Turbofan Rotor/Stator Interaction Noise Reduction Through Trailing Edge Blowing

by

John M. Brookfield

B.S. Aeronautics and Astronautics, University of Washington (1991)
S.M. Aeronautics and Astronautics, Massachusetts Institute of Technology (1993)

Submitted to the Department of Aeronautics and Astronautics in partial fulfillment of the requirements for the

degree of

Doctor of Philosophy

at the

Massachusetts Institute of Technology

June 1998

Author_____
Department of Aeronautics and Astronautics
05 May 1998

Certified by_____
Professor Ian A. Waitz
Director, Aero-Environmental Research Laboratory
Thesis Supervisor

Certified by_____
Professor Jack L. Kerrebrock
Professor of Aeronautics and Astronautics, Emeritus

Certified by_____
Professor K. Uno Ingard
Professor of Aeronautics and Astronautics and Physics, Emeritus

Certified by_____
Dr. Donald B. Hanson
Technical Fellow, United Technologies Pratt & Whitney

Accepted by_____
Professor Jaime Peraire
Associate Professor of Aeronautics and Astronautics
Chairman, Department Graduate Committee

Turbofan Rotor/Stator Interaction Noise Reduction Through Trailing Edge Blowing

by

John M. Brookfield

Submitted to the Department of Aeronautics and Astronautics on 05 May 1998
in partial fulfillment of the requirements for the degree of
Doctor of Philosophy

Abstract

A new technique for reducing rotor wake/stator interaction noise was investigated. The approach involves injecting air from near the trailing edge of the rotating fan blades to fill in the mass/momentum deficit of the rotor wakes. Trailing edge blowing experiments were conducted on a 1/6th scale (22 inch diameter) high-bypass ratio fan stage. Results are presented from measurements downstream of a baseline solid-bladed rotor and a trailing edge blowing rotor with no injection and with three different injection configurations. The mass flow rates of injection ranged from 1.8% to 2.0% of the fan throughflow. Measurements of the flow field downstream of the rotor, the unsteady pressures on the stator, and the duct wall acoustic pressures are presented.

Significant reductions of the wake harmonic amplitudes were obtained at both 0.1 and 1.5 chords downstream of the rotor. The BPF and 2*BPF wake harmonic amplitudes at 1.5 chord were reduced approximately 80% with momentumless wake injection compared to no injection. In addition, the BPF and 2*BPF wake harmonic amplitudes at 0.1 chord with momentumless wake injection were 40% smaller than the wake harmonic amplitudes at 1.5 chord without injection. These results suggest that with appropriate trailing edge blowing blade design, significant noise reductions are possible while maintaining rotor-stator spacing; alternately, the rotor-stator spacing may be significantly reduced while maintaining similar radiated noise levels. The phase angles of the wake harmonics also changed significantly when excess injection was performed.

Stator unsteady pressure measurements showed reductions in unsteady loading, but changes in the stator pressure field did not fully correlate to changes in the wake at 1.5 chord (just upstream of the stator). The reduction in stator unsteady loading was approximately 50 to 70% of that predicted from reductions in the wake harmonic amplitudes using traditional linear strip-theory approximations. Changes in the stator unsteady pressure phase angles also showed only partial agreement with those measured in the wake, particularly when large changes in the radial variation occurred. Large changes were also seen in the duct wall acoustic measurements, with reductions greater than 10 dB observed in the midstage and downstream regions. However, changes in the radiated power could not be conclusively determined due to changes in the radial mode content.

As an adjunct to the trailing edge blowing study, the effect of wake skew on the evolution of wakes downstream of rotating blade rows was quantified and was shown to be significant in geometries with large rotor/stator spacing and low hub-to-tip ratio. The wake is skewed by the freestream swirl and is stretched, increasing the mixing in the wake, result-

ing in a wider and shallower wake. The wake centerline velocity deficit can be reduced up to 50% due to wake skew in typical fan stages, relative to a cascade prediction. Most of the difference observed between the evolution of turbomachinery wakes and two-dimensional models/measurements is attributed to the effect of wake skew/stretching.

Thesis Supervisor: Dr. Ian A. Waitz

Title: Associate Professor of Aeronautics and Astronautics
Director of Aero-Environmental Research Laboratory
Associate Director of Gas Turbine Laboratory

ACKNOWLEDGMENTS

I wish to thank my advisor Prof. Ian Waitz for his guidance, support, and enthusiasm throughout the research. He helped make what seemed nearly impossible into reality. Prof. Jack Kerrebrock offered many interesting and useful insights into compressor flow fields, as well as the experimental facility. Prof. Uno Ingard shared his acoustics expertise and understanding on numerous occasions, and Dr. Donald Hanson provided additional acoustic and industrial experience to make certain that the research was not only relevant, but useful to industry. To have such a well respected committee was really an honor.

Thanks is also given to many people not on my Doctoral Committee who have provided technical support during my research. Prof. Alan Epstein supplied helpful advice on the experimental facility and instrumentation. Prof. Nick Cumpsty shared his vast knowledge of compressor design and noise generation on several "decidedly depressing" occasions. Prof. William Dawes provided the use of his computational code to help us understand the three-dimensionality of the flow field. David Reed and others at The Boeing Company twice calibrated our 4-way probe, and the support of Barry Wagner at Pratt & Whitney was most helpful.

The help of the Gas Turbine Lab staff is also gratefully acknowledged, as their support made many aspects of this research possible. Viktor Dubrowsky not only made things work (by correcting what others nearly ruined), but was very understanding as I made all kinds of noise in the machine shop. The financial services of Holly Anderson and the editorial expertise of Diana Park made life much easier on many occasions. Finally, Lori "Feed Me!" Martinez, in addition to running the entire lab, provided the often needed handful of M&M's.

The other students in the lab also provided their own type of support during the many years, by dragging me kicking and screaming out to a long lunch in front of the Student Center, or out to play hockey, basketball, softball, golf, etc. And of course, the camping trips to the deep woods where we roughed it in the heated swimming pool will never be forgotten. Among the many friends that have come and mostly gone are Scott, Ken & Allison, Dave, Tom, Martin, Jan, Brian, Brian, Brian, Eric, Sonia, Luc, Amit, and many others. Finally, my great thanks to Margarita for keeping me sane the last six months as everything has rapidly come to fruition.

Last, but certainly not least, I wish to thank my family for their continual support and encouragement over the many years.

This work was funded by NASA Langley Research Center under grant NAG1-1512. The support of Doug Stevens and technical monitor, Dr. Carl Gerhold is gratefully acknowledged.

CONTENTS

List of Figures

LIST OF TABLES

NOMENCLATURE

Symbols

a	speed of sound, constant in Fourier series - rotor
A	Area
b	Constant in Fourier series - stator
B	Number of blades in rotor
BPF	Blade passing frequency
c	Chord (usually rotor), constant in Fourier series - wake/stator interaction
C_p	Coefficient of pressure
D_H	Hydraulic diameter
e	Exponential
f	coefficient of friction
k	Integer, for summation of stator harmonics
L	Differential wake element
m	Circumferential harmonic
M	Mach number ($\frac{V}{a}$)
n	Integer, for summation of rotor harmonics (BPF harmonic)
P	Pressure
Pr	Prantl number (Pr = XX)
q	heat
r	Radius
Re	Reynold's number ($Re = rhouL/mu$)
s	Rotor pitch, nondimensional spanwise coordinate

t	Time
T	Temperature
u	Local velocity, velocity along wake centerline in wake skew calculations
U	Mean velocity
v	Velocity perpendicular to wake centerline in wake skew calculations
V	Number of blades in stator, velocity in wake skew calculations
w	velocity in wake relative frame, width of trailing edge blowing ports (perpendicular to camberline)
x	Axial direction, coordinate along wake centerline in wake relative frame
z	axial direction in wake relative frame

Greek Symbols

β	Mach angle
γ	Ratio of specific heats
ϵ	rate of strain
ζ	Wake skew angle (from radial direction)
ν	viscosity
Φ	Rothalpy (rotating enthaply)
ω	angular velocity
Ω	Rotor angular velocity
ρ	Density
θ	Circumferential coordinate (tangential phase angle- radians)

Operators, Superscripts, and Subscripts

$'$	unsteady perturbation, integer constants due to rotor scattering, wake mixing induced quantity
overbar	mean value

∞	at infinite (freestream)
b	blade
j	injection (for trailing edge blowing)
m	for mode order m
r	Rotor relative frame, of the rotor
Re	Real part
s	Stator
t	Rotor blade tip, total condition (as in pressure)
te	At the trailing edge of the rotor blade
x	Axial direction
z	Axial direction in wake skew calculations
θ	Circumferential direction
Σ	Summation

CHAPTER 1

INTRODUCTION

As commercial jet engines have progressed from turbojets to high-bypass ratio turbofans, the primary noise source has shifted from jet noise due to the high turbojet exit velocity, to noise generated by the fan stage. Thus, fan noise is expected to be the most important community noise source for next-generation subsonic aircraft engine technology utilizing ultra high-bypass ratio turbofans. In many situations the radiated noise is dominated by that due to unsteady loading on the stator blades, pylons, and rotor which arises from interaction of these solid surfaces with both random and periodic gusts from a variety of sources. The most significant sources for these gusts are blade wakes and tip clearance flows. During the last twenty years, progress in reducing fan noise has been evolutionary through appropriate choice of rotor-stator blade count, increased rotor-stator spacing, and other methods [25]. Currently available design strategies, however, will be ineffective in meeting the 6 EPNdB engine noise reduction goal established by the NASA Advanced Subsonic Technology Program.

This study focuses on a new approach for reducing fan noise which involves removal and/or addition of fluid through the rotor blades to reduce the blade wakes, thereby making the flow into the stator more uniform. Source control of this nature affects both the time-mean and unsteady aspects of the wake (rotor frame), and thus may impact both tonal and broadband radiated noise from a fan or compressor stage.

The objective of the work is to provide an assessment of wake management strategies for fan noise reduction. Simplified two-dimensional numerical and experimental models

were used to determine the parametric dependence of radiated noise on wake modifications brought about by removal of the blade boundary layer and injection of fluid through the trailing edge of the fan blade. These simplified assessments were followed by rig experiments with trailing edge blowing on a high-speed fan stage. Throughout, the blade geometry and flow conditions investigated were typical of fan designs for next generation high bypass ratio gas turbine engines.

This thesis begins with a discussion of strategies for modifying airfoil wakes, an overview of the wake structure in gas turbine engines, and a description of rotor wake-stator interaction noise generation mechanisms. The numerical and experimental methods used in the study are described in Chapter 2, and the preliminary two-dimensional assessment using cascade experiments and two-dimensional unsteady simulations is then presented in Chapter 3. Predictions of achievable reductions in radiated noise and fan blade design requirements and limitations are also discussed. Chapter 4 describes the kinematics and evolution of the wake downstream of a rotating blade row and presents a model for predicting the effects of the freestream swirl on the decay of the wake. Comparison to experimental data is presented. Wake and stator measurements behind the baseline fan rig rotor are presented in Chapter 5, followed by description of the blade design methodology for wake management in Chapter 6. The trailing edge blowing blade design that was tested is also shown. The results from the wake management rotor are discussed in Chapters 7 and 8, and finally the summary and conclusions are presented in Chapter 9.

1.1 Wake Management Strategies

Control of the initiation of the rotor wakes is sought to minimize the mean velocity deficit and unsteadiness of the wakes and thereby reduce gust amplitude at the inlet to the stator row. The two wake management concepts investigated in this study, blade boundary layer suction and trailing edge blowing, are shown in Figure 1-1. Also shown in Figure 1-1 are simplified schematic diagrams of the desired effects of these treatments on the fan wake: reduction in 1) the mean deficit of the wake and 2) the amplitude of the unsteadiness. Boundary layer suction and trailing edge blowing affect the time-mean width, depth, and shape of the wake by reducing the mass and momentum deficit of the boundary layers

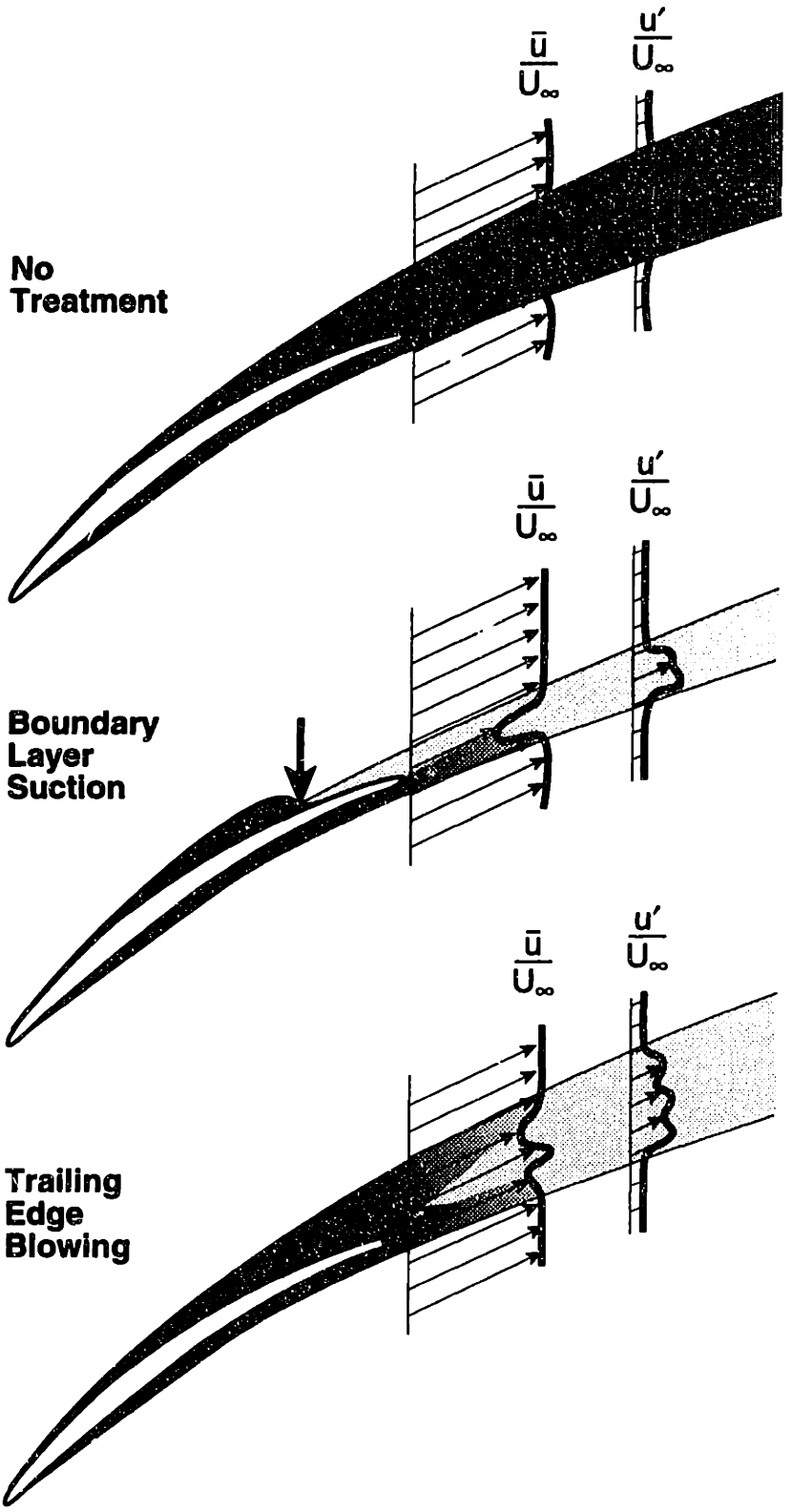

Figure 1-1: Schematic of wake management strategies with a) baseline airfoil, b) boundary layer suction, and c) trailing edge blowing

forming the wake and by adding mass and momentum to the wake, respectively. These effects will be described in more detail in Chapter 3. Changes in unsteady behavior are brought about by control of the sources for unsteadiness in the wakes, specifically 1) control of unsteady boundary layer separation, 2) modification of the trailing edge unsteady vortex shedding, and 3) reduction of turbulence generated by the wake mean shear.

Suction and blowing strategies for wake control have not been investigated previously for fan noise reduction in gas turbine engines because the strategies could not be implemented in practical devices. However, the ideas now merit consideration because of the appreciable size of blades in next-generation gas turbine engines. Indeed some current engines already employ hollow fan blades, with approximately 50 percent open cross-sectional area, in order to reduce weight and structural loading. Wake management is also attractive because it can be used during phases of the flight cycle where community noise impact is most significant and then turned off if necessary during cruise.

1.1.1 Previous Research

Early research on controlling wakes behind bodies has been restricted to geometries and flow conditions not representative of a gas turbine engine environment. Experiments performed by Naumann [26], Corcoran [2], and Park and Cimbala [28], have shown that trailing edge blowing from flat plates can be used to eliminate the time-mean wake deficit and to markedly reduce wake unsteadiness. In particular, Naumann's experiments, carried out in water at Re = 400,000 (based on chord), showed a reduction in time-mean wake deficit of approximately 90% combined with a reduction in the turbulent velocity fluctuations of greater than 50% for several different trailing-edge blowing configurations. Both Naumann, and Park and Cimbala, showed that injection configurations designed to provide more rapid mixing produced more uniform momentumless wake profiles. Further, Leu and Ho [21] have used trailing edge suction to stabilize the wake structure downstream from a flat plate. While the flow conditions and geometries employed in these prior research efforts are different from those in turbomachines, the results do suggest that significant control of both time-mean and unsteady wake phenomena is possible. An objective of the present effort is to study methods for controlling the wake in gas turbine engine fan applications.

In addition, Succi [35] has investigated the use of blowing and suction on propeller and helicopter rotor blades not for reduction of rotor-stator interaction noise, but for the reduction of both thickness and steady loading noise associated with the rotor. He has predicted that significant reductions in noise radiated from a rotor may result from specific spanwise distributions of suction and blowing. It is thus possible that certain suction and blowing strategies designed to reduce rotor-stator interaction noise, could either increase or decrease rotor noise. The additional rotor noise associated with wake management strategies was evaluated by modeling the mass and momentum addition with simple acoustic sources. For the subsonic tip speeds of interest in this study, the rotor tone noise was found to be small compared to the rotor-stator interaction tone noise [17]. Therefore, the impacts of wake management on rotor noise were not addressed further in the current study.

Numerical simulations were completed by Hayden [12] to examine the effect of suction surface boundary layer removal on the wake downstream of the rotor blade. Boundary layer suction was simulated in MISES [6] by specifying a reduction in the boundary layer momentum and displacement thicknesses at the desired chordwise position. The resulting wakes were then examined for changes due to the boundary layer removal. These two-dimensional studies showed reductions in the mean wake velocity deficit of about 40%, and indicated that trailing edge thickness limits the effectiveness of boundary layer suction for wake management purposes.

Cascade experiments by Sell [33] verified the work of Hayden, and also included trailing edge blowing studies. Several different trailing edge blowing geometries were examined, and like the early work of Naumann, Corcoran, etc., significant reductions in the wake were seen. More detailed discussion of Sell's cascade results is presented in Chapter 3.

Work by Houdeville and Fournier [14] on a NACA0015 wing showed similar results to the early cascade experiments of Sell. Suction and blowing (single geometry only) were completed with the wing at zero loading and 6 degrees of incidence for various amounts of mass removal and addition. Large reductions ($> 50\%$) in both the mean wake deficit and unsteadiness were seen.

1.2 Fan Wake Structure

While wake management strategies may seem relatively straightforward to implement, the movement of fluid through internal passages in high speed rotating blades and the highly complex nature of wakes shed from high speed rotating blade rows must be taken into account when examining methods of wake modification. A brief overview of rotor wake structure is therefore appropriate.

Wakes shed from isolated two-dimensional airfoils have uniform profiles along the span and unsteadiness is generated primarily by trailing edge vortex shedding and the wake mean shear. Rotating blade rows, however, generally have nonuniform airfoil geometry and loading along the span, resulting in variation of the width and deficit of the steady wake profile (rotor frame) in the spanwise direction. Variation of 40% is not uncommon in compressor geometries (*e.g.* Prato and Lakshminaryana [30]). In addition, work done by the rotor imparts swirl into the freestream flow field which convects the wakes downstream and skews them in the axial and tangential directions. The amount of skewing depends on the rotor loading distribution (imparted swirl) and complex shapes can result even for nearly radially shed wakes. This effect is discussed in more detail in Chapter 4.

Also, the swirl in the freestream flow establishes radial pressure gradients downstream of the rotor. Since the wake velocities are in general different from the freestream, these pressure gradients act on the wake fluid generating velocities in the spanwise direction. Radial velocities in the wake of approximately 10% of the freestream velocity magnitude are often observed (*e.g.* Lakshminarayana *et al.* [20]). These radial velocities cause migration of the wake in the radial direction, as well as increased mixing. Thus, as discussed above, even the time mean wake structure behind rotating blade rows can vary considerably from an isolated airfoil wake. The impacts of these three-dimensional features on the radiated tonal acoustics is discussed in Section 1.3.

In addition to the mean wake profile, the wake unsteadiness in rotating environments can also differ considerably from the unsteadiness in isolated two-dimensional airfoil flows. While trailing edge vortex shedding and mean shear turbulent production is present in turbomachinery wakes (*e.g.* Epstein *et al.* [7]), there are other contributing factors to the unsteadiness. Blade rows are generally designed for maximum loading and thus have passage

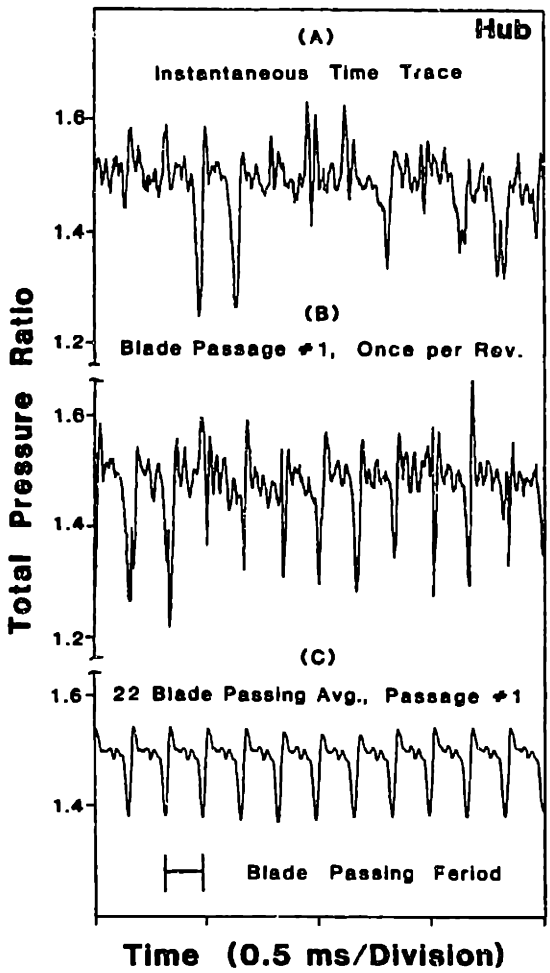

Figure 1-2: Downstream total pressure measurements behind a transonic compressor rotor for a) time accurate data trace, b) same blade passage each revolution, and c) ensemble-averaged profile

flows on the verge of traditional diffuser instability. In fact, many blade designs have airfoil boundary layers which are separated near the trailing edge. These conditions cause the flow field to be susceptible to diffuser-like instabilities and unsteady boundary layer separation, which not only add unsteadiness to the boundary layers which form the wake, but modulate the trailing edge vortex shedding at frequencies on the order of 1/10th blade passing [7].

These sources of unsteadiness, along with generation of turbulence in the wake from the mean shear, result in the amplitude of the unsteadiness in the wake being roughly equal to the mean wake deficit. When measurements downstream of rotating blade rows are examined, as shown in Figure 1-2 from Ng and Epstein [27], time accurate wake data traces

(Figure 1-2a) show considerable complexity and little regular structure. Even examining wakes from a given blade each time it passes the measurement device, eliminating blade-to-blade geometrical differences (Figure 1-2b), shows large variation. It is not until ensemble-averaging is done that a regular wake structure (mean profile) is seen (Figure 1-2c).

Through the use of wake management strategies, it is envisioned that not only can the wake mean velocity deficit and its harmonics be reduced, but the unsteadiness of the wake as well. Boundary layer suction would act to not only reduce the mass and momentum deficit of the flow forming the wake, but would also help stabilize the boundary layer and reduce diffuser-like instabilities and unsteady boundary layer separation. Trailing edge blowing, on the other hand, would suppress the vortex shedding at the trailing edge (much like plates behind circular cylinders) and perhaps also help stabilize the boundary layers. In addition, by reducing the wake velocity deficit, the generation of turbulence in the wake from the mean shear should be reduced as well. As will be discussed in the next section, both the harmonics of the mean wake deficit and the wake unsteadiness are important to the radiated acoustic noise from aircraft engines, and it is thus advantageous to reduce both of these aspects of the wake.

1.3 Noise Generation: Rotor wake-stator interaction

As discussed in the previous section, the amplitude of unsteadiness in rotor wakes is approximately equal to the mean velocity deficit (rotor frame). The resulting broadband noise generated by the random fluctuations in the flow field interacting with downstream solid surfaces (stator blades and/or pylons) is of equal importance in the overall radiated noise generated by gas turbine engines as tonal noise due to the mean wake harmonics (multiples of rotor blade passing frequency) [1]. The acoustic generation mechanisms of these two noise sources will be described in the following sections for subsonic tip speed fan geometries. In addition, impacts of radial wake structure, freestream swirl, blade geometrical differences, inlet distortion, and transonic tip speeds will be discussed.

[1] Analysis by Hanson [11] has shown that elimination of either tones or broadband from a jet engine noise spectrum results in a reduction of approximately 3 EPNdB. These results suggest that both tones and broadband noise have roughly equal importance to the overall perceived noise level.

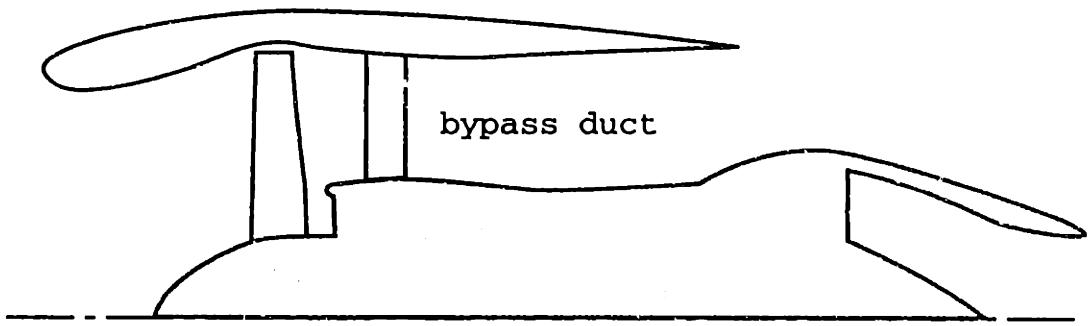

Figure 1-3: Schematic of typical high bypass ratio turbofan engine

1.3.1 Tonal Noise Generation

In this section the basic mechanism for tonal noise due to the wake mean velocity deficit (rotor frame) will be described. Typical turbofan applications incorporate a fan followed by the engine core and bypass duct, as shown in Figure 1-3. The bypass duct houses a stator row to remove the swirl generated by the rotor and may also have additional structural members or pylons. For high-bypass ratio engines, the noise generated by the fan wake-stator row interaction is the dominant acoustic source. Thus, the discussion here will be limited to a rotating blade row (rotor/fan), followed by a stationary blade row (stator) downstream, but can be easily extended to other applications. A schematic of the interaction is shown in Figure 1-4. The fan blades and wakes are moving to the left in the schematic at rotor speed, with the wakes being convected downstream by the freestream flow and intersecting the stationary stator blades.

Before examining all the effects present in flow fields downstream of typical fan geometries (which can have considerable radial variation), the rotor exit flow field will be assumed uniform in the spanwise direction to illustrate the basic interaction mechanism (this two-dimensional approximation would be reasonable for high hub-to-tip ratio applications). With the flow radially uniform, the field in the rotor frame can be written as a sum of harmonics in the tangential direction which are multiples of the number of rotor blades.

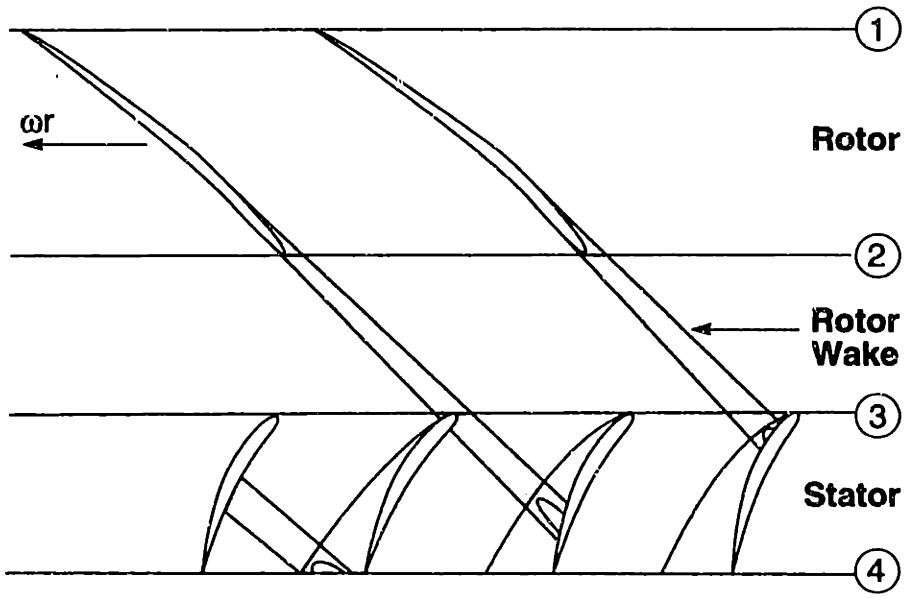

Figure 1-4: Schematic of rotor wake-stator interaction

$$Re\left\{\sum a_n e^{inB\theta_r}\right\}(n = -\infty..., -2, -1, 0, 1, 2, ...\infty) \tag{1.1}$$

Converting to the stationary reference frame, the tangential phase angle θ_r can be written as $\theta_r = \theta - \Omega t$. The flow field (stator inlet flow) is then written as

$$Re\left\{\sum a_n e^{inB\theta} e^{-inB\Omega t}\right\}(n = -\infty..., -2, -1, 0, 1, 2, ...\infty) \tag{1.2}$$

For uniform inlet conditions, the stator row pressure field (like the exit flow field of the rotor) can be written as a sum of harmonics

$$Re\left\{\sum b_k e^{ikV\theta}\right\}(k = -\infty..., -2, -1, 0, 1, 2, ...\infty) \tag{1.3}$$

Typical fan applications have rotor-stator spacings of more than one rotor chord and the wake velocity deficits at the stator row (and thus harmonics) are small compared to the

mean velocity (on the order of 10%). The interaction of these harmonics with the stator row can therefore be linearized and the stator pressure field given by the multiplication of the inlet flow field, Eq. 1.2, with the steady stator pressure field, Eq. 1.3, to obtain

$$P_s = Re\left\{\sum c_{n,k} e^{i(nB \pm kV)\theta} e^{-inB\Omega t}\right\} (n = 0, 1, 2, ...\infty, k = 0, 1, 2, ...\infty) \qquad (1.4)$$

(note that only a one sided series is required for n since both positive and negative values produce identical terms). The assumption of linearity is standard in rotor-stator interaction modeling, and has been numerically validated with good results (this may not be a good approximation for closely spaced rotor-stator stages, such as in the core compressor).

Examining the resulting pressure field (Eq. 1.4) from the interaction of the rotor wake flow field with a downstream stationary stator row, the waves generated are easily identified. Circumferential mode orders, m, (*i.e.* number of wavelengths in the tangential direction) are given by $m = nB \pm kV$, frequencies are given by $nB\Omega/2\pi$ and the rotational speed of the wave is given by $\Omega_m = nB\Omega/(nB \pm kV)$. Note that the modes can rotate both in the rotor direction (positive m) or against it (negative m). These classic results were first published by Tyler and Sofrin [37] and have been reformulated numerous times in the literature.

Whether these waves propagate from the stator row depends on the speed at which they spin and the velocity of the mean flow. If the mean axial velocity of the flow field is ignored, the waves would be cut-on (propagate) when they spin at or above the speed of sound relative to the tangential mean flow velocity. This is equivalent to the classic wavy wall problem shown in Figure 1-5. When the wall travels at a speed below the speed of sound (Figure 1-5a), the pressure waves decay exponentially with distance from the wall. If the wall speed (relative to the velocity above it) is sonic or greater (Figure 1-5b), however, the pressure waves propagate to infinity (in a perfect medium) at the Mach angle, $\beta_M = \cos^{-1}(1/M)$.

Including the effects of the axial velocity, the criterion for propagation (see *e.g.* Hanson [10]) is

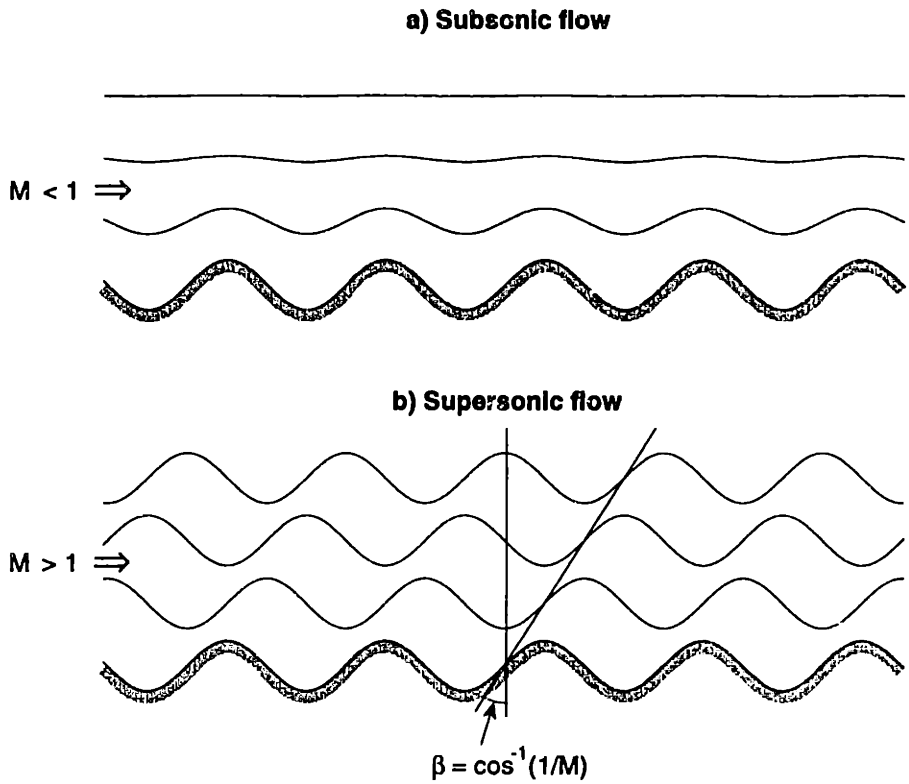

Figure 1-5: Schematic of flow perturbations over a wavy wall for a) subsonic flow and b) supersonic flow

$$(nBM_t + mM_\theta)^2 > (1 - M_x)^2 m^2 \tag{1.5}$$

where M_t is the tip Mach number of the rotor, M_x is the mean axial Mach number of the flow, and M_θ is the mean tangential Mach number, which may be different upstream and downstream of the stator row. When this condition is met, the wave will propagate. An inherent assumption in this analysis is that the acoustic wave is also uniform in the radial direction. Section 1.3.4 will discuss the consequences of radial variation.

The result of this interaction is that specific tangential mode orders at each multiple of rotor blade passing frequency may be cut-on. Of course, there are many complicating factors and several of these will be discussed in later sections. Most important, however, is that acoustic waves at each multiple of blade passing frequency are generated by their harmonic of the wake. *Therefore, it is not the wake velocity deficit itself that must be reduced, but more specifically, the wake harmonic content which generates propagating acoustic waves*

through interaction with the stator row.

1.3.2 Broadband Noise Generation

The basic noise generation mechanism for tonal noise, as described in the previous section, can be extended to gain qualitative understanding of the generation of broadband noise. As was discussed in Section 1.2, the amplitudes of unsteady fluctuation in rotor wakes are of roughly the same magnitude as the mean velocity deficit. The spatial harmonics of the mean wake profile are at multiples of the rotor blade number, and the frequencies of the harmonics (in the absolute frame) are at rotor blade passing frequency. The unsteady fluctuations in the wake, however, can be thought of as having all spatial harmonics at all frequencies. Clearly, certain spatial harmonics will be prominent that are representative of the wake fluctuation length scale, and certain frequencies will dominate which are typical of vortex shedding, *etc.* The result is that B in Eq. 1.4 will take on all positive integer values, producing a broad spectrum of both frequencies and mode orders.

1.3.3 Mode Trapping: Generation of higher harmonics

As described briefly in Section 1.3.1, the propagation of rotor wake-stator interaction tones depends on the freestream flow field. For many turbofan engines, the fan stage is designed such that all modes generated at the rotor blade passing frequency (BPF) are cut-off (decay exponentially) upstream and downstream of the stage. However, often one or more of the modes at BPF is cut-on between the rotor and stator where the freestream flow field has swirl (most fan stages are designed with zero inlet swirl and a stator to remove all swirl generated by the rotor). This results in a phenomena termed 'Mode Trapping', as described by Hanson [10].

In an identical manner as the interaction of the wake flow field with the downstream stator row, the upstream propagating acoustic waves interact with the rotor. This can be seen by transforming the pressure field of the stator, Eq. 1.4, into the rotating reference frame ($\theta = \theta_r + \Omega t$), using it as the unsteady inlet condition to the rotor, calculating the pressure field of the rotor, and then transforming back to the absolute reference frame. The rotor pressure field is then given by

$$P_r = Re\left\{\sum a_{n,n',k} e^{i[(n+n')B \pm kV]\theta} e^{-in'B\Omega t}\right\} \tag{1.6}$$

with $n' = \infty..., -2, -1, 0, 1, 2, ...\infty$. The result is a scattering of the acoustic waves due to the rotor wake-stator interaction into additional circumferential modes, as well as frequencies. Thus, it is possible that even with BPF propagating only between the rotor and stator, higher harmonics (multiples of BPF) will radiate out of the fan stage. Analysis of Hanson [10] has shown that these scattered waves can be significant. Therefore, it is important to remember that for noise suppression through wake management, even if BPF is cut-off outside the fan stage, the BPF harmonic of the wake may need to be reduced in addition to the higher harmonics to gain maximum reduction in the overall noise.

1.3.4 Effects of Radial Variation

In Sections 1.3.1 through 1.3.3 the fan stage geometry and flow field were assumed to be radially uniform. Typical fan applications, however, have low hub-to-tip ratios and large flow variations in the spanwise direction. Both of these complications affect the coupling of the wake-stator interaction with the acoustic modes.

Acoustic modes in cylindrical geometries have Bessel function solutions for the structure of the modes in the radial direction. For high hub-to-tip ratio machines, the duct height is much smaller than the circumference and the solutions for the radial modes are approximately sinusoidal (as the solutions would be for a rectangular duct). For a hub-to-tip ratio of 0.5, the first four radial modes for the m=8 circumferential mode are shown in Figure 1-6. One can see that even the zeroth radial mode has considerable radial variation with maximum amplitude at the tip and virtually zero amplitude at the hub. Of course, the radial structure of the wave also effects the propagation condition, such that only the lower order radial modes for a given tangential mode will in general propagate (see Tyler and Sofrin [37]). The implications of these variations for wake management are discussed in the next section.

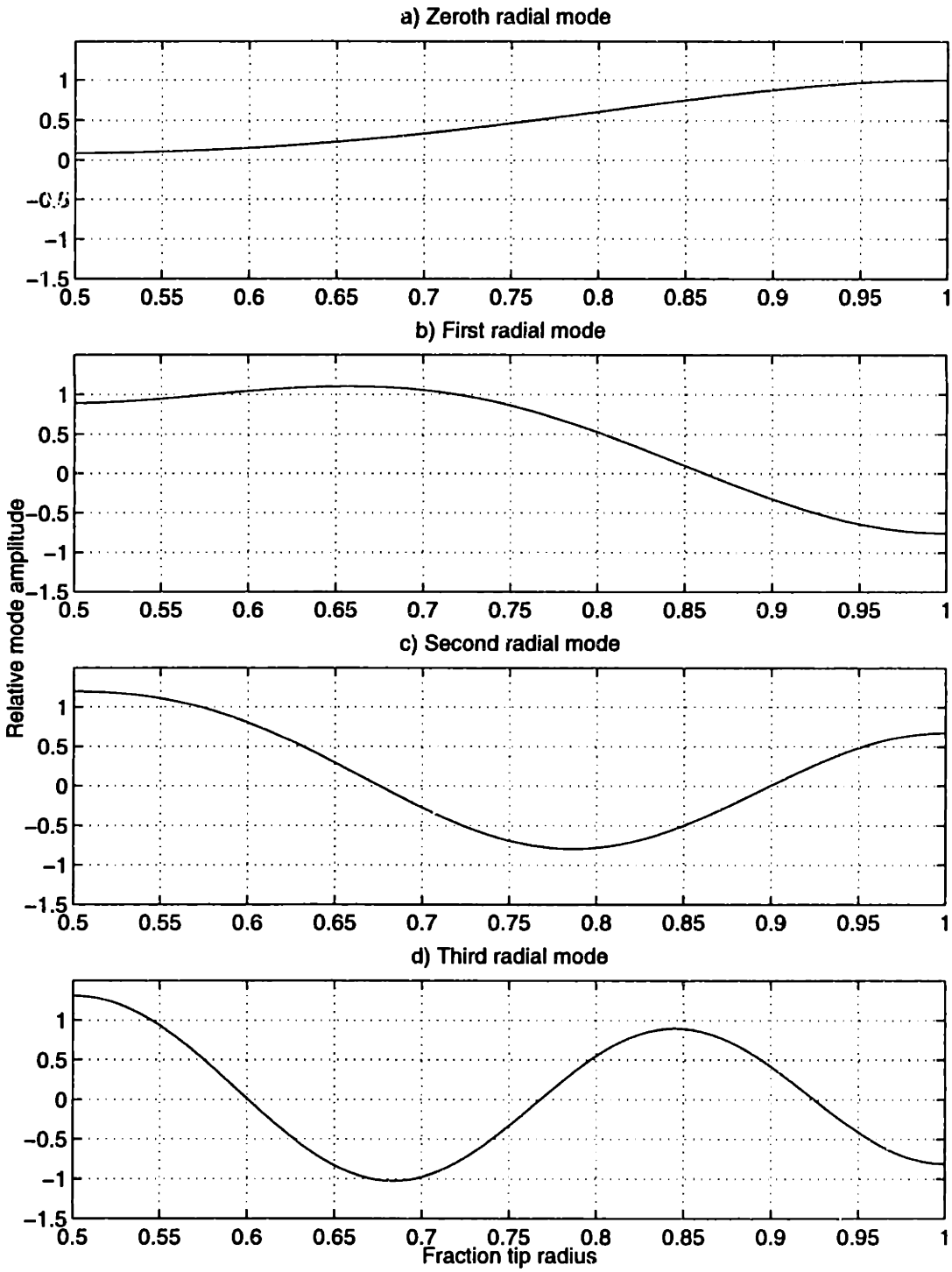

Figure 1-6: Mode shape of the first four radial acoustic modes for a hub-to-tip ratio of 0.5 and m=8 (circumferential mode order)

1.4 Coupling of Fan Wake Structure

In the last several sections the basic interaction mechanisms of rotor wake-stator interaction noise have been discussed. However, real fan flow fields have considerable radial variation which greatly complicates the problem. First, the mean wake profiles have variation of approximately 40% from hub to tip, resulting in radial variation of the wake harmonic amplitudes and stator pressure fluctuations. Thus, the radial mode content is altered such that the sum of generated waves matches the unsteady pressure field of the stator.

In addition, the wake is not oriented radially when interacting with the stator blade, but rather is skewed in a complex shape depending on the rotor loading distribution, as described in Section 1.2. This causes phase variation in the intersection of the wake along the span of the stator blade and in the resulting unsteady pressure field. For certain radial phase variations (wake skews), the integration of the stator pressure field with a given acoustic mode may be very small even if the mode was dominant with radially uniform conditions. The coupling, of course, depends on the radial mode shape which is a function of circumferential mode order and hub-to-tip ratio. In general, wake skew results in stronger coupling to radial modes that have similar radial phase variations as the wake.

Radial coupling is crucial to rotor wake-stator interaction noise production. By shifting the coupling of the wake interaction to the higher order radial modes, the overall acoustic power can be dramatically reduced. Therefore, it is important to understand these effects when attempting wake management concepts. It is certainly possible that through naive smoothing of the wake flow fields, one might actually couple back to lower order radial modes and increase the radiated noise. Equivalently, through very carefully designed wake management, one might perform wake smoothing in only small spanwise sections of the wake and achieve large reductions in the noise. Uniform reduction of the wake along the full span, however, should result in no change in the radial coupling and therefore produce corresponding reductions in the amplitudes of the radiated acoustics.

1.4.1 Effects of Blade-to-Blade Geometrical Differences

Effects of blade-to-blade geometrical differences can be readily seen by once again looking at the basic rotor wake-stator interaction result, Eq. 1.4. Both the rotor and stator can have variations in the blade airfoil geometry, spacing, stagger, etc. Any change in one or more blades in the blade row will result in a broadening of the harmonic content required to describe the resulting pressure and/or flow field.

For example, if one rotor blade is damaged such that the mean wake profile is different from the other blades, the harmonic content of the resulting downstream wake flow field will have all circumferential mode numbers, instead of just multiples of the number of rotor blades. The mean wake-stator interaction tones will still occur, with the interaction of effective blade numbers, B = 1,2,3,..., superimposed. As a result of the blade-to-blade differences, the noise spectrum will contain the standard broadband noise floor, the tones at multiples of rotor blade passing frequency, and tones at multiples of shaft frequency depending on the distribution and severity of the differences from the mean wake harmonics.

Stator blade-to-blade differences cause additional acoustic effects as well, but create additional modes, not frequencies. Any stator blade differences effectively change the number of stator blades, V, such that the radiated acoustic waves still occur at multiples of rotor blade passing frequency, but the mode order number, $m = nB \pm kV$, now take on additional values. As with the rotor blade differences, the basic interaction is still present, but additional effective stator blade number, V, interactions occur depending on the distribution and severity of the variations.

In general, all rotor and stator rows have blade-to-blade differences generating additional frequencies and mode orders. It is desired, therefore, to minimize these variations such that the acoustic waves can be more effectively mitigated. For uniform wake management on all rotor blades, the basic interaction may be reduced, but acoustics generated due to rotor blade-to-blade differences such as blade-to-blade loading variation will likely have limited attenuation (i.e. multiples of shaft frequency).

1.4.2 Effects of Inlet Distortion

While blade-to-blade differences are a concern, the effects of inlet distortion are also very important. Additional acoustic waves generated from blade differences are still a result of interaction with the stator row, whereas inlet distortions interact with the rotating blade row. As a result, acoustic waves at rotor blade passing frequency may be cut-on upstream of the rotor, even if rotor wake-stator interaction BPF tones are not.

The interaction of an inlet distortion can be modeled similarly to the interaction of the wake-stator interaction waves with the rotor. In general, inlet distortions are caused by boundary layer separation in the inlet or ingestion of atmospheric vorticity and are usually stationary in the absolute frame. The distortion is written as a sum of circumferential mode orders, which when transformed in the rotor frame are rotating at rotor speed. The interaction with the rotor is carried out as previously described and then transformed back into the absolute frame. The resulting pressure field is given by

$$P_{r(distortion)} = Re\left\{\sum a_{n,l} e^{i(l+nB)\theta} e^{inB\Omega t}\right\} \tag{1.7}$$

with $l = -\infty..., -2, -1, 0, 1, 2, ...\infty$ and $n = -\infty..., -2, -1, 0, 1, 2, ...\infty$. One can see that the resulting waves are at multiples of rotor blade passing frequency, but the generated circumferential modes depend on the harmonic content of the inlet distortion. Examining the spin velocity of the modes given by $\Omega_m = nB\Omega/(l + nB)$, one can see that it is quite easy to generate propagating BPF modes, since l will have many values for a typical inlet distortion. In fact, the harmonic of the distortion that matches the number of rotor blades ($l = -nB$) will generate a plane wave which is always cut-on. Therefore, minimization of inlet distortion is critical to producing low noise turbofan engines, since a velocity distortion on the order of 1% at the rotor blade number harmonic could generate enough BPF tonal noise upstream of the rotor to dominate all of the rotor wake-stator interaction noise [17]. Example experimental data showing the effects of an inlet distortion on the duct acoustics can be seen in Appendix B.

1.4.3 Transonic Rotor Designs

The discussion thus far has been for subsonic tip speed rotors where pressure fields generated by the rotor itself (clean inlet flow) decay up and downstream. For transonic rotors, however, additional noise sources are present beyond those earlier described. Some of these sources will now be briefly outlined.

Rotors having tip speeds above the speed of sound generate rotor alone noise from their rotor frame steady pressure fields. Because these pressure fields are rotating supersonically at the tip radius of the rotor they may propagate. Again, the condition for propagation depends on the circumferential mode order (multiples of rotor blade number), radial mode order, and the freestream flow field. As before, the radial mode content will depend on the spanwise geometry and loading distribution.

In addition to noise generated by the mean loading of the rotor, blade-to-blade variations cause an often observed condition termed 'buzz saw' noise. This noise is generated by the shock waves from the supersonic sections of the blades. When the blades (and thus shocks) have variations multiples of shaft frequency are produced, since the variations are composed of all circumferential mode orders. These lower order modes can be thought of as two or more blade shocks coalescing to form a strong shock (or several of these occurrences, depending on the distribution of blade variation).

Unlike subsonic fan geometries where propagating tonal noise is only generated by rotor-stator interaction for perfectly uniform inlet flow and blade rows, transonic fans themselves generate tones. These tones are generated by the mean loading on the rotor (the loading required to produce work) and wake management strategies would, therefore, have less effect on the overall noise.

1.5 Summary of Introductory Concepts

As discussed in the previous sections, wake management methods for reduction of turbomachinery rotor wake-stator interaction noise must be implemented with care. Wakes shed from high-speed rotating blade rows have complicated structures due to spanwise loading distributions, freestream swirl effects, and sources of unsteadiness.

In addition, coupling of the interaction of these wakes with downstream stator blades to acoustic modes in low hub-to-tip ratio geometries must take wake skewing and radial acoustic mode structure into account. Without careful analysis, use of wake management could result in an increase in the overall perceived radiated noise.

CHAPTER 2

FAN STAGE GEOMETRY AND NUMERICAL AND EXPERIMENTAL METHODS

This chapter begins with a description of the particular fan stage geometry chosen for this study (Section 2.1), followed by a discussion of the experimental and numerical techniques used to examine the impacts of wake management strategies on rotor wake-stator interaction. Section 2.2 describes two-dimensional unsteady simulations, and Section 2.3 discusses two-dimensional linear cascade analysis for estimating the radiated acoustics. Section 2.4 then describes the experimental cascade testing. The Navier-Stokes solver used to simulate the three-dimensional rotor flow field is described in Section 2.5, and finally, the experimental facility used to test the fan stage is discussed in Section 2.6.

2.1 Description of the Fan Stage Test Geometry

The fan stage used for these wake management studies was a high-bypass ratio fan design typical of next generation engine concepts. It was greatly desired to not only show the impacts of wake management, but to demonstrate these methods on a blade design of interest to industry. Therefore, the Pratt & Whitney 17 inch ADP fan stage design, which is representative of future fan technology, was used for this research.

The fan stage has a mass average pressure ratio (total to static) of approximately 1.2,

a tip Mach number of about 0.8, and an inlet Mach number of approximately 0.45 at the fan leading edge. The hub-to-tip ratio is about 0.45 and the size was scaled to obtain a 22" leading edge tip diameter for installation in the MIT Blowdown Compressor Facility. The fan rotor has 16 wide chord blades, with approximately 40 degrees of twist from hub to tip, followed by a stator row of 40 blades at 1.7 fan midspan axial chords downstream. All testing was completed at the takeoff condition, which is deemed most critical for noise suppression.

The stator blades were redesigned to allow the measurement of stator unsteady loading (the instrumented stator blade will be described in more detail in Section 2.6.3). It was desired to have a uniform stator airfoil along the entire span to facilitate the movement of the instrumented portion of the stator to any spanwise position [1]. Because of this, the midspan airfoil from the originally designed stator blade was used with a modified leading edge. The forward section of the airfoil was thickened to produce a larger leading edge radius to enable the airfoil to accept higher incidence flow. Two-dimensional calculations using MISES [6] were performed to help in the design process.

The two-dimensional simulations and experiments (Chapter 3) were completed using the midspan airfoils from the rotor and stator blades. The take-off conditions at midspan are summarized in Table 2.1. For this design all circumferential acoustic modes at blade passage frequency (BPF) are cut-off upstream and downstream of the stage at the conditions tested, but one BPF mode is cut-on in the midstage region. The primary propagating modes (outside of the fan stage) are listed in Table 2.2.

Fan design parameters	Inlet		Exit
Mach number	0.74		0.52
Flow Angle	39.8 deg.		58.9 deg.
Incidence		11 deg.	
Chord		0.097 m	

Table 2.1: Test fan flow conditions at midspan in relative frame

[1] Since the interaction of wakes with the stator blades is generally believed to be approximately linear for small wake velocity deficits, the effects of camber, thickness, etc. are small. Therefore, the unsteady loading of the stator should be approximately the same for the modified blade as the original design.

Frequency	Circumferential mode order
BPF	None
2*BPF	m = -8
3*BPF	m = 8
	m = -32
4*BPF	m = 24
	m = -16
	m = -56

Table 2.2: Propagating circumferential acoustic modes outside of the test fan stage

2.2 Two-Dimensional, Unsteady Modeling

Two-dimensional unsteady modeling was used by Hayden [12]to 1) parameterize the effects of varying wake width and depth on unsteady stator loading, and 2) investigate the effects of blade boundary layer suction on unsteady stator loading. For the applications of interest, the rotor-stator spacing is large enough that potential flow interaction effects between the rotor and the stator can be neglected. This allowed the boundary layer suction on the rotor and the impact on the stator to be considered in a two part analysis. The first part, a steady, viscous calculation on the rotor, was performed using MISES [6] a two-dimensional cascade code. The second part, an unsteady, thin shear layer Navier-Stokes calculation on the stator was performed using UNSFLO [9]. These computational models are described below.

MISES is a viscous, multiple-blade, cascade code which was modified to model boundary layer suction, and then used to calculate boundary layer and wake characteristics. The code uses a Newton solution method to solve the steady, two-dimensional Euler equations for the outer flow. Boundary layers and wakes are modeled and described with integral equations that are coupled to the inviscid flow (the grid for the inviscid flow region is displaced from the blade by the displacement thickness of the boundary layer). Drela [6] includes a validation of the code with comparisons of blade pressure distributions, displacement thickness, momentum thickness, and boundary layer shape parameter calculations to experimental data. A 1/7-power law velocity profile was assumed for the turbulent portion

of the boundary layer and a Falkner-Skan profile for the laminar region, with the transition point calculated using the e^n method. A cosine velocity profile was assumed in the wake downstream from the blade.

Boundary layer suction was modeled by decrementing the momentum and displacement thicknesses of the boundary layer at a given location along the airfoil chord. The reduction of these parameters was performed by removing a fraction of the bottom of a 1/7-power law velocity profile and recalculating the momentum thickness, displacement thickness, and shape factor for the remaining (top) portion of the profile [12]. These values were then used to re-initiate the boundary layer downstream from the suction location.

The unsteady loading calculations on the stator were performed using UNSFLO, a two-dimensional thin shear layer, Navier-Stokes cascade solver. UNSFLO employs a hybrid Euler/Navier-Stokes scheme, with the Euler algorithm used in inviscid regions and the Navier-Stokes algorithm used in viscous regions. Manwaring and Wisler [22] validated the code for predicting gust response in compressors and turbines through comparison with experimental data. Gaussian wake distributions in the rotor reference frame were converted to stator coordinates and specified at the inlet plane of the stator. The wake deficit, wake width, rotor-stator pitch ratio, and flow angles were also specified. Results of the calculations were corroborated by experimental cascade testing and will not be shown here, but can be found in Hayden [12] and Waitz *et al.* [38].

2.3 Estimating Acoustic Radiation

Estimation of the magnitude of the radiated tone noise for propagating duct acoustic modes associated with the rotor wake-stator interaction was completed using LINSUB, a two-dimensional, linearized panel method written by Smith [34]. The code utilizes flat plate airfoils with zero mean loading and sinusoidal inlet wakes. Both upstream and downstream propagating acoustic waves are calculated as is the downstream convected vorticity wave shed from the stator blades due to the unsteady loading. The code has been used extensively throughout the aircraft engine industry (*e.g.* Hanson [10]). Flow conditions were established by setting the flow angle, Mach number, and rotor-stator pitch ratio. Experimentally and numerically obtained wake profiles were transformed into the stator reference

frame and decomposed into spatial harmonics [2]. LINSUB was then used to calculate the pressure amplitudes of the radiated acoustic waves. The acoustic modes radiated in the two-dimensional cascade model corresponded to the circumferential mode orders in the three-dimensional annular geometry. LINSUB was only used as an estimate for potential changes in the radiated tonal noise, since it does not address the three-dimensionality of either the wake or the acoustic modes.

2.4 Cascade Experiments

As discussed previously, the feasibility of using suction and blowing strategies to control shed wakes has been demonstrated by Houdeville and Fournier [14] and others. However, this prior research has neglected essential features of the gas turbine environment. In particular, realistic fan blade geometries have not been tested, and the previous experiments have been carried out at zero or low incidence, not the higher loading encountered in turbomachinery. Further, cascade effects which introduce normal and axial pressure gradients are not modeled by single plate experiments. All of these effects are important for producing unsteady wake phenomena such as that shown in Figure 1-2. To assess the feasibility of using suction and blowing to reduce fan noise, and in particular the impact on broadband noise sources, a cascade facility was designed by Sell [33] to test fan blade geometries under conditions more representative of those found in turbomachinery.

A schematic diagram of the experimental facility is shown in Figure 2-1. Measurements of time-mean and unsteady wake velocity components were made downstream from a cascade consisting of three of the test fan blades (midspan geometry). The incidence and loading were set to match the take-off conditions listed in Table 2.1, with an inlet-to-exit pressure rise coefficient of Cp = 0.45. The chord of the blades was 0.25m and the span was 0.3m. The Reynolds number based on chord was maintained above 300,000; this is sufficient to simulate the turbulent blade boundary layers and wakes which are present at full-scale conditions [4]. One of the blades was instrumented with 20 static pressure taps on each

[2]Rotor wake-stator interaction calculations are usually conducted in the stator (absolute) reference frame. However, converting the velocity field from the rotor reference frame to the absolute frame results in change of the freestream velocity field, but perturbations remain the same in amplitude and direction. Therefore, wake harmonics calculated in the rotor frame are identical to those in the absolute frame.

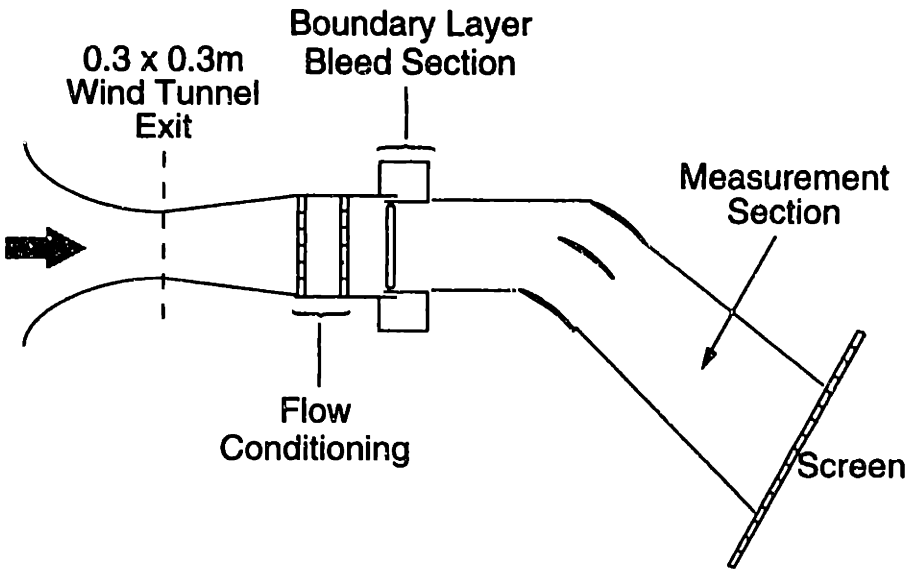

Figure 2-1: Schematic of experimental cascade facility

of the suction and pressure surfaces. The experimentally measured local surface pressure coefficients were compared to results of a numerical simulation obtained using the MISES code described in Section 2.2. The measured and calculated pressure coefficients compared within 5% at all points along the chord. With the exception of three-dimensional effects, the blade boundary layer and wake development in the cascade facility are expected to be representative of the test fan at midspan.

The wake management strategies investigated by Sell [33]include boundary layer suction and blowing at the trailing edge of the blade. A schematic diagram of the original blade used to test these concepts is shown in Figure 2-2. The suction was performed through spanwise slots 2.5 mm wide (chordwise) by 12.5 mm long, separated along the span by 3 mm. The slots were located at chordwise positions $x/c = 0.5$ and 0.8. Suction was applied at rates corresponding to reduction of the local boundary layer momentum thickness of 50% and 70%, based on estimates of the boundary layer thickness calculated using MISES. The suction mass flows for these two cases corresponded to removal of 1.5% and 2.2% of the fan throughflow. The non-uniformity of suction mass flow rate along the span was less than 10%.

Trailing edge blowing was performed through an array of 1.5mm internal diameter

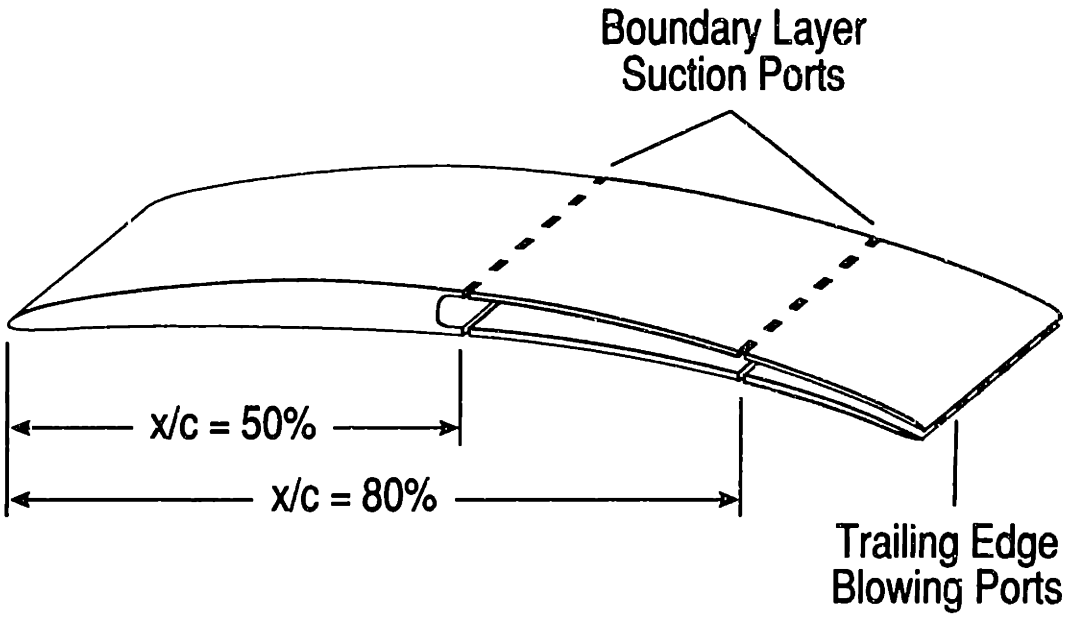

Figure 2-2: Schematic of original cascade wake management blade with boundary layer suction and trailing edge blowing

tubes with a center to center spacing of 3 mm. The tubes were aligned along the mean camber line at the trailing edge. Blowing was performed at rates corresponding to addition of 25%, 75%, and 90% of the natural wake momentum deficit. The mass flows for these cases corresponded to addition of 0.7%, 0.8%, and 0.9% of the fan throughflow, respectively. Results from these early tests are reported in Sell [33] and Waitz *et al.* [38] and indicate that blowing at the metal angle (through the trailing edge) injected fluid primarily into the pressure side of the wake. This effect is a result of the suction surface boundary layer being much thicker than the pressure side causing the flow to deviate from the blade surface metal angle by approximately 6 degrees at the trailing edge.

A second blade was built by Sell with interchangeable trailing edge sections. The four trailing edge sections built are shown in Figure 2-3. The different blowing geometries were 1) solid blade (baseline), 2) blowing at the freestream deviation angle, 3) blowing at the metal angle, and 4) mixed case with every other hole blowing at metal or deviation angle. With these new blowing geometries, injection was performed with addition of 54%, 100%, and 171% of the natural wake momentum deficit. The mass flows for these injection rates

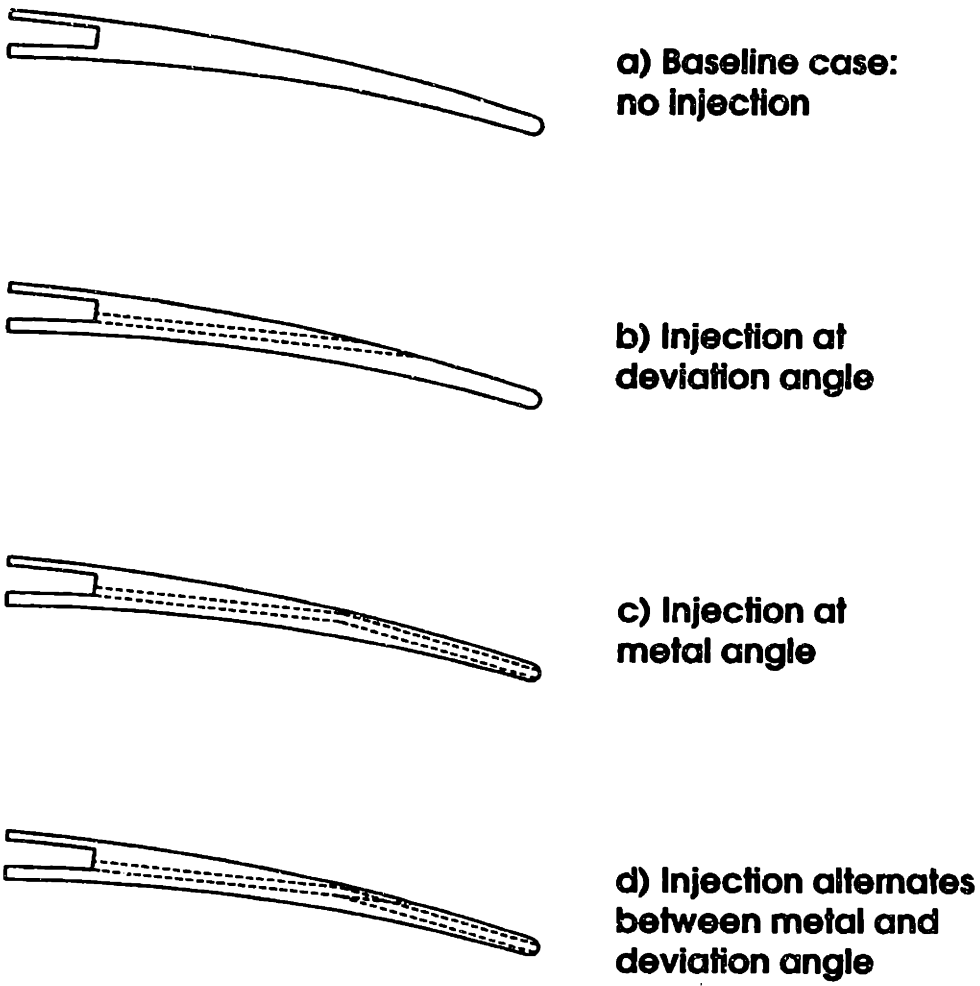

Figure 2-3: Schematic of different trailing edge blowing sections, Sell [33]

corresponded to 0.82%, 1.08%, and 1.36% of the fan through flow.

Measurements of the wake were taken using a single element, hot wire anemometer probe. Sampling was carried out at 25 kHz and frequencies above 10 kHz were filtered. Unsteady flow was resolved below 10 kHz, corresponding to a Strouhal number of 1.4 based on the blade trailing edge thickness of 2.5 mm and the freestream velocity of 18m/s. Thus the time response of the hot wire anemometer was sufficient to resolve the dominant turbulent structures in the wake. The error in the velocity measurements obtained with the hot wire was estimated to be less than 3% with 95% confidence.

Measurements were made at midspan height in the cascade at 0.5, 1.0, 1.5, and 2.5 chord lengths downstream from the blade trailing edge. The probe was traversed along a line parallel to the exit plane of the cascade. Since the axial pressure gradients downstream

from fans are typically near-zero, the area of the downstream duct in which the wakes were measured was adjusted so that the streamwise pressure change was maintained at less than 1.5% of the dynamic head. Results of these experiments are discussed in Section 3.2.

2.5 Navier-Stokes Simulations

Computations were undertaken to elucidate the three-dimensional behavior of the wakes shed from the fan geometry described above. The NEWT flow solver (Dawes [5]) was used for these calculations. The code uses a multiple block, unstructured tetrahedral mesh, and has provisions for adaptive grid refinement. The three-dimensional, Reynolds-averaged, Navier-Stokes equations were solved using a four-step Runge-Kutta time marching algorithm. Turbulence was simulated using the $k - \epsilon$ model. The code has been used in a variety of other investigations to predict rotor through flow, as well as flow in complex internal blade passages, as described by Dawes [5]).

The calculation resulted in an average total pressure rise approximately 1% lower than that measured in the rig tests. The pressure rise and turning were within 1% at the 75% span location, which was chosen for analyzing the effects of freestream swirl on rotor wake decay discussed in Chapter 4. However, approximately 5% less total pressure rise was apparent at the 50% span location in the calculation than at the same location in the experiment. In addition, the calculated wakes were deeper and narrower than those measured experimentally, indicating that the grid was not sufficiently resolved and/or the turbulent viscosity was not accurately being represented. A sample grid at one-half span is shown in Figure 2-4. Nonetheless, the calculations were useful for visualizing the effects of skew in the complicated three-dimensional flow field.

2.6 Rig Experimental Facility

Fan geometries contain many complicating three-dimensional features not present in cascade testing, several of which were discussed in Chapter 1. Therefore, to accurately assess the impact of wake management strategies on noise generated by rotor wake-stator interaction, full rig experiments are required. In this section, the experimental facility used for these

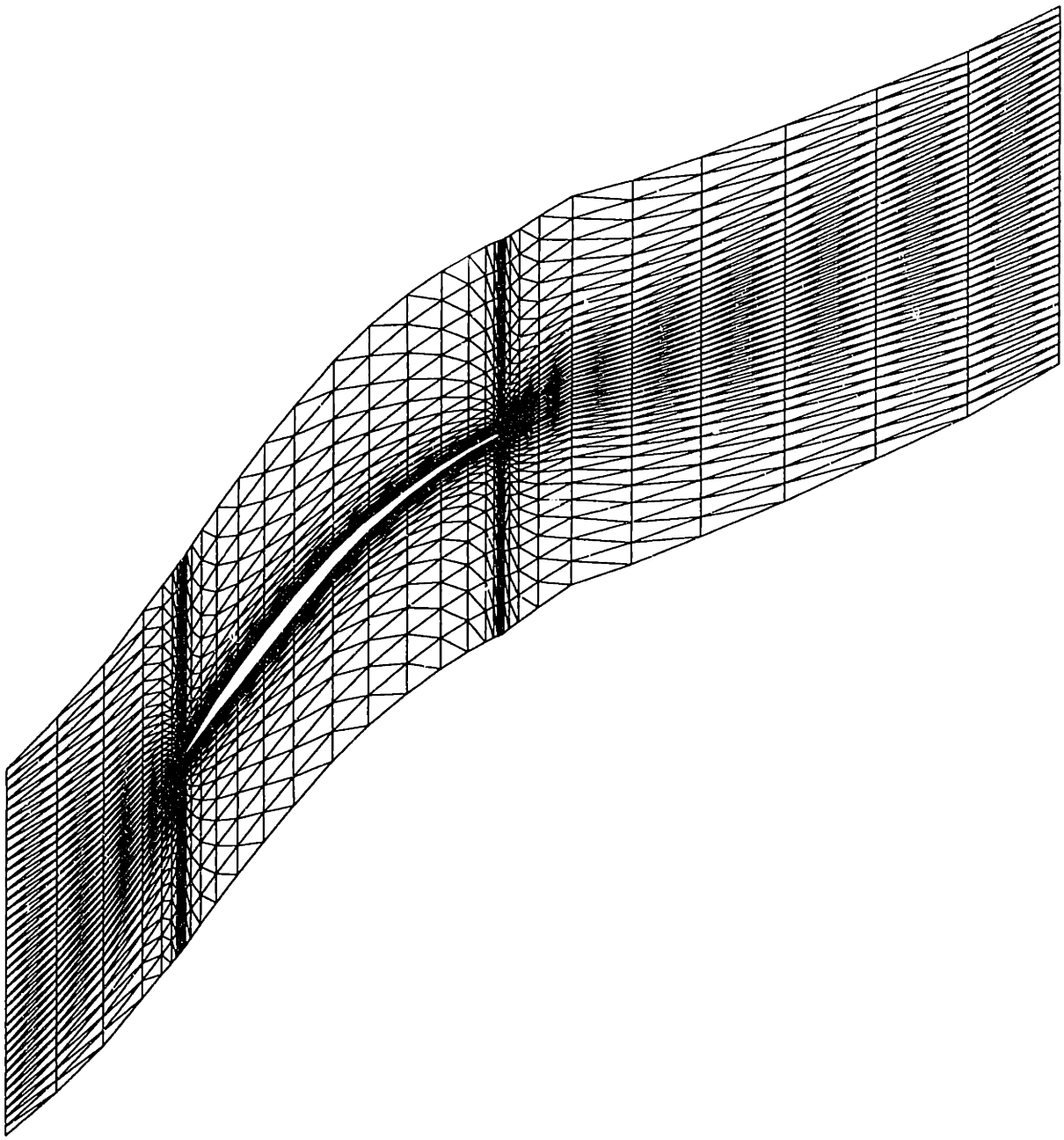

Figure 2-4: Sample grid used for the Navier-Stokes simulations: midspan location

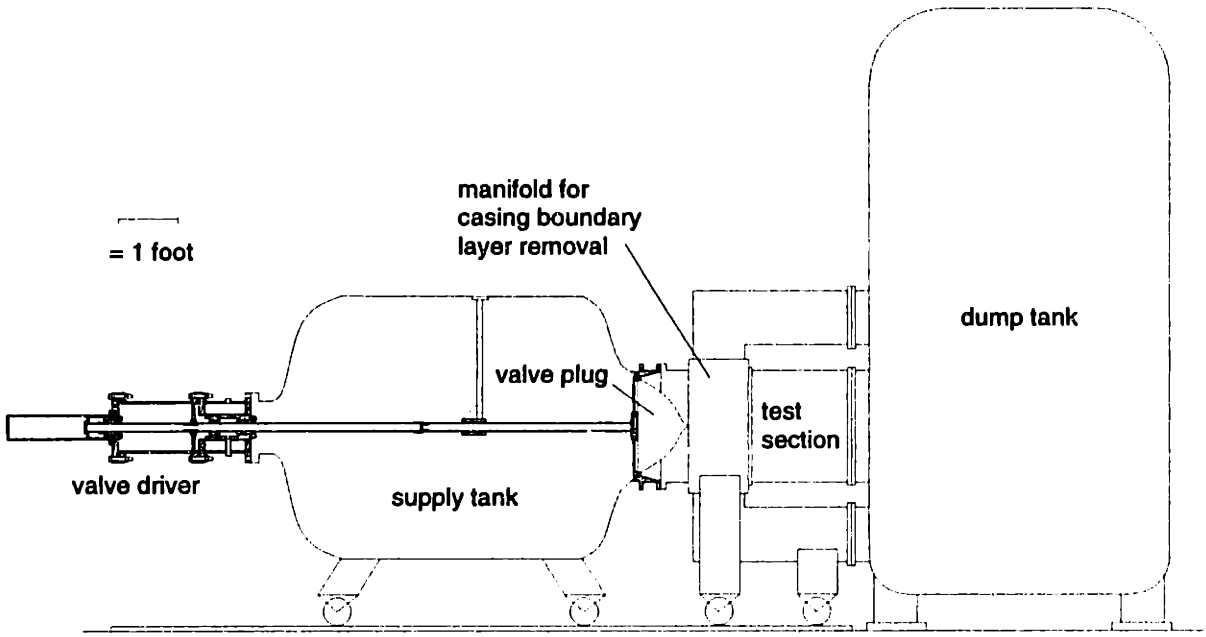

Figure 2-5: Schematic of Blowdown Compressor Facility

tests is described.

The basic test facility used for the study is described in Section 2.6.1. Section 2.6.2 then presents the design of the test section for this particular geometry. The instrumentation used in the test will be discussed in Section 2.6.3, followed by a description of the data acquisition system in Section 2.6.4. Finally, error analysis will be presented in Section 2.6.5.

2.6.1 Blowdown Compressor Facility

Fan rig tests were performed in the Blowdown Compressor Facility in the Gas Turbine Lab at MIT. The basic facility and theory is described in Kerrebrock [19]. A test was originally initiated using a diaghram opened by plastic explosives, but is now performed using a fast acting valve described by Ziminsky [42]. A schematic of the facility is shown in Figure 2-5.

The basic facility is made up of a supply tank (100 ft^3), test section (23.25" inside diameter), and dump tank (300 ft^3). A boundary layer scoop removes the casing boundary layer at the entrance to the test section. Schematic diagrams of all the plumbing of the facility and more detailed description of test running procedure can be found in Reijnen [31].

A blowdown test is conducted in the following manner: 1) the entire facility is brought down to a vacuum (approx. 150 milliTorr) with the valve closed, 2) the supply tank is filled with the appropriate gas mixture, which for the current study was 61.7% CO_2 and 38.3% Argon by mass fraction, 3) the rotor is brought above test speed by an electric motor/generator, 4) the motor is turned off, allowing the rotor to freewheel (speed will slowly decay due to friction and small aerodynamic forces), 5) the system is then armed and when the rotor speed reaches the correct operating condition, the valve opens and the test begins.

The entire test lasts approximately 300 milliseconds in which time data acquisition is carried out (starting at the initial firing) and measurement probes and seals are actuated (the instrumentation is described in more detail in Section 2.6.3). As the test gas flows through the test section, the rotor does work on the flow, thereby decreasing in speed. The rate at which the rotor speed decays depends on the rotor inertia and amount of work performed. As the gas flows out of the supply tank, the pressure and temperature in the supply tank decay as well. With appropriate matching of the rotor inertia and initial supply tank pressure (for given operating condition), the speed of sound of the gas flowing out of the tank and through the test section can be matched to the rotor speed to within 1% over a time period of about 80 milliseconds. In this time, the Mach number and flow angles, and thus operating condition of the rotor, are held constant. This time corresponds to approximately 200 rotor flow through times and about 8 rotor revolutions. For flow phenomena related to passage length scales, this condition corresponds to steady state operation. Phenomena on the time scale of the rotor revolution, such as rotating stall, may not be well captured.

Wake Management Blowing System

Trailing edge blowing wake management required an additional tank to supply gas to the hub of the rotor. When wake management blade design was completed, the required mass flows and pressure for blowing were known, facilitating the design of the blowing system. A supply tank was built with a single fast acting (approx. 50 millisecond opening time) valve to start the flow. A settling chamber was built downstream of the valve with eight 0.50" copper tubes (66 inches long) leading to the outer wall of the test section at 45 degree increments around the circumference. A schematic of the assembly can be seen in Figure 2-6. These ports in the outer wall of the test section connected to tubes leading to the hub

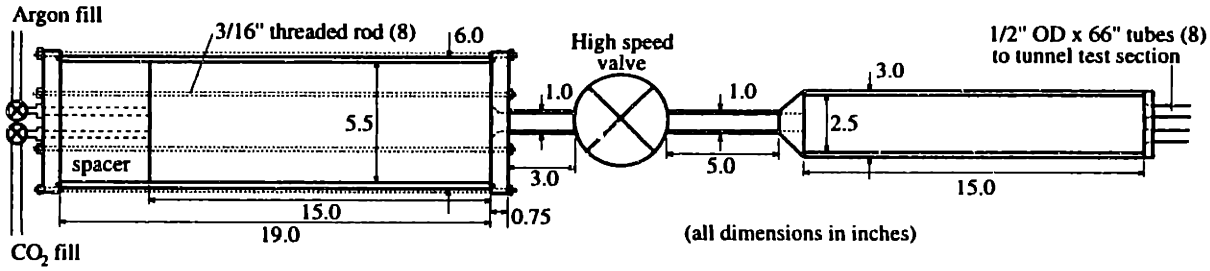

Figure 2-6: Schematic of trailing edge blowing wake management gas supply system

as described in Section 2.6.2. The required tube sizes, supply tank volume and pressure were determined through extensive evaluation of pressure losses and flow conditions due to all corners, expansion/contractions, valve characteristics, *etc.* In addition, the wake management supply tank was designed for installation of internal volume displacement spacers for easy change of tank effective volume.

2.6.2 Design of Fan Stage Test Section

The design of the test section for the installation of the fan stage in the Blowdown Compressor was completed under several requirements. The internal dimensions of the facility, an existing motor/bearing housing, and the rotor/stator spacing limited the available options for the design. Also, the motor/bearing housing bolted to the front of a chamber which was centered in the tunnel by three struts to the tunnel wall (the chamber is open to atmosphere through pipes in the struts for cooling the electric motor).

Removal and/or addition of flow to the test section for previous research efforts was completed with an upstream spider (see Reijnen [31]). However, any upstream disturbance would generate unwanted acoustics (due to rotor inlet distortion) and thus the current study required a new system for the wake management. Piping for the wake management flow was required to be downstream of the choke plate (to reduce upstream influence), but upstream of the main struts (open to atmosphere). Therefore, the wake management piping was brought into the tunnel just in front of the motor/bearing housing attachment in the tunnel (see Figure 2-7), through the outer portion of the motor/bearing housing (bored holes), and into the area under the hub.

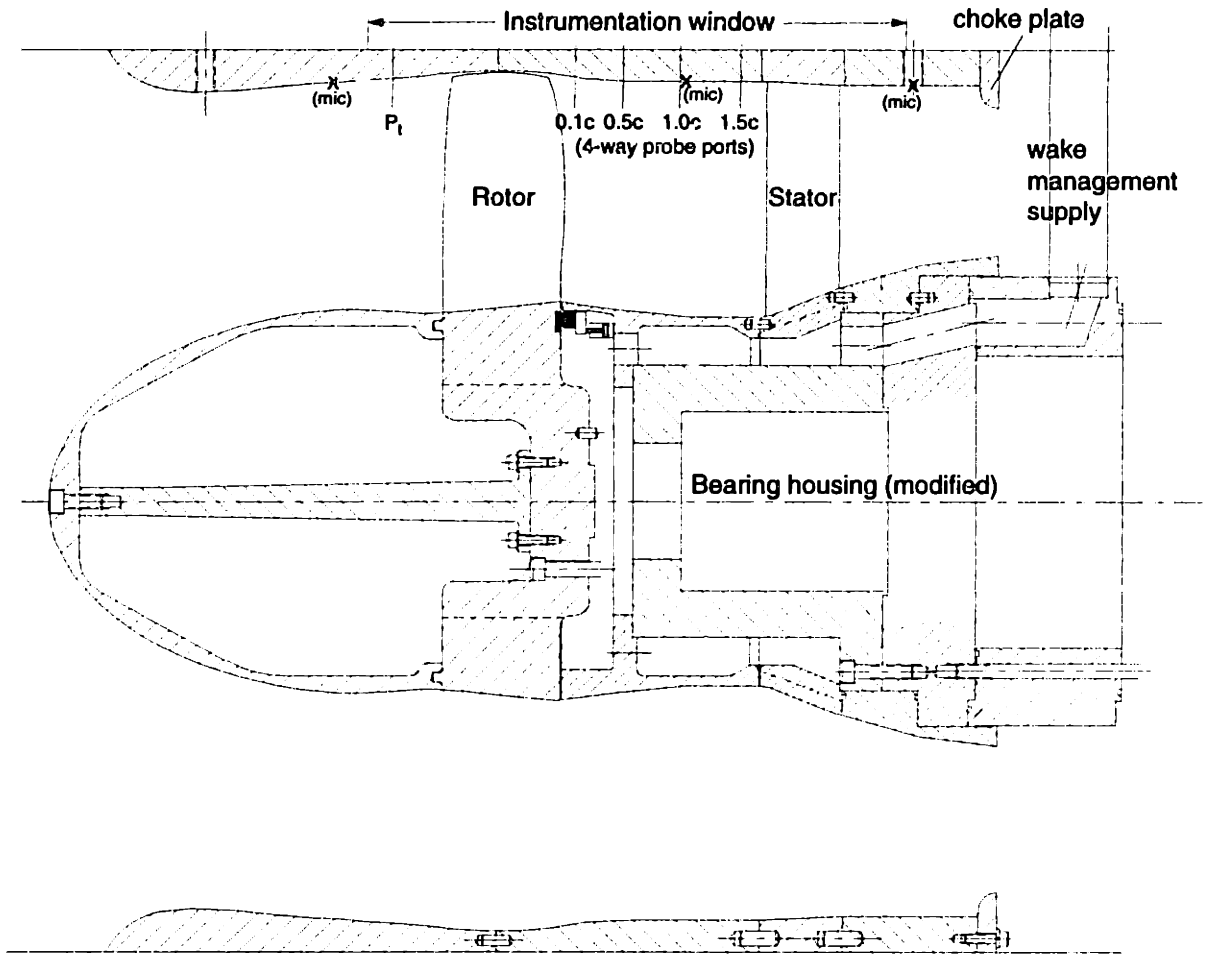

Figure 2-7: Layout drawing of the wake management fan stage in the Blowdown Compressor

With the positioning of the wake management tubes determined, the choke plate was placed approximately one diameter of the originally designed wake management tubes upstream, and the stator row at two stator chords upstream of the choke plate (see Figure 2-7). The positioning of the stator also had to account for the front of the motor/bearing housing, which has a larger diameter than the stator leading edge. With the position of the stator row set relative to the motor/bearing housing, the rotor position was approximately 0.75" in front of the shaft face. This resulted in design of a slightly overhung rotor disk as shown in Figure 2-7. An additional constraint on the position of the fan stage was the location of the instrumentation window in the tunnel wall. Fortunately, the location corresponded to approximately one-half chord upstream of the rotor to one chord downstream of the stator for the positioning described above.

The stator row is pinned through the parts forming the hub to the motor/bearing hous-

ing for both positioning and torque loading. The shroud pieces are centered in the tunnel by the stator row and set screws in the front and rear sections. Additional circumferential and axial constraint is supplied by fixtures in the measurement window opening. Probe holes through the shroud sections also line up with holes in the tunnel wall and instrumentation plates.

With the wake management flow under the hub, a seal is required at the back face of the rotor. The flow passages under the hub, through the motor/bearing housing, and out the tunnel casing were designed for use of either suction or blowing on the fan blades with minimal loss and maximum flow area. To seal the rotor/hub gap, several sealing devices were studied. Labyrinth seals, which are typically used in similar positions, allowed more leakage flow than desired. Graphite face seals, while having good sealing characteristics, would begin to melt the surrounding structure after about 5 seconds of continuous operation for the required geometry (remember that the test section is in vacuum while the rotor is brought up to speed, so there is no convective cooling). Thus, to achieve minimal leakage flow (less than 5% of the wake management flow) at the trailing edge of the rotor, an actuated graphite face seal was designed. The seal was mounted on eight miniature pneumatic actuators, so that the seal could be held back while the rotor was brought up to speed, then seated when the gas flow was initiated. Pressure lines for the seal were brought in through one of the wake management tubes.

Mounting of the rotor blades in the disk was performed in a manner similar to previous Blowdown Compressor blade sets. The rotor blade roots were simple parallelogram sections extended down to a height of 3.000" above the rotor centerline (hub radius is approximately 5.0"). The blades were slid into position, holes drilled along the edge joint of the blade root and disk slot at a height of about 3.5" and rolled pins pressed into the hole (see Figure D-24a). Additional axial containment of the blades was performed by steel rings mounted on the front and back of the disk, which were also used for rotor balancing. In addition, a stainless steel ring was embedded in the back of the disk for seating of the graphite face seal.

Mounting of the stator blades was performed by drilling holes through the blade roots and hub and shroud rings and insertion of rolled pins. The holes were drilled in the opposite direction as the blade stagger (see Figure D-24b in Appendix D).

2.6.3 Instrumentation

Instrumentation for the current study consisted primarily of low and high speed response pressure transducers, position indicators, and thermal-couples. New high response probes were built including wall statics, microphones, a 4-way probe, and an instrumented stator blade. As probe fabrication was completed, many were used for the first time by Reijnen [31]. Low response measurements consisted of supply and dump tank pressures, as well as the pressure at the inlet to the dump tank (just behind the choke plate). Supply tank pressure was low-pass filtered at 10 kHz. In addition, absolute pressure gauges were used to measure supply and dump tanks and vacuum reference system pressures, and thermal-couples were used to measure the temperature of the supply gas.

Microphones and Wall Statics

The wall static probes and microphones were built with Kulite XCQ-062-25D and XCS-062-5D transducers, respectively, mounted in probe bodies shown in Figure 2-8. The head of the probe is 0.25" in diameter, and the body diameter is 0.375". These sizes were chosen for minimum head size allowing an "O" ring in the head shaft (for sealing the probe through the shroud) and reasonable internal area for wiring and vacuum reference connections. Mounting plates were epoxied to the outside of the tunnel, and clamping devices built to hold the probes flush with the inside of the shroud.

Microphone ports were drilled in the tunnel at one fan chord upstream of the rotor, approximately one fan chord downstream of the rotor (which is also approximately one stator chord upstream of the stator), and one stator chord downstream of the stator row. At each axial position, two microphone ports were made at 45 degree apart, or 1/16th of the circumference. This spacing was chosen since the propagating mode orders from rotor wake-stator interaction (see Table 2.2 in Section 2.1) were multiples of 8 for this fan stage geometry, and mode pairs at each multiple of rotor blade passing frequency (up to 5*BPF) could be distinguished by either adding or subtracting the signals from the two microphones at a given axial position (the phase of the mode is either in or out of phase at the two microphones). The microphones were used to measure wall static pressure (mean value), as well as to obtain the qualitative duct acoustic measurements described above.

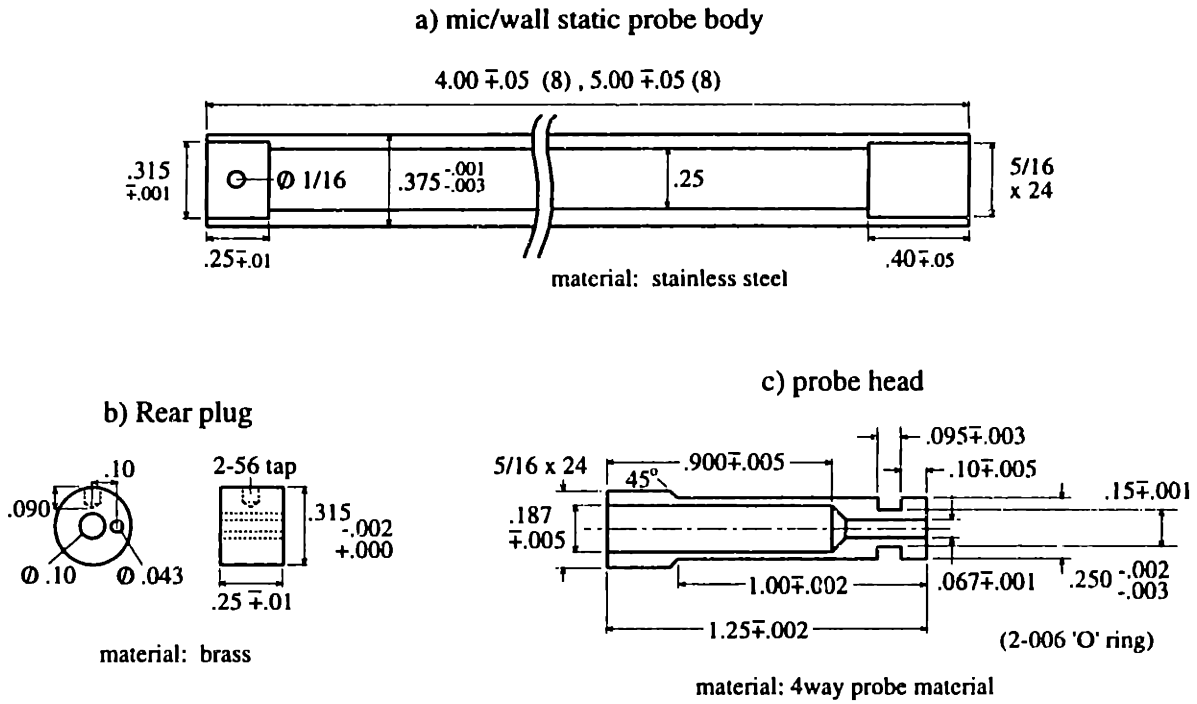

Figure 2-8: Schematic of microphone and wall static pressure probe assemblies

4-Way Probe

To measure the flow field downstream of the rotor, a 4-way probe fitted with four flush mounted pressure transducers (Kulite XCQ-093-25D) was used to determine the total and static pressure and the tangential and radial flow angles. These four quantities also give the three components of Mach number: axial, tangential, and radial. The 4-way probe built for the current study was based on earlier versions used in the Blowdown Compressor, but included vacuum reference to each transducer. One transducer faces the flow, two are at 45 degrees to the flow (± tangential direction) and one is on the tip wedge at 45 degrees (radial direction). A schematic of the probe head section is shown in Figure 2-9 and full drawings can be found in Reijnen [31]. The Kulites are thermally compensated, but the probe included water cooling to maintain the probe at constant temperature.

The probe was taken to Boeing and calibrated (steady state) in their 1" free jet calibration facility. The probe calibration ranged from a Mach number of 0.1 to 0.9 and flow angles of -24 to +24 degrees tangential angle and -20 to +20 degrees radial angle. Details

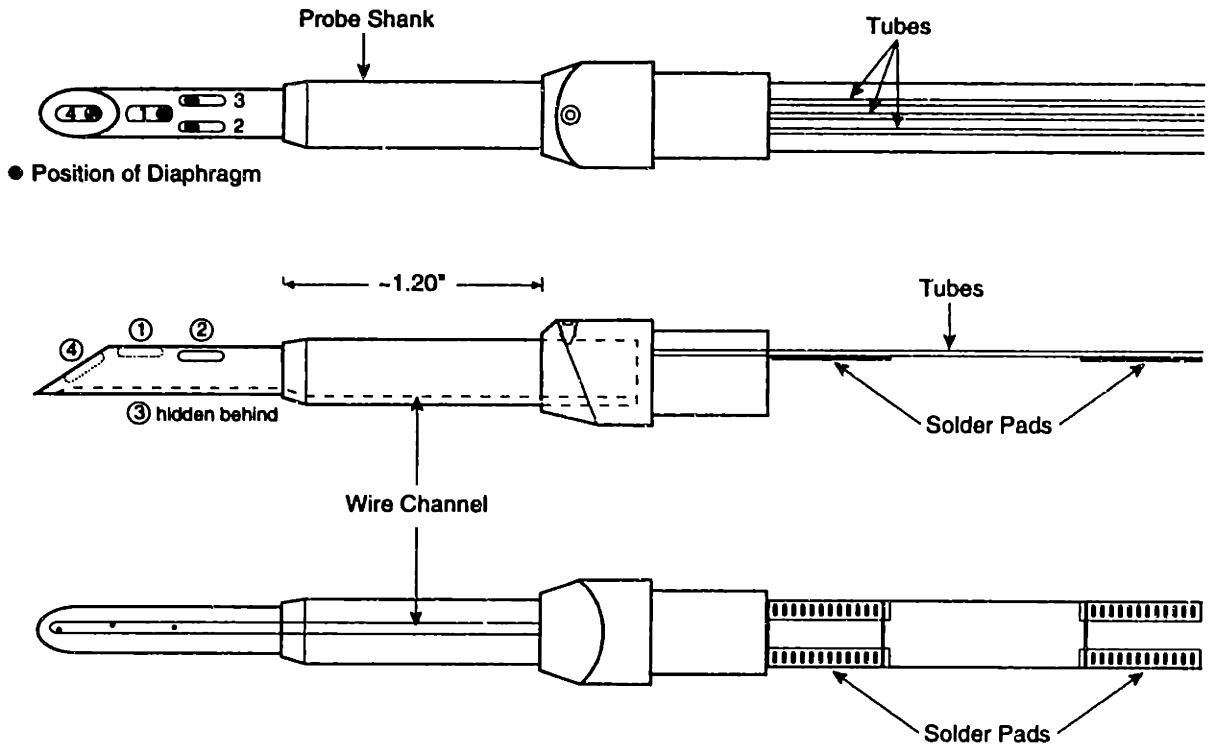

Figure 2-9: Schematic of 4-way probe without wiring and 22" body

of the calibration and data reduction procedure were presented in Reijnen and will not be repeated here. Errors in the steady state data reductions were found to be approximately ± 1 degree in flow angle and ± 1 percent in Mach number and total pressure over the normal operating range (additional errors due to unsteady vortex shedding will be discussed in Section 5.2.2). Above ±15 degrees tangential flow angle, the flow is likely separated over at least one side transducer and the errors increase. However, an appropriate offset angle can be chosen when installing the probe in the test section to minimize errors.

Radial motion of the 4-way probe was provided by a pneumatic actuator. The probe was held in the casing during tunnel start-up, and then translated to the desired spanwise position after the flow was initiated. This was done to avoid damage to the transducers due to any foreign material in the test section (more critical when the diagram was used). Timer circuits were used to offset the time of the translator firing from the firing of the main valve. The final position of the probe was set using calibrated lengths of 1.0" OD rubber tubing as stoppers. This also provided smooth stopping of the probe at the desired depth. A linear potentiometer was used to obtain time accurate probe position.

Wake measurements were taken at 0.1, 0.5, 1.0, and 1.5 rotor axial chords downstream

from the rotor midspan trailing edge. Ensemble-averaging of the wakes was completed over several runs, each having 4 to 6 rotor revolutions (64 to 96 blade passing periods) to obtain the mean wake profiles. Resolution of turbulent fluctuations was limited to a frequency of about 15 kHz (about 7 times blade passing frequency) due to the probe size. Above this frequency, the perturbation wavelength was of the same order, or smaller, than the probe, and thus the perturbation could not be resolved.

Instrumented Stator Blade

In addition to measurements of the flow field downstream of the rotor, it was desired to directly measure the unsteady loading on the stator blade. To do this, one extra length stator blade was built for instrumentation at one spanwise position. As discussed in Section 2.1 the stator was redesigned to allow translation of the instrumented blade for measurement of the entire unsteady pressure field of the stator.

Channels were milled along the stator blade from the root rectangular section (for attachment to the translator) to the transducer seats. A schematic of the blade is shown in Figure 2-10. Stainless steel vacuum reference tubes (0.020" diameter) were placed in the channels and epoxied in holes drilled under the transducer seat which joined to the back of the diaghram, as shown in Figure 2-11. The transducers were mounted in their seats, and the wires run up the channels and connections made on the root section. The channels were then filled and the diaghrams covered with a thin layer of silicon rubber. Like the 4-way probe transducers and microphones, the stator transducers were thermally compensated.

In total, 13 pressure transducers (Kulite XCQ-093-15D) were flush mounted on the blade at the same spanwise position: 7 on the suction surface and 6 on the pressure surface. The chordwise position of the transducers is shown in Figure 2-12. The transducers are concentrated (maximum possible from geometrical and structural constraints) in the leading edge region where the pressure gradients are the largest. A picture of the blade mounted on the stator chamber/translator is shown in Figure 2-13.

To allow the stator to slide into the hub, holes were cut through the stator hub ring and bearing housing. A box fitting through these holes was built to seal the wake management flow in the hub from both the freestream flow field and the gas in the bearing housing. In

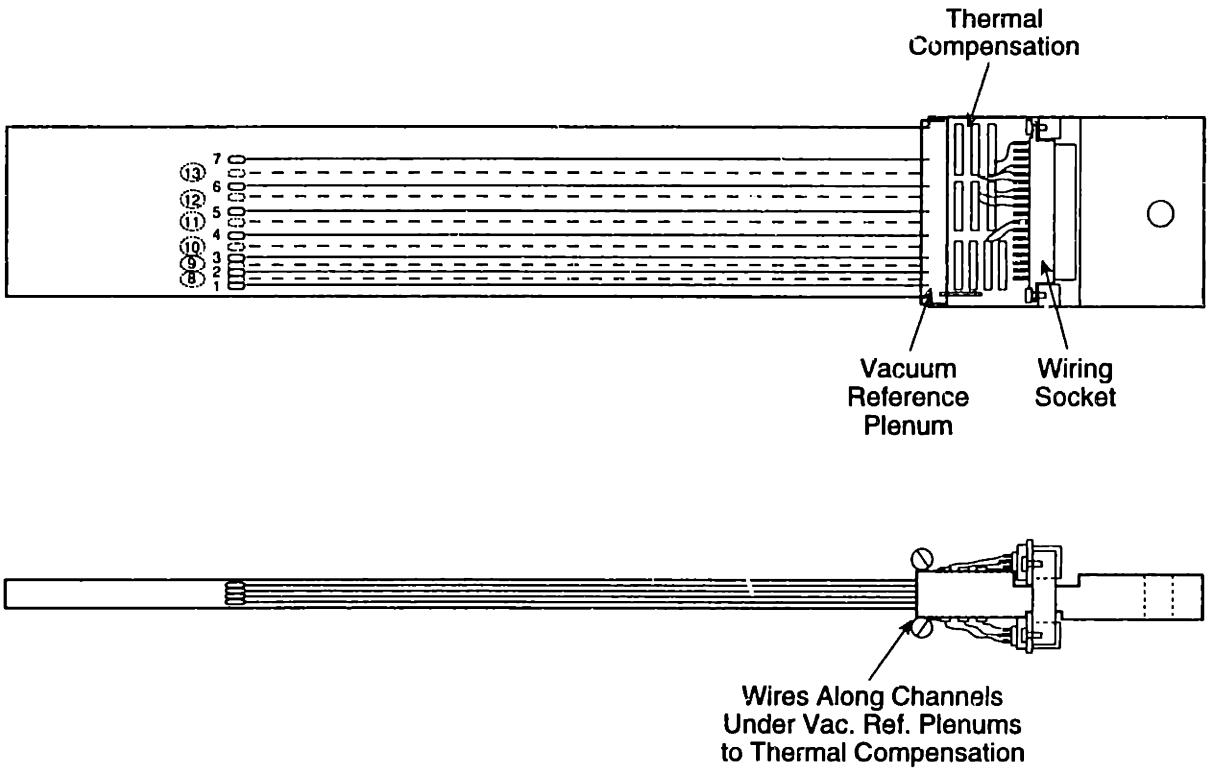

Figure 2-10: Schematic of instrumented stator blade

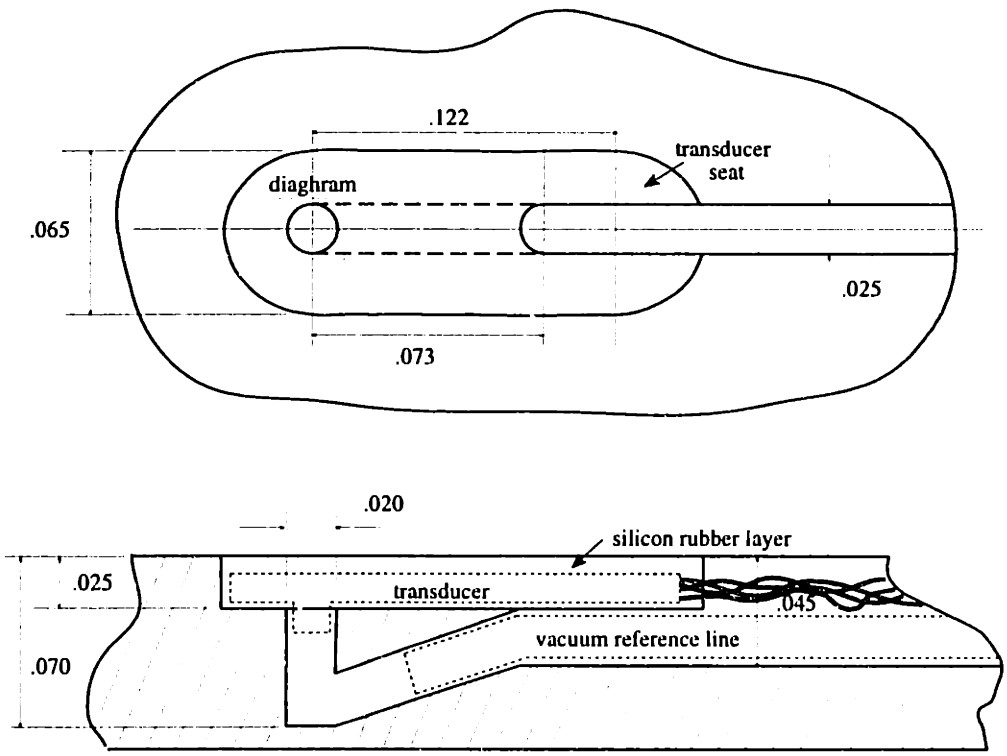

Figure 2-11: Schematic of stator transducer seat

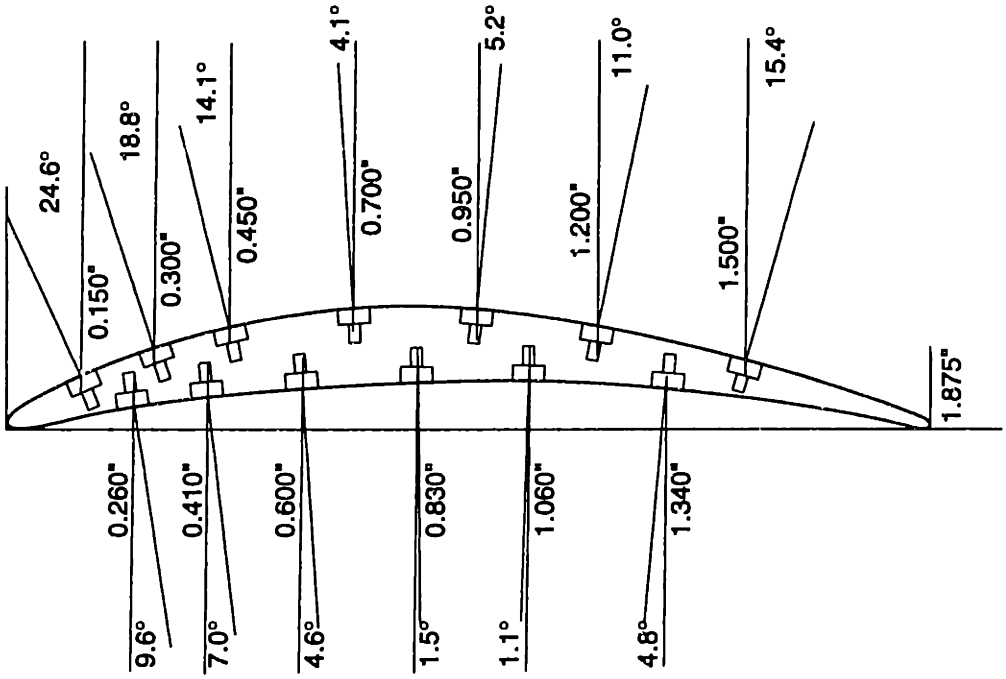

Figure 2-12: Schematic of instrumented stator blade transducer locations

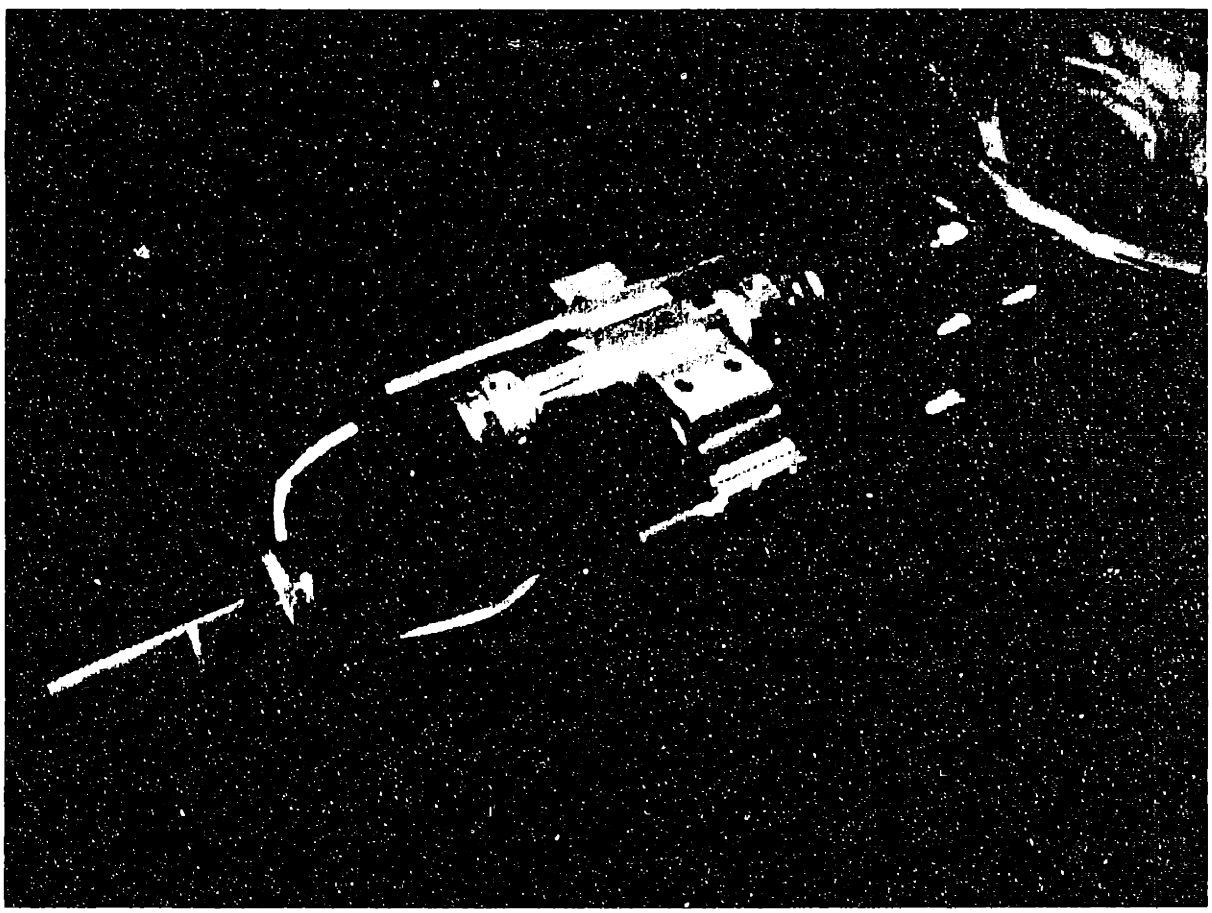

Figure 2-13: Picture of instrumented stator blade mounted in the chamber/translator

addition, the allowable area in the hub for insertion of the blade was only 3.10" deep (the span of the stator in 6.03") so a detachable 3.00" section was built to be placed on the end of the instrumented blade. By use of this section, the entire spanwise distribution of unsteady stator loading could be measured, one-half of the span at a time (*i.e.* lower 50% span with the main blade alone, and the outer 50% span with the 3.00" section attached).

A two-way pneumatic driver was built to translate the stator and a linear potentiometer was used to measure the position. For most of the testing, however, the blade was clamped in position and left in the flow field for the entire test. This was done due to ringing of the pressure transducers when the blade was stopped using the translator. In addition, the stator transducers are less susceptible to damage from foreign material in the flow field than the 4-way probe transducers which face the flow.

With the transducers on the suction and pressure surfaces, not only can the mean pressure envelope be measured, but also the distribution of amplitude and phase of the unsteady pressure fluctuations caused by the interaction with the rotor wakes. These measurements can then be used in acoustic models that integrate the stator unsteady pressure field with the acoustic modes to estimate the radiated acoustic waves.

2.6.4 Data Acquisition

The data acquisition system for acquiring data from the instrumentation described above was a DELL 450DE 80486 32MB RAM EISA computer with three 12-bit, 8 channel ADTEK A/D boards. The sampling frequency was 333 kHz primarily to facilitate calculation of the rotor speed from a 400 pulse per revolution optical shaft encoder. The A/D boards accept input signals from -10 to +10 volts.

Pressure transducers were driven at an excitation voltage of 15.0 volts DC, and the amplifier gains and zero offset were set for maximum use of the A/D input range. Except for the tank pressure transducers, which were driven by previously existing amplifiers (Epstein amps), the high response transducers were driven by 10 Pacific Instruments Model 3210 transducer conditioning amplifiers. Internal 50 kHz low-pass filters were used. For the stator blade, the 6 pressure side transducers were driven by Pacific Instruments Model 8650, F2, J, transducer amplifiers and the signals sent through an independent bank of

25 kHz low-pass filters. Output signal phase shifts from both sets of amplifier/filters were measured up to 10 kHz (5*BPF) and used to correct the data.

Data reduction consisted primarily of MATLAB programs written specifically for the wake management testing. Data was first transformed from A/D board counts to voltage and then pressure. Calibration of the pressure transducers was completed by maintaining atmospheric conditions in the tunnel (transducer faces) and then cycling the vacuum reference line from vacuum to atmosphere. This gave a two point calibration for one atmosphere pressure differential across the transducer. The vacuum reference system was held at vacuum (< 100 milliTorr) during the test time for all experiments.

The linearity of the transducer response (slope = volts/ΔPressure) was checked from zero pressure difference to one atmosphere. The tanks and 4-way probe transducers were linear to well within 1 percent, but the microphones and stator transducers were not. The slope of the transducer response from vacuum to typical pressures seen in the facility during test time (approx. 400 milliTorr) were compared to the slope over a full atmosphere to determine a correction to the two point calibration. Corrections of 5% were typical, and these values were then used in the data reduction procedures. Variations in the two point calibration slopes over the several months of testing were less than 1 percent.

2.6.5 Error Analysis

Error analysis was completed to determine both systematic and random error amplitudes for placement of confidence intervals on the data. Most of the data presented from this study is an average of several runs at the same operating condition. The confidence interval used on the data is a 95% interval estimated by calculating the standard deviation of the particular data point (which typically consists of several runs, each having 64 to 96 blade passing periods) and then using the χ^2 formula $\sigma_{mean} = (1.96/\sqrt{n})\sigma_{samples}$. Estimating the confidence interval in this way accounts for random run-to-run errors, as well as the turbulent fluctuations. Typically, run-to-run variations in measured quantities from the 4-way probe and instrumented stator were less than 1% (less than 20% of the unsteady amplitude).

CHAPTER 3

PRELIMINARY ASSESSMENT

To gain a basic understanding of rotor wake-stator interaction and the effects of wake management strategies on the resulting wake and stator unsteady loading, two-dimensional studies were undertaken by the author and others (Waitz *et al.* [38], Hayden [12] and Sell [33]). Although these studies lack many complicating three-dimensional features that are present in high-speed rotor flow fields, this was seen as an opportunity to develop the basic knowledge required for designing wake management strategies before proceeding to full rig experiments.

Several numerical and experimental studies were completed including numerical parameterization of the wake, boundary layer suction simulations, suction/blowing cascade experiments, and blade design requirements/limitations. The methods used for the studies are described in Chapter 2, and the results presented in Sections 3.1, 3.2, and 3.3. The results are summarized in Section 3.4.

3.1 Numerical Parameterization of Effects of Wake Modifications

As a first step in evaluating wake management techniques, calculations were performed to determine the sensitivity of unsteady stator loading and radiated tone noise to specified modifications of the wake. Gaussian wake distributions in the rotor reference frame, of given width and depth, were specified at the inlet plane of the stator. The 16/40 rotor-stator pitch

ratio of the test geometry and the flow conditions shown in Table 2.1 were used. UNSFLO was used to parameterize the effects of varying wake width and deficit on unsteady forces on the stator blade. The effects on radiated acoustic modes were determined using LINSUB.

The wake deficit was varied over a range of 0 to 30 percent of the freestream velocity while holding the wake width constant at 100% of the rotor pitch. Wake deficits between 5 and 15 percent are typical of fan rotor/stator spacings of technological interest. Over this range the unsteady stator loading harmonics, in multiples of blade passing frequency (BPF), were approximately proportional to the wake deficit. This result is in accord with linear theory which applies for wakes which are small perturbations to the mean flow. Thus, if a particular spatial harmonic of the wake were reduced by 50%, one would expect a reduction of roughly 6 dB in any associated propagating acoustic modes.

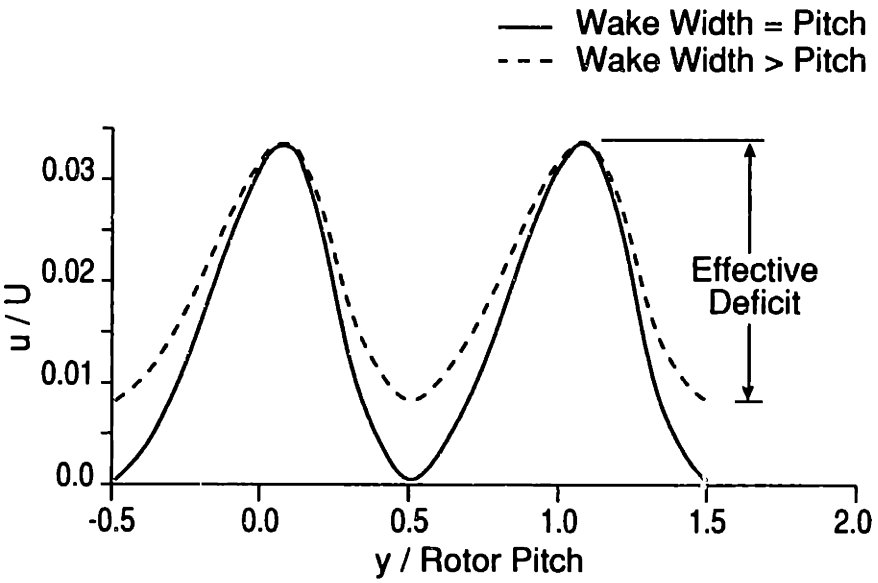

Figure 3-1: Schematic showing effect of wake merging on wake deficit

Similar calculations were performed holding the wake deficit constant at 10 percent while varying the wake width over a range of 0 to 160 percent of the rotor pitch . Reducing the wake width had two effects, both of which were in general deleterious. First, for wake widths greater than one rotor pitch, the wake edges are merged together. Wake deficit profiles for merged and unmerged wakes are shown in Figure 3-1. The wake merging results

in a reduction of the effective deficit seen by the stator row, as the "freestream" velocity is reduced. For fan rotor/stator axial spacings of 1.5 to 2 fan chord lengths, as are typical of current technology engines, the wakes are often merged. Thus reducing the width of wakes so that they are no longer merged can effectively increase the wake velocity deficit, and thus the stator loading and associated tone noise.

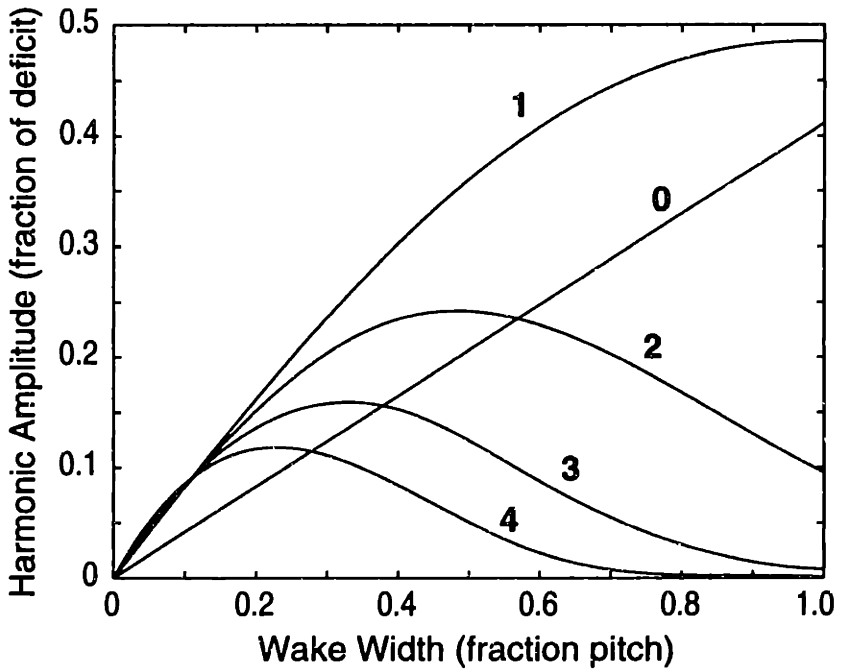

Figure 3-2: Harmonic composition of a Gaussian wake for constant wake centerline deficit

The second effect of changing the wake width is a result of changes in the harmonic content of the gust field which is incident on the stator. Many fan geometries are designed so that acoustic modes associated with the first wake harmonic at blade passing frequency (BPF) are cut off over most of the engine operating envelope. Therefore, the acoustic modes of greatest concern are associated with the 2*BPF, 3*BPF, *etc.*, spatial harmonics of the wake. For constant wake centerline velocity deficit (*i.e.* the same maximum change in incidence angle), these harmonics are increased when the wake width is decreased from full pitch width, as shown in Figure 3-2. Indeed for Gaussian wakes, each spatial mode number, n, peaks at a wake width of approximately 1/n times the rotor pitch. It is thus advantageous for the wake width to be approximately equal to the rotor pitch to minimize

the amplitude of higher order harmonics, *i.e.* multiples of BPF.

Mode	**Mode Amplitudes in dB: Upstream and (Downstream)** All referenced to: m = -8, 2 x BPF upstream and (downstream), respectively, for wake width=rotor pitch			
	Wake Width in fraction pitch			
	0.25	0.5	0.75	1.0
2 x BPF, m = -8	5.5 (5.5)	8.1 (8.1)	5.8 (5.8)	**0 (0)**
3 x BPF, m = 8	6.4 (-21.3)	4.7 (-23.0)	-4.8 (-32.5)	-[illegible].4 (-47.1)
3 x BPF, m = -32	1.5 (-2.5)	-0.1 (-4.2)	-9.6 (-13.7)	-24.2 (-28.3)
4 x BPF, m = 24	2.5 (-9.8)	-4.8 (-17.1)	-26.3 (-38.6)	-42.2 (-54.7)
4 x BPF, m = -16	-16.2 (-7.8)	-23.5 (-15.1)	-45.0 (-36.6)	-61.1 (-52.7)
4 x BPF, m = -56	4.9 (-5.7)	-2.5 (-13.0)	-23.9 (-34.5)	-40.0 (-50.6)

Table 3.1: Radiated acoustic mode amplitudes for varying wake width (constant velocity deficit)

Examples of the changes in amplitude of radiated acoustic modes with varying wake width are shown in Table 3.1. The results were obtained using LINSUB. The mode amplitudes upstream and downstream from the stator are shown referenced to the m = -8, 2*BPF upstream and downstream amplitudes, respectively, for a wake width-to-pitch ratio of 1. (For reference, the downstream amplitude of the m = -8, 2*BPF mode is 15.9 dB greater that the upstream amplitude.) The sensitivity of the higher order modes to wake width is significant. For example, for the 2*BPF mode, a decrease in wake deficit of 50% would be nullified if it were accompanied by a decrease in wake width from 100% of rotor pitch to 75% of rotor pitch. Thus, a general goal for wake management is to strive for

shallow but wide wakes to minimize the propagating tone noise.

3.2 Experimental Cascade Testing of Boundary Layer Suction and Trailing Edge Blowing

Cascade experiments were carried out by Sell [33] for blade boundary layer suction and trailing edge blowing to elucidate the effects of these treatments on both steady and unsteady wake characteristics. The take-off flow conditions and blade incidence angles summarized in Table 2.1 were used. The reduction in tone noise associated with the wake management treatments was estimated using the experimentally obtained time-mean wake signatures as input to LINSUB.

3.2.1 Boundary Layer Suction

Boundary layer suction was applied on the suction side of the blade at 50% and 80% chord for suction mass flow rates corresponding to 50% and 70% reduction of the local boundary layer momentum thickness. The variation in mean velocity deficit with suction at 80% chord is shown in Figure 3-3a as a function of distance downstream from the trailing edge of the fan blade. The narrowing of the wake from the suction side ($y/s > 0$) where the boundary layer was removed is evident. Note that the wake was changed little in going from 50% to 70% boundary layer momentum thickness removal. For the case of 70% momentum thickness reduction the peak wake deficit was reduced 40% at 1.5 chords downstream from the blade. Unfortunately, the suction also resulted in a reduction in width of approximately 15% for this case, slightly reducing the benefits gained by reducing the mean velocity deficit. The reductions in width and deficit are in accord with Hayden's [12] numerical simulations described in Section 2.2.

The change in unsteady wake behavior with suction at 80% chord is shown in Figure 3-3b, where the rms of the velocity fluctuations in the wake is plotted at several locations downstream from the trailing edge. Note the two peaks in turbulent fluctuations which are characteristic of the vortex shedding described by Epstein *et al.* [7]. The peaks correspond roughly to the location of maximum shear in the mean velocity profiles as expected. At 1.5

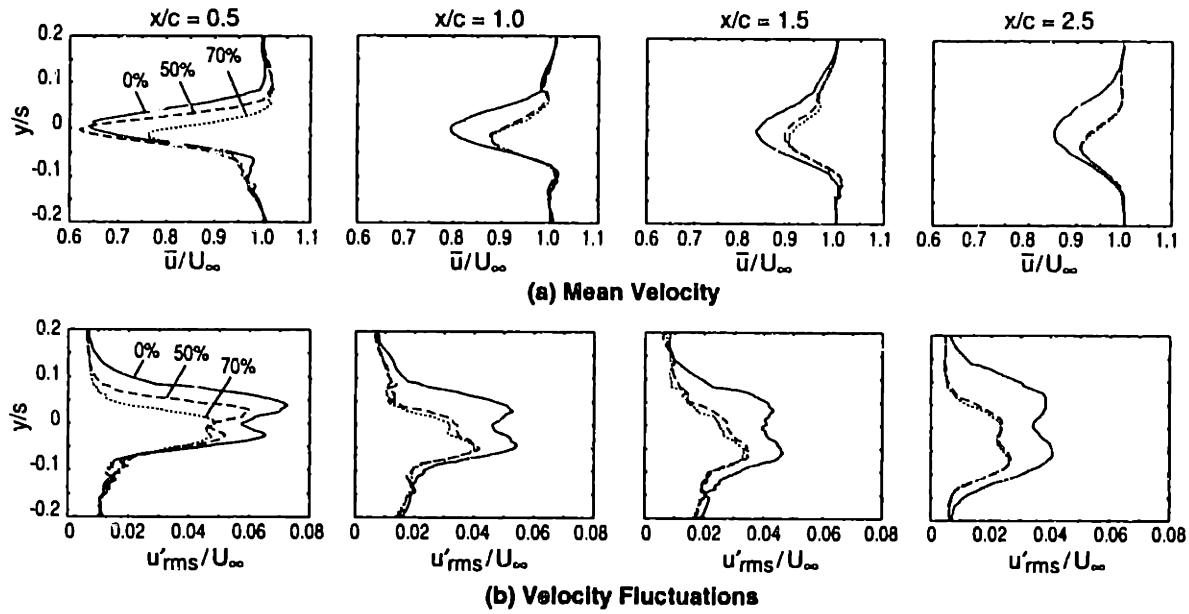

Figure 3-3: Wake measurements for suction surface boundary layer suction at 80% chord: cascade facility

chords downstream, the turbulent velocity fluctuations were reduced approximately 35% for the case of maximum suction. Since there were not significant changes in the turbulence spectrum, this reduction would correspond to approximately a 3.7 dB reduction in the component of broadband noise associated with the wake turbulence.

For the condition of 70% reduction in boundary layer momentum thickness, the time-mean wake signature at 1.5 chord lengths downstream from the trailing edge was converted to the stator coordinate frame and used as input to LINSUB. Recall that for this geometry the 1*BPF acoustic mode is cut-off outside of the fan stage, so it is only the higher spatial harmonics of the wake (2*BPF and higher) which directly influence radiated tone noise (see Section 1.3). The upstream and downstream amplitudes of the propagating acoustic modes were compared to those obtained for the baseline wake profile measured experimentally. (For the baseline m = -8, 2*BPF mode, the downstream amplitude is 15.9 dB greater than the upstream amplitude.) The results of this analysis are shown in Table 3.2. For the case with boundary layer suction the amplitude of the strongest propagating mode (m = -8, 2*BPF, downstream) is reduced by 4.4 dB. Higher order propagating modes show similar

Mode (tonal noise)	Boundary Layer Suction	Trailing Edge Blowing (deviation angle)		
	$\Delta\theta_{b.l.} = 70\%$	-25% mass	$\theta = 0$	+25% mass
2*BPF, m = -8	-4.4	-8.0	-24.4	-3.9
3*BPF, m = 8,-32	-4.5	-8.1	-18.6	-2.6
4*BPF, m = 24,-16,-56	-3.9	-8.3	-13.2	+0.8
Turbulence (broadband)	-3.7	-6.6	-7.0	-0.9

Table 3.2: Cascade acoustic amplitude reduction from wake management

reductions in amplitude. If the treatment were to be applied uniformly along the span of a fan blade, this condition would correspond to removal of approximately 2.2% of the fan through flow. Unfortunately, boundary layer suction effectiveness is limited by the trailing edge thickness of the airfoil. For blades with trailing edge thicknesses comparable to the suction surface boundary layer displacement thickness, the maximum possible reduction in wake harmonic amplitudes is approximately 50%.

3.2.2 Trailing Edge Blowing

Preliminary experiments by Sell [33] with trailing edge blowing were conducted for various amounts of momentum addition (25%, 50%, and 70%) of the natural wake momentum deficit. Mean and unsteady velocity profiles with blowing at the trailing edge metal angle are shown in Figure 3-4 as a function of distance downstream from the trailing edge of the fan blade. Blowing at the metal angle resulted in filling of the pressure side ($y/s < 0$) of the wake due to alignment of the injection ports with the mean camber line which differs from the mean flow direction leaving the blade by the deviation angle, approximately 6 degrees.

Later experiments employing trailing edge blowing with several different jet orifice geometries were also conducted by Sell for mass flow rates corresponding to addition of

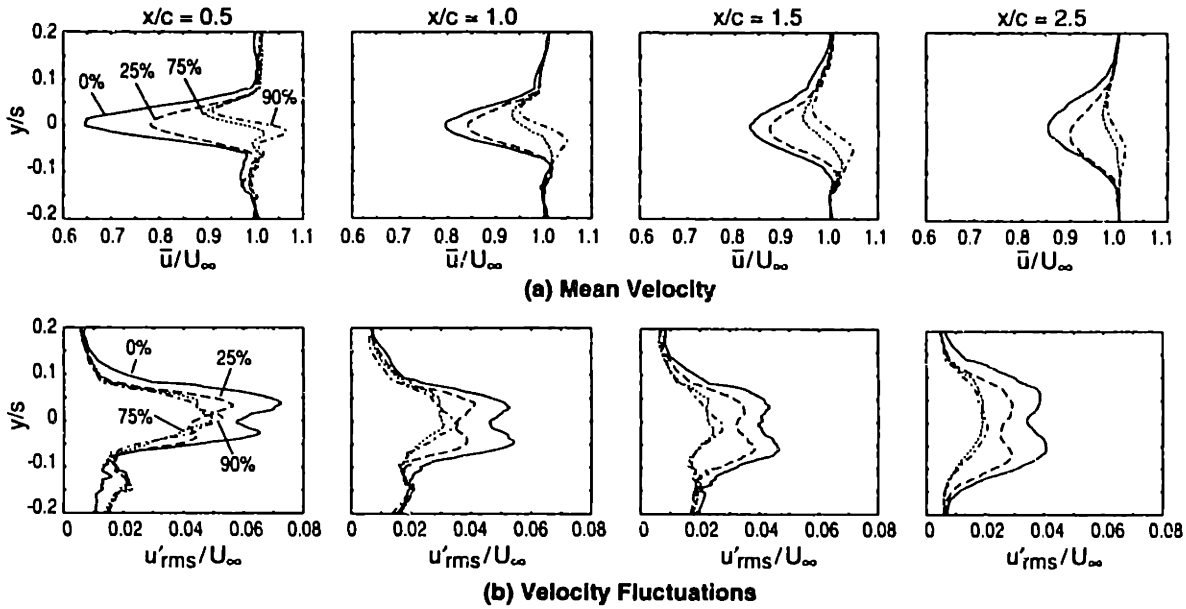

Figure 3-4: Wake measurements with trailing edge blowing at the metal angle: cascade facility)

54%, 100%, and 171% of the natural wake momentum deficit. These momentum additions corresponded to the blowing mass flow rate resulting in a momentumless wake (100% case) and approximately 25% more and less mass flow (54% and 171% cases). Blowing at the deviation angle, which injects fluid into the central portion of the wake, resulted in the largest reduction of the steady wake deficit of approximately 60%, and is shown in Figure 3-5.

The change in unsteady wake character for blowing at the deviation angle is shown in Figure 3-5b, where the rms of the streamwise velocity fluctuations in the wake is plotted at several locations downstream from the trailing edge. The maximum reduction in wake velocity fluctuations is approximately 60% at x/c = 1.5 for the case of 100% filling of the natural wake momentum deficit. Again, since there was little change in the turbulence spectrum, this result implies a reduction of approximately 7 dB in the component of broadband noise associated with the wake turbulence.

For trailing edge blowing at the deviation angle, the time-mean wake signatures at 1.5 chord lengths downstream were decomposed spatially and used as input to LINSUB. The

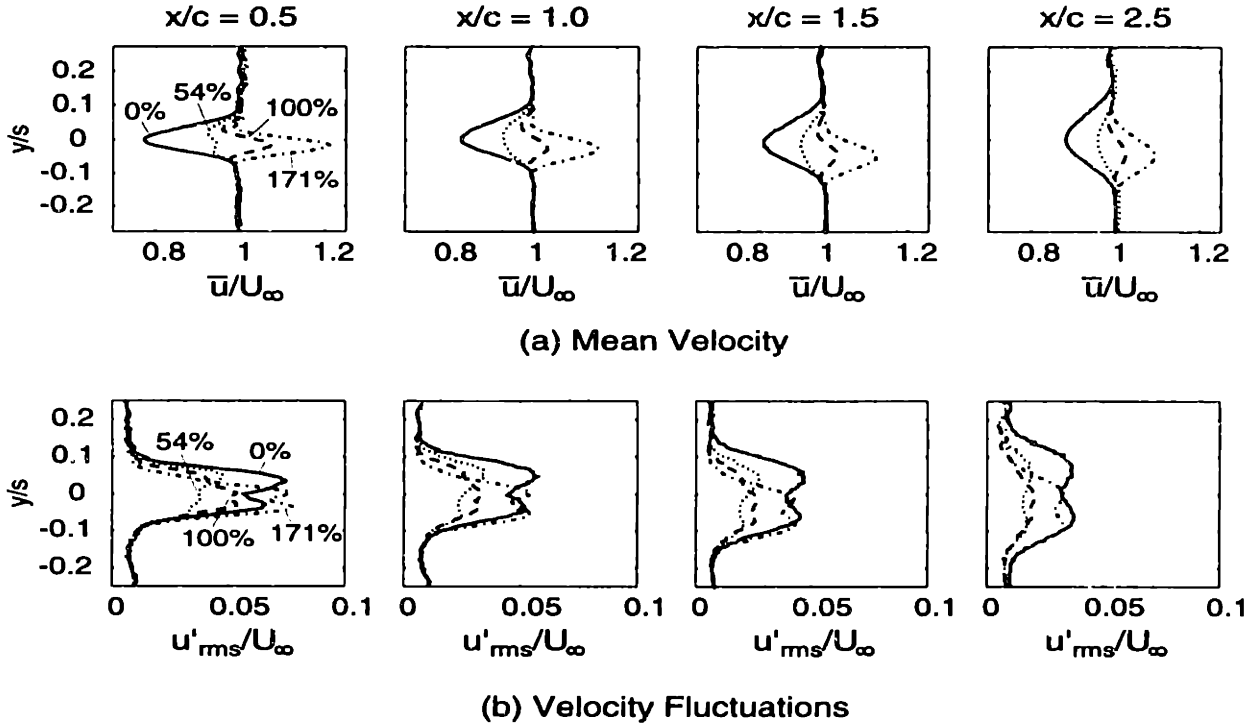

Figure 3-5: Wake measurement with trailing edge blowing at the mean flow deviation angle: cascade facility)

upstream and downstream amplitudes of the propagating acoustic modes were compared to those obtained for the baseline wake profile measured experimentally (again, the downstream reference amplitude is greater than the upstream reference amplitude by 15.9 dB). The results of this analysis are shown in Table 3.2. For trailing edge blowing the amplitude of the strongest propagating mode (m = -8, 2*BPF, downstream) is reduced by 24 dB. Other propagating modes show reductions in amplitude of 7 dB to 18 dB. If the treatment were to be applied uniformly along the span of a fan blade, addition of 100% of the natural wake momentum deficit would correspond to addition of approximately 1.08% of the fan through flow for this particular blowing geometry. Even with 25% less mass addition than that required for a momentumless wake, reductions in the tones were approximately 8 dB with 5 dB broadband reduction.

Unlike cascade geometries, however, rotating blade rows generally have considerable variation in the wake characteristics along the span due to spanwise loading distribution. In addition, three-dimensional phenomena are present, such as wake skewing and radial transport, which effect the wake decay characteristics and the coupling to the acoustic modes. Reductions in radiated acoustic waves from realistic rotor geometries may, therefore,

vary considerably from the cascade results above. Experimental results from rig experiments which include these effects are presented in Chapters 5 through 8.

3.3 Analysis of Fan Blade Design Requirements/Limitations

An analysis was performed to determine the requirements and limitations for internal fan blade passages to allow removal or addition of sufficient mass flow to perform the treatments described in the previous sections. The flow internal to the blades was modeled as a one-dimensional viscous flow in a variable area, rotating channel with heat transfer at the walls. The conservation equations were integrated radially to determine the hub pressure required to obtain a specified flow rate in the passage for a given blade and passage geometry, and operating condition. The viscous and heat transfer terms were approximated using relations given by White [41] and Miller [23]. A more detailed description of the model is provided in Section 6.4.

The analysis was performed for a three-dimensional blade (see Section 2.1) and carried out for both the 0.56m diameter model-scale blade and a full-scale blade (there is roughly a factor of six difference in scale). The analysis was conducted assuming a maximum suction passage open area of 50% of the total blade area at each spanwise location, and uniform percentage reduction in the boundary layer momentum thickness at each spanwise location. An open area of 30% of the total blade area and uniform spanwise reduction in the wake momentum deficit was assumed for trailing edge blowing. These percentages of open area are similar to what is present in the hollow fan blades currently used in some gas turbine engines, and thus are feasible to implement from a structural design perspective.

Figure 3-6 shows solutions for boundary layer suction and trailing edge blowing for the 0.56m model-scale and full-scale blades. The solutions are dependent on the blade passage geometry and the configuration for the suction and blowing ports. Thus while the results are representative, they are not general. For the 0.56m fan model all relevant non-dimensional external flow parameters were matched to full-scale conditions with the exception of the size of the fan. Thus the only difference between the solutions for the model-scale and the full-scale blades is the viscous forces within the blade passages. With much larger flow areas, the full-scale case is driven primarily by rotational effects and behaves essentially

inviscidly.

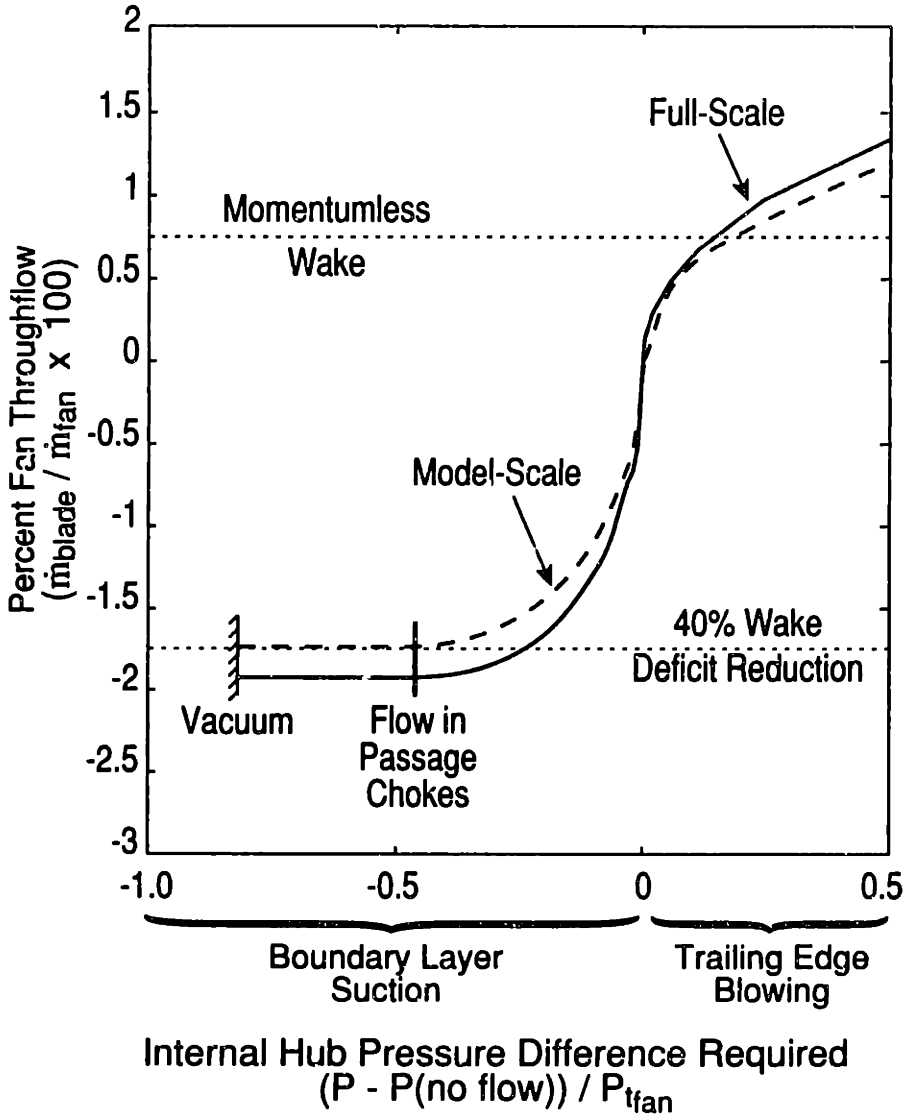

Figure 3-6: Calculated wake management flow requirements/limitations for boundary layer suction and trailing edge blowing for typical high bypass ratio fan geometry

The non-symmetry of the curves for suction and blowing shown in Fig. 3-6 is caused by effects of rotation and different passage geometries for the two cases. The maximum passage mass flow for either suction or blowing is obtained when the fluid chokes in the passage. The choking typically occurs at the hub for suction and the tip for blowing.

The suction is limited to an amount of mass removal which will allow approximately 40% reduction in wake deficit based on the simulations and experiments discussed earlier. This corresponds to removing approximately 2% of the fan through flow.

Trailing edge blowing in general is a more attractive strategy to implement. Note that the hub pressure required for blowing would allow air to be bled from the early stages of the core compressor. In addition, trailing edge blowing requires less mass flow and passage flow area to gain considerably better deficit reduction. This is due to two effects: 1) deficit reduction with boundary layer suction is limited by finite trailing edge thickness; deficit reduction with trailing edge blowing is not; and 2) the radial pressure gradient set up by the blade rotation accelerates the flow moving outward radially, but impedes the removal of air to the hub as required for boundary layer suction through unshrouded blades.

The results shown here were for simple blade passage geometries without extensive estimation of pressure losses due to corners, expansions and contractions, etc. As blade passage geometries become more complex and the losses are more accurately evaluated, as described in Chapter 6, loss estimates will likely increase, requiring larger pressure differentials to drive the flow.

3.4 Summary and Conclusions

These preliminary studies of wake management strategies conducted by the author and others (Hayden [12], Sell [33], and Waitz *et al.* [38]) showed that significant reduction of the harmonics of the mean wake profile, as well as the magnitude of turbulent fluctuations, can be obtained. The results presented suggest that reductions in amplitude of the strongest tonal harmonics of greater than 25 dB may be achievable, as are reductions of approximately 7 dB in the component of broadband noise associated with wake turbulence. In particular:

1) For typical fan designs the blade passing frequency (BPF) acoustic modes are non-propagating. Noise is minimized by reducing 2*BPF and higher spatial harmonics of the wake. For Gaussian wake profiles, this is best achieved by maintaining maximum wake width while reducing the peak deficit.

2) Cascade testing of a representative fan geometry with trailing edge blowing showed

reductions in the time mean wake deficit of approximately 75% and reductions in the rms of the turbulent velocity fluctuations of 60% at 1.5 chord lengths downstream from the trailing edge. The amount of mass addition corresponded to 1.08% of the fan through flow. The reduction in amplitude of the strongest propagating circumferential acoustic mode for this case was estimated to be 24 dB. Other propagating modes were reduced between 7 dB and 18 dB. The reduction in turbulent velocity fluctuations would correspond to a 7 dB reduction in the component of broadband noise associated with wake turbulence.

3) Cascade testing of a representative fan geometry was also carried out with suction surface boundary layer removal. The best results were with suction at 80% chord and a mass flow rate corresponding to removal of 2.2% of the fan through flow. The boundary layer suction produced a reduction in the mean velocity deficit of 40% and mean width of 25% and a reduction in the rms of the turbulent velocity fluctuations of 35%. The reduction in amplitude of the strongest propagating circumferential acoustic mode for this case was estimated to be 4.4 dB. The reduction in the component of broadband noise associated with wake turbulence would be approximately 3.7 dB.

4) Analysis of internal flow requirements for suction and blowing passages in fan blades showed that the primary limitation for mass flow rate for both suction and blowing is choking in the internal passages. For a representative engine fan geometry choking limited the amount of mass removal through boundary layer suction to an amount which would allow reduction of the wake deficit by 40% if applied uniformly along the span. Trailing edge blowing, on the other hand, is not only more effective at smoothing the wake profile, but relatively easier to implement. Mass addition to obtain momentumless wakes along the full span should be possible in most wide chord fan geometries.

3.4.1 Limitations of the Preliminary Study

There are several characteristics typical of compressor flow fields which were not captured by the two-dimensional numerical and experimental models employed in the preliminary studies. In particular, low hub-to-tip ratio fans have radial variation in wake width/pitch and/or deficit, and the wakes are skewed circumferentially and stretched due to swirl downstream from the rotor, as discussed in Chapter 4. These effects could significantly alter

the ability to smooth the wake to the extent shown in the cascade experiments. Further, to accurately evaluate the radiated noise it is important to consider the three-dimensional acoustic mode structure. It is possible that a specific spanwise wake management distribution other than uniform might produce the largest noise reduction, and thus the effects of wake management should be studied in the context of coupling to radial acoustic modes.

Also, as discussed in Section 1.3, the presence of swirl produces different cut-on conditions between the blade rows compared to upstream or downstream, enabling mode trapping to occur. In addition, blades are never perfectly uniform in geometry or spacing, which enriches the harmonic content of the radiated tone noise. In general therefore, reduction of turbomachinery fan noise is expected to be more difficult than in cascade geometries.

CHAPTER 4

WAKE DECAY: EFFECT OF FREESTREAM SWIRL

4.1 Introduction

Understanding the behavior of wakes in turbomachinery is important not only for estimating noise generation, but also for determining overall performance, including efficiency and pressure rise, as well as estimating heat transfer and forced aeroelastic response. The work described in this chapter was carried out as an adjunct to the overall wake management study. The objective was to describe the effect of freestream swirl on the decay of turbomachinery blade wakes. The freestream swirl produced from a loaded, rotating blade row causes the wakes shed from the blades to be stretched and wrapped around the annulus as the wakes are convected downstream. As a result, both the relative orientation of the wakes with respect to the downstream stator blades, as well as the wake velocity deficit and width are changed. It will be shown that the magnitude of the changes in the wake velocity deficit and width are significant, and in general depend on the degree of stretching applied to the wake.

A simplified computational model was developed to illustrate these effects (Brookfield *et al.* [1]). This two-dimensional model allows for stretching of the wake along the wake centerline; factors such as secondary flow and radial wake transport are neglected to show the impact of stretching more clearly. The modeling and experiments were carried out on a M = 0.8 tip speed, low hub-to-tip ratio fan geometry typical of next-generation gas turbine

applications.

In Section 4.2 the kinematics of rotor wake skewing are described, followed in Section 4.3 by description of the simplified model used in the investigation. In Section 4.4 the results of the investigation are presented. The parametric dependence of wake decay on strain rate is first discussed, followed by comparison of the simplified numerical model to 1) data from the two-dimensional cascade facility where no stretching or skewing of the wakes occurs, 2) solutions obtained using the three-dimensional, unstructured mesh, Reynolds-averaged, Navier-Stokes code, and 3) experimental wake measurements taken on a fan stage. Implications for blade design are also discussed with regard to possible influences on fan wake decay for noise reduction. A summary and conclusions are provided in Section 4.5.

4.2 Kinematics of Rotor Wake Skewing

As discussed in Section 1.2, wakes shed by high speed compressors are highly complex. Despite the many detailed investigations that have been presented in the literature, however, many analytical wake mixing models and empirical curve fits used for noise estimation (*e.g.* Hanson [10]) are based on two-dimensional considerations of wake decay and only predict wake profiles to within 20 percent in deficit and/or width. Unfortunately, empirical curve fits based on rig wake data (*e.g.* Philbrick and Topol [29]) and numerical simulation (*e.g.* Suryavamshi and Lakshminarayana [36]) have shown little improvement in prediction of wake evolution. Since acoustic waves produced by the interaction of the wake structure with the stationary stator blades are driven by the spatial harmonics of the wakes, these errors would correspond to approximately 2 dB errors in noise prediction for the first few blade passing harmonics. Therefore, additional understanding of the underlying physics that determine three-dimensional wake decay is needed to not only improve predictions of noise from wake-stator interaction, but compressor and fan design in general.

4.2.1 Wake Kinematics

The freestream swirl downstream from a rotating blade row causes the blade wakes to be skewed tangentially and stretched. The resulting orientation of the wake with respect to the downstream stator row influences the spatial harmonic amplitudes of the wake when decomposed in the tangential and radial directions. Skewing thus affects the coupling of pressure fluctuations associated with wake-stator interaction to the three-dimensional acoustic modes, and as a result, can either increase or decrease the radiated noise. These effects are fairly well known. However, the effect that the stretching, which accompanies the wake skewing, has on the mixing and decay of the wake is less well understood. This phenomenon, which can also impact the radiated noise, is the primary focus of this chapter.

In this section, the kinematics of the wake are described and expressions that relate the skewing and stretching of the wake to the velocity field downstream from the rotor are derived. A wake vortex line that is shed from the rotor blade trailing edge will be followed as it is convected downstream. As the wake element is convected downstream it becomes skewed relative to the radial direction due to the swirl in the mean flow. This is shown schematically in Figure 4-1. The skew angle of the wake, ζ, relative to the radial direction is related to the increase in length of a wake element as a function of distance downstream. The length of a small wake element projected onto an axial plane at a downstream position, z, is given approximately by

$$\Delta L(z) = \sqrt{(dr)^2 + ([\delta\theta_w/\delta r]rdr)^2} \tag{4.1}$$

where θ_w is the angular position of the wake centerline. The angle traversed circumferentially in time, t, by the wake centerline is $\Delta\theta_w(z) = (V_\theta/r)t$, resulting in $\theta_w(z) = \theta_{te} + (V_\theta/r)t$. It is assumed that radial transport effects are small (this assumption will be discussed in greater detail in Section 4.3). The partial derivative of θ_w with respect to radius, r, for small initial wake skew angles, ζ_{te}, is

$$\frac{\delta\theta_w}{\delta r} = \frac{\tan\zeta_{te}}{r} - t\left(\frac{V_\theta}{r}\right)\left[\frac{1}{r} - \left(\frac{1}{V_\theta}\right)\left(\frac{dV_\theta}{dr}\right)\right] \tag{4.2}$$

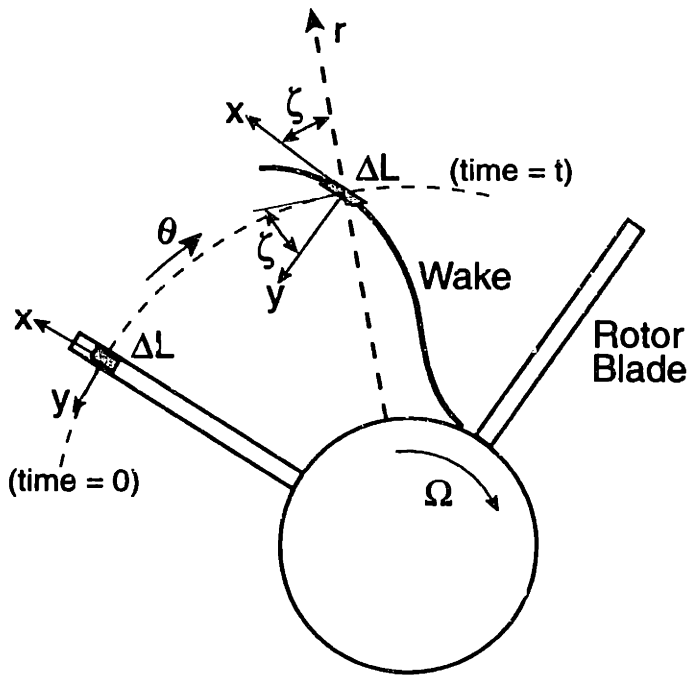

Figure 4-1: Schematic of wake skewing downstream of a rotating blade row

Time is given by $t = z/V_z$, thus the wake element length is

$$\Delta L(z) = dr\sqrt{1 + \left\{\tan\zeta_{te} - z\left(\frac{V_\theta}{V_z}\right)\left[\frac{1}{r} - \left(\frac{1}{V_\theta}\right)\left(\frac{dV_\theta}{dr}\right)\right]\right\}^2} \tag{4.3}$$

which is more conveniently written as $\Delta L = \mathcal{L}dr$.

Observing that the wake skew angle is given approximately by $\zeta(z) = \cos^{-1}(dr/\Delta L(z))$, the wake skew angle as a function of downstream distance is then given by

$$\zeta(r,z) = \cos^{-1}\left(1/\sqrt{1 + \left\{\tan\zeta_{te} - z\left(\frac{V_\theta}{V_z}\right)\left[\frac{1}{r} - \left(\frac{1}{V_\theta}\right)\left(\frac{dV_\theta}{dr}\right)\right]\right\}^2}\right) = \cos^{-1}\left(\frac{1}{\mathcal{L}}\right) \tag{4.4}$$

Further, to satisfy radial equilibrium for an incompressible flow with i) a uniform, non-swirling flow entering the rotor, ii) isentropic flow through the rotor, and iii) no axial pressure gradient downstream from the blade row, gradients in the freestream tangential

velocity are related to gradients in axial velocity by

$$V_z \frac{dV_z}{dr} = \left(\Omega - \frac{V_\theta}{r}\right) \frac{d(rV_\theta)}{dr} \tag{4.5}$$

The axial velocity is constant for a free vortex flow where $V_\theta \propto 1/r$. Note that Eq. 4.5 can be modified to account for more general inlet conditions and non-isentropic rotor flow if required (*e.g.* Kerrebrock [18]). Using Eqs. 4.4 and 4.5, the skew angle of a wake element downstream from the blade row can now be determined as a function of r and z. Equations 4.3 and 4.5 can be used to determine the local change in wake length and the local strain rate, which will be used in the analyses presented in Section 4.3.

In Eqs. 4.3 and 4.4, the influence of the freestream swirl is represented by the two terms in the square brackets. The magnitude of the first term is set largely by the hub-to-tip ratio of the rotor. The second term represents the influence of radial gradients in the tangential velocity field. Depending on the hub-to-tip ratio and the spanwise loading distribution, either term can be dominant, but in typical fan geometries they are of comparable magnitude.

4.2.2 Wake Skewing for Simplified Core Compressor and Fan Stages

To illustrate the behavior of wakes in typical turbomachine situations, the simplified case where the rotor has been designed to provide constant work along the span is considered. For an incompressible flow with uniform, non-swirling inlet conditions, this design strategy results in a free vortex flow field where the mean tangential velocity varies linearly with radius, such that $V_\theta(r) = V_{\theta t}(r_t/r)$, and the axial velocity is radially uniform. The downstream tangential velocity is higher at the hub, decreasing monotonically toward the tip. This causes a radial fluid line to skew as it convects downstream since the hub fluid traverses a longer arc length in the period of time required to reach a given downstream location. For this case, the expression for the skew angle of a wake element as a function of radius and downstream distance is

$$\zeta(r,z) = \cos^{-1}\left(1/\sqrt{1+\left\{\tan\zeta_{te} - \left(\frac{2z}{r}\right)\left(\frac{V_\theta}{V_z}\right)\right\}^2}\right) \tag{4.6}$$

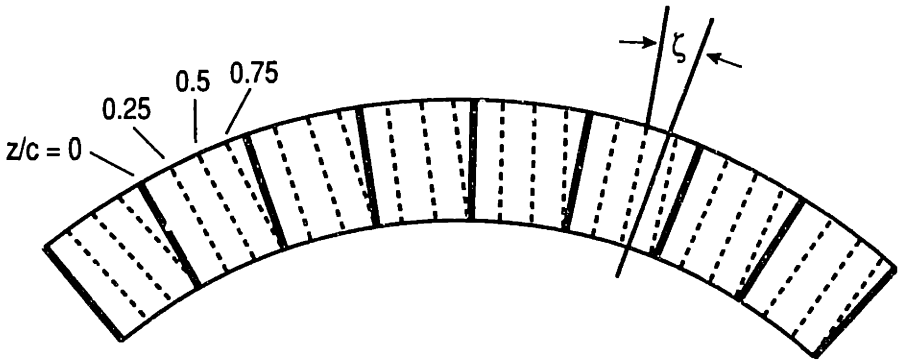

Figure 4-2: Schematic of wake skew for a typical core compressor geometry

Equation 4.6 can be used to determine the conditions for which skewing of the wake is important. For a core compressor, a typical hub-to-tip ratio is 0.8 and a typical rotor-stator spacing is 0.4 rotor chords (approximately 3 percent of the tip radius). Thus, assuming $\zeta_{te} = 0$ and $V_\theta/V_z = 1.0$, the wake skew angle is only about 3 degrees at the stator location, resulting in little stretching of the wake. Plots of the wake orientation with downstream distance for this case are shown in Figure 4-2. For a typical fan geometry, however, the hub-to-tip ratio is 0.5 and the rotor-stator spacing is 1.5 fan chords. The resulting wake skew angle at inlet to the stator is approximately 30 degrees, and the wake is stretched 15 percent. The stretching increases to 38% at 2.5 chords downstream. Plots of wake orientation for a free vortex fan flow are shown in Figure 4-3. Thus, in low hub-to-tip ratio machines with large rotor-stator axial spacing, significant skewing of the wake is possible. In Section 4.4 the effects that the stretching, which is associated with this wake skew, has on the mixing of the wakes will be presented.

Effects of Radial Gradients in Axial Velocity

In general, fan and core compressor stages vary somewhat from free vortex designs. As a result (Eq. 4.5), radial gradients in both axial and tangential velocity are present downstream from the blade row, and the behavior of the wake becomes more complicated to describe. Radial gradients in the mean axial velocity field result in portions of the wake being transported more quickly to the stator location, allowing relatively less time for the

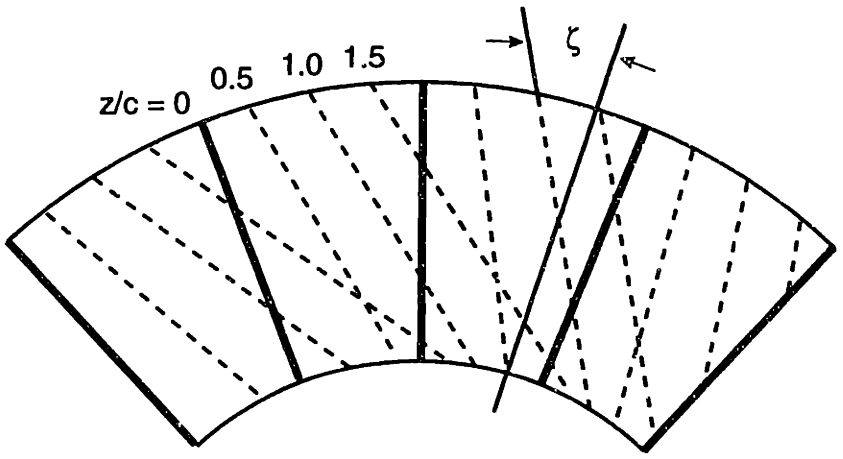

Figure 4-3: Schematic of wake skew for a typical fan stage geometry

wake to skew and mix. Thus wake elements measured at different spanwise locations, in a given axial plane, have been shed from the blade at different times. As a result, the projection onto an axial plane of a wake vortex line, which is shed from the blade at a particular time, is in general different from the intersection that the wake makes with that axial plane when the wake passes through it (the intersection is comprised of many different vortex lines). It is the wake angle associated with the first of these, the projection of a wake vortex line onto the axial plane (given by Eq. 4.4), which is relevant for determining the effect of stretching on wake evolution.

To illustrate these angle differences, a radial equilibrium flow with uniform tangential velocity was examined. For this case the axial velocity as given by Eq. 4.5 increases by approximately 27% from the hub to the tip. The vortex lines in the wake are skewed relative to the radial direction at an angle of approximately 16 degrees at 1.5 chords, as given by Eq. 4.4. However, due to the radial gradient in axial velocity, the wake intersects an axial plane later at the hub than at the tip. As a result, the wake is inclined only 4.5 degrees from the radial direction as it crosses the axial plane at 1.5 chords. Thus, for cases with radial gradients in axial velocity, the angle associated with the intersection of the wake with an axial plane is not a good estimate of the orientation of the vortex lines in the wake, even

for relatively small variations in axial velocity.

4.3 Simplified Numerical Model

As was discussed in the previous section, wakes downstream from fan rotors are typically skewed relative to the radial direction. This skewing stretches the wake and results in an increase in the length of the wake. A simplified numerical model was developed to study the effect of this stretching on the decay of wakes. The development of the model is described below. The cascade facility, Navier-Stokes solver, and fan rig facility that were used to provide data for comparison to the simplified model are described in Chapter 2.

The wake was assumed to be steady and incompressible, and each spanwise section of the wake was assumed to be uniform with constant strain along its centerline (i.e. solved in a strip theory sense). The computational domain is shown in Figure 4-4 in the wake relative frame, as defined in Figure 4-1. The x-axis corresponds to the wake centerline, y is the axis normal to the wake centerline in an axial plane, and z is the freestream flow direction, which would be out of the page in Figure 4-4. The effects of stretching on wake decay were parameterized as a function of the local strain rate as is typical in mixing problems (see *e.g.* Waitz *et al.* [40]).

The local strain rate, ϵ, is given by the expression $\epsilon = (1/\Delta L)[\delta(\Delta L)/\delta t] = (V_z/\Delta L)*$ $[\delta(\Delta L)/\delta z]$. Taking the derivative of the wake element length, ΔL, with respect to z, and rewriting Eq. 4.3 as $\Delta L = \mathcal{L}dr$, then

$$\frac{\delta(\Delta L)}{\delta z} = -dr\left(\frac{V_\theta}{V_z}\right)\left(\frac{\sqrt{(\mathcal{L}^2-1)}}{\mathcal{L}}\right)\left[\frac{1}{r}-\left(\frac{1}{V_\theta}\right)\left(\frac{dV_\theta}{dr}\right)\right] \tag{4.7}$$

Using this expression in the relation for the strain rate provides the local wake strain rate as a function of downstream distance, z, and radial position:

$$\epsilon(r,z) = -V_\theta\left(\frac{\sqrt{(\mathcal{L}^2-1)}}{\mathcal{L}^2}\right)\left[\frac{1}{r}-\left(\frac{1}{V_\theta}\right)\left(\frac{dV_\theta}{dr}\right)\right] \tag{4.8}$$

In the simplified numerical model, the velocities in the x, y, and z directions respectively are u, v, and w. Stretching of the wake was prescribed by imposing a velocity $u_s = \epsilon x$ for

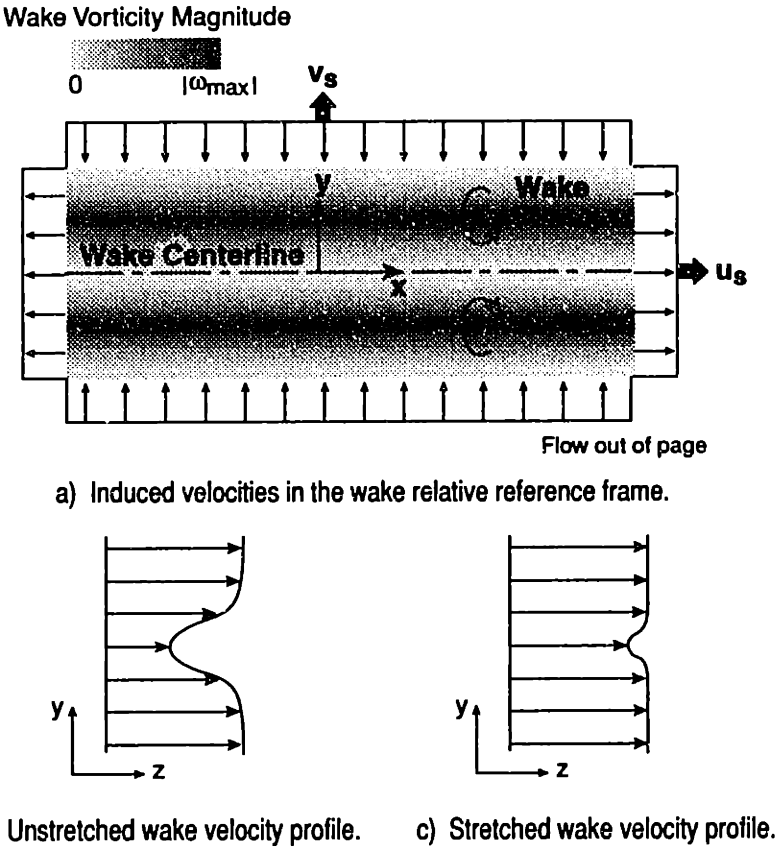

Figure 4-4: Schematic of computational domain used to model effect of strain on wake decay

uniform strain rate, ε, in the x-direction. Continuity of mass dictates that the stretch velocity is balanced by $v_s = -\varepsilon y$, to maintain zero axial pressure gradient. The velocities in the x and y directions are then given by $u = u_s + u'$ and $v = v_s + v'$, respectively, where u' and v' are the velocities induced by wake mixing, and u' is assumed to be zero. Assuming derivatives in x and z are much smaller than derivatives in y, the equations for continuity of mass and y and z-momentum are written as:

$$\frac{\delta(u_s + u')}{\delta x} + \frac{\delta(v_s + v')}{\delta y} + \frac{\delta w}{\delta z} = 0 \tag{4.9}$$

$$w\frac{\delta w}{\delta z} + v\frac{\delta w}{\delta y} = \nu\frac{\delta^2 w}{\delta y^2} \tag{4.10}$$

$$w\frac{\delta v}{\delta z} + v\frac{\delta v}{\delta y} = \nu\frac{\delta^2 v}{\delta y^2} \tag{4.11}$$

Note that the stretch induced velocities, u_s and v_s, will cancel from the mass continuity equation, such that only the entrainment or mixing induced velocity, v', appears in the y-direction giving

$$\frac{\delta v'}{\delta y} + \frac{\delta w}{\delta z} = 0 \tag{4.12}$$

In the analysis, it was assumed that the effect of axial pressure gradients on the wake is negligible and that radial velocities are small. Analyses based on Hill [13] can be used to show that the first of these assumptions is good for duct area changes of less than 2%, which are typical of many fan duct designs. For these situations the change in wake centerline velocity due to the pressure gradient is expected to be less than 3%. The validity of the second assumption, that of small radial velocities is more difficult to evaluate. In the experiments and numerical simulations presented in Section 4.4, outward velocities along the wake axis (the x-direction in the wake-relative frame) of approximately 10% of the freestream velocity magnitude were found. Such velocities would result in a relatively small redistribution of wake fluid (movement on the order of 7% of span by the time the wake reaches the stator location). It is also expected that radial wake transport will increase the

rate of turbulent exchange in the wake. Indeed there was a difference in effective viscosity apparent between the cascade experiments and the rig tests presented in Section 4.4. This difference scales approximately with the increase in mean shear found by adding the radial velocity measured in the rig tests to the two-dimensional wake velocity profile measured in the cascade. Such an approximation for the effective viscosity might be applied if the simplified model were to be used to predict wake evolution without *a priori* knowledge of the flow field.

The equations were solved using centered finite difference methods. Validation of the method and comparisons to experimental results are presented in Section 4.4.

4.4 Results and Discussion

In Section 4.4.1 the simplified numerical model is compared to measurements taken in the cascade facility. Then, the effects of skewing and stretching of the wake on the wake velocity deficit and width are parameterized in Section 4.4.2. Section 4.4.3 presents the comparison of the model to the three-dimensional computations, and in Section 4.4.4 estimates from the model are compared to measurements obtained from the fan rig. A brief discussion of implications for the design of turbomachine blades for more rapid wake decay (and thus less noise production from wake/stator interaction) is given in Section 4.4.5.

4.4.1 Validation of the Simplified Numerical Model with 2-D Cascade Data

The numerical scheme used to integrate Equations 4.10-4.12 was first validated by comparing the results of the simplified numerical model to an exact error function solution for a double diffusion layer problem. The computed diffusion layer profile matched the analytical solution with less than 1 percent error. Following this, the model was compared to cascade wake measurements. For two-dimensional wakes the turbulent viscosity is approximately constant with downstream distance (see *e.g.* Schlichting [32]). Therefore, a constant effective viscosity, ν, of 0.0275 m^2/s was chosen for these comparisons. This value of viscosity provided the best match between the modeled and measured two-dimensional wake decay

rates. The calculations were initiated using a Gaussian velocity profile that was specified to approximate the measured wake profile at 0.5 chords downstream. The calculated velocity profiles at 0.5, 1.0, 1.5, and 2.5 chords are compared to the measured cascade (see Section 2.4) profiles in Figure 4-5. For this two-dimensional case with no stretching, both the velocity deficit and width are accurately captured by the model. The calculated velocity deficit is within 5 percent of the measured values at 1.5 and 2.5 chords.

4.4.2 Effect Of Wake Skew

Stretching of the vorticity associated with the wake increases the strength of the vorticity and thus the gradients in $w(y)$. At the same time, the induced normal velocity, v_s, moves the shear layers closer together, as illustrated qualitatively in Figure 4-6. This effectively results in more rapid mixing and an increase in the wake centerline velocity, but also smaller wake width in the y-direction than with no stretching. Thus, the momentum thickness of the wake measured normal to the wake centerline decreases with applied stretching. However, because the stretching is a result of wake skewing, the wake is oriented at some angle relative to the radial direction. Thus, when the velocity deficit is measured in the circumferential direction (*i.e.* at the skew angle, ζ, through the model wake) the width is increased over the unstretched wake. This results in constant wake momentum thickness downstream (when measured in the circumferential direction) as is required for momentum conservation under conditions of zero axial pressure gradient and no spanwise transport of wake fluid.

The effects of stretching on wake mixing will now be examined quantitatively using the simplified model. Different strain rates were applied to the wake to determine the parametric trends for wake velocity deficit and width. The initial conditions and effective viscosity obtained from the comparison to the cascade measurements were used for the investigation. Constant strain rates downstream from the rotor ranging from $\epsilon = 0$ to 600 were specified. These strain rates cover the range of interest for typical turbomachine applications.

Figure 4-7 shows the wake velocity profiles in the wake relative frame at 1.5 chords downstream for the different strain rates examined. The reductions in both velocity deficit and width of the wake with increased strain rate are shown. The reductions in deficit and

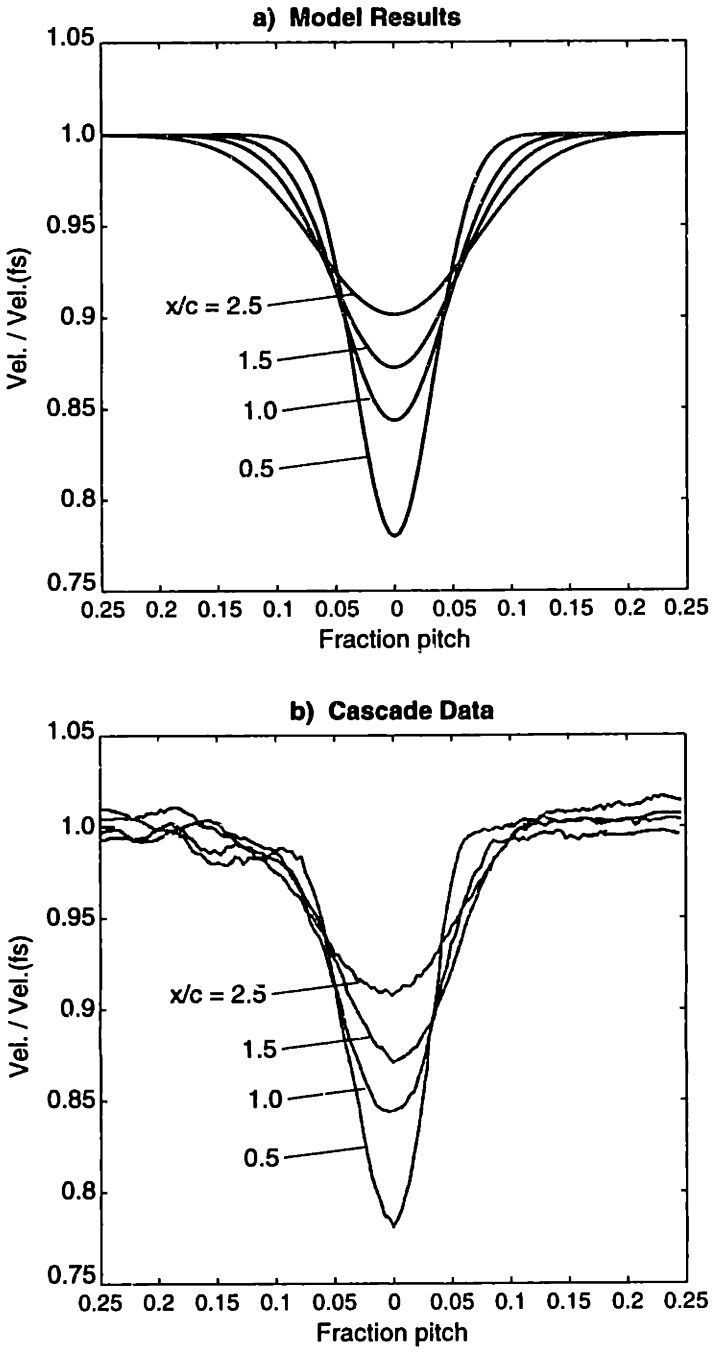

Figure 4-5: Comparison of simplified model to measured cascade data

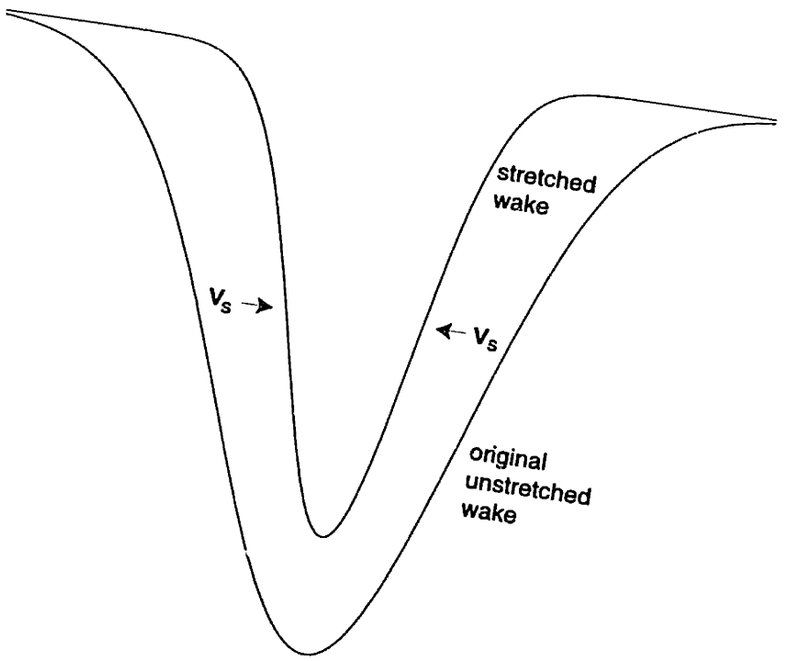

Figure 4-6: Qualitative schematic of the effect of applied strain (out of the page) on the wake profile

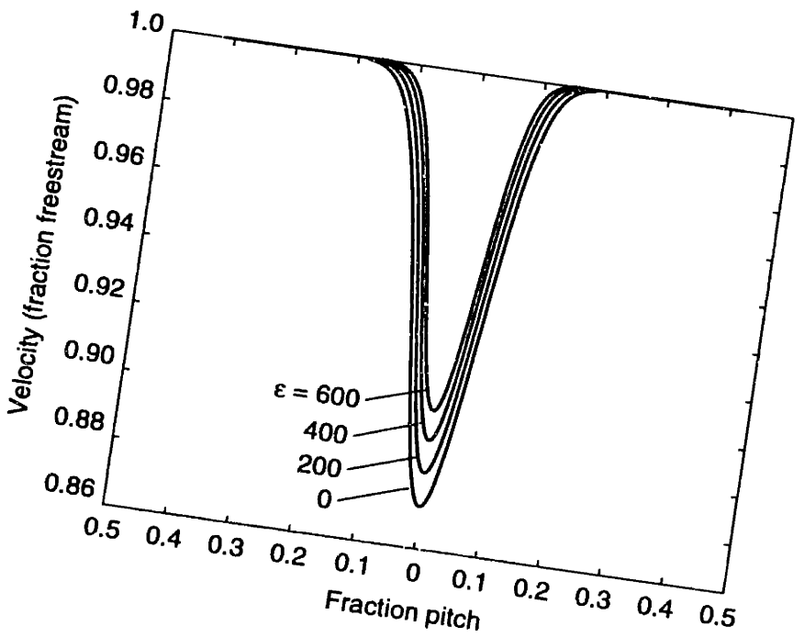

Figure 4-7: Calculated wake profiles at 1.5 chords downstream with various amounts of applied strain

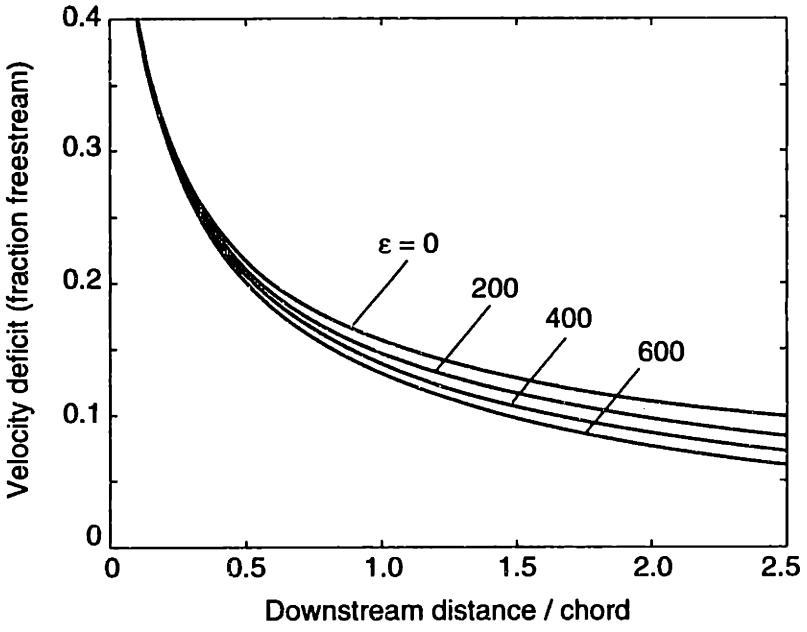

Figure 4-8: Decay of wake centerline velocity deficit versus downstream distance for various amounts of applied strain

width increase with downstream distance, since the wake is stretched to ever increasing length. The decay of the centerline velocity deficit with downstream distance is plotted in Figure 4-8 for the different strain rates. There is rapid decay of the velocity deficit in the near-wake region (up to about 0.5 chords), followed by a decrease in decay rate with downstream distance. For a typical fan rotor-stator spacing of approximately 1.5 chords and a strain rate of 600 (which would roughly correspond to the local strain rate near the hub for a rotor designed for constant radial work input and a hub-to-tip ratio of 0.5), the wake at the stator position will have a velocity deficit of about 78 percent of that which would be predicted with an unstretched cascade wake. For prediction of unsteady loading on the stator blade and radiated noise, this would result in an error of approximately 2 dB. A more detailed discussion of the effect of wake skew and stretch on wake harmonic amplitudes, and thus the effect on radiated tonal noise, is presented in Section 4.4.5.

As discussed previously, the wake momentum deficit measured normal to the wake (the y-direction in the wake relative frame) decays with downstream distance as the wake is stretched. A plot of this decay is presented in Figure 4-9. For the example given above of a

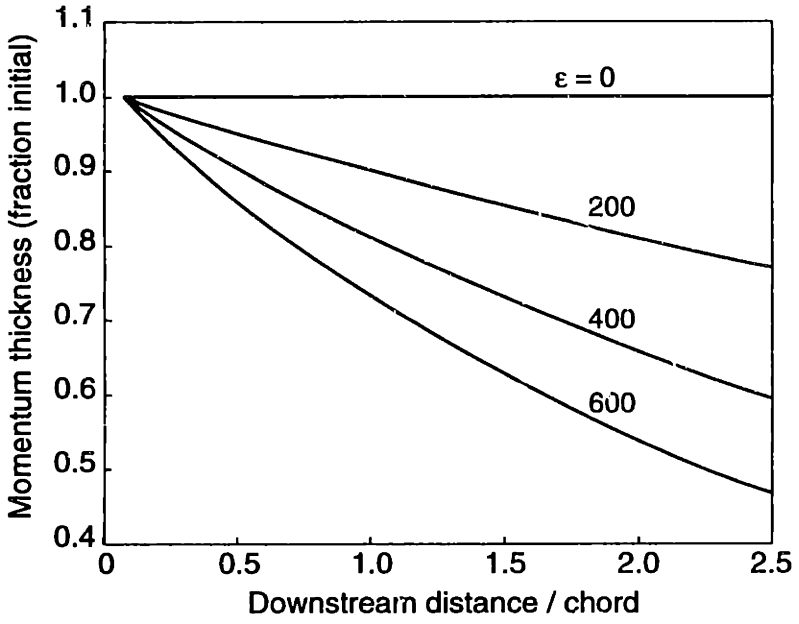

Figure 4-9: Decay of momentum deficit (in wake relative frame) versus downstream distance with various amounts of applied strain

constant radial work fan with a hub-to-tip ratio of 0.5, the momentum thickness is decreased by approximately 37 percent compared to the unstretched case at 1.5 chords downstream from the rotor. This decay in the momentum thickness in the wake relative frame is related to the wake skew angle by $\theta/\theta(0) = \cos\zeta$.

4.4.3 Comparison with Navier-Stokes Simulations for High Speed Fan Rotor

Rotors typically have radial gradients in both axial and tangential velocity resulting in a radial variation of the wake skew angle, and thus spatial variations in the strain rate applied to the wake. Also, radial wake transport is often observed. To investigate the effects of stretching on wake mixing in a situation that is more representative of a fan application, the wake velocity profiles obtained from the simplified numerical model were compared to the results of three-dimensional computations (see Section 2.5). The appropriate strain rates were obtained by plotting contours of relative Mach number to determine the skew angle of the wake at 0.1, 0.5, 1.0, and 1.5 chords downstream. These plots are shown in Figure

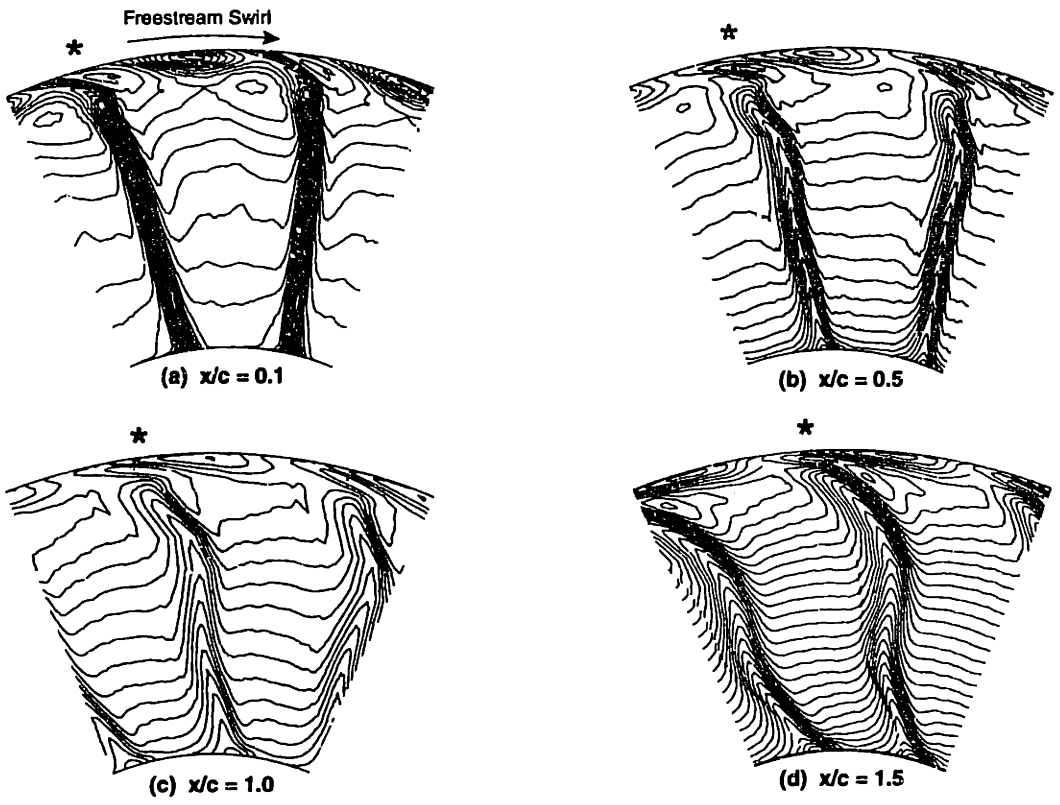

Figure 4-10: Calculated flow contours in axial planes downstream of the fan showing the wake skew

4-10.

Seventy-five percent span was chosen for the comparison since it is a region of high wake stretching, and this spanwise location is outside the tip clearance flow region. Further, since there is approximately zero radial gradient in axial velocity at 75% span, the angle of intersection of the wake with an axial plane (as shown plotted in Figure 4-10) corresponds approximately to the angle of the projection of a wake vortex line onto that plane. (Recall that the projection is the relevant angle for determining the effects of wake stretching due to swirl, as discussed in Section 4.2.2) A Gaussian profile that approximates the computational wake profile at 0.1 chords was used for the initial condition, and the effective viscosity, ν = 0.040 m^2/s, was set in the simplified model to match the change in the computational wake profile between 0.1 and 0.5 chords. This is an acceptable procedure for setting the effective viscosity because there is negligible wake stretching between the trailing edge and 0.5 chords downstream. (Indeed, the effect of wake stretching on velocity deficit in this

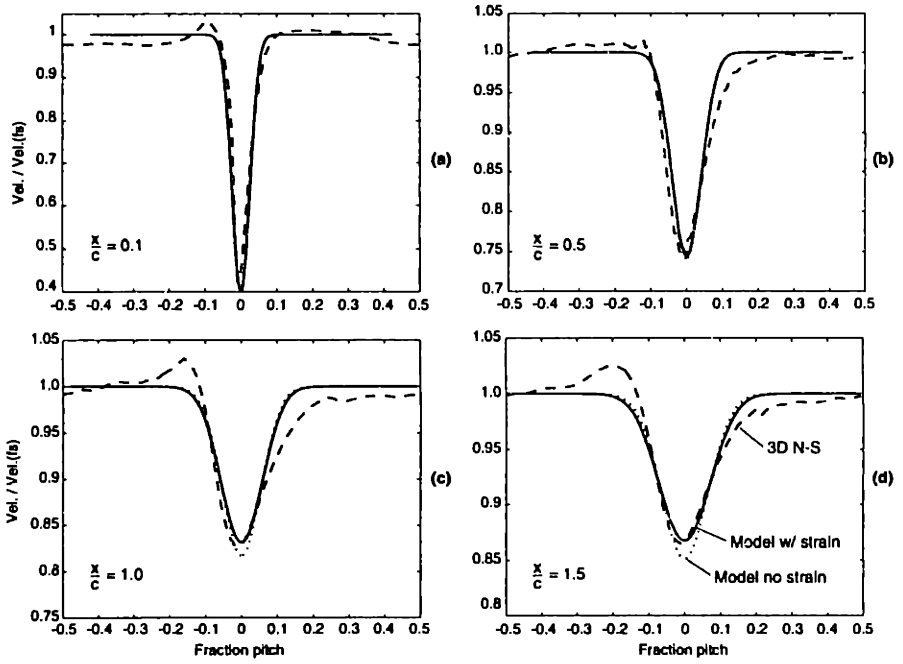

Figure 4-11: Comparison of simplified model to Navier-Stokes simulation

region is less than 2 percent.) A comparison of the wake profile from the three-dimensional simulation, the unstretched model wake, and the stretched model wake at 0.5 chord is shown in Figure 4-11b. The model wake captures the overall features of the wake obtained from the three-dimensional simulation.

The wake velocity profiles at 1.0 and 1.5 chords downstream are compared to the results of the three-dimensional computations in Figures 4-11c and 4-11d. The predicted wake velocity deficits compare within 3.5 percent. Also plotted are the wake profiles that would result if no stretching were introduced into the simplified model. The reduction in wake velocity deficit due to stretching corresponds to approximately 12 percent of the unstretched deficit at 1.5 chords downstream from the blade.

4.4.4 Comparison with Fan Wake Measurements

In this section the results of the simplified calculation procedure are compared to measurements behind a rotating blade row (see Section 2.6). To accomplish this, measured wake data immediately downstream from the blade row was used to set the initial wake profile

for the computation, and the change in measured wake profiles between 0.1 and 0.5 chords was used to set the effective viscosity. This is the same procedure that was used for the comparison to the Navier-Stokes solution presented in Section 4.4.3. Wake measurements at 1.0 and 1.5 chords downstream were then compared to the simplified model with and without strain imposed.

The wake initial condition was established by matching the momentum deficit measured downstream from the fan and the measured wake velocity profile at 0.1 chords to within 3 percent of velocity deficit and 32 percent of the width. Because the wake at 0.1 chords was relatively small compared to the 4-way probe, the measurements were less accurate at this location. Further, oscillations in measured flow Mach number were observed that are believed to have resulted from amplification of unsteady vortex shedding on the probe due to wake impingement. These oscillations (which can be seen in Figures 4-12a and 4-12b) are thus an artifact of the measurement device and were not present in the flow (see Section 5.2.2). It was found, however, that the initial condition used at 0.1 chords had little impact on the comparison between calculated and measured wake characteristics, provided the momentum thickness of the model wake at 0.1 chord was set to match that measured downstream. The effective viscosity was set to obtain the measured velocity deficit at 0.5 chords, resulting in $\nu = 0.044$ m^2/s. As discussed in Section 4.3, the difference between this viscosity and that required to match the results of the cascade experiments scales roughly with the increase in mean shear due to the additional radial transport velocity measured in the rig tests. Therefore, setting the model viscosity in this manner may approximately capture the increased turbulent exchange associated with radial wake transport.

Wake measurements taken at 50 and 75 percent span in the experiment were used with a rotor shaft speed encoder signal to estimate the tangential position of the wakes. The wake unsteadiness and variability made it difficult to discern the center of the wake in raw data traces to better than 2 percent pitch, and a more detailed mapping of the wake position as a function of radius was not possible at this time. However, the measurements taken at 50 and 75 percent span indicate that the wake was more highly skewed in the outer one-half span than the results of the three-dimensional computations presented in Section 4.4.3 suggest. The measured data show the 75 percent span wake to be shifted an additional 10 percent in pitch from the calculation relative to the 50 percent span wake location at

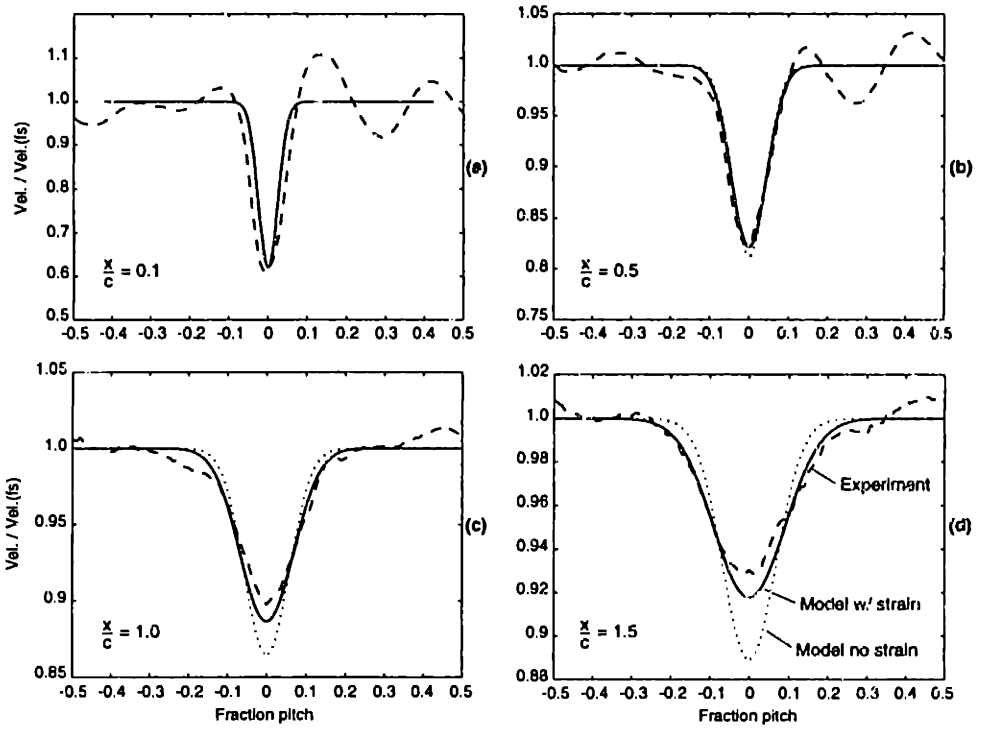

Figure 4-12: Comparison of simplified model to fan rig wake measurements

1.5 chords. This is caused by a slightly different loading distribution in the Navier-Stokes solver as discussed in Section 2.5. With the loading shifted relatively further outboard on the blade in the simulations, the simulated skew angle is lower than that measured in the experiment. The wake skew angle in the rig test was approximately 55 degrees at 1.5 chords and 75 percent span.

The strain rates corresponding to the wake skew angles measured in the data were specified in the simplified numerical model. The results are compared to the measured wake velocity profiles in Figures 4-12a-d. As in Section 4.4.3, all of the wake comparisons were carried out for the 75 percent span location. Addition of stretching to the model accounts for 73 percent of the difference between two-dimensional wake evolution and the wake decay in the flow field downstream from the rotating fan. The additional differences between the estimated wake and the measured wake may be due to experimental uncertainty and/or redistribution of wake fluid and increased mixing due to radial transport. Nonetheless, the results imply that wake stretching has a significant effect on the behavior of the wake.

4.4.5 Wake Stretching Effects on Radiated Acoustics

The effects of wake skewing on the radial coupling of the wake-stator interaction to the duct acoustic modes are relatively well known and are discussed in more detail in Section 1.4. These effects are due to the radial variation in time at which the wake intersects the stator leading edge, and changes in this distribution can either increase or decrease the resulting acoustic amplitudes. In addition to these changes, however, the effect of skewing on the mixing rate of the wake can further affect the radiated noise. To examine these effects, the modeled wakes at 1.5 chords for the stretched and unstretched cases were spatially decomposed into harmonics of blade passing frequency (BPF). The resulting harmonic amplitudes for the two cases are plotted in Figure 4-13. These are compared to the harmonic amplitudes obtained from the wakes measured in the fan rig tests. Since the amplitudes of radiated acoustic modes associated with wake-stator interaction are approximately linear with the amplitudes of the wake harmonics impinging on the stator blades, reductions in acoustic levels can be estimated from the reductions in the wake harmonics. The reductions are given by ΔdB = 20 log10 (A_{st}/A), where A is the harmonic amplitude of the unstretched wake and A_{st} is the harmonic amplitude of the stretched wake. Stretching of the wakes results in noise reductions of about 2.5 dB for the 2*BPF mode, and more than 5 dB for the higher harmonics.

These reductions imply that fan loading could be tailored to produce perhaps 3 dB reductions in radiated tonal noise[1] above present designs. If studies are conducted to determine the most dominant spanwise sections of the stator with respect to coupling with the propagating acoustic modes, then the blade loading can be designed to give greatest stretching in that region. This would be done through designing the blades to give appropriate radial gradients in the tangential and axial velocities. The reductions associated with more rapid wake decay must be considered with respect to additional changes (either increases or decreases) in radiated noise due to variation in coupling to duct modes as the wakes are skewed relative to the stator blades. Further, design changes to achieve noise reductions

[1]It is also expected that wake stretching will have some impact on the turbulent fluctuations in the wake which give rise to broadband noise. Studies of wakes downstream from wings presented by Miranda and Devenport [24] generally showed large increases in turbulence levels in regions of the wake undergoing straining *when the turbulence stresses were normalized by the local length and velocity scales.* However, the absolute (dimensional) magnitudes of the turbulent stresses changed little with increased strain rate.

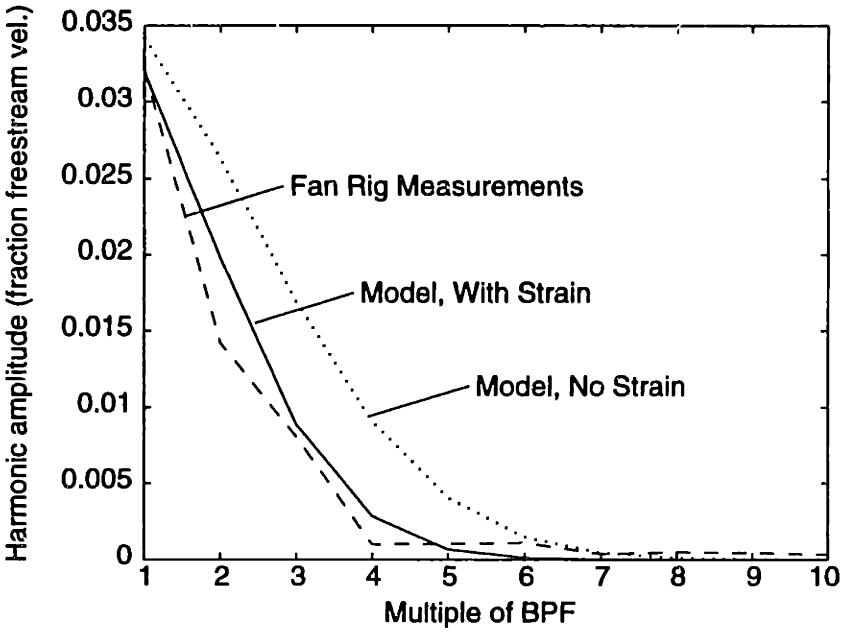

Figure 4-13: Harmonic composition of wake profiles at 1.5c for the experimental data, the simplified model with applied strain, and the model with no strain

must be balanced against efficiency and performance issues to determine the best overall design.

4.5 Summary and Conclusions

A simplified numerical model was developed to quantitatively describe the effects of swirl on the decay of wakes downstream from rotating blade rows. Freestream swirl skews the wake tangentially and stretches the wake as it is convected downstream. These effects cause the velocity deficit to be reduced and the width of the wake measured in the circumferential direction to be increased. Wake skewing has little impact on wake decay when rotor-stator axial spacing is less than 40% chord, and/or the hub-to-tip ratio is over 0.9. However, for low hub-to-tip ratio machines with large rotor-stator spacing, typical of fans in high bypass ratio turbomachines, stretching of the wake and the associated effects on the wake decay characteristics can be large. In such situations, 50 percent reduction in the wake velocity deficit and associated harmonics is possible.

Cascade wake profiles were estimated to within 5 percent of the velocity deficit by the simplified numerical model with no stretching. With the introduction of stretching into the model, the wake velocity deficit downstream of a next-generation high bypass ratio turbofan was estimated to within 13 percent. It was shown that the change in wake decay with stretching may be responsible for between 2.5 and 5 dB changes in radiated tone noise.

Use of constant effective viscosity, constant average strain rate, and spanwise uniform wake elements were seen to capture most of the essential physics of the wake mixing behavior. However, better comparison might be achieved by incorporation of a more realistic three-dimensional wake geometry, the variation in strain rate, and the increase in effective viscosity due to radial transport with downstream distance (as the ratio of radial velocity to wake velocity deficit in the freestream direction increases).

Finally, this study suggests that the use of cascade data and two-dimensional wake mixing models for the prediction of unsteady aerodynamics and noise associated with wakes interacting with downstream blade rows must be done with care. However, the application of wake stretching to simplified models of wake mixing can be used to extend the range of applicability of two-dimensional cascade data.

CHAPTER 5

BASELINE FAN DATA

To provide a reference data set for later comparison to the wake management blades, a solid-bladed rotor was built and tested. Measurements of the downstream flow field were then used in conjunction with data obtained from the preliminary assessment (Chapter 3) to design the trailing edge blowing rotor blades.

In this chapter, data reduction techniques will first be briefly described in Section 5.1, followed by experimental measurements from the baseline rotor. Downstream flow field measurements using the 4-way probe will be presented in Section 5.2, stator pressure measurements will be presented in Section 5.3, and a discussion of the physical mechanisms of stator unsteady loading will follow in Section 5.4. Results from the in-duct microphones will be shown in Section 5.5, and a brief summary and conclusions will follow in Section 5.6.

5.1 Data Reduction Methodology

Before presenting the baseline fan rig data, a brief description of the data reduction techniques used to generate the plots is appropriate. Most of the data presented in this thesis is the ensemble-average of several runs (with each run comprising of 4 to 6 rotor revolutions). For various flow variables, average profiles (periodic components) and harmonic content are often presented, as well as the profiles of the unsteadiness in the signal. The errors in the presented quantities were estimated from the standard deviation of the signals and

are presented as 95% confidence intervals. In addition, spectra of the signals are shown for estimation of the spectral content of the random fluctuations. A more detailed discussion of the data reduction procedure is presented in Appendix A.

5.2 Flow Field Measurements: 4-way probe (Baseline rotor)

Downstream of the rotor, the flow field was measured at four axial locations: 0.1, 0.5, 1.0, and 1.5 rotor midspan axial chords (hereafter referred to simply as chord, c). The first location (0.1c) is directly behind the trailing edge of the blade, and 1.5c is just in front of the stator row, which has its leading edge at 1.7c. The primary measurement location is 1.5c, since the flow field entering the stator row is of most interest. Measurements at 1.5c were taken at 25, 50, 75, and 87.5 percent span, and at 50 and 75 percent span for the other three axial locations. Since each measurement location required several runs to obtain enough blade passing periods for adequate determination of the mean profile and its harmonics, there was not adequate time to obtain a more complete mapping of the flow field.

5.2.1 Measurements at 1.5 chords

Flow field measurements at 1.5 chords downstream of the rotor were of the most interest, since they most closely represent the flow field entering the stator blades. At this location, the blade passing period ensemble-averaged relative Mach number profiles will be shown. 95 percent confidence intervals are included on the relative Mach number profiles, as well as all other ensemble-averaged flow profiles presented in this thesis. Harmonic content of the relative Mach number profile and the turbulence intensity profile (standard deviation) will also be shown. Additional flow variables including Mach number components, flow angles, and static and total pressures are presented in Section 7.2 in comparison to the trailing edge blowing rotor without injection. However, it should be noted here that the absolute Mach number typically has about one-half the variation of the relative Mach number across the blade pitch. Thus, the wake velocity perturbations seen by the stator blades are partially due to flow speed variations and partly due to angle of attack variation. The distribution of tangential flow angle harmonic content was observed to be virtually identical to the

distribution of relative Mach number harmonic content.

Note, all data traces were set by the index of the rotor and thus the beginning of the blade passing period of each plot is with the rotor in the same position. Therefore, the relative location of the wake in a plot indicates the relative position of the wake in the flow field. The skew of the wake can thereby be determined. In addition, to allow ease of comparison between different data sets, the scales used in the plots is kept consistent (except for the high-loading data presented in Appendix C). For example, all Mach number profile plots at 1.5 chord use a range of $\Delta M=0.15$, and plots at 0.1, 0.5, and 1.0 chord use a range of $\Delta M=0.30$.

25% span

The ensemble-averaged relative Mach number profile at 25% span, 1.5c is shown in Figure 5-1 a, along with its harmonic content (first five multiples of BPF) and the turbulence intensity (b and c, respectively). Ninety-five percent confidence intervals are shown for each quantity. At this position, the wake deficit (relative frame) is approximately 16% of the freestream, with the harmonic content decreasing rapidly with multiple of BPF. Note that the level of turbulence intensity is roughly equal to the mean wake deficit and larger than the wake harmonics. This turbulence intensity is the measure of all fluctuations in the time-accurate signal that are not periodic on the rotor blade passing period. Therefore, blade-to-blade variations in the flow field (multiples of shaft frequency) will also be included in the measure of turbulence intensity, in addition to the true turbulence level.

The other flow variables for the solid blades are shown as solid lines in Figures 7-2 through 7-17 and are not repeated here. The absolute Mach number has about 60% of the mean deficit as the relative Mach number. This is because the wake velocity perturbation is approximately in the direction of blade stagger, not in the mean absolute flow direction. For a given loading condition, the mean absolute Mach number may be perfectly uniform across the pitch. If this was the case, the wake perturbation would be composed entirely of a change in tangential flow angle. For 25%, 1.5c, however, the wake perturbation imposed on the stator blades is partly flow speed (absolute Mach number), and partly angle of attack variation (tangential flow angle).

Variations in all three components of Mach number (axial, tangential, and radial) are roughly equal and are approximately 8% of the freestream Mach number. Like Mach number, the absolute total pressure has about one-half the variation of the relative total pressure, with very little variation in the static pressure across the wake.

50% span

Midspan profiles of relative Mach number (ensemble-averaged profile), its harmonics, and the turbulence intensity are shown in Figure 5-2 a,b, and c. Additional 50% span flow variables can be seen in Figures 7-7 through 7-9. At this midspan position, the absolute profiles have less than one-half the variation of the relative profiles, and the relative Mach number wake velocity deficit (8%) manifests itself in the absolute velocity field primarily as tangential flow angle variation (4.5 degrees).

75% span

The same flow quantities shown at 25% and 50% span locations are plotted for 75% span in Figure 5-3 and in Figures 7-11 through 7-13. This 75% spanwise location is approximately at the maximum loading position (in terms of total pressure rise). Again, variation in absolute Mach number and total pressure are less than one-half that of their relative frame counterparts, resulting in the perturbations being primarily angle of attack in the absolute frame. Also, the relative Mach number turbulence intensity is approximately equal to the relative Mach number mean profile deficit.

87.5% span

The flow field at 87.5% span is presented in Figure 5-4 and in Figures 7-15 through 7-17. Observe the wide width of the velocity deficit at this position. This large increase in wake width compared to the other spanwise locations is due to wake skewing. In the outer 25% span, the wake is highly skewed, and thus by conservation of momentum, the width is significantly increased. A more detailed discussion of the effects of wake skew is presented in Chapter 4.

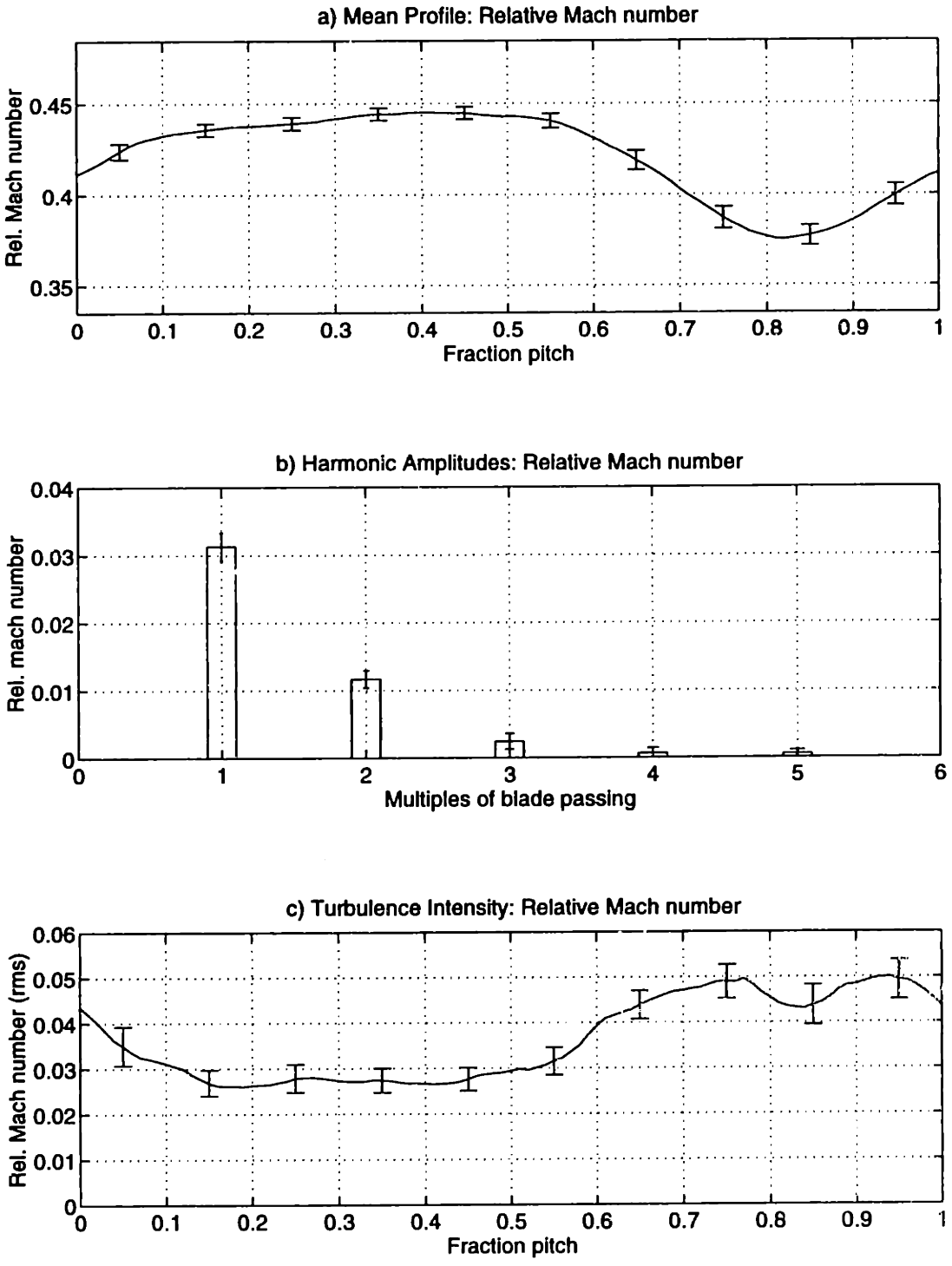

Figure 5-1: Relative Mach number ensemble-averaged profile, mean harmonic content, and turbulence profile at 25% span, 1.5c for the baseline rotor

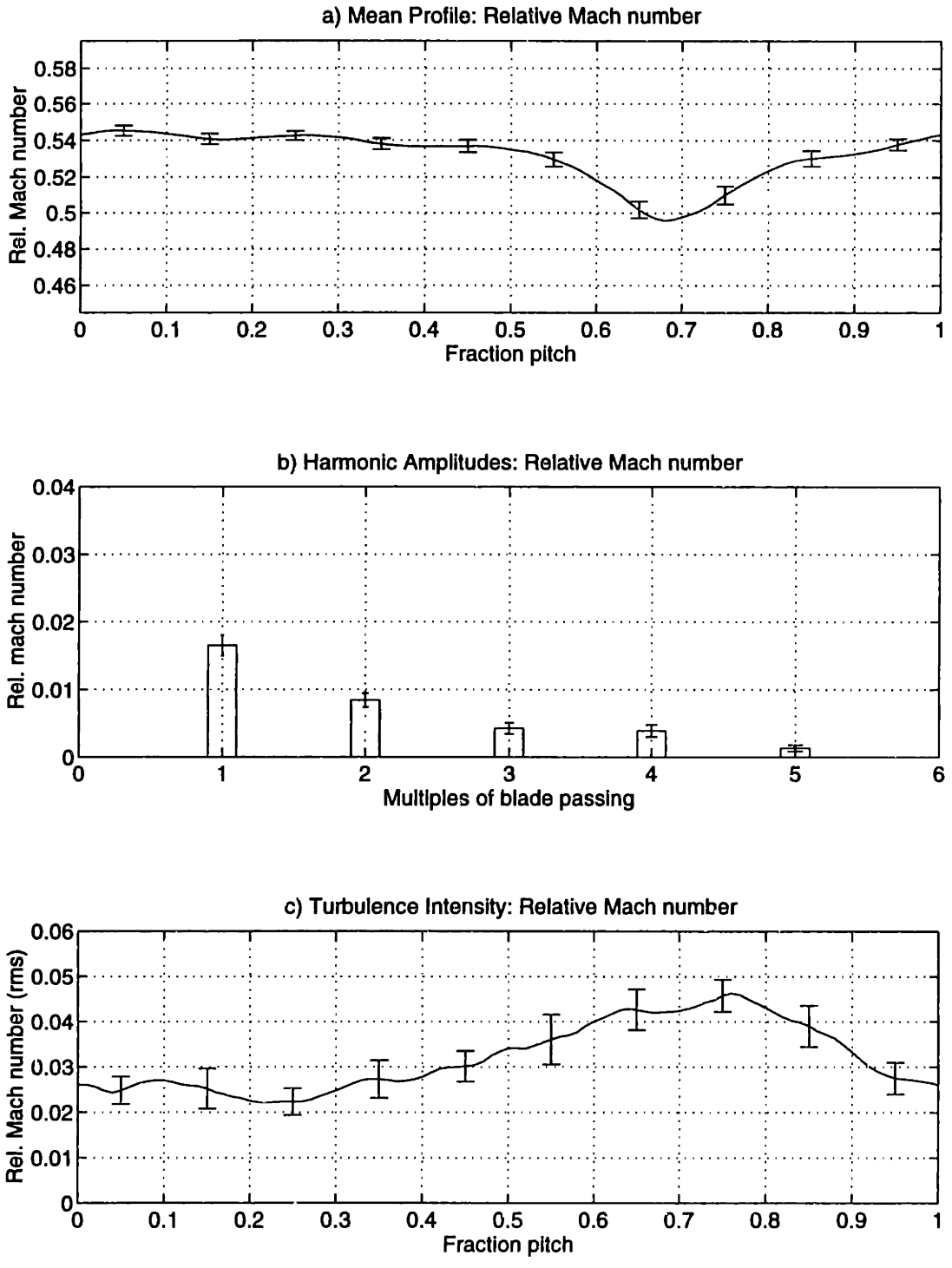

Figure 5-2: Relative Mach number ensemble-averaged profile, mean harmonic content, and turbulence profile at 50% span, 1.5c for the baseline rotor

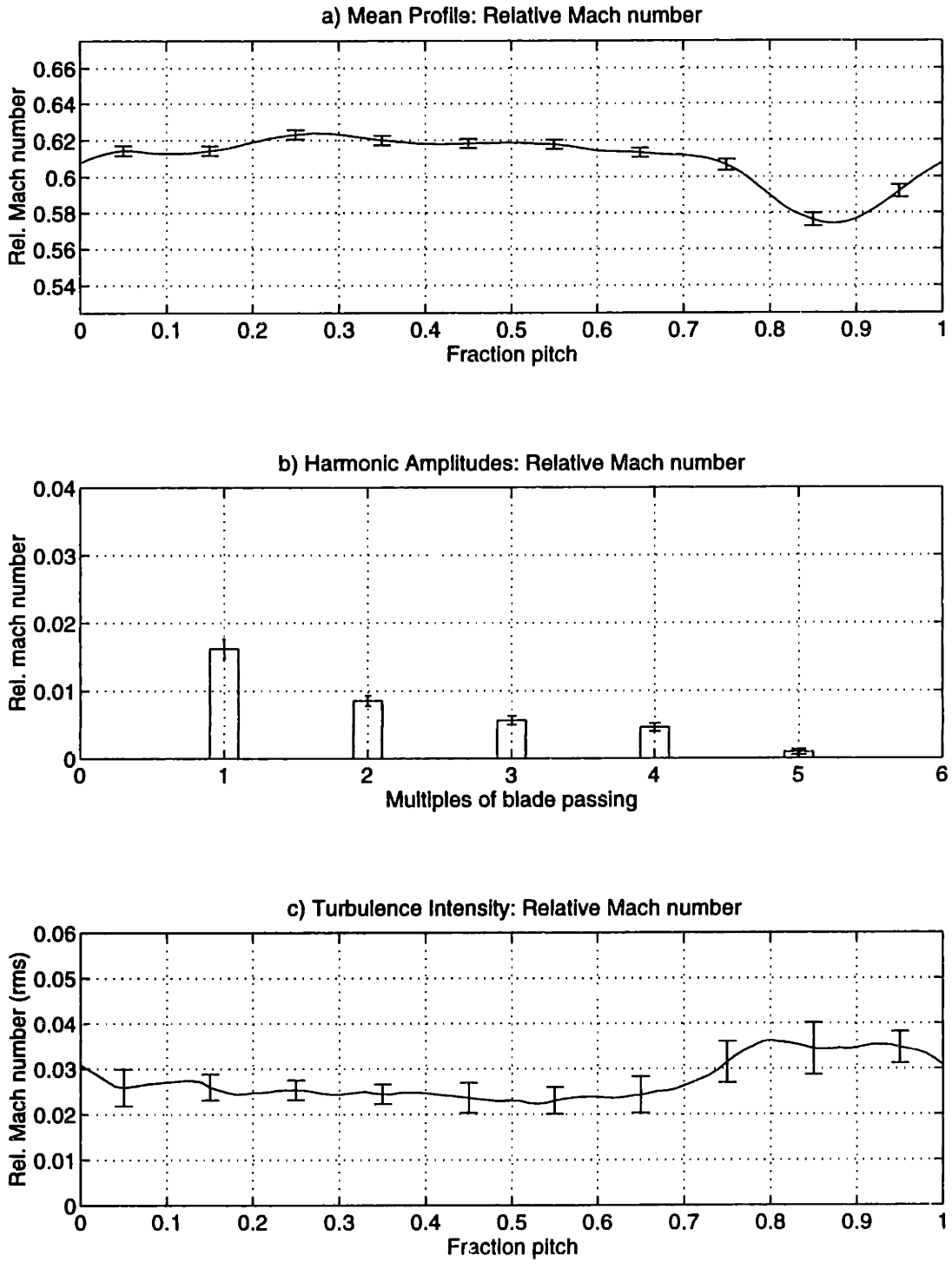

Figure 5-3: Relative Mach number ensemble-averaged profile, mean harmonic content, and turbulence profile at 75% span, 1.5c for the baseline rotor

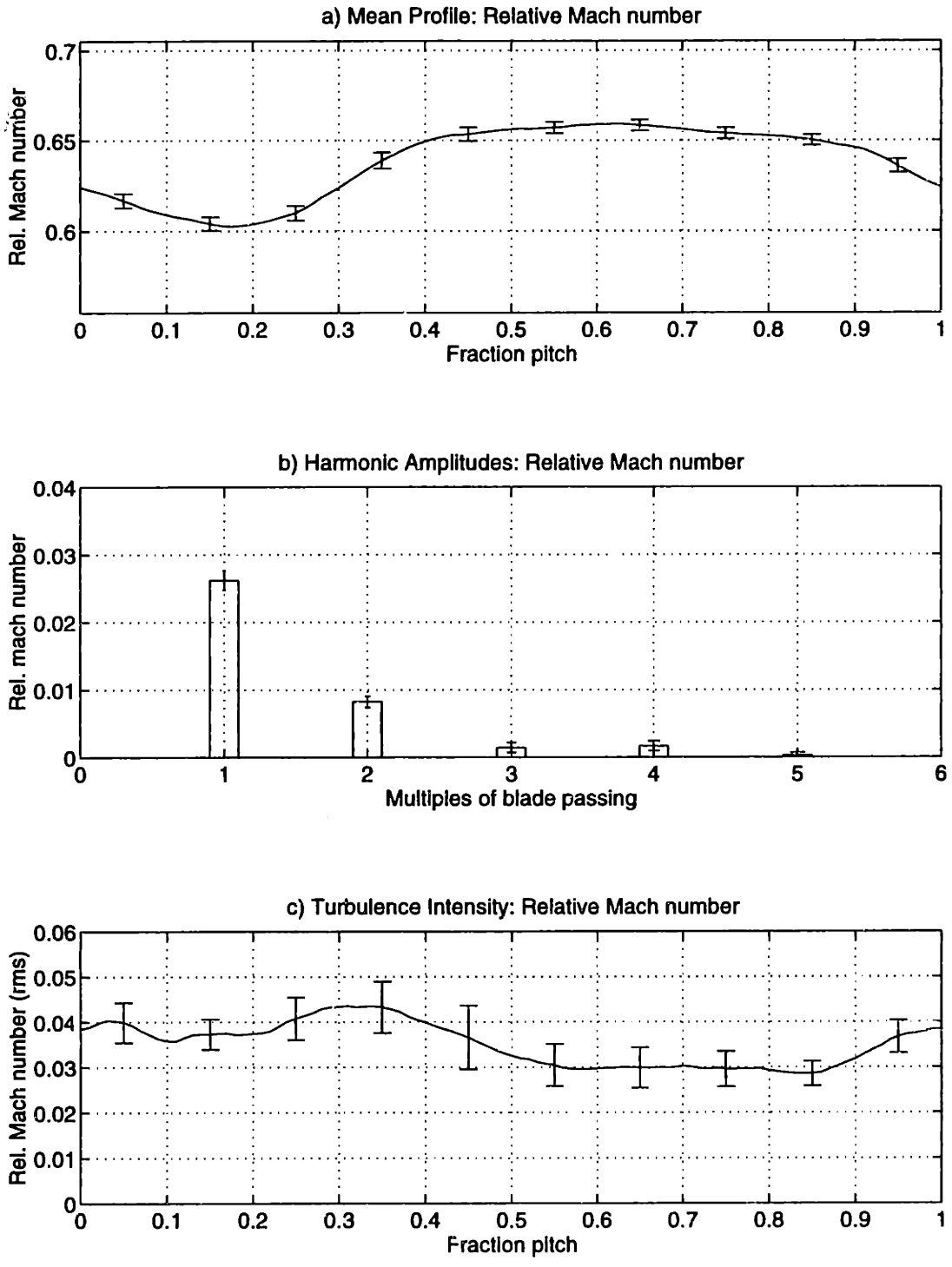

Figure 5-4: Relative Mach number ensemble-averaged profile, mean harmonic content, and turbulence profile at 87.5% span, 1.5c for the baseline rotor

In addition to wake skewing, the tip clearance flow begins to merge with the wake in the outer 10-15% span at 1.5 chords downstream of the rotor. However, since tip clearance flows at 1.5 chords downstream of the rotor are typically spread across a large portion of the pitch, the increase in flow field harmonic content associated with the tip clearance flow is primarily blade passing frequency, BPF. Note that the 2,3,...*BPF harmonic amplitudes, as well as the turbulence intensity are roughly the same as at 50% and 75% span. For this fan geometry, only the higher harmonics, 2,3,...*BPF, directly generate radiating acoustic waves (with 2*BPF dominating by approximately 16 dB), so it is believed that the tip clearance flow does not greatly increase the overall radiated tonal noise.

Relative Mach number spectra

The ensemble-averaged relative Mach number profiles and harmonics, as well as the calculated turbulence intensity profiles, have been presented, but thus far no information regarding the spectral content of the turbulence has been presented. The turbulence intensity is certainly important, but the spectral distribution of the turbulence is crucial to the impact on perceived noise level. Therefore, the full spectra of the relative Mach number data traces were calculated and are presented (up to 6*BPF) in Figures 5-5 through 5-8 for measurements taken at 25%, 50%, 75%, and 87.5% span, 1.5 chords downstream of the rotor. As with the previously presented data, the spectra are averages of four runs each.

The tone amplitudes (at multiples of BPF) are the same as the harmonic amplitudes presented earlier, but now the full turbulence spectrum can be seen. The electrical noise in the experimental facility was measured to be approximately .0001 (above about 1/20 BPF), so it is less than 1/4th of the turbulence level over the range shown. The turbulence spectra bulge above the "floor" value around the tones, as is typically seen in noise spectra from gas turbine engines. In Chapter 8 these spectra will be compared to the spectra with trailing edge blowing wake management to examine changes to both turbulence amplitude and distribution.

As stated, the spectrum of the turbulence is important for estimating and modeling broadband noise generation, but an additional aspect of the spectrum is also important. The turbulence intensity presented earlier is that due to any fluctuation in the flow field other

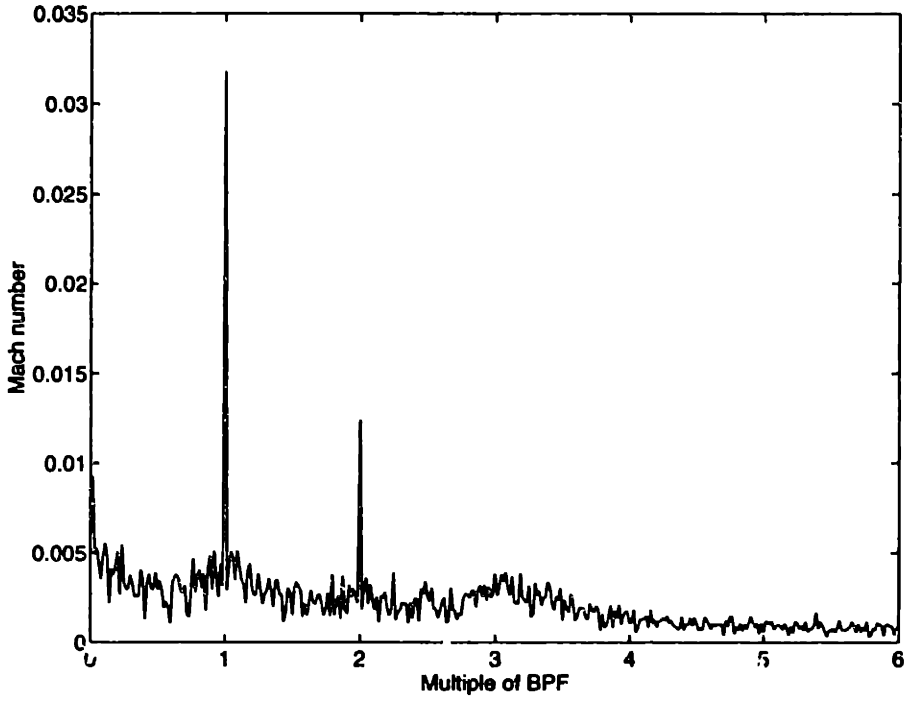

Figure 5-5: Rotor flow field relative Mach number spectrum (4 run average) at 25% span, 1.5c for baseline rotor

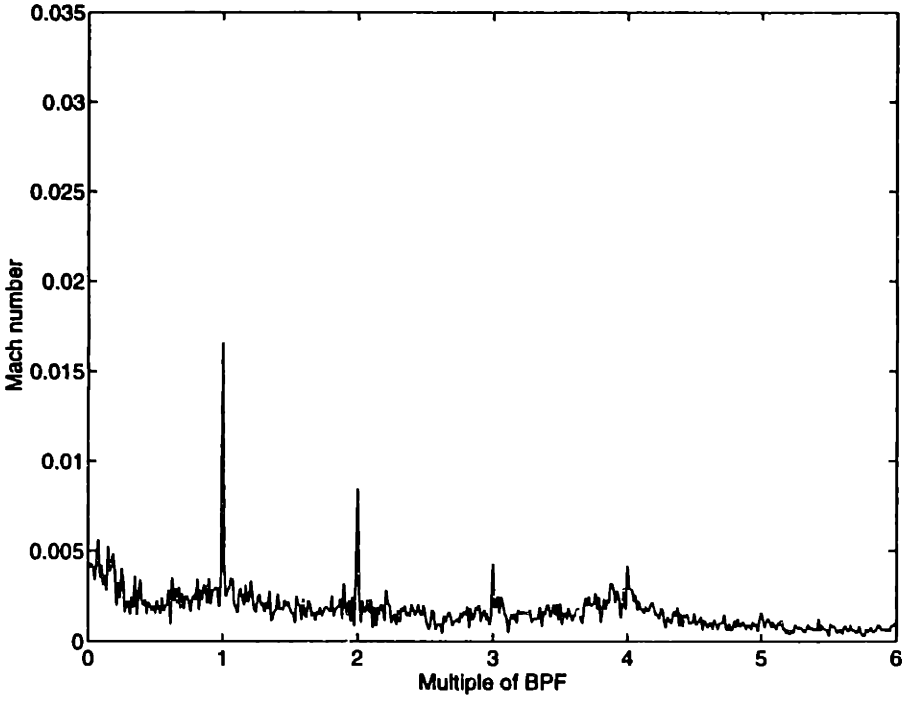

Figure 5-6: Rotor flow field relative Mach number spectrum (4 run average) at 50% span, 1.5c for baseline rotor

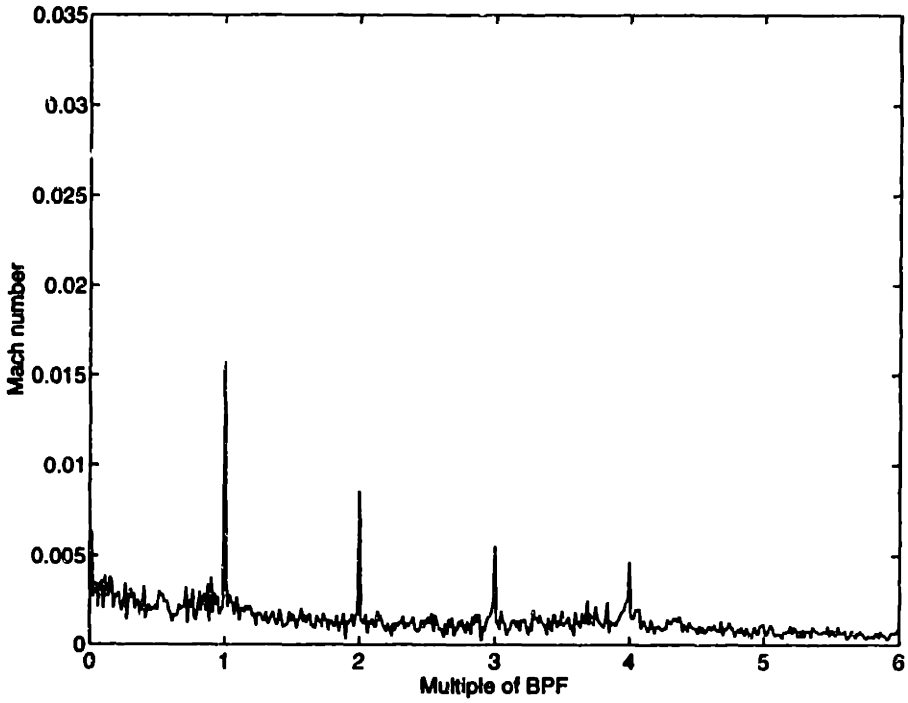

Figure 5-7: Rotor flow field relative Mach number spectrum (4 run average) at 75% span, 1.5c for baseline rotor

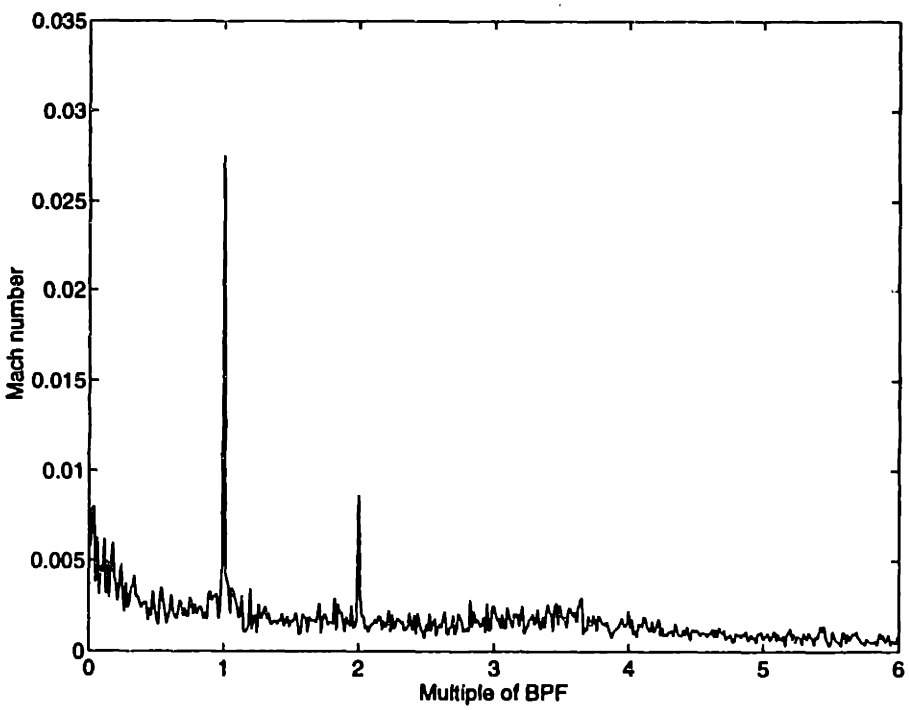

Figure 5-8: Rotor flow field relative Mach number spectrum (4 run average) at 87.5% span, 1.5c for baseline rotor

than multiples of rotor blade passing period (BPF). Since rotor blade-to-blade variations will cause modes at all multiples of shaft frequency to be generated in the rotor wake/stator interaction (and rotor blades can never be perfectly uniform in shape, spacing, and tip clearance) these modes can greatly influence the turbulence intensity. Therefore, the full spectrum should always be analyzed for not only the turbulence spectrum, but also the presence of any multiples of shaft frequency. The presence of these shaft multiples can be seen in Figure 5-8 where small spikes are seen protruding above the broadband noise floor at the first four multiples of shaft frequency (*i.e.* at 1/16th, 1/8th, 3/16th , and 1/4 BPF), as well as at some higher multiples. Since these spurious tones are not much larger than the broadband in this case, they should not greatly effect the overall measure of the turbulence intensity.

Summary of measurements at 1.5 chord

As discussed in Section 1.3, the important quantities for rotor wake-stator interaction are the harmonic content of the flow field for tonal noise and the turbulent intensity for broadband noise. In addition, however, the phasing of the wake intersecting the stator is very important for the generation of tonal noise.

Examining the harmonic content of the relative Mach number profiles (Figures 5-1, 5-2, 5-3, and 5-4 b) the amplitude of the 2*BPF harmonic is seen to be roughly constant along the span. The tip region is often thought to the most critical to noise generation because the propagating modes are often only rotating supersonically in the outboard regions. However, since the velocity deficit associated with the tip clearance flow is broad at the face of the stator, it is made up primarily of blade passing frequency and does not impact the higher harmonics to a significant degree. Therefore, the tip clearance flow does not appear to be the dominant tonal noise source for this fan stage.

In addition, note the relative location of the wake centerlines for the different spanwise locations in the blade pitch. Using these positions, the skew of the wake can be estimated. The offset of 50% span from 25% span is approximately -13% pitch, the 75% span location is shifted from the midspan location by approximately 19% pitch, and the 87.5% location is shifted an additional 30% pitch from the 75% span location. This results in a wake that is

bowed dramatically in the tangential direction, which matches (qualitatively) the contour plots in Section 4.4.3 from computations. The wake skew creates phase variation in the intersection of the wake on the stator and thus strongly affects the coupling to the acoustic modes, which have large radial variation for low hub-to-tip ratio geometries.

Like the relative Mach number harmonics, the peak turbulence intensity appears to be approximately constant with spanwise position. Even into the tip clearance flow region, where the area of high turbulence level is broader, the peak intensity is approximately the same. However, the total amount of turbulent kinetic energy is much larger in the tip region than along the span. Unfortunately, the relative importance of the turbulence peak level versus circumferential extent on radiated broadband noise is not known and is expected to be design dependent.

5.2.2 Measurements at 0.1, 0.5, and 1.0 chords

Since the primary measurement location was 1.5c, data gathered at upstream locations was limited to 50% and 75% spanwise locations. As will be discussed, unsteady vortex shedding on the 4-way probe measurement device created oscillations in the measured quantities, limiting their usefulness particularly at the 0.1 and 0.5 chord axial positions.

The plot scales for each measurement position at 0.1, 0.5, and 1.0c are all identical. This is done for easy comparison of profiles with downstream distance and spanwise position. However, the scale of relative Mach number plots are 3 times that used at 1.5c, and the scales of the harmonics and turbulence intensity are 2 times those used at 1.5c. Ensemble-averaged plots of total pressures, static pressure, Mach numbers, and flow angles (all with 3 times the scale used at 1.5c) for 0.1, 0.5, and 1.0c are given in Appendix E.

Trailing edge measurements

Measurements at 0.1 chords downstream of the rotor were made at both 50% and 75% span. Plots of the averaged relative Mach number profile, its harmonics, and the turbulence intensity are shown in Figures 5-9 and 5-10 for 50% and 75% span, respectively. The oscillations at approximately 4*BPF are quite evident. Since the width of the wake is

about 25% pitch, the amplitude of the 4*BPF harmonic is expected to be large, but the oscillations in the freestream flow have no physical basis other than being induced by the probe. Additional flow variables are presented in Appendix E.

Upon examination of the flow around the elliptical head of the 4-way probe, the frequency of vortex shedding (assuming a Strouhal number of 0.2) was calculated to be approximately 4*BPF for this fan stage geometry operating condition[1]. For flow field measurements at 1.5 chord, the 4th harmonic of the wake is relatively small and therefore does not amplify the shedding significantly. However, at positions closer to the rotor, 0.1c in particular, the 4th harmonic of the wake is larger and amplification of the natural vortex shedding of the probe is evident. The pressure field around the probe oscillates enough to significantly alter the unsteady measurement of the flow field.

To test the above hypothesis, a fin was carefully glued to the back of the probe head, as shown in Figure 5-12. The fin was made out of foam and thus made insignificant change to the structural characteristics of the probe. Since the addition of the fin turns the probe head into a lifting body, any measured flow oscillations caused by amplification of natural structural modes of the probe would increase. The fin, however, should dramatically decrease any vortex shedding from the probe.

With the addition of the fin, a test was completed at 0.1 chord and 75% span. The resulting relative Mach number data is plotted in Figure 5-11. Comparing this data to Figure 5-10, the near complete elimination of the 4*BPF oscillation is evident. Because the fin would change the calibration of the probe, however, it was decided to use the probe in the original state until a permanent fin could be manufactured and the probe recalibrated. This permanent modification was indeed done for the results presented in Chapter 7. In addition, the most important measurements were at 1.5 chords where the oscillations were relatively small.

[1]The shedding frequency was also estimated for a transonic rotor geometry previously tested in the Blowdown Compressor. The shedding frequency for that geometry was approximately 2*BPF, and the downstream data indeed showed 2*BPF oscillations in the freestream flow field.

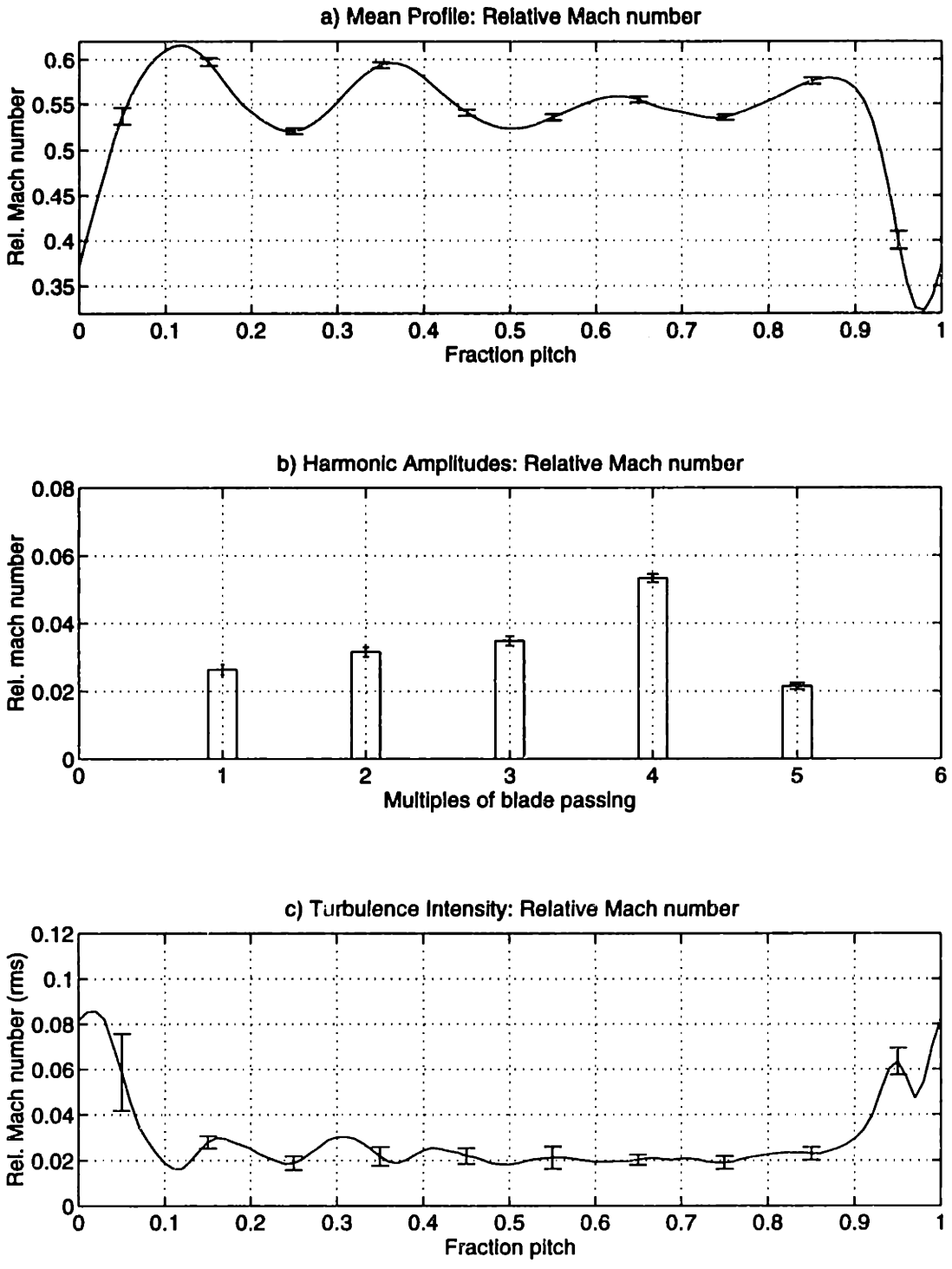

Figure 5-9: Relative Mach number ensemble-averaged profile, mean harmonic content, and turbulence profile at 50% span, 0.1c for the baseline rotor

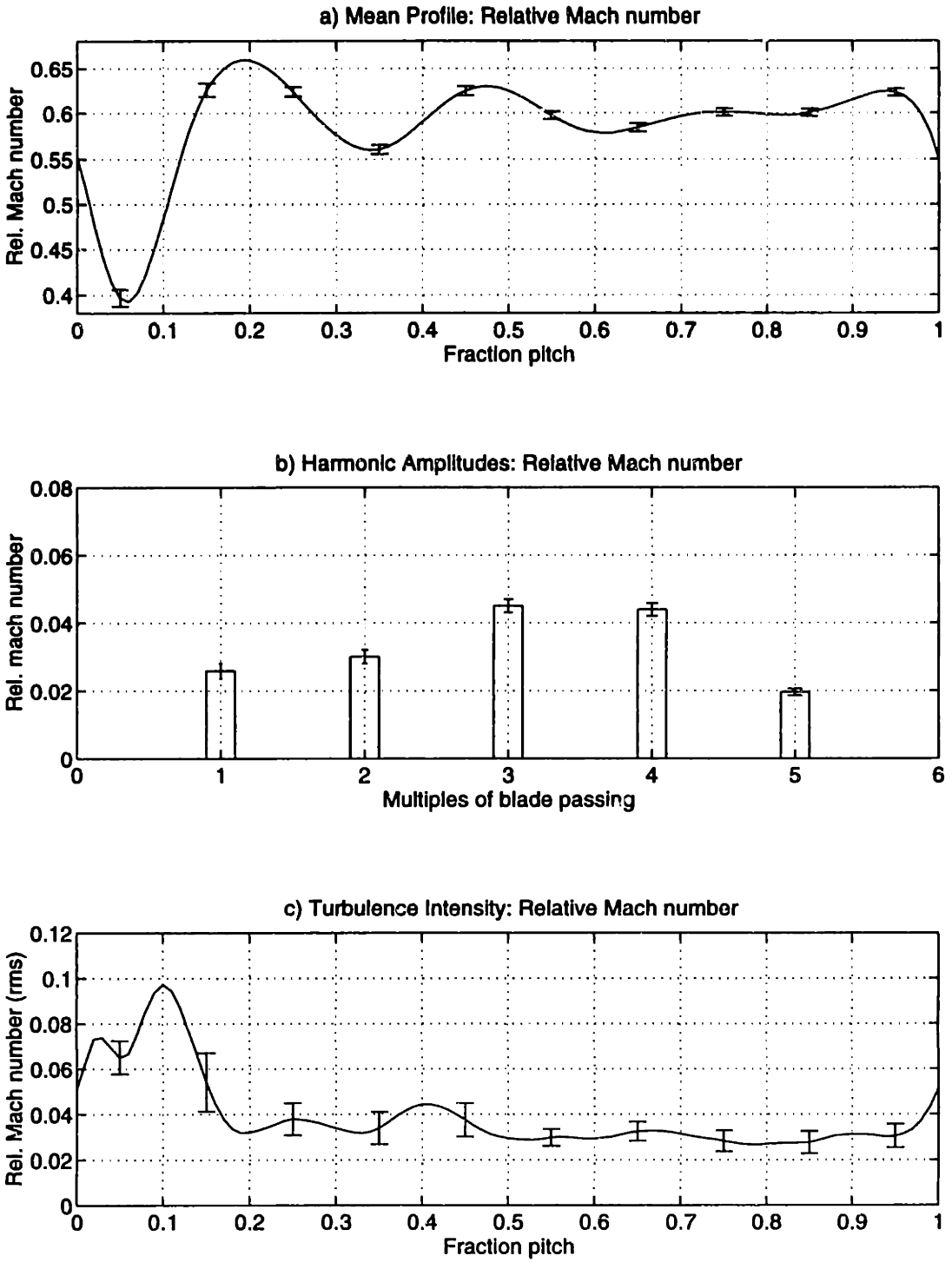

Figure 5-10: Relative Mach number ensemble-averaged profile, mean harmonic content, and turbulence profile at 75% span, 0.1c for the baseline rotor

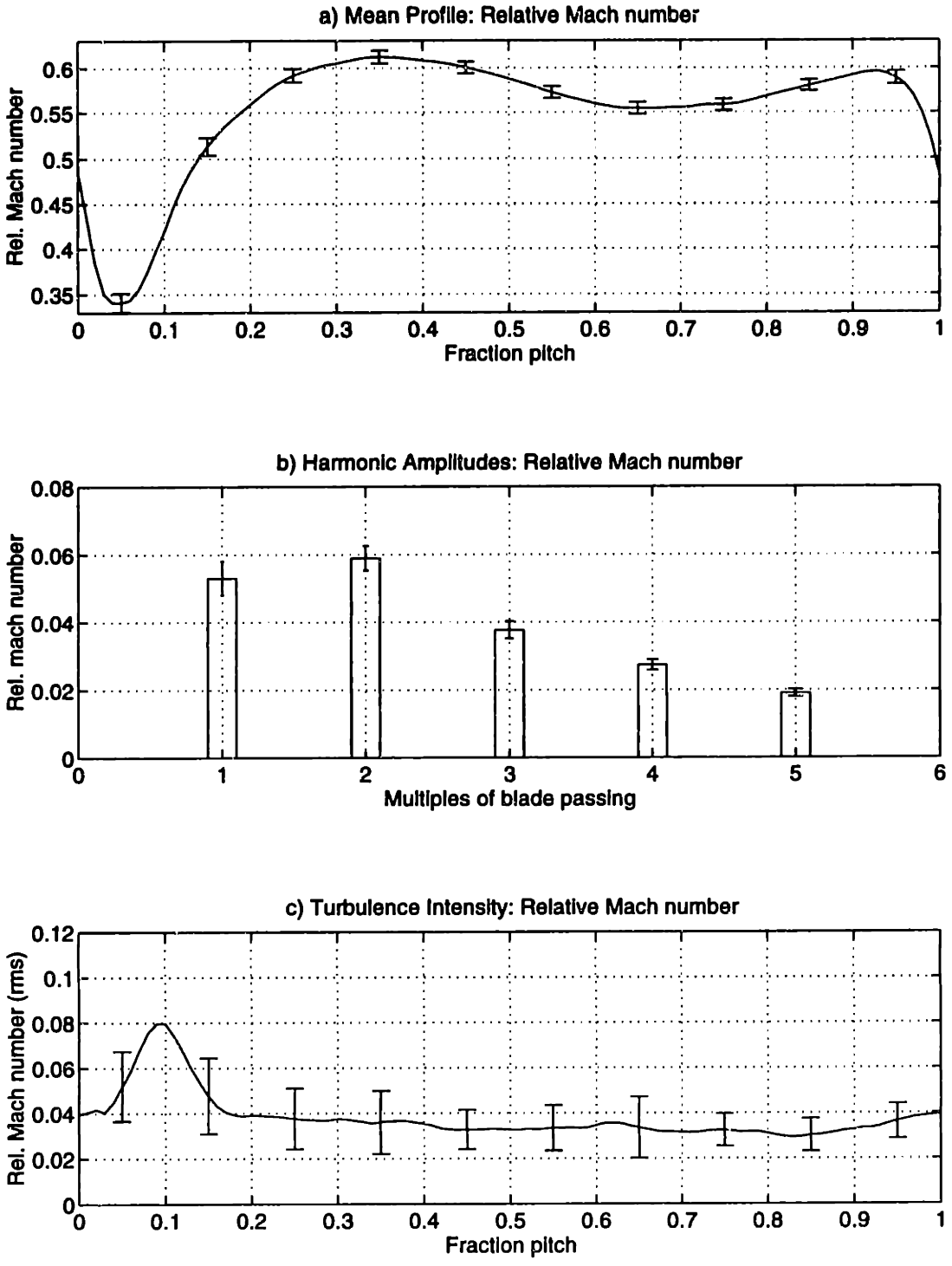

Figure 5-11: 4-way probe with fin: Relative Mach number ensemble-averaged profile, mean harmonic content, and turbulence profile at 75% span, 0.1c for the baseline rotor.

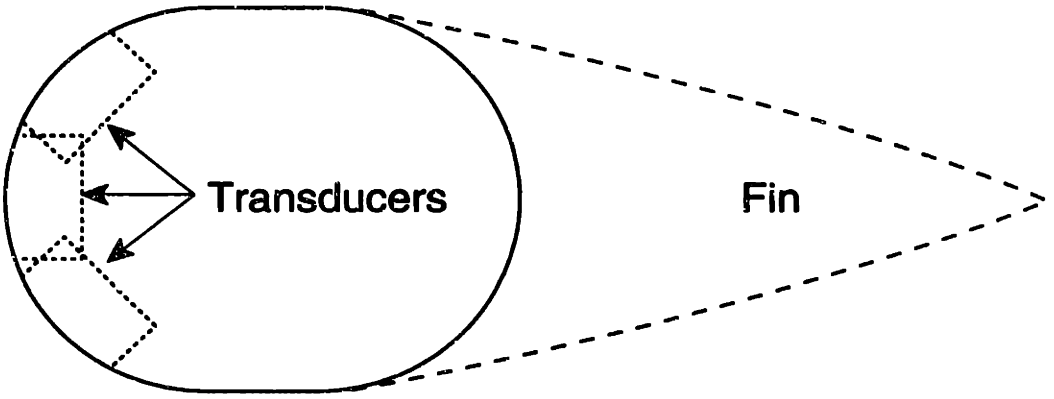

Figure 5-12: Cross section of 4-way probe head with attached fin to suppress vortex shedding

0.5 chord position

Relative Mach number mean profiles, harmonics, and turbulence intensity are shown in Figures 5-13 and 5-14 for 50% and 75% span, respectively. As with the 0.1 chord position, significant vortex shedding oscillations are seen. The reduction in the velocity deficit from 0.1c is clear, however, as well as the reduction in amplitude of the higher wake harmonics. Because the rotor index is approximately lined up with the tip trailing edge (blade number 14) at the instrumentation position in the tunnel, the wakes at 0.1c are approximately at the beginning of the pitch. By 0.5c, however, the wakes have moved circumferentially approximately 20% pitch. With the mean swirl angle in the flow of about 35 degrees, the wake tangential movement from the rotor to the stator (at 1.7c) is about 70% pitch at midspan, and 85% pitch at 75% span. Additional flow variables can be seen in Appendix E.

1.0 chord position

The ensemble-average relative Mach number profile, its harmonics, and turbulence intensity are plotted for 50% and 75% span in Figures 5-15 and 5-16 at 1.0 chords downstream of the rotor. As before, the decay in the velocity deficit and the tangential movement of the wake is evident. The decay in the 2*BPF wake harmonic amplitude from 0.1c to 1.0c is about 60%, and the decay in maximum turbulent intensity from 0.1c to 1.0c is approximately 35% for 50% span. Additional flow variables are presented in Appendix E.

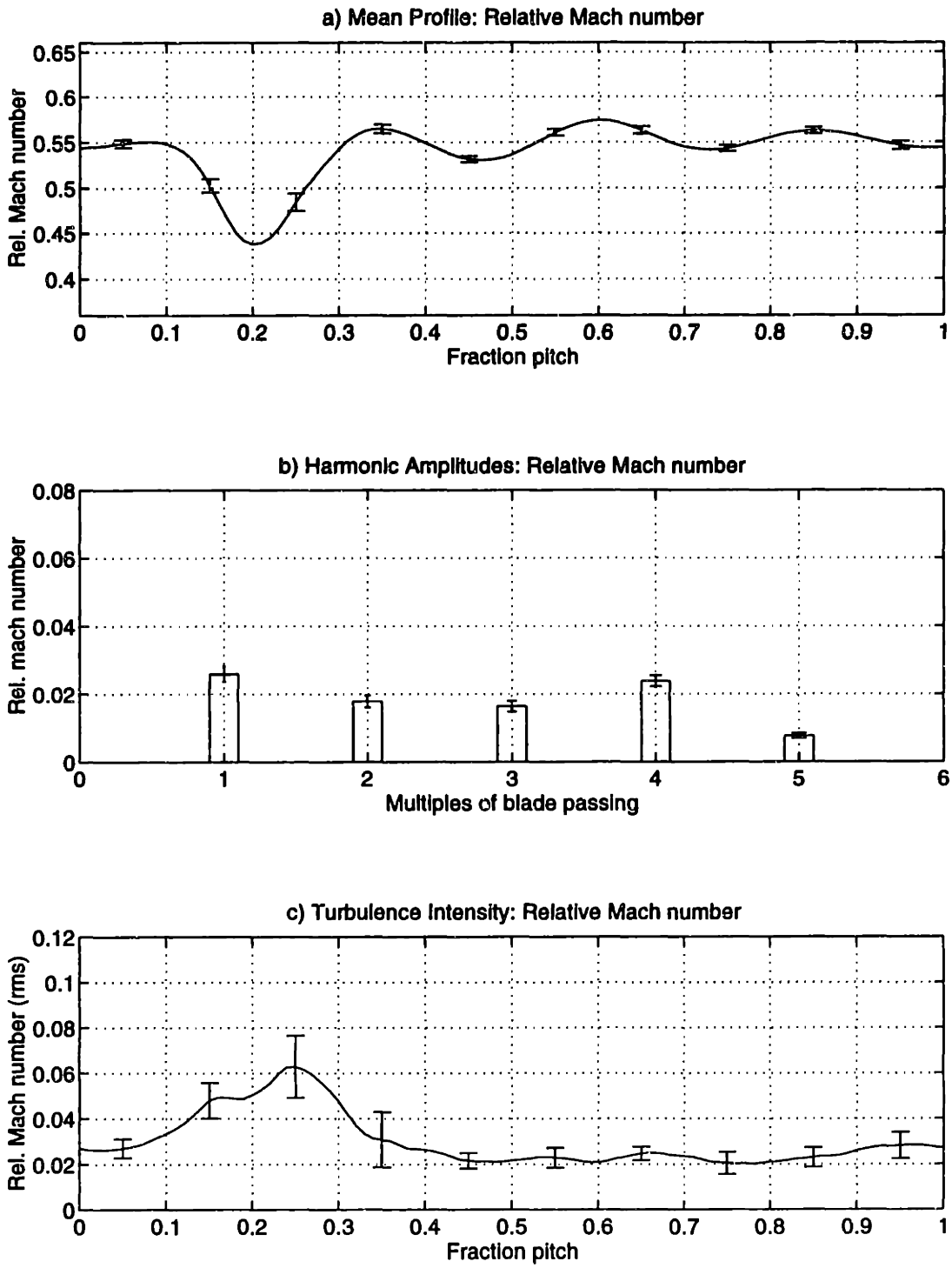

Figure 5-13: Relative Mach number ensemble-averaged profile, mean harmonic content, and turbulence profile at 50% span, 0.5c for the baseline rotor

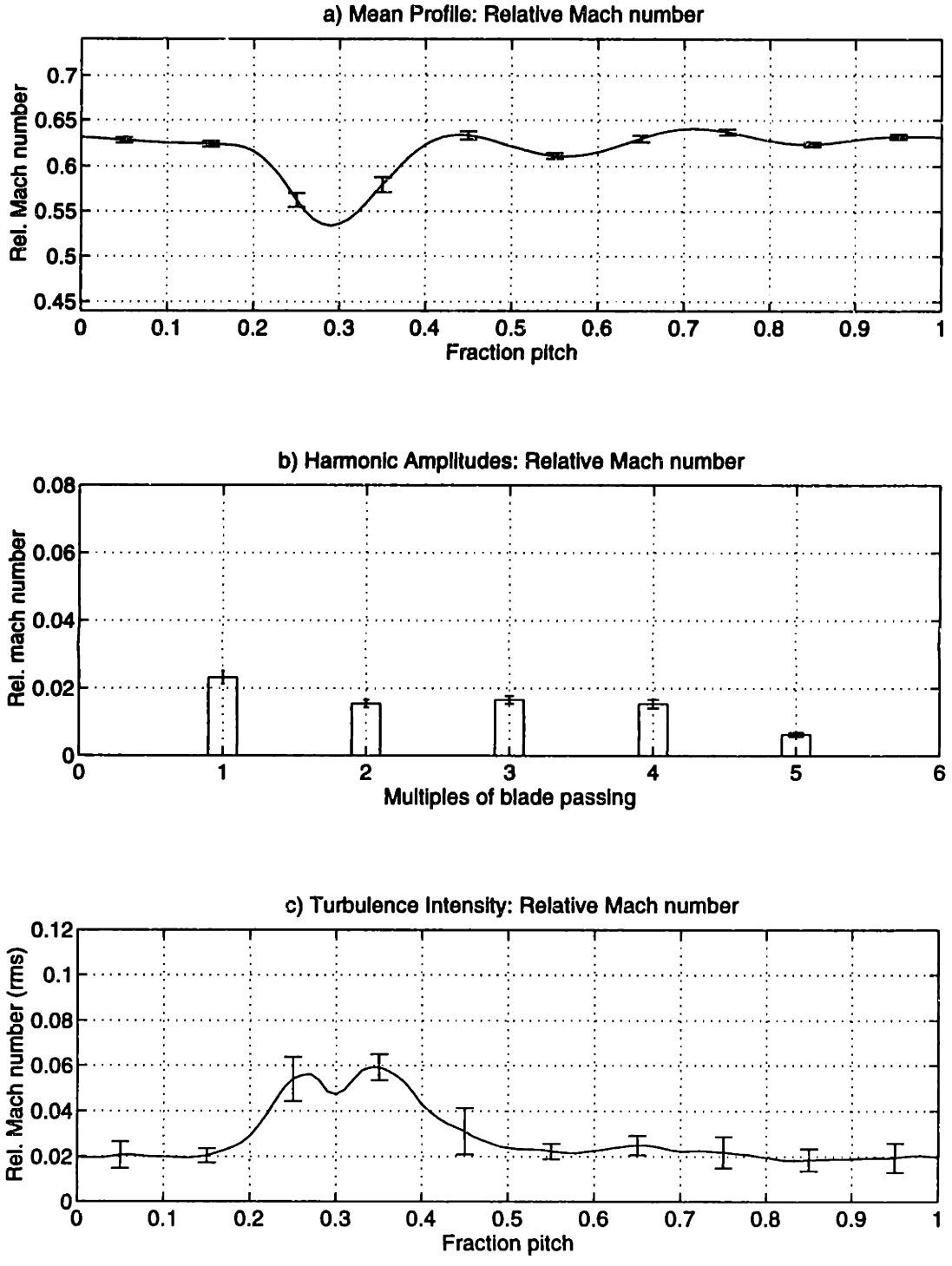

Figure 5-14: Relative Mach number ensemble-averaged profile, mean harmonic content, and turbulence profile at 75% span, 0.5c for the baseline rotor

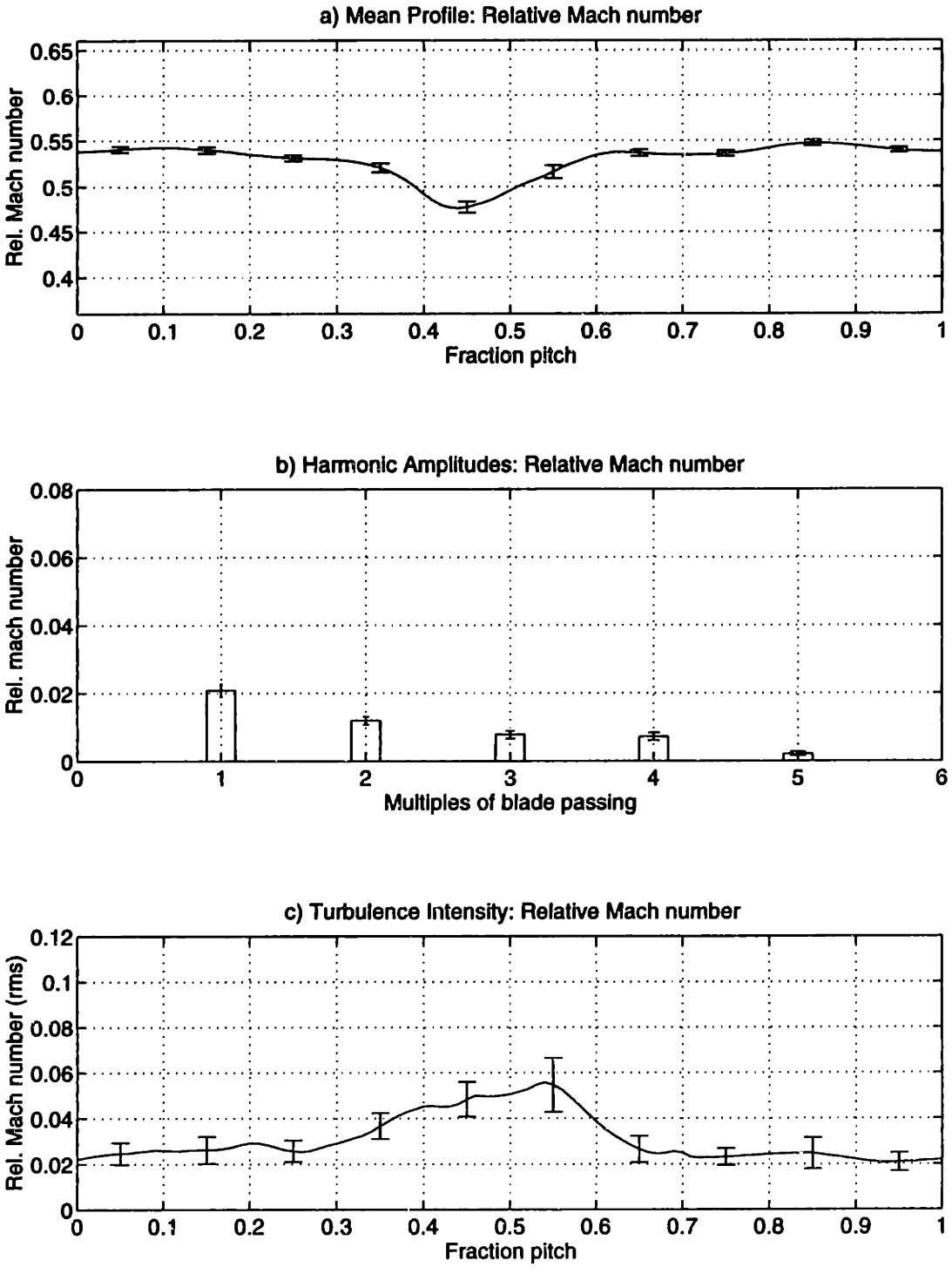

Figure 5-15: Relative Mach number ensemble-averaged profile, mean harmonic content, and turbulence profile at 50% span, 1.0c for the baseline rotor

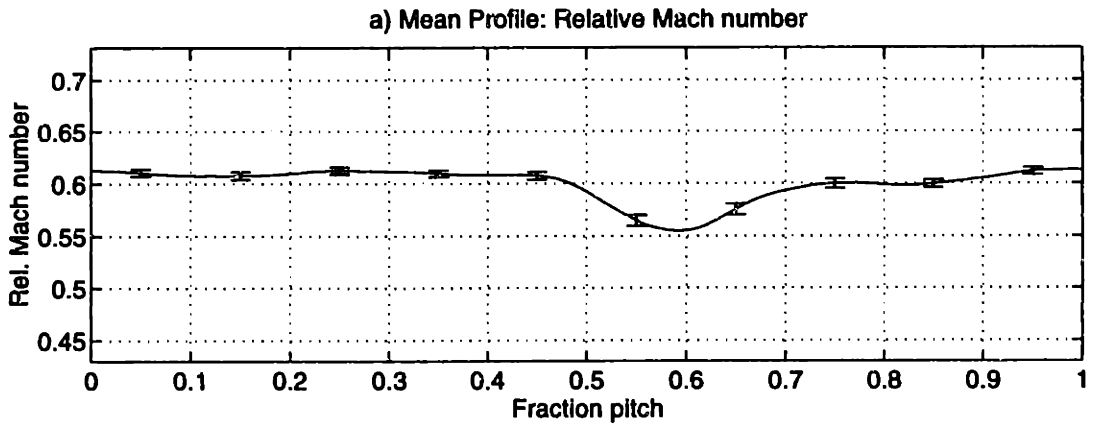

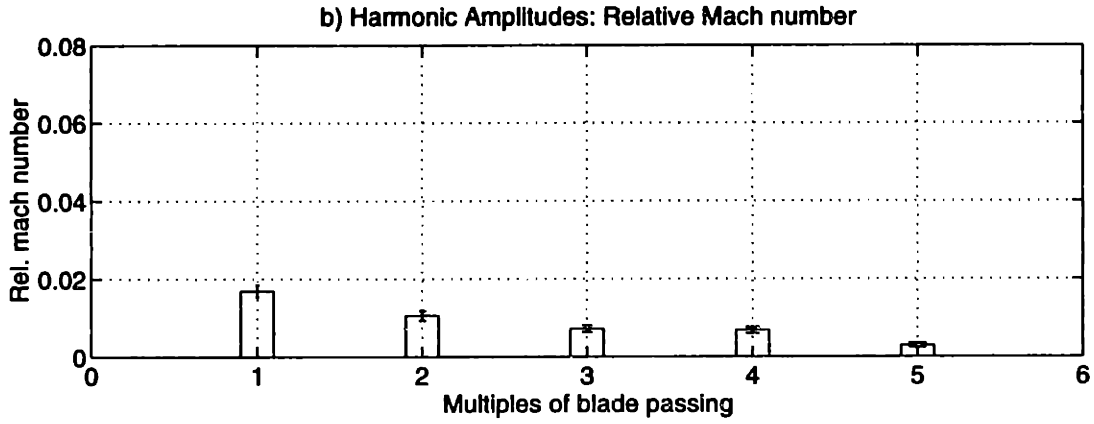

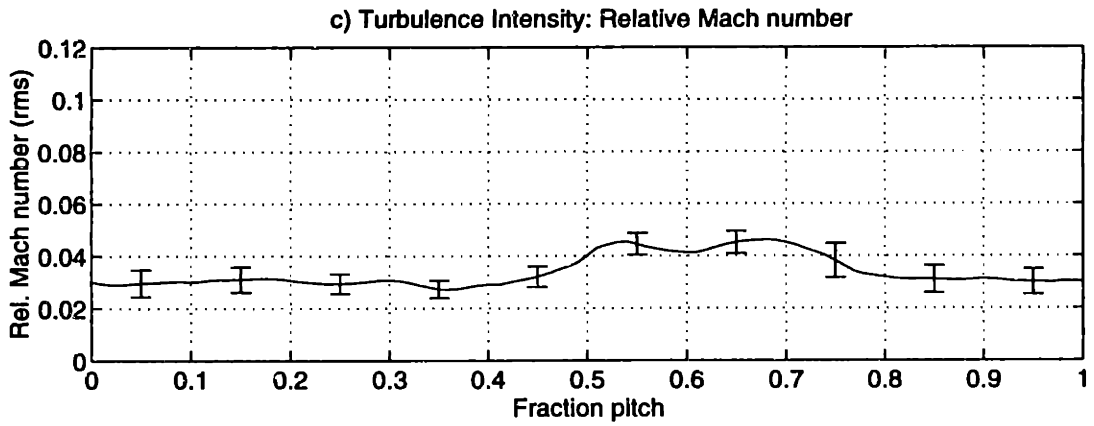

Figure 5-16: Relative Mach number ensemble-averaged profile, mean harmonic content, and turbulence profile at 75% span, 1.0c for the baseline rotor

5.2.3 Summary of Baseline Rotor Flow Field Measurements

Examining the profiles and harmonic content for the wake flow field from 0.1c to 1.5c, it is clear that the wake undergoes significant mixing and reduction of its mean relative Mach number deficit (approximately 85%) and maximum turbulent amplitude (approximately 50%). The wake evolution behind rotating blade rows is largely driven by turbulent mixing and the effects of wake stretching due to the freestream swirl. It was estimated in Chapter 4 that swirl causes a decrease in the mean velocity deficit of approximately 20% at 1.5c over a wake in non-swirling flow.

In addition, the wake in the absolute frame generally has about one-half the variation in Mach number and total pressure as the relative frame, so perturbations at the inlet to the stator row manifest themselves to a large degree as changes in angle of attack. It is for this reason (and because the velocity perturbations are small) that linear approximations for stator unsteady loading with wake harmonic amplitude agree so well with experiments (most airfoils have linear lift curve slopes, C_p vs.α, over the typical operating range).

Also, the skew of the wake can be visualized by examining the position of the wake centerline at the different spanwise locations. The wake is severely distorted at 1.5c from its near radial shape at 0.1c, and the wake skew angle at 75% span, 1.5c is approximately 55 degrees. This angle corresponds to about 75% increase in the wake length, which causes an increase in the mixing rate of the wake (see Chapter 4) and will also greatly alter the coupling to acoustic modes (see Section 1.3.)

It was also pointed out previously that the harmonic content of the wakes at 1.5c does not vary greatly in the radial direction. In particular, any merging of the tip clearance flow to the wake at 87.5% span does not appear to alter the harmonic content of the flow field, except for the 1*BPF harmonic. For this fan geometry, rotor-stator interaction BPF tones are cut-off outside the fan stage, and thus increases in BPF harmonic near the tip can only influence tones scattered due to mode trapping. The harmonics of unsteady pressure on the stator blade, which show similar trends, are presented in the next section.

Finally, turbulence intensities and spectrums were also observed to be roughly constant along the span in the flowfield measurements at 1.5c. This may indicate that the tip clearance flow does not dominate broadband noise generation.

5.3 Stator Unsteady Pressure Measurements (Baseline)

As with the 4-way probe flow field measurements described above, the primary stator measurements were made at 25, 50, 75, and 87.5% span locations. All stator measurements are with the stator row at 1.7 chords rotor/stator spacing. The data presented at these locations are the average of four runs, each having 96 blade passing periods.

5.3.1 Mean Pressure Envelopes

The mean, or steady, pressure envelopes for 25%, 50%, 75%, and 87.5% span locations are plotted in Figures 5-17 through 5-20. 4-way probe data at the 1.5c location was used to nondimensionalize the pressure coefficients with the formula $C_p = (P_{local} - P_{upstream})/(P_t - P)_{upstream}$. The mean pressure is the zeroth harmonic of the ensemble-averaged profile. The mean pressure envelopes are not very important for noise generation purposes, but do indicate the overall behavior of the flow field. It is clear from the envelope at 25% span (Figure 5-17) that the stator is partially separated. The flow field at 1.5c, 25% span showed a very wide wake, which may be a result of hub corner separation and/or pressure gradients caused by the hub contour. Regardless, the hub flow field is not very clean, and it will be seen in Chapter 7 whether wake management has a positive impact on this flow.

In addition to the mean pressure envelope, the plots show 95% confidence intervals for the data, as well as the unsteady envelope at each measurement position (dash-dot lines). This unsteady envelope is the minimum and maximum pressure (periodic) seen at the transducer over the ensemble-averaged blade passing period.

5.3.2 Stator Pressure Harmonic Amplitudes and Phase

After averaging the stator pressure data over the blade passing periods of interest, the signals were decomposed spatially to obtain the complex Fourier coefficients (the mean profiles were obtained from the zeroth harmonic). As described in Section A.0.3, the confidence intervals of the harmonics were also calculated. The amplitude and phase of the coefficients were then plotted for all thirteen stator transducers to obtain the distribution of amplitude and phase along the stator chord. In all plots for the stator blade, solid lines represent the

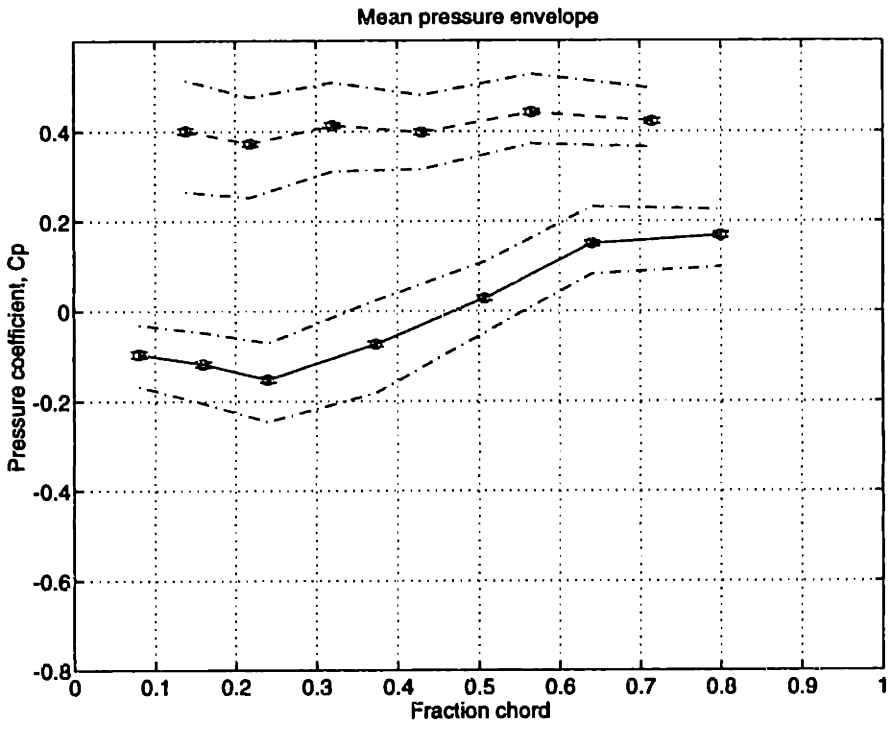

Figure 5-17: Stator mean pressure envelope at 25% span for the baseline rotor: suction surface (—) and pressure surface (- -), with range of periodic pressure fluctuations (– .)

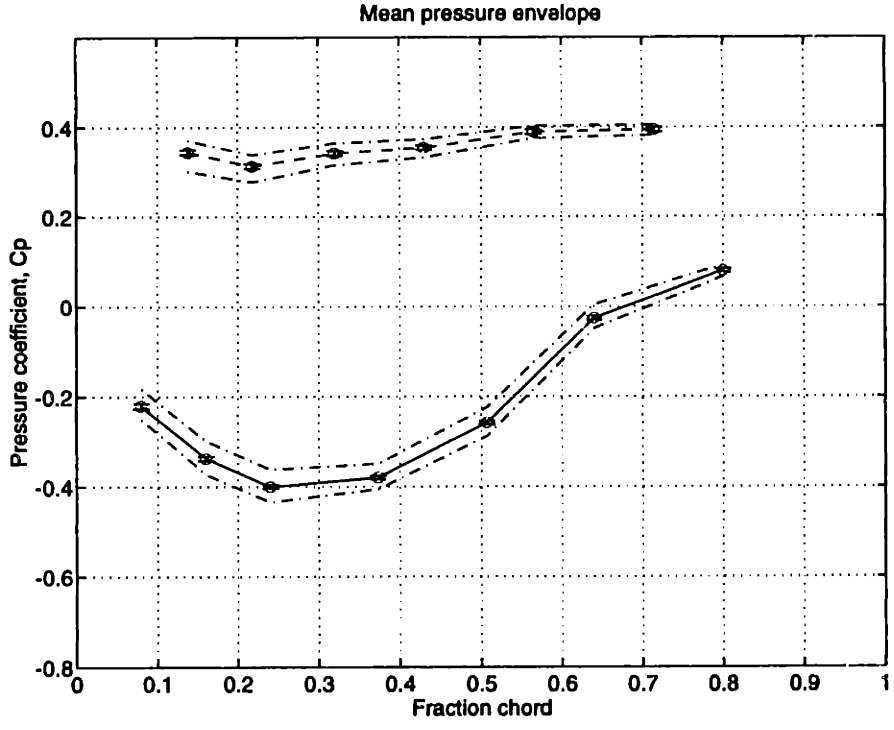

Figure 5-18: Stator mean pressure envelope at 50% span for the baseline rotor: suction surface (—) and pressure surface (- -), with range of periodic pressure fluctuations (– .)

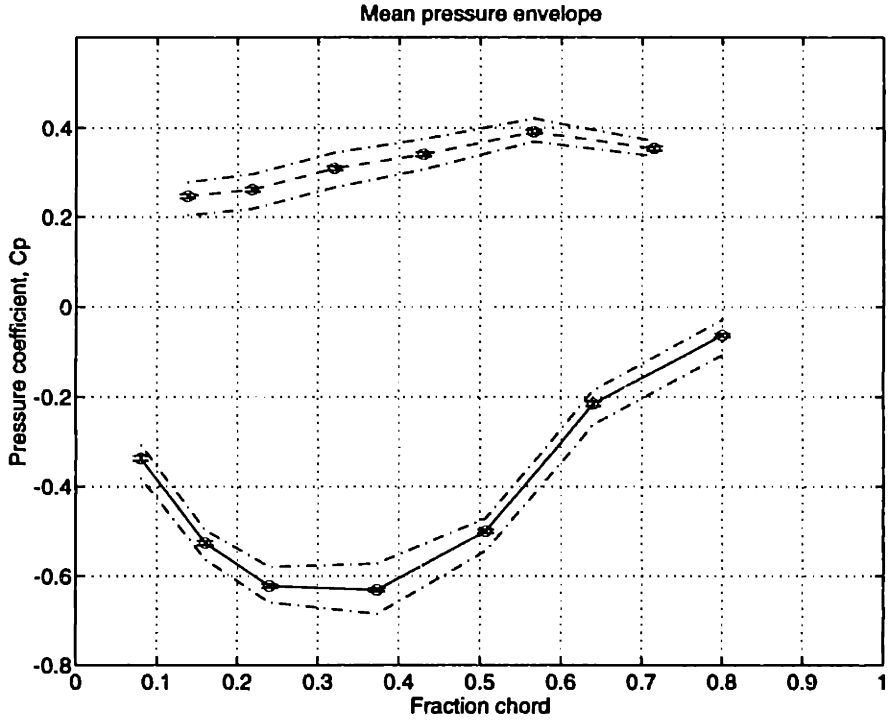

Figure 5-19: Stator mean pressure envelope at 75% span for the baseline rotor: suction surface (—) and pressure surface (- -), with range of periodic pressure fluctuations (– .)

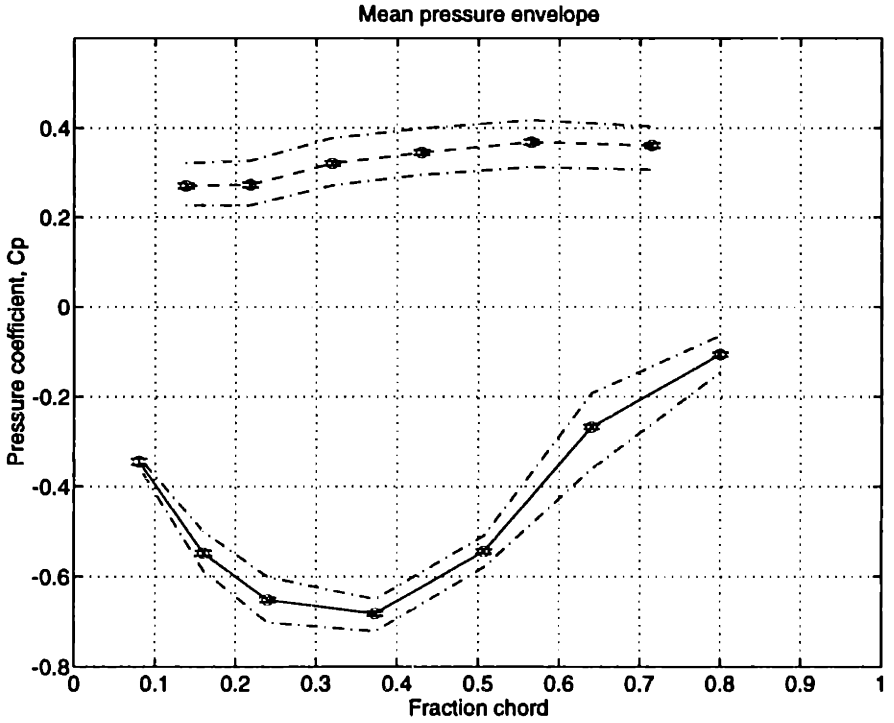

Figure 5-20: Stator mean pressure envelope at 87.5% span for the baseline rotor: suction surface (—) and pressure surface (- -), with range of periodic pressure fluctuations (– .)

suction surface and dashed lines the pressure surface. Harmonic amplitudes are given as dB noise levels (dB = $20\log_{10}(P'_{rms}/2x10^{-5})$) scaled to an inlet total pressure of one standard atmosphere.

Figure 5-21 and 5-22 show the harmonic amplitudes and phase, respectively, for the first three blade passing harmonics at 25% span. The relative amplitude of the harmonics can be seen, as well as the phase variation along the chord of the stator. The BPF harmonic is virtually 180 degrees out of phase on the pressure and suction surfaces along the full chord, with the minimum pressure point moving upstream on the stator surface. With the wake traveling over the stator chord from the leading to trailing edge, one might expect to see decreasing phase along the stator in the pressure response (minimum pressure traveling downstream). Computations using UNSFLO [9], however, confirmed the experimental result, and are discussed in more detail in Section 5.4. The effect is a result of the closely coupled stator blades. Because of the particular fan geometry of 16 rotor blades and 40 stator blades, the wake pitch is 2.5 stator pitches. Therefore, the blades on either side of the instrumented blade are ±144 degrees out of phase and the combination of the total pressure difference in the wake with the induced velocities on the blade surface, result in the minimum pressure traveling upstream. This has been seen previously in measured data [3].

Plots of the harmonic amplitudes and phase for 50%, 75%, and 87.5% span are shown in Figures 5-23 through 5-28. The phase variation of BPF at the different spanwise locations is seen to match the wake skew (approximately 180 degree phase difference between 50 and 87.5% span), and the harmonic amplitudes of pressure variations on the stator are fairly constant (within a factor 2) along the span. An additional test at 95% span, which is well within the tip clearance flow region, is shown in Figures 5-29 and 5-30. There is little change in the amplitudes of the periodic unsteady pressure due to the tip clearance flow, and thus the wake is expected to be the primary noise source. This result, as previously explained, is thought to be due to the fact that the tip clearance flow is over one-half pitch in width at the stator row and is therefore made up primarily of 1*BPF. In fact, the amplitude of 2*BPF, which generates the strongest propagating acoustic mode, is smallest in the tip region.

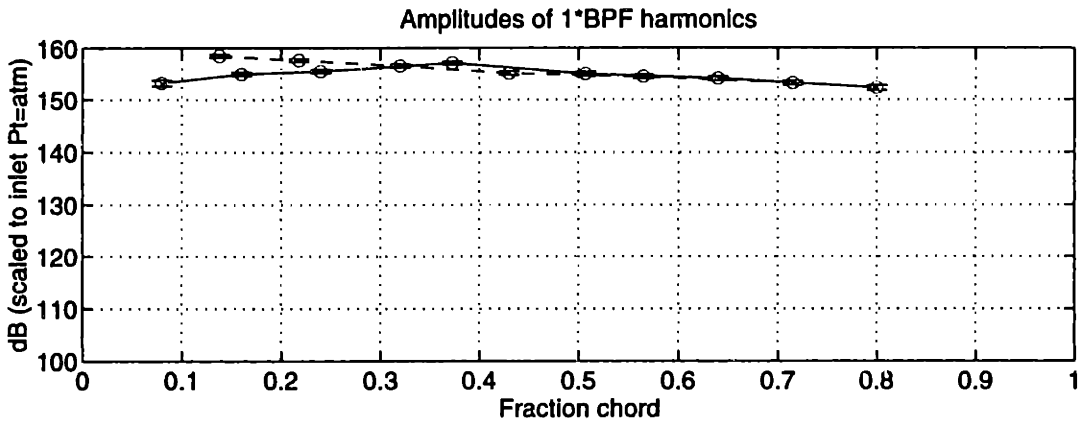

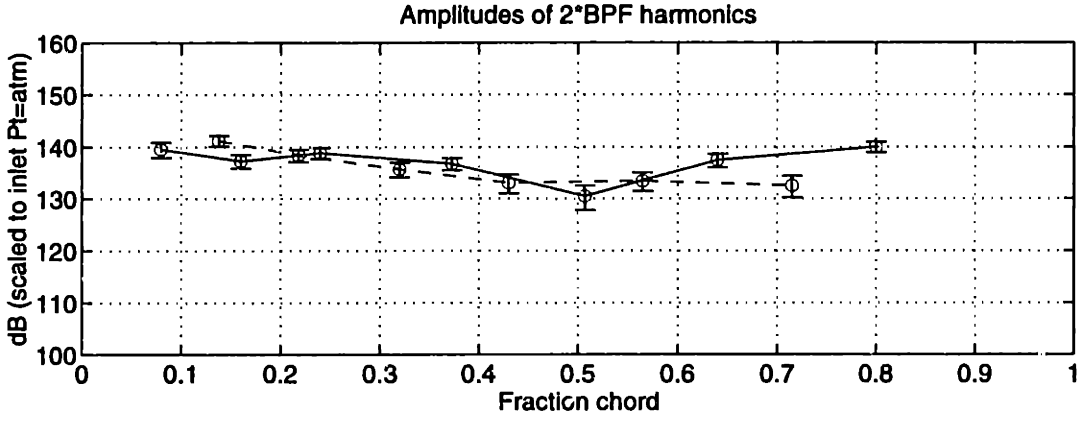

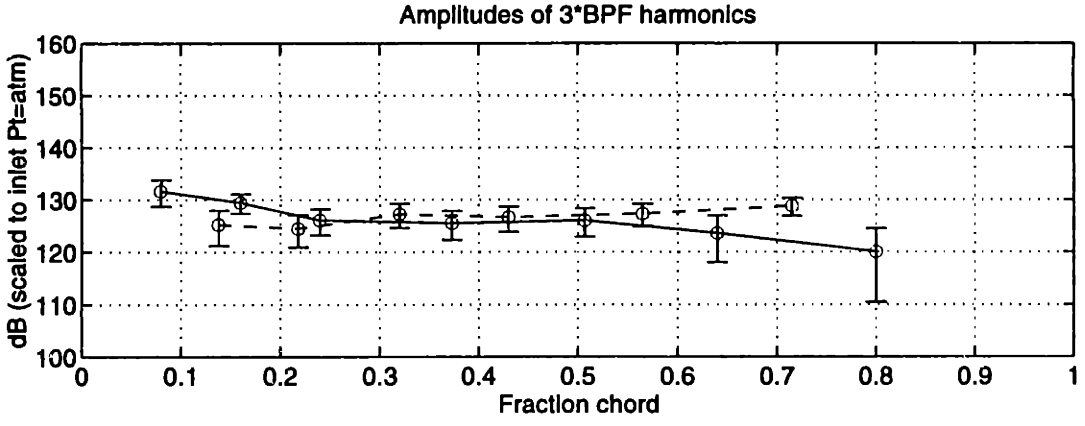

Figure 5-21: Amplitudes of BPF harmonics at 25% span for the baseline rotor: suction surface (—) and pressure surface (- .)

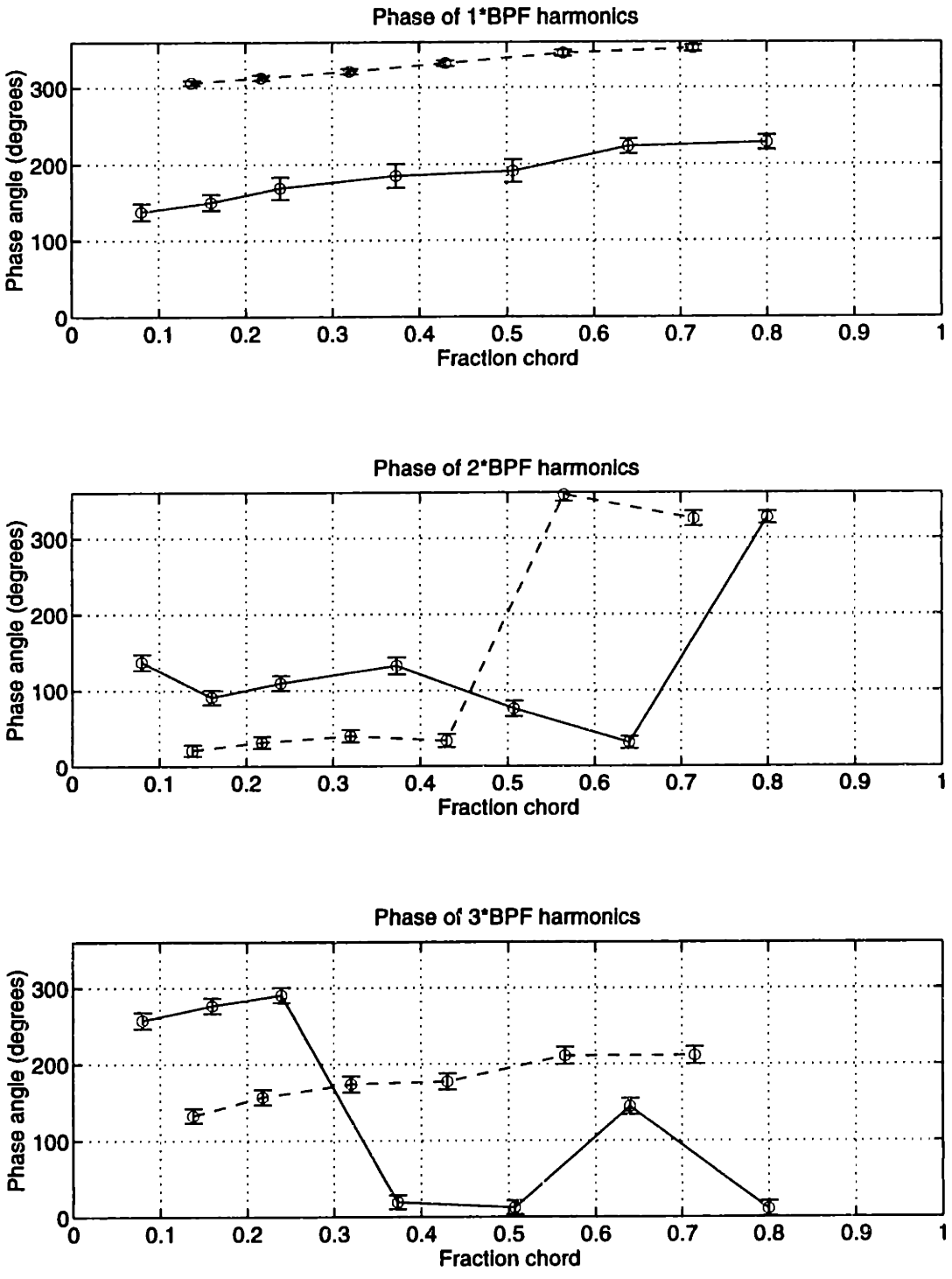

Figure 5-22: Phases of BPF harmonics at 25% span for the baseline rotor: suction surface (—) and pressure surface (- .)

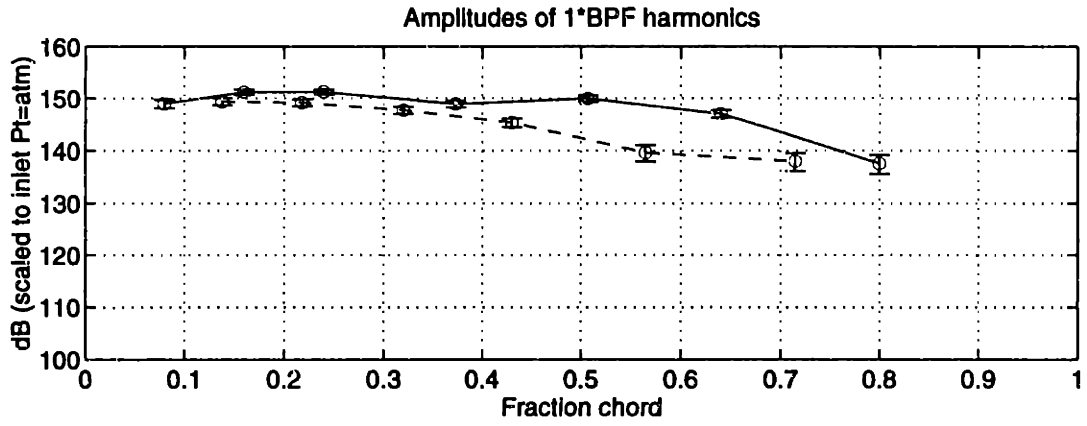

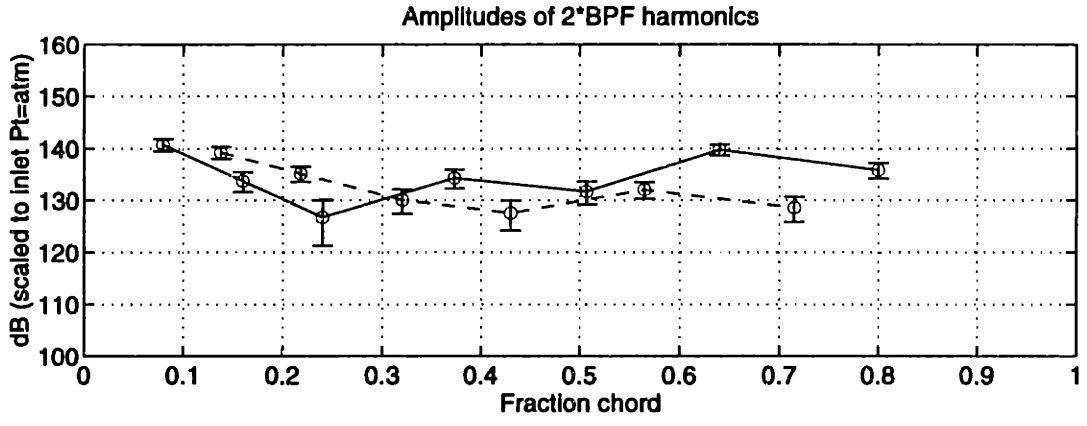

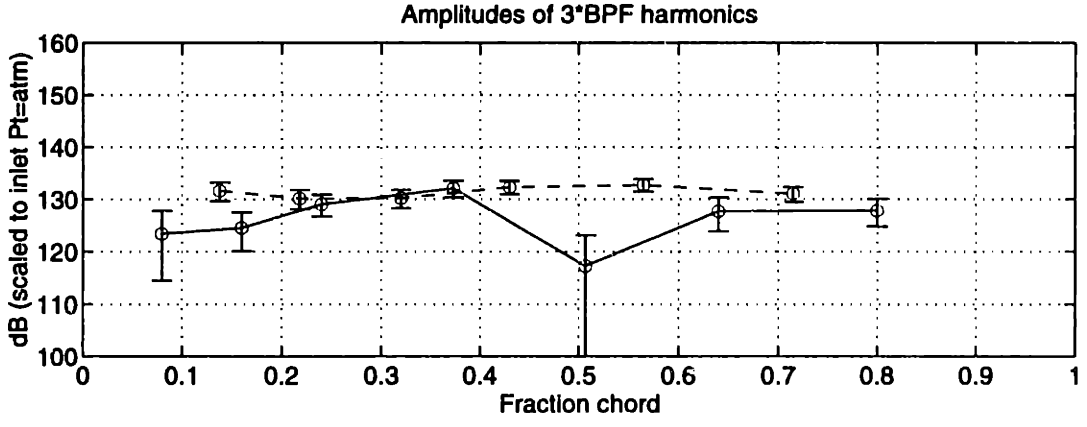

Figure 5-23: Amplitudes of BPF harmonics at 50% span for the baseline rotor: suction surface (—) and pressure surface (- .)

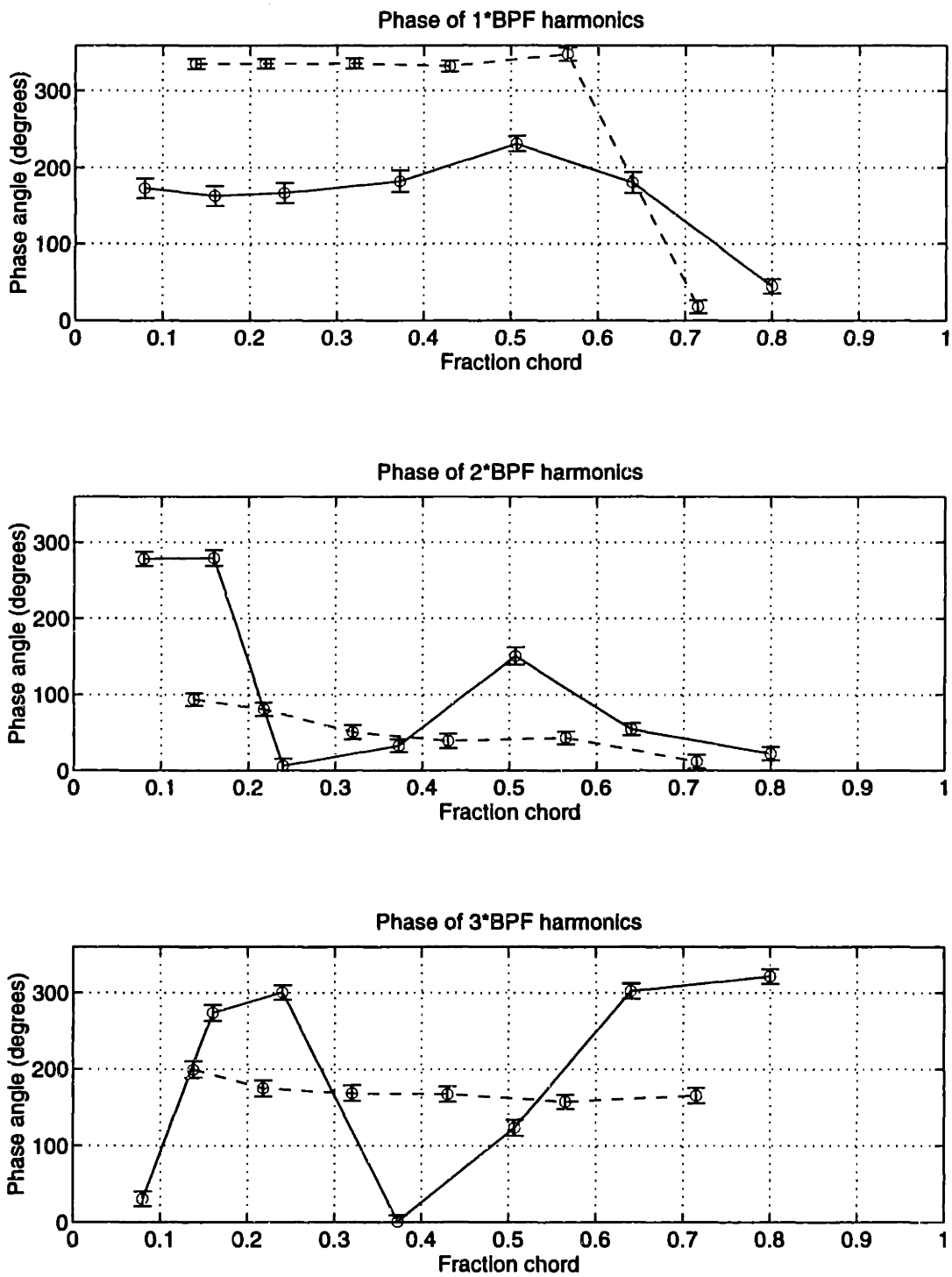

Figure 5-24: Phases of BPF harmonics at 50% span for the baseline rotor: suction surface (—) and pressure surface (- .)

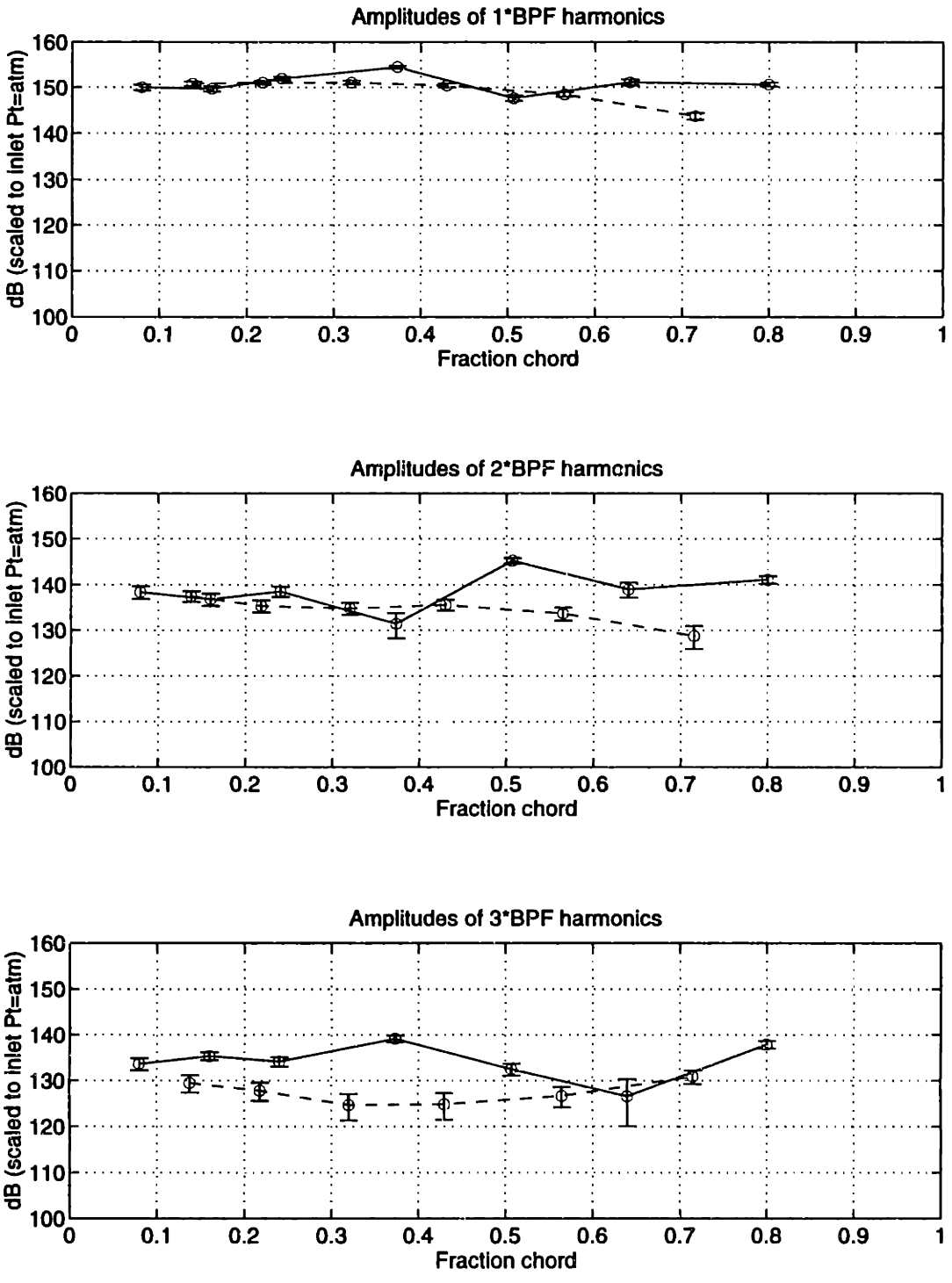

Figure 5-25: Amplitudes of BPF harmonics at 75% span for the baseline rotor: suction surface (—) and pressure surface (- .)

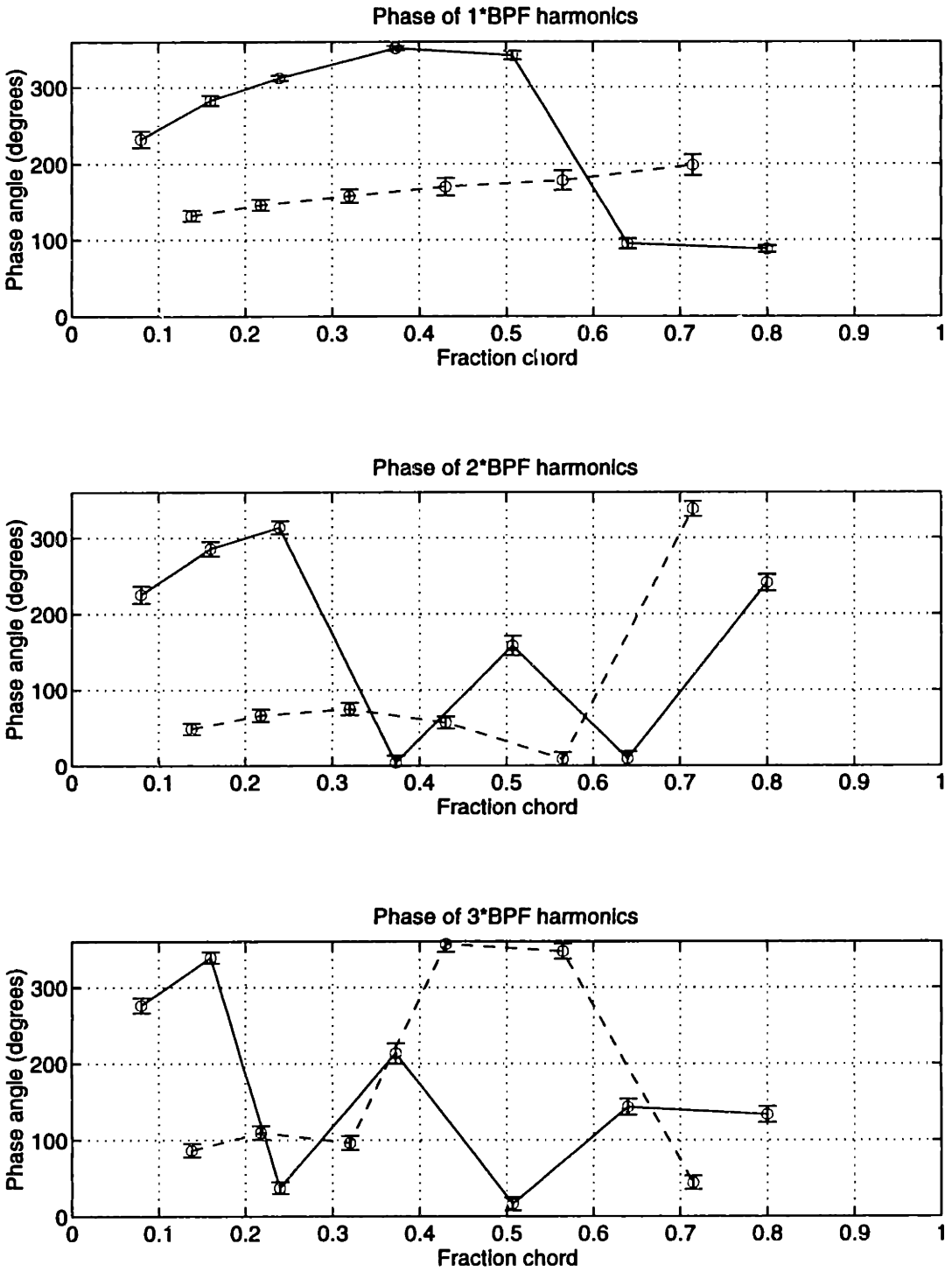

Figure 5-26: Phases of BPF harmonics at 75% span for the baseline rotor: suction surface (—) and pressure surface (– .)

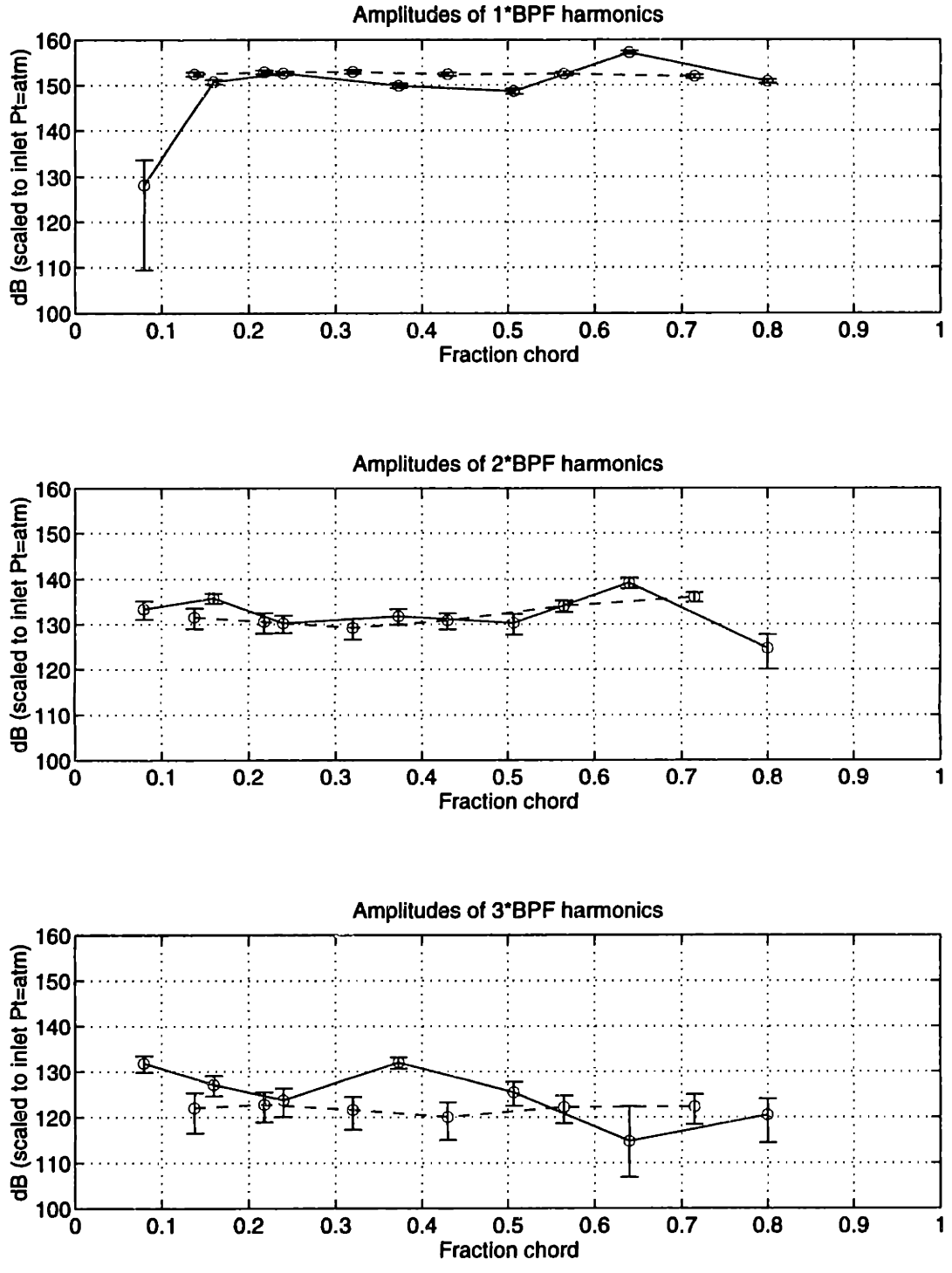

Figure 5-27: Amplitudes of BPF harmonics at 87.5% span for the baseline rotor: suction surface (—) and pressure surface (– .)

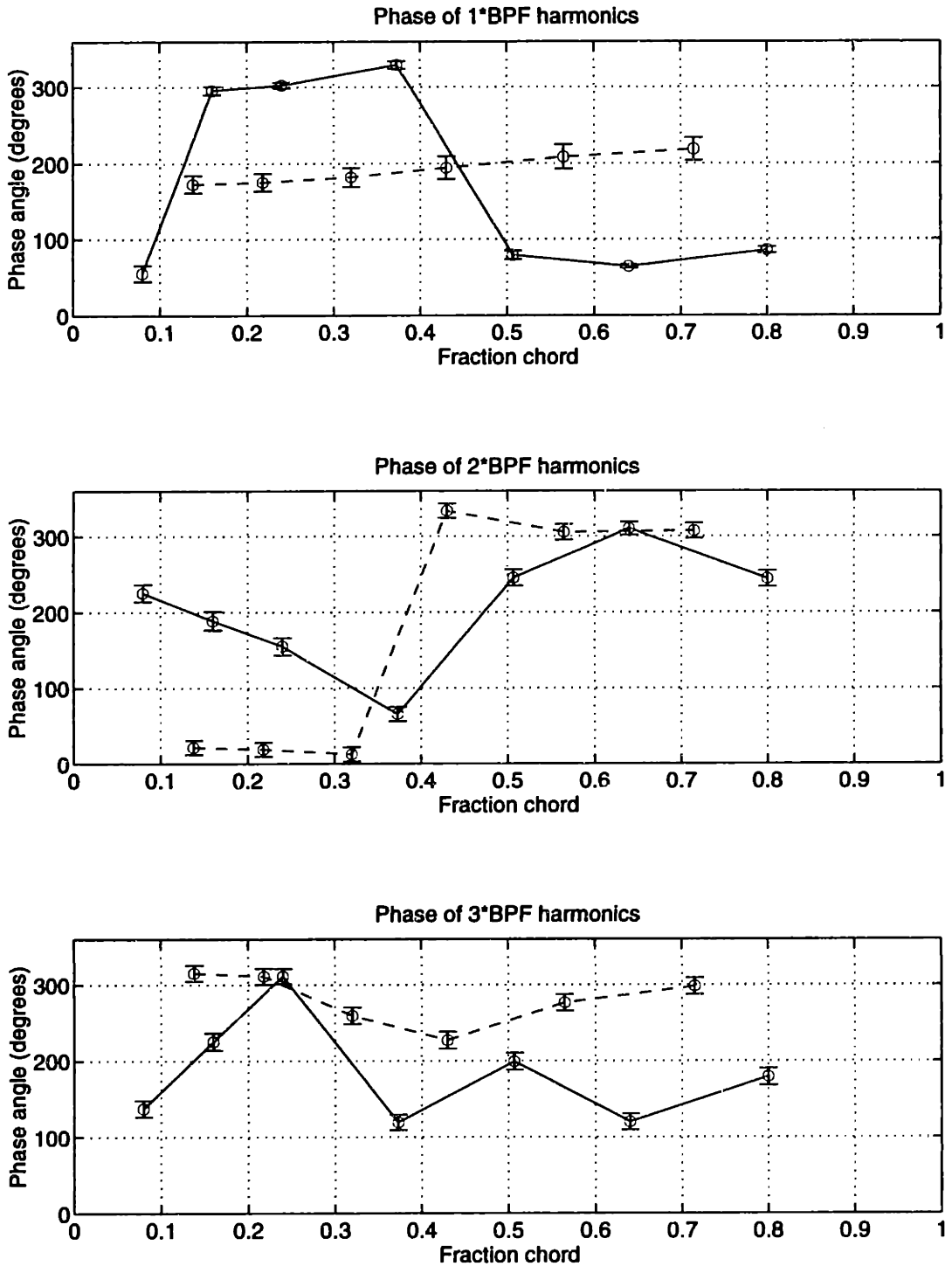

Figure 5-28: Phases of BPF harmonics at 87.5% span for the baseline rotor: suction surface (—) and pressure surface (- .)

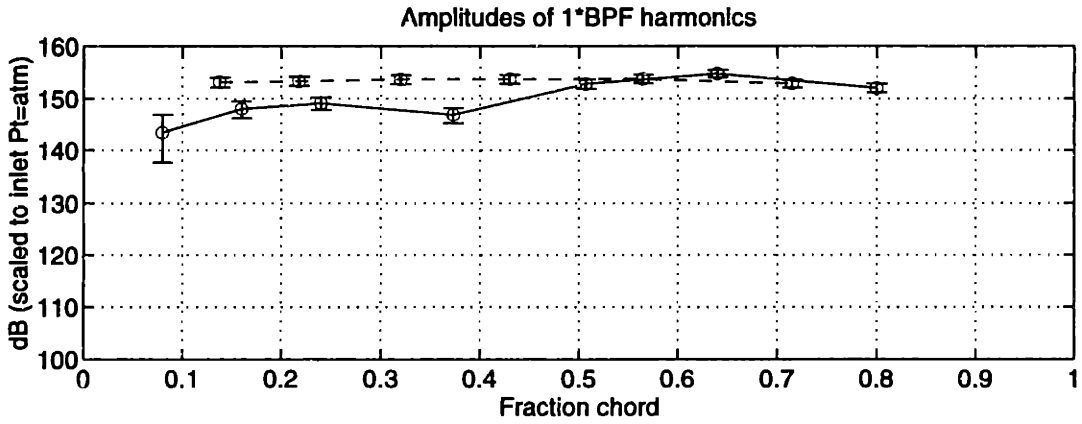

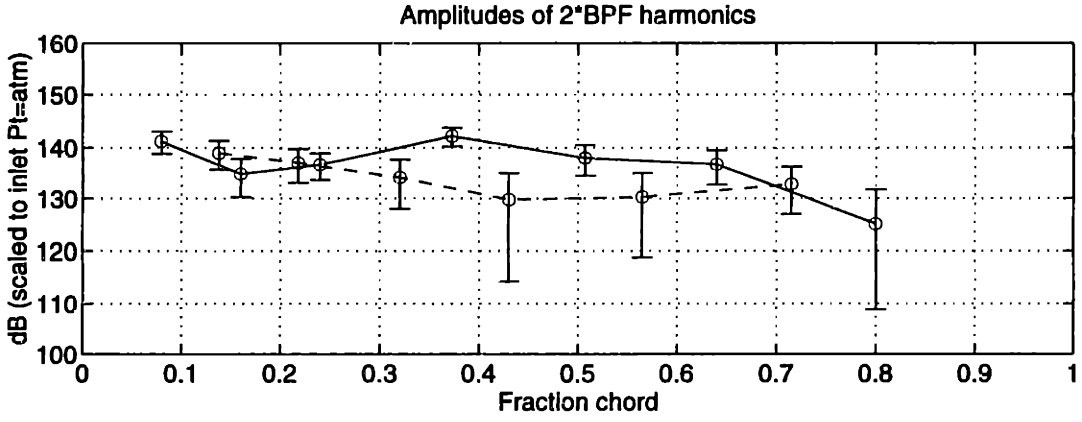

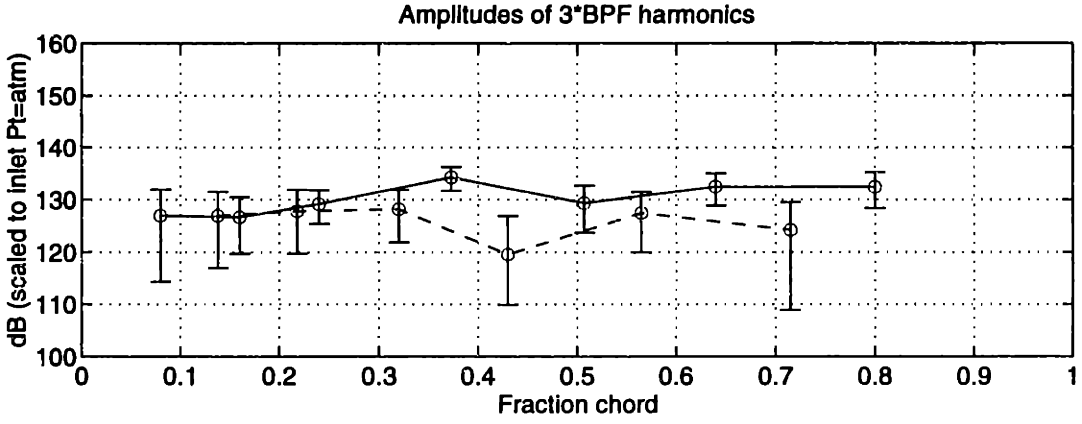

Figure 5-29: Amplitudes of BPF harmonics at 95% span for the baseline rotor: suction surface (—) and pressure surface (- .)

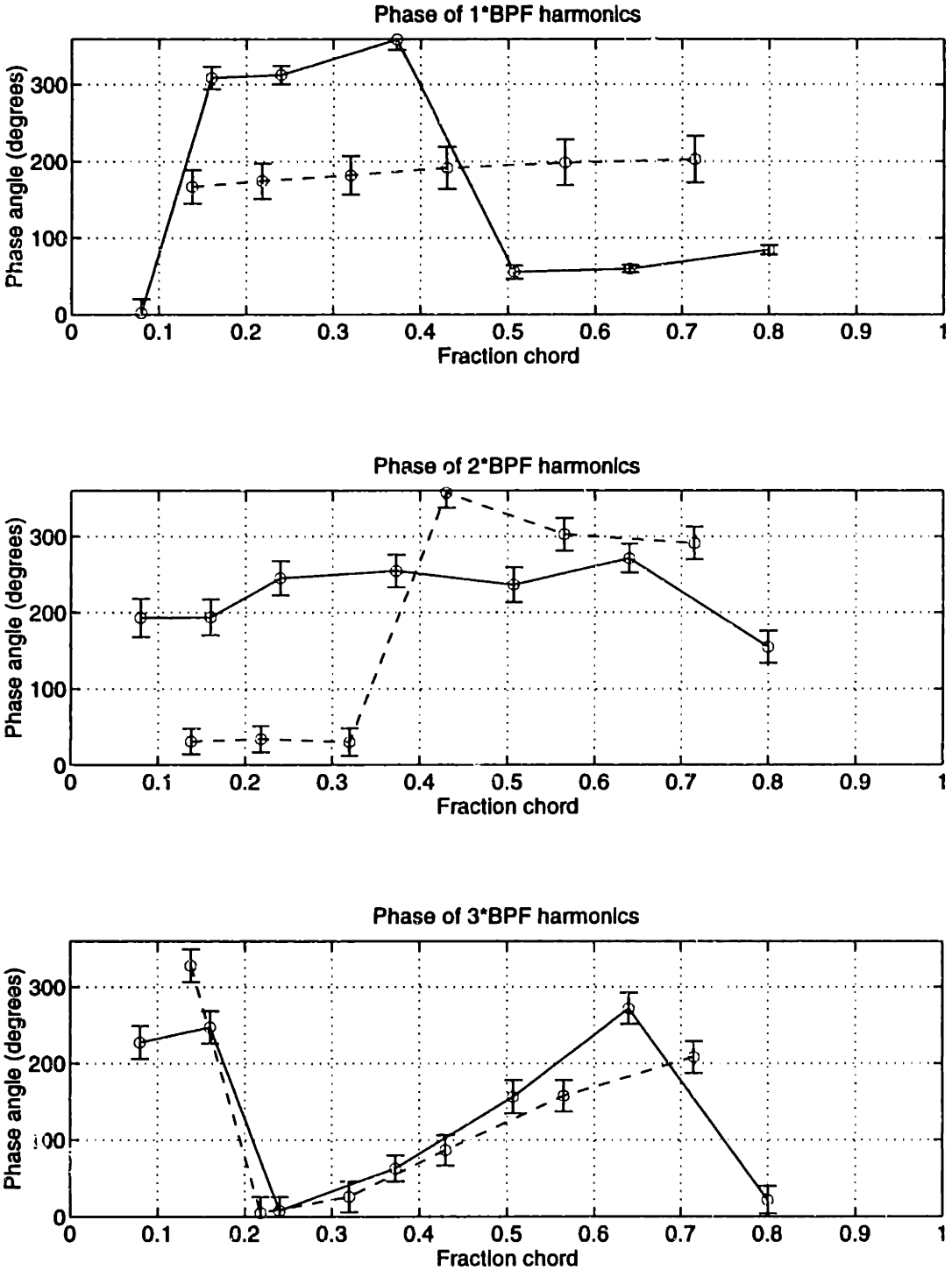

Figure 5-30: Phases of BPF harmonics at 95% span for the baseline rotor: suction surface (—) and pressure surface (- .)

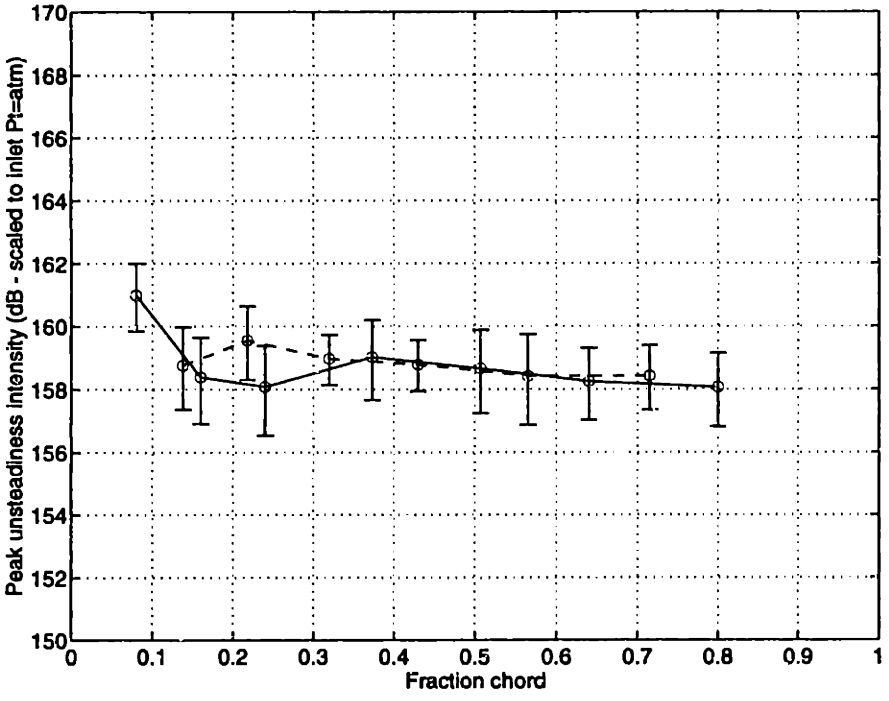

Figure 5-31: Amplitudes of random fluctuations at 25% span for the baseline rotor: suction surface (—) and pressure surface (- .)

5.3.3 Stator random pressure fluctuation amplitudes

In addition to the harmonics of the mean periodic unsteady pressures on the stator blade, the magnitude of the random perturbations was also calculated. Since these random fluctuations are the source of broadband noise the magnitude of the fluctuations are some indication of the level of broadband noise generated. For each rotor revolution within the data window of interest, the root mean square (rms) pressure was calculated over the blade passing period for each stator transducer. These profiles (4 runs with 6 rotor revolutions/run, except at 95% span) were ensemble-averaged and the maximum amplitude determined for each transducer. The magnitudes along the stator chord are plotted in Figures 5-31 through 5-35. The 95% confidence intervals were determined by calculating the standard deviation of the 24 samples for each transducer and the χ^2 formula (described earlier) applied with the appropriate constant for 24 samples.

The plots show that the peak random fluctuations are fairly constant in both the chordwise and spanwise directions. The amplitudes are generally a little higher near the

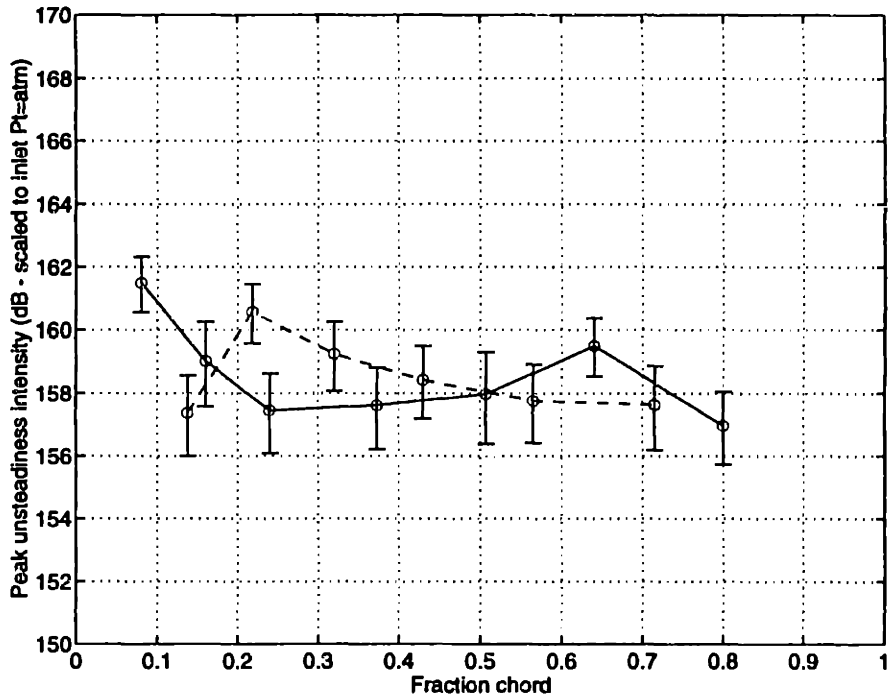

Figure 5-32: Amplitudes of random fluctuations at 50% span for the baseline rotor: suction surface (—) and pressure surface (- .)

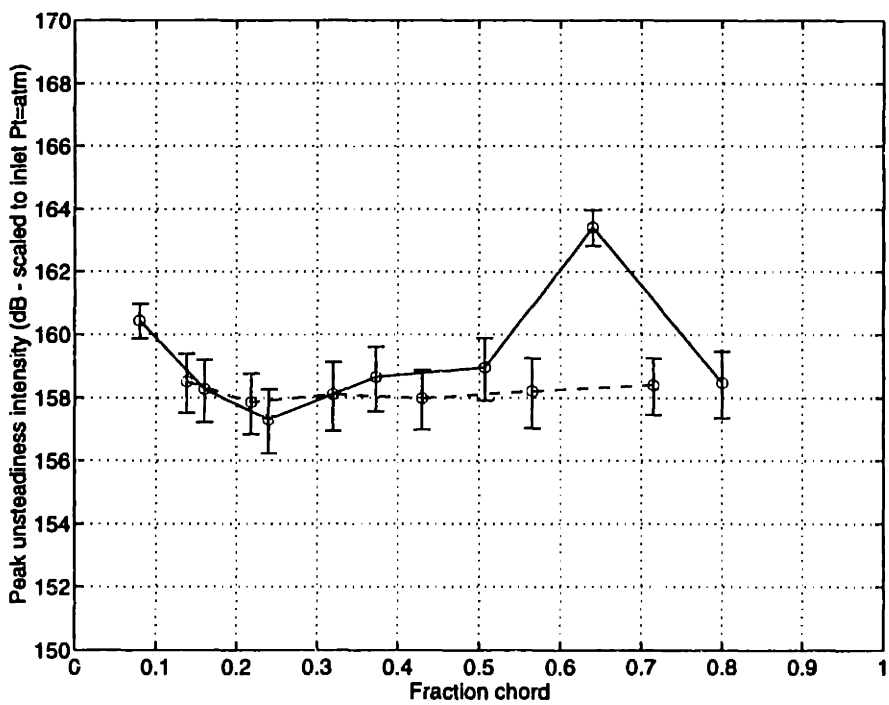

Figure 5-33: Amplitudes of random fluctuations at 75% span for the baseline rotor: suction surface (—) and pressure surface (- .)

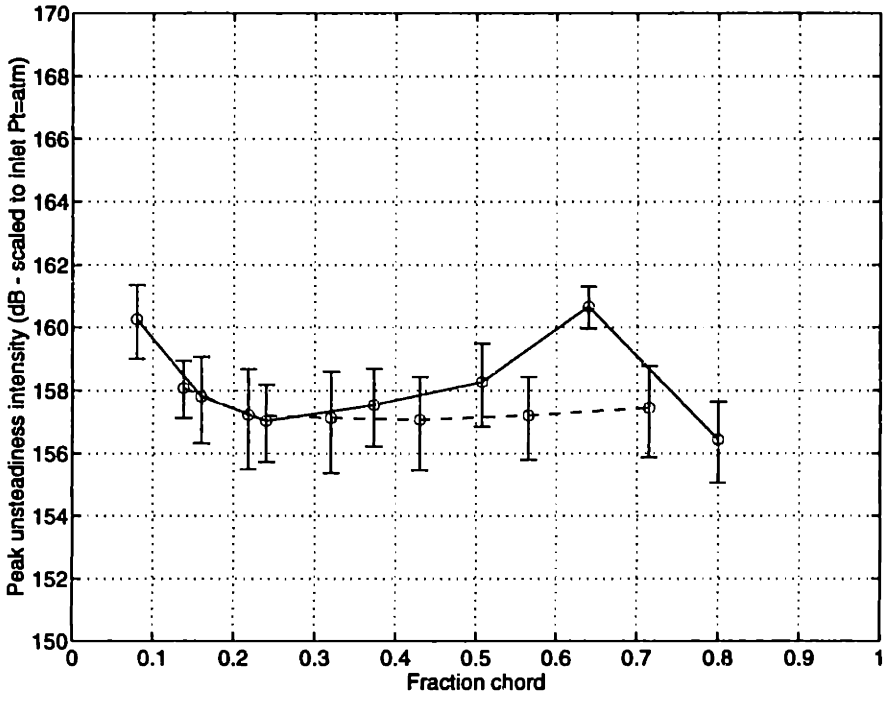

Figure 5-34: Amplitudes of random fluctuations at 87.5% span for the baseline rotor: suction surface (—) and pressure surface (- .)

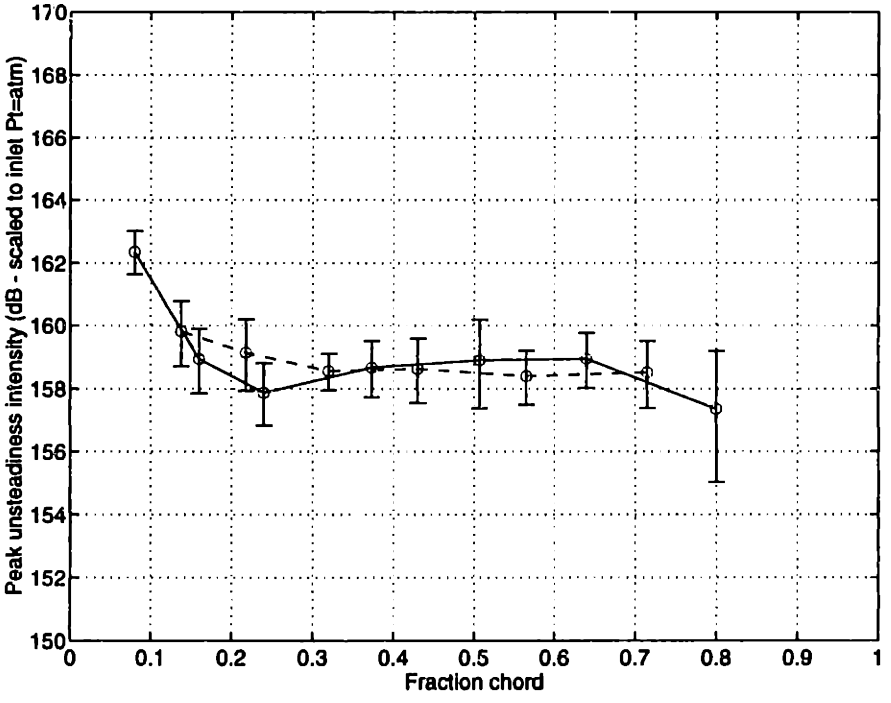

Figure 5-35: Amplitudes of random fluctuations at 95% span for the baseline rotor: suction surface (—) and pressure surface (- .)

leading edge and at transducer 6 on the suction surface at 75% and 87.5% span locations. Like the periodic signal harmonics, the turbulent fluctuations are not higher in the tip region. However, the extent of high turbulence level over a blade passing period is higher in the tip region than along the span, just like the fluctuations in the relative Mach number. The relative dominance of the wake and tip clearance flow turbulence on radiated broadband noise for this fan stage is not known at this time.

5.3.4 Stator pressure spectra

The previous section presented the peak pressure fluctuation intensity on the stator blades, but did not include any information regarding the spectral content of the random perturbations. To examine this, the full spectrum of the pressure signals at transducer 3 (24% chord on the suction side, near the minimum mean pressure) was calculated for 25%, 50%, 75%, and 87.5% span and is presented in Figures 5-36 through 5-39. The pressure amplitudes were scaled to a standard atmosphere inlet total pressure condition and the dB sound pressure level calculated [dB = $20\log_{10}(P'_{rms}/2x10^{-5})$]. As with the relative Mach number spectra (Section 5.2.1) the tonal amplitudes are the same as those calculated from the ensemble-averaged pressure signals.

The spectra are very similar to the spectra from the flow field measurements (relative Mach number), and can be analyzed for shaft frequencies (due to rotor blade-to-blade variations) as well as the random fluctuation spectrum. As in the relative Mach number spectra, some multiples of shaft frequency are evident, but their amplitudes are not significantly higher (approximately 3 dB) than the broadband noise floor. For the stator blade measurements, the electrical noise measured with no flow in the tunnel was approximately 90dB, over 20dB below the pressure fluctuations in the flow up to 6*BPF.

5.3.5 Summary of Stator Unsteady Measurements

Measurements from the instrumented stator blade were a little unexpected, but were explained through numerical simulation. Both the phasing of the minimum pressure moving upstream on the stator surface and the general roller coaster pattern of both amplitude and phase along the chord for higher harmonics was qualitatively verified. In general, how-

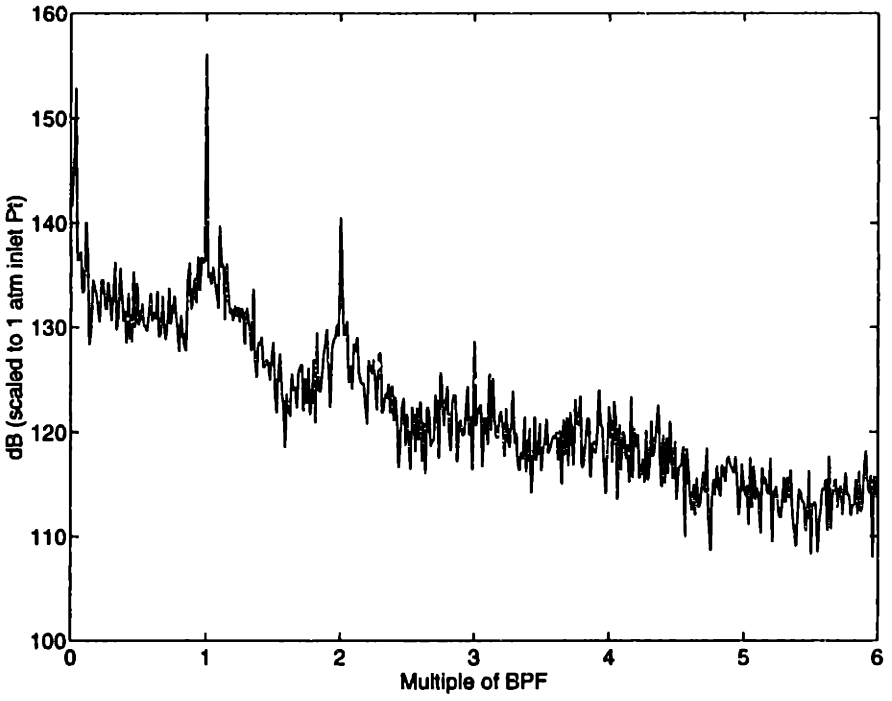

Figure 5-36: Spectra of stator transducer 3 pressure signal (4 run average) at 25% span for baseline rotor

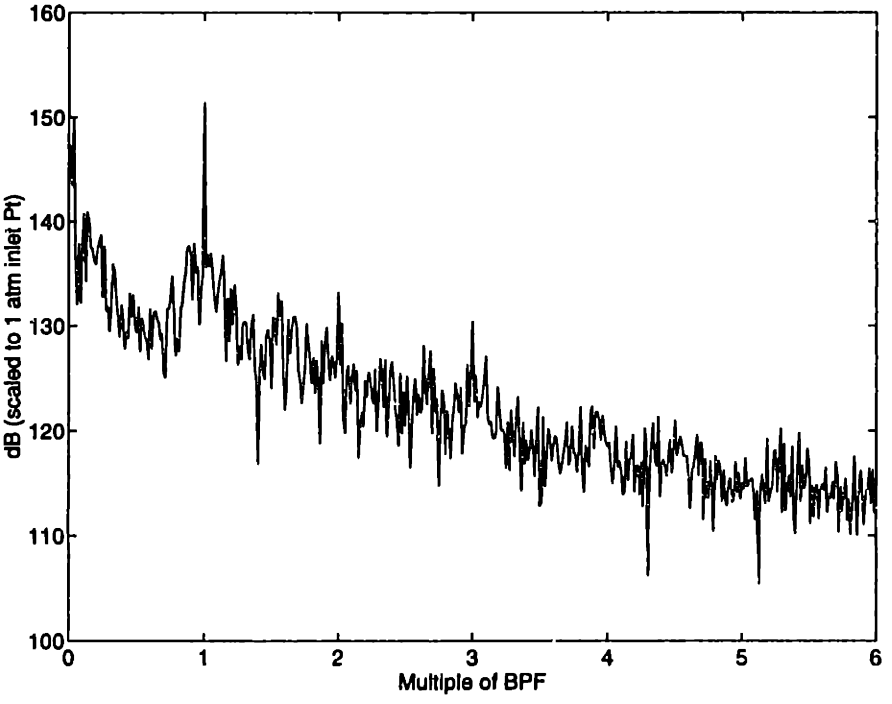

Figure 5-37: Spectra of stator transducer 3 pressure signal (4 run average) at 50% span for baseline rotor

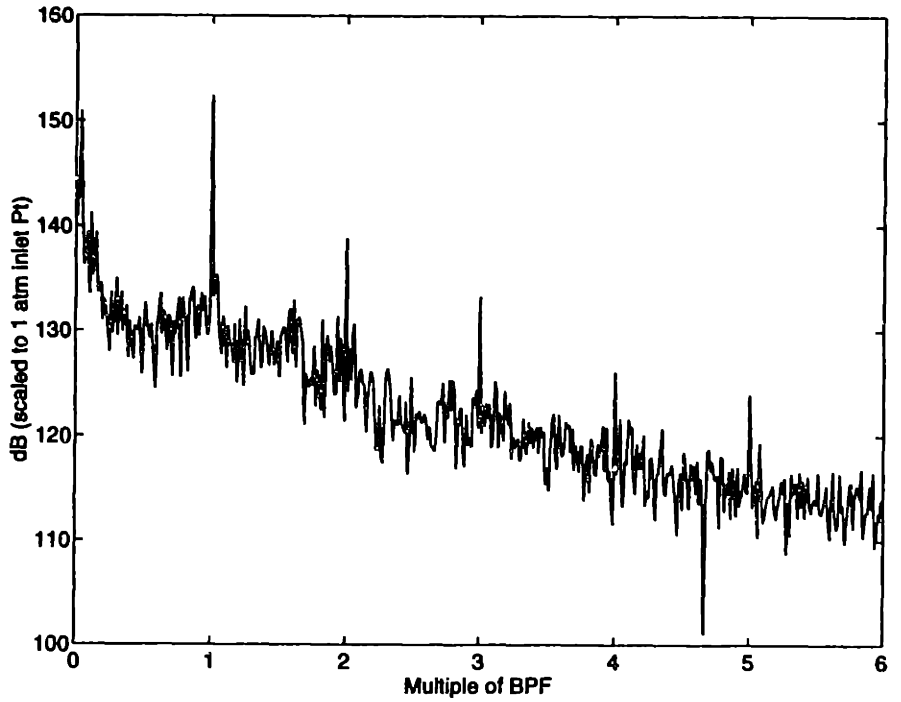

Figure 5-38: Spectra of stator transducer 3 pressure signal (4 run average) at 75% span for baseline rotor

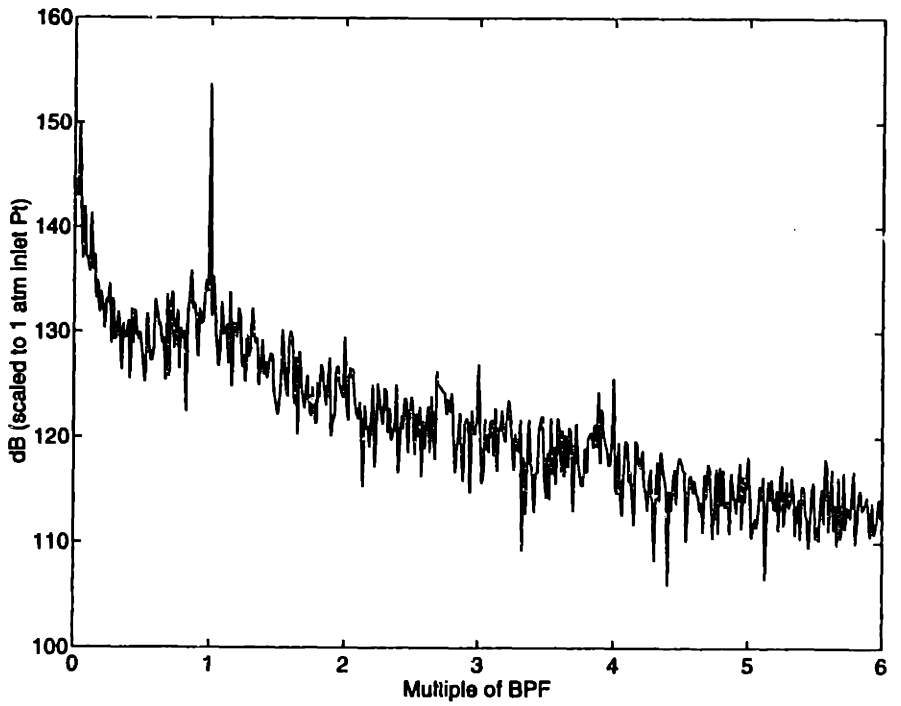

Figure 5-39: Spectra of stator transducer 3 pressure signal (4 run average) at 87.5% span for baseline rotor

ever, the amplitude of the harmonics was seen to be approximately constant along the span, which would be expected since the wake harmonics were fairly constant as well. In addition, the spanwise phase variations in 1*BPF were observed due to the wake skew. These stator measurement results could be input into acoustic models to estimate the radiated modes. Unsteady amplitudes and spectra, which were also fairly uniform along the span, could be used for broadband noise prediction.

5.4 Stator Unsteady Loading: Physical Mechanisms

The interaction of rotor wakes with downstream stator blade rows is complex. Although three-dimensional effects, such as spanwise variation and wake skew, greatly complicate the interaction, even purely two-dimensional (cascade) wake/stator interaction can be complicated. In particular, the minimum static pressure (perturbation) was found to propagate upstream along the stator chord for the fan stage geometry used in this study. To analyze this flow field, two-dimensional numerical simulations were performed with UNSFLO [9]. The conditions were similar to those found in the experimental rig.

Intuitively, one would expect to observe the minimum pressure (unsteady perturbation) to be closely associated with the position of the wake as it convects through the stator blade passage, and thus travel downstream over the stator chord. For the fan geometry used, the wake transport away from the suction side of the stator surface, toward the pressure surface, is only about 5% chord through the stator passage. Therefore, the flow field on the stator suction surface is expected to be closely coupled to the wake perturbations.

In core compressor applications, the rotor/stator blade count is usually close to one so the stator blade pressure fields are approximately in phase. Advanced turbofan geometries, however, typically have wide chord fan blades and high rotor/stator blade ratios. For the fan stage design used in this study, the rotor/stator blade number ratio is 2.5 (16 rotor blades to 40 stator blades). This results in an inlet flow field to the stator where an individual stator blade only sees 40% of the rotor (and wake) pitch, and thus the phase angle between stator blades is 144 degrees. The interaction can be seen in Figure 5-40, where contours of total pressure perturbations from the mean flow field are plotted. For low solidity (chord/pitch) blading, the blade flow fields may not interact strongly, but with

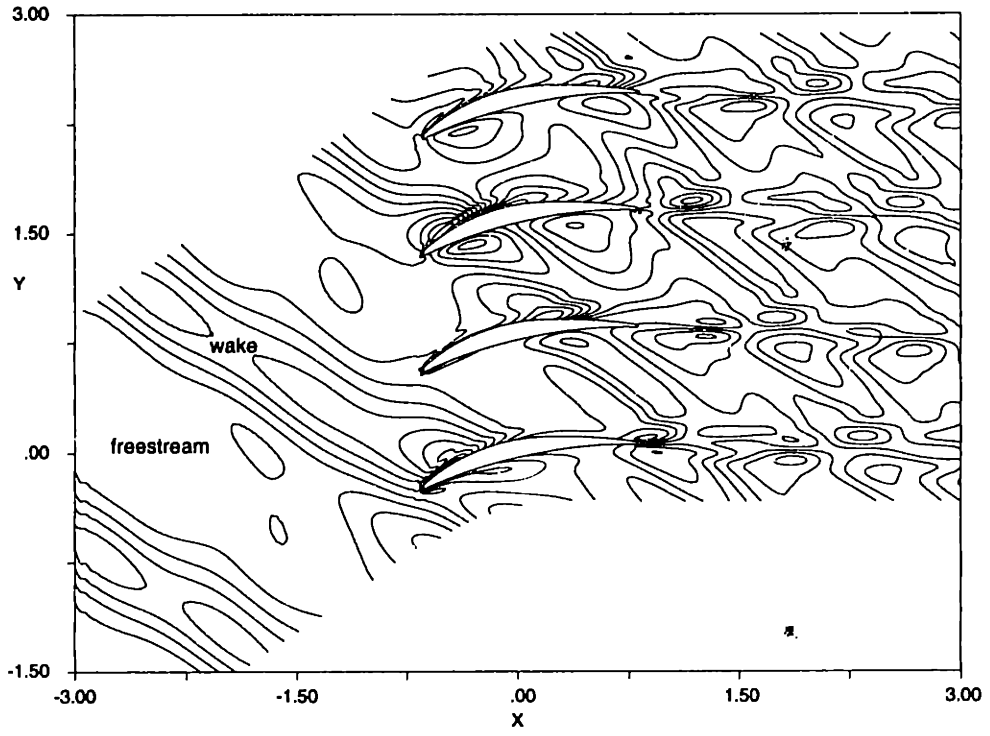

Figure 5-40: Contours of stator flow field total pressure perturbations showing wake:stator count (1:2.5) and wake angle (approx. 35 degrees)

higher solidity, a given stator blade flow field is influenced by the neighboring blade flows to a larger degree. Because of the fairly high solidity for the geometry used in this study and the large phase differences blade-to-blade, the resulting wake/stator interaction is more complicated than the interaction of a wake with an isolated airfoil.

Examining the static pressure field of the calculation shown above, it was found that the minimum static pressure perturbation traveled upstream on the stator blade surface, rather than downstream. To illustrate this effect, static pressure perturbation contours are plotted at five different times (t=0, .2, .4, .6, and .8) during the wake passing period in Figures 5-41 through 5-45, where the static pressure perturbations are nondimensionalized by the inlet stagnation pressure. Figure 5-41 is at the same time as Figure 5-40, where the wake centerline is just downstream of the lower stator's leading edge (all of the following plots show the bottom two blades of Figure 5-40 and description of minimum pressure points refer to the bottom blade). At this time (t=0) the minimum static pressure perturbation (from now on referred to simply as minimum pressure) is at the leading edge.

Examining the flow field at t=.2 (Figure 5-42), there is still a negative pressure at the

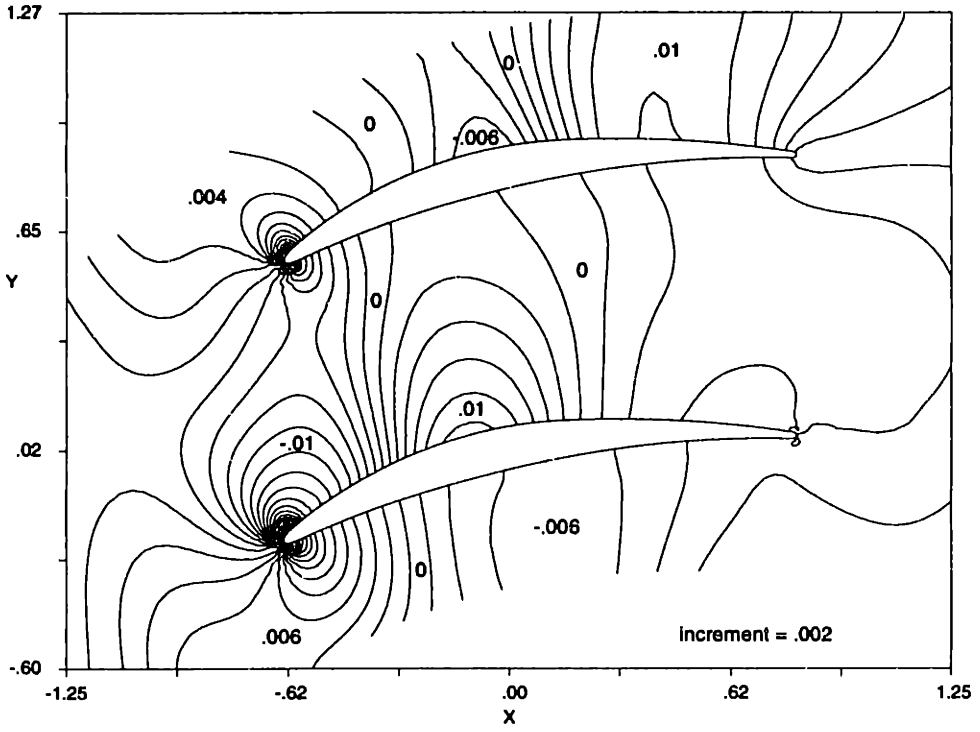

Figure 5-41: Stator flow field static pressure perturbation contours at time, t=0 wake passing periods

leading edge, but a low pressure region has appeared on the back one-half chord (minimum at approx. 75% span). Progressing to t=.4 (Figure 5-43) the minimum pressure point has moved forward to about 50% span, and the minimum pressure point moves slightly forward by t=.6 (Figure 5-44). At t=.8 (Figure 5-45), however, the minimum pressure point has moved up to about 25% chord, and the minimum pressure moves again to the leading edge at t=1.0 (same as t=0). As one can see, the migration of the minimum pressure point is not only progressing upstream, but does so in a non-uniform manner.

To understand the complex interaction that is causing the minimum pressure point (perturbation) to travel upstream, plots of total pressure perturbation contours and flow field velocity perturbation vectors are shown in Figures 5-46 through 5-55. The lower total pressure fluid in the wake traverses through the stator blade passage from t=0 to t=.8 (Figures 5-46 through 5-50, where the total pressure perturbations are nondimensionalized by the inlet stagnation pressure and multiplied by 100) as one would expect. In addition, the induced velocities (Figures 5-51 through 5-55) near the suction surface of the blade are toward the wake centerline as the wake convects away from the suction surface, also as one

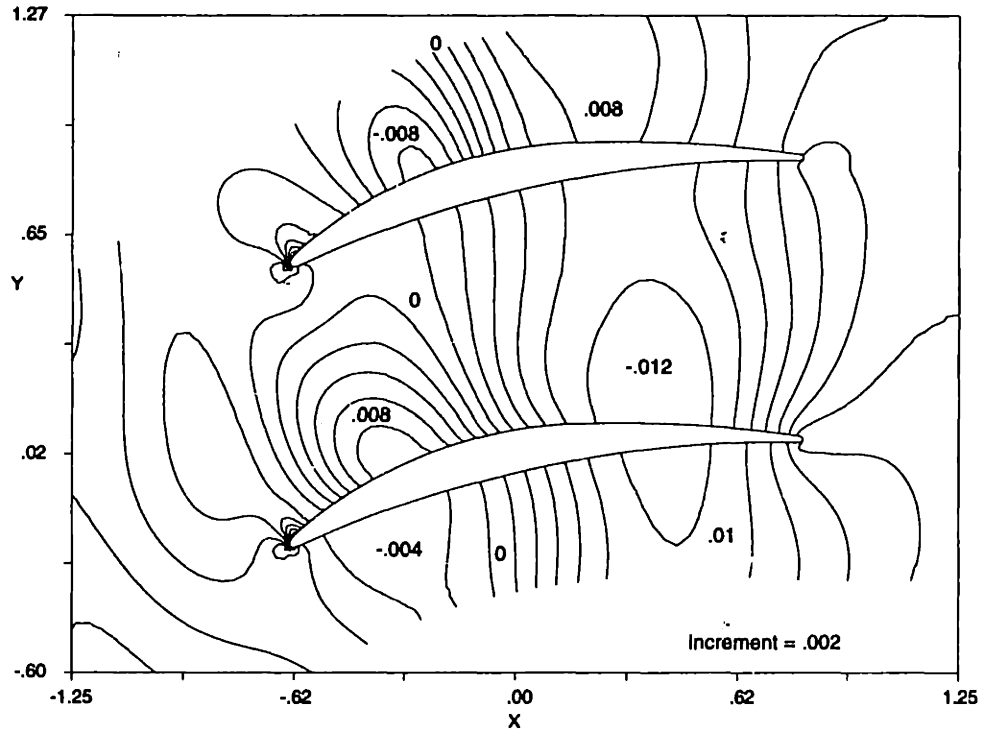

Figure 5-42: Stator flow field static pressure perturbation contours at time, t=.2 wake passing periods

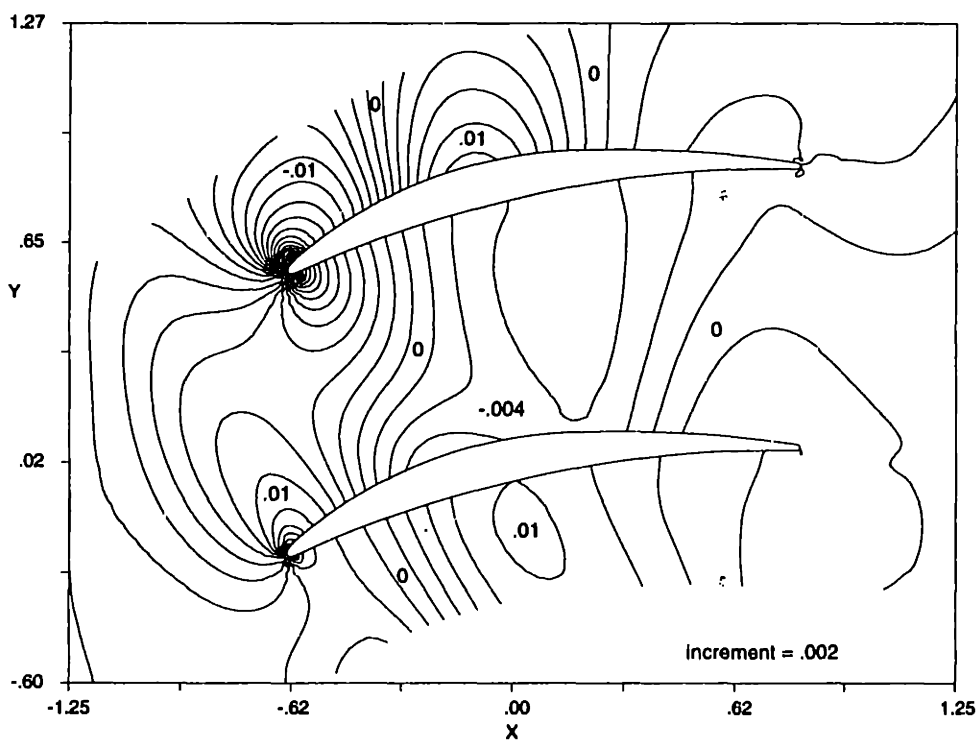

Figure 5-43: Stator flow field static pressure perturbation contours at time, t=.4 wake passing periods

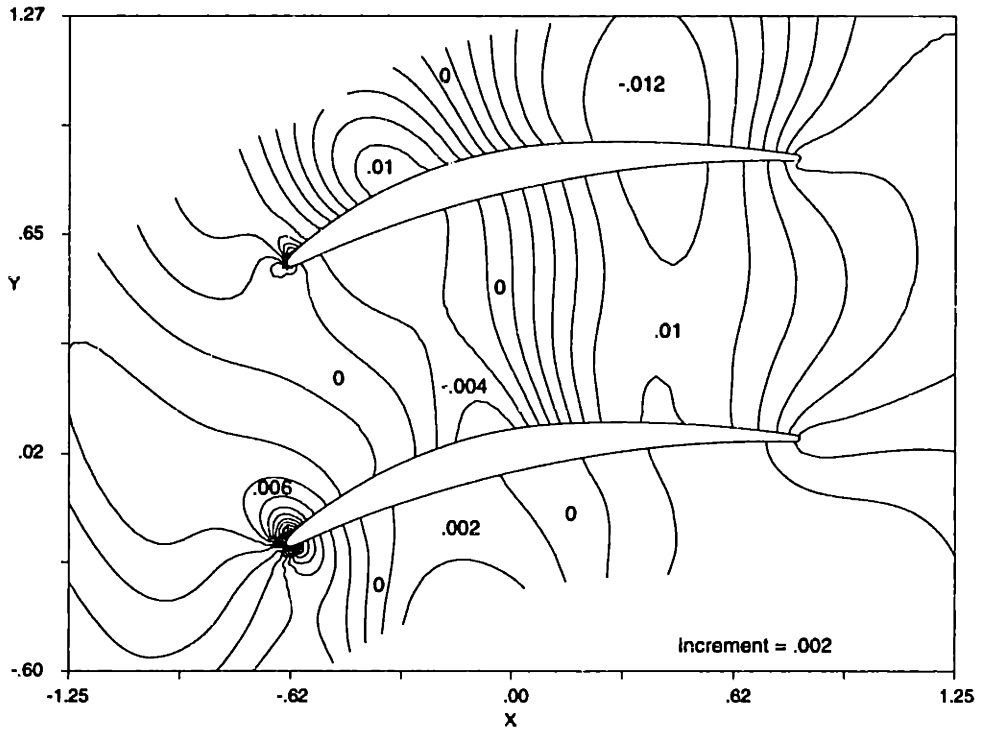

Figure 5-44: Stator flow field static pressure perturbation contours at time, t=.6 wake passing periods

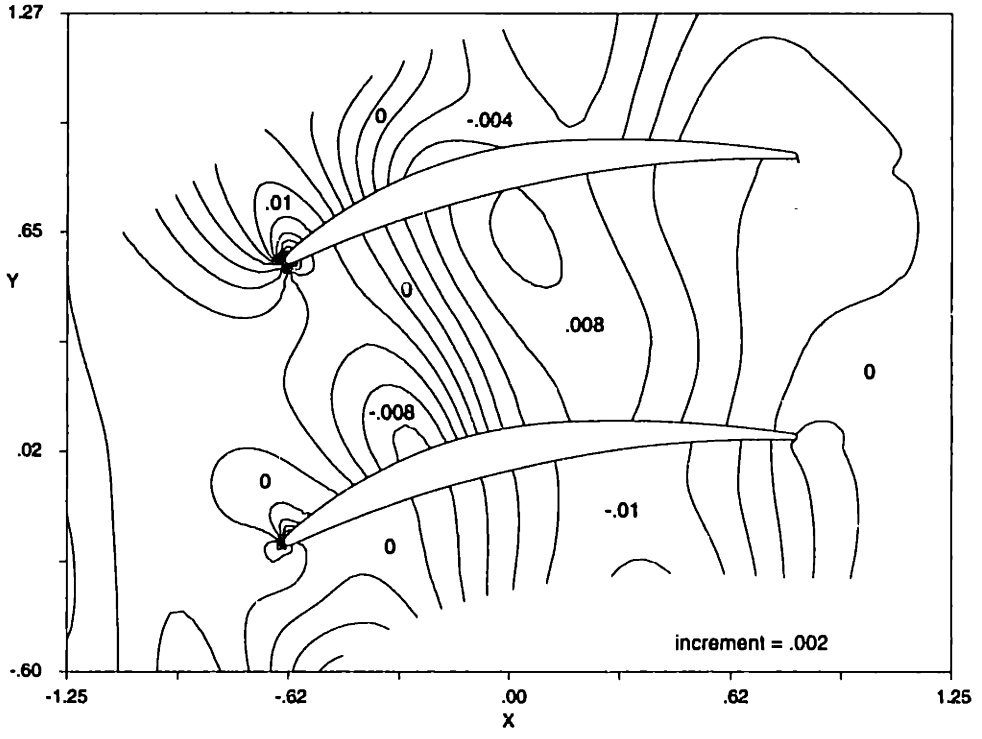

Figure 5-45: Stator flow field static pressure perturbation contours at time, t=.8 wake passing periods

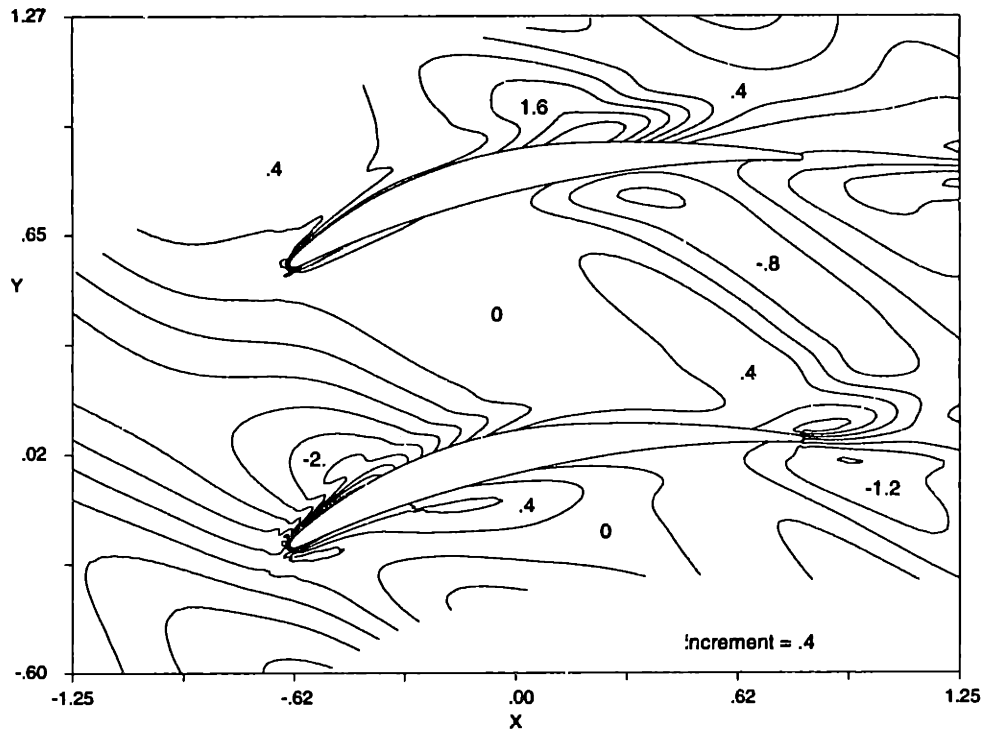

Figure 5-46: Stator flow field total pressure perturbation contours at time, t=0 wake passing periods

would expect. However, as the wake convects through the passage, the velocity perturbations that are induced near the blade surface (influenced by the neighboring blades) may either amplify or counteract the variations in total pressure of the flow field. For instance, at t=.6 the minimum static pressure perturbation (Figure 5-44) is at approximately 45% chord (lower blade in plots). Examining the total pressure contours (Figure 5-49), there is fairly high total pressure at this location (about +1.5), but there is also a large positive (in streamwise direction) velocity perturbation (Figure 5-54) caused by wake entrainment. In this instance, the velocity perturbation dominates and the net effect is a negative static pressure perturbation.

However, like the wake measurements, where it was not the centerline deficit that was important but the harmonic content of the wake profile, it is the harmonics of the static pressure perturbations on the stator that is crucial. Thus, to better quantify the effects seen above, the amplitude and phase of the static pressure perturbations on the stator blade surface (lower blade) were calculated and are shown in Figures 5-56 and 5-57 for the first three multiples of blade passing frequency (BPF). One can see that the phase of the

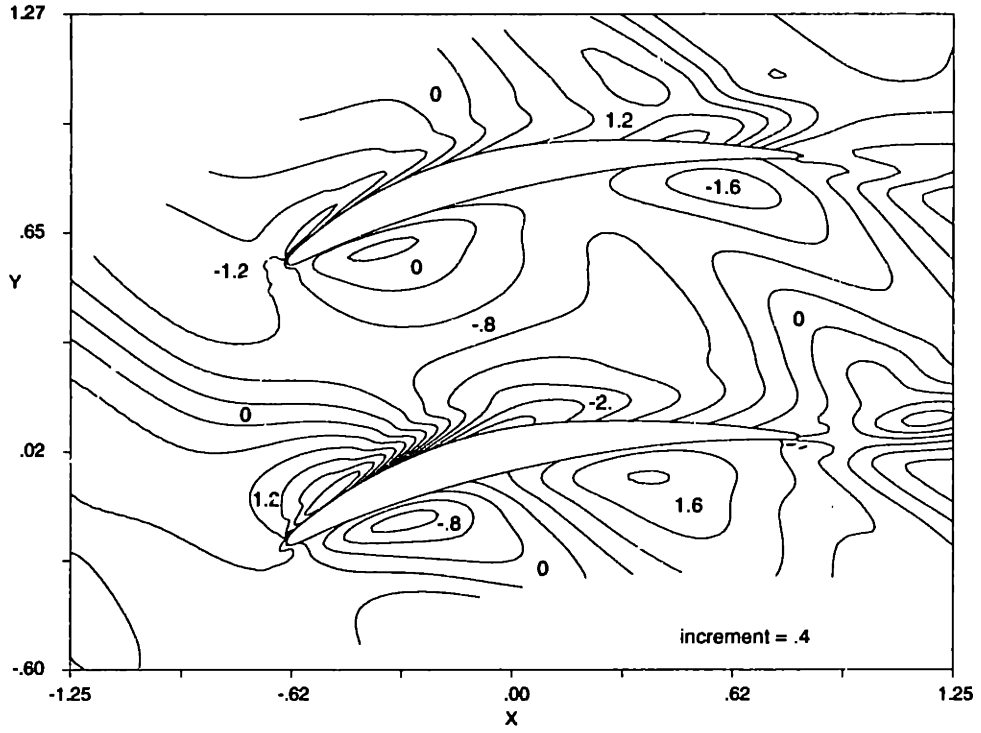

Figure 5-47: Stator flow field total pressure perturbation contours at time, t=.2 wake passing periods

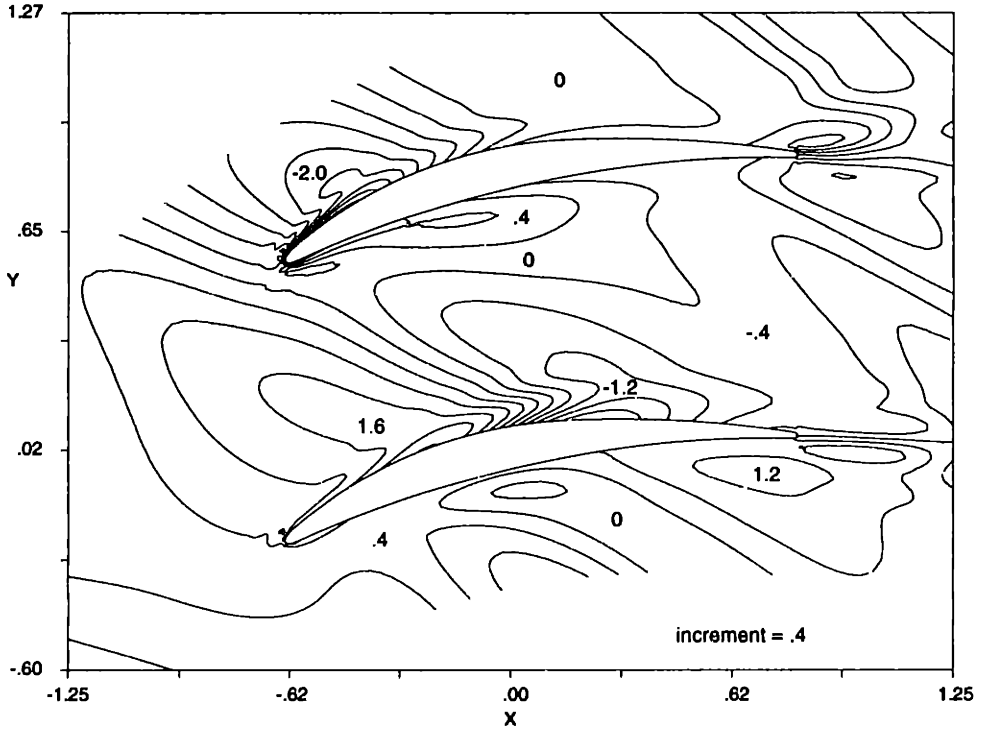

Figure 5-48: Stator flow field total pressure perturbation contours at time, t=.4 wake passing periods

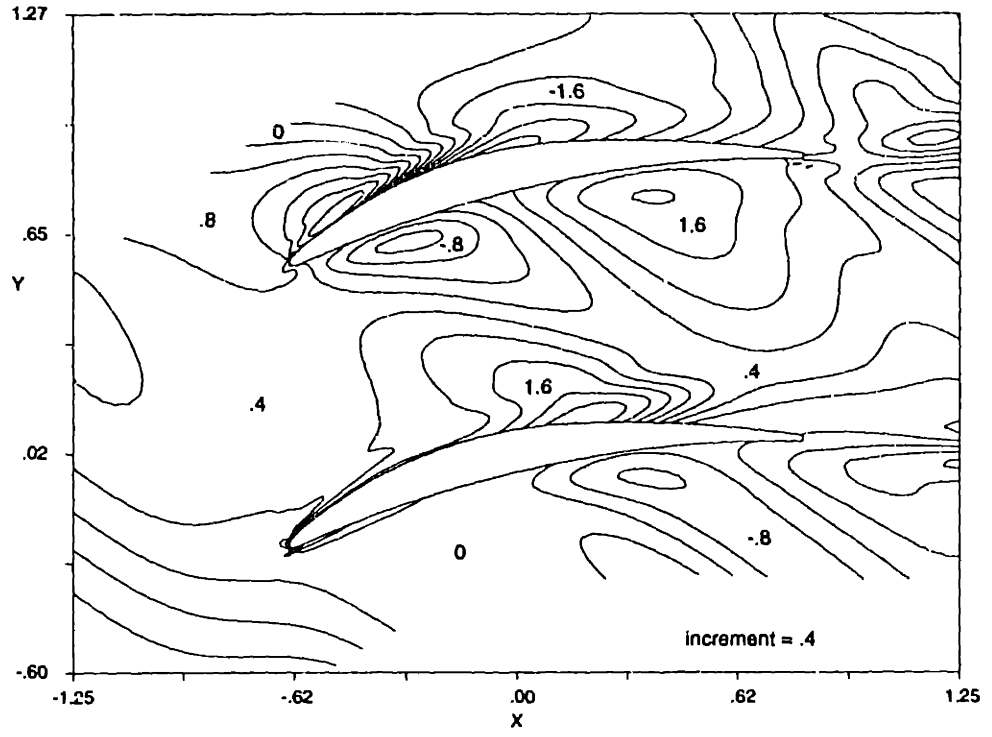

Figure 5-49: Stator flow field total pressure perturbation contours at time, t=.6 wake passing periods

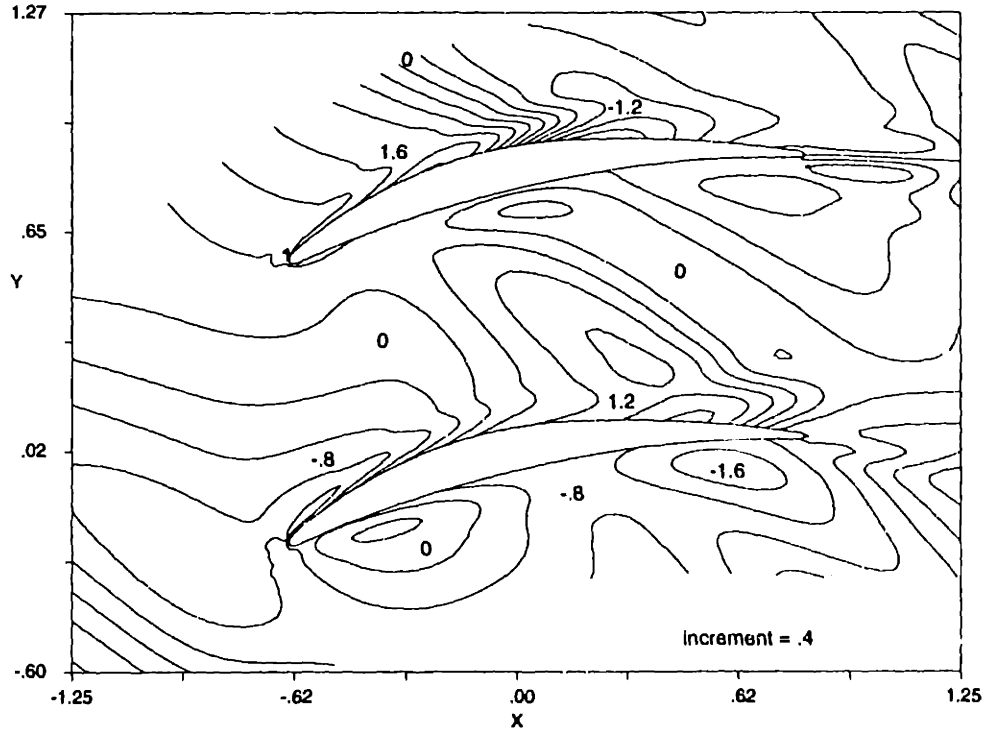

Figure 5-50: Stator flow field total pressure perturbation contours at time, t=.8 wake passing periods

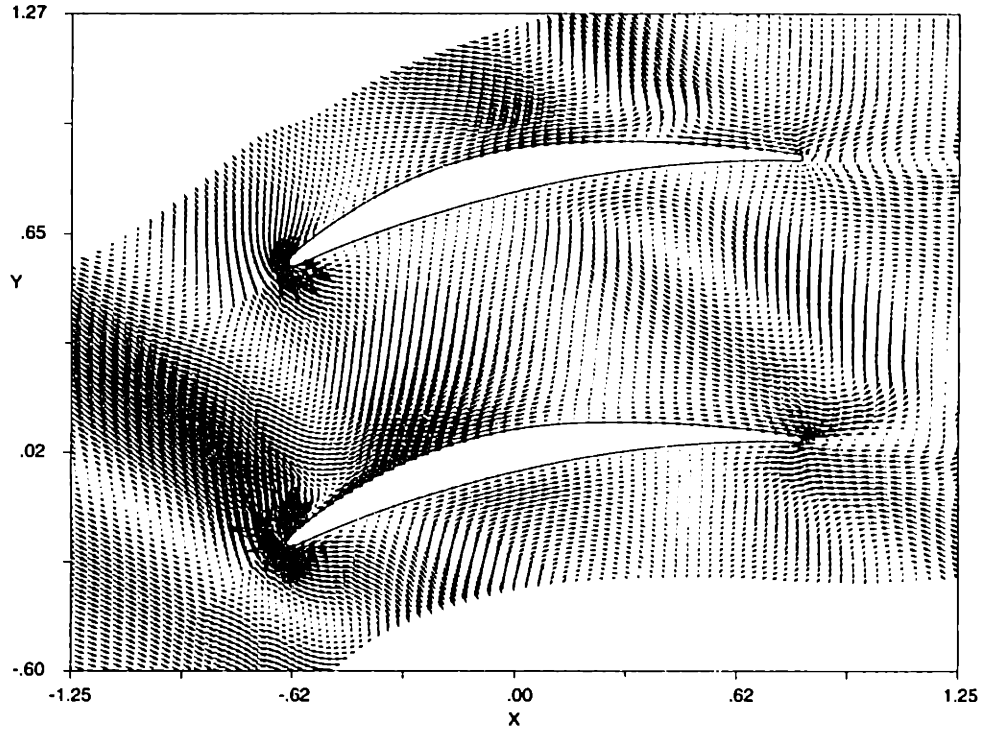

Figure 5-51: Stator flow field velocity perturbation vectors at time, t=0 wake passing periods

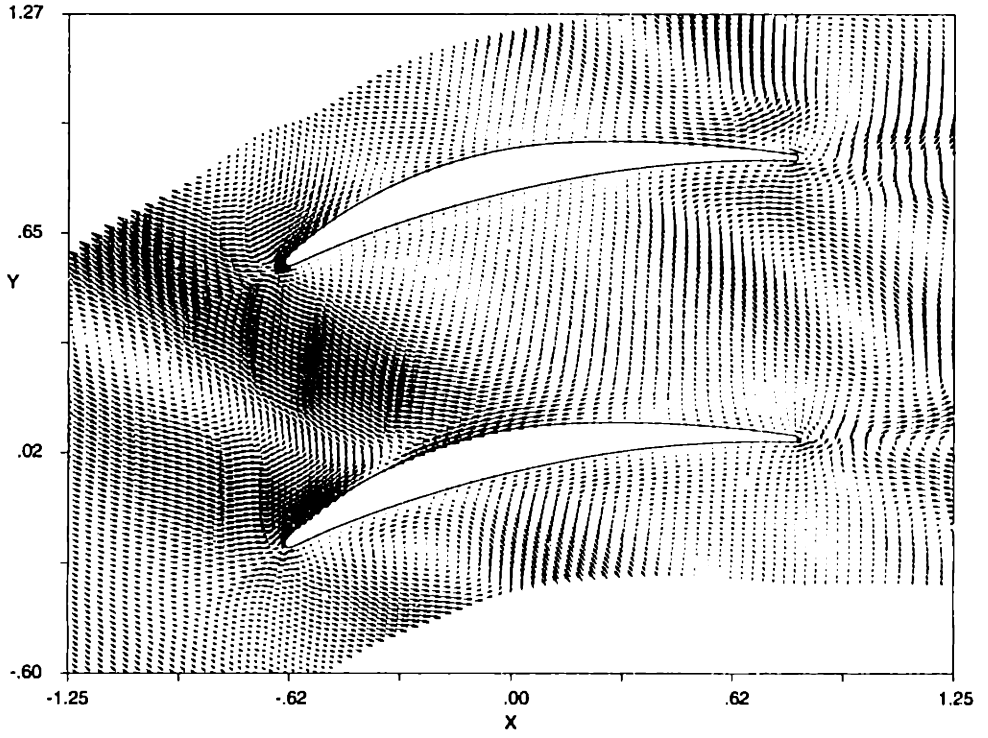

Figure 5-52: Stator flow field velocity perturbation vectors at time, t=.2 wake passing periods

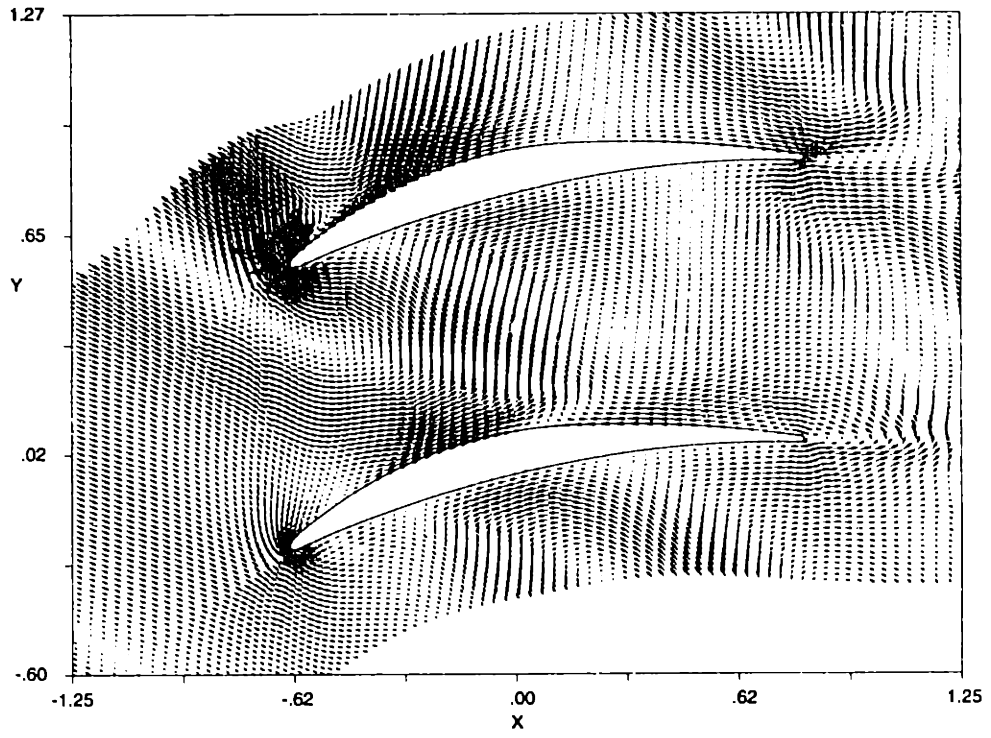

Figure 5-53: Stator flow field velocity perturbation vectors at time, t=.4 wake passing periods

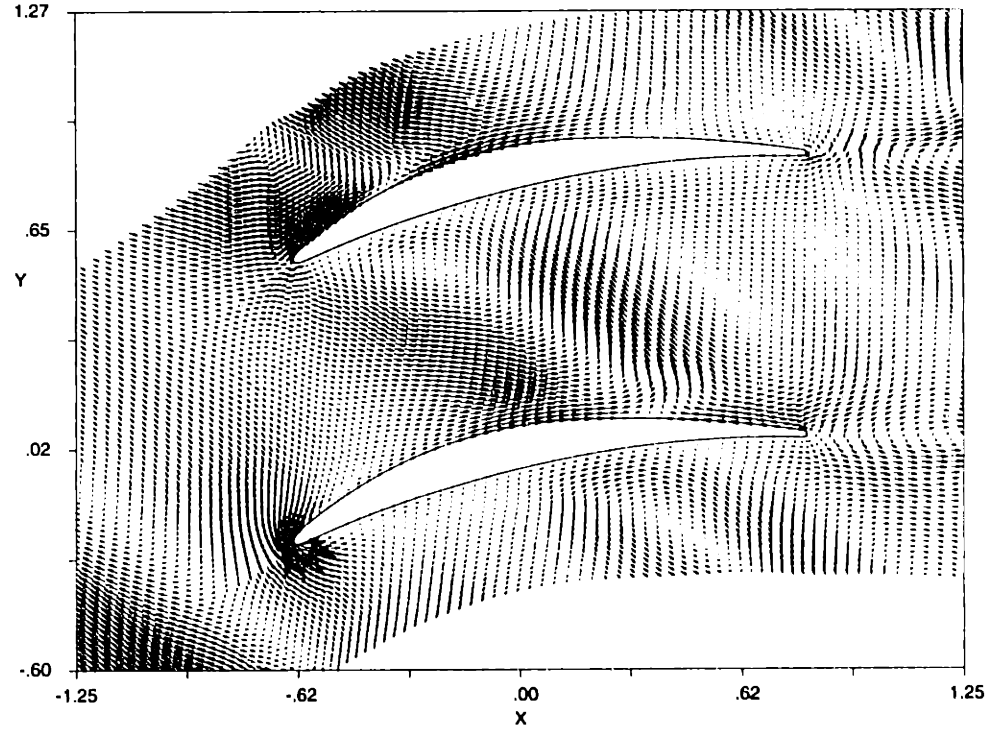

Figure 5-54: Stator flow field velocity perturbation vectors at time, t=.6 wake passing periods

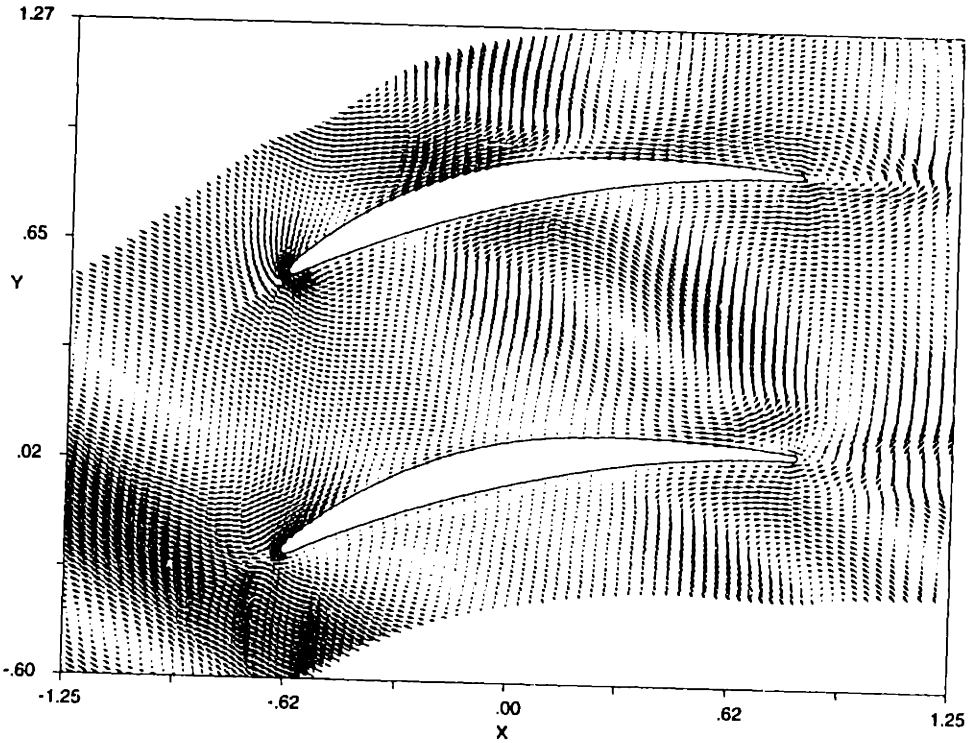

Figure 5-55: Stator flow field velocity perturbation vectors at time, t=.8 wake passing periods

BPF static pressure fluctuation is approximately linear and travels upstream (increasing phase angle). In general, however, the amplitudes and phases of the perturbations are complicated functions of stator chordwise position, particularly for higher harmonics, which can strongly influence the coupling to acoustic modes. While the simulation was not run to match a particular condition in the experimental rig, the results show qualitative agreement in minimum pressure phase direction and overall nonlinear behavior.

Conclusions

The minimum static pressure perturbation on the stator surface due to rotor wake/stator interaction may travel either upstream or downstream. Experimental data on compressor stages with equal blade counts have shown phases traveling downstream [8], and other geometries have demonstrated phases traveling upstream [3] (in addition to the geometry used in this study). The complex interaction depends strongly on the rotor/stator blade number ratio and the stator solidity. The position of the minimum unsteady static pressure at any given time is a result of the competing effects of total pressure variations (wake to

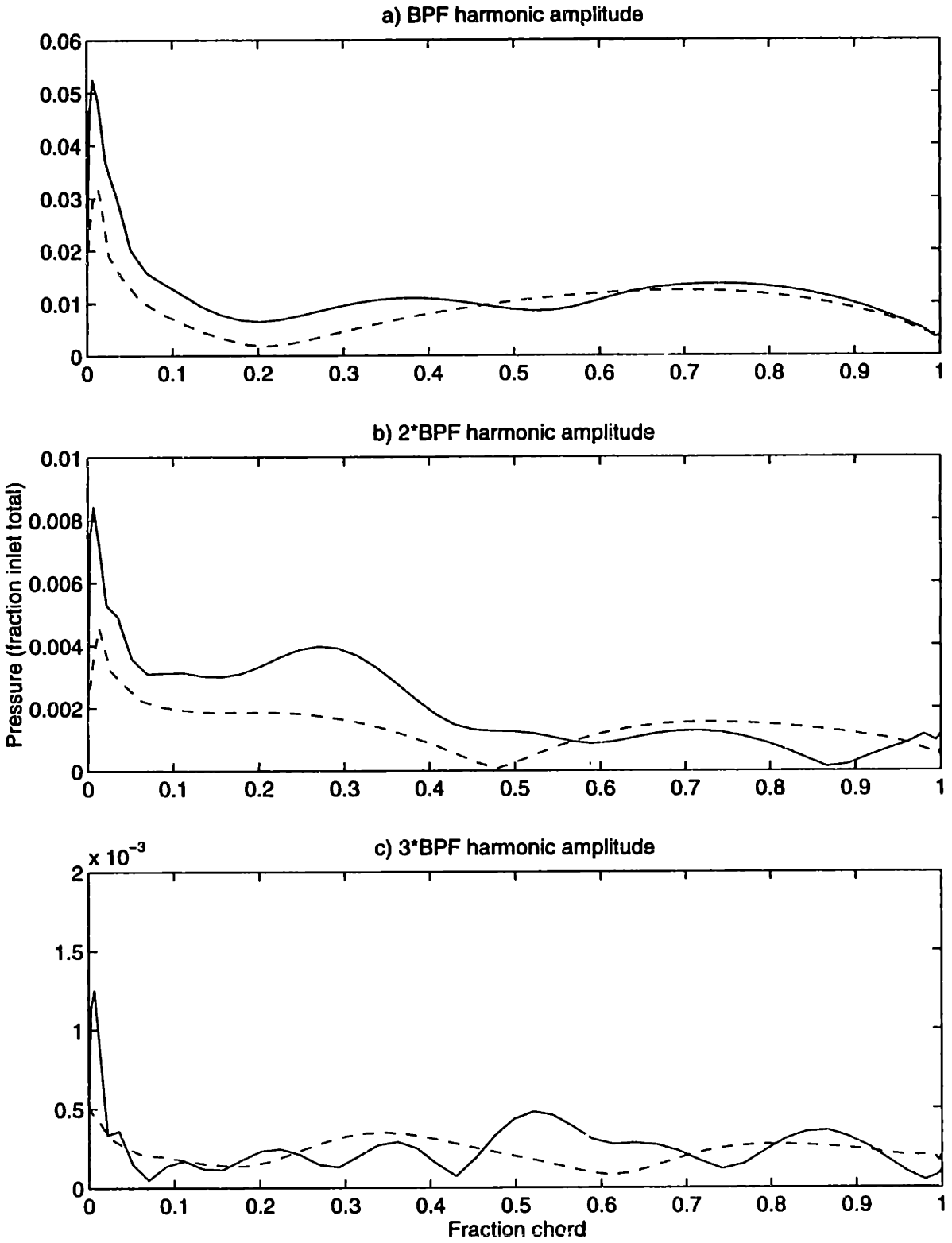

Figure 5-56: Stator unsteady loading harmonic amplitudes versus chordwise position: suction surface (—) and pressure surface (– .)

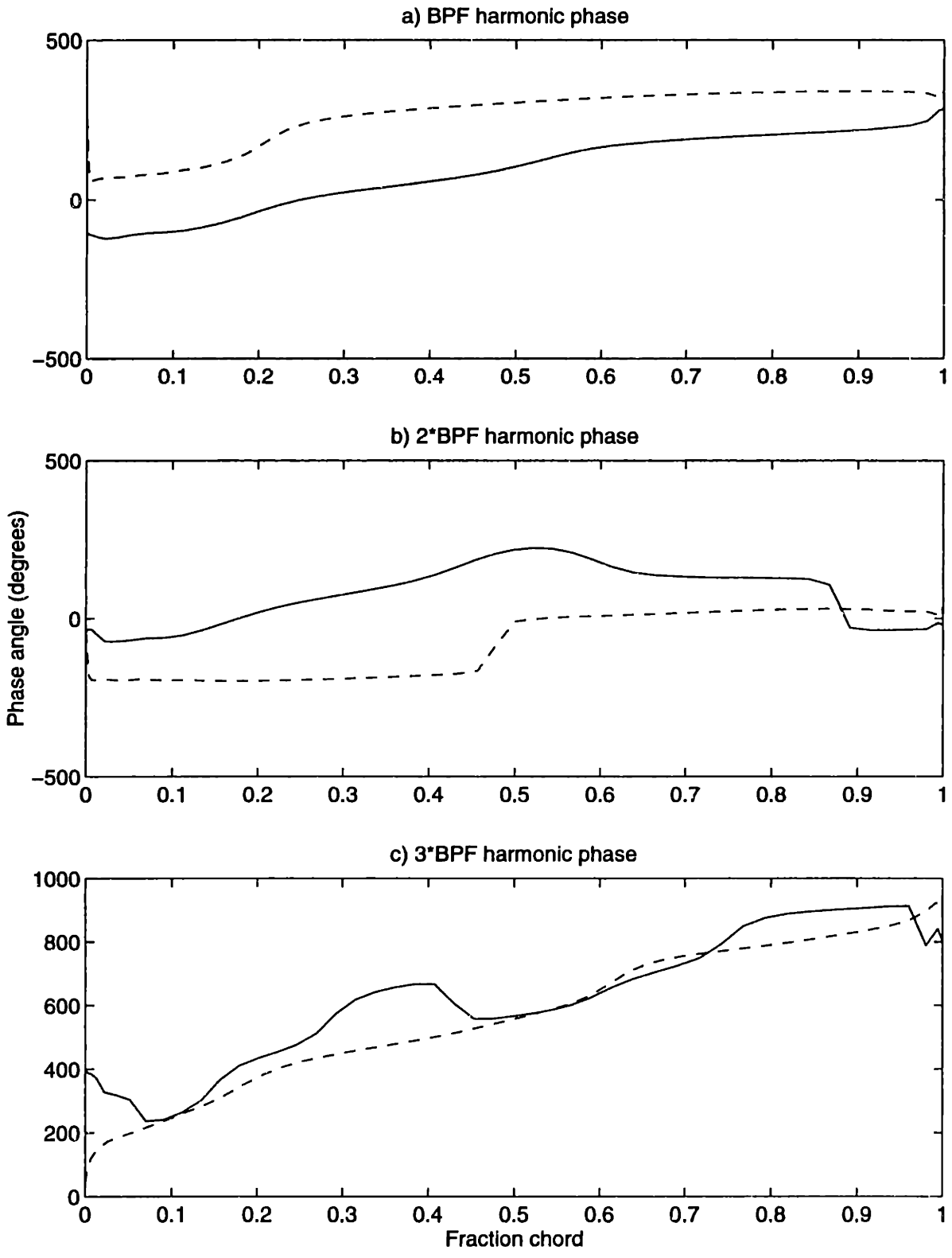

Figure 5-57: Stator unsteady loading harmonic phases versus chordwise position: suction surface (—) and pressure surface (- .)

freestream) and the induced velocities in the blade passage (which are influenced by the flow fields of the neighboring blades). The phase of the minimum pressure perturbation along the stator chord may therefore vary from linear to more complex than those shown above, and the amplitudes vary considerably as well, both depending on the geometry of interest. Since both the phase and amplitude distributions are important for coupling to acoustic modes, the complex nature of both must be taken into account when modeling noise generated by rotor wake/stator interaction. Further, it can be inferred that geometries with low hub-to-tip ratios (large radial variation in stator solidity) and large spanwise flow field variations (rotor loading distribution) may have minimum pressure perturbations on the stator blades that travel in different directions at different spanwise locations.

5.5 Measured Acoustic Modes: Microphones

Acoustic duct modes were measured using pairs of microphones at three axial locations. The pairs were located upstream and downstream of both the rotor and stator, and each pair was spaced $1/16^{th}$ of a circumference apart at the same axial location. Since all the propagating acoustic modes due to perfect rotor wake-stator interaction were multiples of 8 (see Table 2.2) and each multiple of blade passing frequency (3 to 5*BPF) had mode pairs with one mode in and one mode out of phase at the two microphones, each mode up to 5*BPF could be distinguished. Naturally, any additional mode present due to blade-to-blade differences or inlet distortion would effect the measurement of the expected modes.

Acoustic data was taken during all tests, but the data presented here will be primarily that taken during stator measurement tests. These tests had no probes in the flow field, and thus represent clean flow conditions. The instrumented stator blade acts simply as any other stator blade.

To obtain the individual acoustic modes, the signals from the microphone pair at a given axial location were either added or subtracted to obtain the in or out of phase mode, respectively. As alluded to earlier, the 2*BPF mode downstream of the stator is the strongest mode in the system (due to rotor wake-stator interaction). This was observed in the acoustic calculations using LINSUB [34] in the preliminary assessment in Section 3.1, where the 2*BPF mode downstream of the stator was approximately 16 dB higher than

any other propagating mode.

The in and out of phase harmonic amplitudes of the averaged microphone signals (sum and difference) downstream of the stator are plotted in Figure 5-58 a and b. The m = -8 mode at 2*BPF is out of phase at the two microphones and can be clearly seen in Figure 5-58b. The in phase 2*BPF amplitude in Figure 5-58a is approximately 16 dB smaller than the out of phase. There is a significant BPF harmonic present which is believed to be due to a combination of the evanescent BPF mode downstream of the stator and acoustic modes due to inlet distortion and/or blade-to-blade differences.

An estimate of the broadband noise is provided in Figure 5-59, which is the noise spectra from one microphone downstream of the stator row. 2*BPF is clearly seen, but the higher harmonic tones are nearly in the noise floor, since the 2*BPF, m = -8 tone is only about 15 dB above the broadband noise. Additional tones can be seen at multiples of shaft frequency (1/16th BPF) due to blade-to-blade differences, and the electrical noise at 60 Hz is quite evident.

In general, the acoustic modes are not easily measured due to the geometry of the facility. However, the strongest propagating mode (that which is dominant in the noise spectrum and must be reduced the most) can be easily distinguished from the noise floor. Additional data showing the acoustics upstream and downstream of both the rotor and stator for test conditions with and without an inlet distortion generated by a 1/2 inch rod is presented in Appendix B.

5.6 Summary and Conclusions of Baseline Rotor Measurements

Measurements were taken for a solid fan geometry to establish the baseline flow field, stator unsteady loading, and acoustics. This data was then used to facilitate the design of the wake management trailing edge blowing blades, as well as to establish necessary data reduction routines. The principal conclusions from the baseline experiments are discussed below.

1) The ensemble-averaged mean wake profiles showed little variation in harmonic content for multiples of blade passing frequency (BPF) in the spanwise direction. At 1.7c

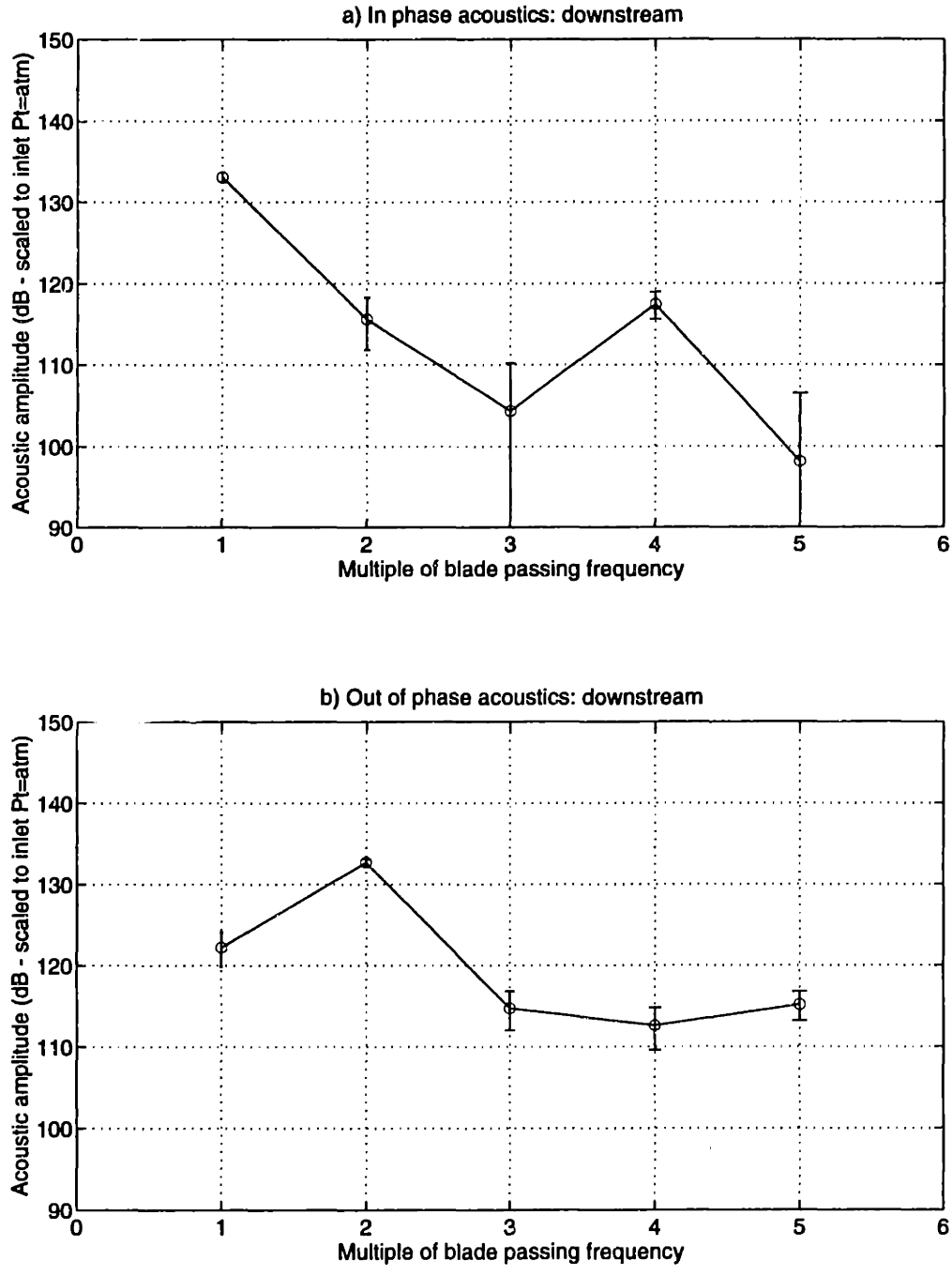

Figure 5-58: Measured duct acoustic mode amplitudes downstream of the stator row (scaled to an inlet total pressure of one standard atmosphere)

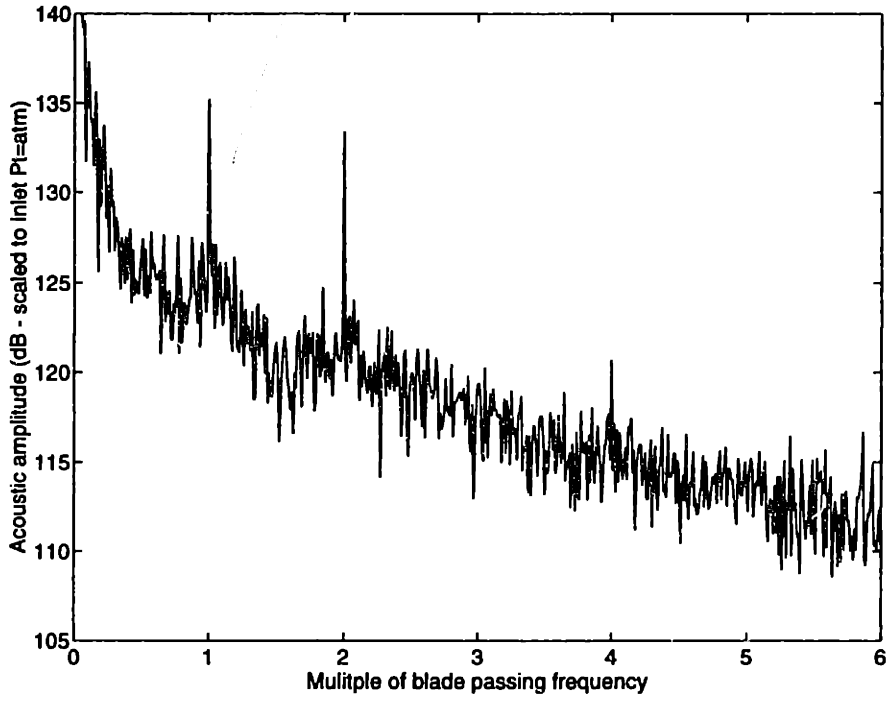

Figure 5-59: Measured duct acoustic noise spectrum downstream of the stator row

rotor/stator spacing, the tip clearance flow is over one-half pitch in width and in thus made up primarily of 1*BPF. It is therefore expected that the tip clearance flow is not the dominant tonal noise source for propagating modes of this fan stage geometry. In addition, the turbulence intensity was virtually constant along the span of the wake, but broader in the endwall flow regions. Further analysis is required to determine the relative importance of the peak turbulence intensity versus the circumferential extent of the fluctuations on the radiated broadband noise.

2) Like the wake profiles, the unsteady loading on the stator blade showed little variation in harmonic amplitude for the higher BPF harmonics along the span. The amplitude of the unsteady fluctuations was nearly constant with spanwise position as well.

3) Minimum phase of pressure on the stator blade was found to propagate in the upstream direction on the stator surface. This is believed to be the result of the combination of total pressure difference between the wake and the freestream and the induced velocity field in the stator passage. This phenomena would be design dependent, being influenced largely by rotor/stator blade count and pitch-to-chord ratio of the stator row.

4) The dominant propagating acoustic mode (2*BPF downstream) is clearly seen in the microphone data and is approximately 15dB above the broadband. However, because this mode is 15-16dB above all other propagating modes, higher harmonic modes are near, or in, the broadband noise floor. Changes in the 2*BPF mode downstream of the stator row due to wake management treatment should be identifiable.

CHAPTER 6

DESIGN METHODOLOGY FOR WAKE MANAGEMENT BLADES

Upon completion of the preliminary flow field measurements downstream of the baseline fan rotor, results from the two-dimensional studies (Chapters 1 and 3) were coupled with the measured wake characteristics to facilitate the design of wake management blades. Because the effectiveness of boundary layer suction was limited by trailing edge thickness, as well as blade internal flow area, only trailing edge blowing blades were designed and built. However, the design process for blades with boundary layer suction or a combination of boundary layer suction and trailing edge blowing, as discussed in a patent application filed on wake management blade design [39], would be very much the same.

The design methodology utilized information from both fluidic and structural measurements and analysis. In the following sections, the information gathered to facilitate the final design is presented. First the results of the two-dimensional study are briefly summarized in Section 6.1, followed in Section 6.2 by the results of the baseline rig tests. Section 6.3 then describes some of the structural limitations imposed on internal blade passages, and Section 6.4 presents the simplified model used to estimate the passage flow. The generic injection geometry used is then described in Section 6.5, followed by the estimation of the flow characteristics for the actual blade design in Section 6.6. Finally, schematics of the blade design are shown in Section 6.7 and the fabrication strategy is discussed in Section 6.8.

6.1 Results from Two-Dimensional Studies

The results from two-dimensional cascade testing presented in Chapter 3 showed reductions in the wake harmonic amplitudes of greater than 75% and a decrease in the unsteady fluctuations of 60%. Trailing edge blowing was completed using several different injection port geometries (results of each are presented in Sell, [33]), with blowing at the deviation angle of the mean flow field providing the best wake smoothing (both mean and unsteady components).

Flat plate experiments of Naumann [26] and Corcoran [2] used several different port geometries as well, and showed that discrete spanwise ports provide increased mixing in the wake compared to a continuous slot. Thus, two-dimensional results would imply that the geometry for maximum reduction of the wake mean deficit and unsteadiness is trailing edge blowing through discrete ports at the deviation angle[1].

6.2 Fan Flow Field Characteristics

To design the trailing edge blowing wake management blades, the wake characteristics and the freestream flow field must be known. With these quantities, the amount of injection required to obtain a momentumless wake can be calculated as a function of span. This calculation requires the knowledge of the pressure, density, and flow velocity of the freestream flow at the blade trailing edge, as well as the boundary layers and wake momentum and displacement thicknesses. Since the 4-way probe can only measure pressure and Mach number quantities downstream, the flow variables in the blade passage were obtained through numerical simulation (with comparison to experimental data when possible). The flow variables used in the design process, as well as trailing edge thicknesses, are shown in Table 6.2.

In addition to the wake measurements, calculations were performed to determine both the boundary layer characteristics on the blade surfaces, as well as the downstream wake mass and momentum thicknesses. Ideally, injection would be performed to eliminate both

[1]This excludes the addition of vortex generators and other devices which increase mixing, but have potentially deleterious effects on the blade row performance with the blowing turned off.

Flow variable	Spanwise location (fraction span)			
	.20	.50	.75	.85
P/Pt(up)	.98	1.02	1.0575	1.07
ρ/ρ(up)	1.11	1.15	1.16	1.17
M(rel)	.45	.54	.61	.625
θ(wake)/r(tip)	.0045	.0032	.0034	.0042
t.e. thickness / r(tip)	.0021	.0020	.0019	.0018
M(injection) (continuous t.e. slot)	.90	1.03	1.153	1.35

Table 6.1: Fan flow field conditions used for wake management trailing edge blowing blade design

the mass and momentum deficit in the resulting wake so the freestream flow is unchanged as the wake mixes out. However, as the injection port size decreases relative to the boundary layer thickness, the required velocity increases (as the square root of size) for the same momentum addition, resulting in lower mass addition. For typical blade airfoils, blowing ports will have this characteristic due to finite trailing edge thickness and a compromise must be made. For complete filling of the momentum deficit, the required injection velocity is given by $u_j/U = \sqrt{\theta_{wake}/w}$, with θ_{wake} = wake momentum thickness, w = injection port width, and U = freestream velocity for density of the injection fluid equal to the freestream value. This results in less than complete filling of the mass deficit of the wake. Further, since most of the base pressure effect is eliminated by blowing, injection at this velocity may slightly over-compensate the wake momentum deficit. The resulting injection Mach numbers are shown in Table 6.2 for continuous slot injection at one-half the trailing edge thickness, using the experimentally measured wake momentum thickness. Throughout the design process, the required mass flow and the flow area necessary to deliver that flow were conservatively estimated. In addition, the passages were designed to be easily throttled (at the root inlet) for maximum flexibility.

With the flow variables known and the injection port velocities calculated, a minor obstacle to the design process becomes apparent. The resulting injection flow velocities on

the outer portion of the span are supersonic. This results because of the thin airfoils near the tip and the high freestream flow velocities (relative frame)[2]. The velocities calculated thus far were obtained assuming the injection port width to be one-half the trailing edge thickness, while injection at the deviation angle would occur upstream where the blade airfoil is thicker (enabling larger injection port width). At the tip, however, the injection flow with these larger port widths was still calculated as being supersonic. To eliminate the need of a convergent/divergent nozzle the outer span jets were designed to be under-expanded, sonic flow. In addition, subsonic injection would be susceptible to unsteady behavior and would not remain non-dimensionally constant throughout the test time. Therefore, the lower span injection ports were adjusted to ensure sonic flow as well, such that the flow was choked at the injection orifices (with the correct mass flow and total pressure) along the full span.

6.3 Structural Limitations

In addition to the complicated fluid mechanics involved in the design of blades with internal wake management passages, limitations imposed by mechanical loading must be considered. There are several issues that must be examined: 1) centrifugal loading, 2) aerodynamic loading, and 3) blade internal pressures. Each of these issues will be discussed in this section. Since the tests are completed in a blowdown manner, the total testing time anticipated for the blades is short (on the order of a few hours), so fatigue issues were not addressed.

Centrifugal Loading

The loading due to centrifugal acceleration is the dominant source of stress on typical high speed rotating blades. The loading causes the blades to grow radially and to untwist. This causes both stresses along the span of the blade and torsional shear. By designing internal blade passages which are everywhere the same percent of local blade thickness and chord (as illustrated in Figure 6-1a), the stresses along the span of the blade should be virtually unchanged, since each section of airfoil is still carrying the same amount of outboard material

[2]It should be stated at this point that if designing an engine from scratch incorporating wake management strategies, the fan blade airfoils, as well as many other aspects of the engine, may be designed quite differently from those used in this study However, the basic design strategy discussed here would remain the same.

as the solid blade.

In addition, by removing the inner area of an circular rod (as shown in Figure 6-1b), the torsional strength is reduced to $1 - (d/D)^4$ of the solid rod. Therefore, if the blade internal passages are 50% of the local blade thickness ($d/D = 0.5$), the torsional loading should not be significantly increased (less than 10%). Of course, the opening of the passage near the trailing edge will basically remove that portion of the airfoil as a torsion load member. This is one reason to have multiple internal passages, each with turning vanes and discrete injection slots, so that the shear loop is not greatly altered due to the injection port opening (shear stress is approximately inversely proportional to the length of the solid material loop, *i.e.* airfoil skin and/or internal ribs).

Aerodynamic Loading

Aerodynamic loading of rotating blades is typically much smaller than the forces due to centrifugal loading, but still must be addressed. The rotor does work by turning the flow about 35 degrees in the tangential direction. Through this turning process, the blade is loaded perpendicular to the direction of the inlet velocity field, imposing a bending moment on the blade, as well as torque. The aerodynamic torque is generally in the opposite direction as that due to centrifugal loading, and the bending moment applies tensile spanwise stresses on the pressure side of the blade and compression on the suction side. Therefore, the maximum stress levels (tensile) are typically near the root on the pressure side of the blade. Like the decrease in torsional strength, the decrease in bending strength can be estimated by removing the middle area from a square rod (see Figure 6-1c). Removing the central section of the thickness, the strength is reduced to $1 - (h/H)^3$ of the solid bar. For removal of the middle fifty percent of the thickness, the decrease in bending strength is only 12.5%. If both the blade skins (pressure and suction sides) are left intact, internal passages should not significantly increase the stresses due to aerodynamic loading.

Wake Management Pressure

Lastly, the effects of internal blade pressure must be estimated. To drive the flow through the blade passages, the pressure of the flow in the blade must be several times that outside

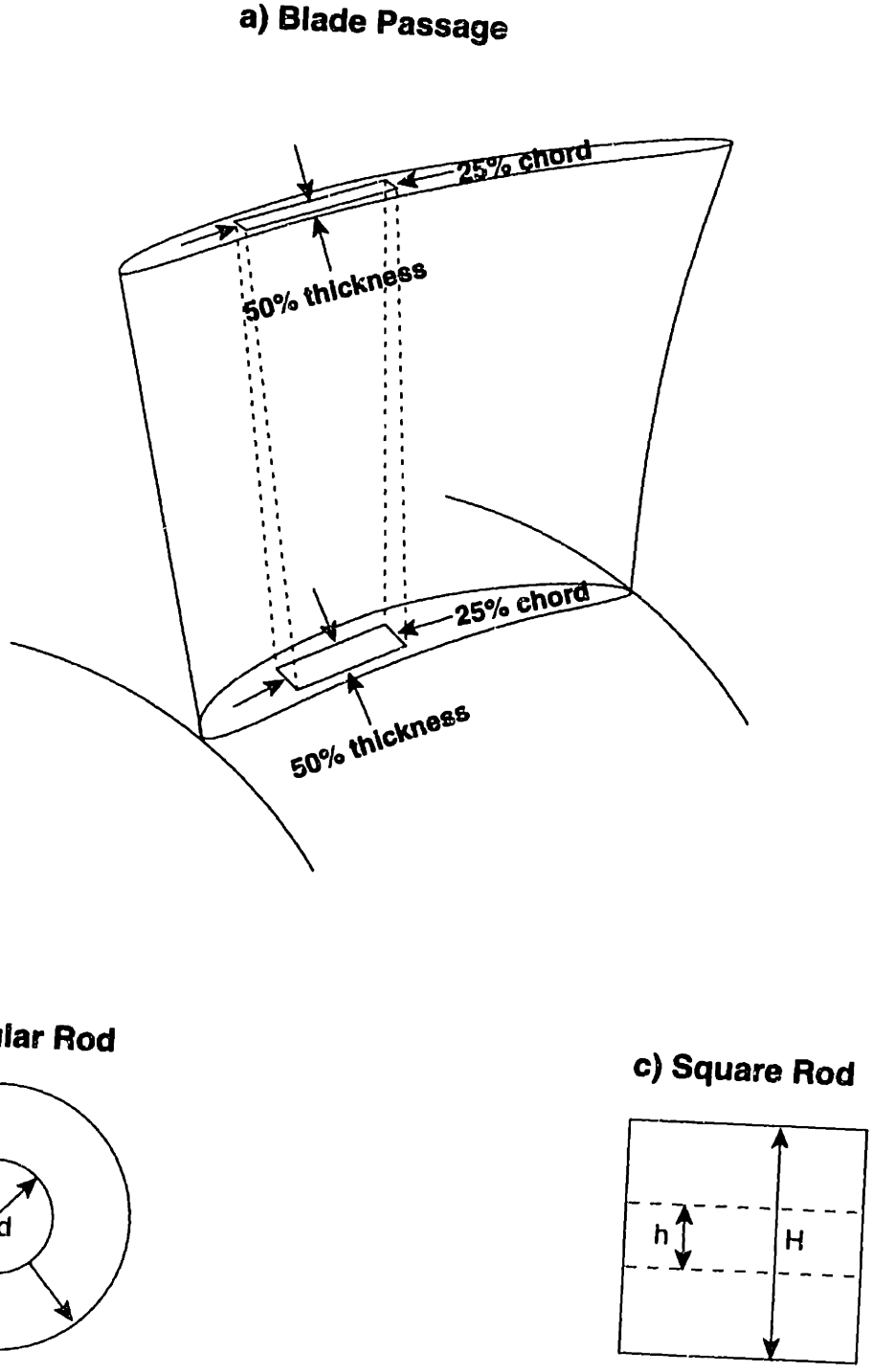

Figure 6-1: Schematics of structural considerations for blade internal passages: a) channel with constant percent blade area cross section, b) circular rod with hollow center, and c) square rod with middle section removed

(actual pressures will be shown in Section 6.6). The stresses in the blade surfaces are fairly small, but the displacement of the airfoil surface must be examined. The displacement of the blade skin due to a pressure differential typical of the pressures that will be seen in the blade was calculated for a plate element with two free sides and two fixed sides (attachment to the ribs between blade passages). A section of the blade skin covering a passage is not free at two sides, but this was seen as the maximum possible deflection. Using these results, the minimum blade surface thickness and width of blade passages could be determined. This was another reason for using turning vanes within the blade passages.

As discussed, the stress levels in correctly designed hollow blades should not be significantly different than those in solid blades. To better estimate any differences, a finite element analysis was completed [16] on the solid blade and a preliminary boundary layer suction blade design. A schematic of this design, which included boundary layer suction slots at 60% chord, is shown in Figure 6-2. The results showed lower stress levels in the hollow blade and smaller blade untwist at the tip than the solid blade. While the calculation was completed on a different blade design than the trailing edge blade, the results are expected to be similar. Clearly, differences will be present due to injection port geometry and slightly different internal open area. If less total blade airfoil area is removed on the outer portion of the span in proportional to the lower, one would expect to see increased stress levels. For this reason, hollow regions (voids) may need to be used to alleviate the blade loading at the root.

6.4 Simplified Passage Flow Model

A simplified model was used to estimate the flow characteristics in the blade internal passages. The conservation equations were written for a one-dimensional, viscous, rotating channel, with variable area and heat transfer. This model could then be used to estimate the flow from the base of the blade (passage inlet) to the top of the passage where it begins to turn toward the trailing edge. Estimation of the flow from the top of the blade 'radial' passage to the injection ports was completed with empirical curves as described in more detail in Section 6.5. Some early calculations using this model were described in Section 3.3.

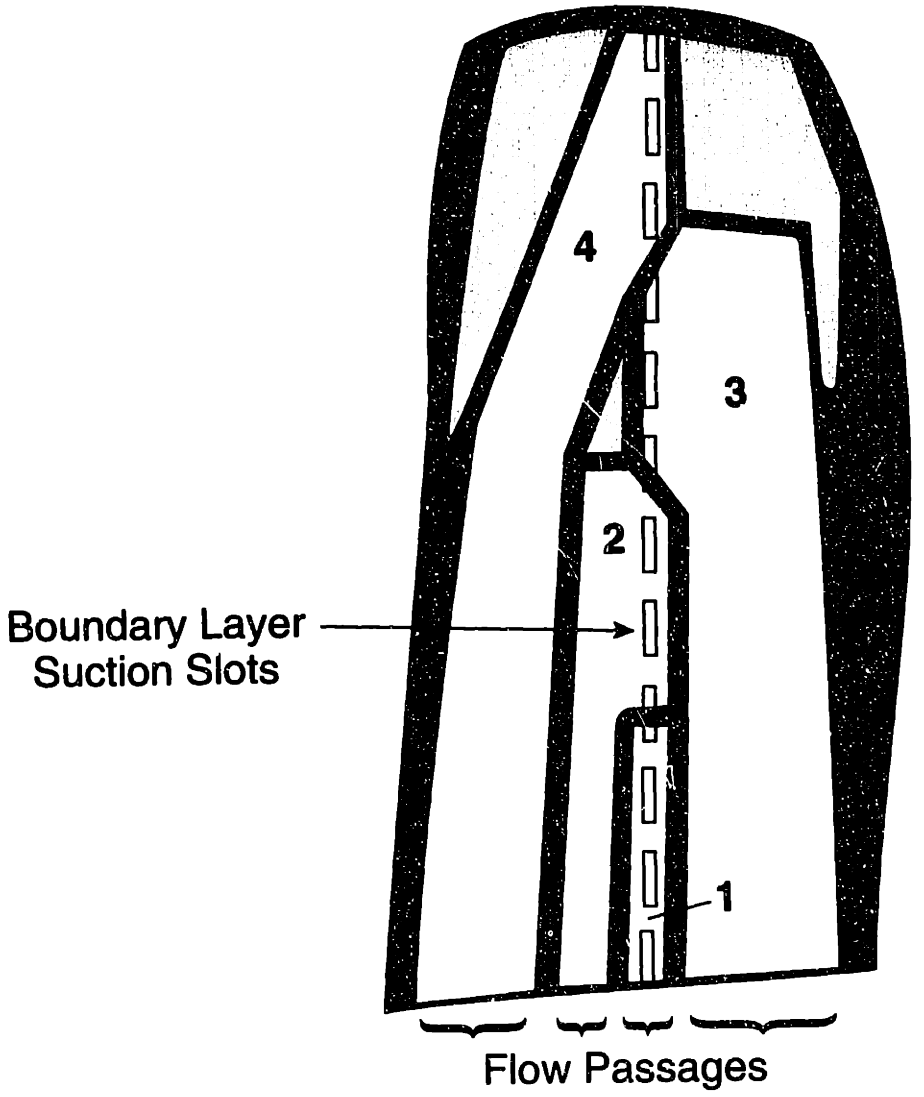

Figure 6-2: Blade passage design for boundary layer suction at 60% chord used for finite element analysis

The conservation equations in the rotating reference frame can be written as:

(mass)

$$\frac{d\rho}{\rho} + \frac{du}{u} + \frac{dA}{A} = 0 \tag{6.1}$$

(eq. of state)

$$\frac{dP}{P} = \frac{d\rho}{\rho} + \frac{dT}{T} \tag{6.2}$$

(momentum)

$$\rho u du = -dP + \rho\Omega^2 r dr + \frac{f}{2D_H}\rho u^2 dr \tag{6.3}$$

(energy- rothalpy)

$$d\Phi = d(h + \frac{u^2}{2} - \frac{r\Omega V_\theta}{2}) = dq \tag{6.4}$$

where P = static pressure, ρ = density, T = temperature, u = passage flow velocity (relative frame), A = passage area, Ω = rotor angular velocity, f = coefficient of friction, D_H = hydraulic diameter, Φ = rothalpy (rotating total enthalpy), h = enthalpy, q = heat, and V_θ = tangential velocity ($r\Omega$ in this case).

The heat transfer term is approximated by the expression given in White [41] and the coefficient of friction is estimated from the empirical curve fit to the Moody diagram given in Miller [23].

$$\frac{dq}{c_p T} = \frac{f/2D_H}{\left[1 + 13\left(Pr^{2/3} - 1\right)(f/8)^{1/2}\right]}\left(\frac{T_b}{T} - 1\right) dr \tag{6.5}$$

$$f = .25/\left\{log_{10}\left[\frac{k}{3.7D_H} + \frac{5.74}{Re_{D_H}^{.9}}\right]\right\}^2 \tag{6.6}$$

where C_p = coefficient of specific heat, Pr = Prantl number, T_b = blade temperature, k =

roughness factor, and Re_{D_H} is the Reynold's number based on passage hydraulic diameter.

Combining the conservation equations and using the non-dimensional spanwise coordinate, ds = dr/r, the static pressure is given by

$$\frac{dP}{P} = \frac{\frac{dA}{A} - \frac{dq}{C_pT} + \frac{\Omega^2 r^2}{u^2} ds + \frac{f}{2D_H}[1 + (\gamma - 1)M^2] r ds}{\frac{[1+(\gamma-1)M^2]}{\gamma M^2} - 1} \tag{6.7}$$

The change in velocity and density (and thus temperature) can then be found using

$$\frac{du}{u} = -\frac{dP}{\rho u^2} + \frac{\Omega^2 r^2 ds}{u^2} + \frac{f}{2D_H} r ds \tag{6.8}$$

$$\frac{d\rho}{\rho} = -\frac{du}{u} - \frac{dA}{A} \tag{6.9}$$

These equation can be stepped along the span of the blade passage to determine the flow field for a given initial condition. Clearly, the procedure fails as the Mach number approaches unity.

Note that the equations depend on several non-dimensional parameters given by M, dA/A, $\Omega^2 r^2/u^2$, and fr/D_H. Experimental tests in the Blowdown Compressor are run with the same flow Mach numbers as the full-scale engine, so all the non-dimensional variables are the same except for the viscosity parameter fr/D_H. This parameter is a combination of friction factor (f) and the fan size (r and D_H). The radius and hydraulic diameter will scale together, but the friction factor is a function of hydraulic diameter, and thus decreases with increase in fan size. Therefore, viscous losses are expected to be smaller in full-scale engine blade passages.

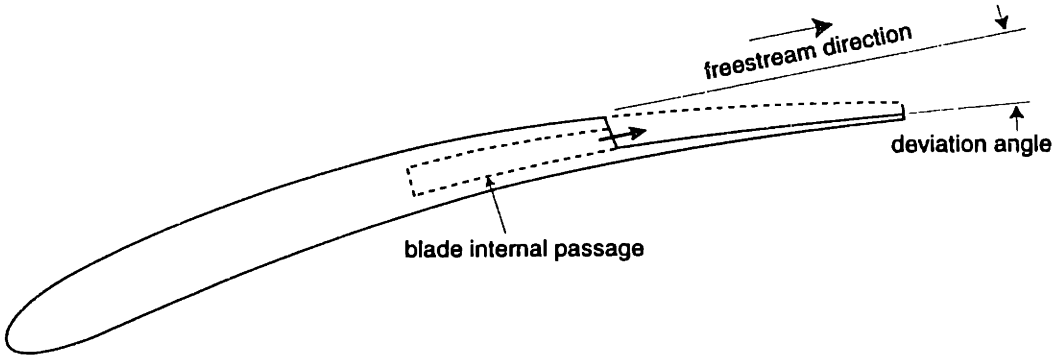

Figure 6-3: Schematic of airfoil with blowing orifice for injection at the mean flow deviation angle

6.5 Blade Internal Passage Geometries

To determine the mass flow and total pressure required for injection, the exit port dimensions must first be determined. As discussed in Section 6.1, two-dimensional studies showed that blowing at the deviation angle produced the smoothest wakes. Since the trailing edge thickness introduces additional displacement thickness beyond that in the boundary layer, the injection ports were opened on the wake management fan blade from approximately the deviation angle position on the suction surface of the blade to the trailing edge, as illustrated in Figure 6-3. This not only decreased the effective trailing edge thickness, but increased the injection port width. In the hub region where the injection velocity would be subsonic, the opening to the suction surface was moved aft a few percent chord to obtain a choked orifice. The tip region ports were similarly moved forward a few percent chord to decrease the required Mach number of the injection flow ($M_{required} \leq 1.23$), and thus the degree of under-expansion of the sonic jets.

To estimate the performance of the resulting blade with the blowing turned off, the flow field for an airfoil with the trailing edge step, as shown in Figure 6-3, was calculated using MISES [6]. The resulting wake was within 1 percent of the original airfoil wake in width, velocity deficit, and momentum thickness. The increase in boundary layer thickness caused by the separation at the step is counteracted by the decrease in the trailing edge thickness to produce virtually no change to the wake mean characteristics.

When these injection port orifice sizes (widths) were determined, the total pressures and mass flows required as a function of span were set. Incorporated in these calculations was the open area of the injection, 3:1, which was chosen from both structural and wake

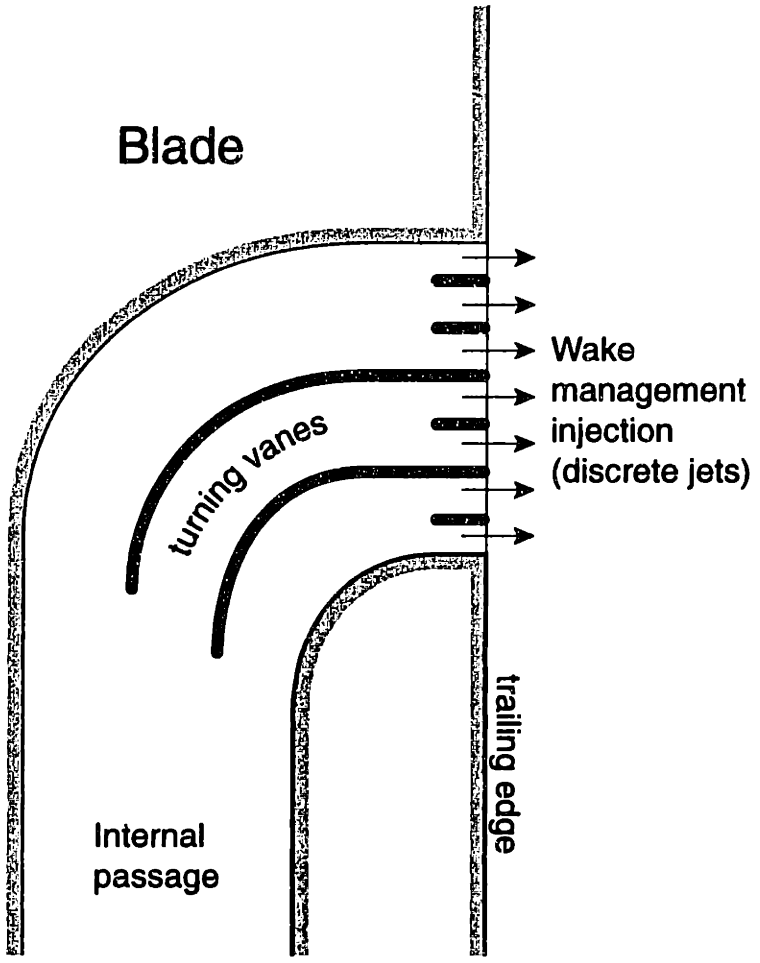

Figure 6-4: Schematic of blade internal passage trailing edge blowing section

mixing considerations, and a discharge coefficient of unity was used for the sonic orifices. This open area resulted in structural vanes comprising 25% of the span at the trailing edge, which were also used for flow straightening before injection (particularly for the hub region). Because of the total pressure distribution required along the blade span (and some structural concern), 5 internal passages were used, each responsible for a 20% section of the span. The injection ports used are approximately 3mm high (approximately 2% span), with 1mm vanes in between (35 ports, 7/section).

In addition, vanes were put into the internal passages for structural support, as well as to help turn the flow from the spanwise to the chordwise direction for injection. Since the flow at the bottom corner of each passage was in greatest danger of separation, a vane was

inserted to turn the flow for the two bottom injection ports, and then another for the next two ports. This is shown schematically in Figure 6-4. These vanes provided flow turning, structural support to limit the blade surface deflections due to the internal pressure, and shear strength for torsional loading.

6.6 Calculation of Passage Flow

With the geometry of the injection section determined and the mass flows and total pressures known for the trailing edge blowing fluid, the internal blade passages could be designed. This process required several iteration loops as better estimations of the flow losses, required driving pressures, and passage areas were made. The passages were placed in the blade airfoils after each iteration to ensure maximum usage of the blade internal flow area (center 50% of the thickness).

The process of estimating the flow for a given passage was completed as follows. The required mass flow and total pressure at the injection port outlets was known from previous calculations. Empirical data (Idelchick [15]) was used to estimate the losses for the contractions into the discrete injection ports, flow along the chordwise passage between the turn and the injection ports, and the flow around the turning vane corners. The flow at the beginning of each of these regions was calculated to obtain the required flow at injection. Fortunately, the losses through the turns were adequate to approximately obtain the spanwise total pressure variation desired along each 20% span section.

With the required flow known at the top of each internal passage (just before the turn for each 20% blowing section) the simplified model (Section 6.4) was used to estimate the passage size and pressure at the blade root required to obtain the desired injection. Empirical data was then again used to determine the losses in the flow entering the rotor disk, through the passage to the passage inlet, and in the inlet itself.

This calculation was done for all five passages and the resulting areas used in the blade airfoils. After a couple iterations, passages were determined that used the full chordwise extent of the hub airfoil internal area (always 50% of the local blade thickness). Since the tip section required the largest driving total pressure, the other sections (particularly

the hub) would have flow of much higher total pressure than desired. To reduce the total pressure, a throttle plate was designed for insertion at the blade root (between the passage inlets and the hole bringing flow from the rear face of the disk). By correctly setting the throttle hole size for each passage, the correct total pressure drop was obtained for the mass flow required. In addition, this served as a relatively easy way to adjust the flow into each passage if the original design did not produce the spanwise distribution desired, or if different distributions were to be tested.

Following the preliminary design of the blade internal passages, one passage was run with a three-dimensional Navier-Stokes solver. This calculation confirmed that the loss and flow calculations described above were reasonable. However, it was still expected that some adjustments to the throttle plates would need to be made, so all calculations were done conservatively and the throttle plates designed so that maximum flexibility was ensured.

6.7 Blade Design

The trailing edge blowing wake management fan blade design is shown in Figures 6-5 through 6-8. A view of the blade at the hub stagger angle is shown in Figure 6-5. The leading edge is on the left with the fan through flow from left to right. The five passages can be seen with their internal turning/splitter vanes and the discrete injection ports. A void can also be seen forward of the tip passage to alleviate stress in the front part of the blade. The line just to the right of the beginning of the discrete port vanes is the opening of the passages to the suction surface of the blade. This location varies from approximately 82% to 95% chord, from the tip to the hub, respectively.

Figure 6-6 shows the blade in a perspective view where the blade twist and the passage inlets can be seen at the hub. In this picture, the leading edge is on the right. A step can also be seen above the passage inlets on the pressure side of the blade, which was used for additional support of the centrifugal load on the pressure surface blade skin. A cut into the trailing edge of the root platform is also seen just above the root passage openings. This step is for placement of the stainless steel ring on which the graphite face seal seats.

The hub and midspan airfoils are shown in Figures 6-7 and 6-8. The hub airfoil shows

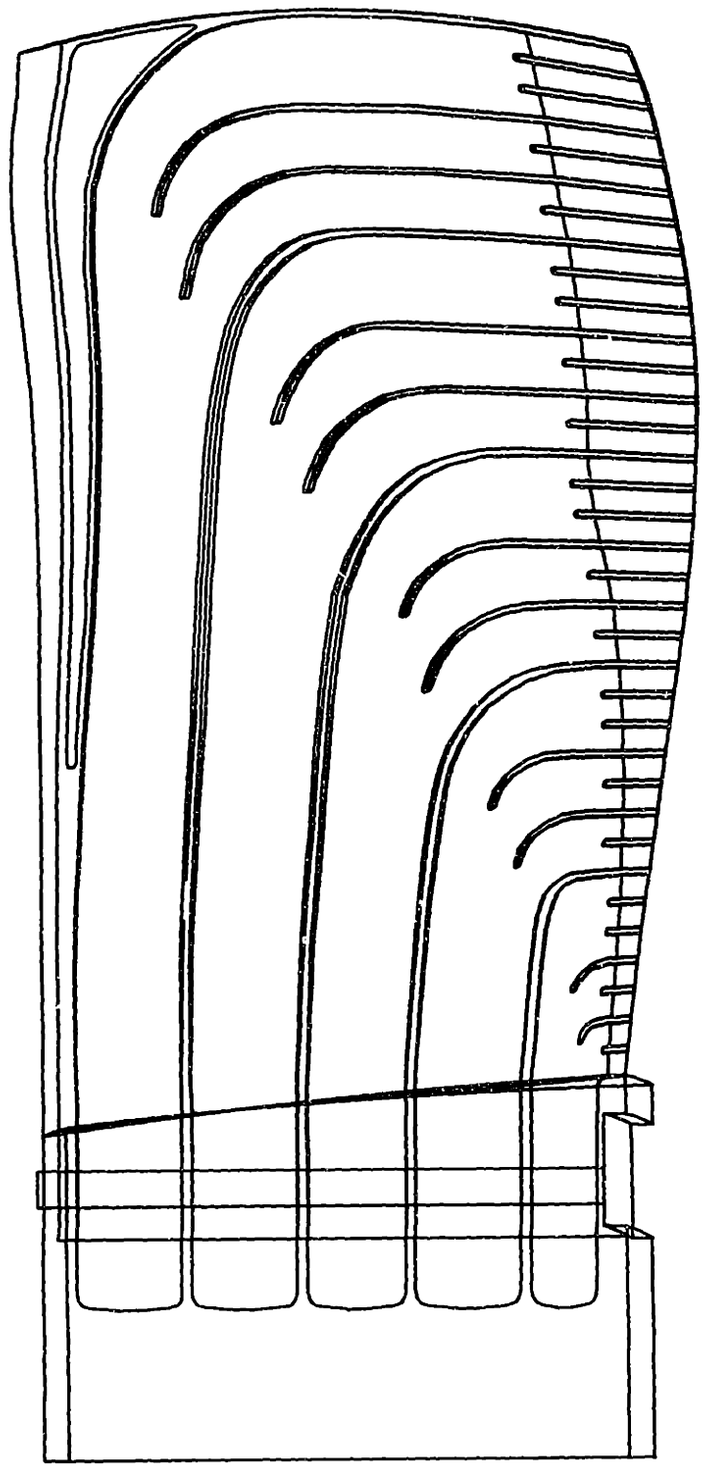

Figure 6-5: Deviation angle trailing edge blowing wake management fan blade: stagger angle view

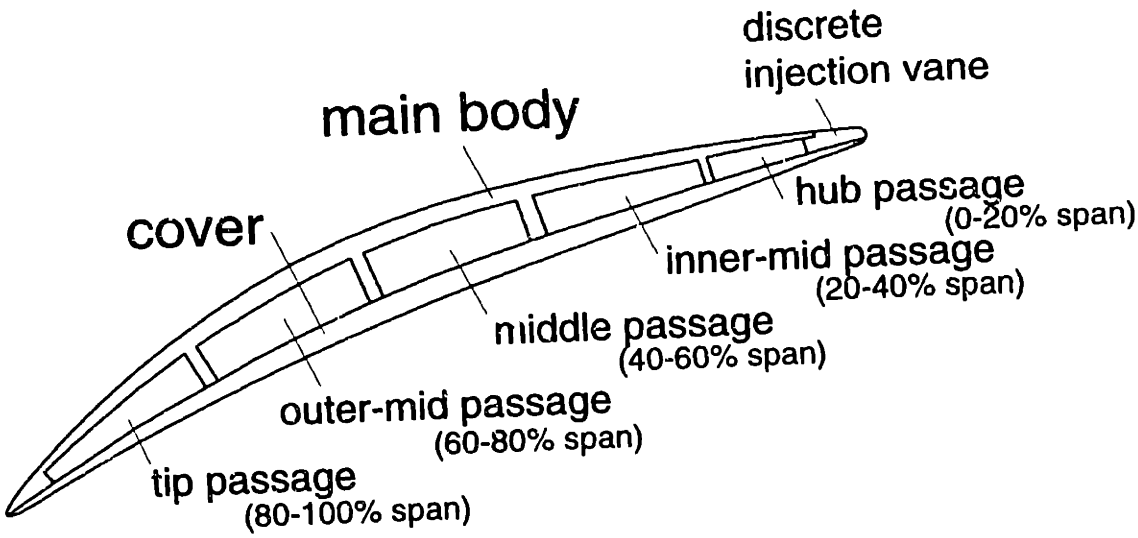

Figure 6-7: Hub cross section of trailing edge blowing wake management blade (150% actual scale)

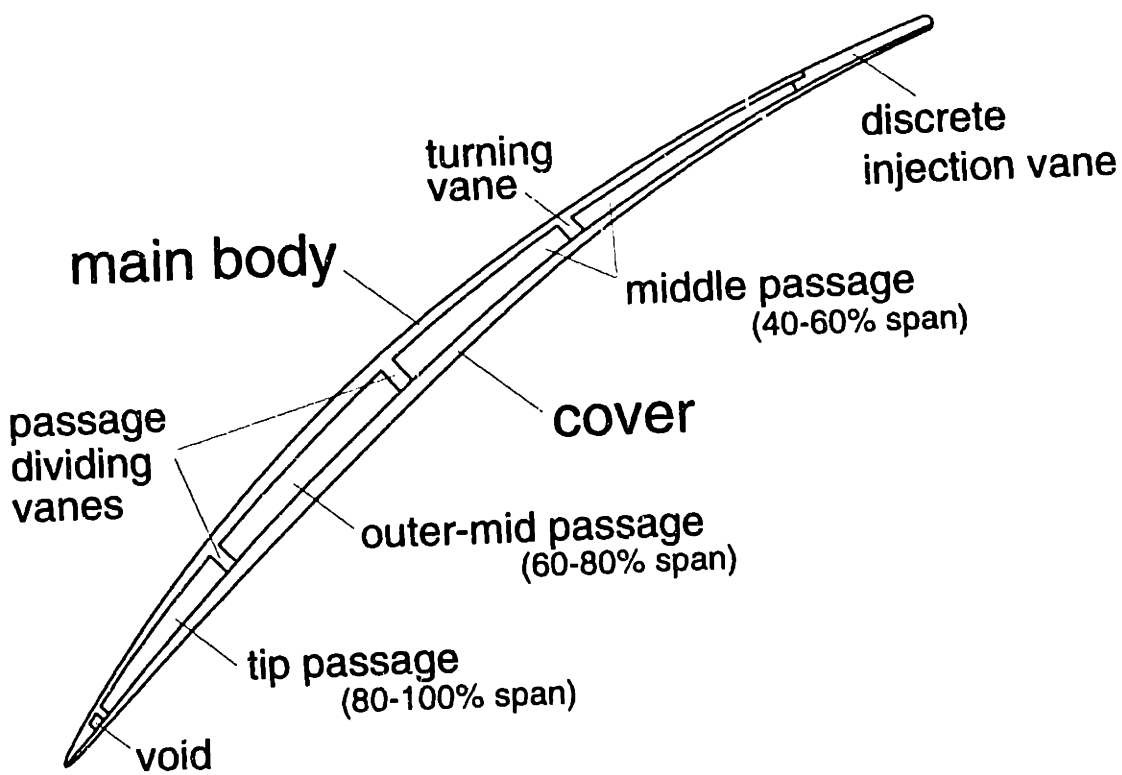

Figure 6-8: Midspan cross section of trailing edge blowing wake management blade (150% actual scale)

the five passages in the center 50% of the blade thickness, and the location of the injection port (95% span). The midspan airfoil, similarly, has the two outer span passages visible, as well as the midspan passage in two parts due to a turning/splitter vane. Again, the location of the injection opening to the suction surface is visible. The deviation angle of the flow at midspan is about 6 degrees. In addition, the bottom of the void can be seen near the leading edge.

6.8 Blade Fabrication

The fabrication process used for the manufacturing of the trailing edge fan blades was chosen after considering several different methods. Casting with ceramic cores and investment casting from stereolithography were examined. Unfortunately, stereolithography did not have the required resolution (particularly minimum blade thickness), and ceramic core casting was estimated to be prohibitively expensive. Therefore, the chosen process was machining two blade halves and then joining them together to form the completed blade. Since it was desired for the blade joint to have considerable strength for structural support, the blade was made out of 6061-T6 aluminum and brazed together. This was the highest strength aluminum that was brazable. All the blade ribs (between passages) and vanes were brazed. This process not only sealed each passage from the others, but maintained maximum possible strength of the hollow blade.

The main blade part was machined as a solid blade and then the passages machined into the surface. These passages were cut to 75% of the local blade thickness. In addition, the blade ribs and vanes were cut down to 25% of the local blade thickness. The blade cover, which was the pressure surface of the blade and 25% of the local blade thickness, was then machined. This part was then fixtured to the main blade and the assembly dip-brazed. After reheat treatment, the passage openings to the suction surface were machined. During the dip-brazing and reheat treatment processes, the blades exterior shapes were known to move. The blades cupped by 0.030 to 0.040 inches at midspan, such that the pressure surface of the blade created a concave surface, and the blade twisted by 1 to 1.5 degrees at the tip, relative to the hub.

Pictures of the two blade pieces are shown in Figure 6-9, and a close up of the blade

internal passages machined into the main blade half is shown in Figure 6-10. The tabs around the blade were used to pin the parts in position, hold the blade together during the brazing process, and secure the blade for machining the injection orifices in the suction surface. A picture of a trailing edge blowing rotor is shown in Figure 6-11, and a close up of the trailing edge of the blades is shown in Figure 6-12. The holes in the disk supplying injection fluid to the blade internal passages, as well as the stainless steel ring for the graphite face seal, can be seen.

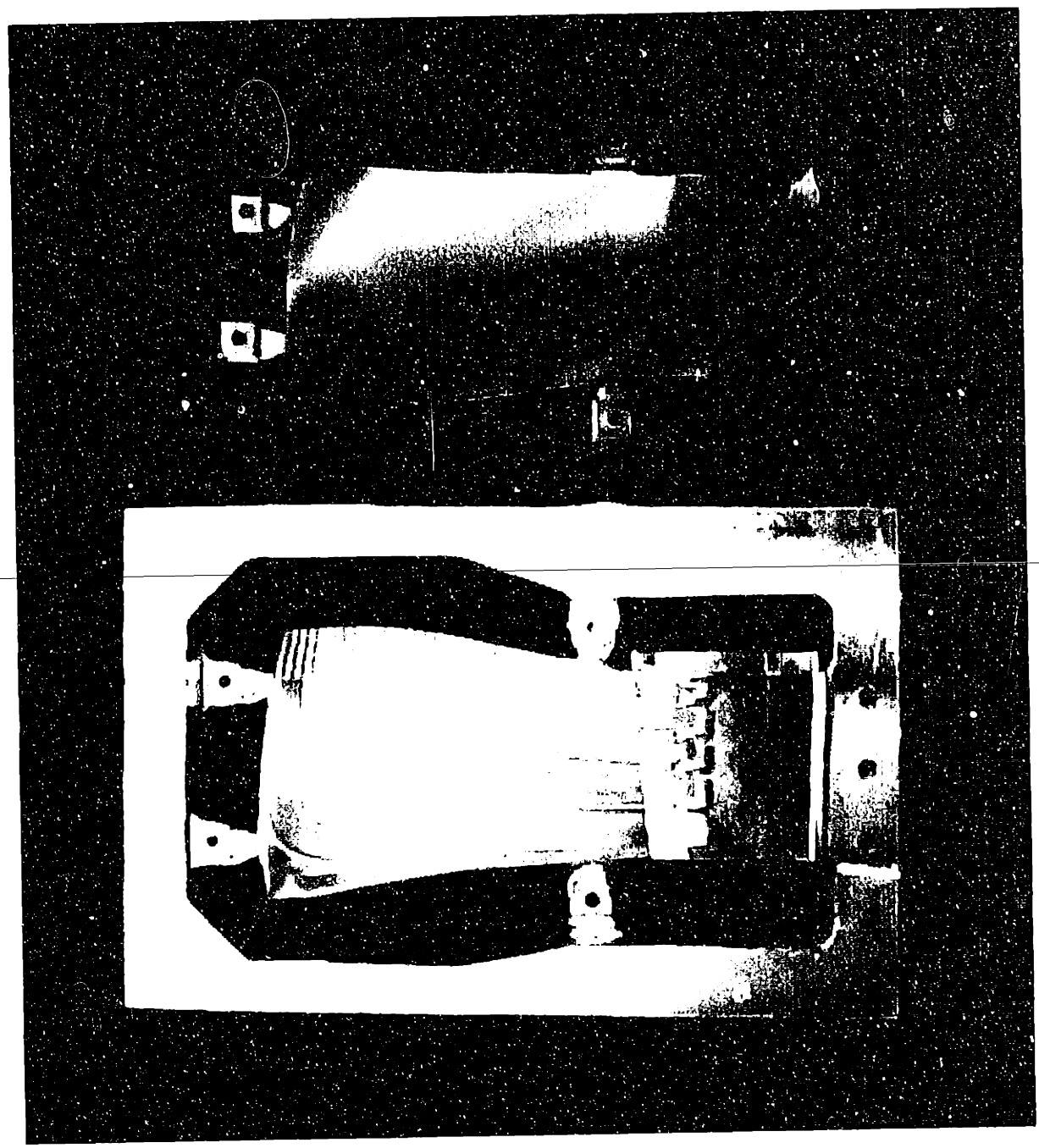

Figure 6-9: Picture of two blade halves of trailing edge blowing fan blade before brazing operation

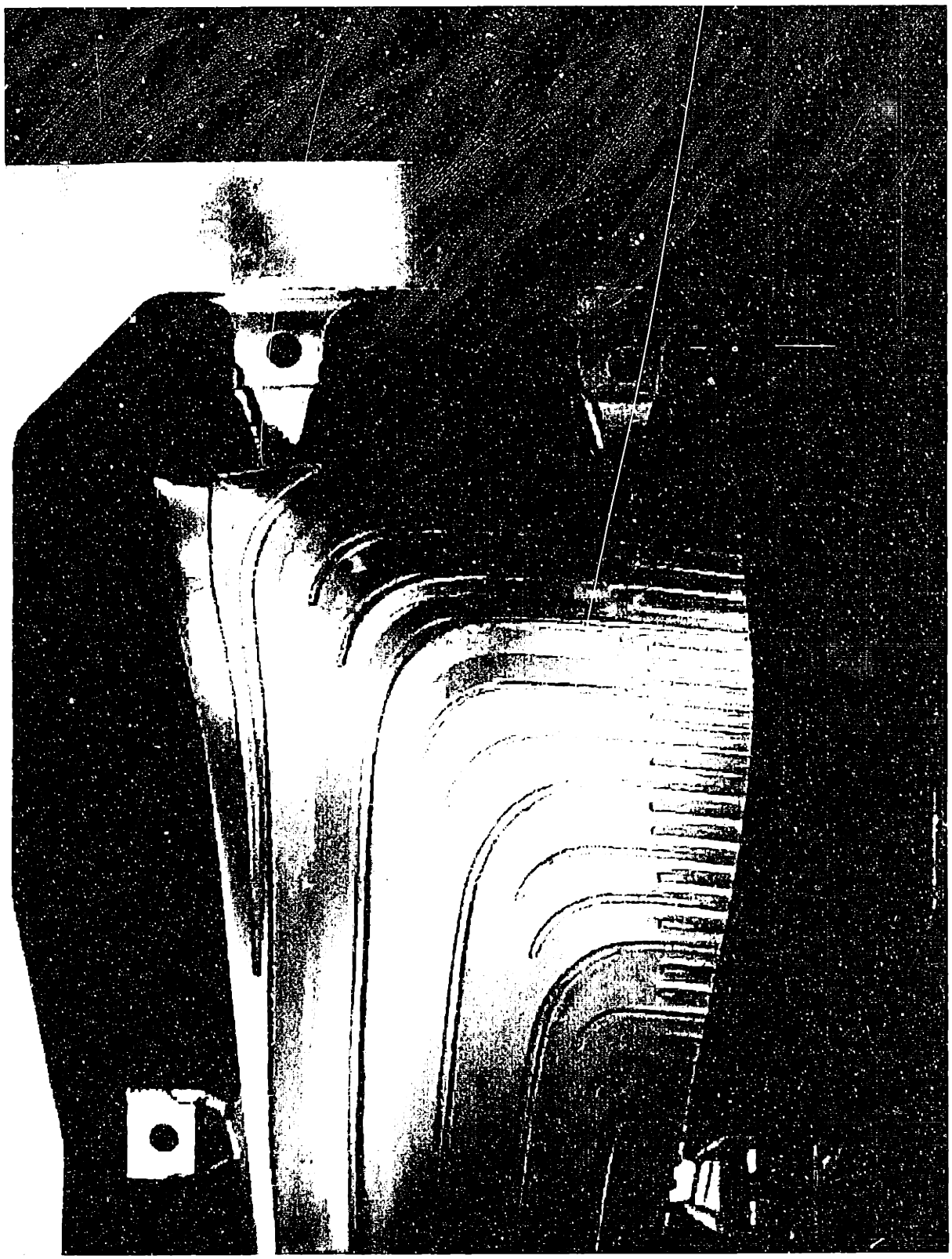

Figure 6-10: Close-up picture of the internal passages machined into the main blade half

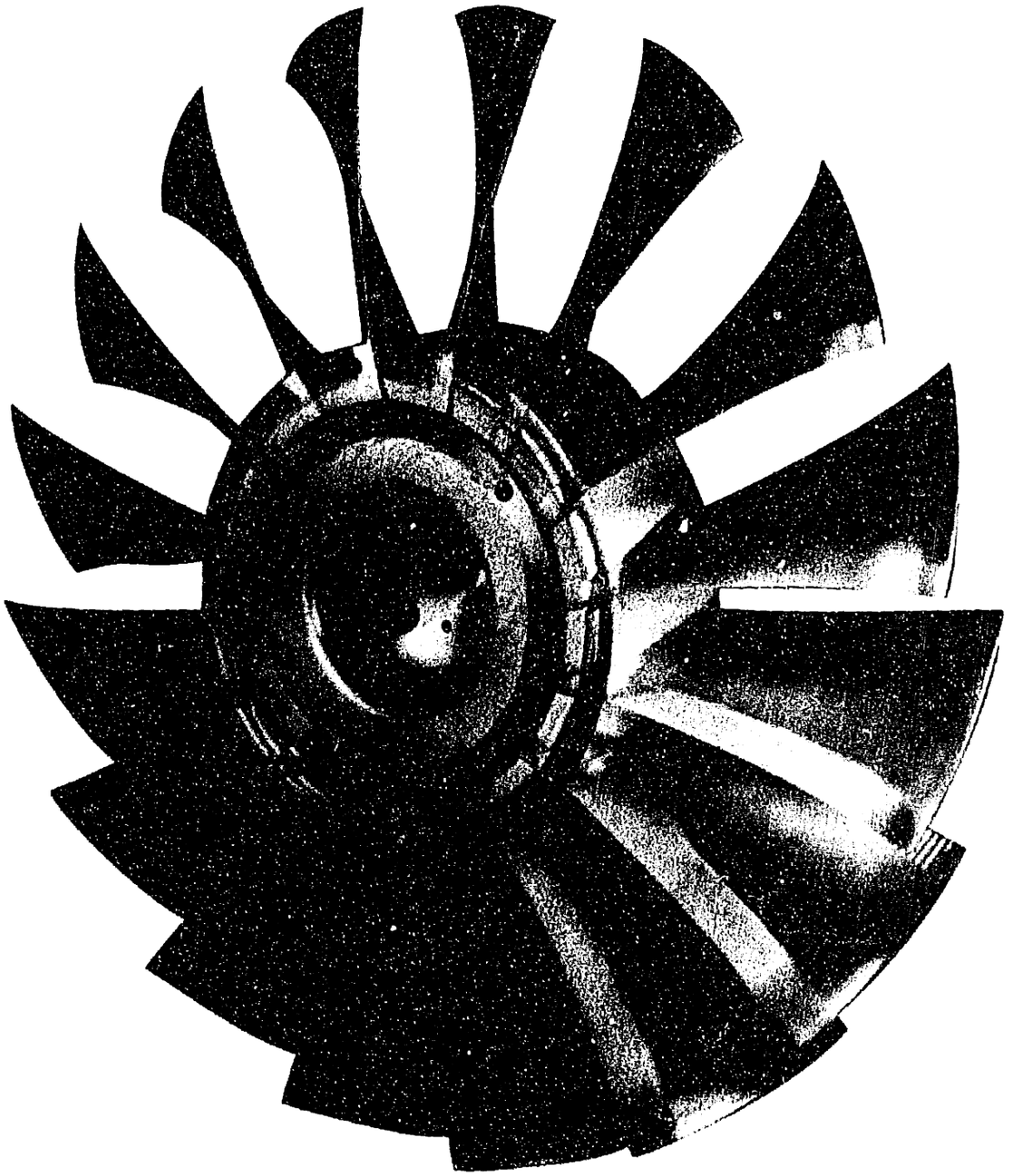

Figure 6-11: Picture of assembled trailing edge blowing rotor

Figure 6-12: Close-up picture of the trailing edges of the assembled trailing edge blowing rotor

CHAPTER 7

TRAILING EDGE BLOWING FAN: FLOW FIELD MEASUREMENTS

Following the design and manufacture of the wake management fan, testing began to demonstrate the ability of trailing edge blowing to mitigate both the wakes downstream of the rotor and the resulting noise generated from rotor wake/stator interaction. As for the baseline solid-bladed rotor, testing consisted of 4-way probe flow field measurements, instrumented stator unsteady pressure measurements, and duct acoustic measurements. However, the main thrust of the research was the fluid mechanics of trailing edge injection to demonstrate reduction of the flow field unsteadiness downstream of the rotor. Thus, the flow field measurements for several different fan configurations will first be presented, followed by stator and acoustic measurements in Chapter 8.

In this chapter modifications to the 4-way probe will first be addressed, followed in Section 7.2 by comparison of the trailing edge blowing rotor without injection to the baseline rotor with solid blades. Results from the initial testing of the trailing edge blowing rotor with injection favoring the tip of the blade will then be shown in Section 7.3. Flow field measurements downstream of the trailing edge blowing rotor modified to achieve midspan-weighted injection are then presented in Sections 7.5 and 7.6 for two different trailing edge injection mass flow rates. Finally, efficiency calculations are discussed in Section 7.7, followed by a summary of the trailing edge blowing flow field results.

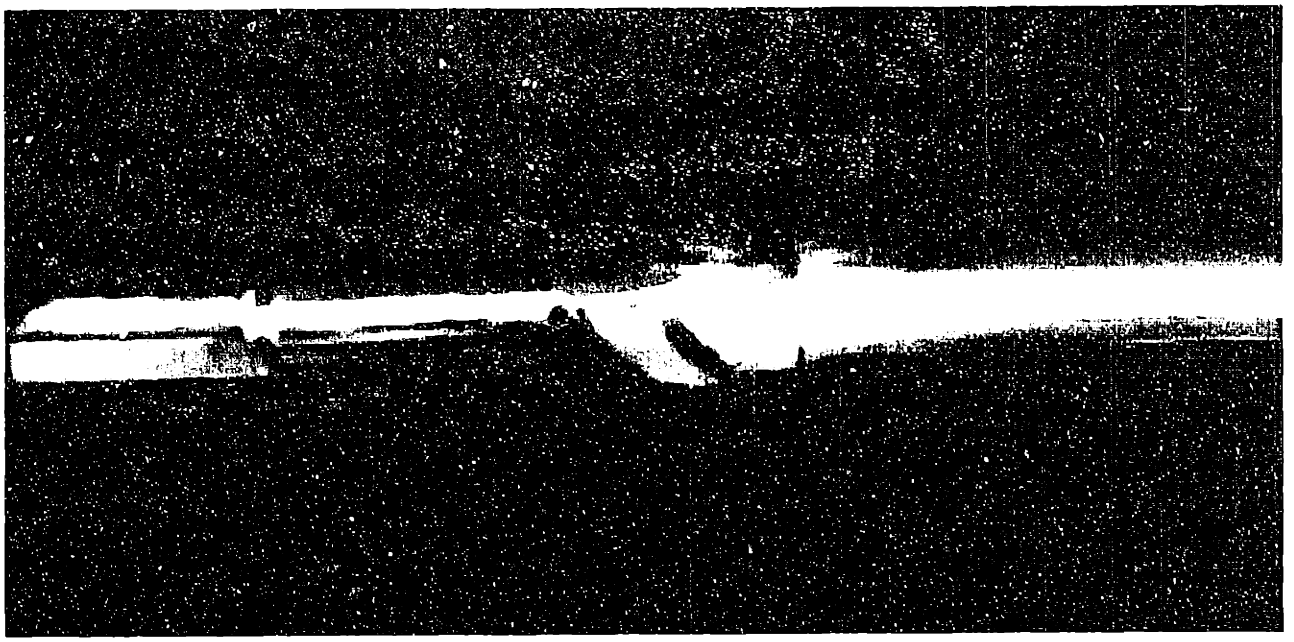

Figure 7-1: 4-way probe with fin modification for vortex shedding suppression

7.1 4-way Probe Modification

Before testing began on the trailing edge blowing rotor, a permanent modification was made to the 4-way probe used for flow field measurements. As discussed in Section 5.2.2, unsteady vortex shedding from the body of the probe was causing four times blade passing frequency (4*BPF) oscillations in the data. These oscillations corrupted the measurements, particularly just downstream of the rotor. A foam fin had been used previously to test this hypothesis, but could not be used as a permanent fix.

To permanently alleviate the vortex shedding problem, a fin was machined from stainless steel, which ran the entire length of the probe tip. The fin was screwed directly into the probe tip/shaft joint, since attachment with epoxy might interfere with the transducer wiring. A picture of the 4-way probe with the attached fan is shown in Figure 7-1. After completion of the modification, the probe was recalibrated in a steady-flow facility at The Boeing Company.

7.2 Comparison of Trailing Edge Blowing Rotor (No Injection) to the Baseline Solid-Bladed Rotor

With the inclusion of trailing edge blowing on a fan stage, comparisons must be made to determine the impact of the design changes to the fan performance. While the introduction of fluid injection at the trailing edge will clearly change the flow field exiting the rotor, this condition would only apply to takeoff and landing portions of the flight where noise reductions are necessary. Equally as important, however, is the performance at cruise where most of the fuel burn occurs. Therefore, performance comparison of the trailing edge blowing rotor without injection to the baseline solid-bladed rotor were made.

Measurements at 25, 50, 75, and 87.5% span, 1.5 chord will be presented comparing the trailing edge blowing rotor without injection to the baseline rotor with solid blades. With the results of both plotted in the same figure, direct comparison of the effects due to the internal passages and the scalloped suction surface can be observed. However, since the fan blade with internal passages will have slightly different untwist characteristics than a solid blade and the exterior shape may have slight variations due to manufacture, the spanwise loading distribution of the wake management rotor is not expected to be exactly the same as for the solid-bladed rotor. Production blades incorporating trailing edge blowing would be designed to account for untwist changes, etc. In addition, since the fan used in this study is in the takeoff configuration, testing at true cruise conditions can not be completed. The fan performance, therefore, was compared at the takeoff conditions.

7.2.1 Flow field measurements

25% span, 1.5 chord

Flow field measurements at 25% span, 1.5 chords downstream of the rotor are presented in Figures 7-2 through 7-5. The flow variables for the baseline rotor with solid blades are shown in solid lines, and the measurements for the trailing edge blowing rotor (no injection) are shown in dash-dot lines. The average relative Mach number is seen to be approximately 5% higher with the trailing edge blowing rotor, and the ensemble-averaged relative Mach number BPF harmonic is about 17% higher. The increase in the relative Mach number is

due to the increase in axial Mach number, which unloads the airfoil and results in lower tangential Mach number and total and static pressure rise. The absolute total pressure ratio is about 1.5% lower with the trailing edge blowing rotor.

50% span, 1.5 chord

Ensemble-averaged flow variable profiles at 50% span, 1.5 chords downstream of the rotor are shown in Figures 7-6 through 7-9. Like the flow characteristics at 25% span, the axial Mach number at 50% span is about 4% high with the trailing edge blowing rotor causing an increase in the BPF harmonic of the relative Mach number of approximately 24% and a decrease in the absolute total pressure ratio of about 1%. Most of the total pressure reduction is due to lower static pressure rise.

75% span, 1.5 chord

Flow field measurements at 75% span, 1.5 chord are presented in Figures 7-10 through 7-13 for the baseline solid-bladed rotor and the trailing edge blowing rotor with no injection. The Mach numbers for the two configurations are seen to be much closer than at 25 and 50% span, with the relative and axial Mach numbers about 1% higher with the trailing edge blowing rotor. The total pressure ratio is approximately 1.5% low, relative to the solid-bladed rotor.

87.5% span, 1.5 chord

Measurements at 87.5% span, 1.5 chords downstream of the baseline solid-bladed rotor (solid lines) and the trailing edge blowing rotor with no injection (dash-dot lines) are presented in Figures 7-14 through 7-17. Again, the average relative Mach number is higher with the trailing edge blowing rotor, but the primary cause at 87.5% span does not appear to be due to changes in the inlet flow. The axial Mach number is within 1% for the two configurations, but the tangential Mach number (imparted swirl) and total pressure ratio are about 5% and 2% low, respectively, for the trailing edge blowing rotor. This result may be due to the scalloped suction surface near the trailing edge and/or the blade exterior shape at full

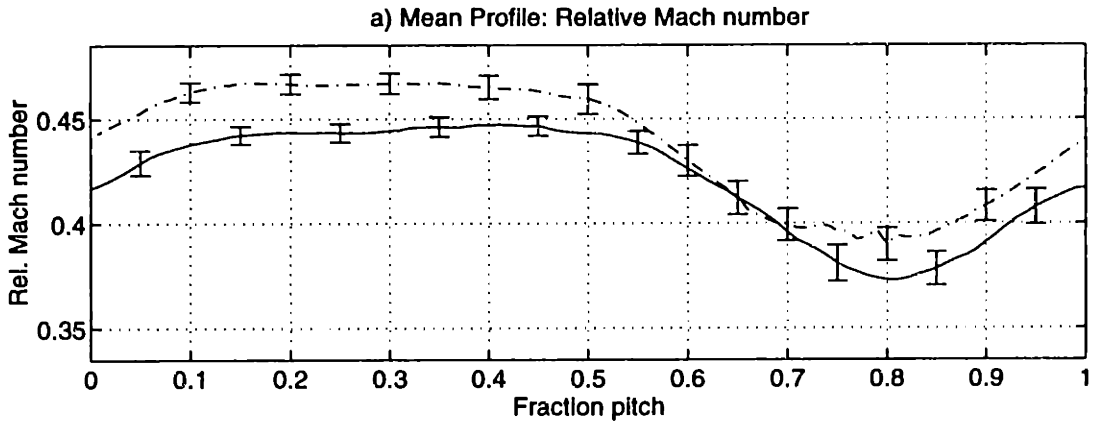

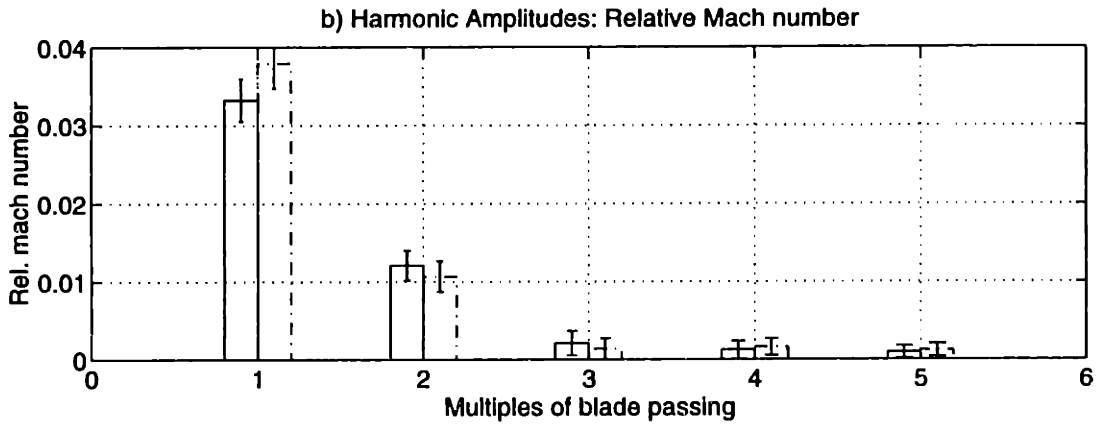

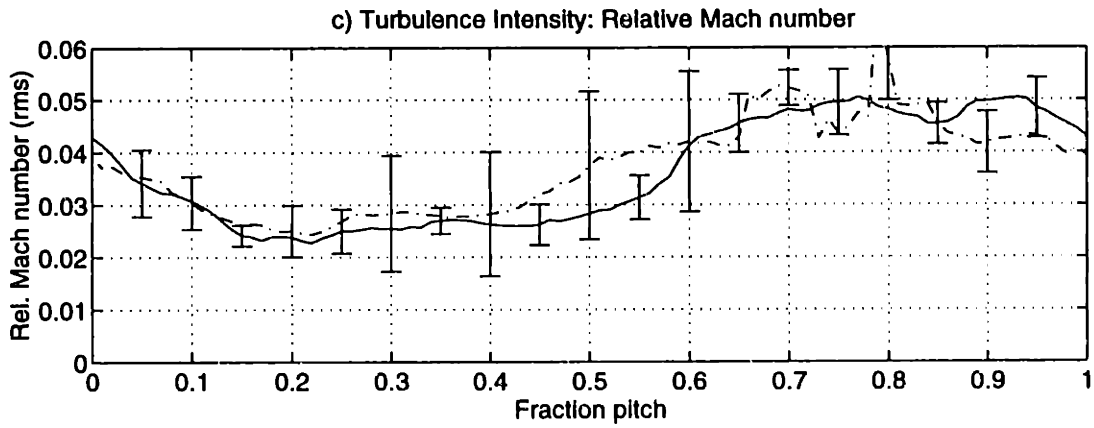

Figure 7-2: Relative Mach number ensemble-averaged profile, mean harmonic content, and turbulence profile at 25% span, 1.5c for the baseline solid-bladed rotor (—) and the trailing edge blowing rotor with no injection (- .)

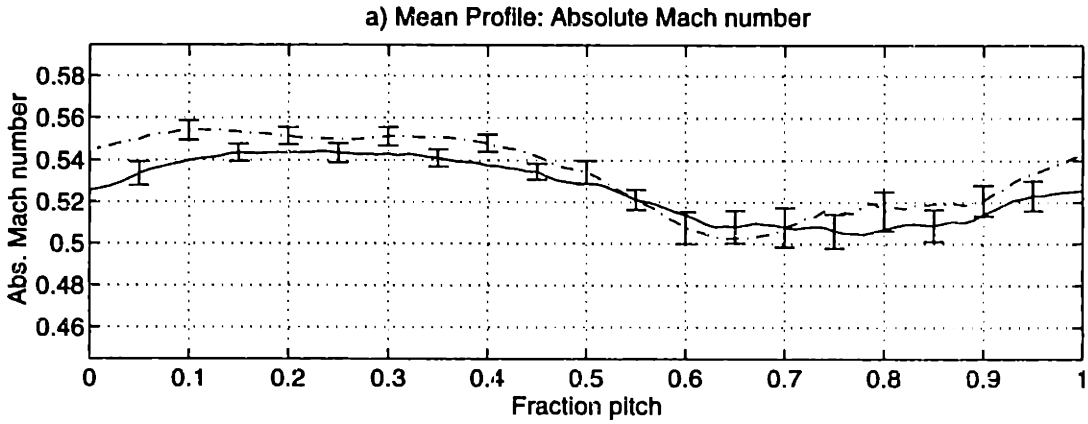

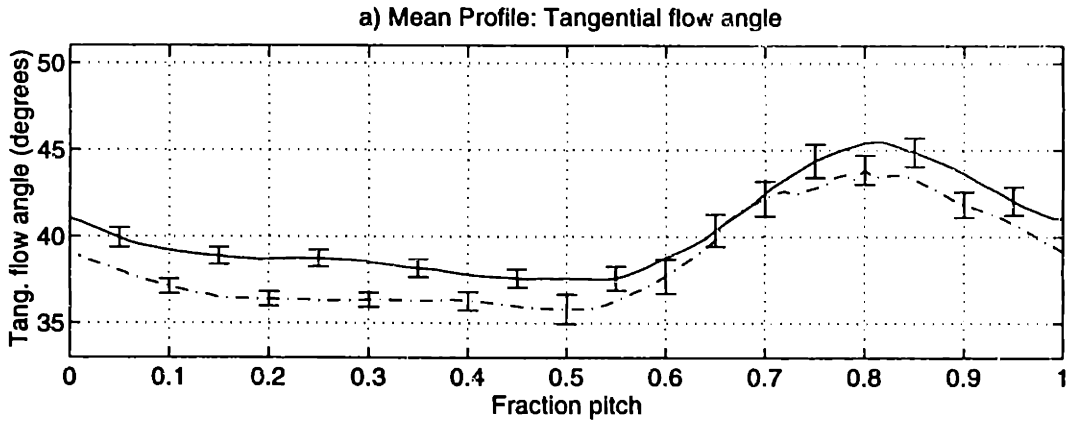

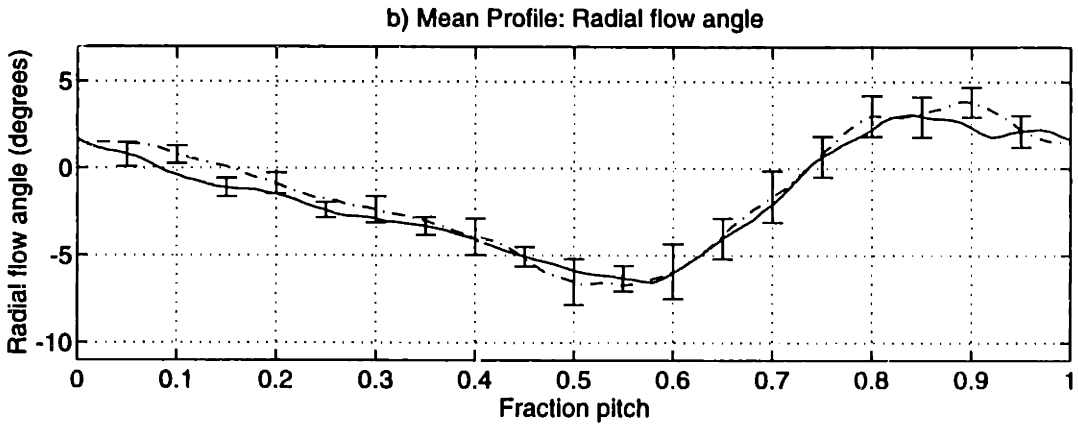

Figure 7-3: Ensemble-averaged profiles of absolute Mach number and tangential and radial flow angles at 25% span, 1.5c for the baseline solid-bladed rotor (—) and the trailing edge blowing with no injection (- .)

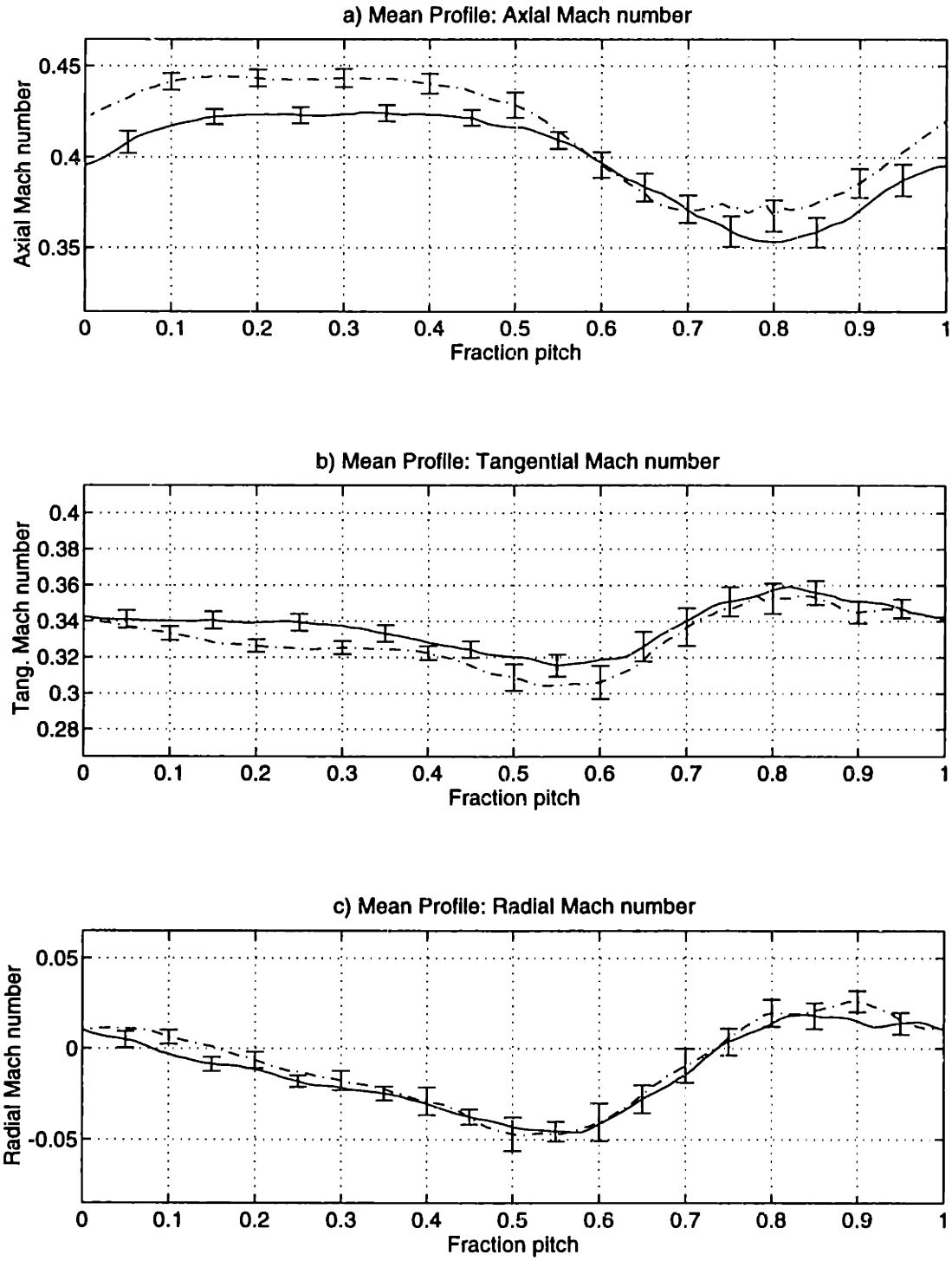

Figure 7-4: Ensemble-averaged profiles of axial, tangential, and radial Mach number at 25% span, 1.5c for the baseline solid-bladed rotor (—) and the trailing edge blowing rotor with no injection (- .)

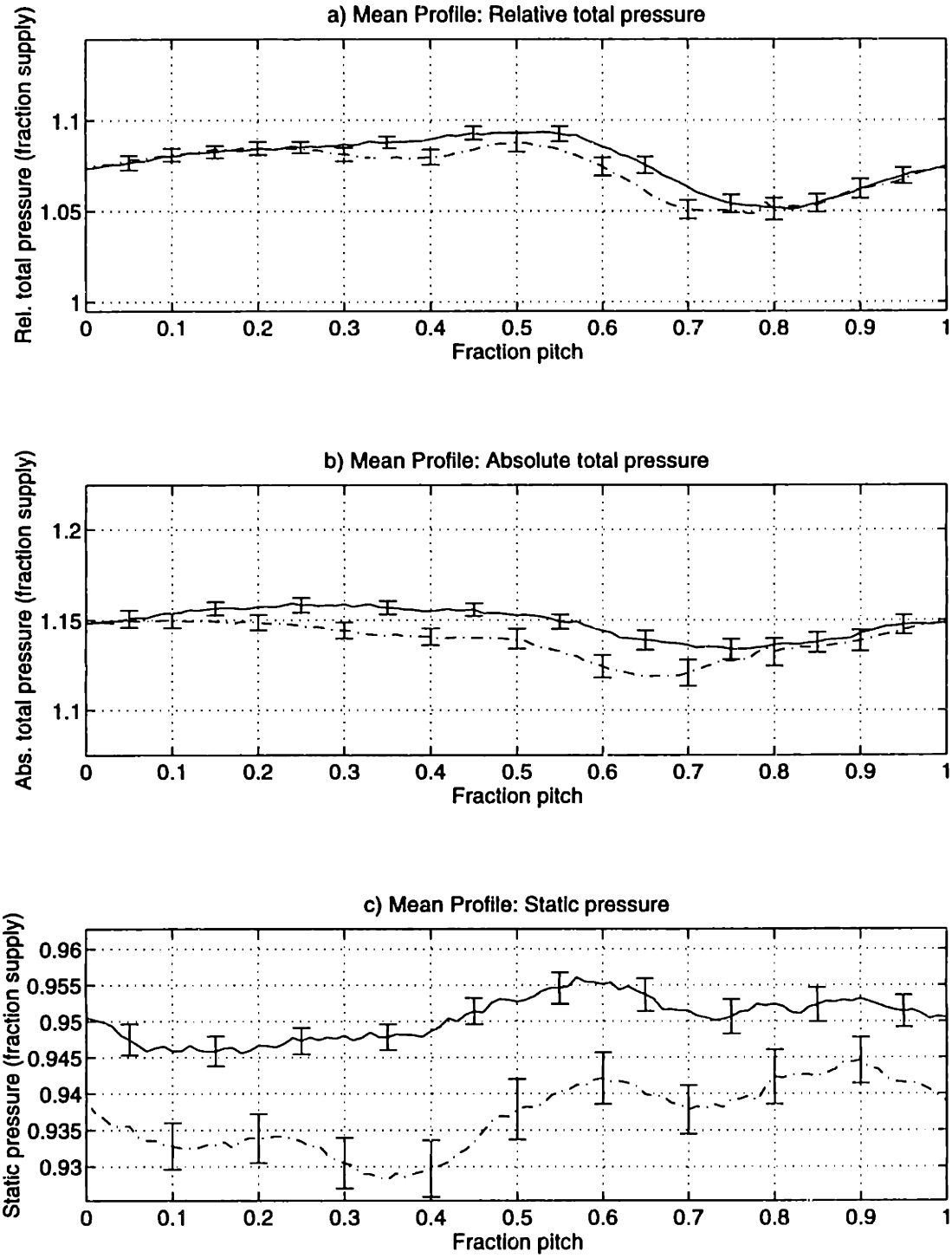

Figure 7-5: Ensemble-averaged profiles of relative and absolute total pressure and static pressure at 25% span, 1.5c for the baseline solid-bladed rotor (—) and the trailing edge blowing rotor with no injection (- .)

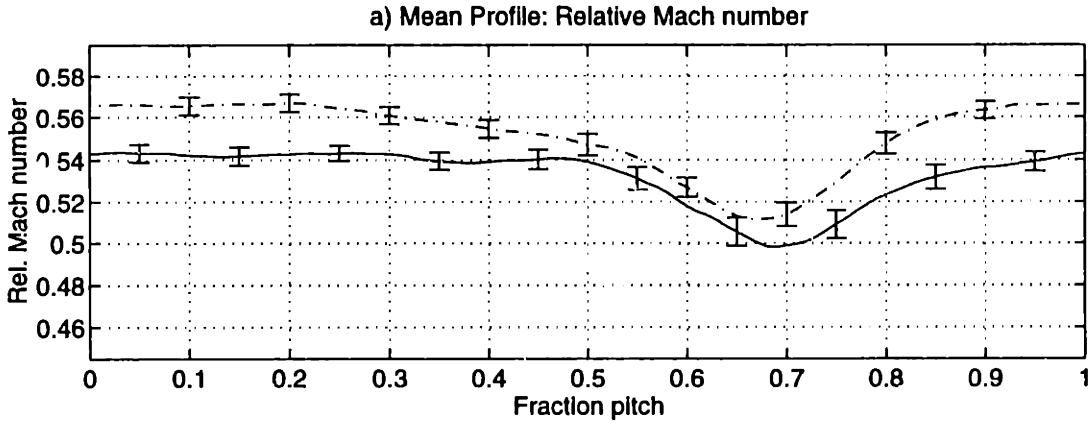

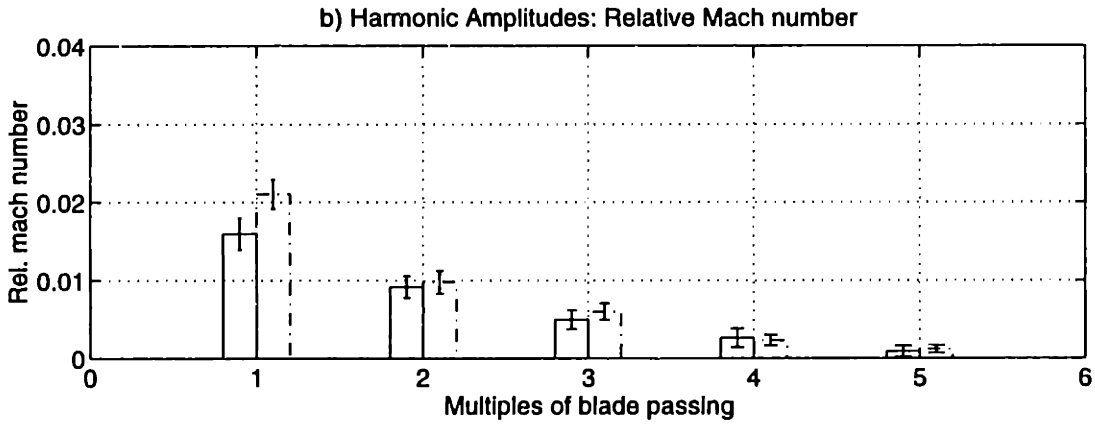

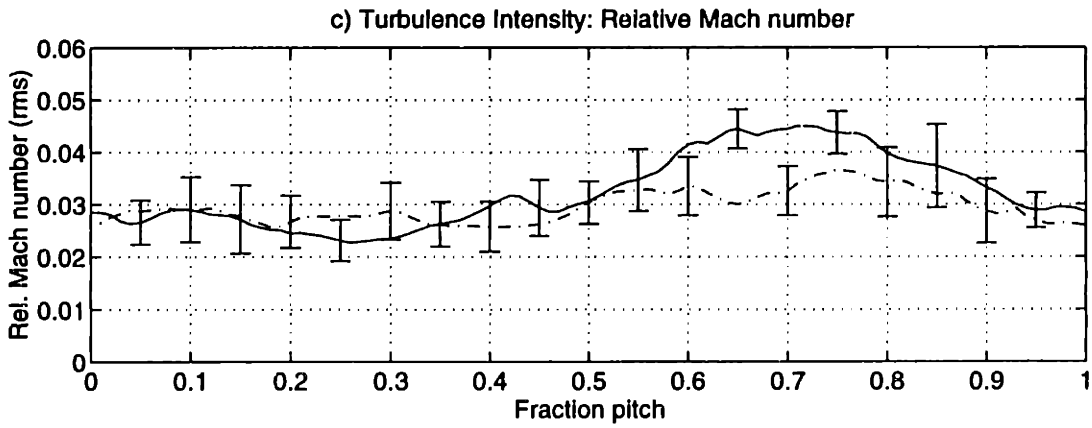

Figure 7-6: Relative Mach number ensemble-averaged profile, mean harmonic content, and turbulence profile at 50% span, 1.5c for the baseline solid-bladed rotor (—) and the trailing edge blowing rotor with no injection (- .)

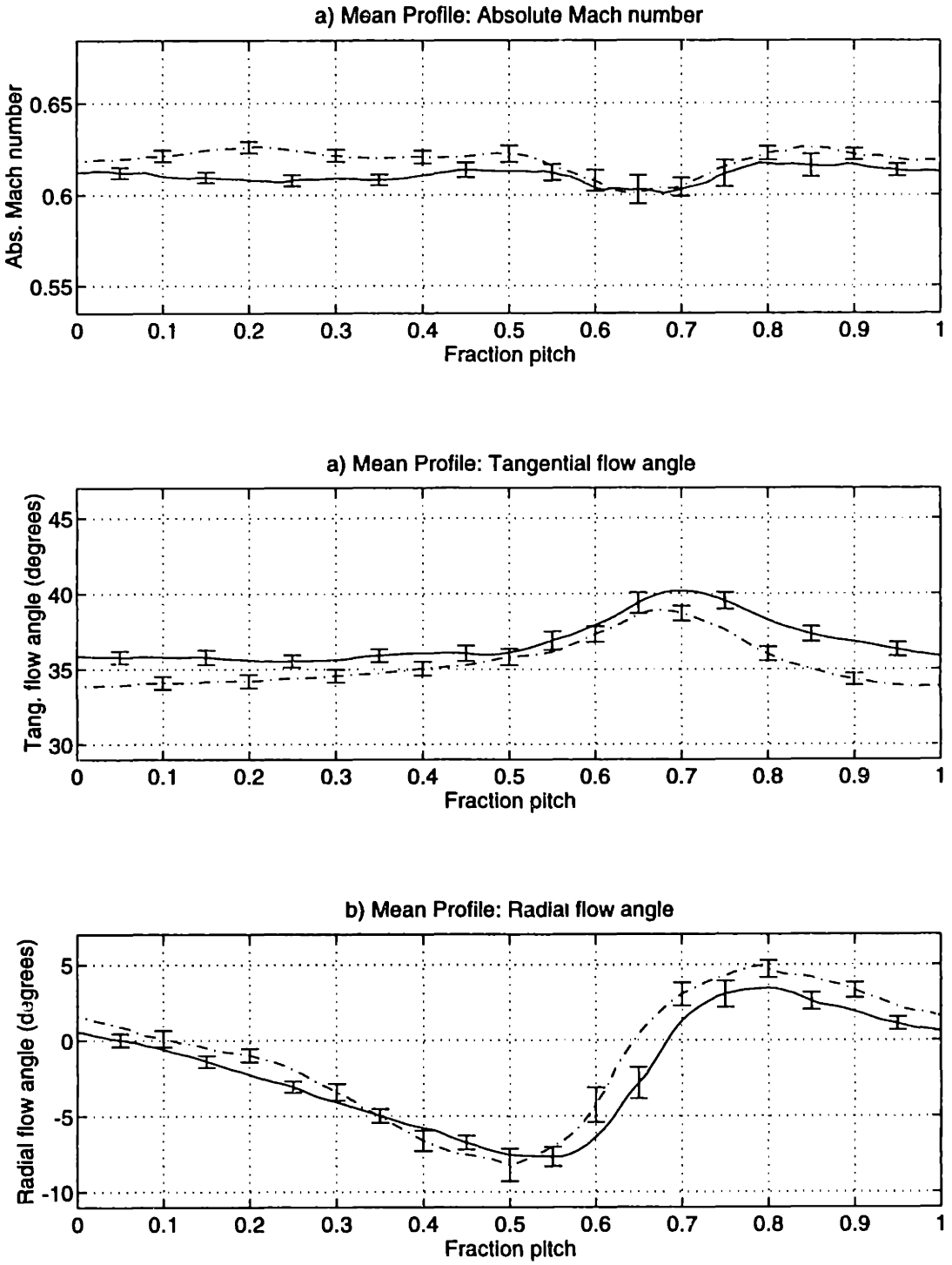

Figure 7-7: Ensemble-averaged profiles of absolute Mach number and tangential and radial flow angles at 50% span, 1.5c for the baseline solid-bladed rotor (—) and the trailing edge blowing with no injection (- .)

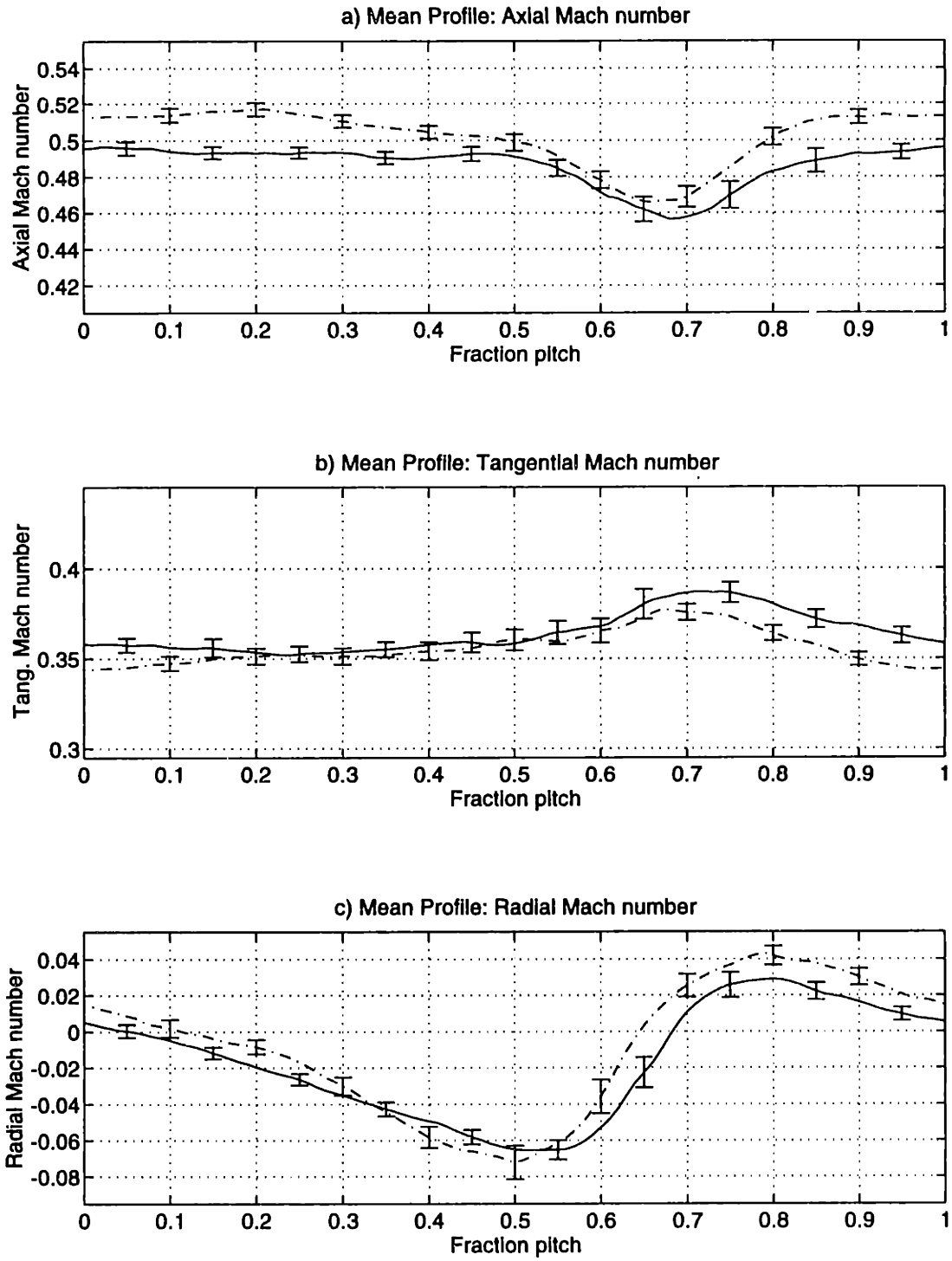

Figure 7-8: Ensemble-averaged profiles of axial, tangential, and radial Mach number at 50% span, 1.5c for the baseline solid-bladed rotor (—) and the trailing edge blowing rotor with no injection (– .)

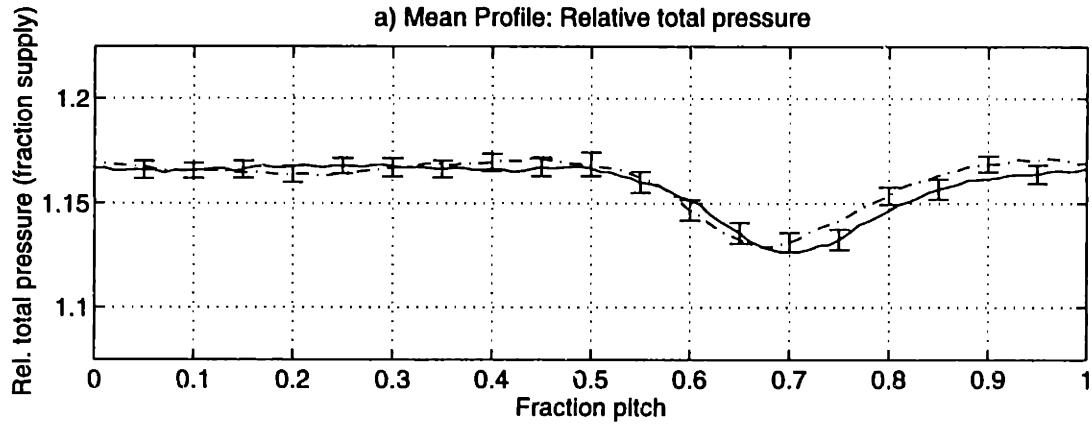

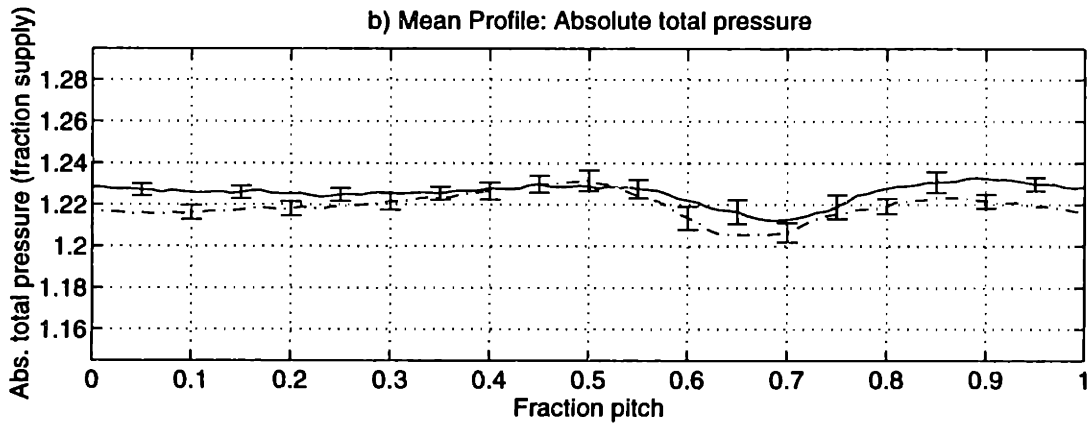

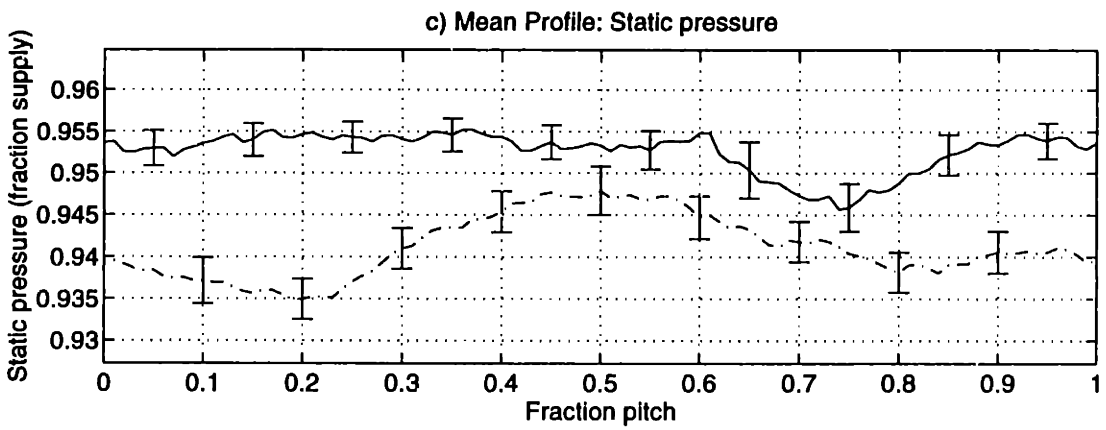

Figure 7-9: Ensemble-averaged profiles of relative and absolute total pressure and static pressure at 50% span, 1.5c for the baseline solid-bladed rotor (—) and the trailing edge blowing rotor with no injection (– .)

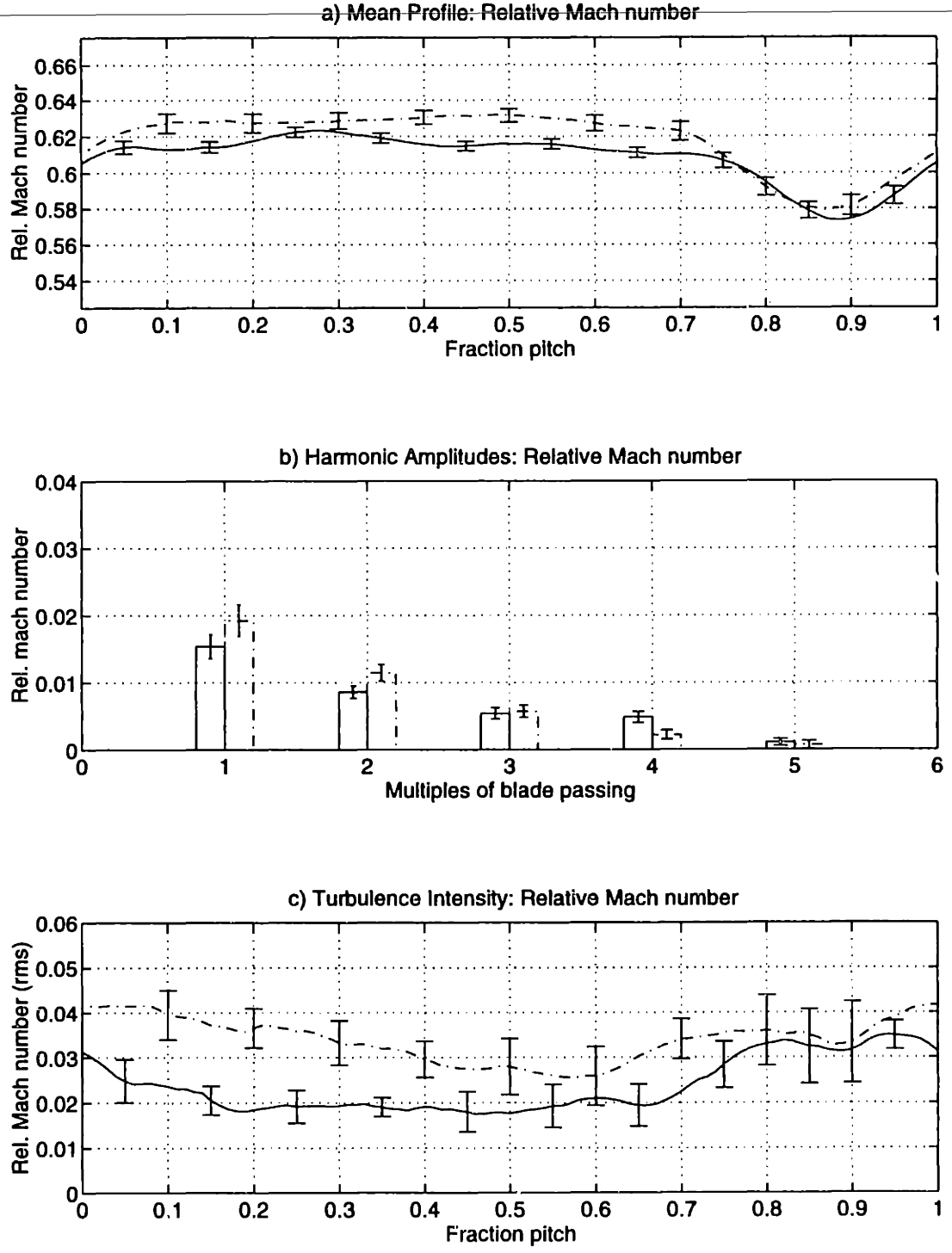

Figure 7-10: Relative Mach number ensemble-averaged profile, mean harmonic content, and turbulence profile at 75% span, 1.5c for the baseline solid-bladed rotor (—) and the trailing edge blowing rotor with no injection (- .)

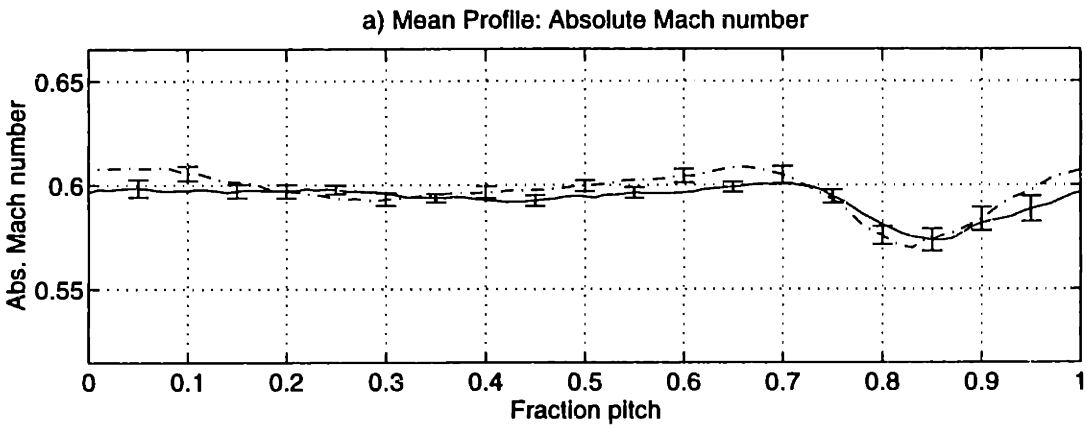

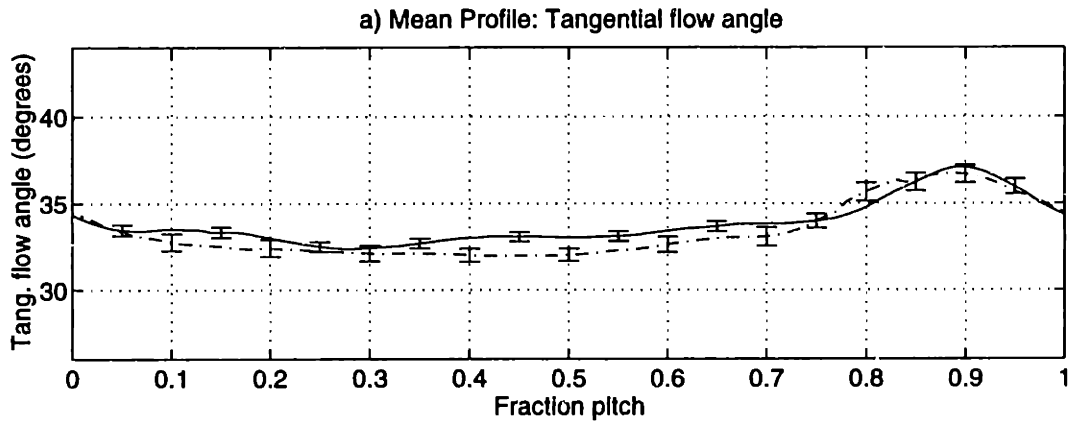

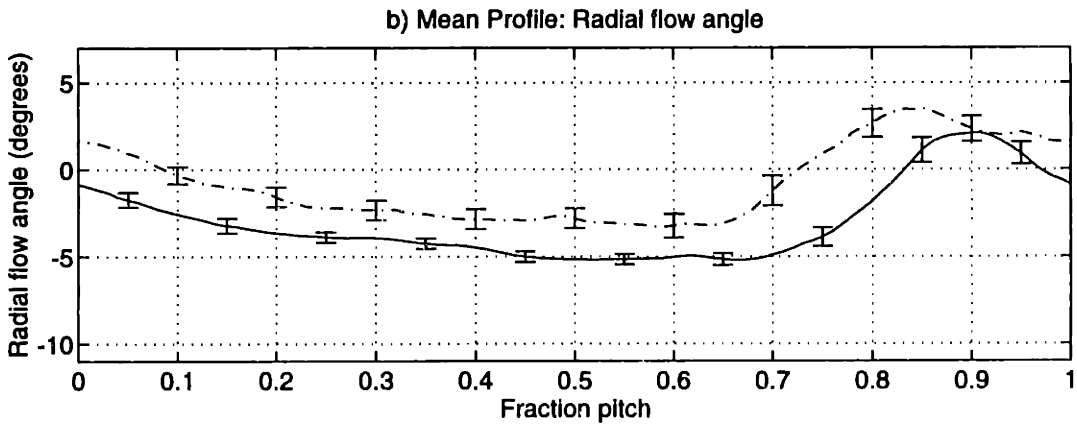

Figure 7-11: Ensemble-averaged profiles of absolute Mach number and tangential and radial flow angles at 75% span, 1.5c for the baseline solid-bladed rotor (—) and the trailing edge blowing with no injection (- .)

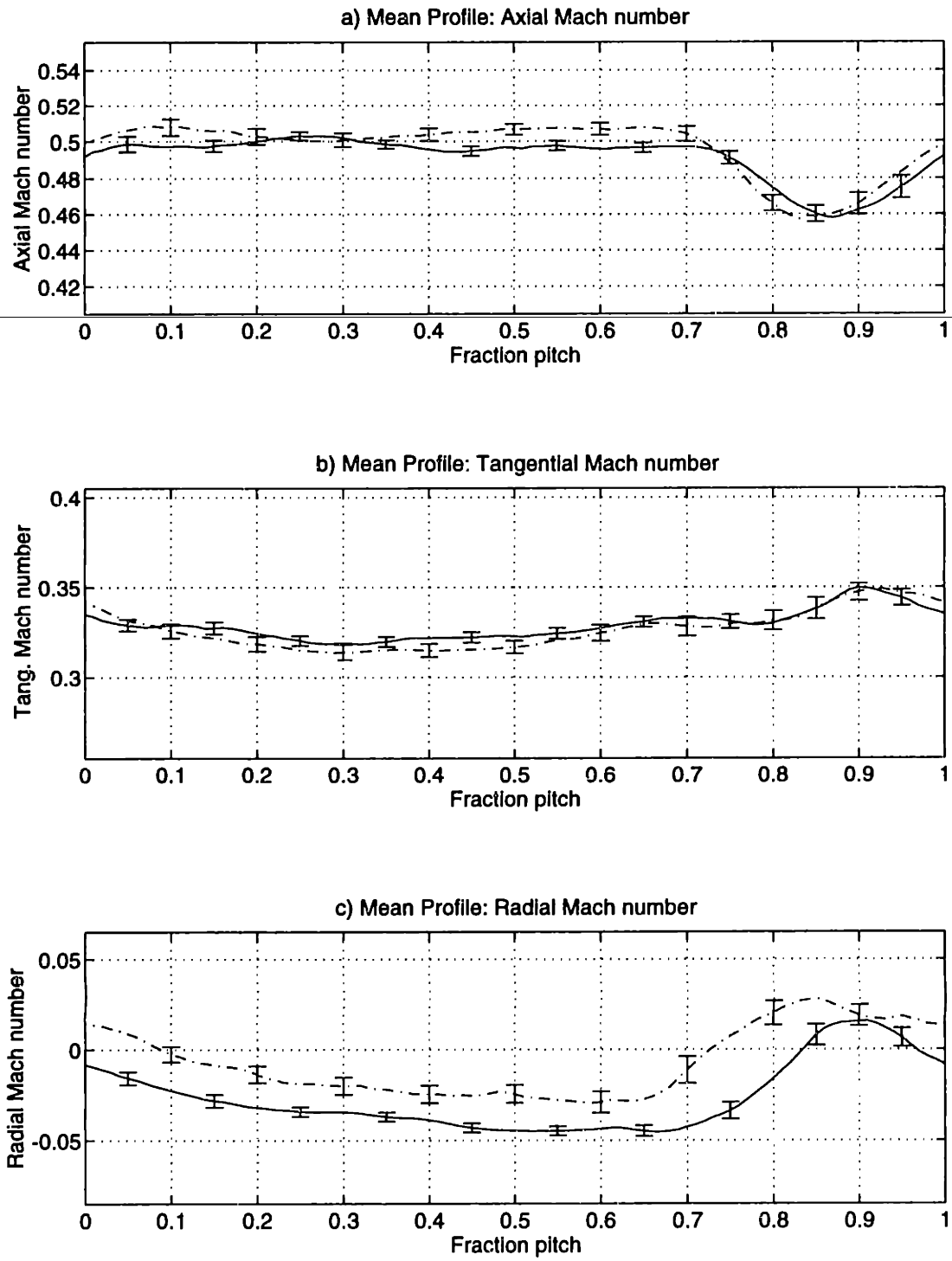

Figure 7-12: Ensemble-averaged profiles of axial, tangential, and radial Mach number at 75% span, 1.5c for the baseline solid-bladed rotor (—) and the trailing edge blowing rotor with no injection (- .)

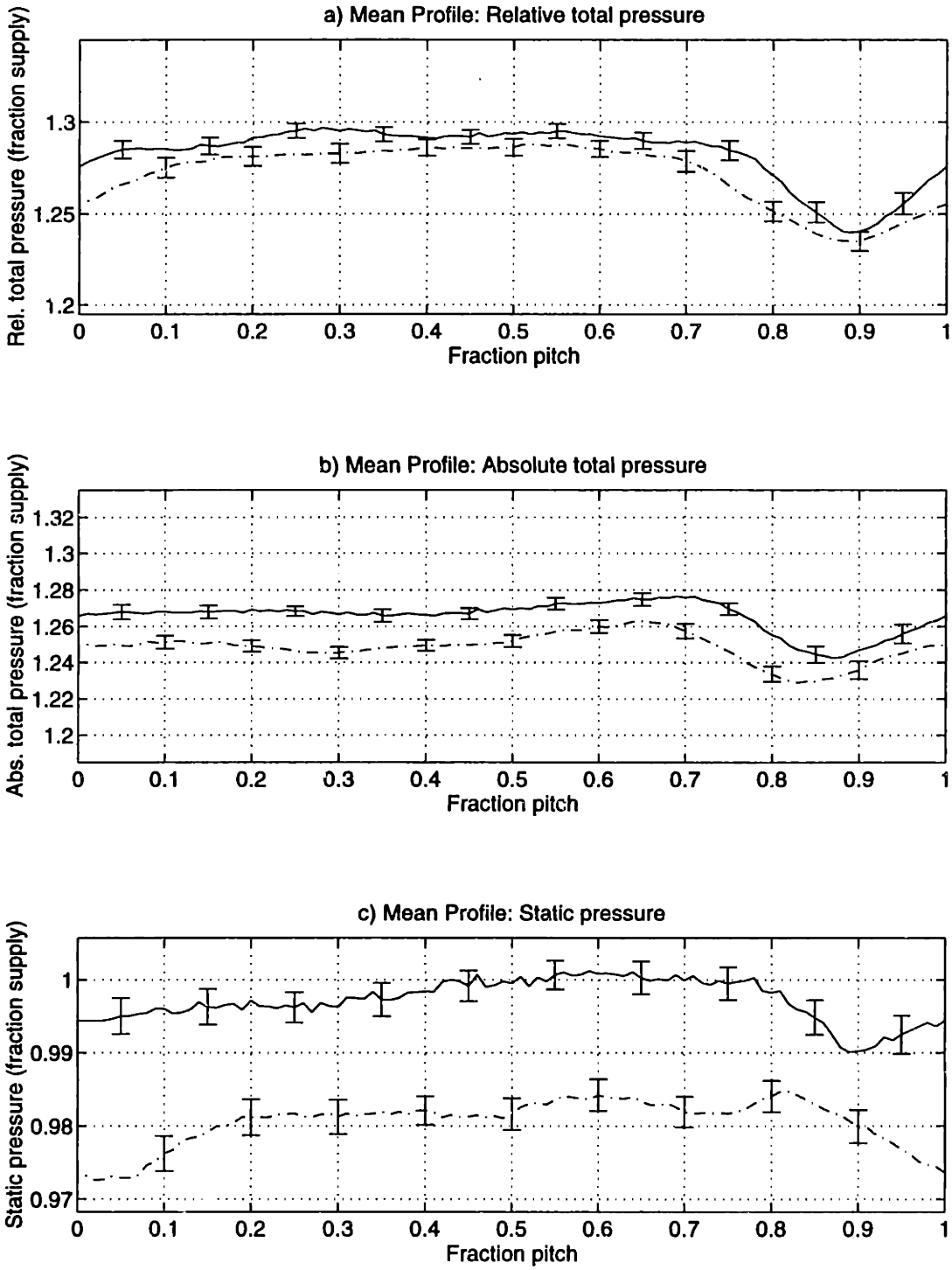

Figure 7-13: Ensemble-averaged profiles of relative and absolute total pressure and static pressure at 75% span, 1.5c for the baseline solid-bladed rotor (—) and the trailing edge blowing rotor with no injection (- .)

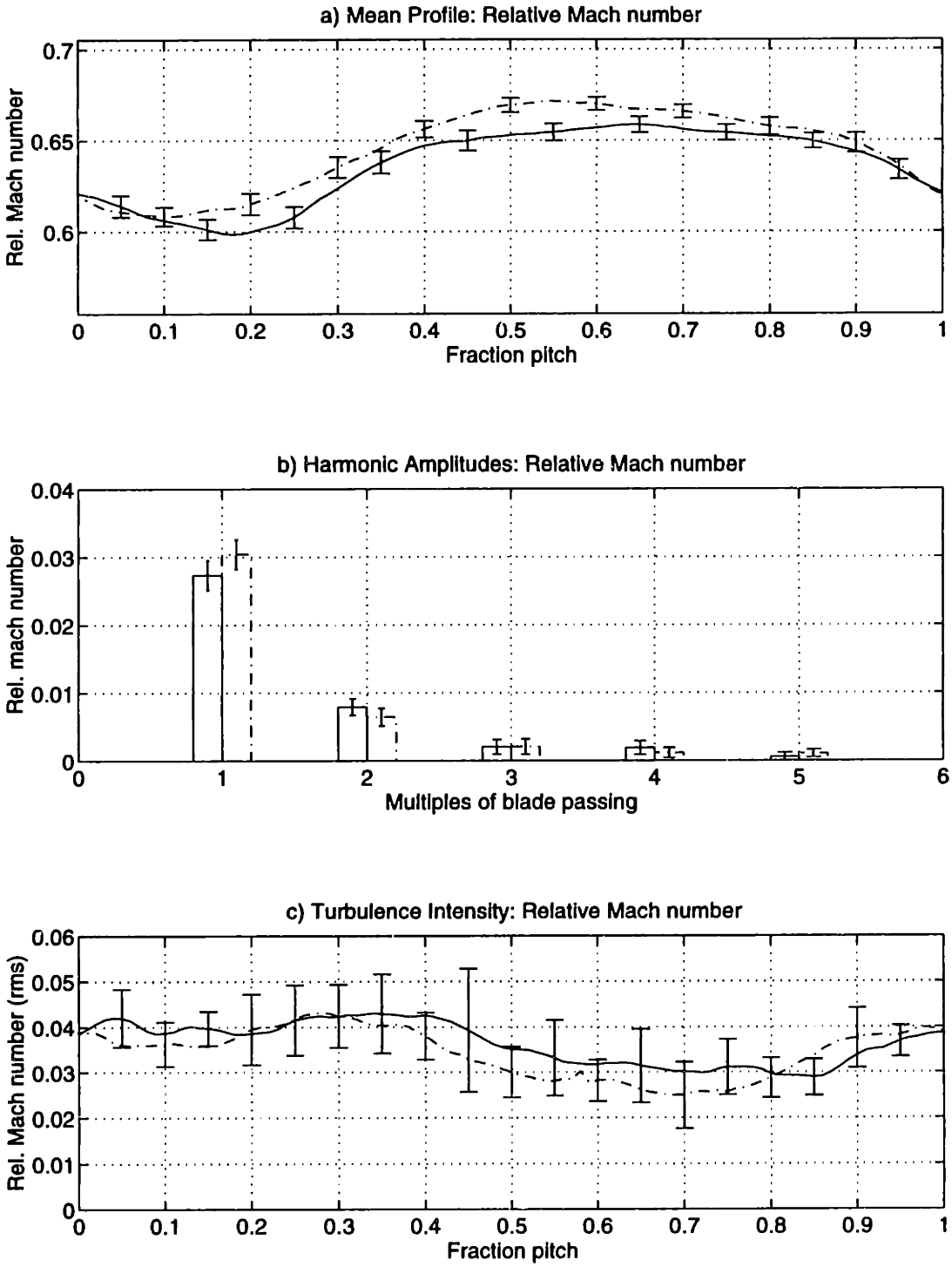

Figure 7-14: Relative Mach number ensemble-averaged profile, mean harmonic content, and turbulence profile at 87.5% span, 1.5c for the baseline solid-bladed rotor (—) and the trailing edge blowing rotor with no injection (- .)

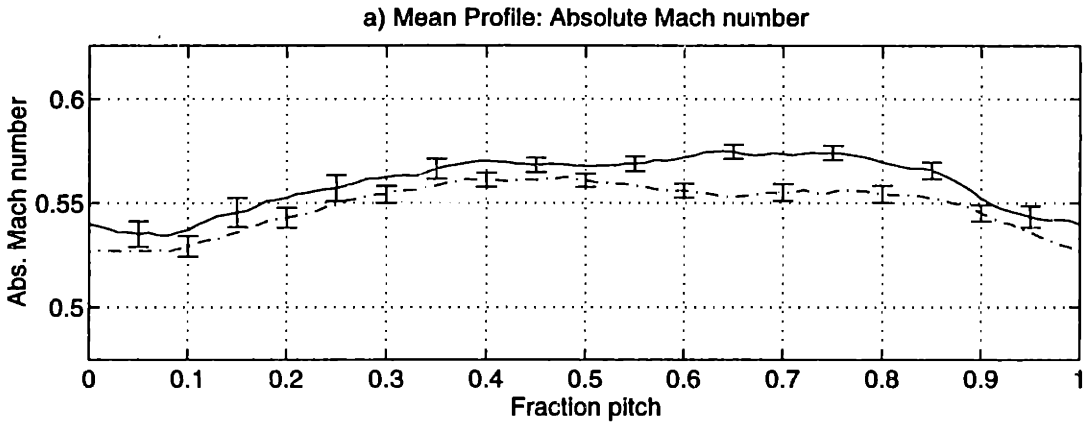

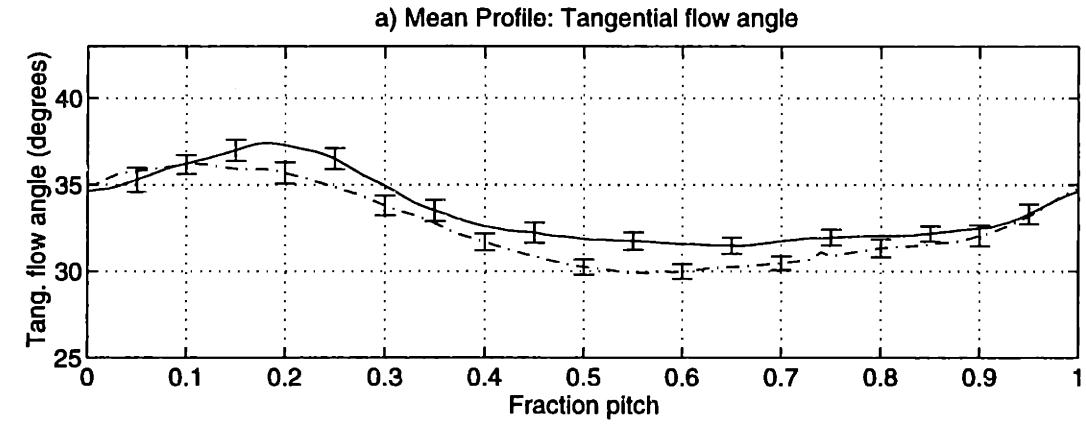

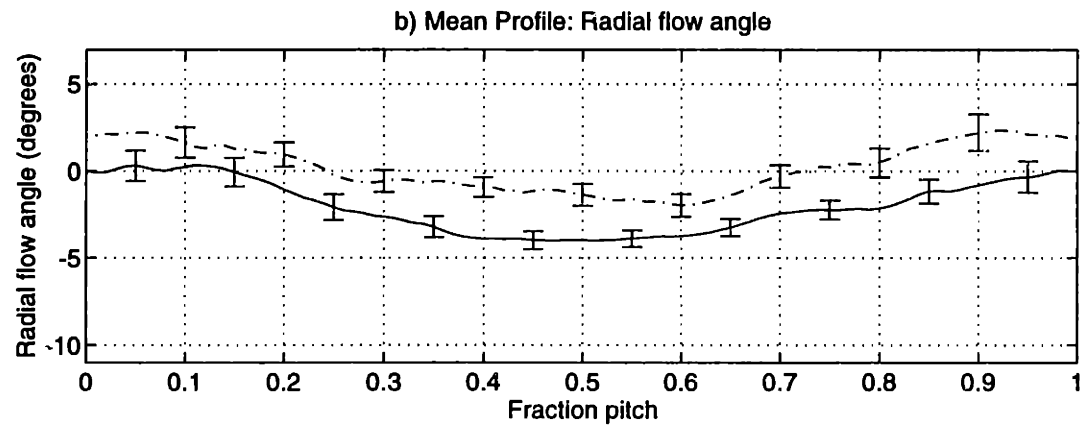

Figure 7-15: Ensemble-averaged profiles of absolute Mach number and tangential and radial flow angles at 87.5% span, 1.5c for the baseline solid-bladed rotor (—) and the trailing edge blowing with no injection (- .)

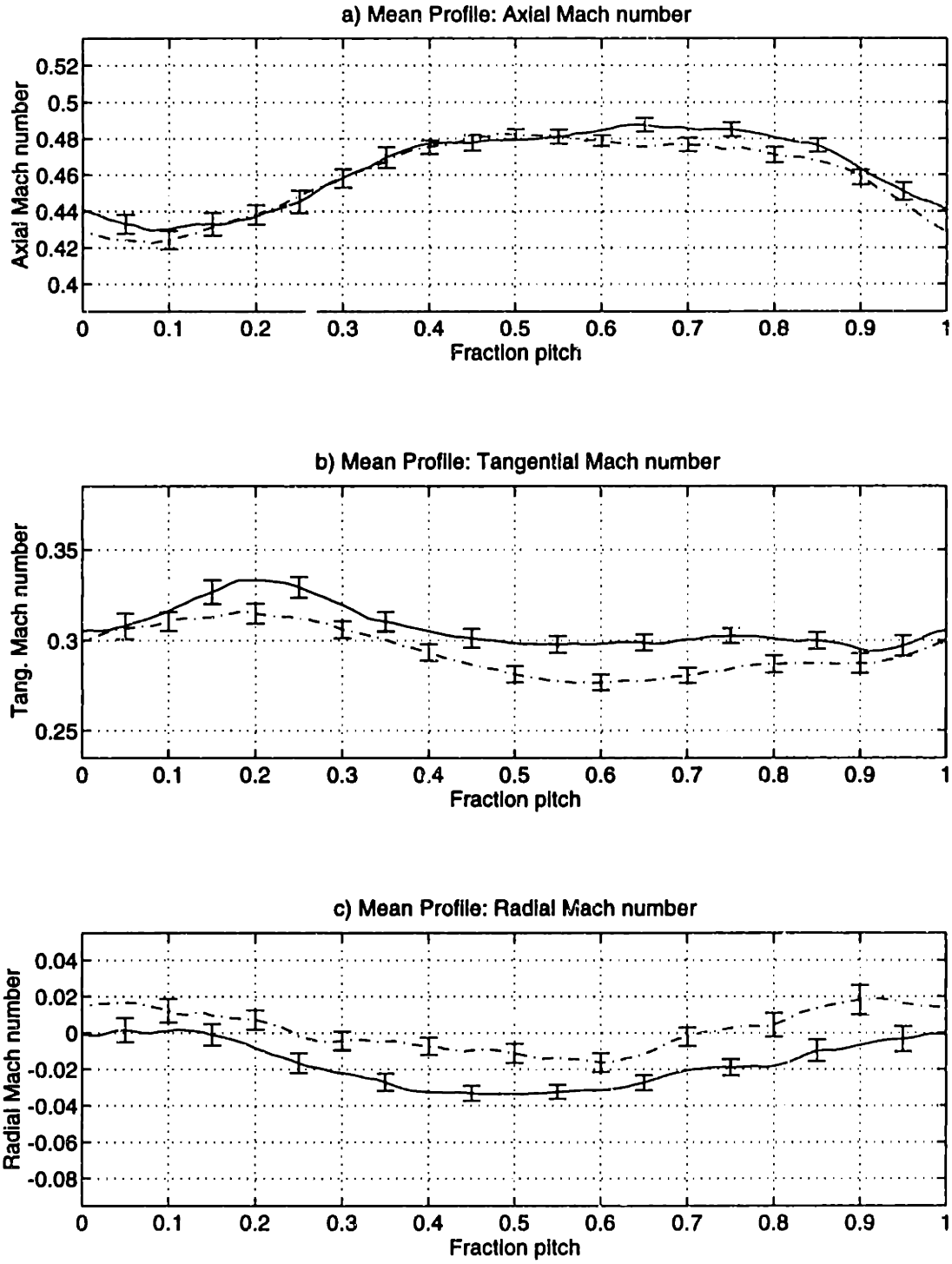

Figure 7-16: Ensemble-averaged profiles of axial, tangential, and radial Mach number at 87.5% span, 1.5c for the baseline solid-bladed rotor (—) and the trailing edge blowing rotor with no injection (- .)

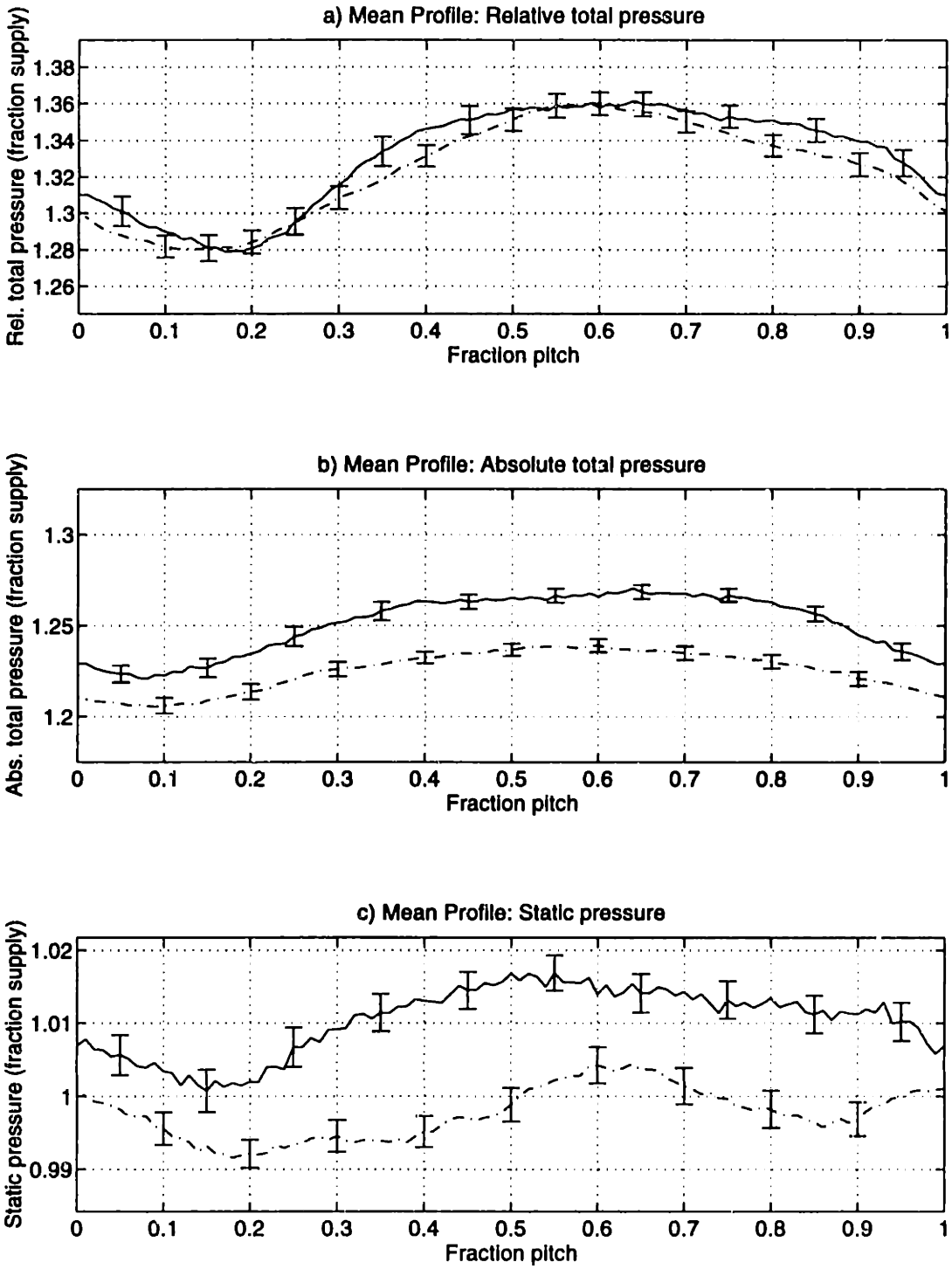

Figure 7-17: Ensemble-averaged profiles of relative and absolute total pressure and static pressure at 87.5% span, 1.5c for the baseline solid-bladed rotor (—) and the trailing edge blowing rotor with no injection (- .)

Baseline rotor	BPF	2*BPF	3*BPF	4*BPF	5*BPF
25% span, 1.5c	.0333	.0117	.0024	.0006	.0005
50% span, 1.5c	.0165	.0084	.0043	.0039	.0013
75% span, 1.5c	.0162	.0085	.0056	.0046	.0009
87.5% span, 1.5c	.0262	.0082	.0015	.0017	.0002
T.e. blowing rotor (no injection)	BPF	2*BPF	3*BPF	4*BPF	5*BPF
25% span, 1.5c	.0386 (1.16)	.0118 (1.01)	.0006 (0.26)	.0012 (2.01)	.0011 (2.06)
50% span, 1.5c	.0206 (1.25)	.0095 (1.13)	.0057 (1.34)	.0024 (0.60)	.0013 (0.98)
75% span, 1.5c	.0193 (1.19)	.0114 (1.34)	.0057 (1.02)	.0022 (0.49)	.0007 (0.82)
87.5% span, 1.5c	.0304 (1.16)	.0065 (0.79)	.0021 (1.45)	.0012 (0.69)	.0011 (4.57)

Table 7.1: Wake relative Mach number harmonic amplitudes at 1.5 chord for the baseline rotor and the trailing edge blowing rotor with no injection (trailing edge blowing rotor harmonic amplitudes also shown as fraction of baseline harmonic amplitudes)

speed (changes due to manufacture and untwist).

7.2.2 Wake harmonic amplitudes

The wake relative Mach number harmonic amplitudes are tabulated in Table 7.1 for the first five multiples of rotor blade passing frequency, BPF. The amplitudes are shown for the baseline rotor with solid blades and for the trailing edge blowing rotor with no injection. The harmonic amplitudes of the trailing edge blowing rotor are also shown as a fraction of the baseline rotor. In general, the amplitudes are reasonably close, and the amplitudes of the fourth and fifth harmonics are within the turbulence level of the flow field and thus changes are not significant. The amplitudes are also shown graphically versus span in Figure 7-18 for the first four multiples of BPF.

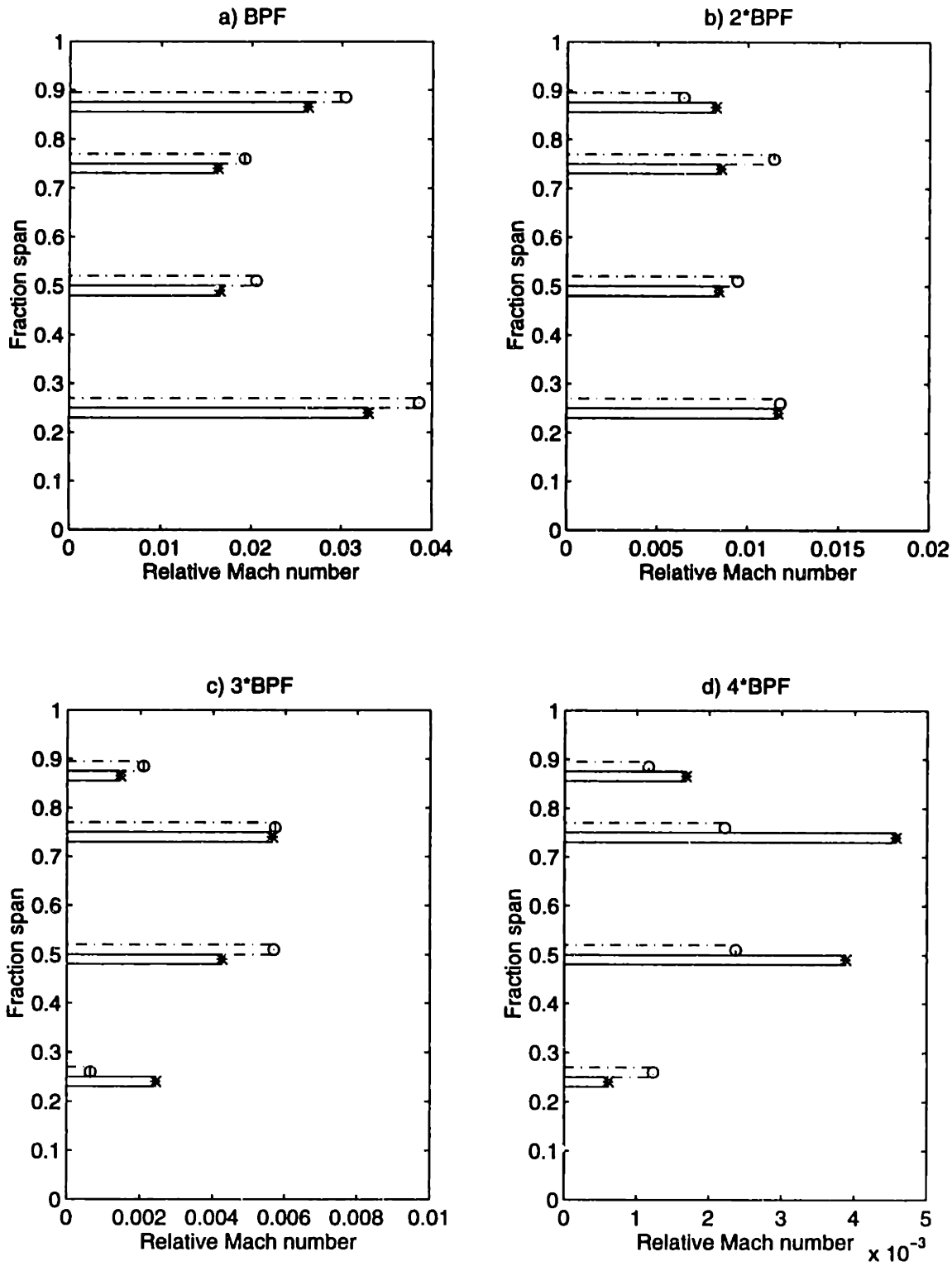

Figure 7-18: Wake relative Mach number harmonic amplitudes at 0.1 chord versus span: baseline rotor (—) and trailing edge blowing rotor, no injection (– .)

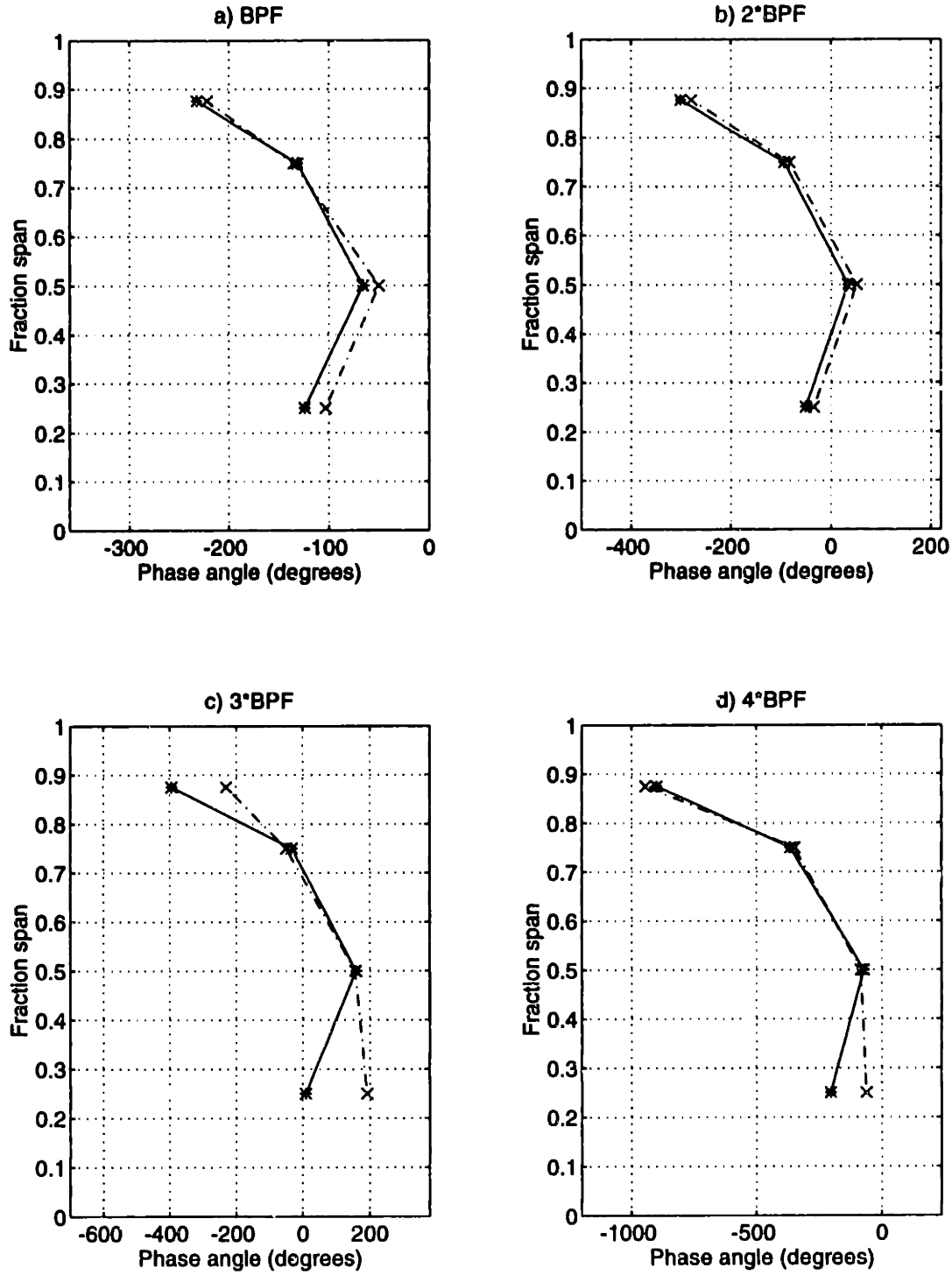

Figure 7-19: Phase angles for the first four BPF harmonics of relative Mach number at 1.5 chord for the rotor with solid blades (—) and the trailing edge blowing rotor with no injection (– .)

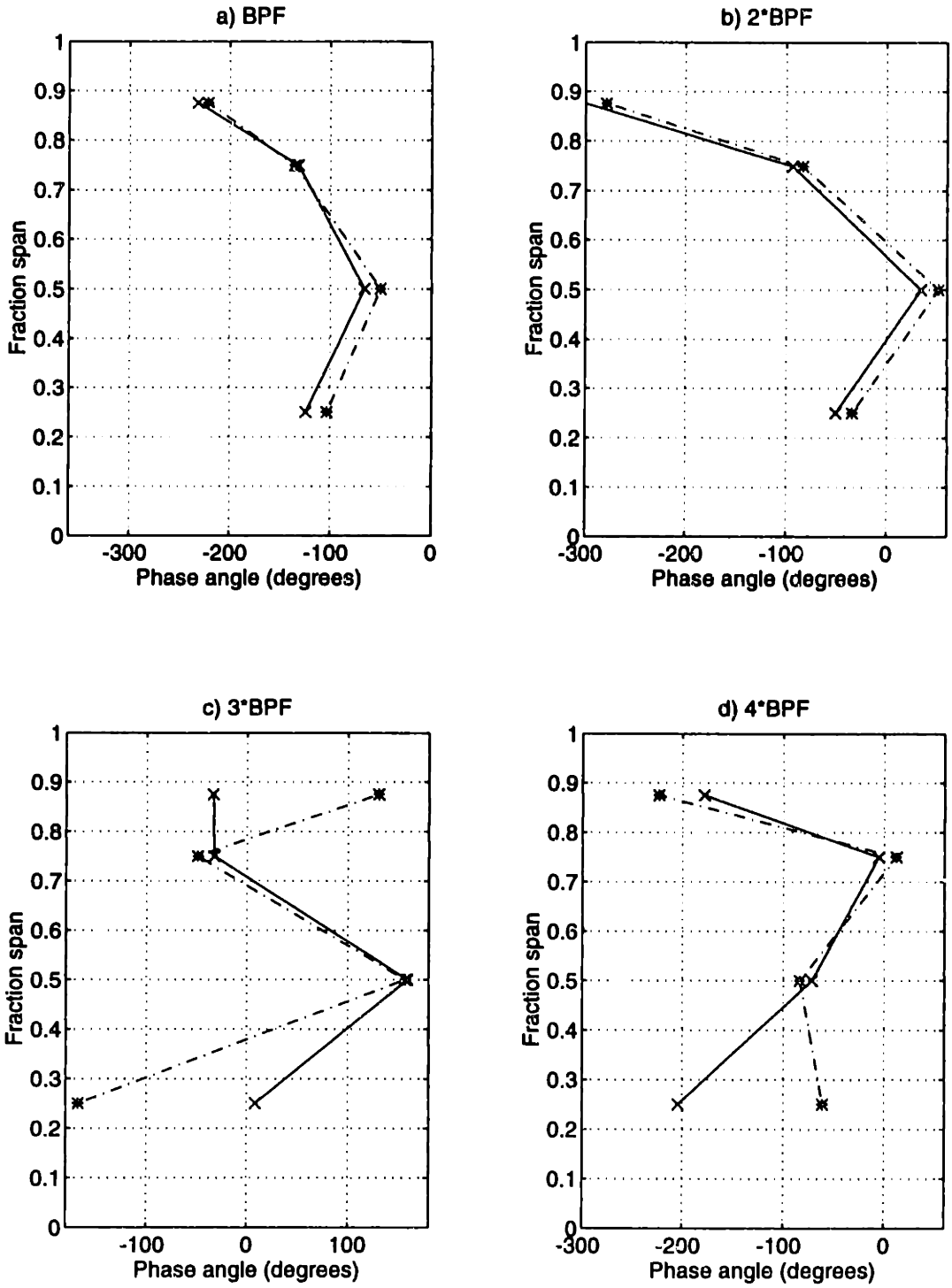

Figure 7-20: Phase angles (360 degrees) for the first four BPF harmonics of relative Mach number at 1.5 chord for the rotor with solid blades (—) and the trailing edge blowing rotor with no injection (- .)

7.2.3 Wake radial phase variation

The phases of the wake relative Mach number harmonics were calculated and are presented in Figure 7-19 for the first four multiples of BPF. The phase angles of the 1*BPF harmonics approximately match the centerline of the wake profiles. In the wake profile plots, a phase angle of zero degrees corresponds to the minimum at 0.5 pitch, and +-180 degrees corresponds to the minimum at 0.0 or 1.0 pitch.

For a given wake profile, the phases of the wake harmonics are locked at specific values. Thus, if the wake profile was the same at all spanwise locations, the radial phase variation of the BPF harmonic would exactly match the wake centerline skew. Also, the radial phase variation of the higher harmonics would have exactly the same shape as BPF, but the variation would be 'n' times the BPF variation, where 'n' indicates the multiple of BPF (n*BPF).

The radial phase variation shapes are seen to be approximately the same for BPF through 4*BPF in Figure 7-19, particularly for the baseline rotor. The trailing edge blowing rotor shows some differences at the hub and tip, but overall it matches quite well with the baseline rotor.

In addition to the radial phase curves shown in Figure 7-19, the same phase angles are shown in Figure 7-20. When the wake phases are calculated, the phase angles are only known within multiples of 360 degrees. For a standard wake, as shown in this section, the appropriate multiple of 360 degrees can be added/subtracted to obtain the plots shown in Figure 7-19, where the actual phase variation along the span is observed. In general, however, this will not be possible unless the wake is measured at many radial stations.

This ambiguity in the wake harmonic phase angle is critical when attempting to understand how changes to the wake will affect the coupling of the stator unsteady pressure fields to the acoustic modes. For example, the 3*BPF harmonic phases at 75 and 87.5% span appear to be nearly the same for the baseline rotor in Figure 7-20c. For standard wakes, this is fairly easily adjusted to produce the actual 360 degrees of phase variation over this 12.5% span section. However, with the addition of injection from the trailing edge, adjustments to the wake phases are no longer straight-forward. If the wake transitions from being underfilled to being overfilled along the span, the 'wake' turns into a 'jet'. The phase of the

wake BPF harmonic changes about 180 degrees (with similar shifts in the higher harmonics) when a jet is produced. Therefore, care must be given to judging the wake phase angle variations. Between any two spanwise data points, 360 degrees (or multiples, thereof) of phase variation may be present.

7.2.4 Summary of comparison of the baseline solid-bladed rotor and the trailing edge blowing rotor with no injection

Flow field measurements downstream of the trailing edge blowing rotor (no injection) were found to be sufficiently close to those of the rotor with solid blades to assure that the performance of the blades with internal passages was representative of typical fan geometries. The average axial Mach number was seen to be several percent higher for the trailing edge blowing rotor, causing slightly lower loading. This resulted in lower exit tangential Mach number (lower swirl and tangential flow angle) and lower static and total pressure ratio (about 1-1.5%). However, the wake relative Mach number harmonic amplitudes were seen to be approximately the same for the two configurations, as were the wake harmonic radial phase variations. Again, extreme care must be used when interpreting the wake phase angles in attempting to understand changes in acoustic coupling to the stator pressure field.

A couple notes regarding this comparison of data should be made. A large portion of the changes seen in the flow measurements between the baseline rotor and the trailing edge blowing rotor are within the 95% confidence intervals shown. In addition, the flow measurement probe was modified and recalibrated between measurements on the solid and trailing edge blowing rotors. While best estimates of the errors in the flow measurements were used in the plots, additional offsets in Mach number and/or pressures may be present. Additional measurements should be taken with the modified probe downstream of the baseline rotor before significant weight is placed on the performance changes due to the trailing edge blowing blades.

7.3 Trailing Edge Blowing Rotor: tip-weighted injection

As described in Chapter 6 the trailing edge blowing fan blades were designed to inject fluid such that a momentumless wake would be achieved along the entire blade span. Since each of the five blade passages required a different inlet total pressure (the tip needing the highest), throttle plates were inserted in the disk beside the blade root to throttle the injection flow into each passage. The hole sizes were designed such that each would provide the necessary total pressure drop required for each passage relative to that for the tip.

To ease later modification, the throttle holes were initially machined smaller than the ideal design value. This allowed the plates to be easily removed and the holes enlarged if necessary. These original throttle plates resulted in injection that was weighted toward the tip of the blade. The effective momentum thickness added with injection as a fraction of the local wake momentum thickness (no injection) along the span is shown in Figure 7-21. The curve with '*' symbols are measurements at 0.1 chord, and the curve with '+' symbols are measurements at 1.5 chord. The measured momentum thickness of the flow is quite sensitive to the choice of 'freestream', and thus the momentum thicknesses shown (as fraction of pitch) have potential errors of approximately 0.1 to 0.2. A value of 1.0 indicates that the momentum added with injection was equal to the wake momentum deficit and the resulting flow field has zero net momentum deficit.

The injection is seen to be weighted toward the tip of the blade, with a momentumless wake at approximately 80% span. The lower one-half of the span has only about 40% momentum addition, and the tip is overblown. This condition had been previously considered as a configuration for future testing, however, so the throttle plates were left as is and measurements taken. The plates could then be later modified to achieve more uniform injection along the span. The injection mass flow of this tip-weighted configuration was approximately 1.9% of the fan throughflow.

7.3.1 Flow field measurements at 0.1 chord

Measurements were taken just behind the trailing edge of the rotor at 0.1 chord downstream. One run was performed with and without 1.9% tip-weighted injection (each having 96 blade

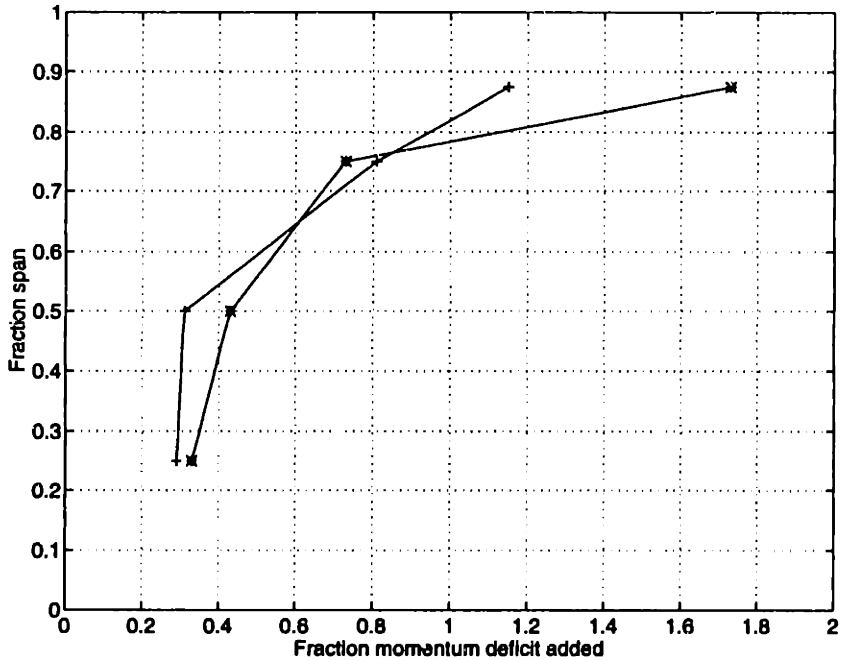

Figure 7-21: Wake momentum deficit addition with injection versus span: tip- weighted injection ('*' at 0.1 chord and '+' at 1.5 chord)

passing periods of 'steady state' data) at 25, 50, 75 and 87.5% span. The curves with no injection are plotted with the injection curves for direct comparison.

25% span, 0.1 chord

The relative Mach number measurements at 25% span, 0.1 chord are shown in Figure 7-22 with and without tip-weighted injection. The other flow variables are shown in Figures 7-23 through 7-25. The solid line is with no injection, and the dashed line is with injection of approximately 1.9% of the fan throughflow. The wake centerline deficit is reduced more than 50%, but the width is slightly increased with injection. The mean relative Mach number harmonic content is reduced approximately 50% for the first five harmonics, and except for the radial flow component, the other flow variables show similar smoothing. There is virtually no change in the turbulence intensity. The consistency of the radial flow is good news in the respect that the injection is in the freestream direction and not blowing radially outward in the hub region. This was a concern due to the very limited volume for turning the flow in the chordwise direction in the hub injection passage.

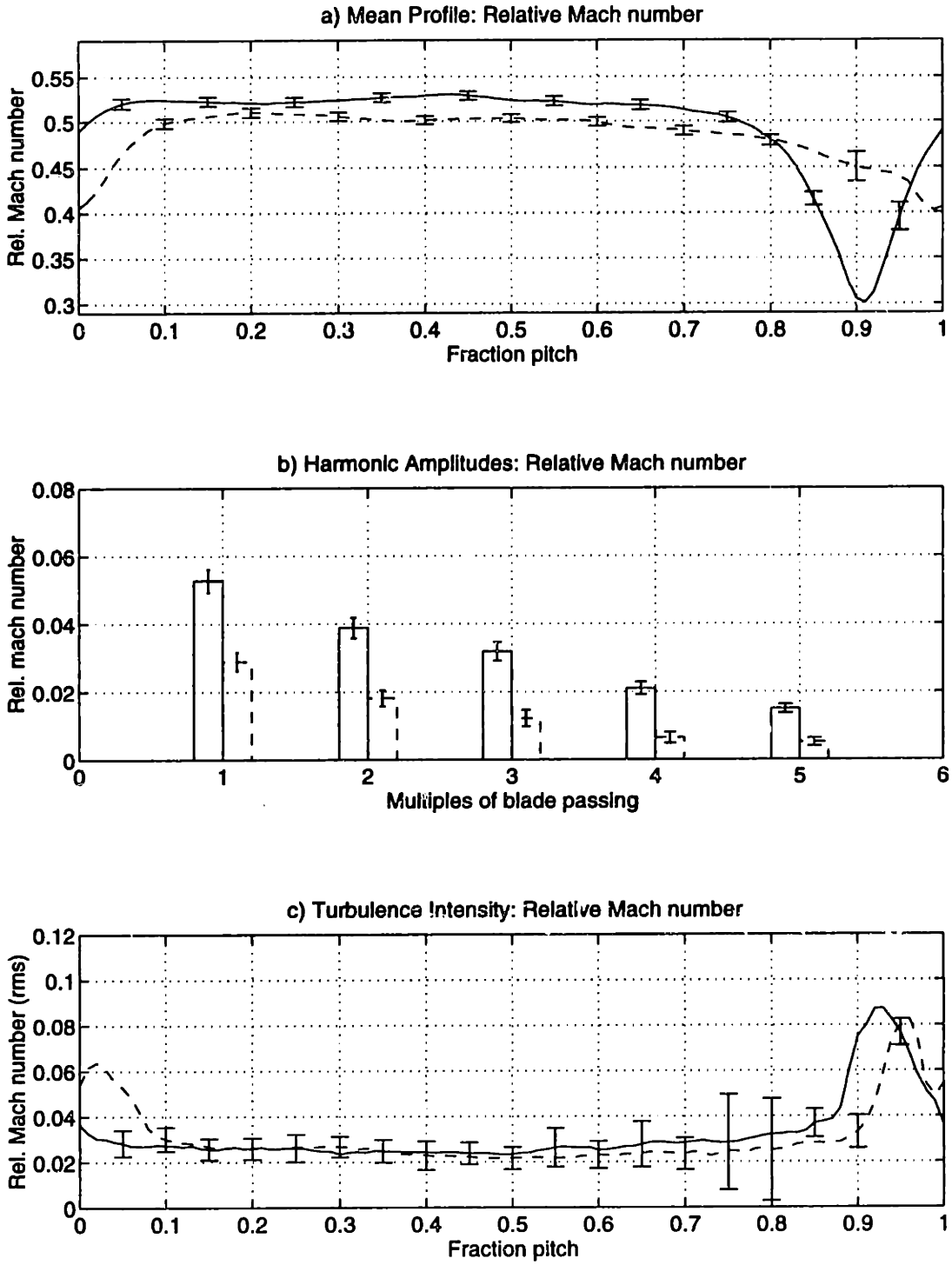

Figure 7-22: Relative Mach number ensemble-averaged profile, mean harmonic content, and turbulence profile at 25% span, 0.1c for the trailing edge blowing rotor with (- -) and without (—) tip-weighted injection

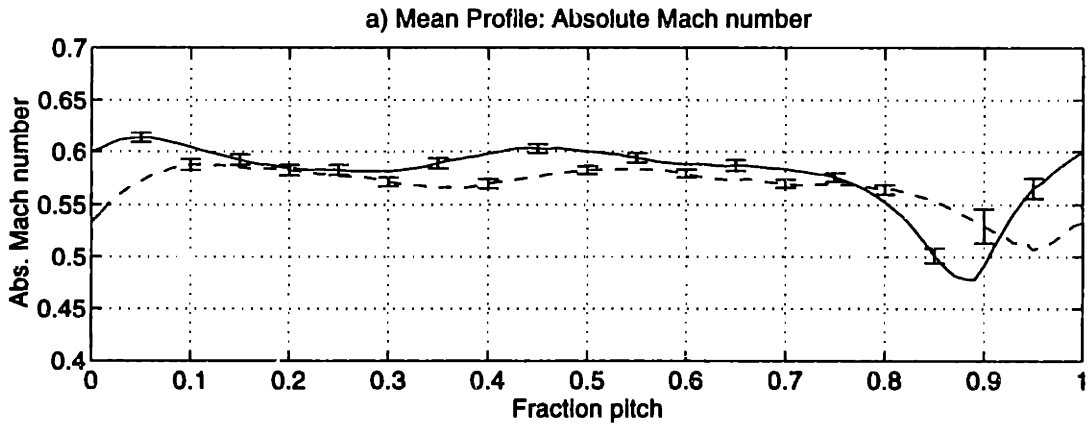

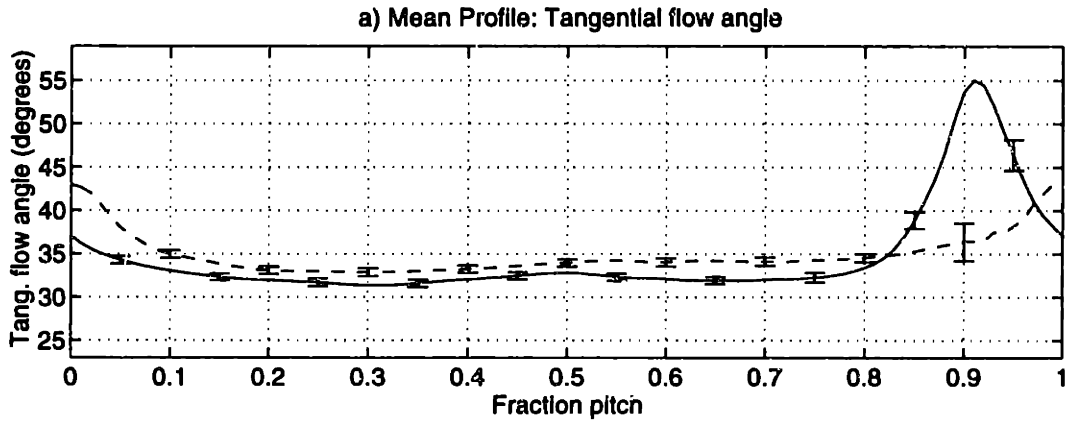

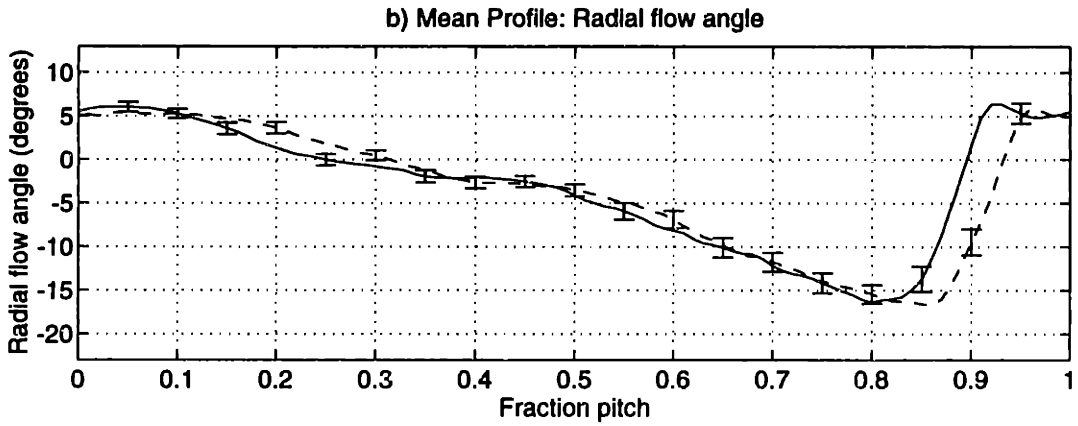

Figure 7-23: Ensemble-averaged profiles of absolute Mach number and tangential and radial flow angles at 25% span, 0.1c for the trailing edge blowing rotor with (- -) and without (—) tip-weighted injection

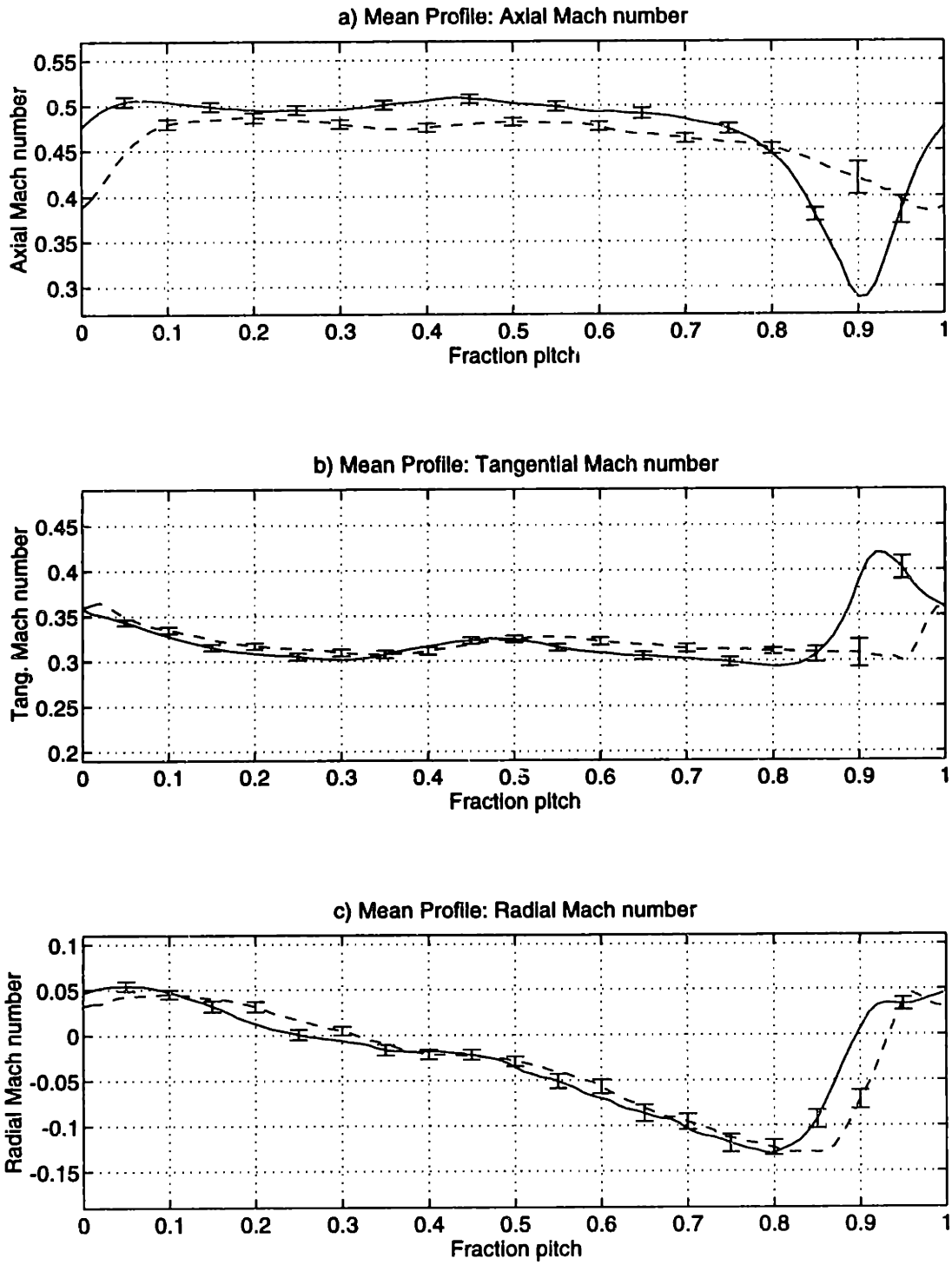

Figure 7-24: Ensemble-averaged profiles of axial, tangential, and radial Mach number at 25% span, 0.1c for the trailing edge blowing rotor with (- -) and without (—) tip-weighted injection

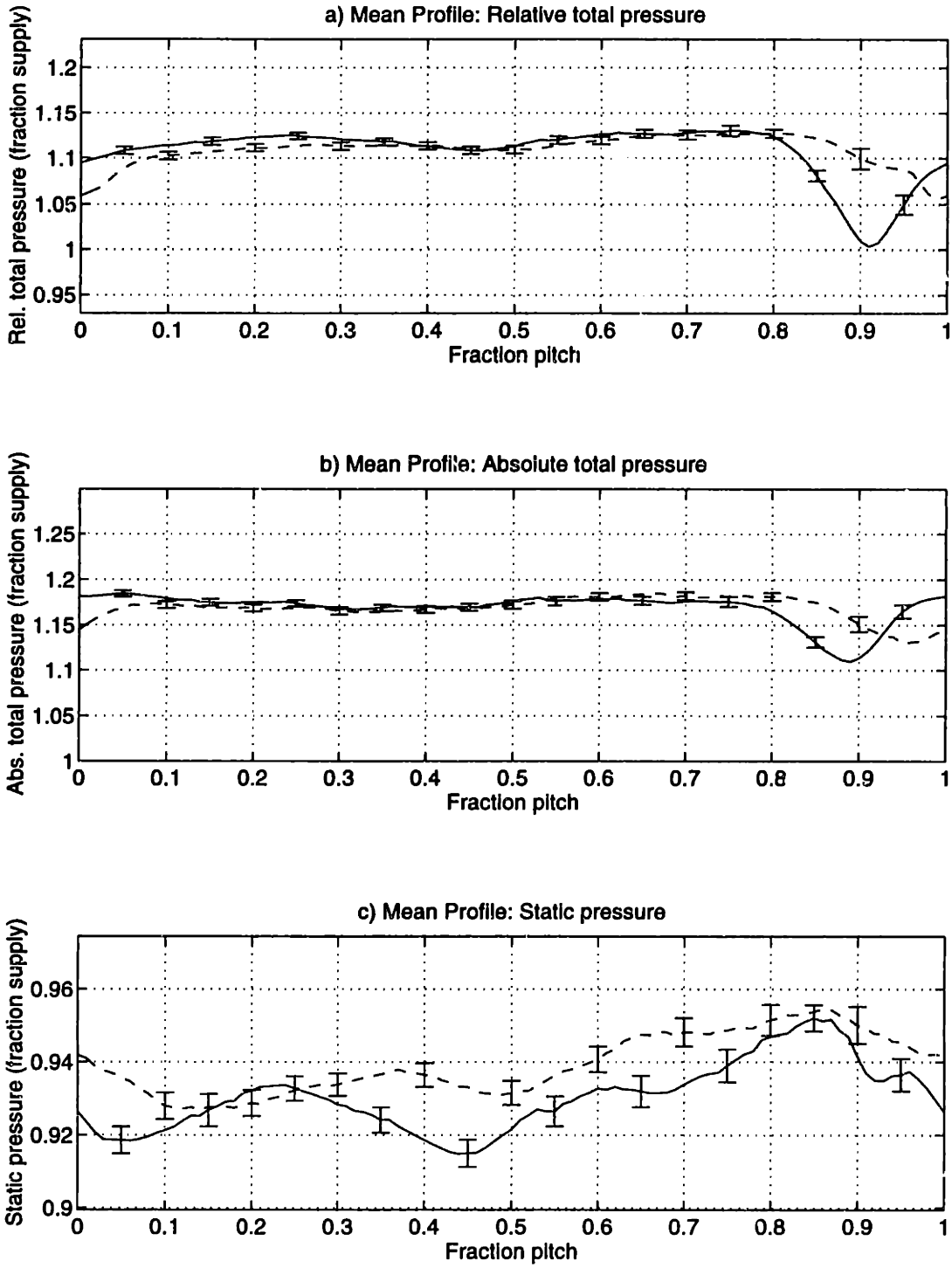

Figure 7-25: Ensemble-averaged profiles of relative and absolute total pressure and static pressure at 25% span, 0.1c for the trailing edge blowing rotor with (- -) and without (—) tip-weighted injection

50% span, 0.1 chord

The flow variables at 50% span, just behind the rotor trailing edge, are shown in Figures 7-26 through 7-29. The freestream axial Mach number is approximately 2% lower with injection. The blowing results in a wake that is about 45% filled (momentum deficit). In addition, the blowing 'jet' is seen to be very near the center of the wake. This was the intention of blowing at the deviation angle and appears to be successful. The changes in the turbulence intensity at this position are not significant.

75% span, 0.1 chord

At 75% span, 0.1 chord the flow variables are significantly smoothed with injection and are plotted with the no injection results in Figures 7-30 through 7-33. The variations in relative Mach number and tangential flow angle are reduced about 75% with injection. Although the wake is not completely filled, note that only a small jet results in the wake due to injection. This smooth profile at 0.1 chord suggests that the injection 'slots' from the deviation angle to the trailing edge results in injection at near the freestream velocity, versus a narrow, high velocity jet. The result is quicker smoothing of the wake. In fact, the relative Mach number harmonics at 75% span have only small reductions from 0.1 to 1.5 chord, since most of the mixing has already occurred. The peak turbulence intensity in the wake at 75% span, 0.1 chord is also reduced about 40% with injection.

The rapid mixing results described above could be very useful in production engines. If the rotor/stator spacing could be significantly reduced without increasing the rotor wake/stator noise, the engine weight can be decreased. Of course, the wake skewing is also important and must be considered, but the 75% span BPF and 2*BPF harmonics are smaller at 0.1 chord with injection than at 1.5 chord without injection.

87.5% span, 0.1 chord

Figures 7-34 through 7-37 show that the injection rate at 87.5% span is to high. The wake is completely eliminated and a jet of approximately 20% of the wake momentum thickness without blowing is seen on the pressure side of the wake relative Mach number profile (lower

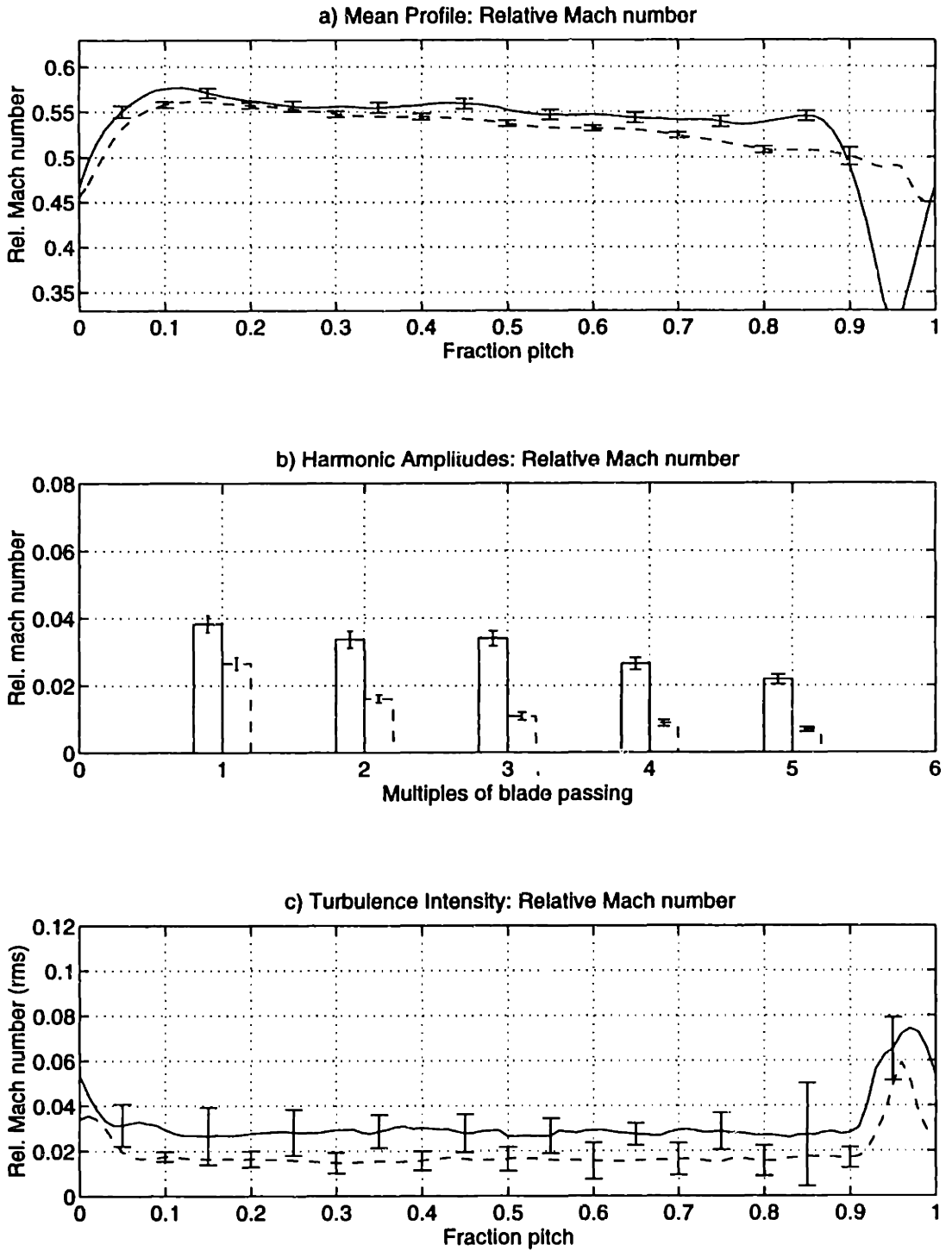

Figure 7-26: Relative Mach number ensemble-averaged profile, mean harmonic content, and turbulence profile at 50% span, 0.1c for the trailing edge blowing rotor with (- -) and without (—) tip-weighted injection

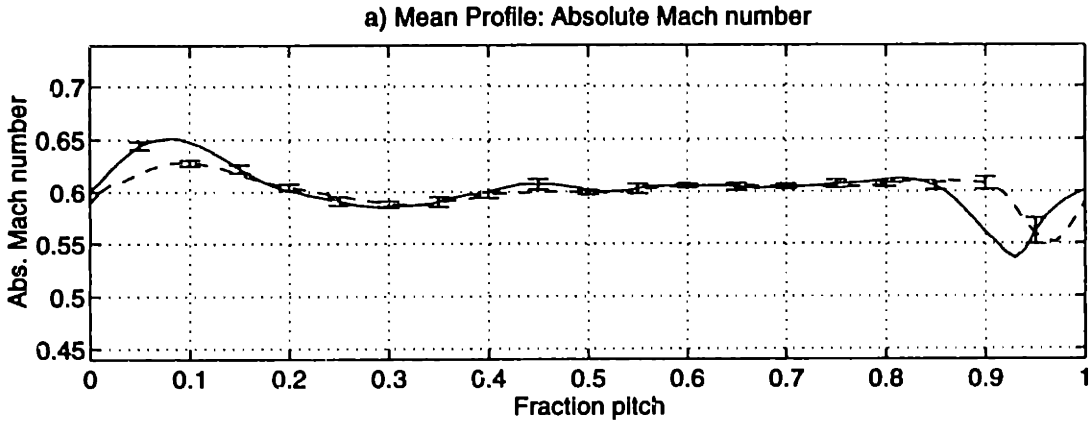

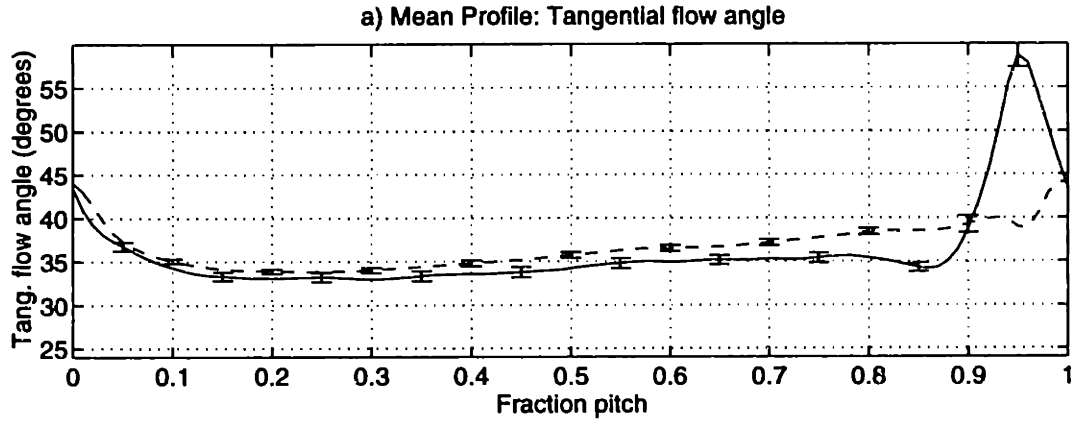

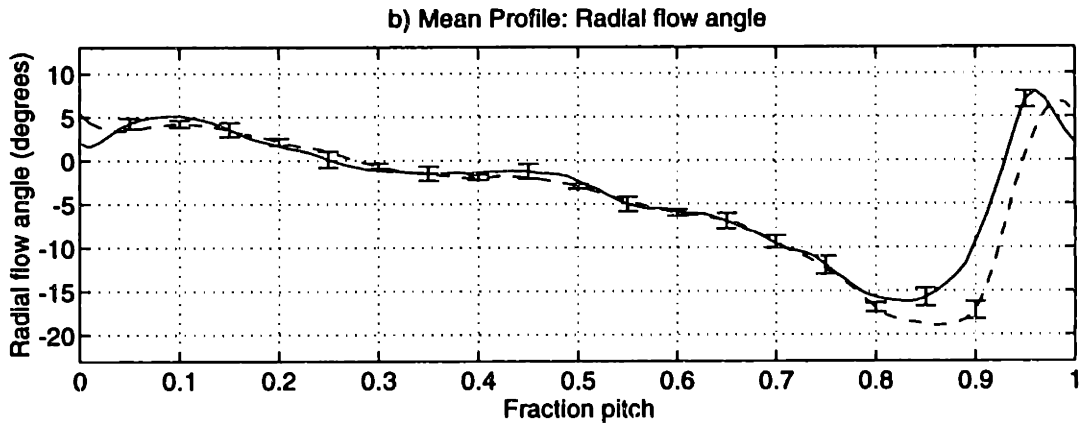

Figure 7-27: Ensemble-averaged profiles of absolute Mach number and tangential and radial flow angles at 50% span, 0.1c for the trailing edge blowing rotor with (- -) and without (—) tip-weighted injection

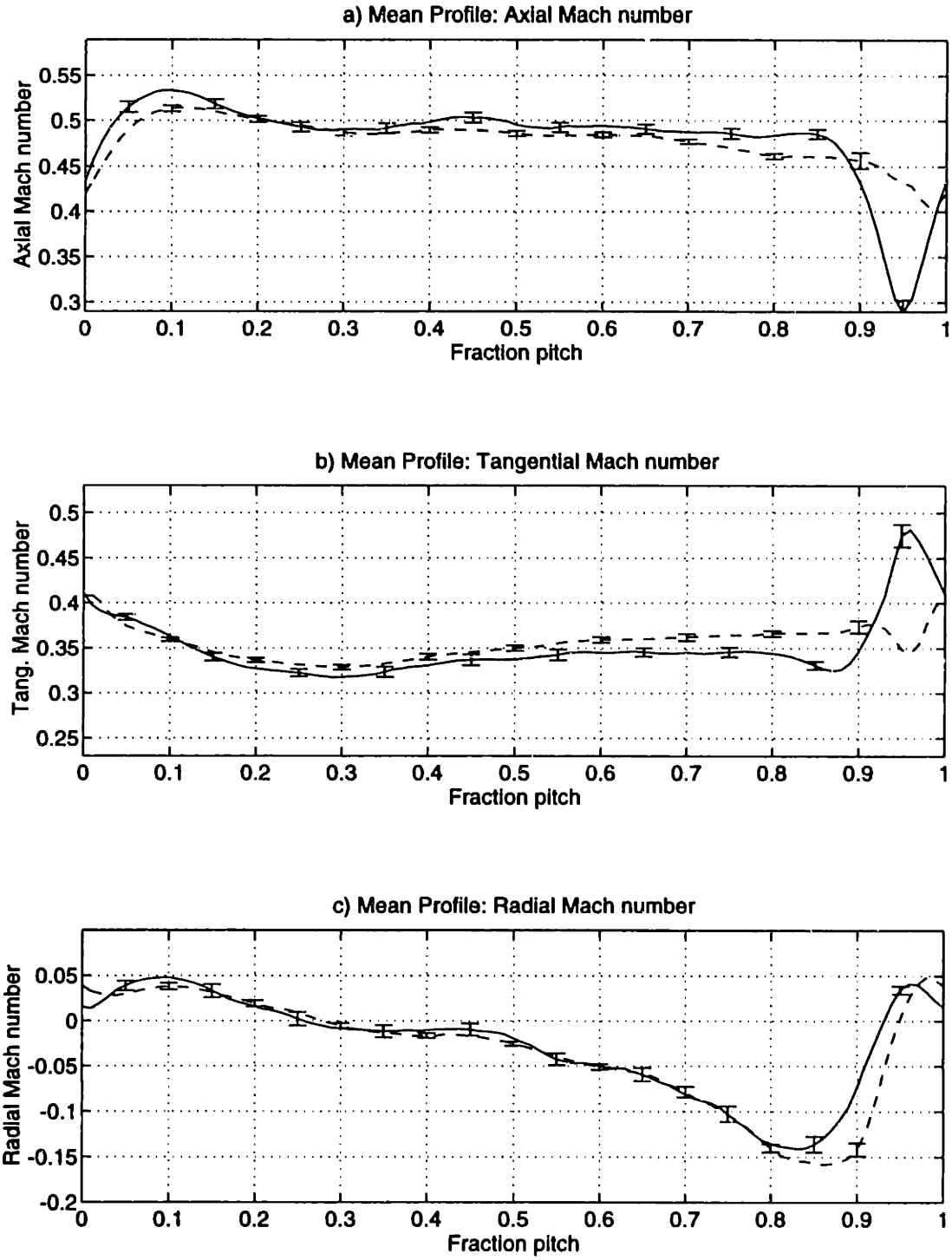

Figure 7-28: Ensemble-averaged profiles of axial, tangential, and radial Mach number at 50% span, 0.1c for the trailing edge blowing rotor with (- -) and without (—) tip-weighted injection

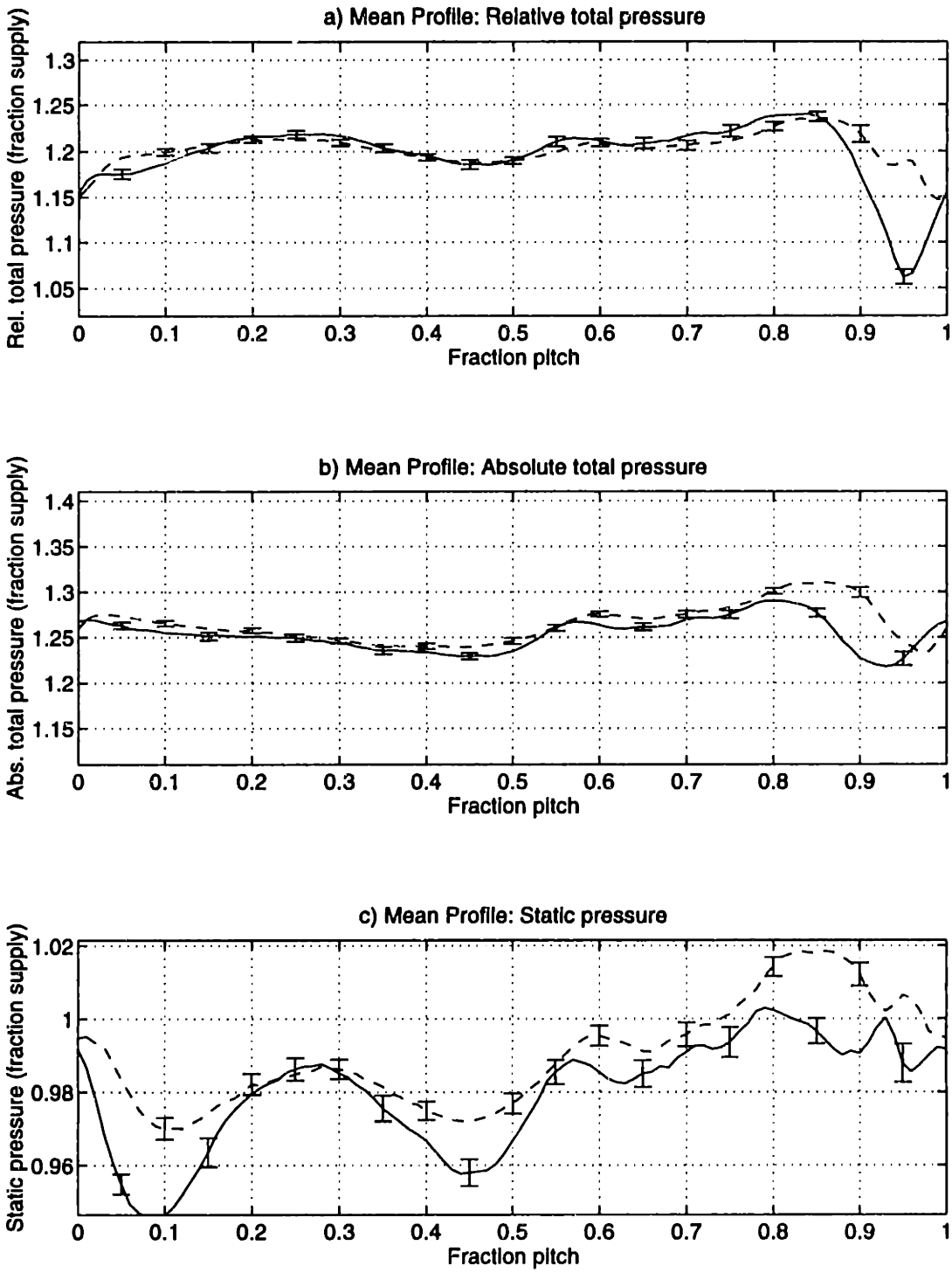

Figure 7-29: Ensemble-averaged profiles of relative and absolute total pressure and static pressure at 50% span, 0.1c for the trailing edge blowing rotor with (- -) and without (—) tip-weighted injection

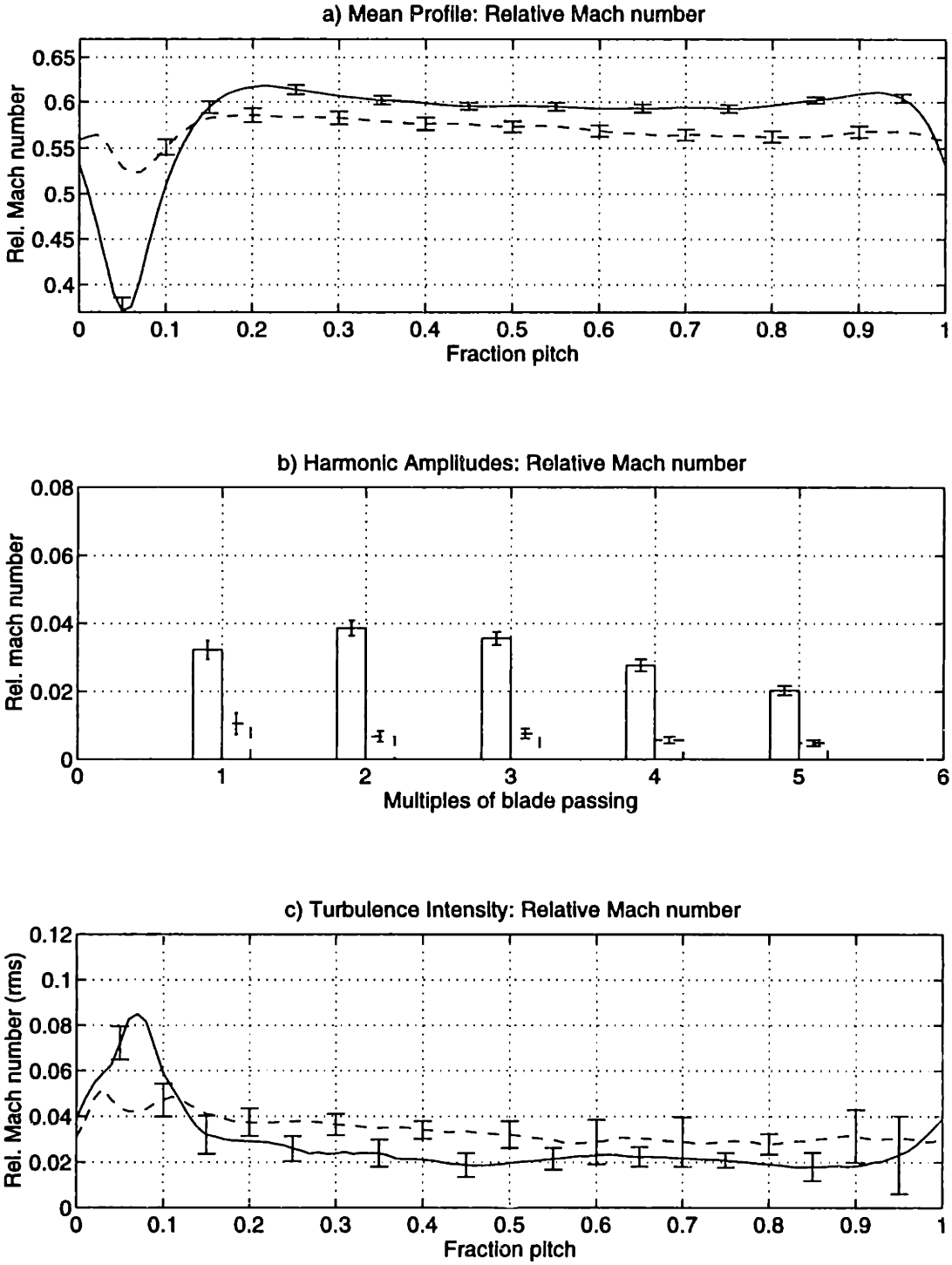

Figure 7-30: Relative Mach number ensemble-averaged profile, mean harmonic content, and turbulence profile at 75% span, 0.1c for the trailing edge blowing rotor with (- -) and without (—) tip-weighted injection

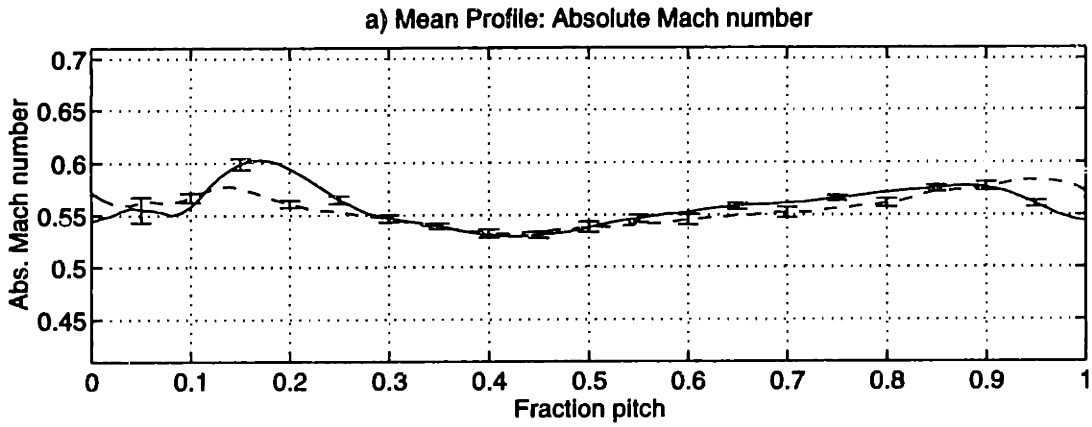

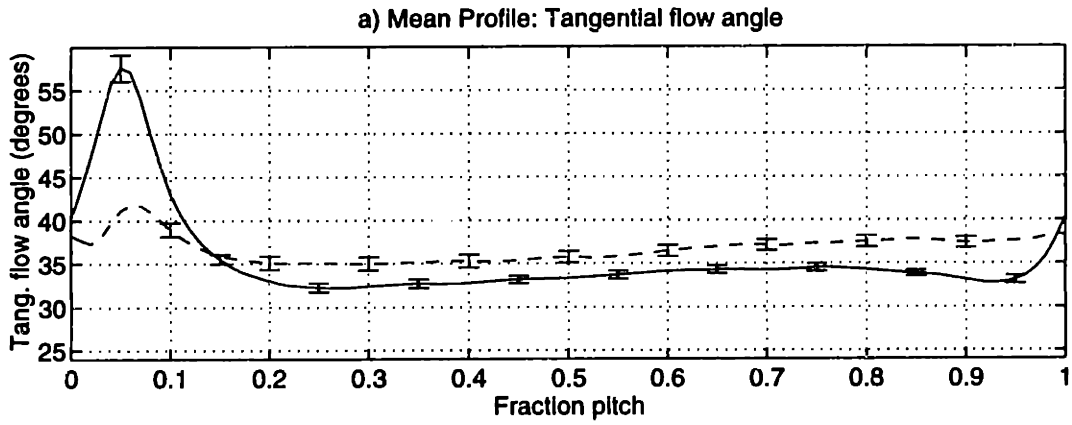

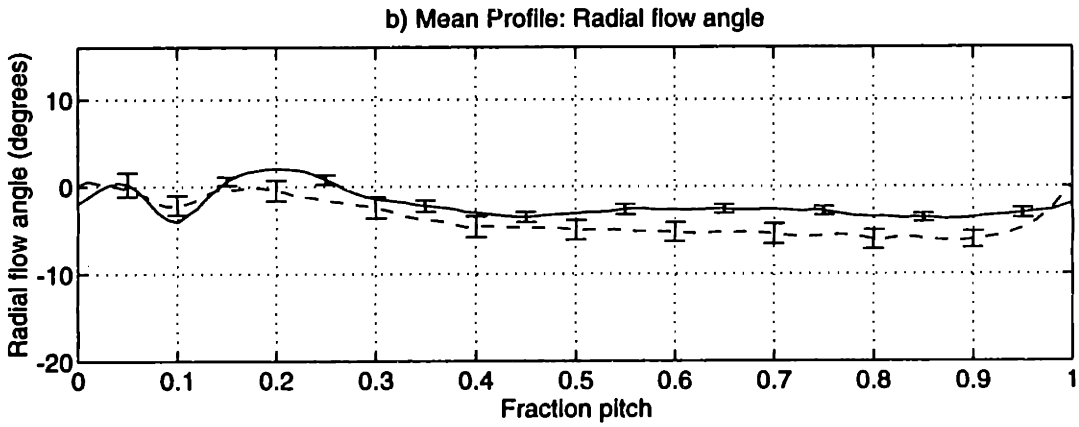

Figure 7-31: Ensemble-averaged profiles of absolute Mach number and tangential and radial flow angles at 75% span, 0.1c for the trailing edge blowing rotor with (- -) and without (—) tip-weighted injection

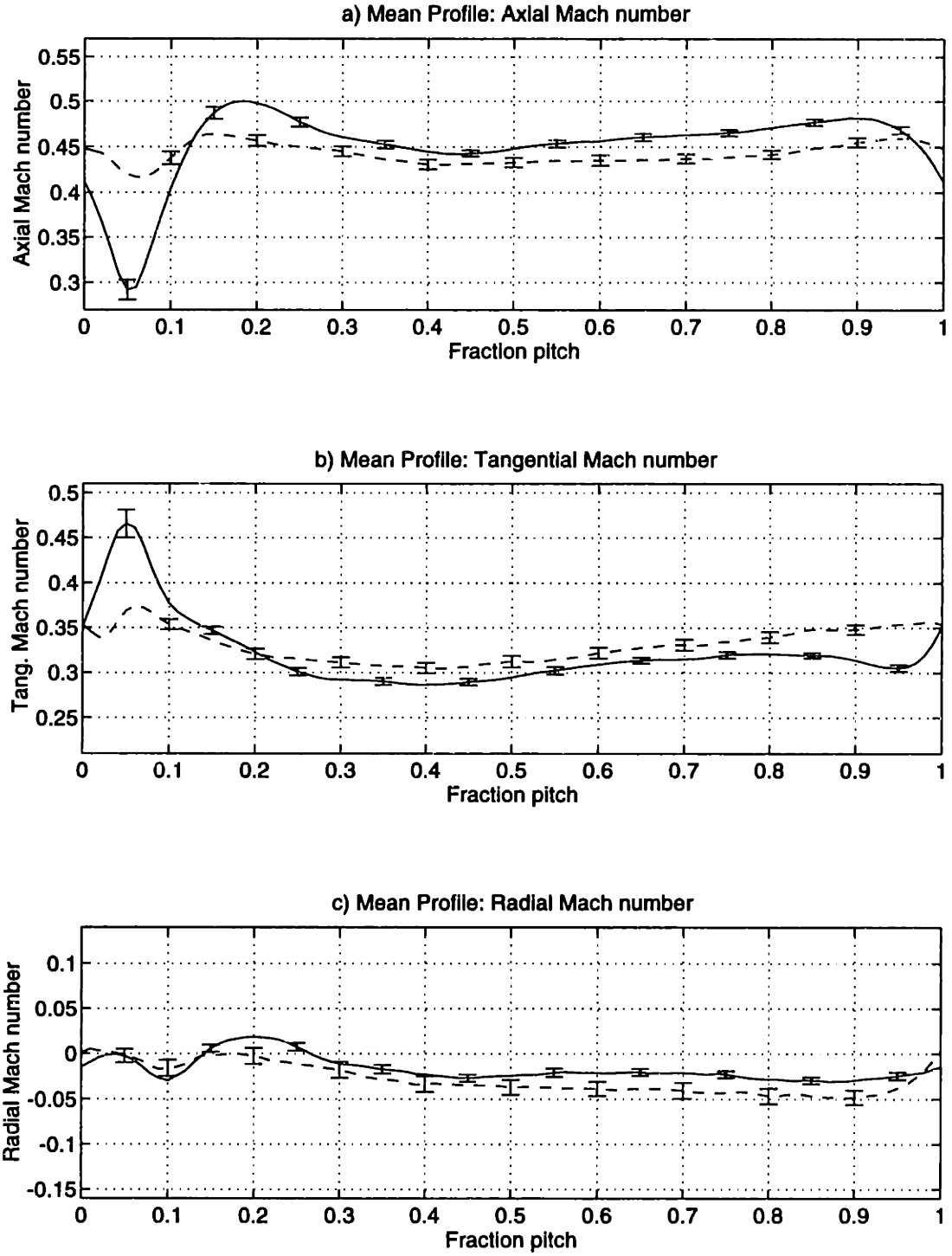

Figure 7-32: Ensemble-averaged profiles of axial, tangential, and radial Mach number at 75% span, 0.1c for the trailing edge blowing rotor with (- -) and without (—) tip-weighted injection

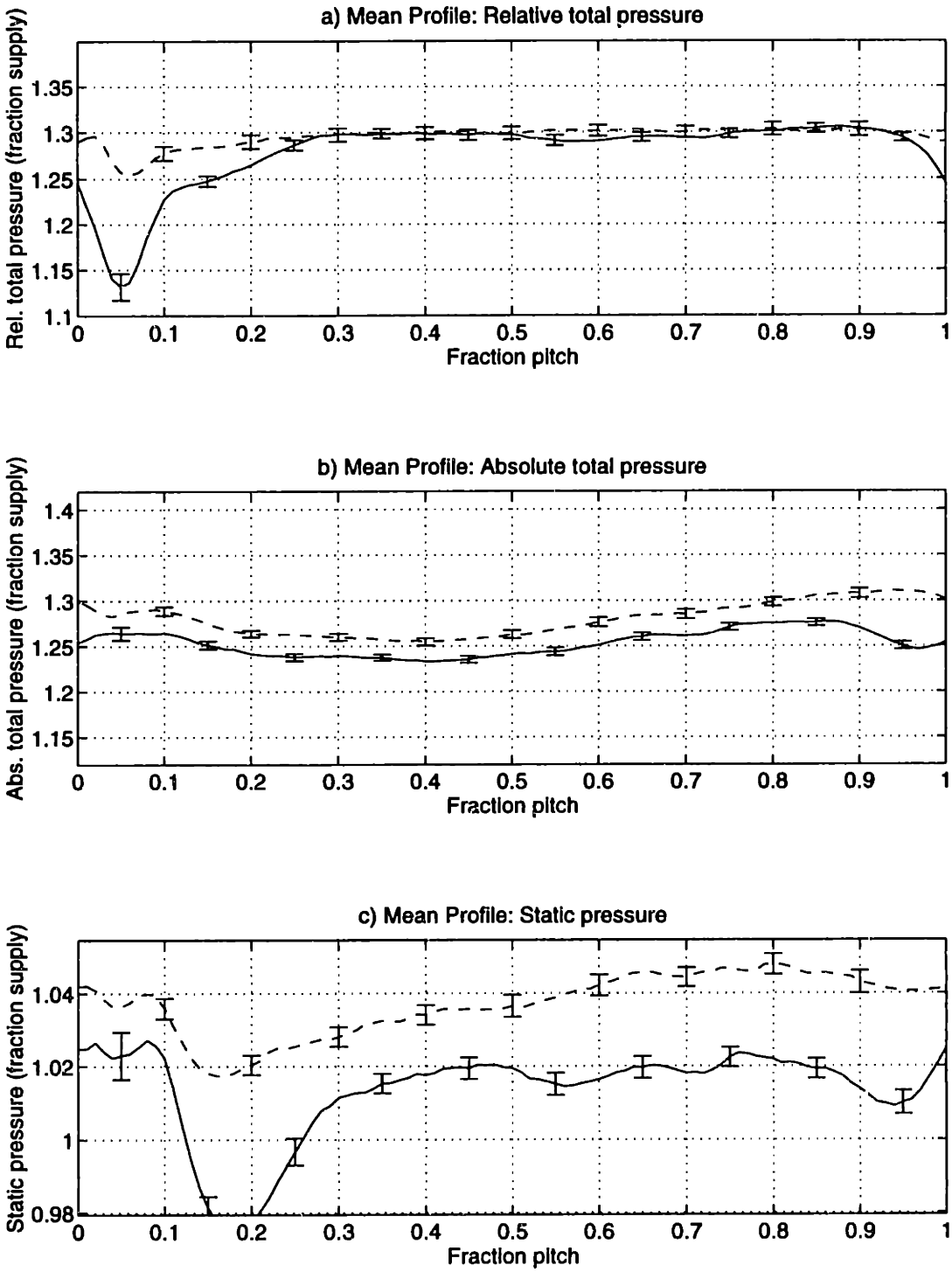

Figure 7-33: Ensemble-averaged profiles of relative and absolute total pressure and static pressure at 75% span, 0.1c for the trailing edge blowing rotor with (- -) and without (—) tip-weighted injection

T.e. blowing rotor (no injection)	BPF	2*BPF	3*BPF	4*BPF	5*BPF
25% span, 0.1c	.0528	.0388	.0319	.0210	.0149
50% span, 0.1c	.0383	.0336	.0339	.0264	.0217
75% span, 0.1c	.0322	.0386	.0356	.0277	.0203
87.5% span, 0.1c	.0245	.0259	.0155	.0077	.0035
T.e. blowing rotor (tip-weighted injection)	**BPF**	**2*BPF**	**3*BPF**	**4*BPF**	**5*BPF**
25% span, 0.1c	.0289	.0181	.0122	.0064	.0051
(fraction no inj. at 0.1c)	(0.55)	(0.47)	(0.38)	(0.31)	(0.34)
[fraction no inj. at 1.5c]	[0.75]	[1.53]	[19.1]	[5.22]	[4.81]
50% span, 0.1c	.0265	.0160	.0108	.0087	.0068
	(0.69)	(0.48)	(0.32)	(0.33)	(0.31)
	[1.29]	[1.70]	[1.90]	[3.66]	[5.37]
75% span, 0.1c	.0105	.0067	.0076	.0057	.0049
	(0.32)	**(0.17)**	**(0.21)**	**(0.21)**	**(0.24)**
	[0.54]	**[0.59]**	[1.33]	[2.58]	[6.94]
87.5% span, 0.1c	.0205	.0139	.0088	.0079	.0061
	(0.84)	(0.53)	(0.57)	(1.03)	(1.74)
	[0.67]	[2.15]	[4.24]	[6.82]	[5.83]

Table 7.2: Wake relative Mach number harmonic amplitudes at 0.1 chord for the trailing edge blowing rotor with and without tip-weighted injection (tip-weighted injection harmonic amplitudes also shown as fraction of no injection harmonic amplitudes at 0.1c ( ) and as fraction of no injection harmonic amplitudes at 1.5 chord [ ])

fraction pitch). The wake harmonics are reduced up to 4*BPF, and the peak relative Mach number turbulence intensity is reduced by approximately 45%.

Summary of tip-weighted injection: 0.1 chord wake measurements

There is rapid mixing between the injection jets and the wake, such that at 0.1 chord (axial distance) downstream of the rotor trailing edge, the wake profiles are already quite smooth. The relative Mach number wake mean profile harmonic amplitudes with and without injection are tabulated in Table 7.2 and are shown graphically versus span for the first four BPF harmonics in Figure 7-38. At 75% span, where the injection results in

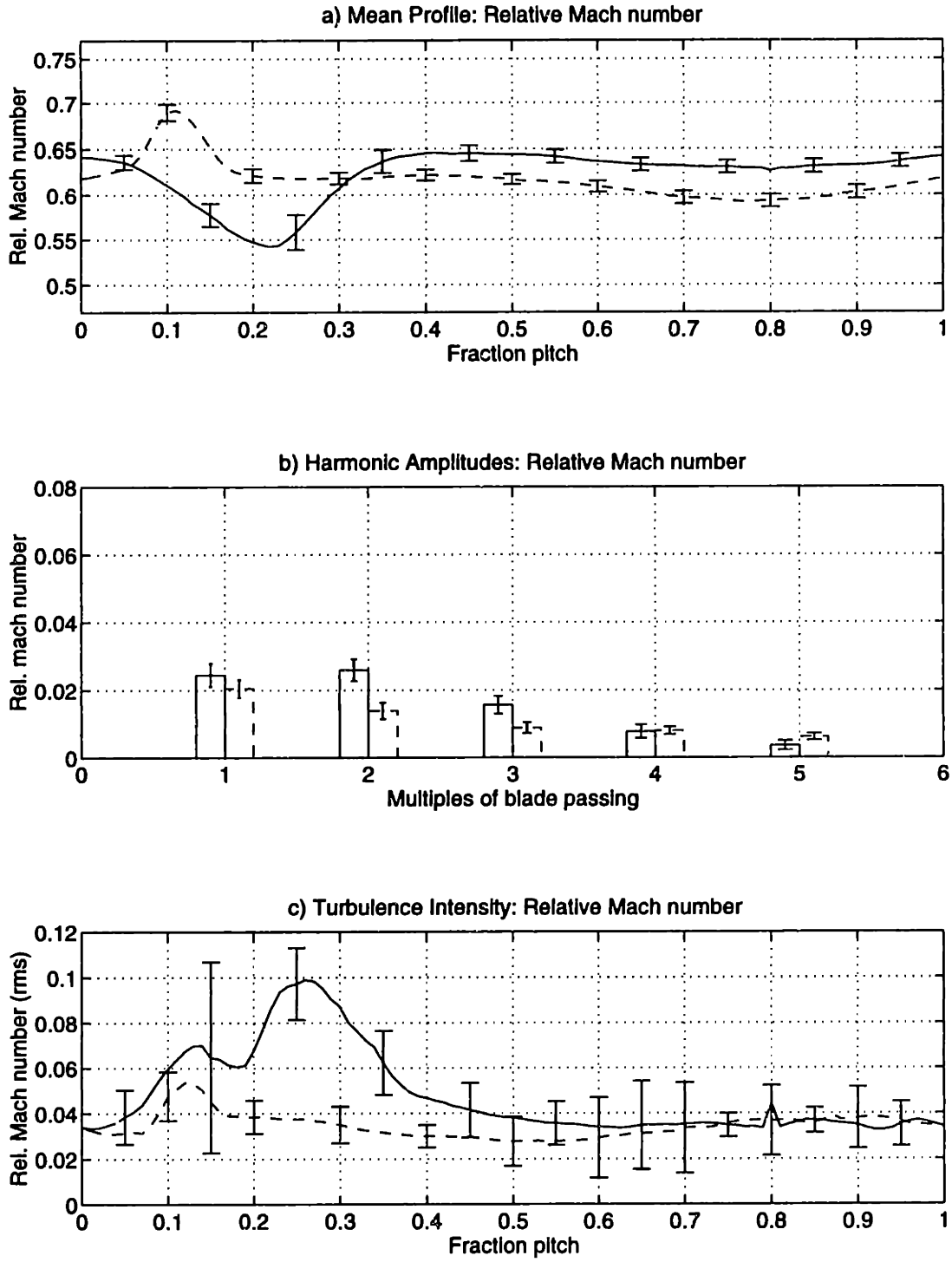

Figure 7-34: Relative Mach number ensemble-averaged profile, mean harmonic content, and turbulence profile at 87.5% span, 0.1c for the trailing edge blowing rotor with (- -) and without (—) tip-weighted injection

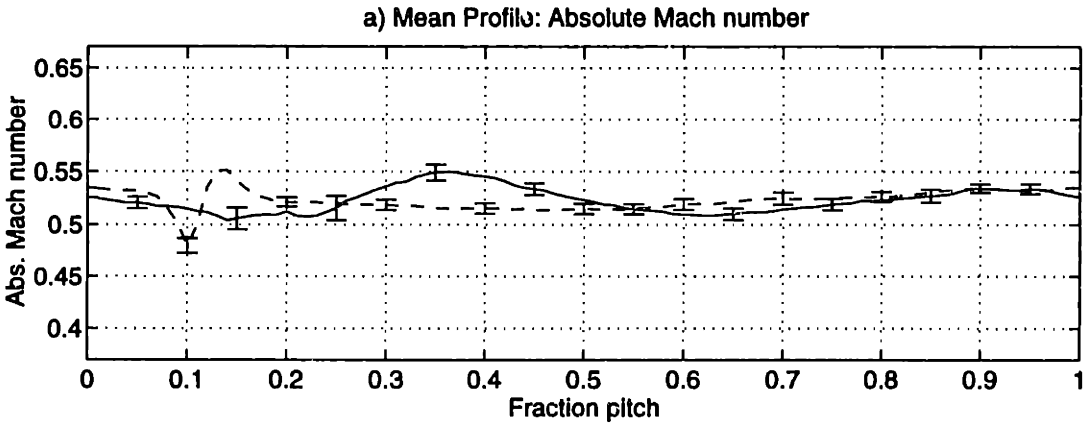

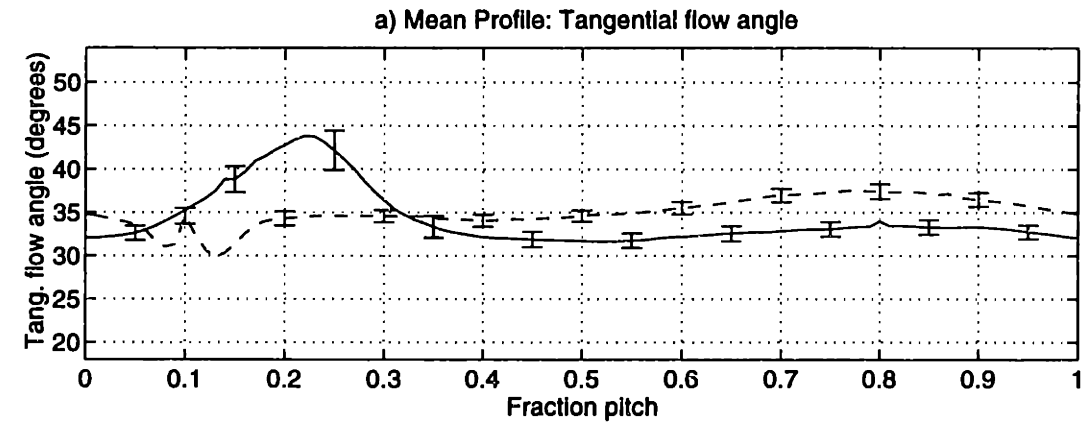

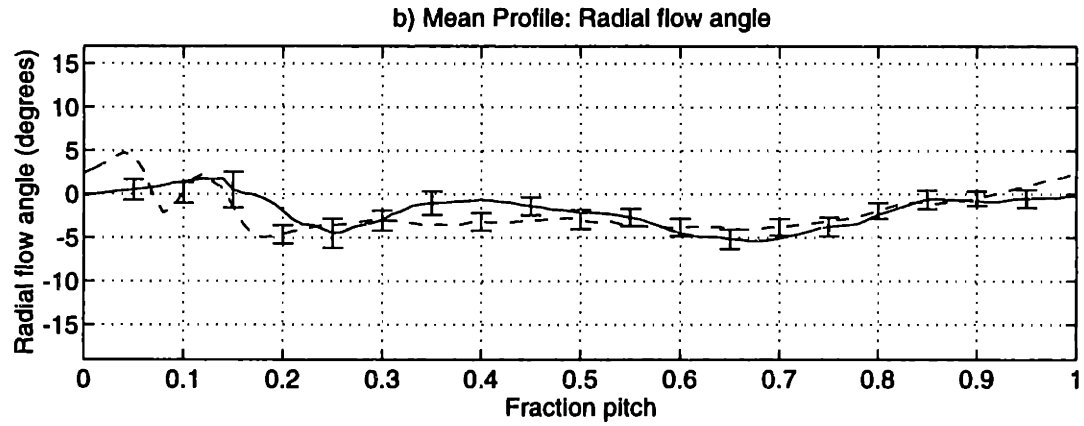

Figure 7-35: Ensemble-averaged profiles of absolute Mach number and tangential and radial flow angles at 87.5% span, 0.1c for the trailing edge blowing rotor with (- -) and without (—) tip-weighted injection

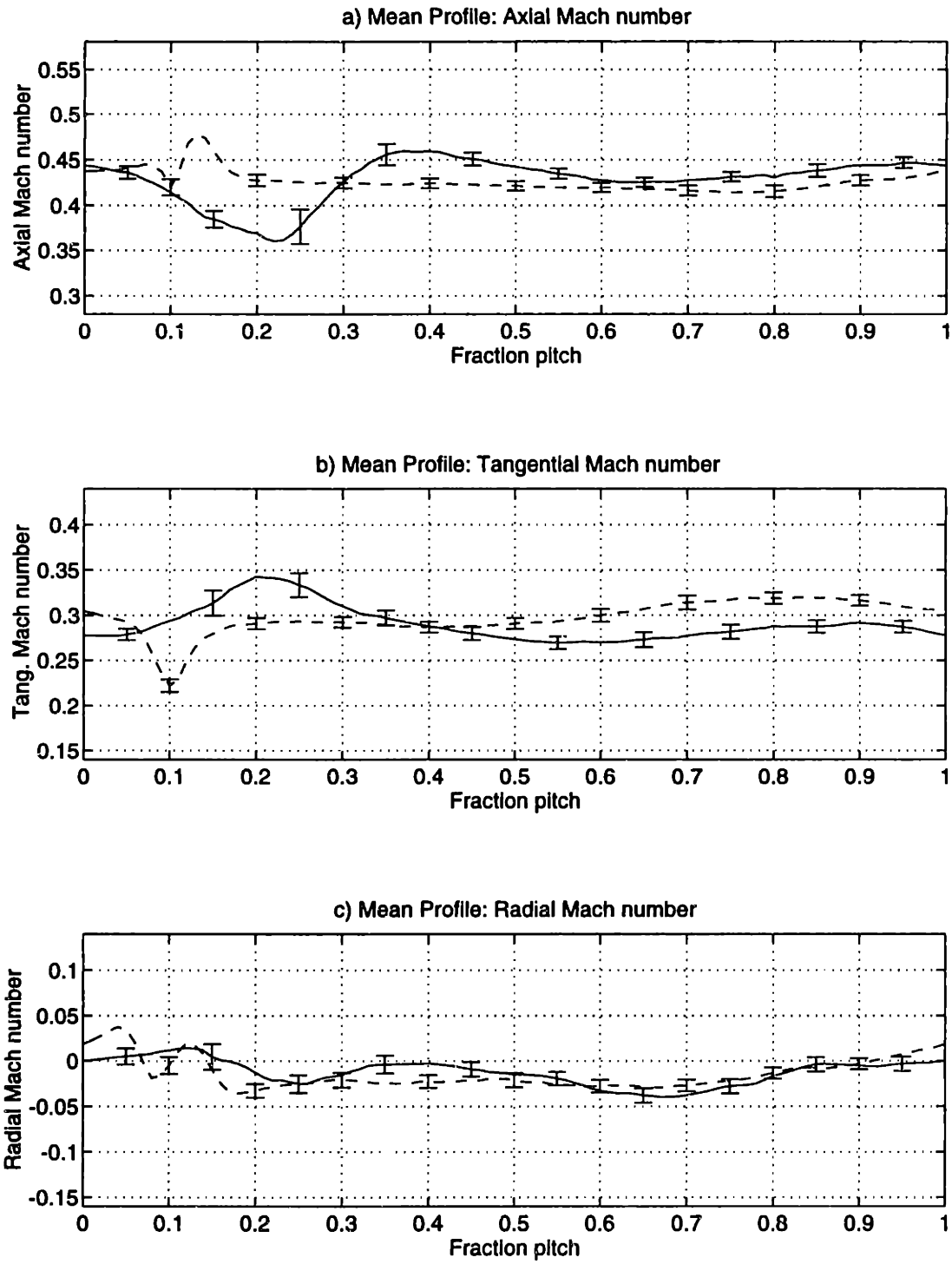

Figure 7-36: Ensemble-averaged profiles of axial, tangential, and radial Mach number at 87.5% span, 0.1c for the trailing edge blowing rotor with (- -) and without (—) tip-weighted injection

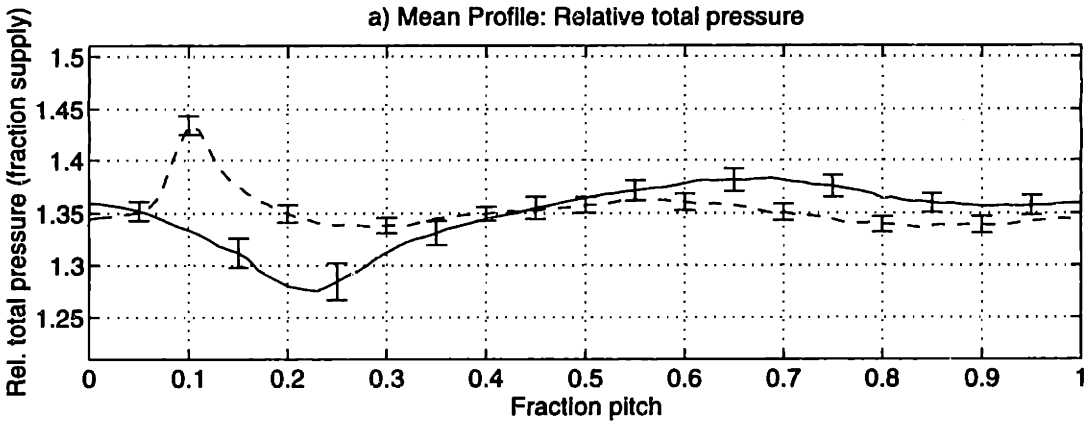

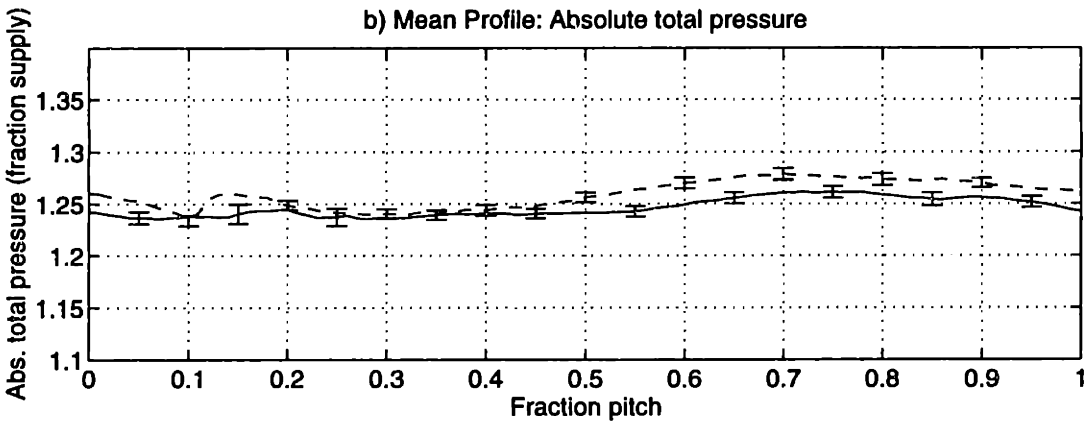

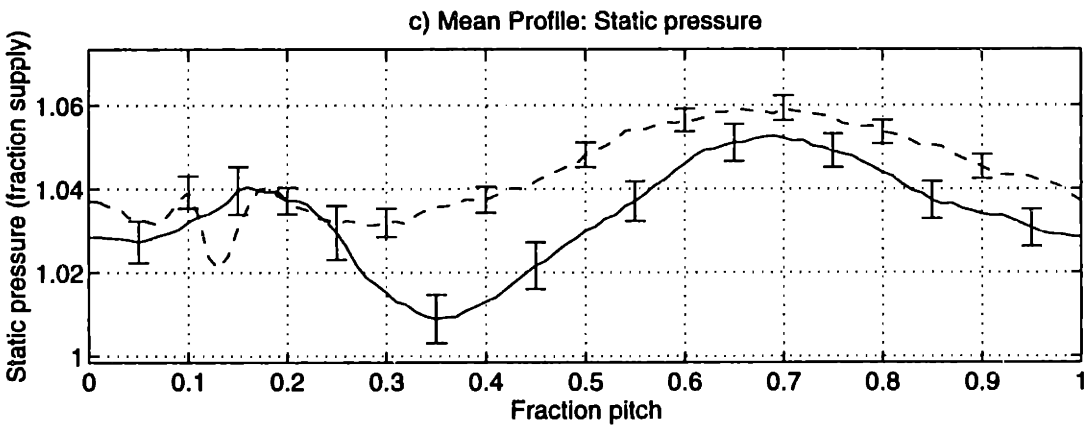

Figure 7-37: Ensemble-averaged profiles of relative and absolute total pressure and static pressure at 87.5% span, 0.1c for the trailing edge blowing rotor with (- -) and without (—) tip-weighted injection

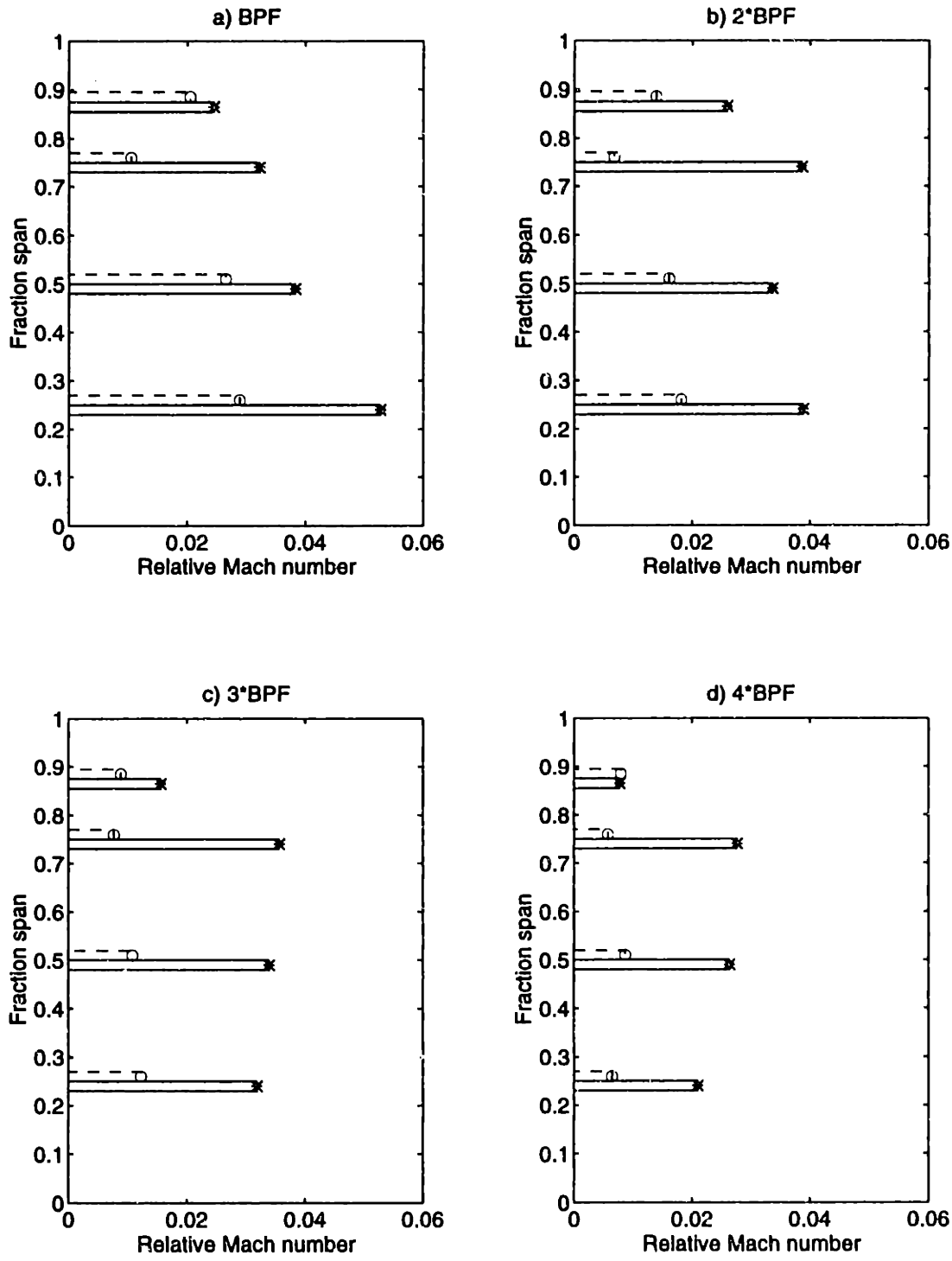

Figure 7-38: Wake relative Mach number harmonic amplitudes at 0.1 chord versus span: no injection (—) and 1.9% tip-weighted injection (- -)

nearly a momentumless wake, the BPF and 2*BPF harmonic amplitudes at 0.1 chord with injection are 46% and 41% smaller, respectively, than the harmonic amplitudes at 1.5 chord with no injection. In many of the preliminary studies on trailing edge blowing discussed in Chapter 1, small high velocity jets were used for injection. These narrow jets resulted in a 'jet/wake' combination that persisted far downstream. By opening the injection slot from the deviation angle position to the trailing edge (creating a scalloped suction surface), the injection has resulted in a wide low velocity jet and quicker mixing.

The important conclusion from this rapid mixing is that the wake harmonic amplitudes at 0.1 chord with tip-weighted injection are close to and often smaller than the wake harmonic amplitudes at 1.5 chord without injection. If the injection distribution is adjusted to achieve a momentumless wake along the entire span, similar harmonic amplitude reduction to that observed at 75% span (with tip-weighted injection) should be attainable in the entire flow field. This result offers the opportunity to significantly reduce the rotor/stator spacing and not increase the radiated acoustics. Of course, the wake phases must be taken into account when considering such design modifications, as well as effects due to the rotor potential field.

In addition to reductions in the mean wake harmonics, the turbulence intensity with injection is reduced at 0.1 chord relative to no injection. The injection jets introduce additional turbulence into the flow field, but the smoothing of the mean wake profile reduces the generation mechanism of turbulence downstream of the blade trailing edge. The injection of fluid may also partially control unsteady oscillations in the suction surface boundary layer near the trailing edge, where the boundary layer is separated, or close to separation.

7.3.2 Flow field measurements at 1.5 chord

In addition to the measurements at 0.1 chord, measurements were taken at 1.5 chords downstream, just in front of the stator row, for the tip-weighted injection distribution. The flow field at 1.5 chord is that incident to the stator row, and thus it is the most relevant for rotor wake/stator interaction. Two runs were performed at each test condition, each consisting of six revolutions of data (96 blade passing periods). The two data sets were then averaged together and plotted versus the data without injection for comparison. The

no injection data is shown as solid lines and the injection data is shown as dashed lines.

25% span, 1.5 chord

The results of the measurements at 25% span, 1.5 chords downstream of the rotor are shown in Figures 7-39 through 7-42. Figure 7-39a shows the ensemble-averaged relative Mach number mean profile, with the harmonic content of the mean profile shown in Figure 7-39b. With the injection mass flow rate adjusted to achieve a momentumless wake at approximately 80% span, the resulting decrease in the wake profiles at 25% span are fairly small. The relative Mach number BPF harmonic is reduced approximately 25%, and the higher harmonics are virtually unchanged. Similarly, the turbulence intensity in Figure 7-39c is not significantly reduced. The decrease in the average relative Mach number is believed to be caused by the increase in overall mass flow through the choke plate and flow redistribution downstream of the rotor.

Comparing the Mach number profiles at 0.1 and 1.5 chord, the flow at 25% span is seen to diffuse significantly between the rotor and stator. Without injection, the average axial Mach number decreases by approximately 13% from the rotor trailing edge (0.1c) to just in front of the stator row (1.5c). This expansion is due primarily to the hub contour and was confirmed with results from streamline curvature calculations. In fact, the calculations showed that the flow measured at 25% span, 1.5 chord corresponds to the flow leaving the rotor trailing edge at approximately 19% span. Since the amount of injection decreases rapidly toward the hub, it is not surprising that the wake measured at 25% span, 1.5 chord has only moderate smoothing.

With injection, the decrease in average axial Mach number from the rotor exit to the stator is even larger than without injection. The average axial Mach number at 0.1 chord with injection is 2.3% lower than without injection and is 4.1% lower at 1.5 chord. This result indicates that the large injection rates in the outer one-half span region energizes the flow forcing the hub to expand even more than without injection. The expansion of the flow causes an increase in the wake momentum deficit as it is convected from 0.1 to 1.5 chord. The mass average axial Mach number at a given position downstream of the rotor should be roughly equal with and without injection due to the downstream choke plate.

The changes in the absolute Mach number, flow angles, and Mach number components due to injection can be seen in Figures 7-40 and 7-41. With a decrease in the inlet axial Mach number, the loading will be slightly higher, resulting in a slight increase in the exit tangential Mach number and flow angle. This is indeed the result with injection. The total pressure (relative and absolute) and static pressure can be seen in Figure 7-42, where a slight decrease in the total pressures and an increase of about 0.7% in the static pressure is observed with injection.

50% span, 1.5 chord

The comparison of downstream flow field variables with and without blowing at 50% span, 1.5 chords is shown in Figures 7-43 through 7-46. Again, the axial Mach number is lower with injection at this location, resulting in a lower relative Mach number and higher flow angle. The wake momentum deficit is about 40% filled at this spanwise location, resulting in wake harmonic reductions of approximately 30% for BPF, 50% for 2 and 3*BPF, etc. Since the higher harmonics are generally within the amplitude of random flow unsteadiness, reductions are not strictly discernible within the 95% confidence intervals. While the mean wake harmonics are reduced, the turbulence intensity is not significantly changed. The total pressure ratio is reduced by approximately 1% with injection.

With the diffusion of the hub flow, the rest of the flow is accelerated since the flow area remains constant within 0.3% from the rotor trailing edge to 1.5 chord. The average axial Mach number at 50% span increases by approximately 4% from 0.1 to 1.5 chord without injection and 1.5% with injection.

75% span, 1.5 chord

At 75% span the wake is mostly filled with injection, resulting in reductions in the relative Mach number harmonics of approximately 68% for BPF, 80% for 2*BPF, and 45% for 3*BPF. These reductions and the other flow variables can be seen in Figures 7-47 through 7-50. The turbulence intensity in Figure 7-47c is reduced down to the no injection freestream value, a reduction of approximately 24% in the peak intensity. At 75% span, the total pressure rise is increased due to injection by about 2%, and the static pressure is increased

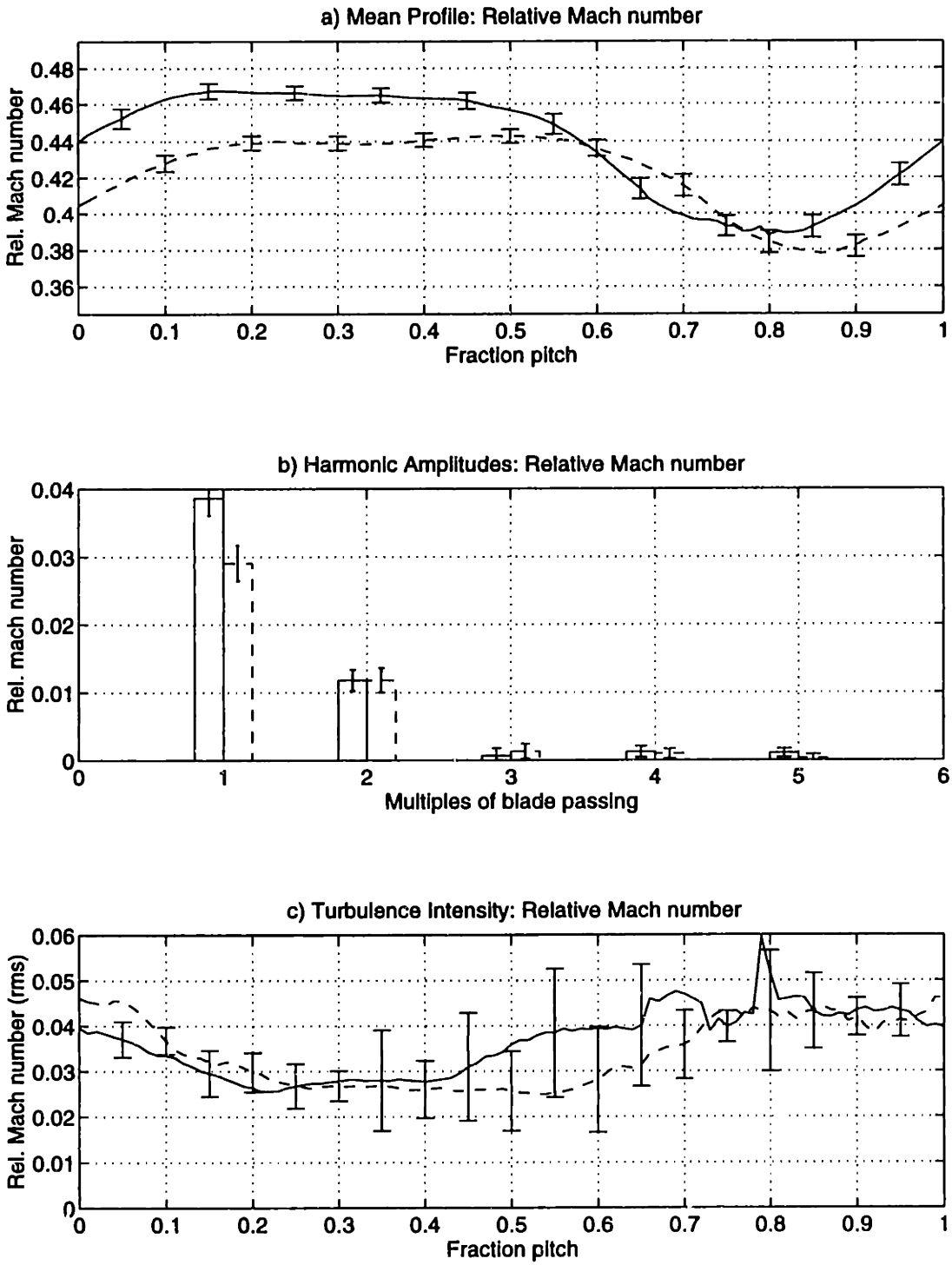

Figure 7-39: Relative Mach number ensemble-averaged profile, mean harmonic content, and turbulence profile at 25% span, 1.5c for the trailing edge blowing rotor with (- -) and without (—) tip-weighted injection

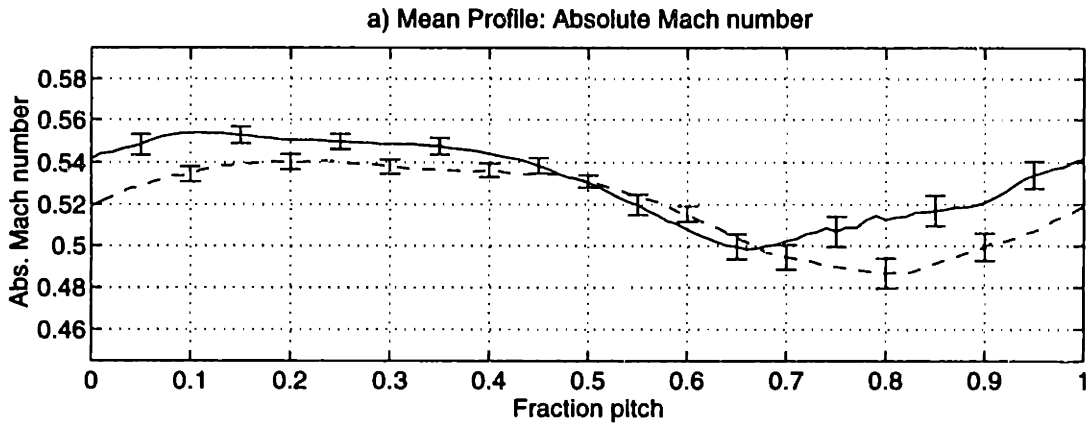

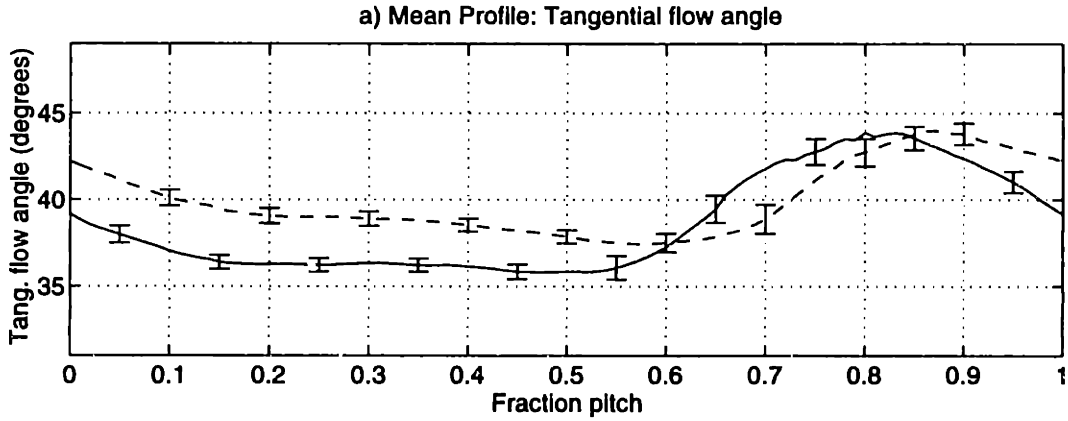

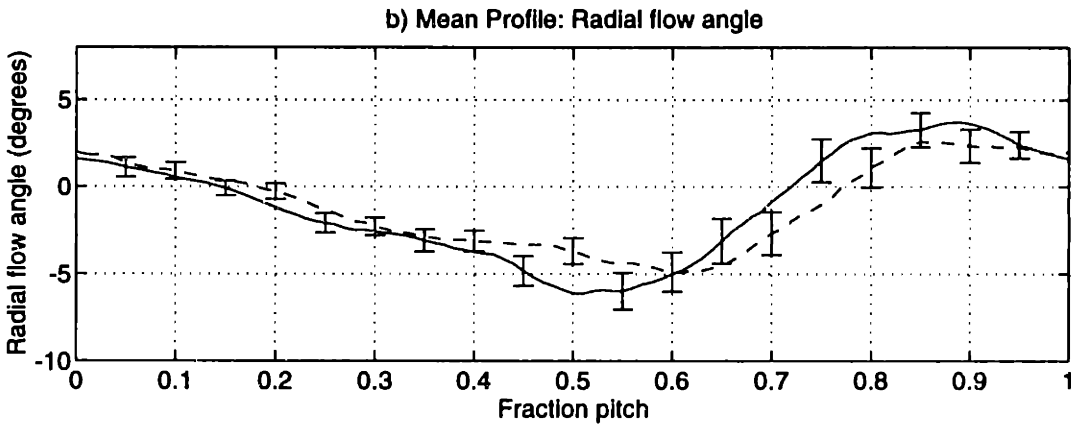

Figure 7-40: Ensemble-averaged profiles of absolute Mach number and tangential and radial flow angles at 25% cpan, 1.5c for the trailing edge blowing rotor with (- -) and without (—) tip-weighted injection

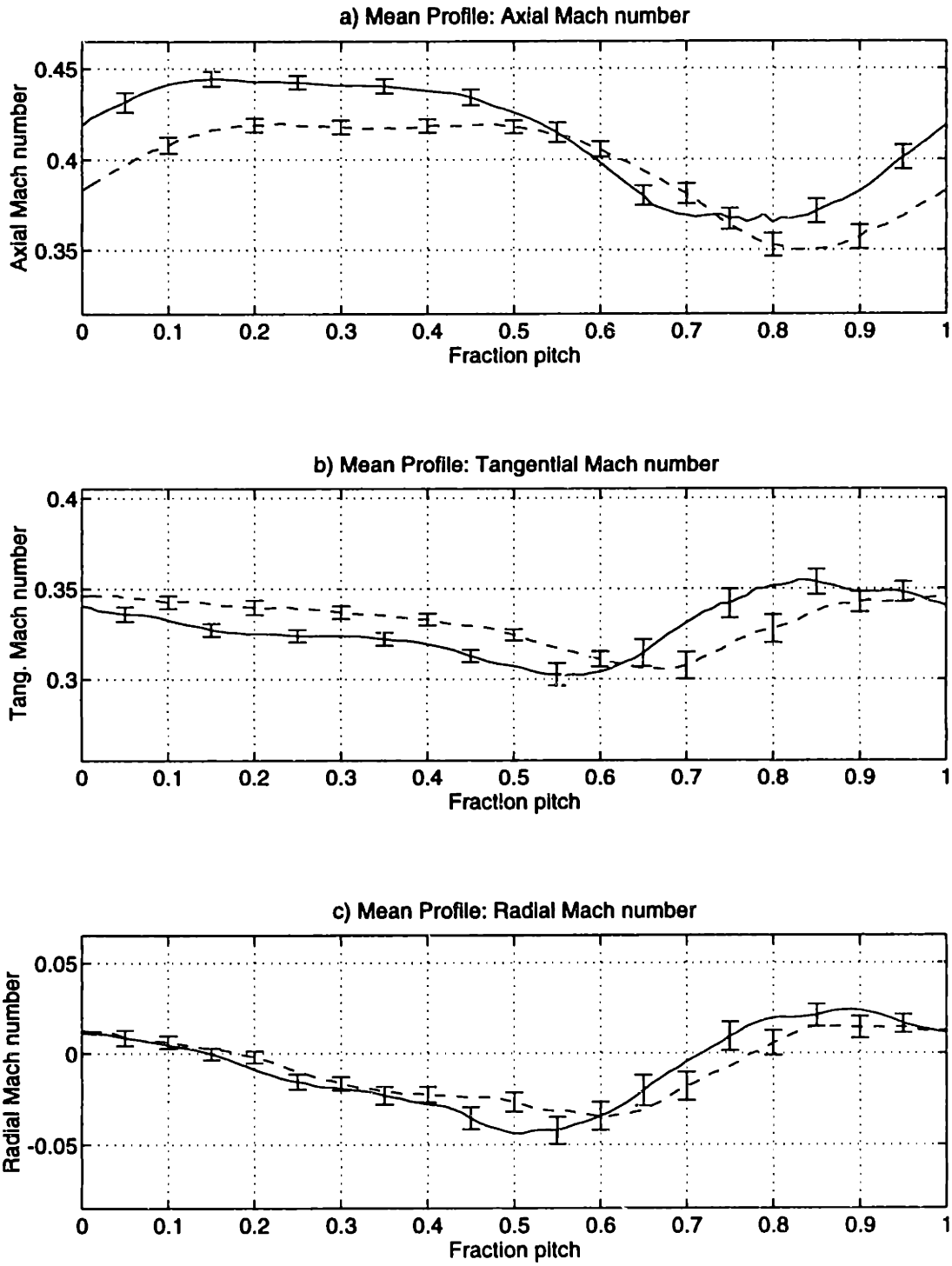

Figure 7-41: Ensemble-averaged profiles of axial, tangential, and radial Mach number at 25% span, 1.5c for the trailing edge blowing rotor with (- -) and without (—) tip-weighted injection

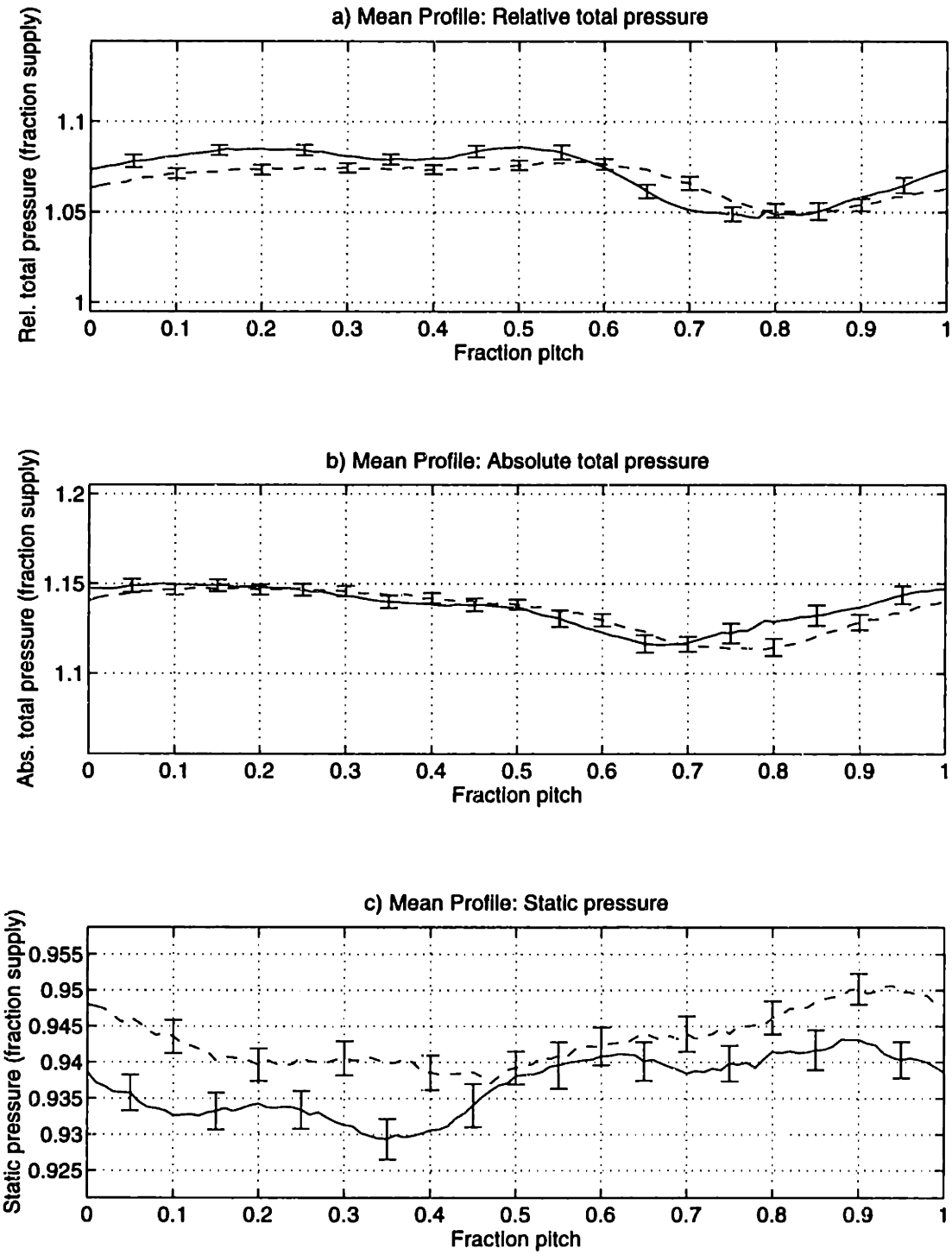

Figure 7-42: Ensemble-averaged profiles of relative and absolute total pressure and static pressure at 25% span, 1.5c for the trailing edge blowing rotor with (- -) and without (—) tip-weighted injection

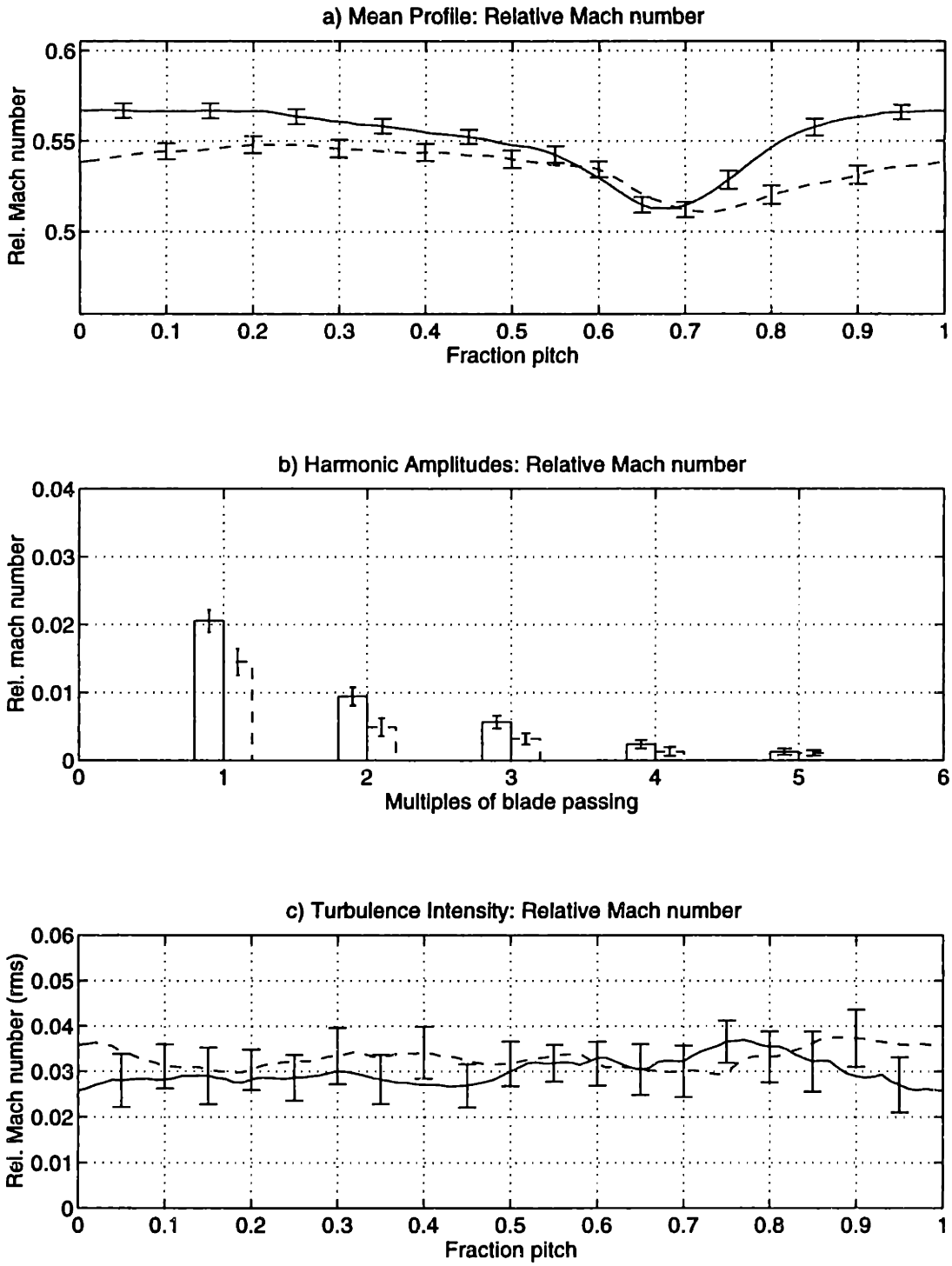

Figure 7-43: Relative Mach number ensemble-averaged profile, mean harmonic content, and turbulence profile at 50% span, 1.5c for the trailing edge blowing rotor with (- -) and without (—) tip-weighted injection

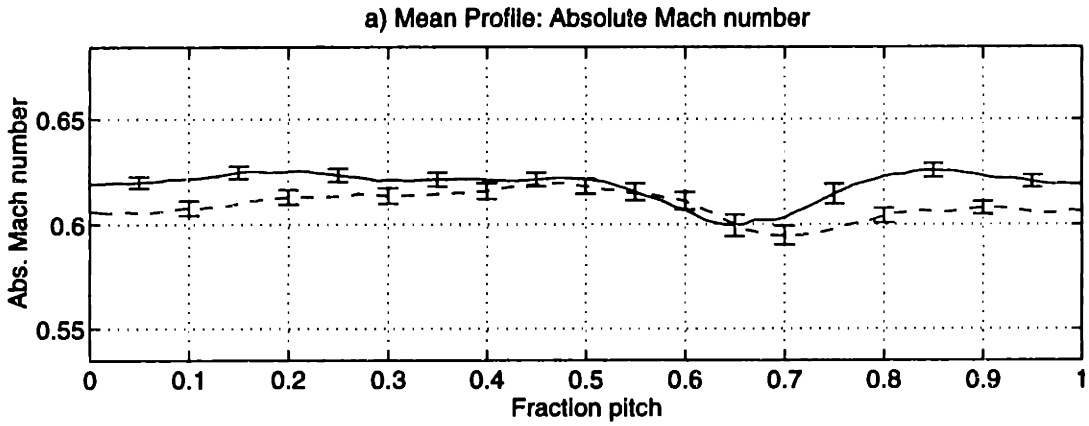

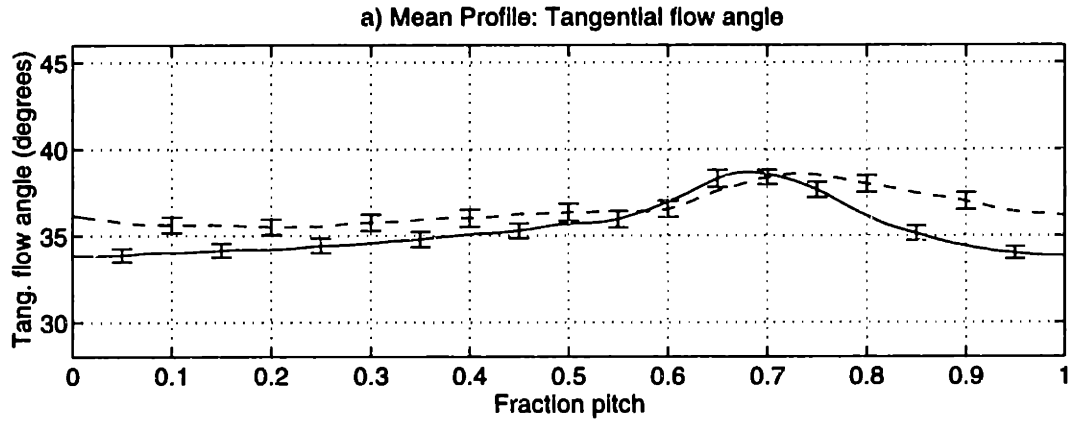

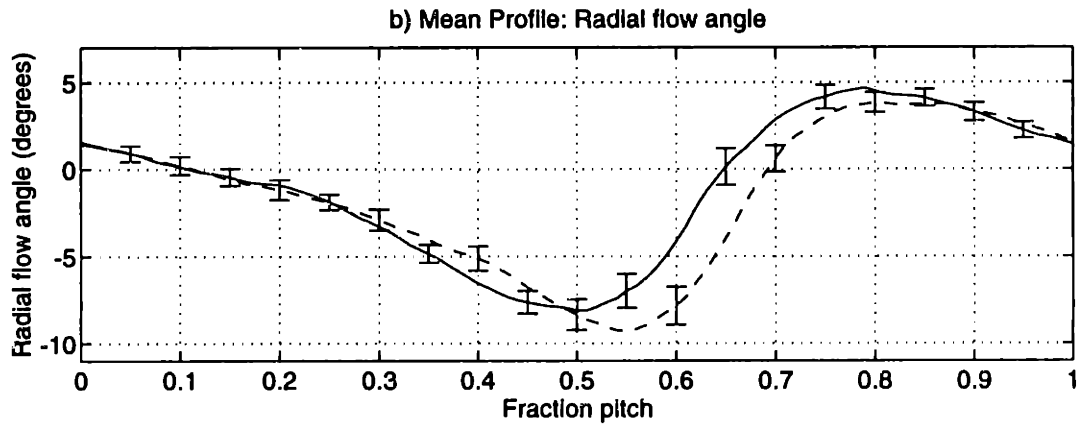

Figure 7-44: Ensemble-averaged profiles of absolute Mach number and tangential and radial flow angles at 50% span, 1.5c for the trailing edge blowing rotor with (- -) and without (—) tip-weighted injection

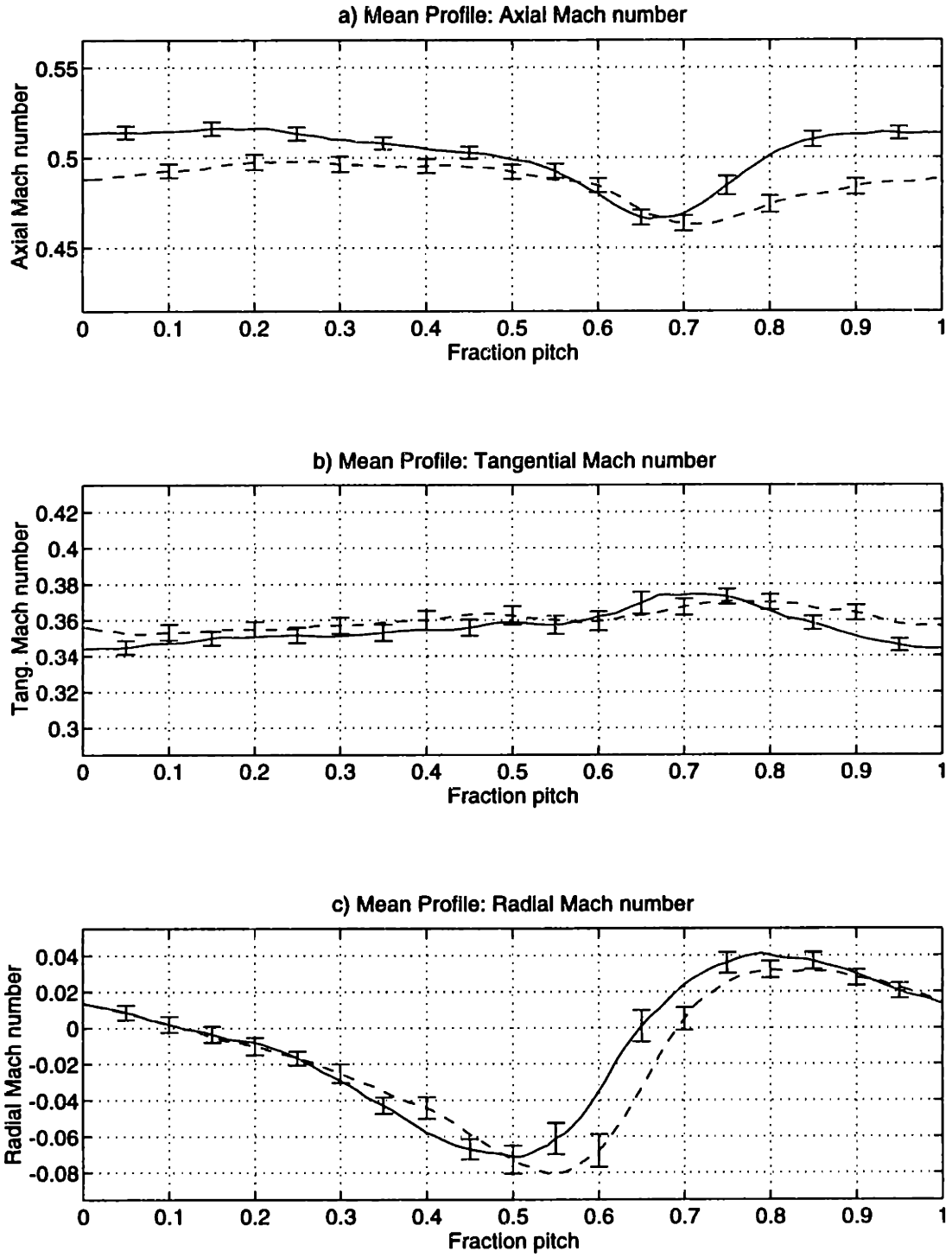

Figure 7-45: Ensemble-averaged profiles of axial, tangential, and radial Mach number at 50% span, 1.5c for the trailing edge blowing rotor with (- -) and without (—) tip-weighted injection

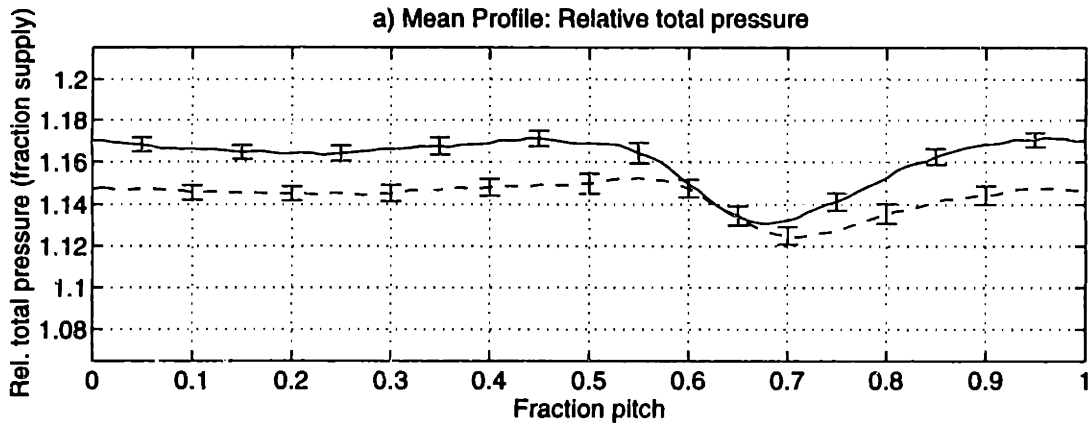

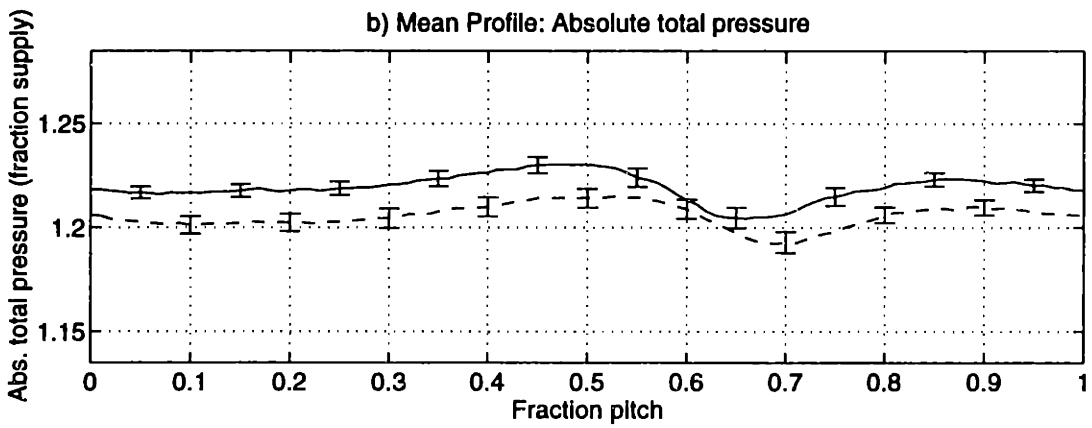

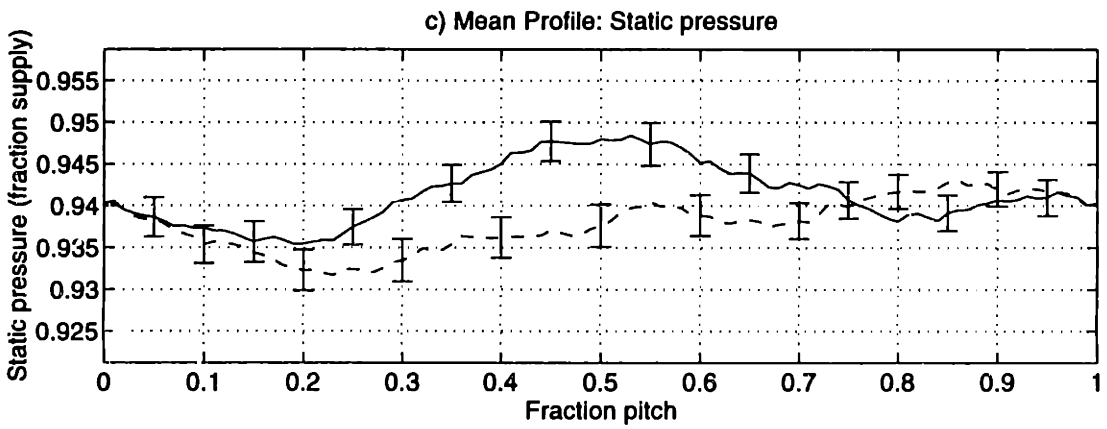

Figure 7-46: Ensemble-averaged profiles of relative and absolute total pressure and static pressure at 50% span, 1.5c for the trailing edge blowing rotor with (- -) and without (—) tip-weighted injection

by about 1%. In addition, the variation in absolute Mach number and tangential flow angle has been reduced by about 50% with injection.

87.5% span, 1.5 chord

The flow field at 87.5% span with blowing is seen to be significantly smoothed relative to the no injection configuration in Figures 7-51 through 7-54. The mean values of nearly all the flow variables are within two percent for the two cases, and the pitchwise variations due to the wake are smaller (with injection) by about 80% (except for the radial flow component). Since the wake is highly skewed in the outer span region, the wake is mostly composed of BPF at 87.5% span. Thus, the higher wake harmonics are not greatly reduced by the injection, but the BPF harmonic is reduced by approximately 80%. The total pressure rise is also increased with injection by about 2%. The average axial Mach number at 87.5% span is accelerated approximately 7% without injection from 0.1 to 1.5 chord and about 10% with injection.

Wake Harmonic Phases: 1.5 chord

In addition to the wake harmonic amplitudes, the phase of the harmonics is also very important to the acoustic mode coupling. The phase of the first four relative Mach number BPF harmonics are plotted in Figure 7-55 for the trailing edge blowing rotor with and without tip-weighted injection. It is quite clear from the plots that the phases change significantly with injection. For example, the 2*BPF harmonic has approximately 330 degrees of phase variation from 50 to 87.5% span with no injection, but only about 80 degrees of phase variation with injection (with a possible multiple of 360 degrees). This is crucial in determining the dominant radial modes. With large phase variations, as is the case without injection, the dominant coupling is to the higher radial modes that have similar phase variations to the wake and stator unsteady pressure field. This usually results in fairly low radiated noise levels since only the first few radial modes typically propagate. However, if the wake phase variations are reduced with injection, the dominant coupling may be with the low order radial modes that propagate. Thus, even if the harmonic amplitudes are reduced significantly, the propagating radial acoustic modes may be even larger than

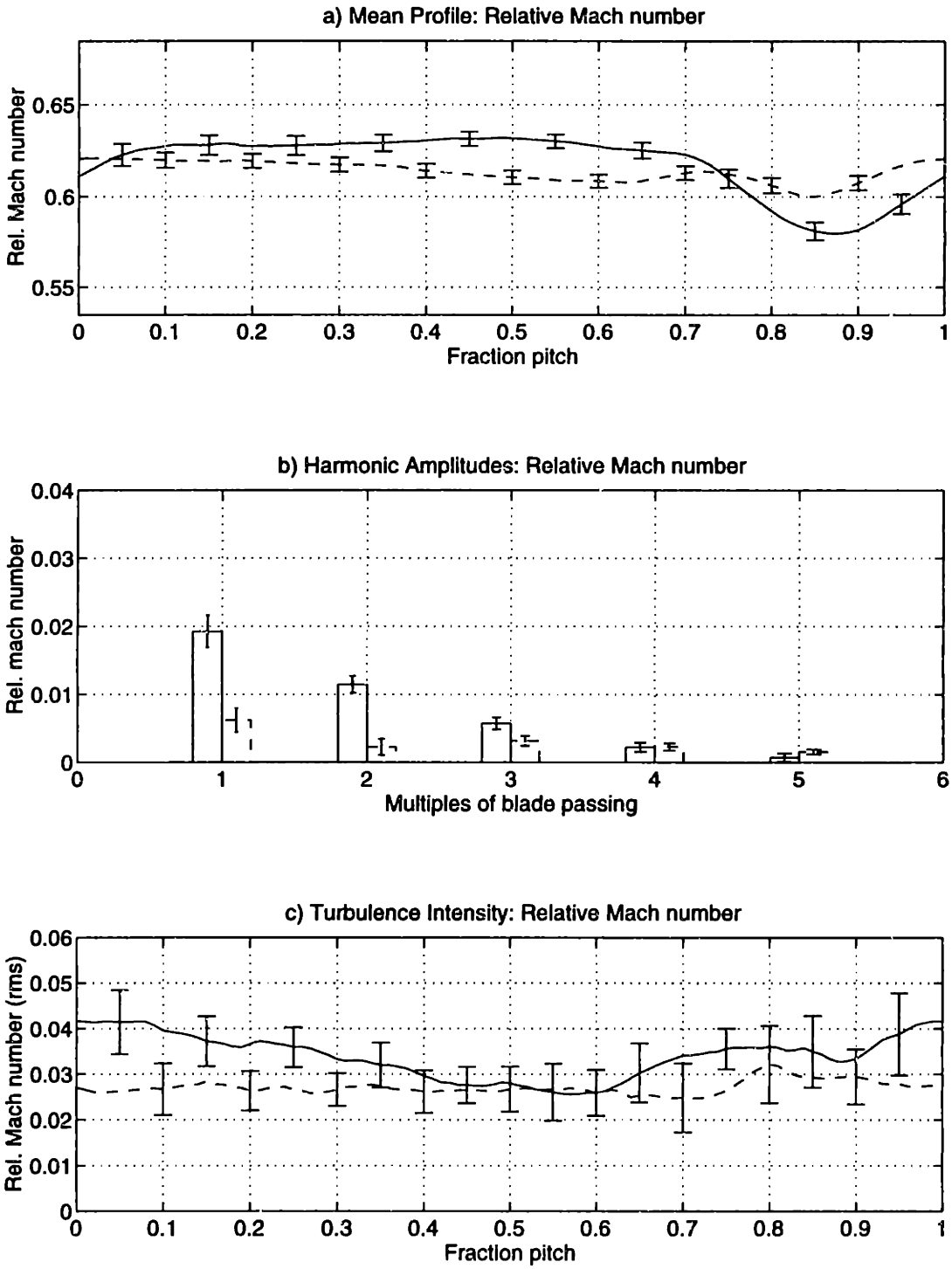

Figure 7-47: Relative Mach number ensemble-averaged profile, mean harmonic content, and turbulence profile at 75% span, 1.5c for the trailing edge blowing rotor with (- -) and without (—) tip-weighted injection

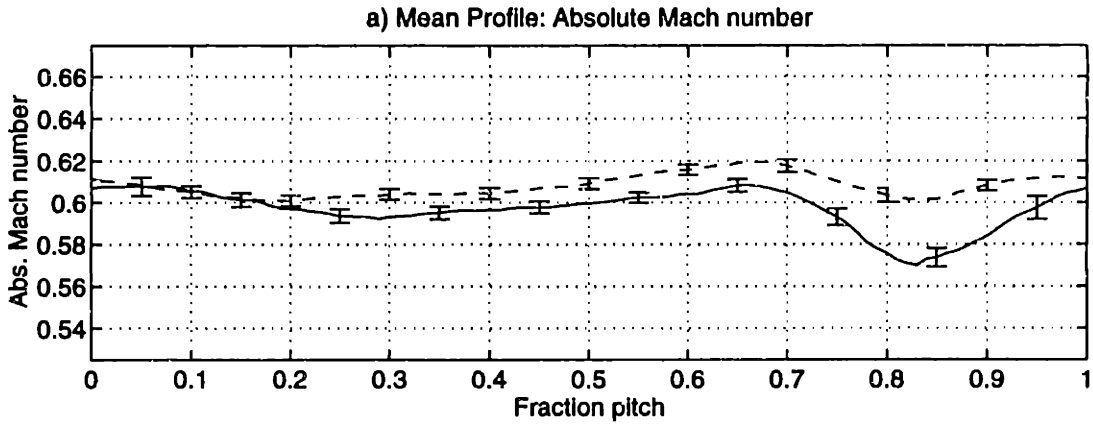

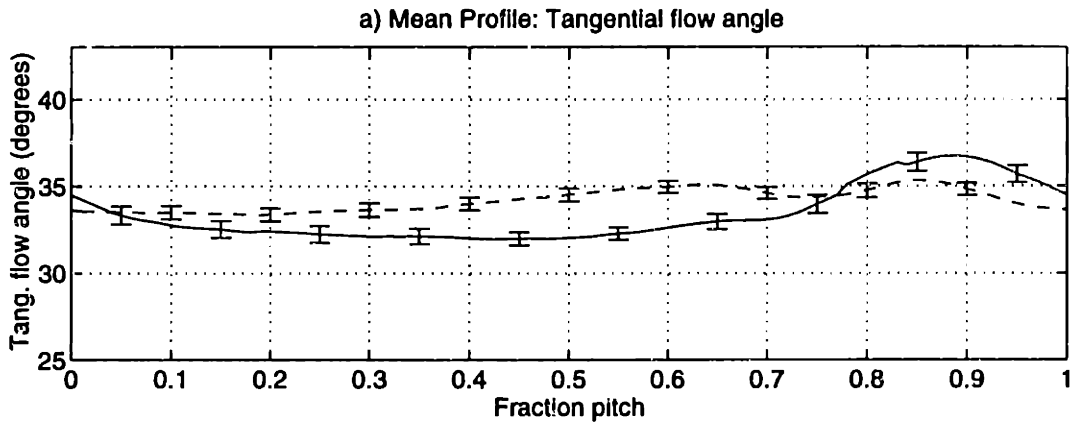

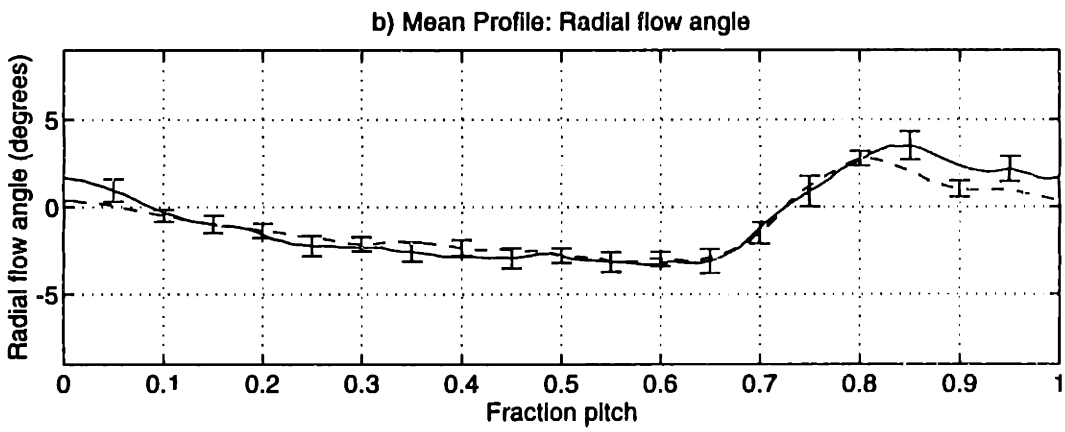

Figure 7-48: Ensemble-averaged profiles of absolute Mach number and tangential and radial flow angles at 75% span, 1.5c for the trailing edge blowing rotor with (- -) and without (—) tip-weighted injection

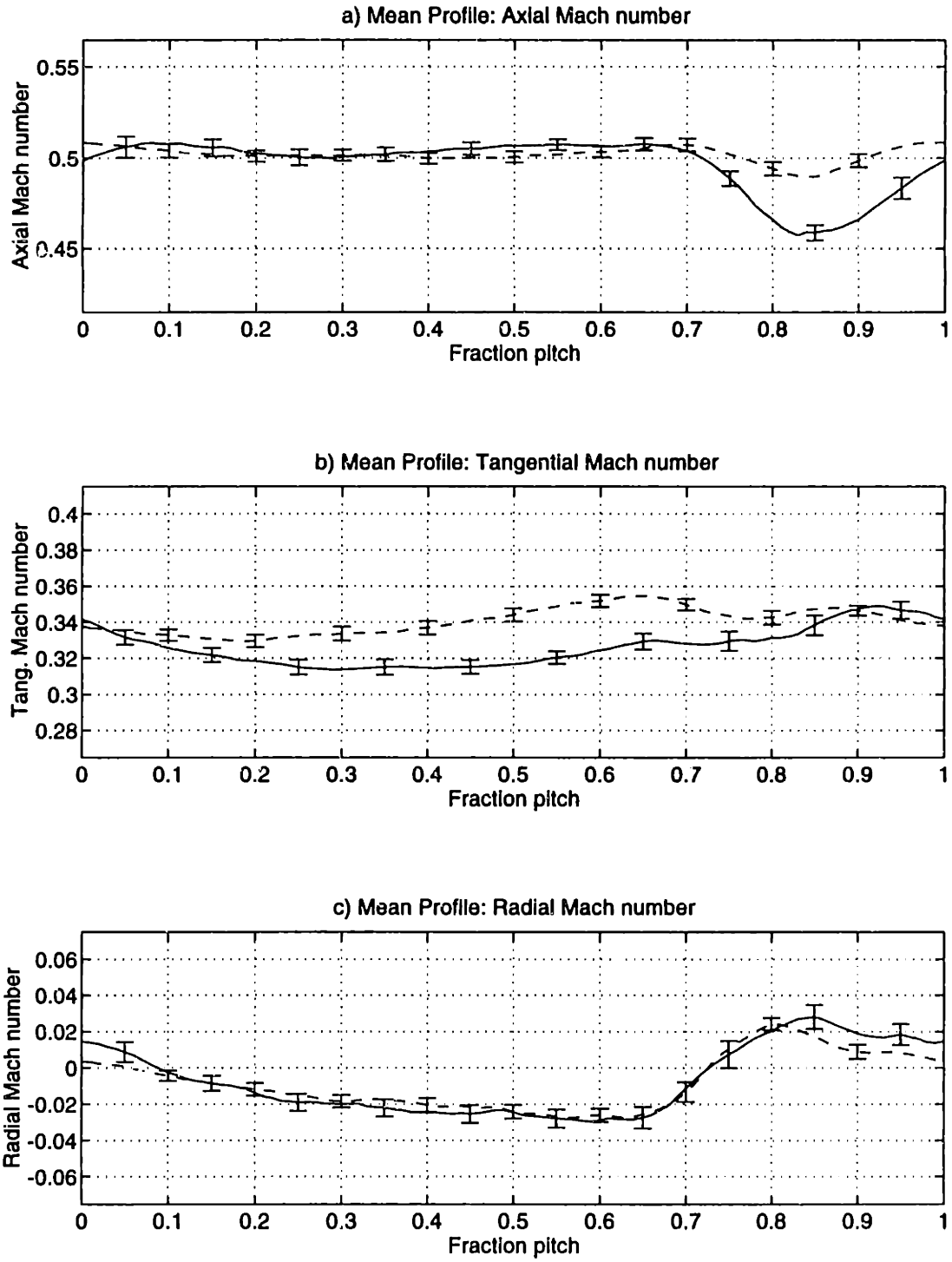

Figure 7-49: Ensemble-averaged profiles of axial, tangential, and radial Mach number at 75% span, 1.5c for the trailing edge blowing rotor with (- -) and without (—) tip-weighted injection

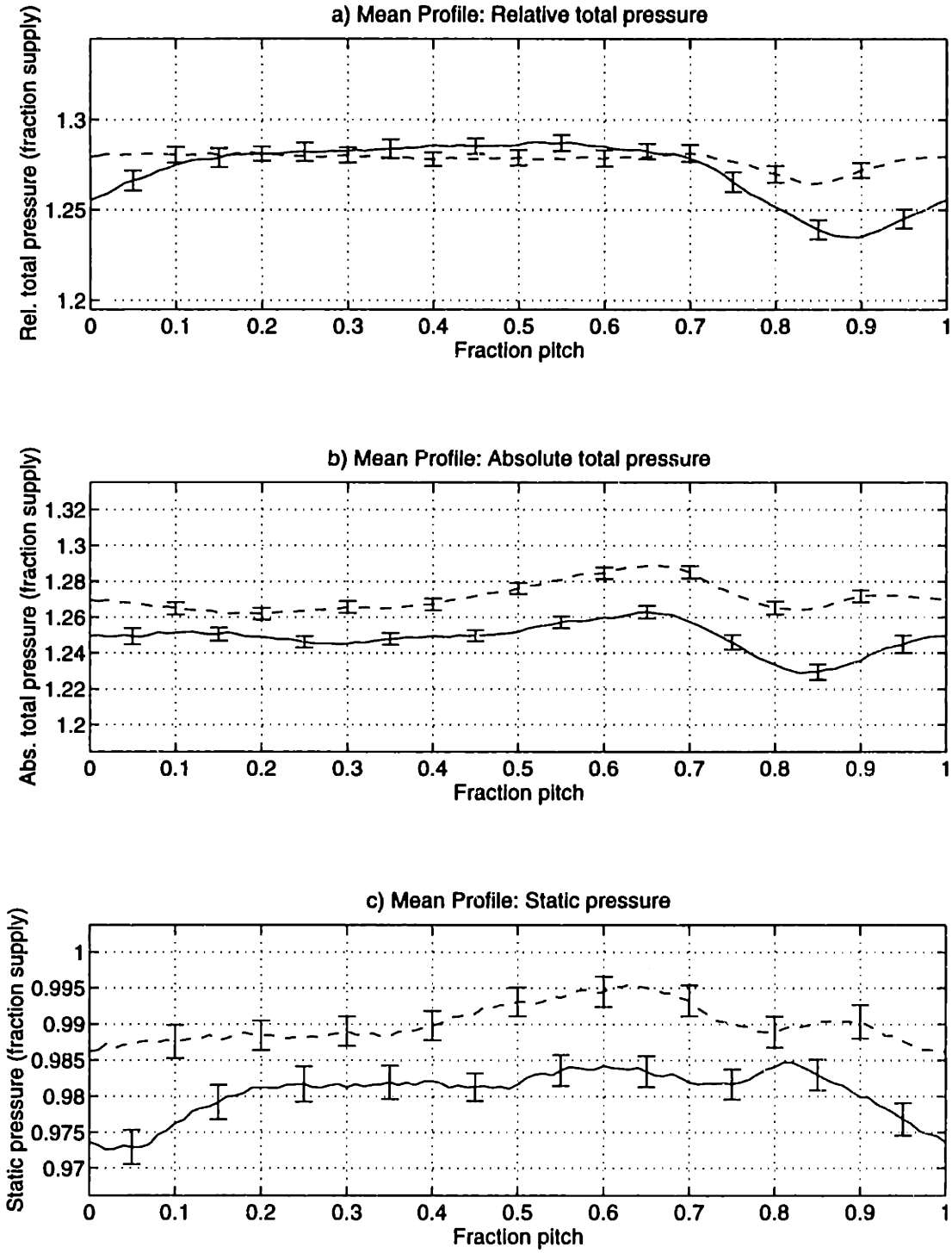

Figure 7-50: Ensemble-averaged profiles of relative and absolute total pressure and static pressure at 75% span, 1.5c for the trailing edge blowing rotor with (- -) and without (—) tip-weighted injection

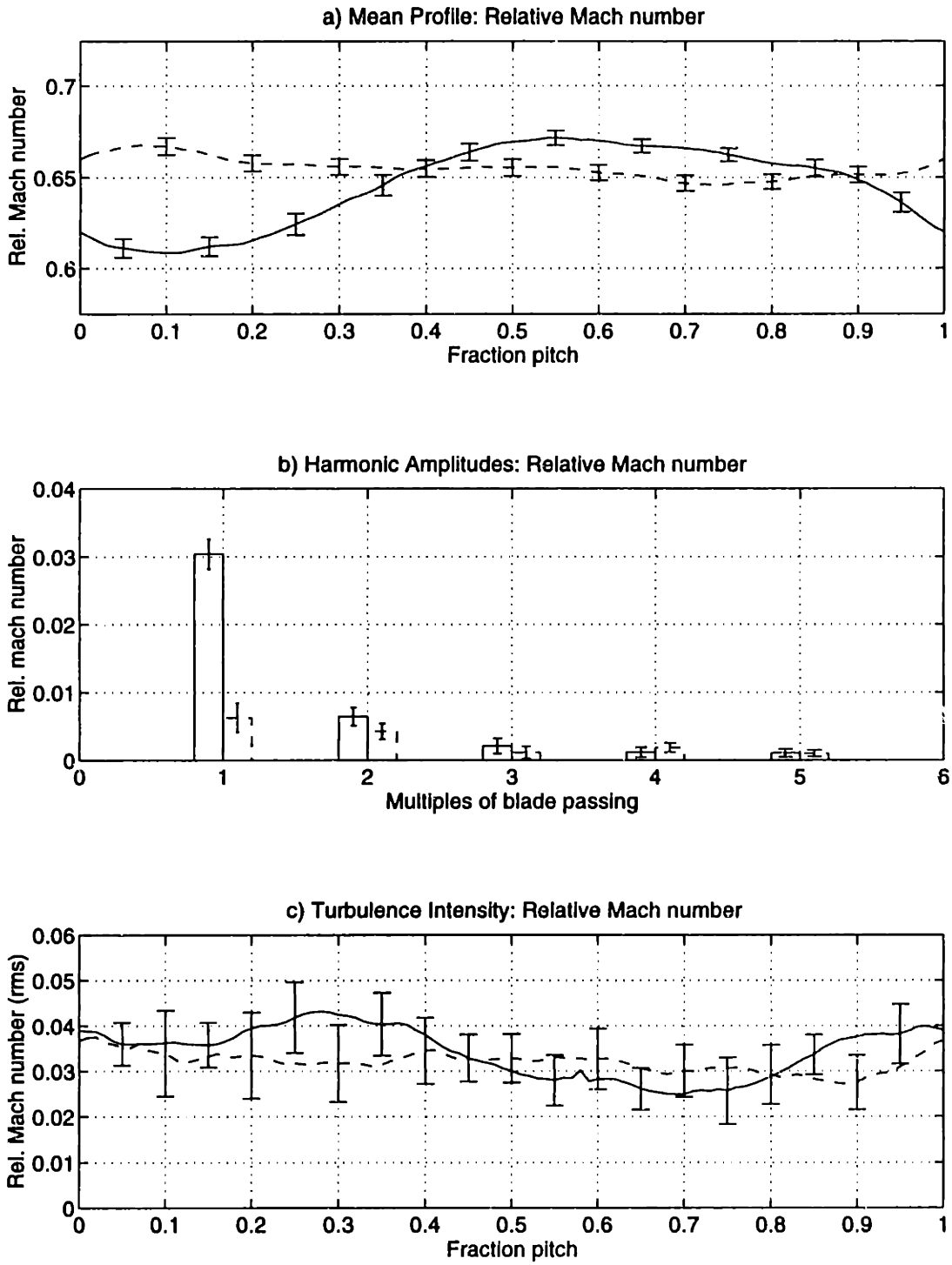

Figure 7-51: Relative Mach number ensemble-averaged profile, mean harmonic content, and turbulence profile at 87.5% span, 1.5c for the trailing edge blowing rotor with (- -) and without (—) tip-weighted injection

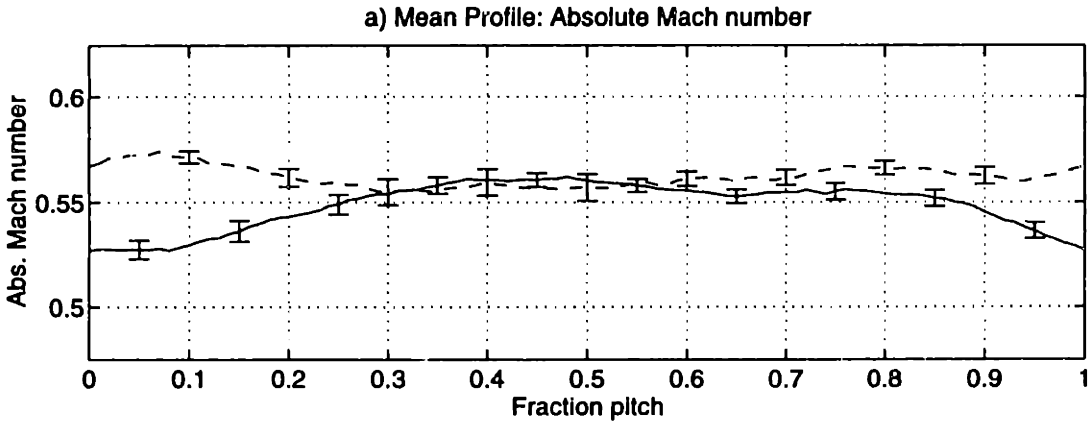

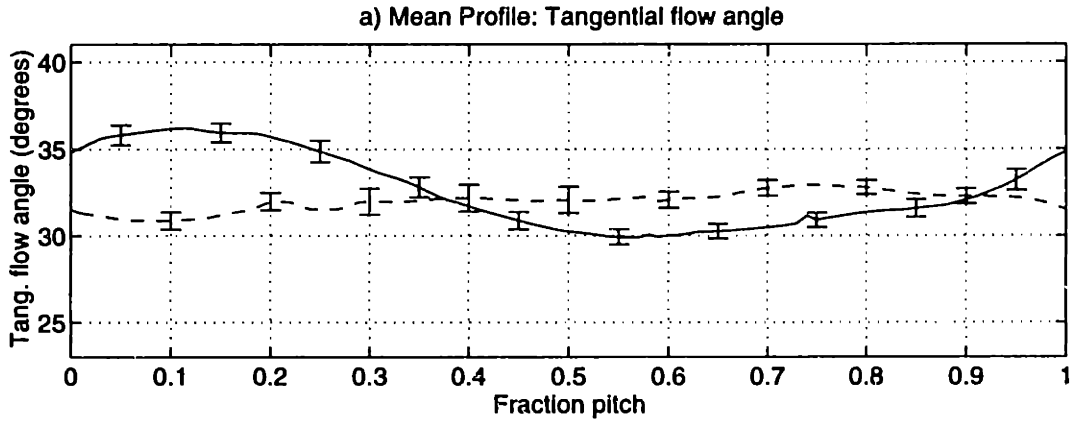

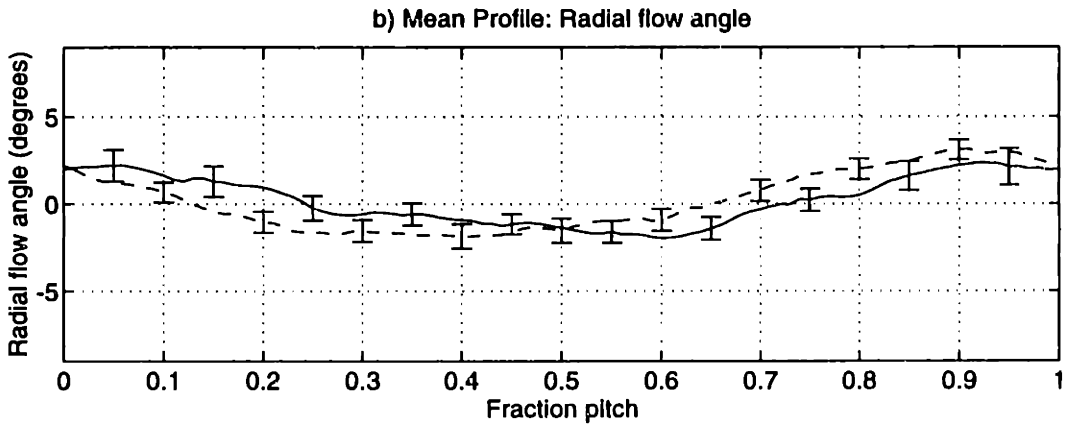

Figure 7-52: Ensemble-averaged profiles of absolute Mach number and tangential and radial flow angles at 87.5% span, 1.5c for the trailing edge blowing rotor with (- -) and without (—) tip-weighted injection

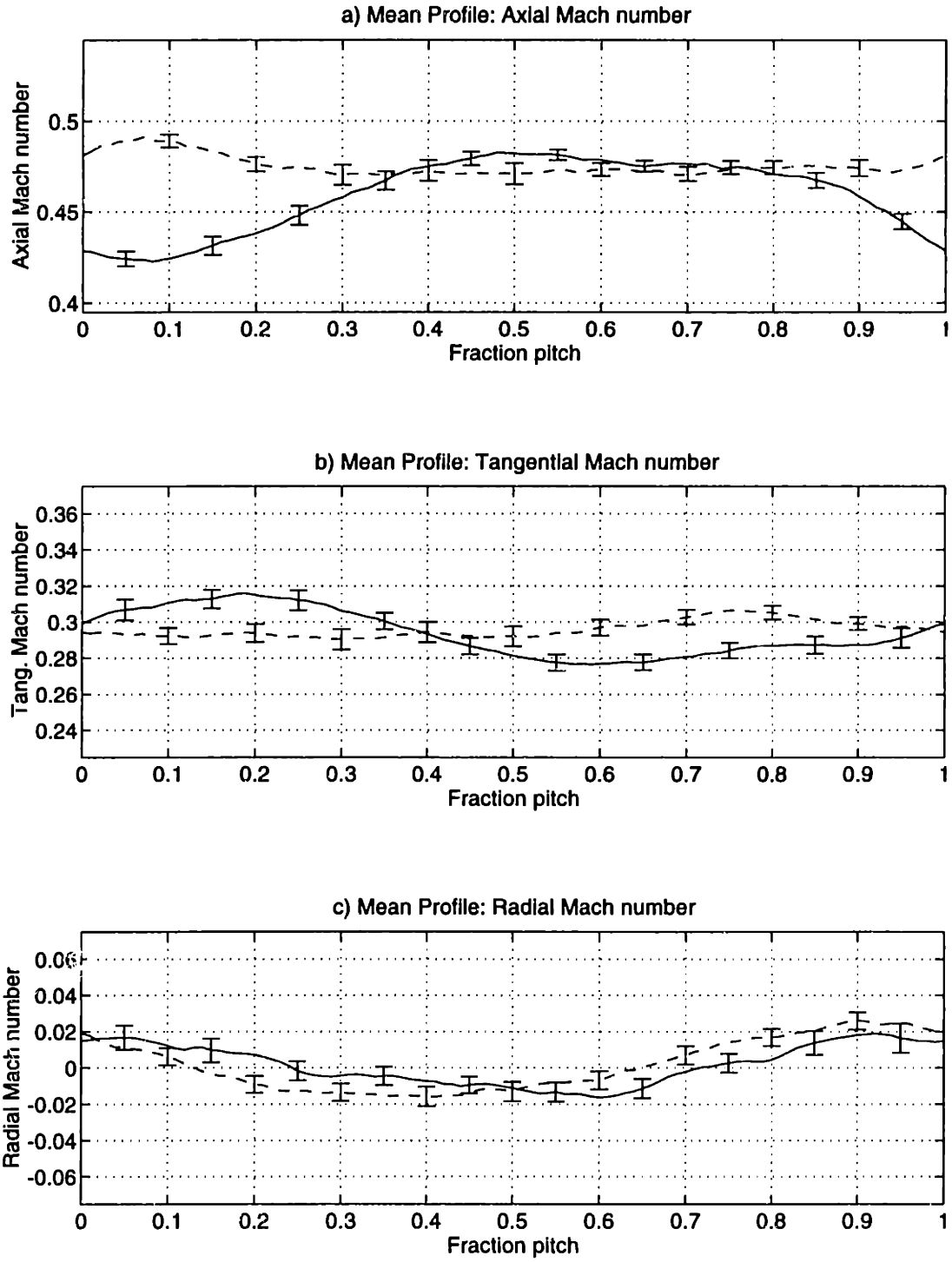

Figure 7-53: Ensemble-averaged profiles of axial, tangential, and radial Mach number at 87.5% span, 1.5c for the trailing edge blowing rotor with (- -) and without (—) tip-weighted injection

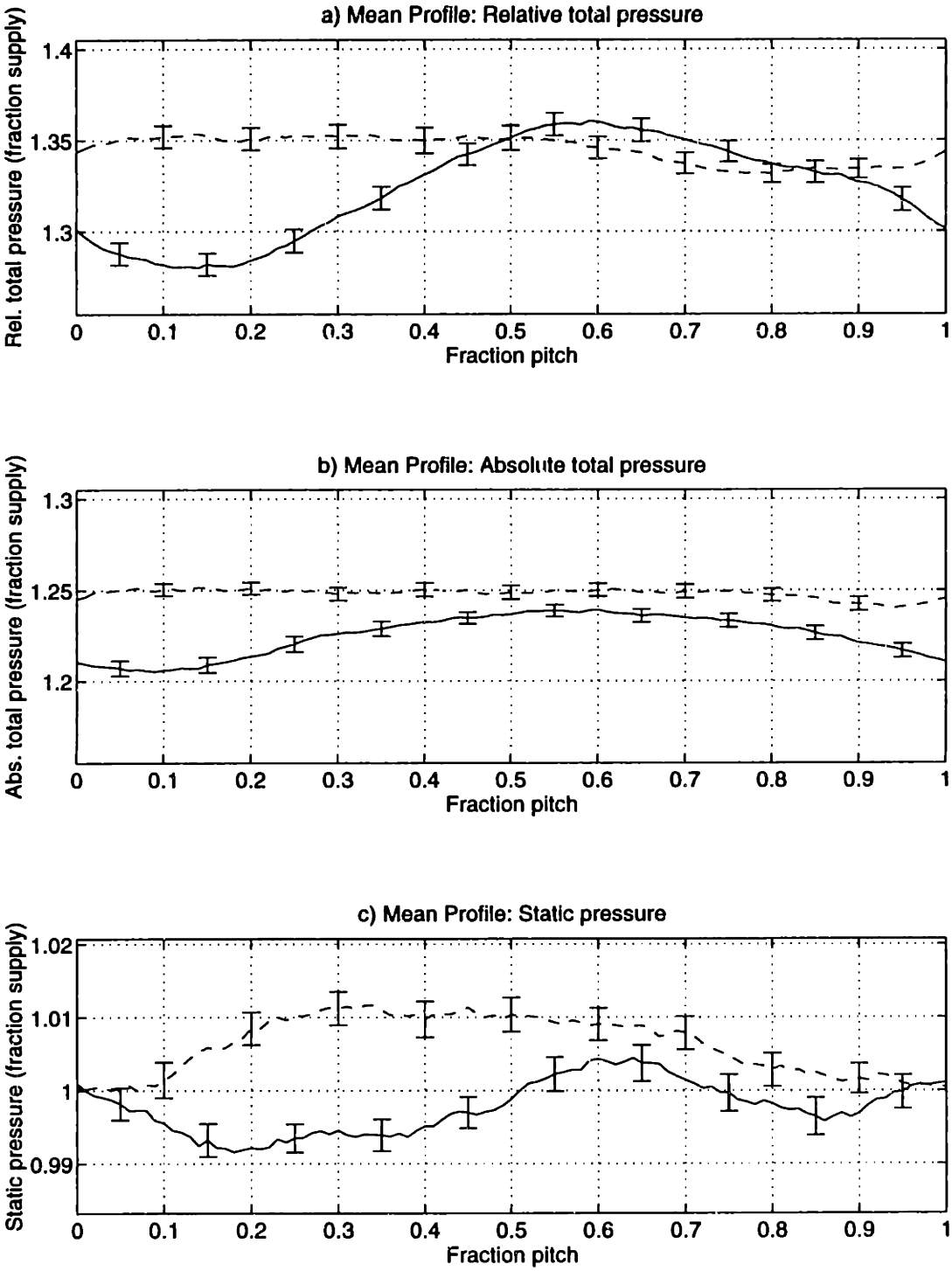

Figure 7-54: Ensemble-averaged profiles of relative and absolute total pressure and static pressure at 87.5% span, 1.5c for the trailing edge blowing rotor with (- -) and without (—) tip-weighted injection

without injection if the phase variations are altered such that the low radial modes couple well.

As is observed at 87.5% span in Figure 7-55, overblowing the wake results in a 'jet' that causes the wake phases to shift considerably. A resulting jet shifts the BPF harmonic phase by approximately 180 degrees, and likely shifts the higher harmonic phases by similar amounts (this depends on the shape of the jet). This result can significantly affect the acoustic coupling and offers potential leverage on noise reduction. If a specific radial wake phase variation can be determined that causes the lowest radiated noise, it may be possible to generate it through underblowing and overblowing specific regions of the span.

For example, the wake skew and harmonic phases for the baseline and no injection configurations show a bow in the spanwise direction (see Figure 7-19). It is certainly possible that straightening the phase variation from the hub to tip may reduce the noise. By overblowing the hub region, the phases would be shifted by approximately 180 degrees and the radial phase variation significantly straightened.

Summary of tip-weighted injection: 1.5 chord results

As was shown in Figures 7-39 through 7-54, the tip-weighted trailing edge blowing filled in the outer one-half span wakes quite nicely, but left the hub sections significantly underblown. While the wake harmonics were only slightly reduced at 25% span (BPF approximately 25% lower, with no change to the higher harmonics), the harmonics were significantly reduced at 75 and 87.5% span. BPF was reduced 68% at 75% span and 79% at 87.5% span. Similarly, 2*BPF was reduced 76% at 75% span and 34% at 87.5% span. The harmonic amplitudes (first five multiples of BPF) are tabulated in Table 7.3, and the amplitudes with injection are also shown as a fraction of the amplitudes without injection. In addition, the amplitudes for the first four BPF harmonics versus spanwise position are shown graphically in Figure 7-56

In addition to the wake reductions, the mass flow through the rotor decreases by approximately 2% due to injection. From the hub to midspan at 1.5 chords, the freestream axial Mach number is about 4% lower and the freestream tangential Mach number about 3% higher with injection. This results in a higher tangential flow angle, but lower total

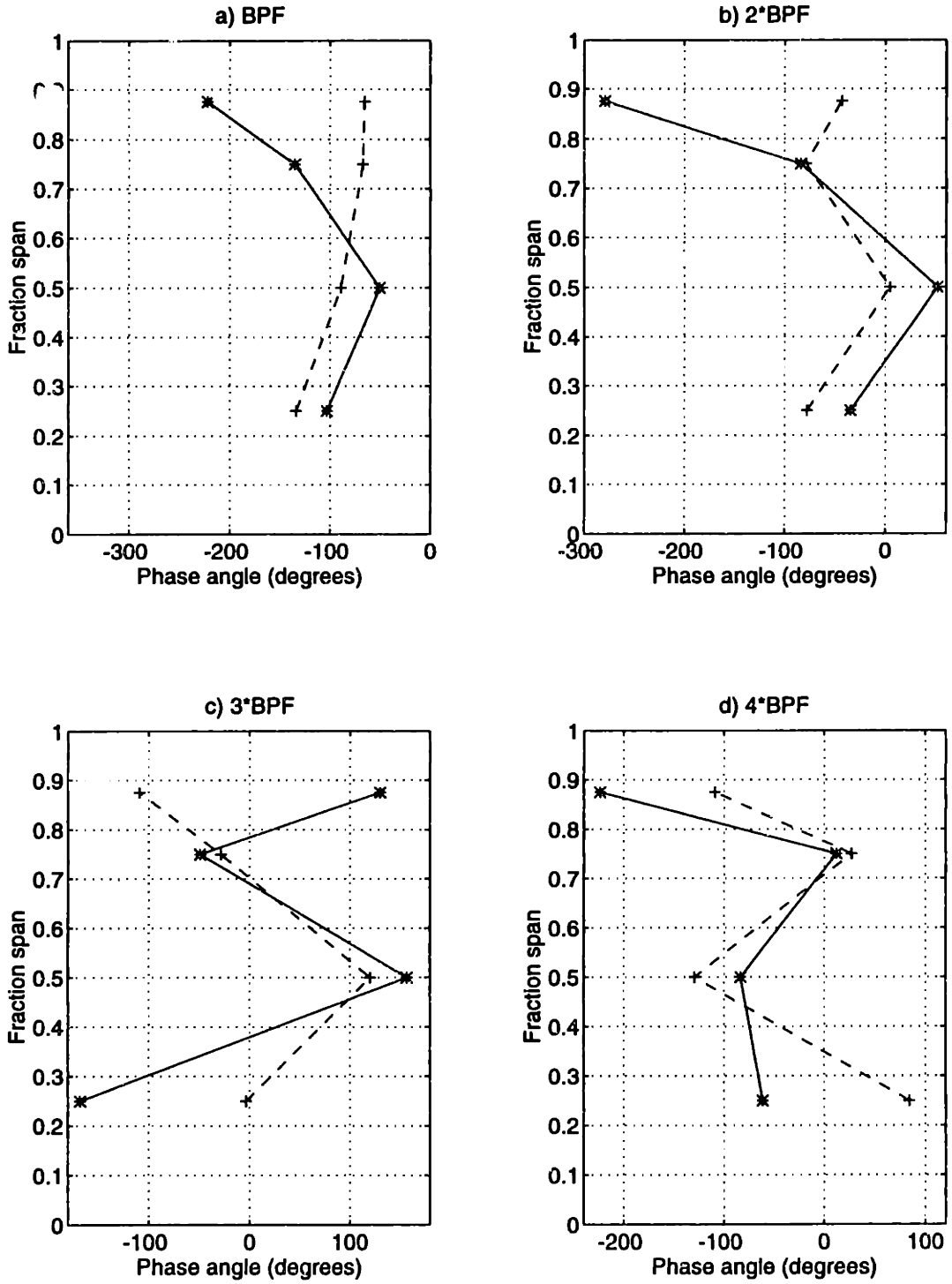

Figure 7-55: Phase angles for the first four BPF harmonics of relative Mach number at 1.5 chord for the trailing edge blowing rotor with (- -) and without (—) tip-weighted injection

T.e. blowing rotor (no injection)	BPF	2*BPF	3*BPF	4*BPF	5*BPF
25% span, 1.5c	.0386	.0118	.0006	.0012	.0011
50% span, 1.5c	.0206	.0095	.0057	.0024	.0013
75% span, 1.5c	.0193	.0114	.0057	.0022	.0007
87.5% span, 1.5c	.0304	.0065	.0021	.0012	.0011
T.e. blowing rotor (tip-weighted injection)	BPF	2*BPF	3*BPF	4*BPF	5*BPF
25% span, 1.5c	.0291 (0.75)	.0118 (1.00)	.0013 (2.03)	.0010 (0.79)	.0003 (0.28)
50% span, 1.5c	.0145 (0.71)	.0049 (0.52)	.0032 (0.56)	.0013 (0.56)	.0011 (0.84)
75% span, 1.5c	.0062 **(0.32)**	.0022 **(0.24)**	.0032 **(0.55)**	.0023 **(1.02)**	.0015 **(2.19)**
87.5% span, 1.5c	.0063 (0.21)	.0043 (0.66)	.0012 (0.55)	.0018 (1.59)	.0010 (0.93)

Table 7.3: Wake relative Mach number harmonic amplitudes at 1.5 chord for the trailing edge blowing rotor with and without tip-weighted injection (tip-weighted injection harmonic amplitudes also shown as fraction of no injection harmonic amplitudes)

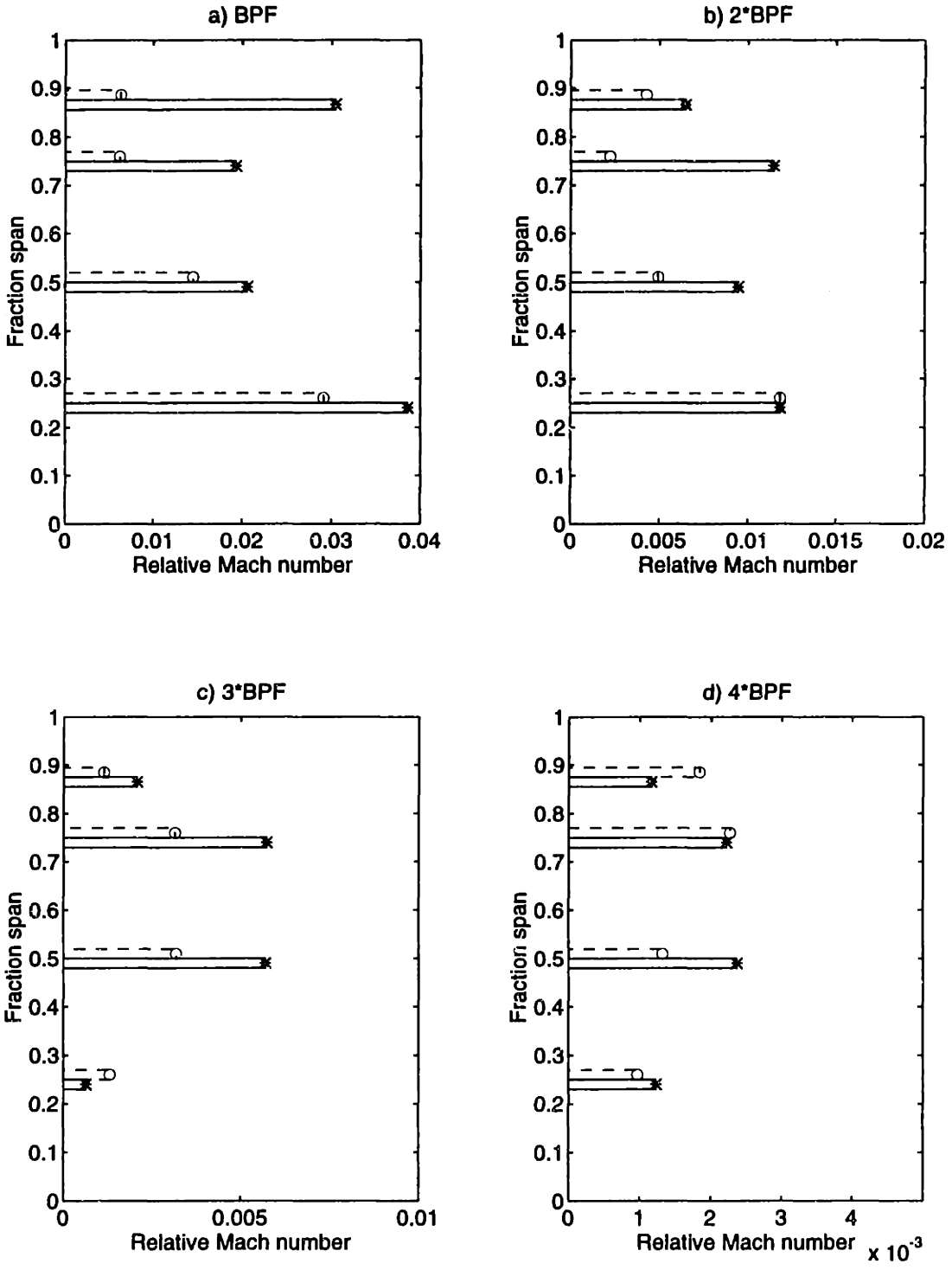

Figure 7-56: Wake relative Mach number harmonic amplitudes at 1.5 chord versus span: no injection (—) and 1.9% tip-weighted injection (- -)

pressure rise with injection (about 1%). From midspan to the tip, however, the average axial Mach number and tangential flow angle are slightly increased and the total pressure ratio is increased by about 2% with injection. Thus, the mass average total and static pressure ratios increase with injection.

With the downstream choke plate, the mass average axial Mach number should be approximately the same at a given position downstream of the rotor with and without injection. Thus, with a high injection rate at the tip, the hub region is forced to diffuse even more than without injection, and thus the flow downstream of the rotor goes through significant redistribution in the midstage region. The flow in the lower 25% span region undergoes large diffusion and thus the wake momentum deficit downstream is larger than at the rotor trailing edge. Knowing the distribution of injection with the original throttle plates allows modification to achieve more uniform injection.

7.4 Injection Modification

The tip-weighted injection results discussed in Section 7.3 showed that significant reductions in the wake harmonic amplitudes can be obtained, particularly if a momentumless wake is achieved. To try to obtain a more uniform injection distribution, the momentum deficit reductions with the tip-weighted injection were examined to determine the necessary changes in mass flow required in each blade internal passage. In addition, the dependence of the pressure used for the blowing on the addition of momentum to the wake was examined by using a higher initial blowing tank pressure (mass flow rate), for measurements at 50 and 87.5% span, 1.5 chords downstream of the rotor.

The momentum thickness reduction observed with the 1.9% mass injection rate at 50% span was about 45% at 0.1 chord. In order to obtain approximately a momentumless wake at 50% span, the blowing initial supply pressure was set approximately 22% higher, resulting in a total mass injection flow rate of approximately 2.35% of the fan throughflow. The measured flow quantities at 50% span, 1.5 chord with 2.35% injection are shown in Figures 7-57 through 7-60. The variations in the flow are much smaller than either the no injection case or the 1.9% tip-weighted injection case; reductions greater than 50% in the first five multiples of blade passing frequency were obtained. The BPF and 2*BPF harmonic

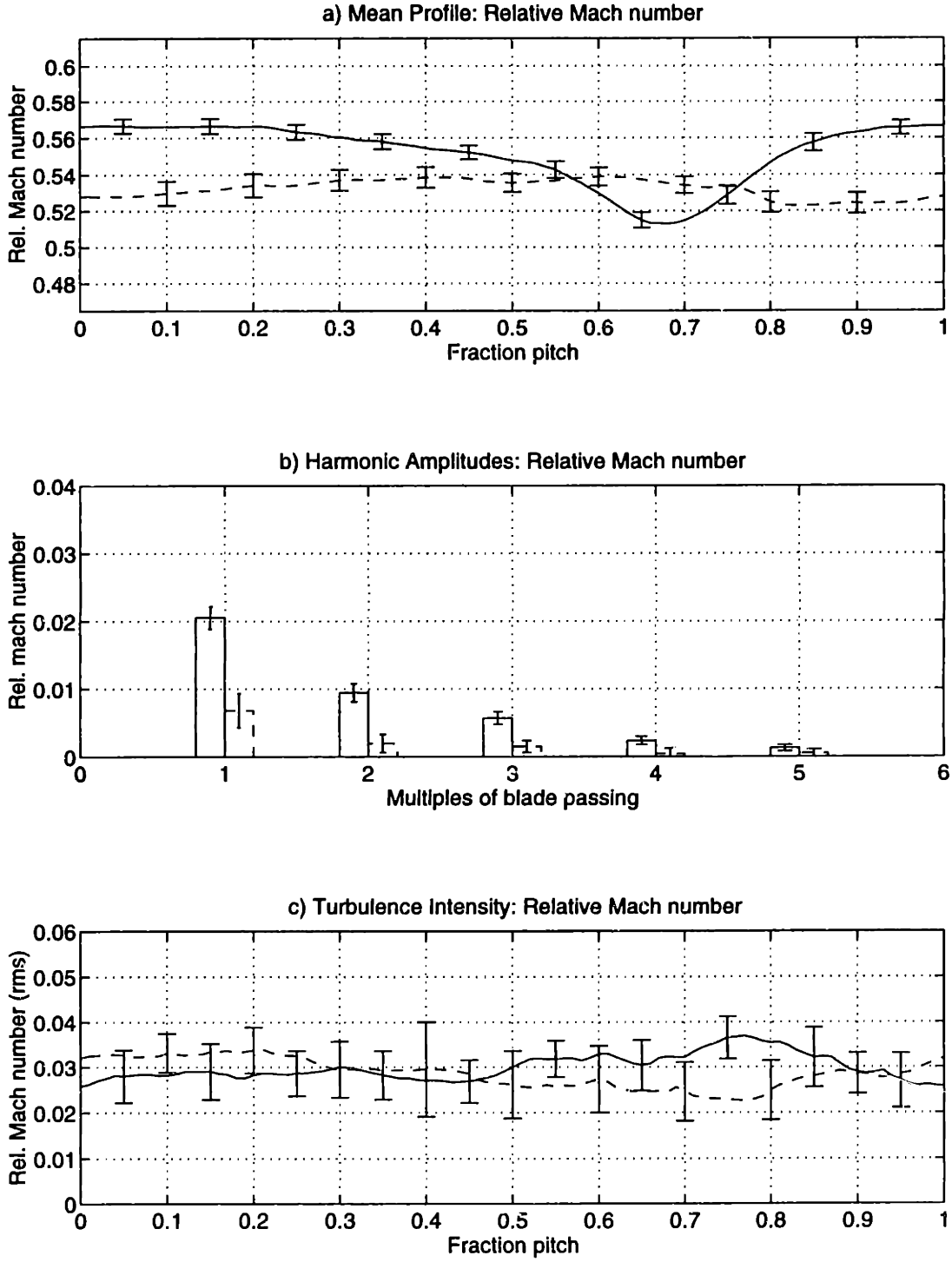

Figure 7-57: Relative Mach number ensemble-averaged profile, mean harmonic content, and turbulence profile at 50% span, 1.5c for the trailing edge blowing rotor with 2.35% (- -) and without (—) tip-weighted injection

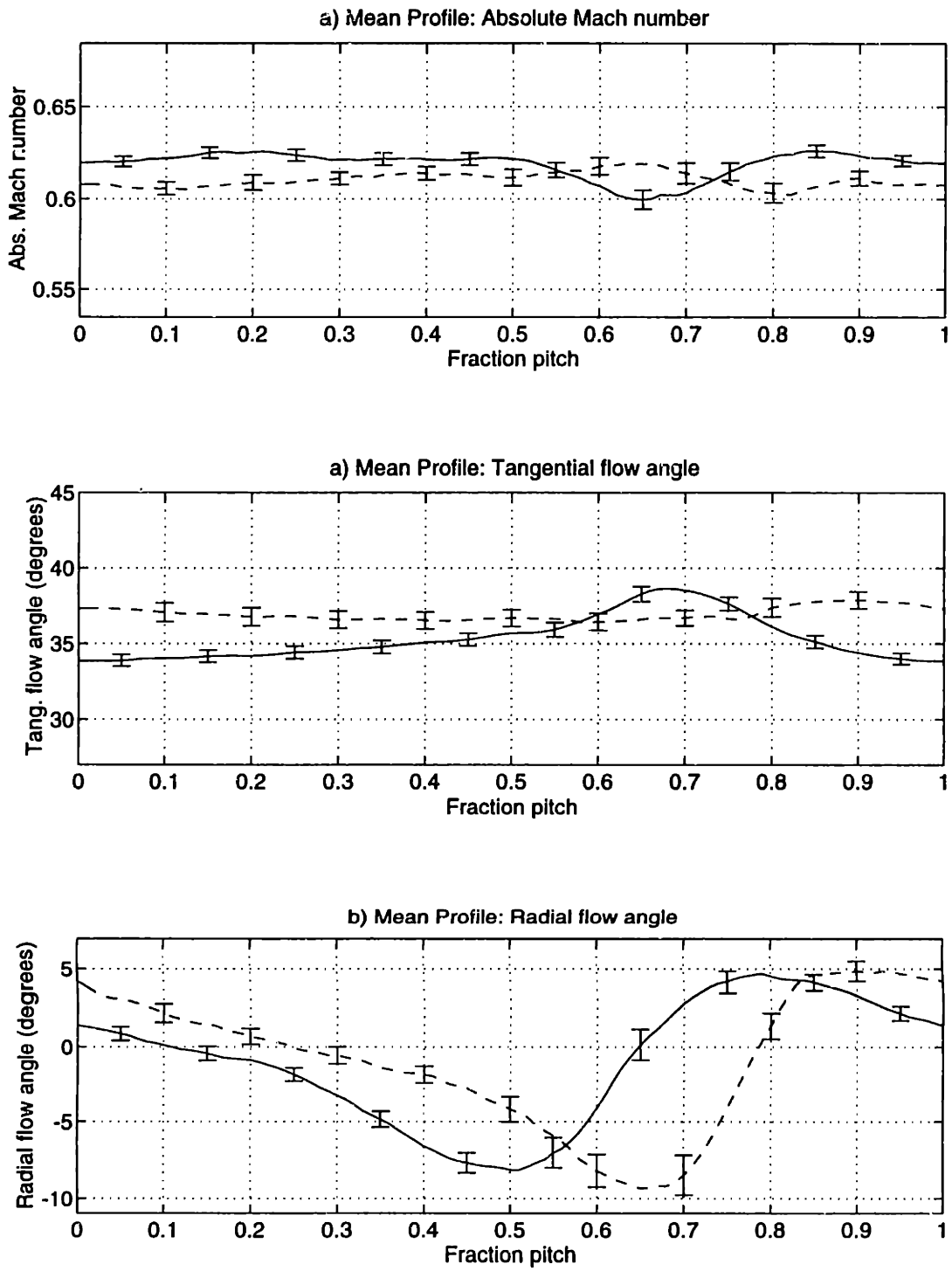

Figure 7-58: Ensemble-averaged profiles of absolute Mach number and tangential and radial flow angles at 50% span, 1.5c for the trailing edge blowing rotor with 2.35% (- -) and without (—) tip-weighted injection

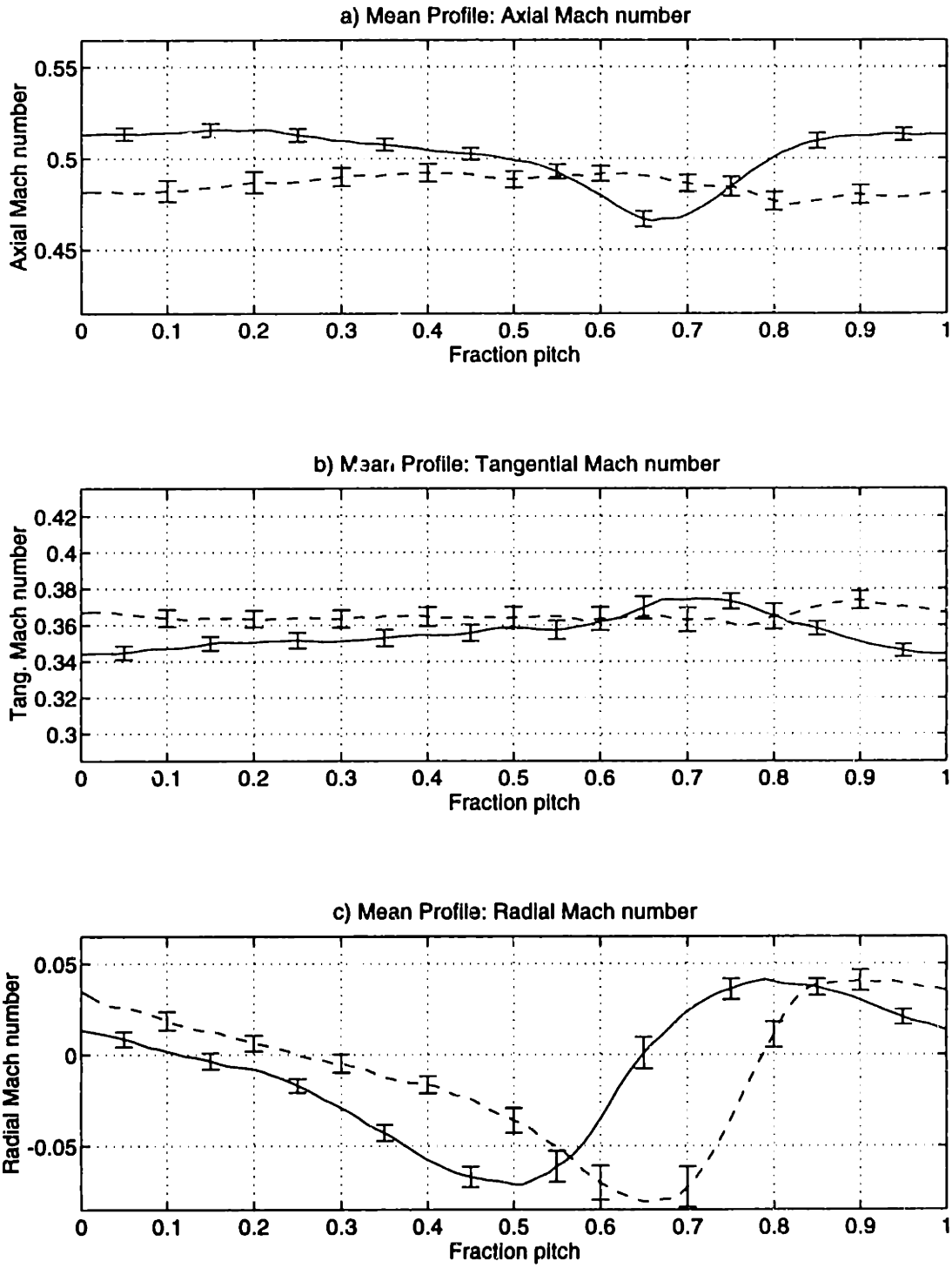

Figure 7-59: Ensemble-averaged profiles of axial, tangential, and radial Mach number at 50% span, 1.5c for the trailing edge blowing rotor with 2.35% (- -) and without (—) tip-weighted injection

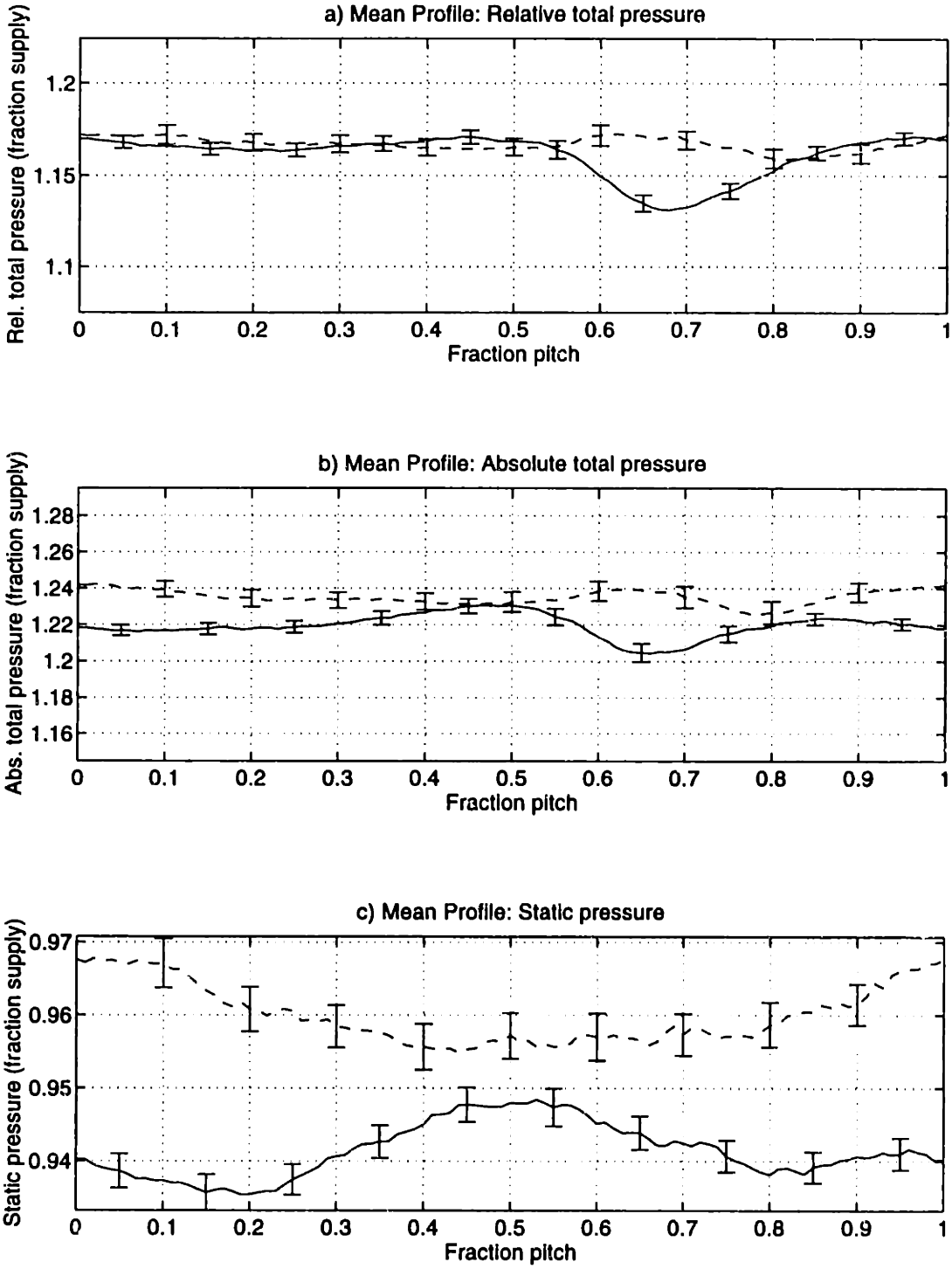

Figure 7-60: Ensemble-averaged profiles of relative and absolute total pressure and static pressure at 50% span, 1.5c for the trailing edge blowing rotor with 2.35% (- -) and without (—) tip-weighted injection

amplitudes are reduced 67% and 79%, respectively, from the no injection measurements at 50% span, 1.5 chord.

With the momentum deficit reductions calculated from 1.9% tip-weighted injection (blade throttle plates in place), and determination that 50% span required approximately 25% higher blowing supply pressure/mass flow to generate a momentumless wake, the necessary changes to the throttle plates were determined. The result of the calculations was that the removal of the throttle plates would result in much of the required change needed to obtain a momentumless wake along the entire span. Also, since flow field measurements with the original throttle plates and no throttle plates would give two data points for later fine tuning of the blade passage throttling (and time was limited), the throttle plates in the rotor hub were simply removed.

7.5 Trailing Edge Blowing Rotor: 2.0% midspan-weighted injection

After removal of the rotor blade throttle plates, the rotor was reinstalled in the test section of the Blowdown Compressor Facility. Measurements were first taken at 0.1 chord to set the initial blowing tank pressure. The axial position just downstream of the rotor (0.1c) was chosen since only one run is required at each spanwise position to obtain confidence intervals much smaller than the flow field variations. The same initial blowing tank pressure was used as for the 1.9% tip-weighted injection, and the results are shown in the next sections.

The distribution of injection for this midspan-weighted configuration is shown in Figure 7-61 as a function of spanwise position. The '+' symbols are measurements at 1.5 chord, and the '*' symbols are measurements at 0.1 chord. The wake momentum deficit appears to have been approximately uniformly filled along the entire span at 0.1 chord, but the wake momentum deficit at 1.5 chord shows a midspan-weighted distribution. [Note: The changes in wake momentum deficit reduction downstream may be partly due to the flow redistribution between the rotor and stator, as discussed in Section 7.3.1] Due to variability in the momentum deficit calculation with choice of 'freestream', however, the error in the measured momentum thickness fractions shown is about 0.1 at 1.5 chord and about 0.2 at

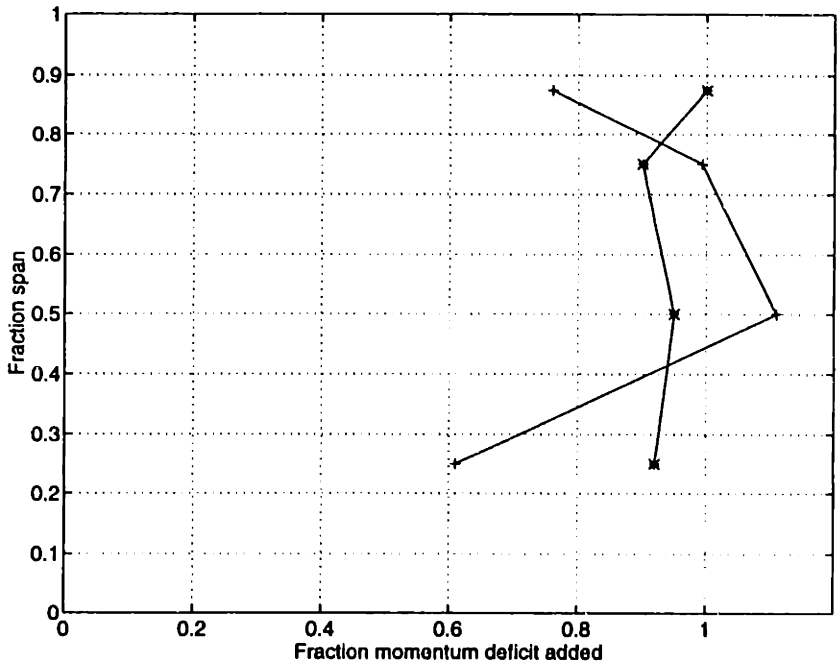

Figure 7-61: Momentum deficit addition with injection versus span: 2.0% midspan-weighted injection

0.1 chord. The mass flow rate for this injection configuration was approximately 2.0% of the fan throughflow.

7.5.1 Flow field measurements at 0.1 chord

Measurements were obtained at 25, 50, 75, and 87.5% span, 0.1 chord downstream of the rotor. The ensemble-averaged relative Mach number mean profile, its harmonic content, and the profile of relative Mach number turbulence intensity are shown in Figures 7-62 through 7-65. The other flow variables are shown in Appendix E. As with the tip-weighted injection, the injection data (dashed lines) is plotted with the no injection data (solid lines) for direct comparison.

The relative Mach number profiles appear to be well filled (close to momentumless wakes) at all spanwise positions with large reductions in the harmonic amplitudes. At the four spanwise positions, the BPF harmonic amplitudes are reduced 52 to 81% with injection compared to the no injection harmonics at 0.1c, and the 2*BPF amplitudes are reduced 57 to 91%. All the harmonic amplitudes are tabulated in Table 7.4, and are shown graphically

T.e. blowing rotor (no injection)	BPF	2*BPF	3*BPF	4*BPF	5*BPF
25% span, 0.1c	.0528	.0388	.0319	.0210	.0149
50% span, 0.1c	.0383	.0336	.0339	.0264	.0217
75% span, 0.1c	.0322	.0386	.0356	.0277	.0203
87.5% span, 0.1c	.0245	.0259	.0155	.0077	.0035
T.e. blowing rotor (2.0% midspan-weighted inj.)	BPF	2*BPF	3*BPF	4*BPF	5*BPF
25% span, 0.1c	.0098	.0083	.0088	.0087	.0091
(fraction no inj. at 0.1c)	(0.19)	(0.21)	(0.28)	(0.41)	(0.61)
[fraction no inj. at 1.5c]	[0.25]	[0.70]	[13.7]	[7.07]	[8.62]
50% span, 0.1c	.0184	.0077	.0023	.0052	.0044
	(0.48)	(0.23)	(0.07)	(0.20)	(0.20)
	[0.89]	[0.81]	[0.40]	[2.20]	[3.50]
75% span, 0.1c	.0093	.0033	.0036	.0024	.0024
	(0.29)	(0.08)	(0.10)	(0.09)	(0.12)
	[0.48]	[0.29]	[0.62]	[1.08]	[3.41]
87.5% span, 0.1c	.0053	.0110	.0100	.0052	.0036
	(0.22)	(0.42)	(0.65)	(0.67)	(1.03)
	[0.17]	[1.70]	[4.83]	[4.47]	[3.47]

Table 7.4: Wake relative Mach number harmonic amplitudes at 0.1 chord for the trailing edge blowing rotor with and without 2.0% midspan-weighted injection (injection harmonic amplitudes also shown as fraction of no injection harmonic amplitudes at 0.1c ( ) and as fraction of no injection harmonic amplitudes at 1.5 chord [ ])

(1-_*BPF) versus spanwise position in Figure 7-66.

7.5.2 Flow field measurements at 1.5 chord

After the measurements were completed at 0.1 chord, the flow measurement probe was moved to 1.5 chords, just in front of the stator row. While the data at 0.1 chord suggested that the injection was achieving close to a momentumless wake along the entire span, the measurements at 1.5 chord were not as encouraging. There are a couple possible reasons for this result. First, the calculation of momentum deficit at 0.1 chord has errors of approximately 0.2 due to the choice of wake edge in the nonuniform freestream. In addition,

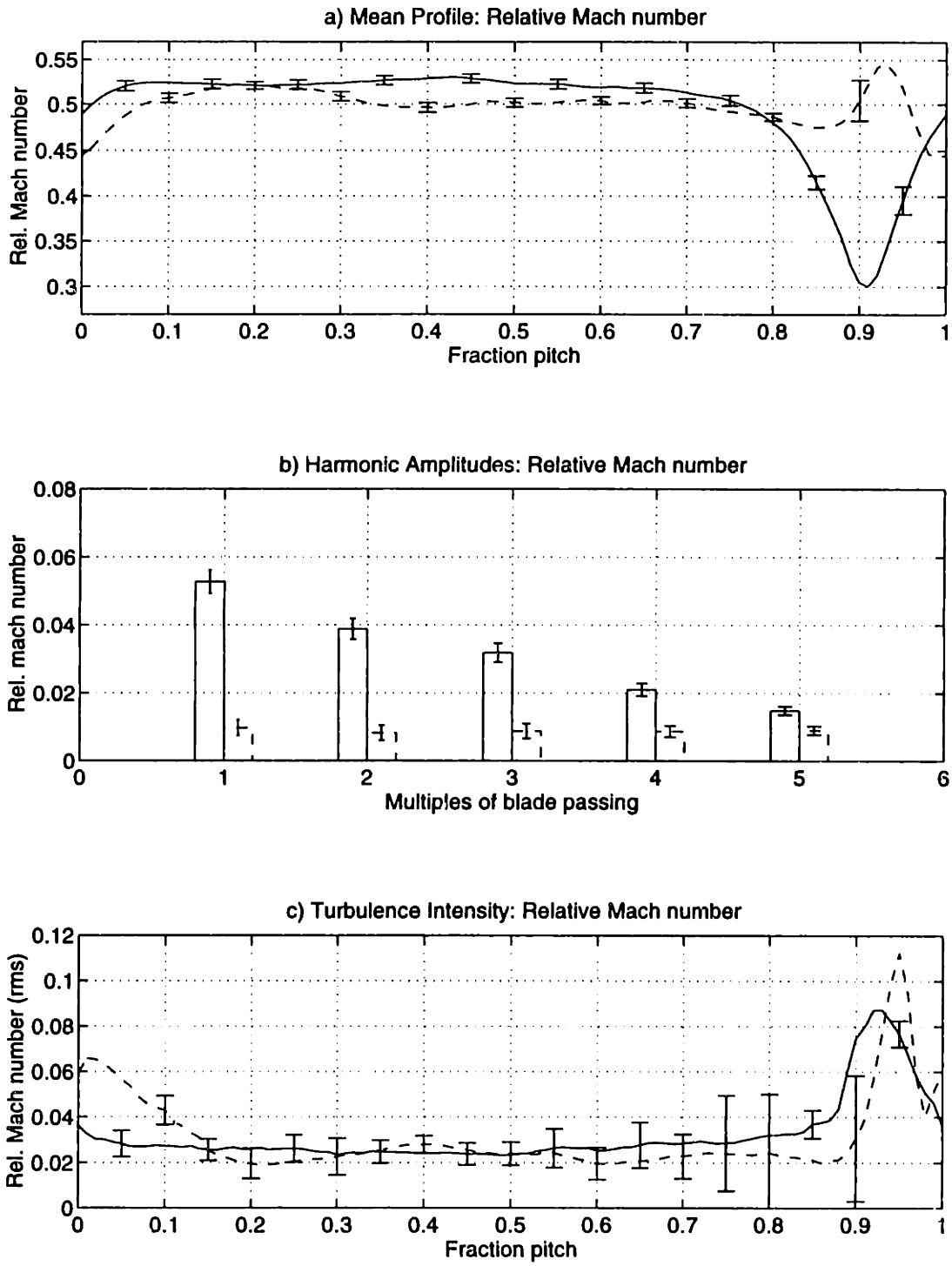

Figure 7-62: Relative Mach number ensemble-averaged profile, mean harmonic content, and turbulence profile at 25% span, 0.1c for the trailing edge blowing rotor with 2.0% (- -) and without (—) midspan-weighted injection

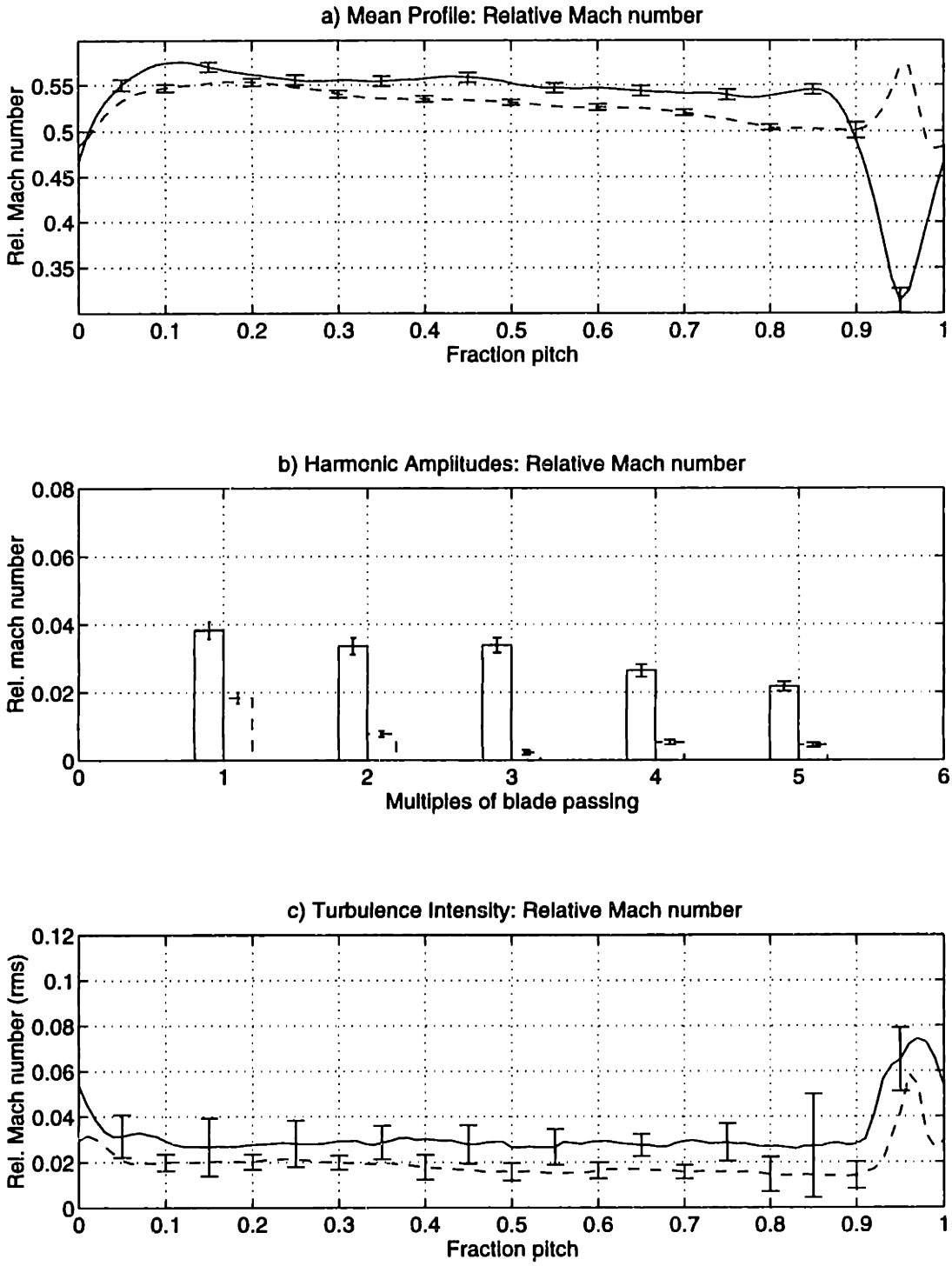

Figure 7-63: Relative Mach number ensemble-averaged profile, mean harmonic content, and turbulence profile at 50% span, 0.1c for the trailing edge blowing rotor with 2.0% (- -) and without (—) midspan-weighted injection

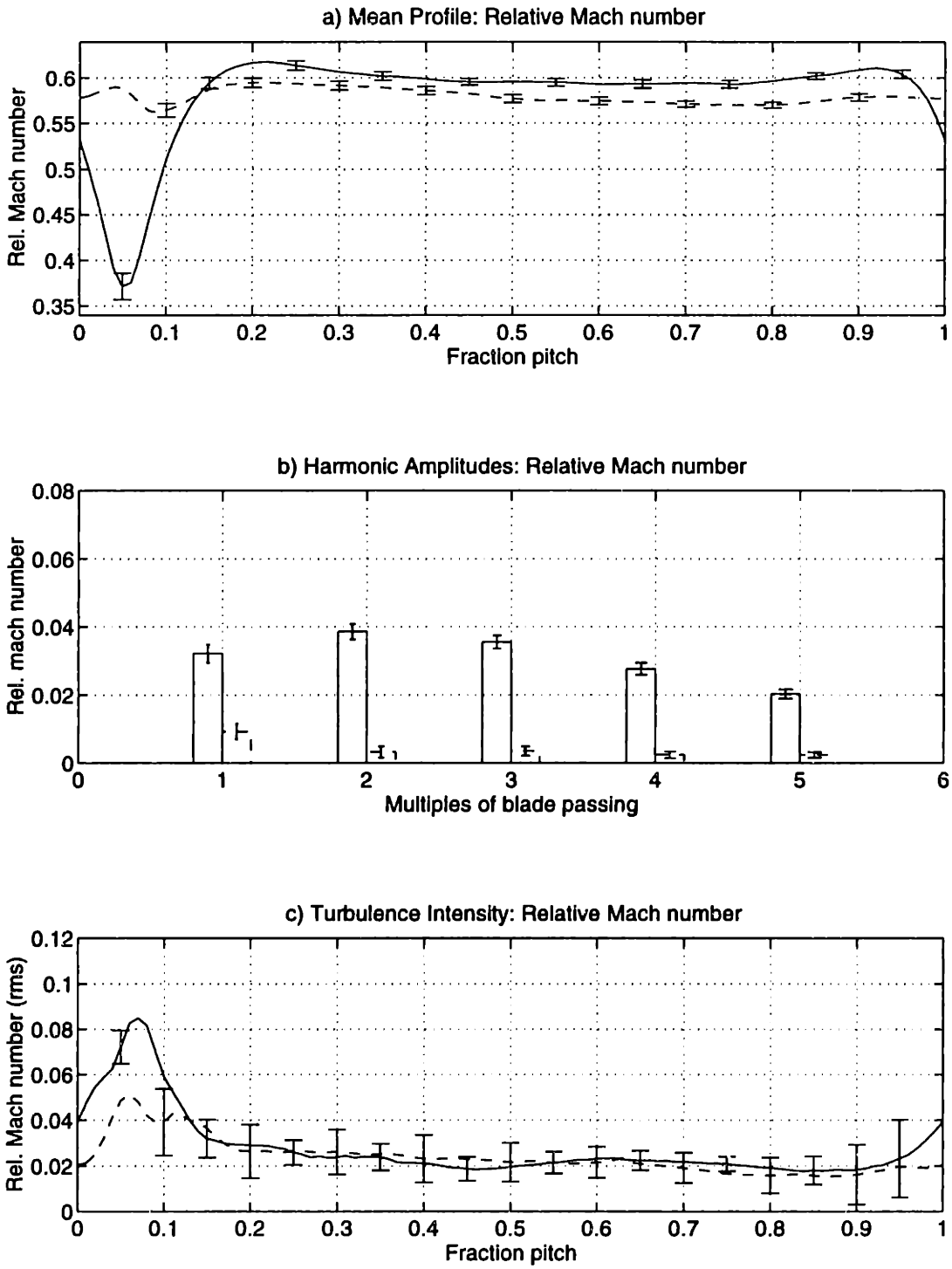

Figure 7-64: Relative Mach number ensemble-averaged profile, mean harmonic content, and turbulence profile at 75% span, 0.1c for the trailing edge blowing rotor with 2.0% (- -) and without (—) midspan-weighted injection

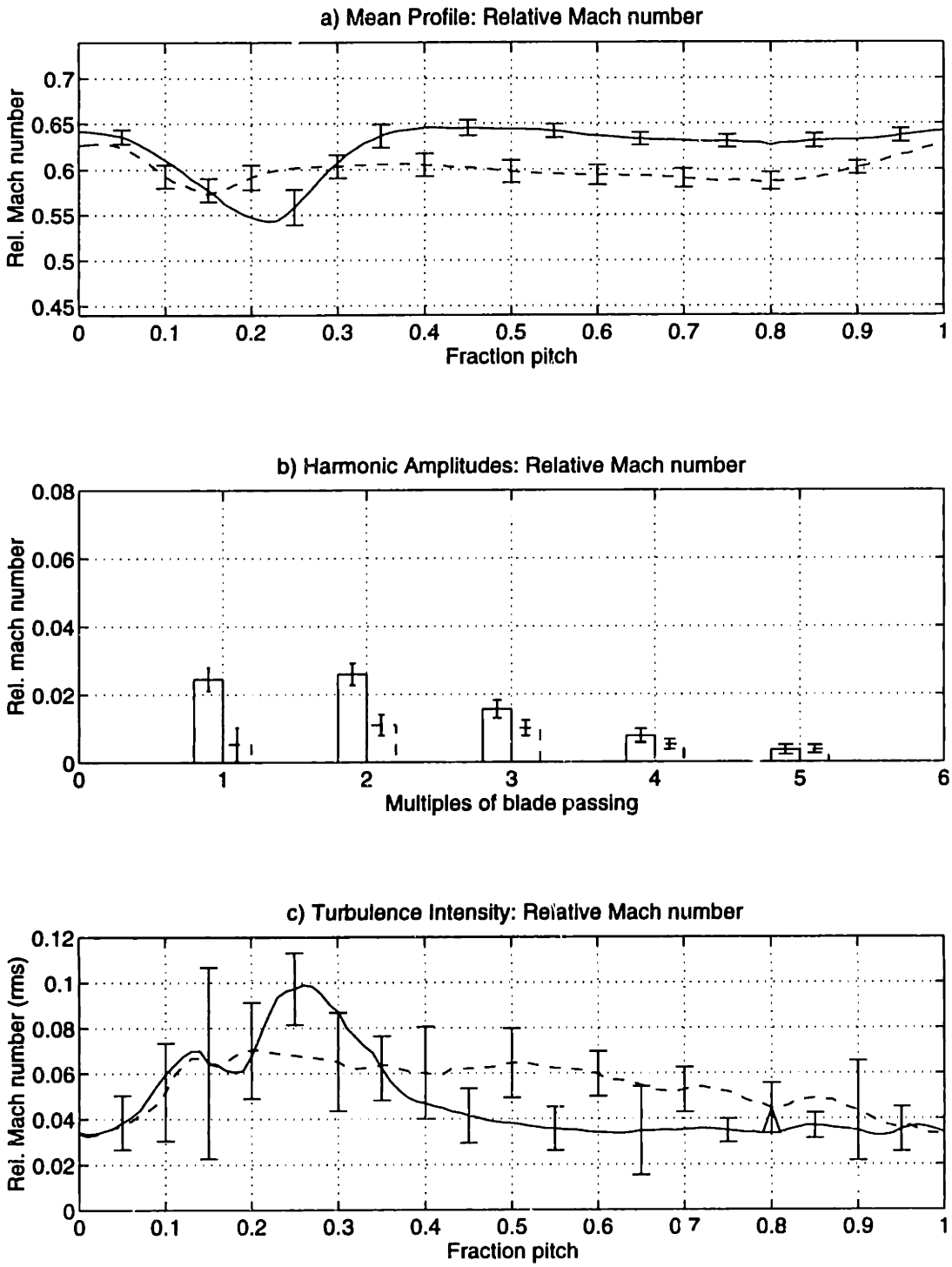

Figure 7-65: Relative Mach number ensemble-averaged profile, mean harmonic content, and turbulence profile at 87.5% span, 0.1c for the trailing edge blowing rotor with 2.0% (- -) and without (—) midspan-weighted injection

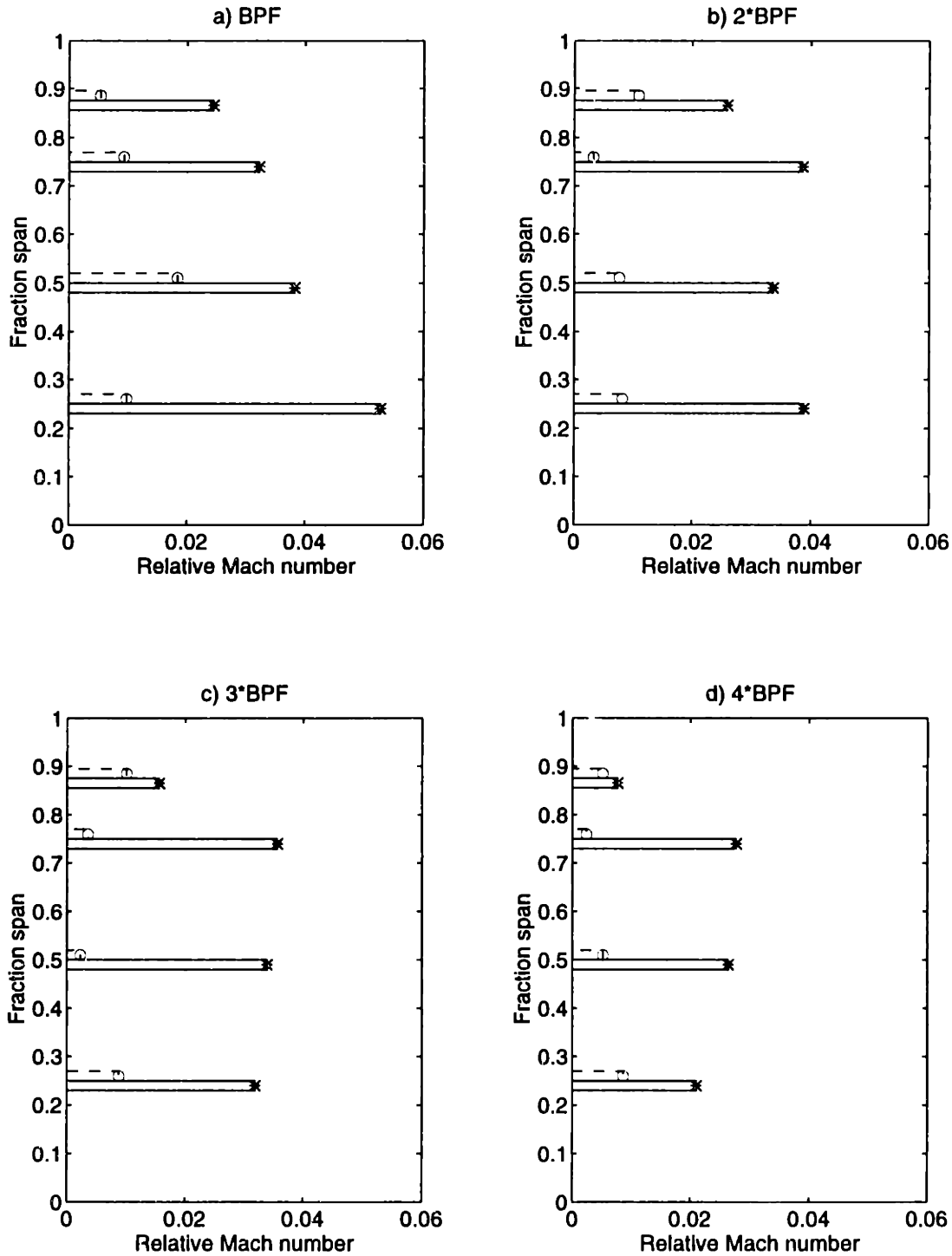

Figure 7-66: Wake relative Mach number harmonic amplitudes at 0.1 chord versus span: no injection (—) and 2.0% midspan-weighted injection (- -)

because of the flow redistribution between the rotor and stator, the flow measured at 1.5 chord did not necessarily originate at the same spanwise position on the rotor. This is particularly true below 50% span, where it was previously mentioned that the wake at 25% span, 1.5 chord originated at approximately 19% span on the rotor blade.

Relative Mach number data at 25, 50, 75, and 87.5% span, 1.5 chords for the 2.0% midspan-weighted injection is presented in Figures 7-67 through 7-70, compared to the no injection results. Additional flow quantities can be seen in Appendix E. The wake momentum deficit appears to be underblown at 25% span by approximately 40%, overblown at 50% span by about 10%, approximately filled at 75% span, and about 25% underblown at 87.5%. The BPF harmonic amplitudes are reduced 40 to 78% with injection compared to the no injection data at 1.5 chord, and the 2*BPF amplitudes are reduced 15 to 56%. All the harmonic amplitudes are tabulated in Table 7.5 and are shown graphically (1-4*BPF) versus span in Figure 7-71. The turbulence intensity is largely unchanged, except for an increase at 87.5% span of approximately 25%.

The relative Mach number wake harmonic phases are plotted in Figure 7-72 for the first four multiples of blade passing frequency. Because of the overblown midspan wake, the wake phase angles at 50% span are seen to be shifted about 180 degrees. This injection configuration, like the tip-weighted injection, causes large changes to the radial variation in wake harmonic phase and will significantly change the radial coupling of the acoustic modes. It would appear that the 2*BPF wake harmonics have virtually no phase variation from the hub to 75% span (although there could be 360 degree variations between any two points, see Section 7.2.3). If this is true, then the 2*BPF injection harmonics could couple strongly with the lower order radial acoustic modes that originally did not couple well due to the high wake skew. Even with large reductions in the harmonic amplitudes, this strong coupling could result in increased radiated noise. It was therefore decided to decrease the injection mass flow to achieve a momentumless wake at 50% span.

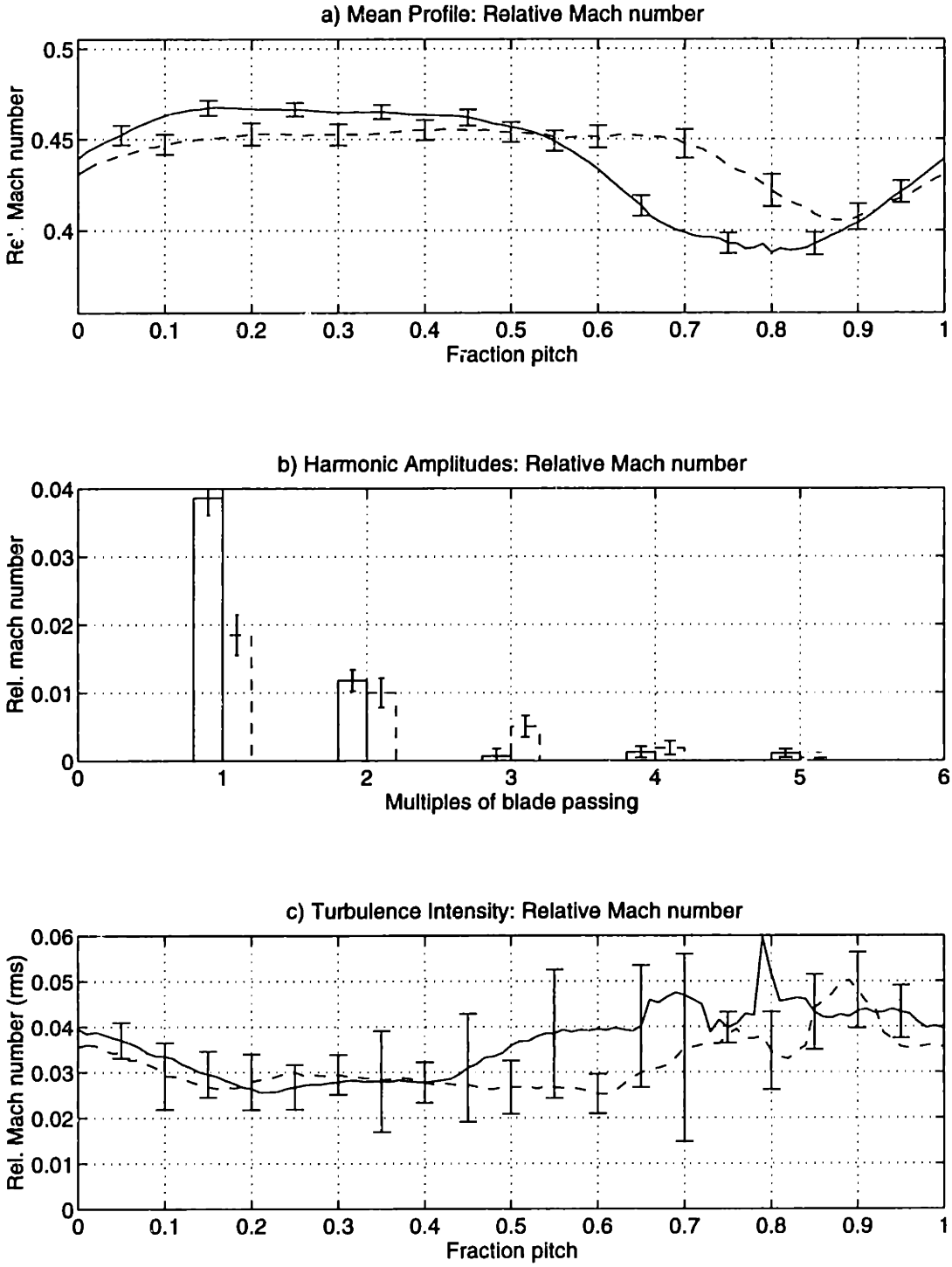

Figure 7-67: Relative Mach number ensemble-averaged profile, mean harmonic content, and turbulence profile at 25% span, 1.5c for the trailing edge blowing rotor with 2.0% (- -) and without (—) midspan-weighted injection

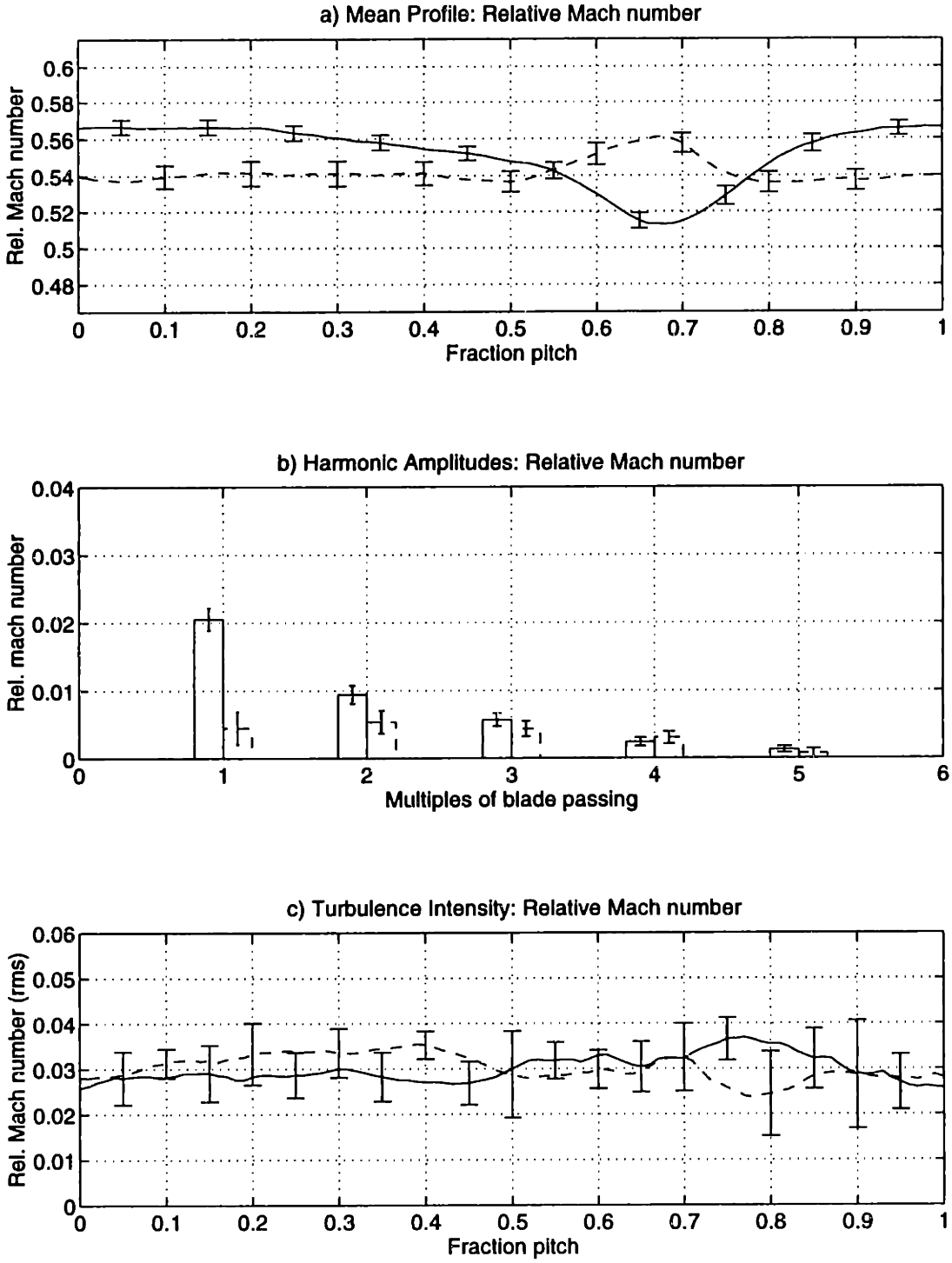

Figure 7-68: Relative Mach number ensemble-averaged profile, mean harmonic content, and turbulence profile at 50% span, 1.5c for the trailing edge blowing rotor with 2.0% (- -) and without (—) midspan-weighted injection

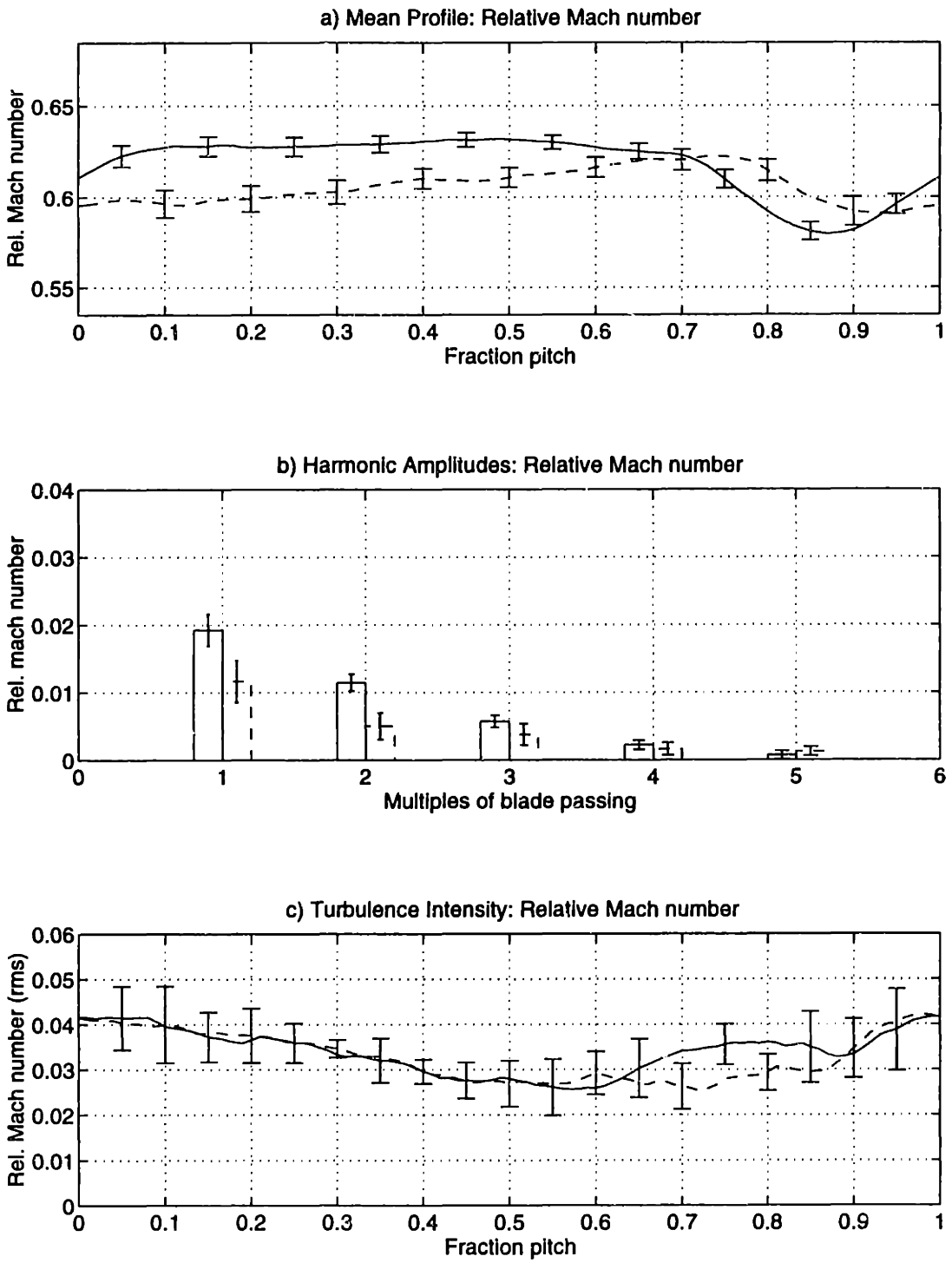

Figure 7-69: Relative Mach number ensemble-averaged profile, mean harmonic content, and turbulence profile at 75% span, 1.5c for the trailing edge blowing rotor with 2.0% (- -) and without (—) midspan-weighted injection

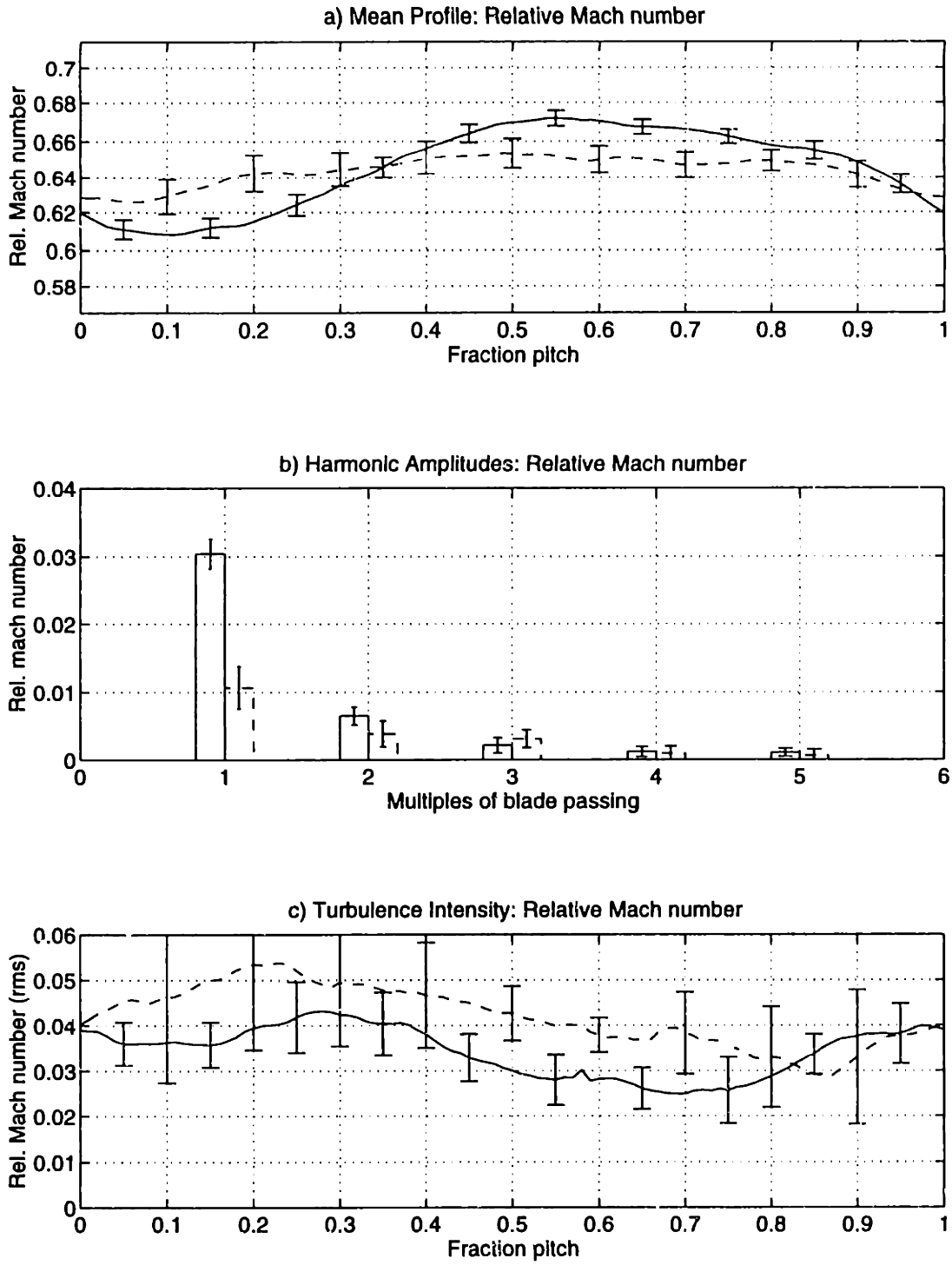

Figure 7-70: Relative Mach number ensemble-averaged profile, mean harmonic content, and turbulence profile at 87.5% span, 1.5c for the trailing edge blowing rotor with 2.0% (- -) and without (—) midspan-weighted injection

T.e. blowing rotor (no injection)	BPF	2*BPF	3*BPF	4*BPF	5*BPF
25% span, 1.5c	.0386	.0118	.0006	.0012	.0011
50% span, 1.5c	.0206	.0095	.0057	.0024	.0013
75% span, 1.5c	.0193	.0114	.0057	.0022	.0007
87.5% span, 1.5c	.0304	.0065	.0021	.0012	.0011
T.e. blowing rotor (2.0% midspan-weighted inj.)	**BPF**	**2*BPF**	**3*BPF**	**4*BPF**	**5*BPF**
25% span, 1.5c	.0185 (0.48)	.0100 (0.85)	.0050 (7.86)	.0019 (1.50)	.0004 (0.36)
50% span, 1.5c	.0045 (0.22)	.0054 (0.57)	.0044 (0.76)	.0030 (1.28)	.0007 (0.57)
75% span, 1.5c	.0116 (0.60)	.0050 (0.44)	.0038 (0.66)	.0016 (0.73)	.0013 (1.81)
87.5% span, 1.5c	.0107 (0.35)	.0038 (0.59)	.0031 (1.47)	.0009 (0.78)	.0006 (0.58)

Table 7.5: Wake relative Mach number harmonic amplitudes at 1.5 chord for the trailing edge blowing rotor with and without 2.0% midspan-weighted injection (injection harmonic amplitudes also shown as fraction of no injection harmonic amplitudes at 1.5 chord)

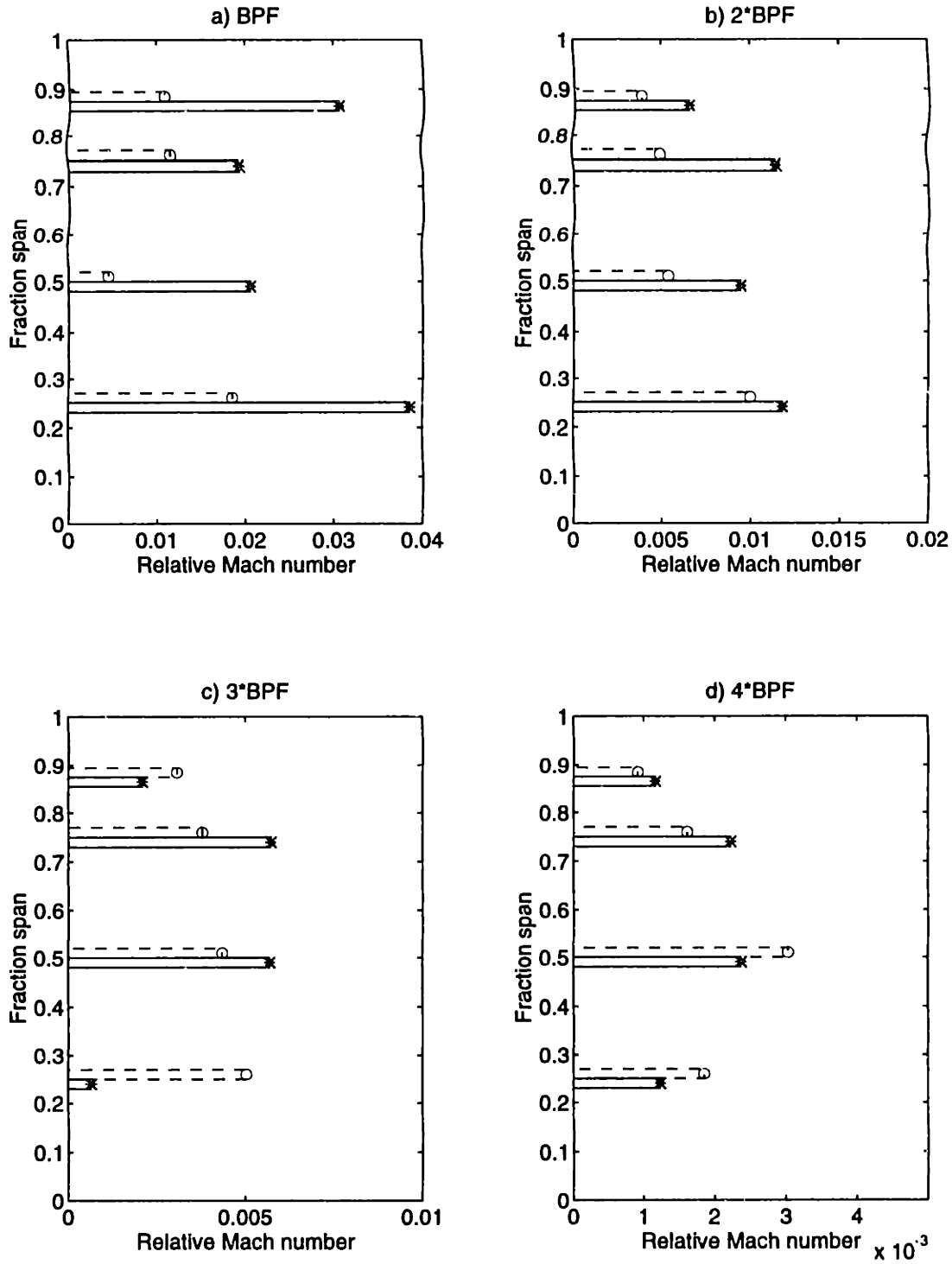

Figure 7-71: Wake relative Mach number harmonic amplitudes at 1.5 chord versus span: no injection (—) and 2.0% midspan-weighted injection (- -)

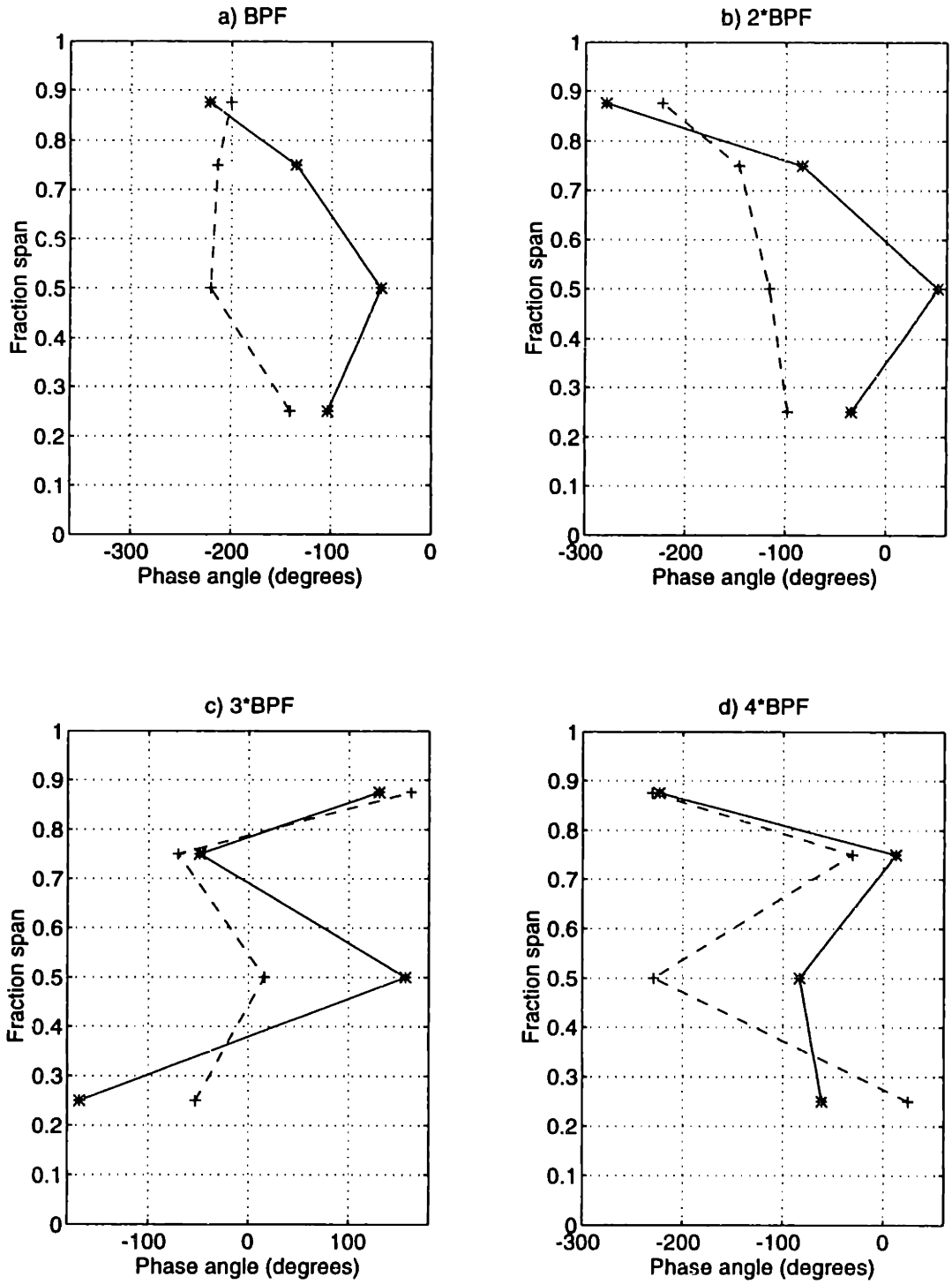

Figure 7-72: Phase angles for the first four BPF harmonics of relative Mach number at 1.5 chord for the trailing edge blowing rotor with 2.0% (- -) and without (—) midspan-weighted injection

7.6 Trailing Edge Blowing Rotor: 1.8% midspan-weighted injection

Because of the high injection rates in the midspan region with the 2.0% injection rate, the mass flow rate for the midspan-weighted injection was decreased to approximately 1.8% of the fan throughflow. If the injection was held low enough such that all sections of the span remained underblown, then there was a reasonable chance of maintaining the same radial wake harmonic phase variation as the no injection configuration. Maintaining the same phase variation and achieving reasonably uniform reduction in the wake harmonic amplitudes along the span was the only way to assure reduction of the total radiated noise.

Time only allowed for one set of flow measurements at 1.5 chord, and these are presented in Figures 7-73 through 7-76. Additional flow quantities are shown in Appendix E. The wake is seen to be just slightly overblown at 50% span, and underblown over the rest of the span. The wake harmonic amplitude reductions at 50% are very large, and the peak turbulence intensity is decreased at 50 and 75% span by approximately 25%. The wake harmonic amplitudes (1 through 5*BPF) are tabulated in Table 7.6 and shown graphically (1-4*BPF) versus span in Figure 7-77. The harmonic phases are plotted in Figure 7-78 for the first four multiples of BPF. The phase variation of BPF is seen to be almost the same as with no injection, but the 2*BPF harmonic phase at 50% span was shifted about 180 degrees.

For maximum noise reduction, the best advice the author can give at this time is to design the injection to achieve a momentumless wake, and then slightly reduce the injection flow rate. This strategy will assure that all spanwise locations are slightly underblown, keep the wake harmonic phase angles approximately the same as without injection, and reduce the wake harmonic amplitudes significantly. However, if the wake is skewed into a 'C' shape (like the fan used in this study), the use of overblowing to increase the phase angle variation of the wake harmonics along the span of the stator may produce additional noise reduction.

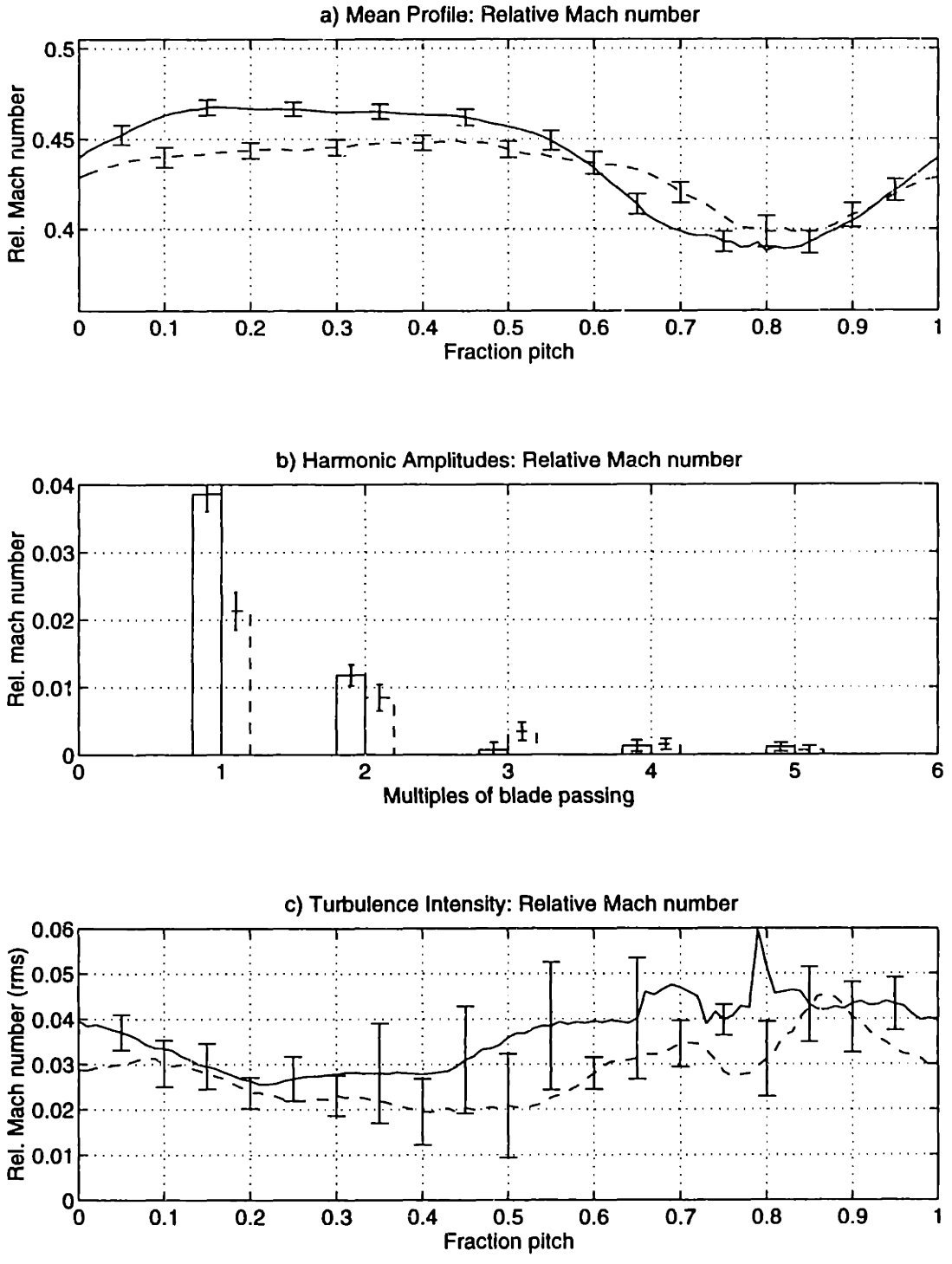

Figure 7-73: Relative Mach number ensemble-averaged profile, mean harmonic content, and turbulence profile at 25% span, 1.5c for the trailing edge blowing rotor with 1.8% (- -) and without (—) midspan-weighted injection

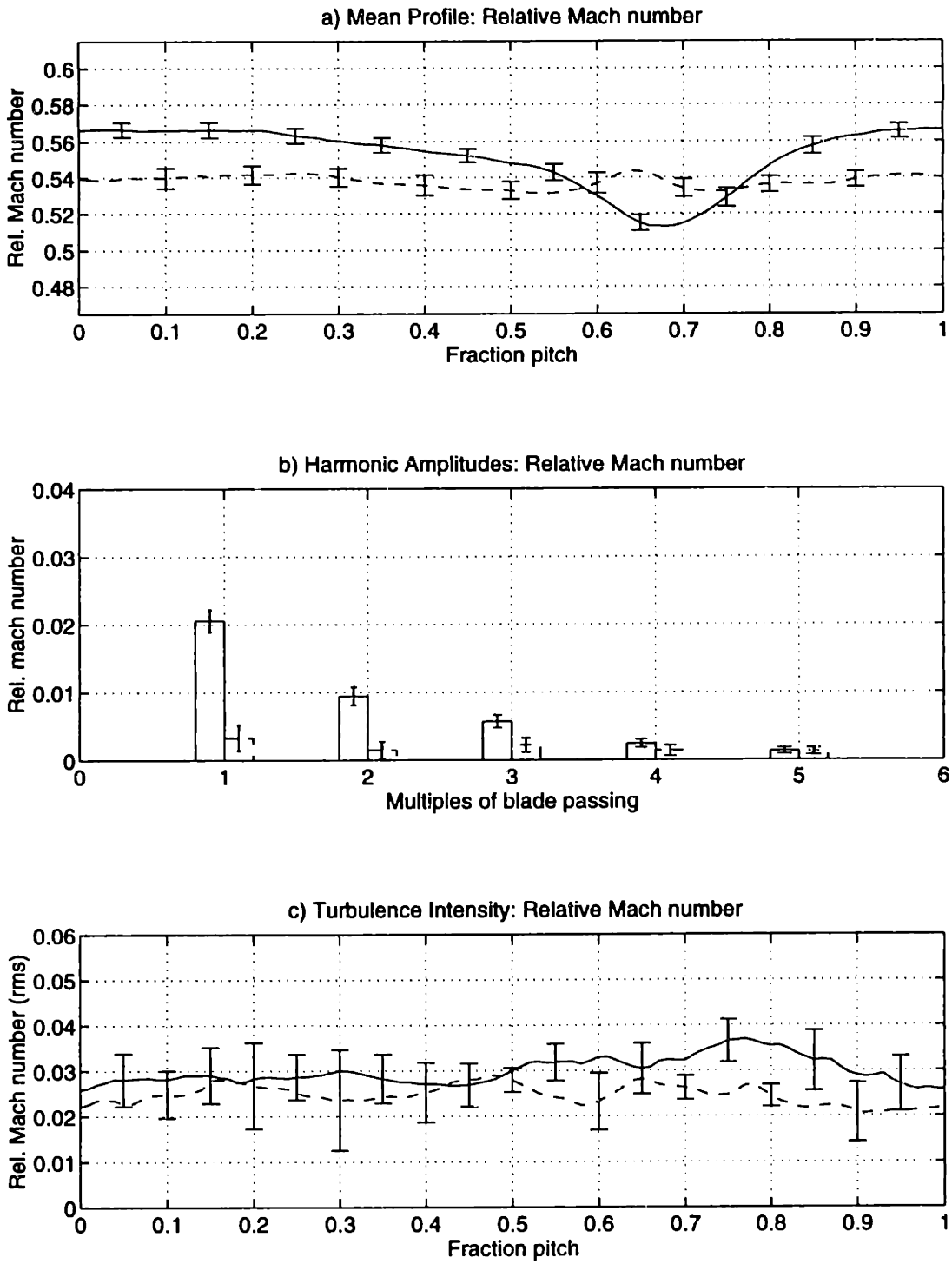

Figure 7-74: Relative Mach number ensemble-averaged profile, mean harmonic content, and turbulence profile at 50% span, 1.5c for the trailing edge blowing rotor with 1.8% (- -) and without (—) midspan-weighted injection

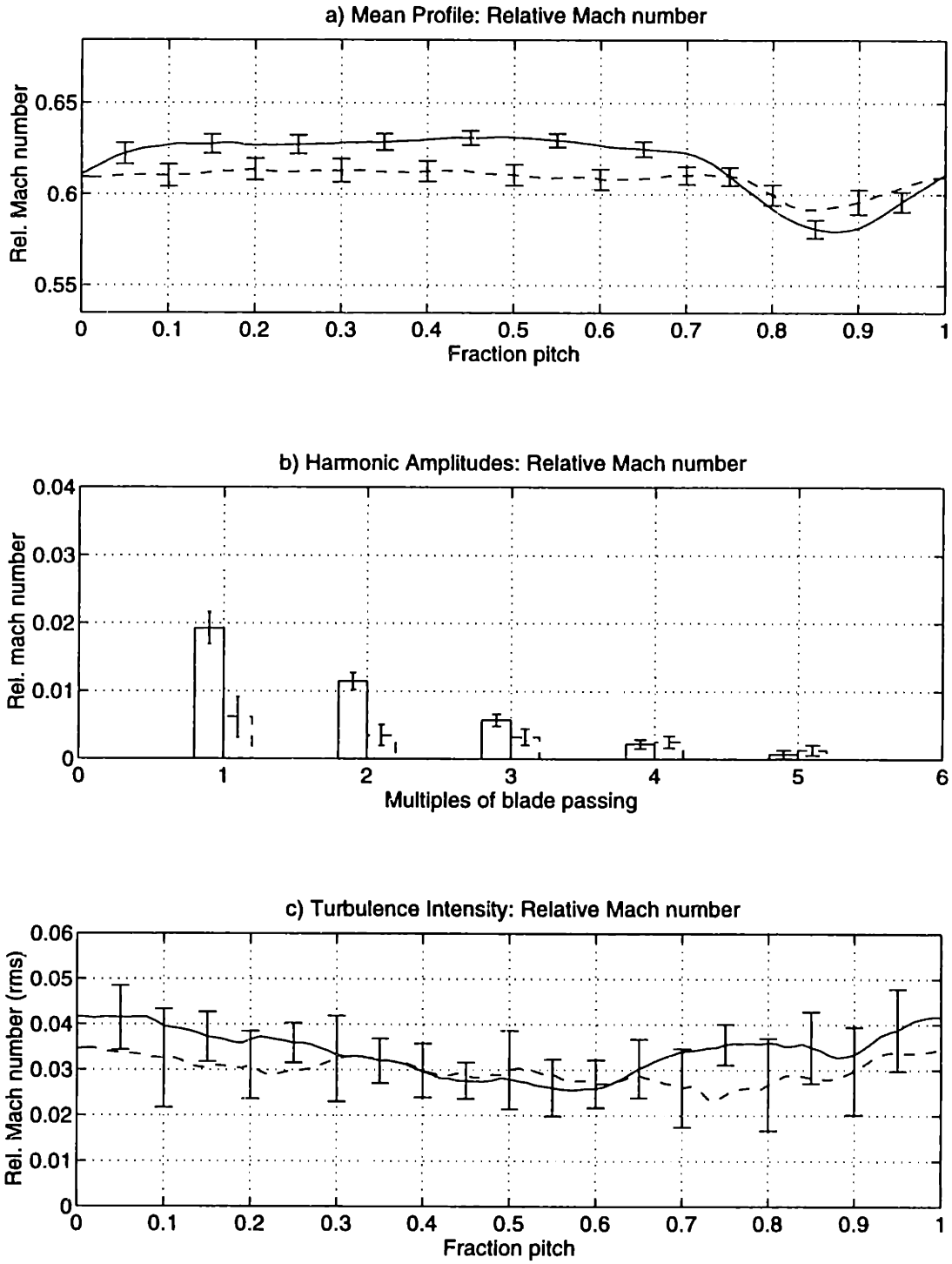

Figure 7-75: Relative Mach number ensemble-averaged profile, mean harmonic content, and turbulence profile at 75% span, 1.5c for the trailing edge blowing rotor with 1.8% (- -) and without (—) midspan-weighted injection

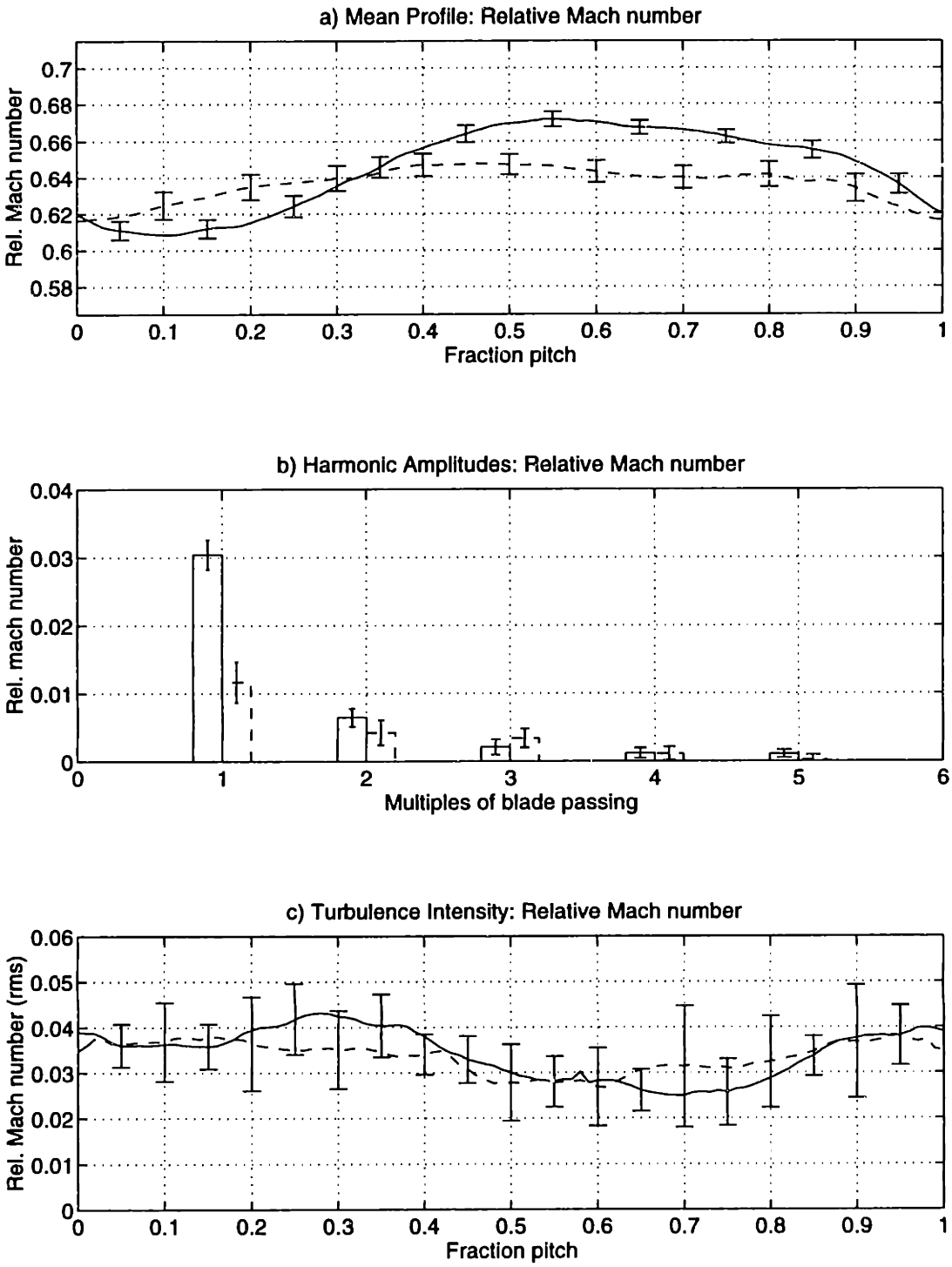

Figure 7-76: Relative Mach number ensemble-averaged profile, mean harmonic content, and turbulence profile at 87.5% span, 1.5c for the trailing edge blowing rotor with 1.8% (- -) and without (—) midspan-weighted injection

T.e. blowing rotor (no injection)	BPF	2*BPF	3*BPF	4*BPF	5*BPF
25% span, 1.5c	.0386	.0118	.0006	.0012	.0011
50% span, 1.5c	.0206	.0095	.0057	.0024	.0013
75% span, 1.5c	.0193	.0114	.0057	.0022	.0007
87.5% span, 1.5c	.0304	.0065	.0021	.0012	.0011
T.e. blowing rotor (1.8% midspan-weighted inj.)	**BPF**	**2*BPF**	**3*BPF**	**4*BPF**	**5*BPF**
25% span, 1.5c	.0213 (0.55)	.0085 (0.72)	.0034 (5.33)	.0015 (1.20)	.0006 (0.54)
50% span, 1.5c	.0033 **(0.16)**	.0014 **(0.15)**	.0022 **(0.38)**	.0013 **(0.56)**	.0012 **(0.94)**
75% span, 1.5c	.0062 (0.32)	.0035 (0.30)	.0032 (0.57)	.0025 (1.14)	.0013 (1.84)
87.5% span, 1.5c	.0117 (0.38)	.0042 (0.65)	.0034 (1.63)	.0011 (0.97)	.0002 (0.15)

Table 7.6: Wake relative Mach number harmonic amplitudes at 1.5 chord for the trailing edge blowing rotor with and without 1.8% midspan-weighted injection (injection harmonic amplitudes also shown as fraction of no injection harmonic amplitudes at 1.5 chord)

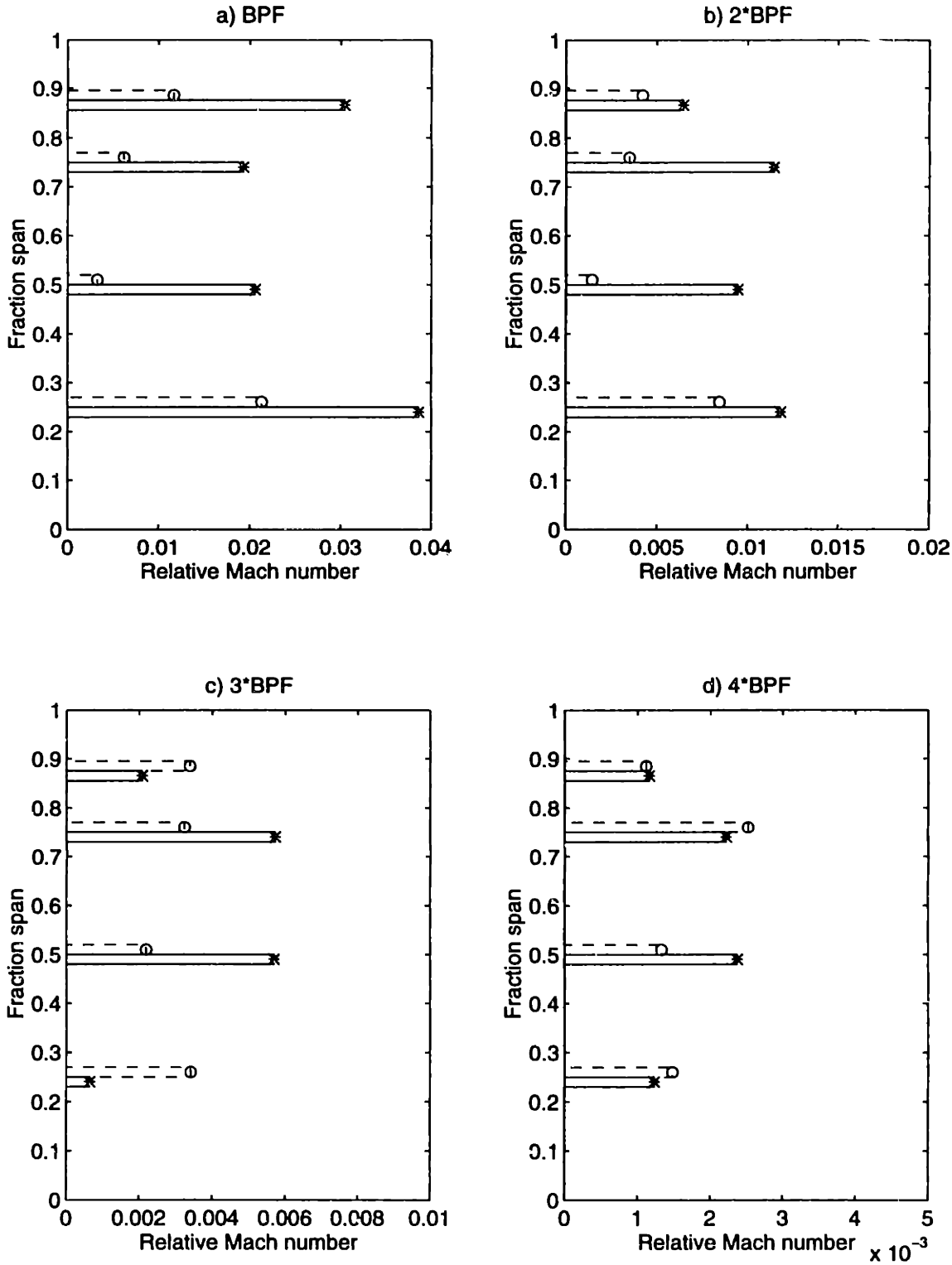

Figure 7-77: Wake relative Mach number harmonic amplitudes at 1.5 chord versus span: no injection (—) and 1.8% midspan-weighted injection (- -)

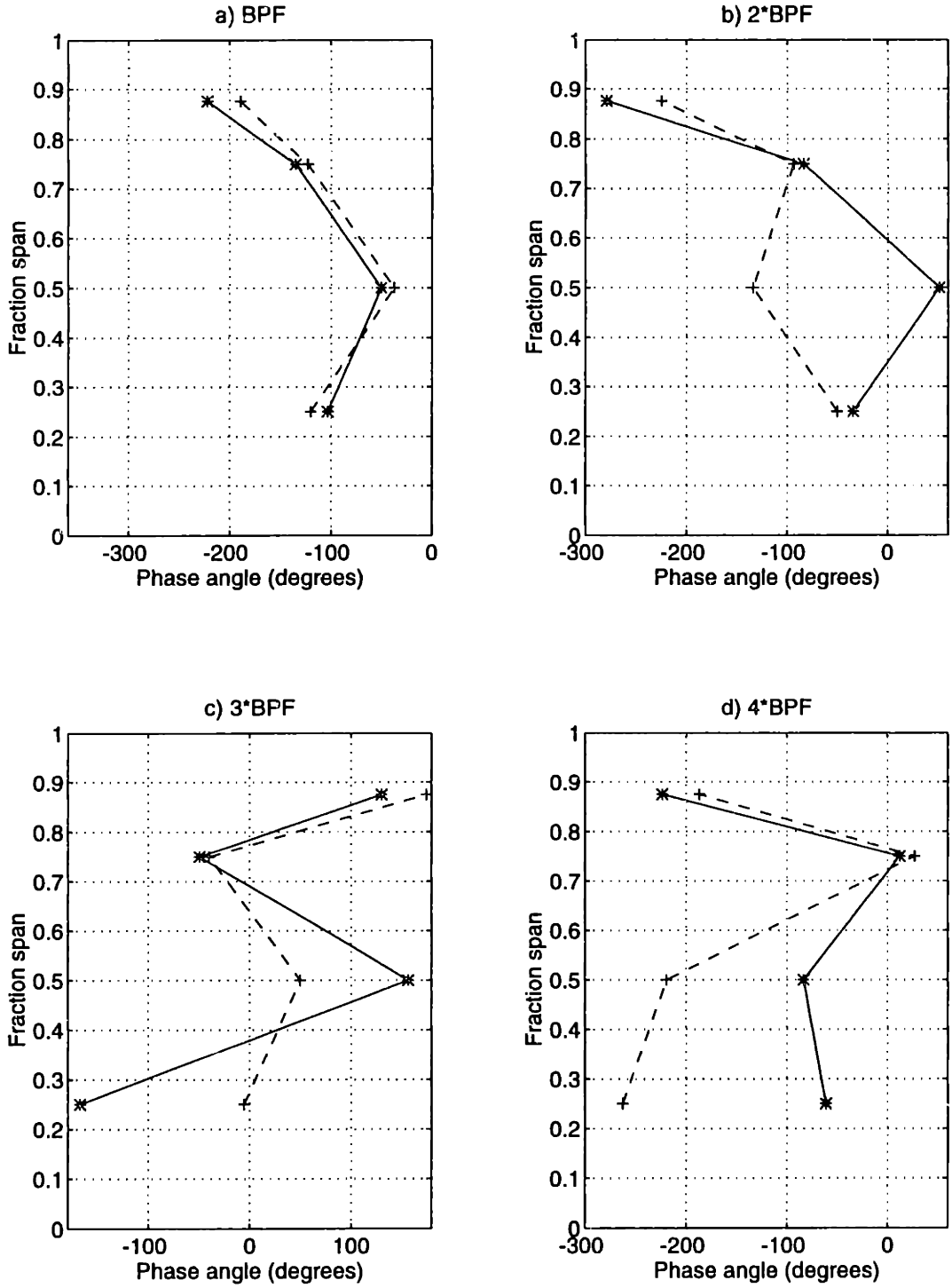

Figure 7-78: Phase angles for the first four BPF harmonics of relative Mach number at 1.5 chord for the trailing edge blowing rotor with 1.8% (- -) and without (—) midspan-weighted injection

7.7 Efficiency Measurements

The rotor adiabatic efficiency was calculated for the baseline solid-bladed rotor and for the trailing edge blowing rotor with and without injection. Direct calculation of efficiency requires total pressure and total temperature measurements upstream and downstream of the rotor, but only pressure and Mach number measurements were completed in the facility. The upstream total temperature was estimated by assuming isentropic expansion in the supply tank, and the downstream total temperature was written in terms of speed of sound and Mach number. The Euler Turbine equation was then used to iteratively solve for the total temperature ratio across the rotor (see Reijnen [31]).

The efficiency of the trailing edge blowing rotor (no injection) was found to be 0 to 4.9% lower than the baseline solid-bladed rotor, depending on radial position. However, the 95% confidence interval in the calculated efficiency is approximately 4 percent, and the external blade shapes (besides the injection orifices) are slightly different.

The efficiency with injection was calculated by summing the energy contributions from the main flow and from the injection flow, which has an initial total pressure under the hub of approximately 3 times the throughflow total pressure. The efficiency with injection is given by

$$\eta = \frac{\left[\left(\frac{P_{t_2}}{P_{t_{1,p}}}\right)^{(\gamma-1)/\gamma} - 1\right] + \frac{m_s}{m_p}\left(\frac{T_{t_{1,s}}}{T_{t_{1,p}}}\right)\left[\left(\frac{P_{t_2}}{P_{t_{1,s}}}\right)^{(\gamma-1)/\gamma} - 1\right]}{\left[\frac{T_{t_2}}{T_{t_{1,p}}} - 1\right] + \frac{m_s}{m_p}\left(\frac{T_{t_{1,s}}}{T_{t_{1,p}}}\right)\left[\frac{T_{t_2}}{T_{t_{1,s}}} - 1\right]} \tag{7.1}$$

The total pressure and total temperature are given by P_t and T_t, respectively, with '1' corresponding to inlet conditions and '2' corresponding to conditions downstream of the rotor. The mass flows are m_p and m_s, with the subscript p referring for the primary flow and s referring to the secondary (injection) flow. The efficiency without injection is obtained by setting $m_s = 0$.

The primary result of the efficiency calculations was that injection does not significantly alter the efficiency of the rotor. Changes of about one percent were observed with injection, but no definite conclusions could be reached, since the changes were smaller than the estimated 95% confidence intervals. The trailing edge blowing rotor without injection

showed some spanwise positions with efficiency reductions relative to the baseline solid-bladed rotor up to about 5 percent, but these changes were also generally within the error bars of about 4 percent.

7.8 Summary of Trailing Edge Blowing Rotor Flow Field Measurements

The results presented in Sections 7.2 through 7.6 have shown that about 80% reduction of the relative Mach number wake harmonic amplitudes (first five harmonics of BPF) is possible. For injection that does not completely fill in the momentum deficit of the wake, the harmonic amplitudes are reduced (depending on the amount of momentum addition) and the harmonic phases remain approximately the same as without blowing. When the injection adds additional momentum beyond a momentumless wake and a 'jet' results, the harmonic phases shift by approximately 180 degrees, and significant changes in the radial wake harmonic phase variations occur. These phase changes, together with the changes in harmonic amplitudes, cause the coupling of the stator unsteady pressure fields to the acoustic modes to change in radial mode content. Depending on the change in radial variation in the wake harmonics due to injection, the total radiated noise can either be increased or decreased, even if the wake harmonic amplitudes are reduced.

Because trailing edge blowing offers leverage on both the wake harmonic amplitude and phase, the radial variation of the wake can be tailored to achieve a wide range of possible wake configurations entering the stator row. To fully utilize this potential, additional understanding of the stator pressure field and acoustic coupling is required to determine the optimal injection distribution for maximum noise reduction.

In addition to reducing the wake harmonic amplitudes at 1.5 chords downstream of the rotor, trailing edge blowing was shown to significantly reduce the wake harmonics just downstream of the rotor at 0.1 chord. For injection that resulted in approximately a momentumless wake (1.9% tip-weighted and 2.0% midspan-weighted injection at 75% span) the BPF and 2*BPF wake harmonic amplitudes at 0.1 chord were 40% or more smaller than the wake harmonic amplitudes at 1.5 chord with no injection (see Tables 7.2 and 7.4).

These results imply that significant reduction of the rotor/stator spacing may be possible without increasing the radiated noise. Although the wake skew will be reduced by decreasing the axial spacing, radial phase variations can be applied to the wake harmonics through underblowing and overblowing different spanwise regions of the wake.

Large reductions in the turbulence intensity at 1.5 chord were not obtained with trailing edge blowing due to the high level of turbulence in the freestream. The turbulence level was measured upstream of the rotor and found to be approximately equal to the freestream value at 0.1 chord (about 4% of the inlet Mach number) and about 30% lower than the freestream value at 1.5 chord. Some of the turbulence intensity measured downstream of the rotor may be due to blade-to-blade differences, which will manifest themselves at multiples of shaft frequency. Therefore, even with complete smoothing of the wake, the turbulence intensity can only be reduced by approximately 50% at the face of the stator row for the experimental set-up used in this research. These reductions may not be true for in-service turbofan engines, however, if the turbulence level at the fan face is below 4% of the mean inlet Mach number and the rotor blade-to-blade differences are minimal.

Finally, the trailing edge blowing rotor does not have a large reduction in performance in comparison to the solid-bladed rotor. The total pressure ratio was approximately 1% lower with the trailing edge blowing blades (no injection) and the wake harmonic amplitudes were slightly higher. The efficiencies of the two rotors (with and without injection) were generally within the 95% confidence intervals of about 4% in the efficiency calculations.

CHAPTER 8

TRAILING EDGE BLOWING ROTOR: STATOR UNSTEADY PRESSURE AND MICROPHONE ACOUSTIC MEASUREMENTS

It was shown in Chapter 7 that significant smoothing of the wake mean profiles can be achieved with trailing edge blowing. While uniform spanwise reduction of the wake profiles was not obtained, the measurements showed that the wake can be filled to the point of overblowing, and thus there is sufficient volume within next generation fan blades for inclusion of trailing edge blowing passages. If the distribution of wake modification is determined for maximum noise reduction, it should be possible to design the appropriate blades.

While smoothing the wakes downstream of the rotor was the main thrust of the research, the final goal was to reduce the radiated acoustics due to rotor wake/stator interaction. To gain some understanding of the effects of trailing edge blowing on the stator unsteady pressure fields, stator unsteady surface pressure measurements were taken. These measurements on the stator surface could then be compared to the wake measurements just upstream of the stator at 1.5 chord. The results of the stator measurements are discussed in Sections 8.1 and 8.2.

Duct acoustic measurements were also taken. Because of the restrictive nature of the test facility geometry, acoustic data was only taken with microphones flush-mounted in the

outer shroud up and downstream of both the rotor and stator. While these measurements were only taken at the outer shroud and thus provide the sum of all the radial modes at a given multiple of blade passing frequency, qualitative conclusions can be drawn. The results of the acoustic measurements are presented in Section 8.4

8.1 Stator Unsteady Pressure Measurements: Baseline rotor vs. trailing edge blowing rotor (no injection)

Stator unsteady surface pressure measurements were taken with an instrumented stator blade. The blade was instrumented with 13 flush mounted Kulite pressure transducers on the suction and pressure surfaces (see Section 2.6.3). The location of the transducers along the chord is shown in Figure 2-12.

Stator measurements were taken with and without rotor trailing edge blowing, and the results of the no injection configuration are presented here. The data downstream of the trailing edge blowing rotor (no injection) is shown in dash-dot lines and is plotted with the data for the baseline rotor with solid blades for comparison. Measurements were taken at 50, 75, and 87.5% span.

The transducer data at each spanwise position will first be presented in Sections 8.1.1 through 8.1.3. The data includes the mean stator pressure envelope and the ensemble-averaged harmonic amplitudes and phases at each transducer. The difference in pressure across the blade was also calculated from the data. The amplitude and phase of the pressure difference at blade passing frequency between the suction and pressure surfaces is then plotted for the three spanwise positions in Section 8.1.4. As for the flow measurements, 95% confidence intervals are shown.

8.1.1 50% span

The mean pressure envelopes at 50% span for the baseline solid-bladed rotor and the trailing edge blowing rotor (no injection) are shown in Figure 8-1. The pressure is shown as a pressure coefficient, where the pressures are nondimensionalized by the upstream static

pressure and dynamic head for each rotor configuration. The trailing edge blowing rotor is seen to have a slightly higher pressure coefficient (overall offset) due to the lower upstream static pressure, but the envelope is almost identical. The range of periodic unsteady pressure at each transducer is also shown in the plots as dash-dot lines. These curves show the amplitude of the periodic pressure fluctuations on the blade surface for the sum of the first five multiples of blade passing frequency.

The harmonic amplitudes of the first three multiples of blade passing frequency, BPF, unsteady pressure are shown for the suction surface in Figure 8-2. Again, the baseline solid-bladed rotor is shown as solid lines, and the trailing edge blowing rotor is shown as dash-dot lines. In general, the harmonic amplitudes agree within approximately 5 dB, but the data is not expected to match exactly due to the change in wake harmonic amplitudes at 1.5 chord.

Similarly, the pressure surface harmonic amplitudes are shown in Figure 8-3. Again, differences on the order of 5 dB are seen at some transducers, particularly BPF where the wake harmonic amplitudes at 1.5 chord were different by approximately 25% for the baseline rotor and the trailing edge blowing rotor (no injection).

The phases of the stator pressure harmonics are shown in Figures 8-4 and 8-5 for the suction and pressure surfaces. Differences between the data downstream of the two rotors is again observed, with the phases of BPF and 2*BPF offset by approximately 30 degrees along most of the stator chord. This offset matches the change in wake phase angles observed in the wake measurements shown in Figure 7-19 at 50% span.

8.1.2 75% span

The stator mean pressure envelopes at 75% span are plotted in Figure 8-6 for the baseline and trailing edge blowing (no injection) rotors. As at 50% span, the pressure coefficients are offset for the two configurations due to the difference in upstream static pressure, but the envelopes are very similar.

The unsteady pressure harmonic amplitudes for the suction and pressure surfaces are shown in Figures 8-7 and 8-8. There are some differences in the stator harmonic amplitudes

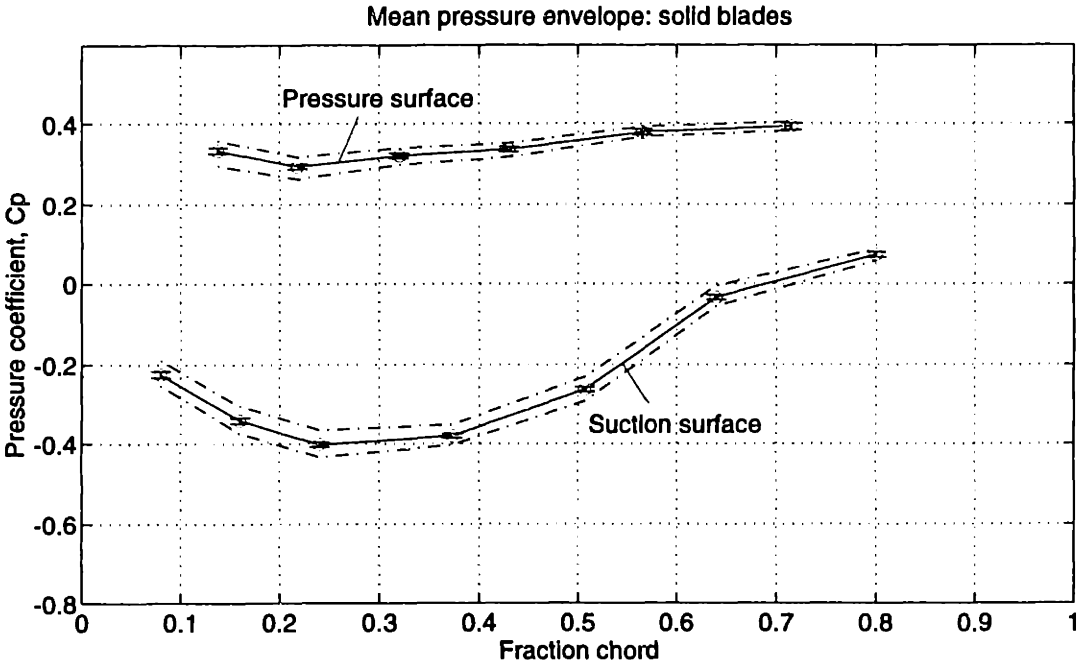

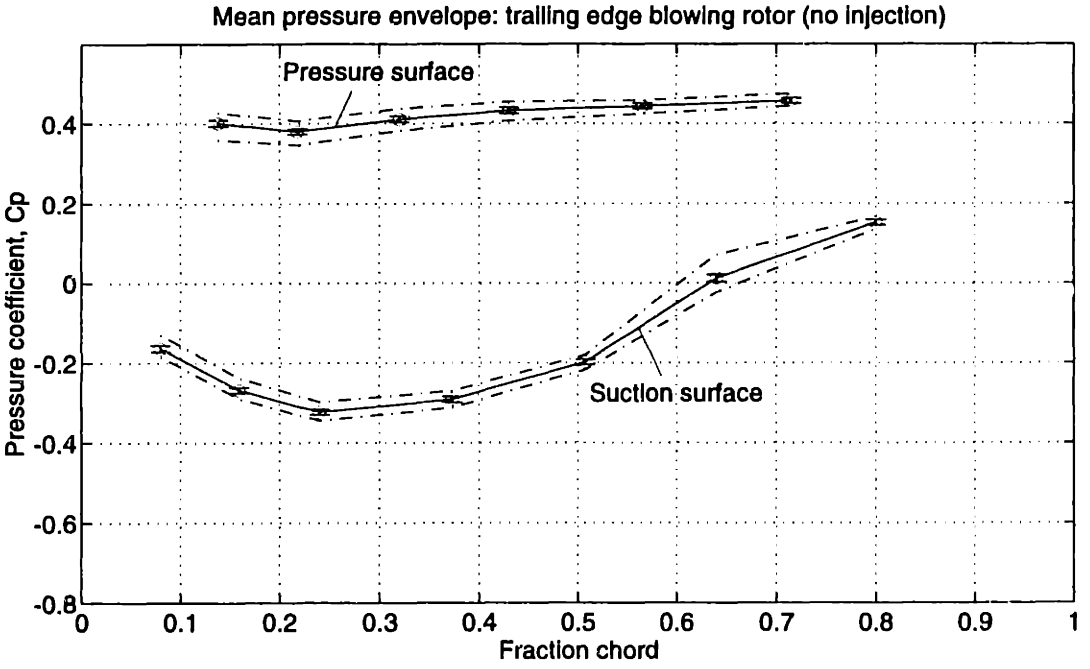

Figure 8-1: Stator time-mean pressure envelope at 50% span for the baseline solid-bladed rotor and the trailing edge blowing rotor with no injection [with periodic unsteady pressure envelope (- .)]

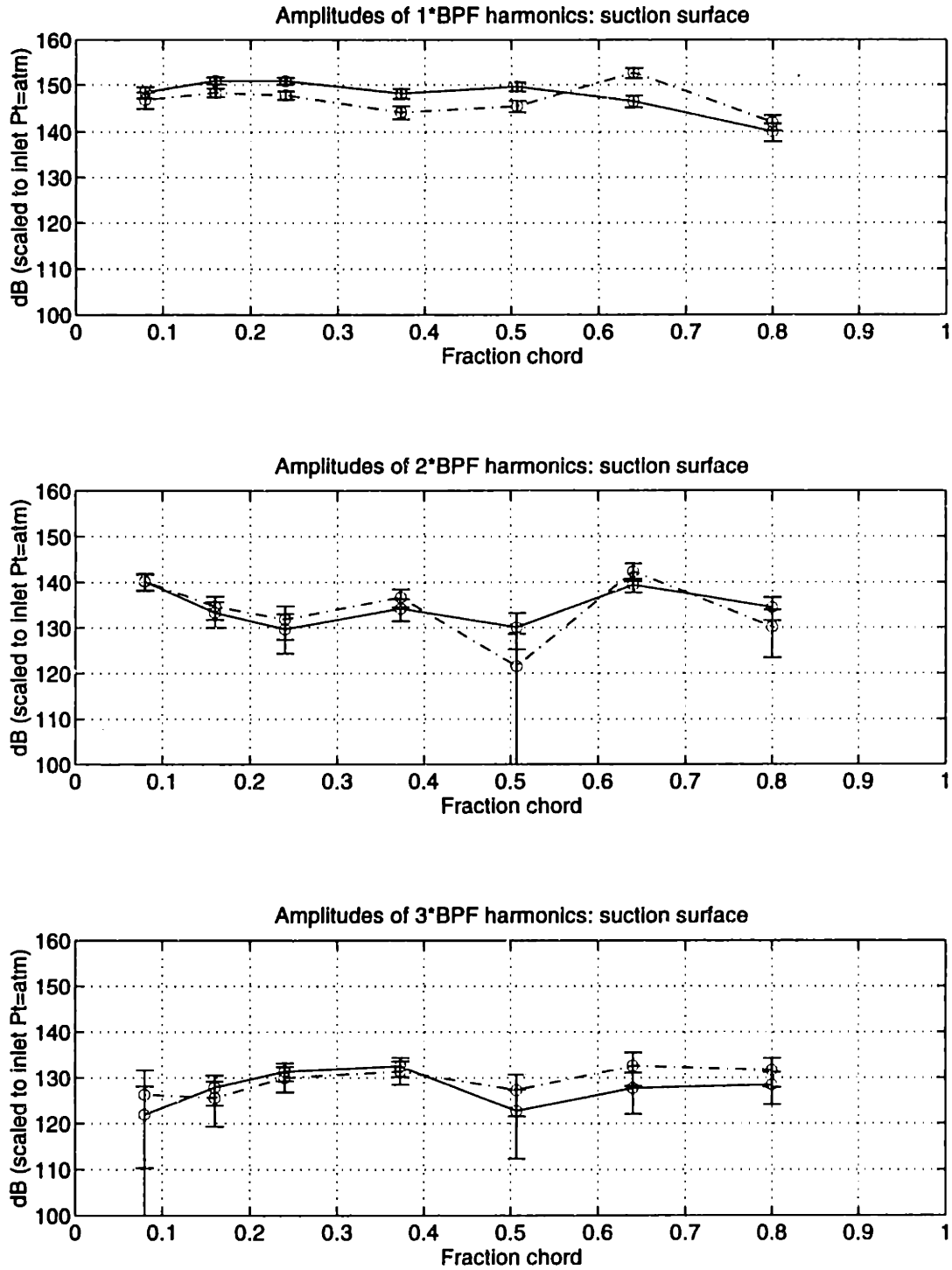

Figure 8-2: Stator suction surface harmonic amplitudes at 50% span for the baseline solid-bladed rotor (—) and the trailing edge blowing rotor with no injection (- .)

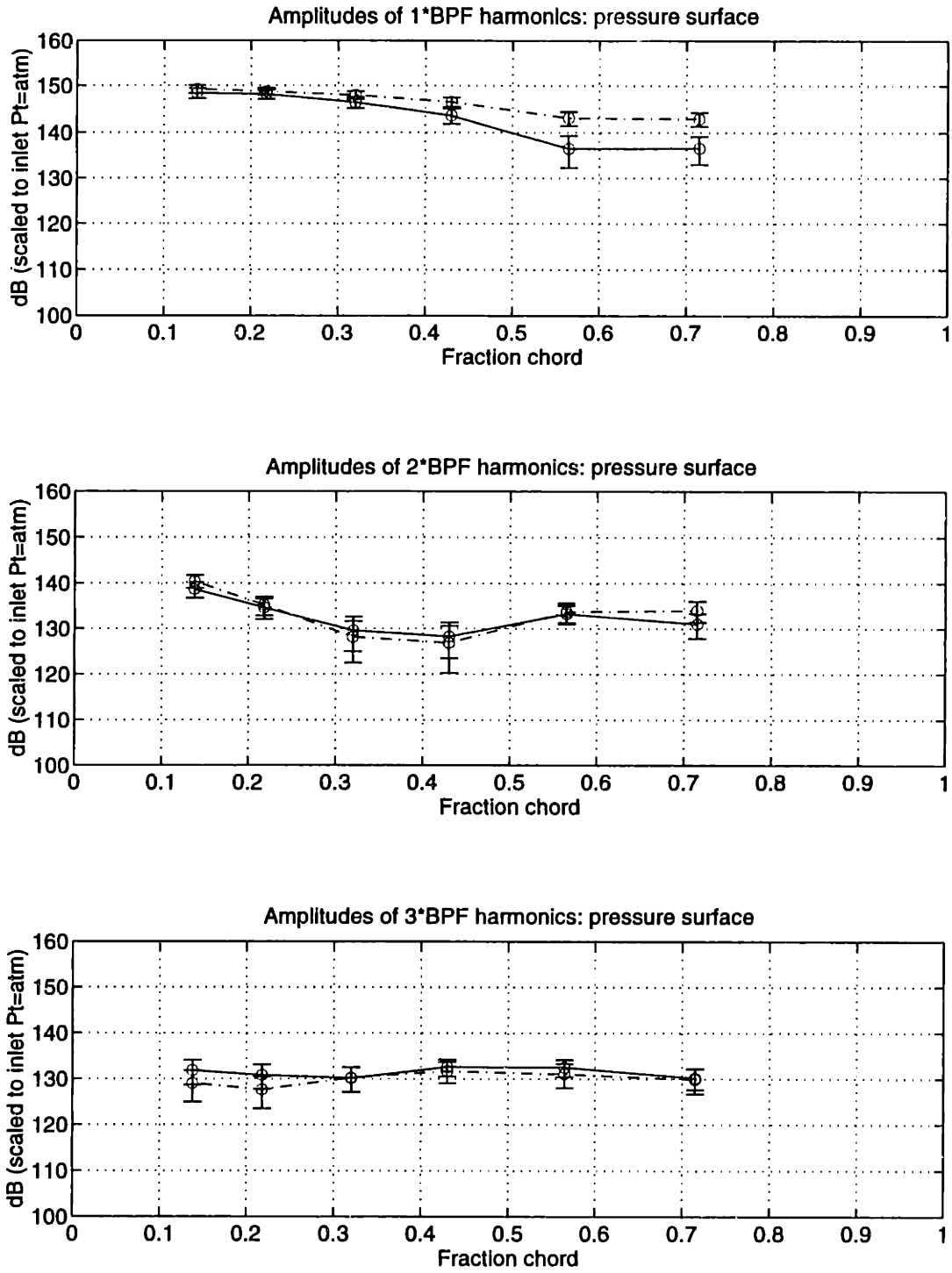

Figure 8-3: Stator pressure surface harmonic amplitudes at 50% span for the baseline solid-bladed rotor (—) and the trailing edge blowing rotor with no injection (- .)

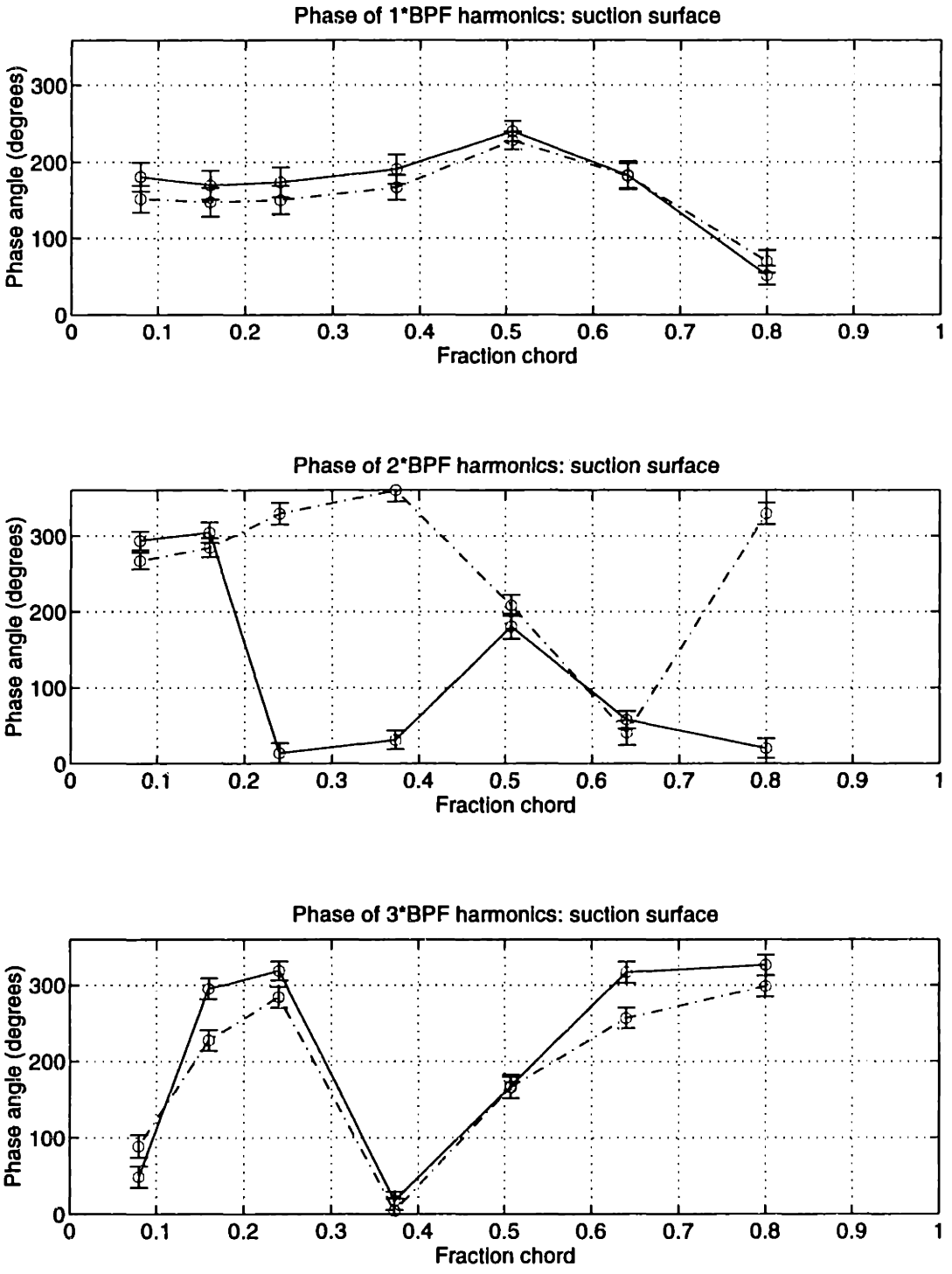

Figure 8-4: Stator suction surface harmonic phases at 50% span for the baseline solid-bladed rotor (—) and the trailing edge blowing rotor with no injection (– .)

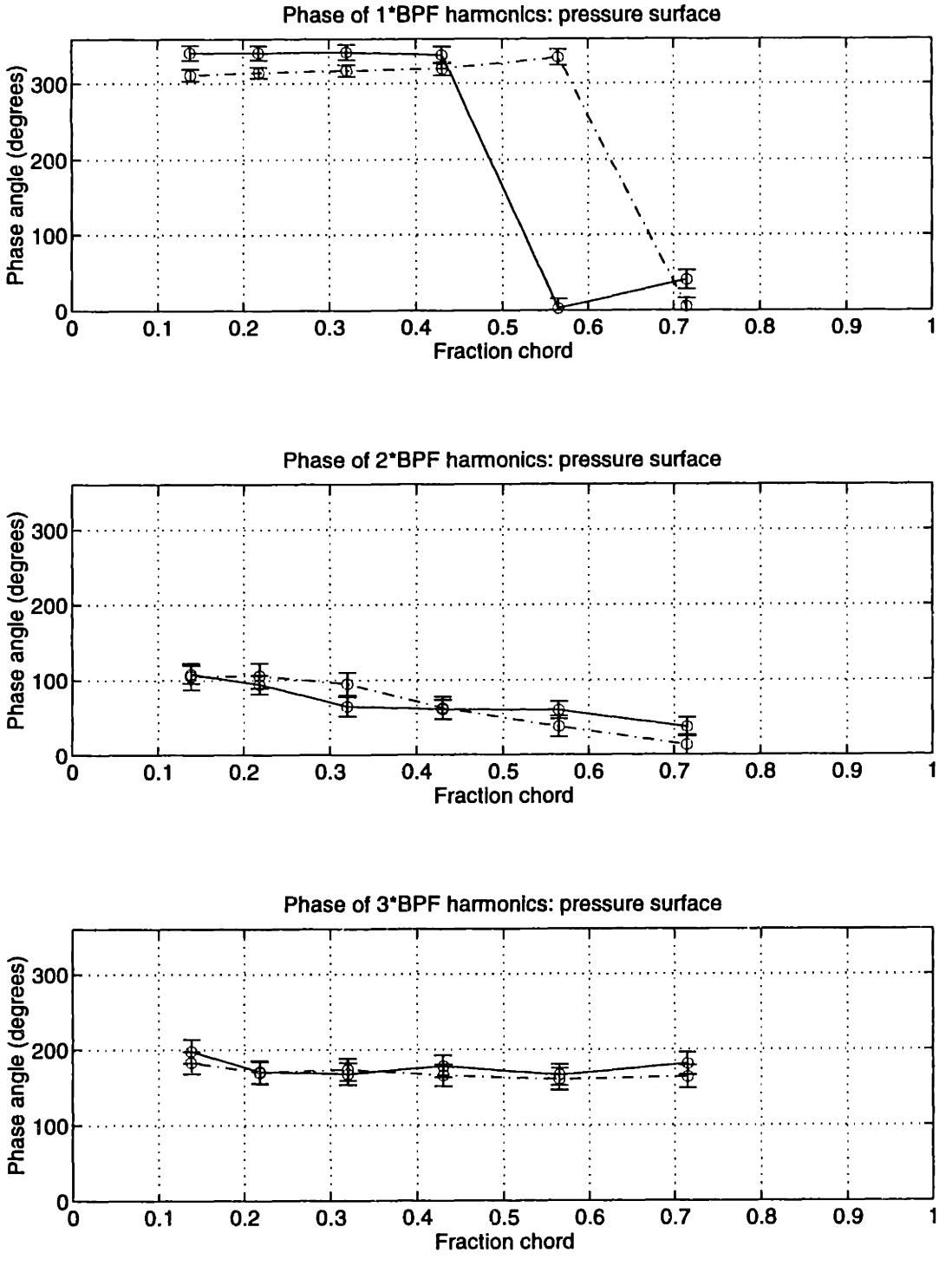

Figure 8-5: Stator pressure surface harmonic phases at 50% span for the baseline solid-bladed rotor (—) and the trailing edge blowing rotor with no injection (- .)

between the two rotors at 75% span, where the wake harmonics are different at 1.5 chord by approximately 18% for BPF and 30% for 2*BPF. The amplitudes at BPF are within approximately 3 dB along the chord on both the suction and pressure surfaces; an increase in wake harmonic amplitude of 18% would correspond to about 1.4 dB change in the stator pressure perturbations according in linear strip theory.

The harmonic phases for the suction and pressure surfaces are shown in Figures 8-9 and 8-10. Again, the phases are slightly different for the two rotor configurations, approximately matching the difference in wake harmonic phases at 1.5 chord of approximately 3.5 degrees at BPF and 10 degrees at 2*BPF.

8.1.3 87.5% span

The mean pressure coefficient envelopes at 87.5% span are plotted in Figure 8-11. With the higher upstream static pressure, the pressure coefficients are again offset for the two rotors. The unsteady pressure ranges are observed to be quite close.

The suction and pressure surface harmonic amplitudes are shown in Figures 8-12 and 8-13, and the harmonic phases are shown in Figures 8-14 and 8-15. The wakes at 1.5 chord have differences in the harmonic amplitudes of about 16% at BPF, 22% at 2*BPF, and 40% at 3*BPF, and the phases are different by about 10 degrees at BPF, 20 degrees at 2*BPF, and 160 degrees at 3*BPF. The amplitudes of the stator pressure harmonics appear to follow these wake differences fairly well, but the stator phases are more difficult to distinguish. The BPF harmonics on the stator seem to be offset by approximately 10 degrees, but the higher harmonics have more inconsistent behavior, particularly 3*BPF. Because the wake 3*BPF harmonic phase variation from 75% span to the tip is substantially different between the baseline rotor and the trailing edge blowing rotor, it may not be appropriate to directly compare stator unsteady pressure phases at 87.5% span.

8.1.4 Amplitude and phase of pressure difference

While the higher harmonics of unsteady pressure on the stator appear to exhibit some strange behavior when the wake harmonic phases change their radial variation, the wake

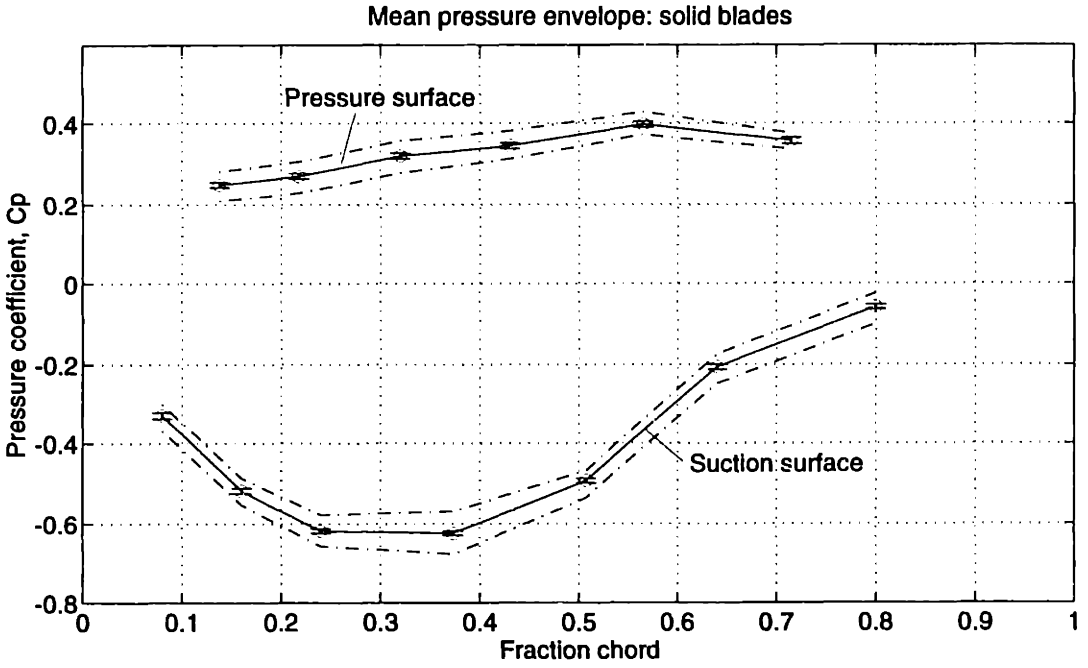

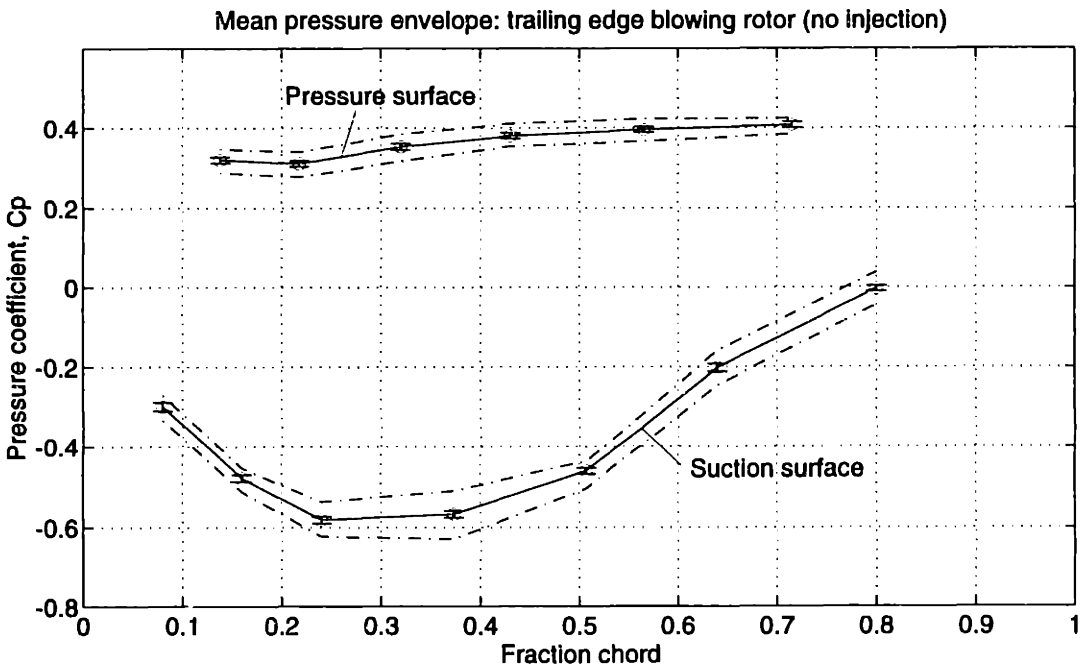

Figure 8-6: Stator time-mean pressure envelope at 75% span for the baseline solid-bladed rotor and the trailing edge blowing rotor with no injection [with periodic unsteady pressure envelope (– .)]

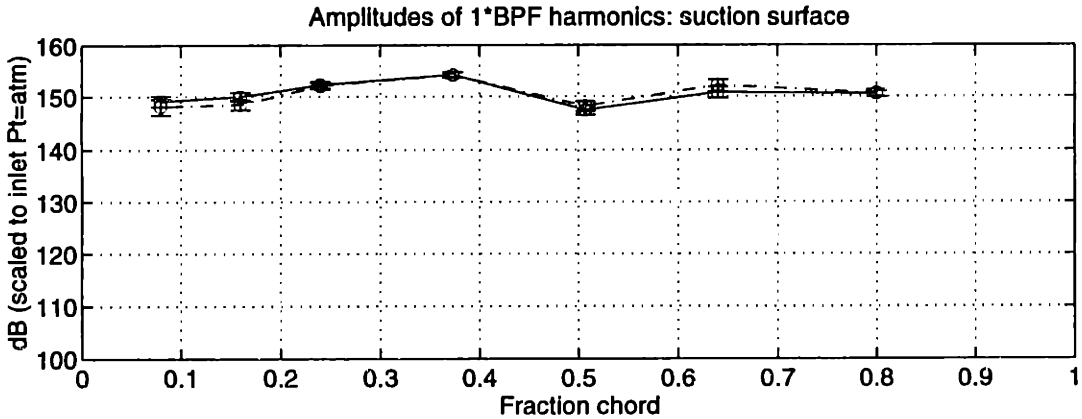

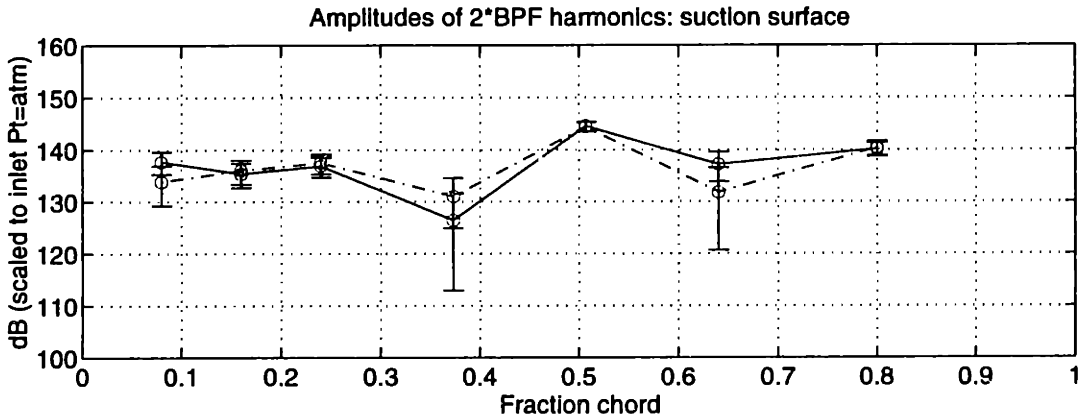

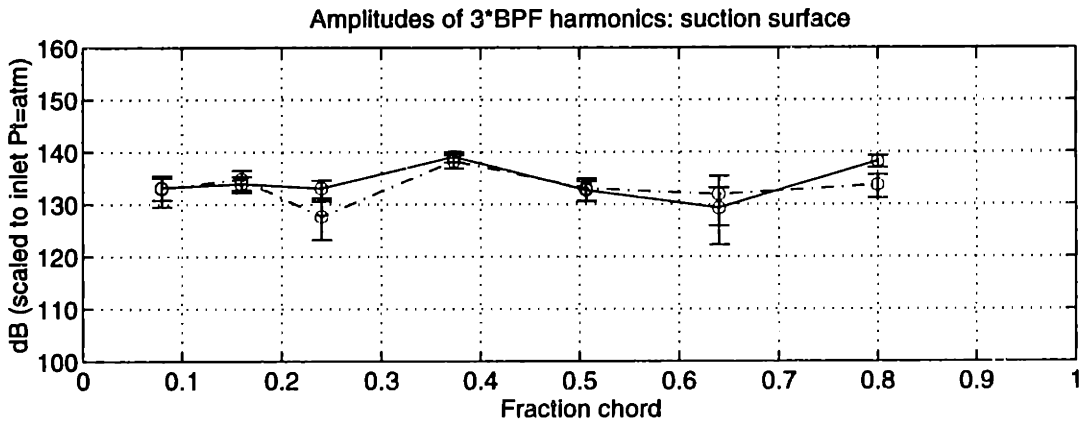

Figure 8-7: Stator suction surface harmonic amplitudes at 75% span for the baseline solid-bladed rotor (—) and the trailing edge blowing rotor with no injection (- .)

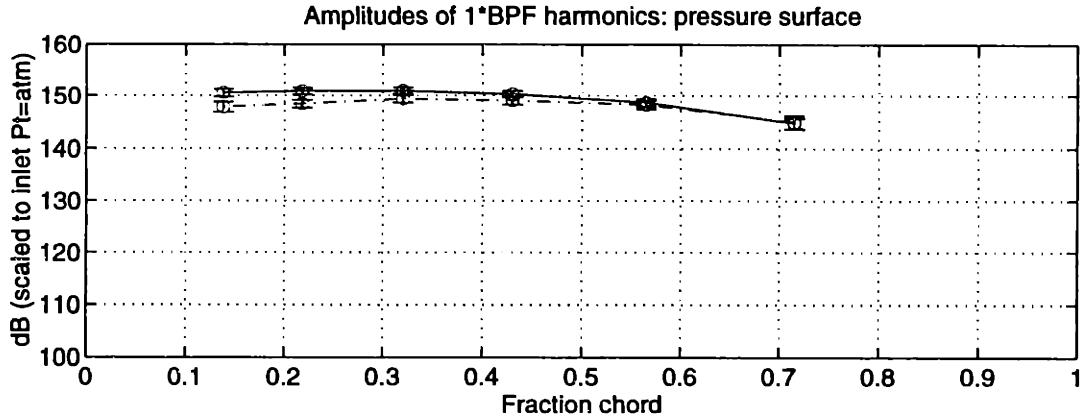

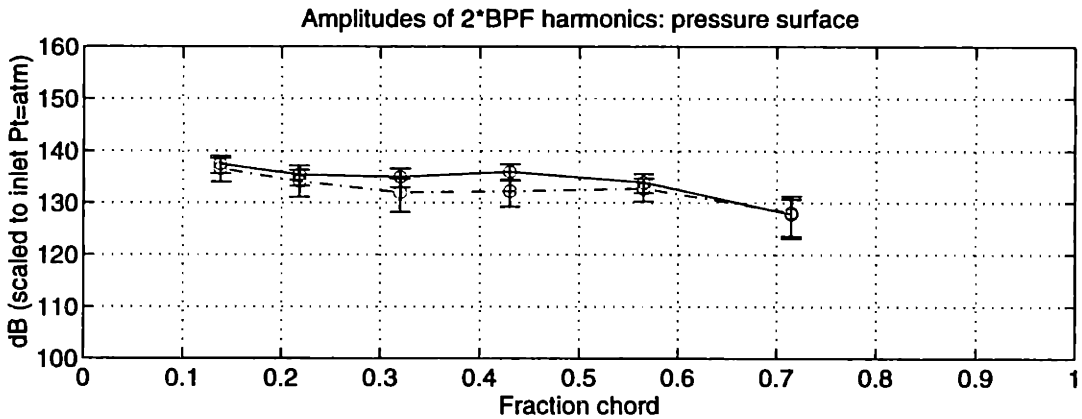

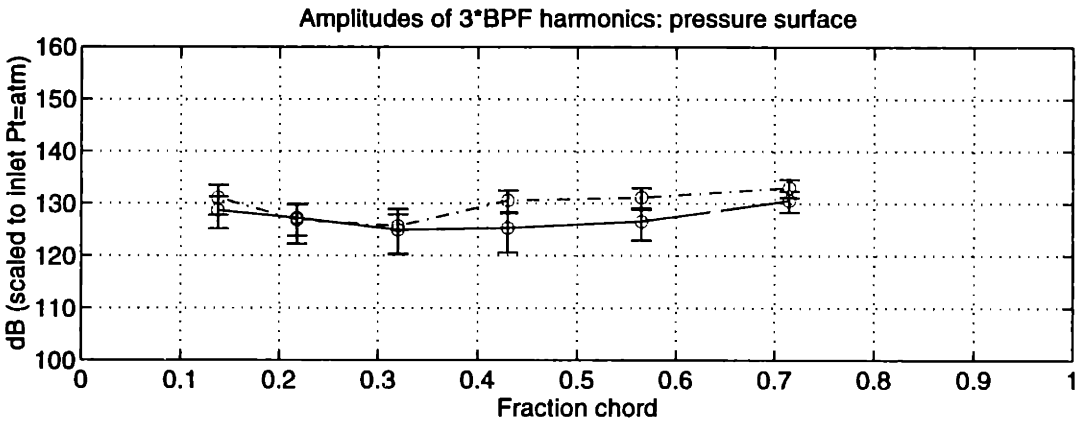

Figure 8-8: Stator pressure surface harmonic amplitudes at 75% span for the baseline solid-bladed rotor (—) and the trailing edge blowing rotor with no injection (- .)

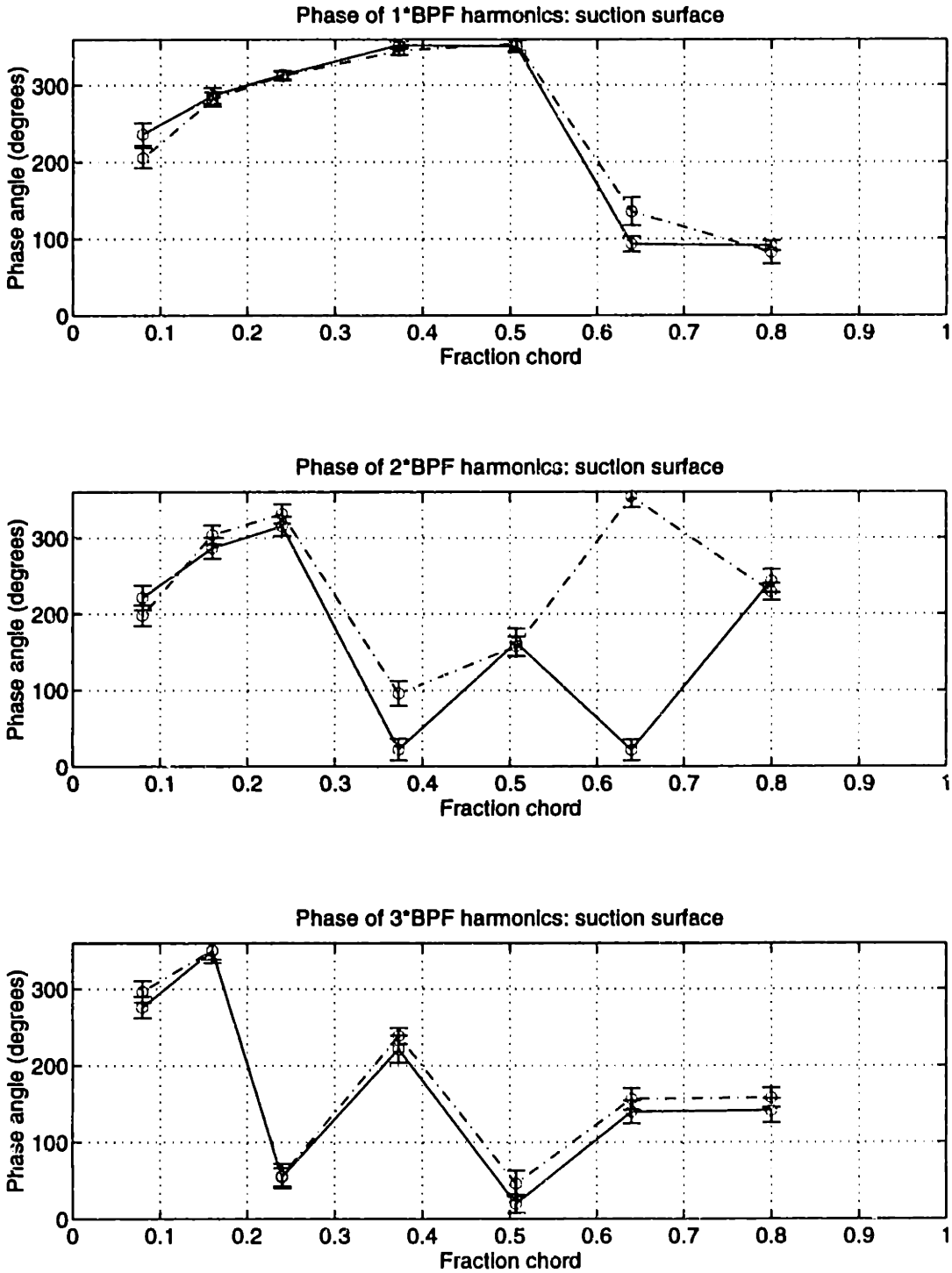

Figure 8-9: Stator suction surface harmonic phases at 75% span for the baseline solid-bladed rotor (—) and the trailing edge blowing rotor with no injection (- .)

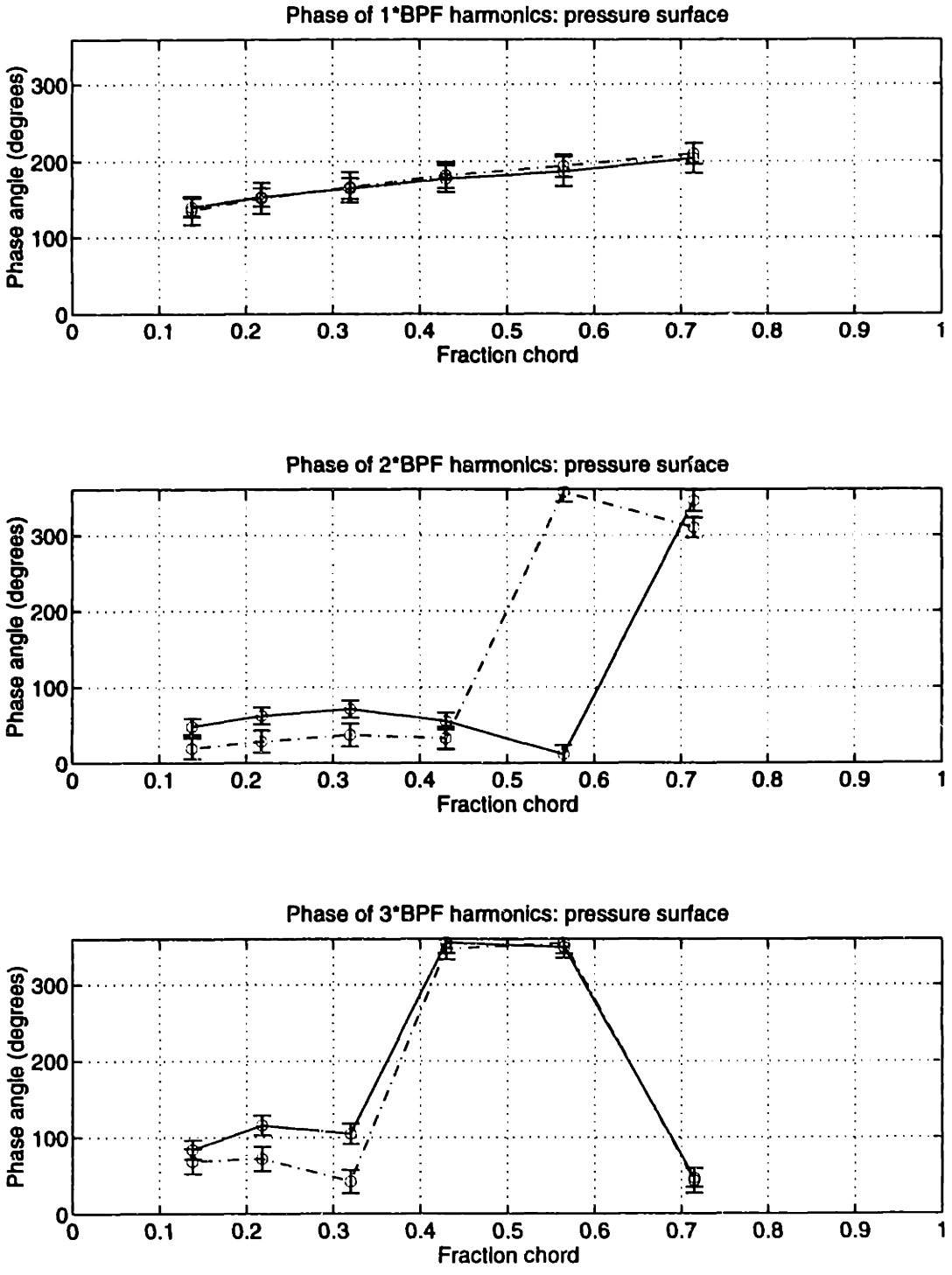

Figure 8-10: Stator pressure surface harmonic phases at 75% span for the baseline solid-bladed rotor (—) and the trailing edge blowing rotor with no injection (- .)

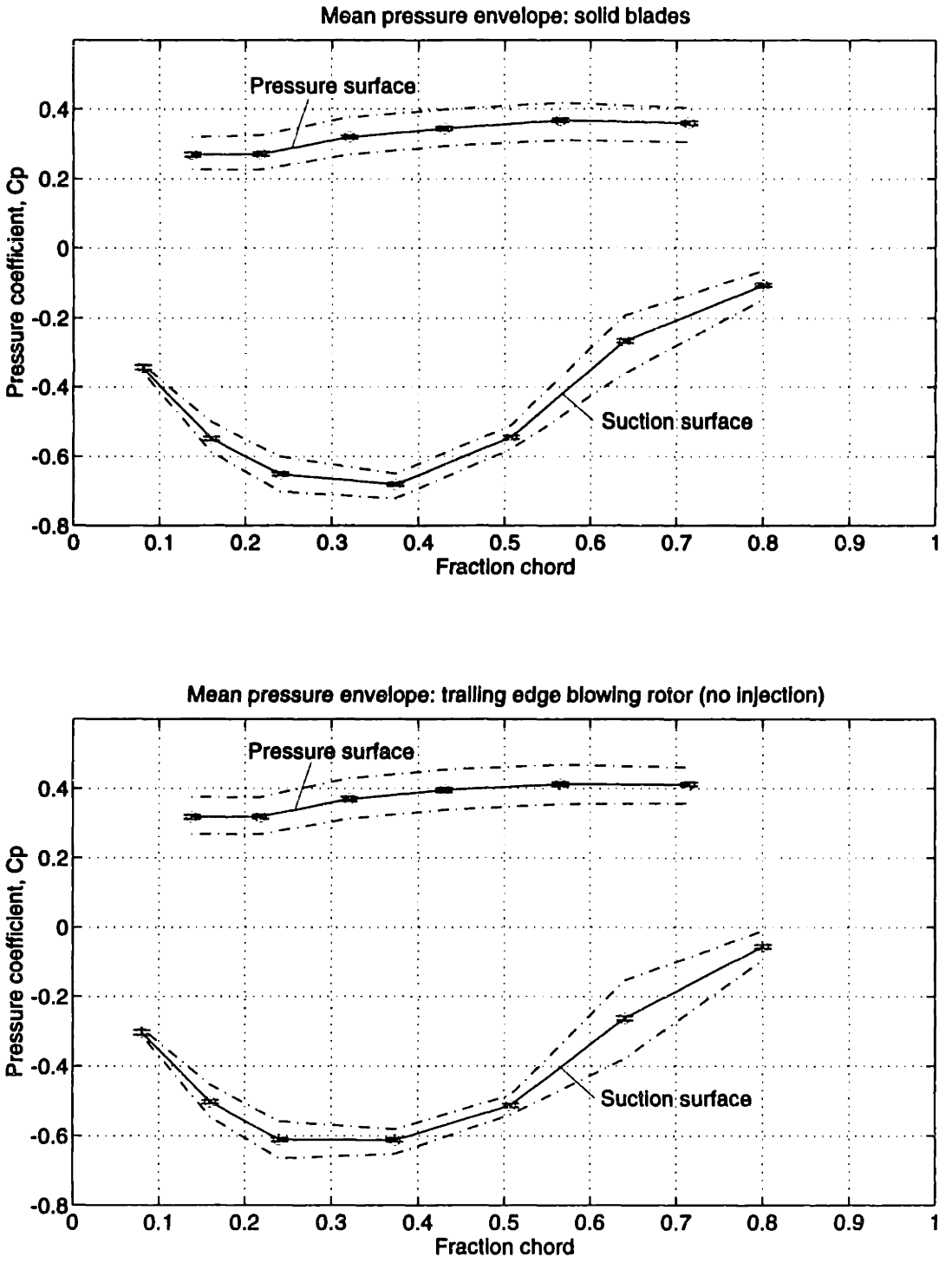

Figure 8-11: Stator time-mean pressure envelope at 87.5% span for the baseline solid-biaded rotor and the trailing edge blowing rotor with no injection [with periodic unsteady pressure envelope (– .)]

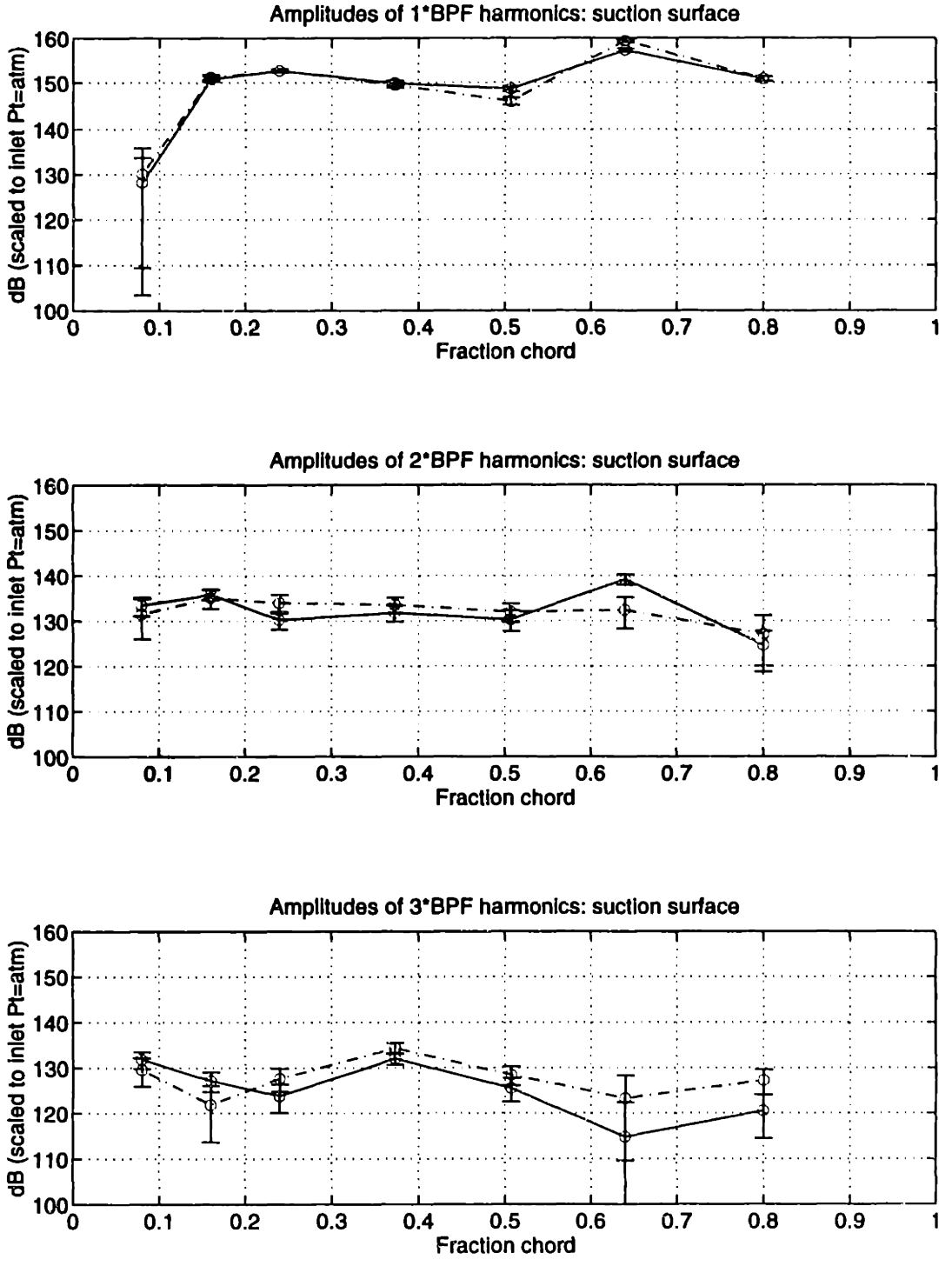

Figure 8-12: Stator suction surface harmonic amplitudes at 87.5% span for the baseline solid-bladed rotor (—) and the trailing edge blowing rotor with no injection (- -)

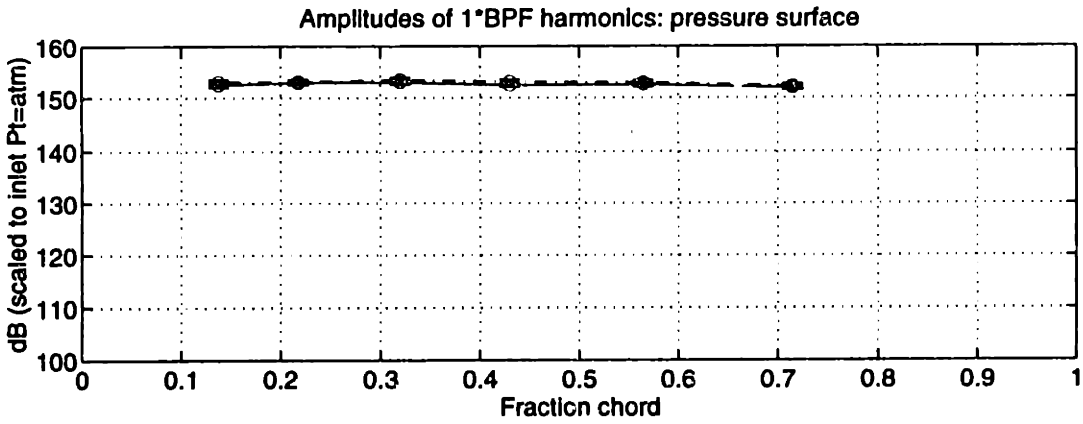

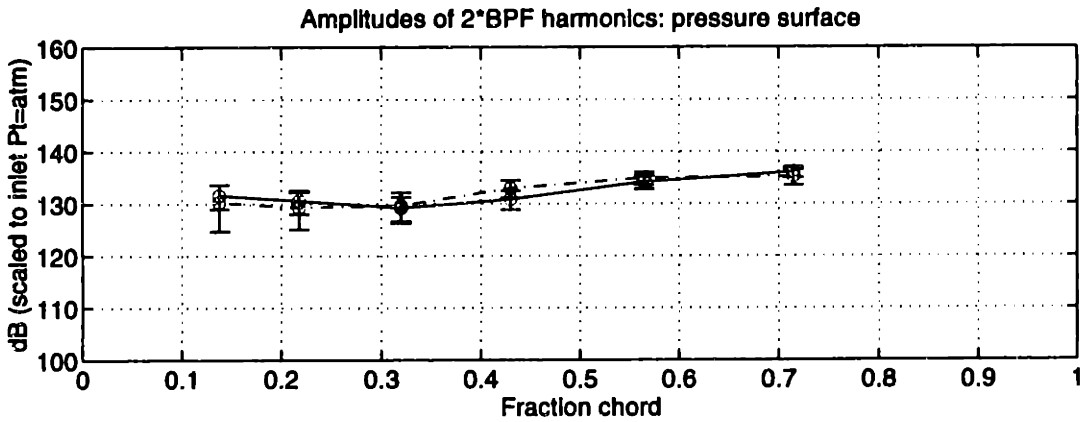

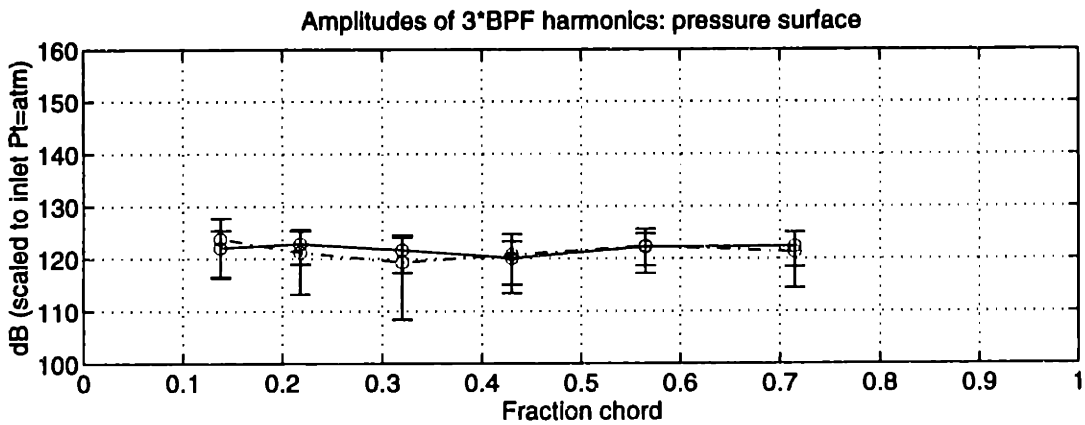

Figure 8-13: Stator pressure surface harmonic amplitudes at 87.5% span for the baseline solid-bladed rotor (—) and the trailing edge blowing rotor with no injection (- .)

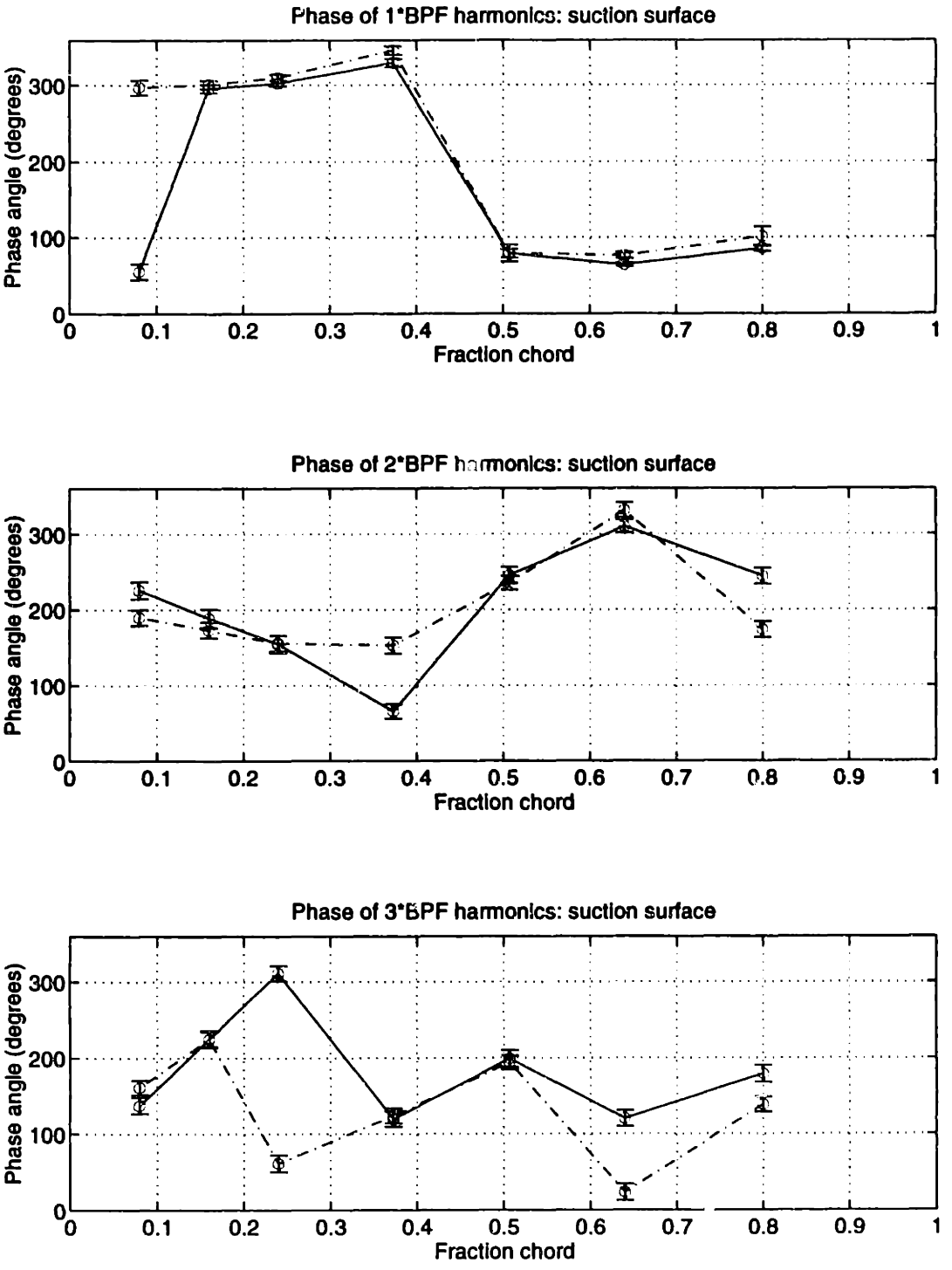

Figure 8-14: Stator suction surface harmonic phases at 87.5% span for the baseline solid-bladed rotor (—) and the trailing edge blowing rotor with no injection (- .)

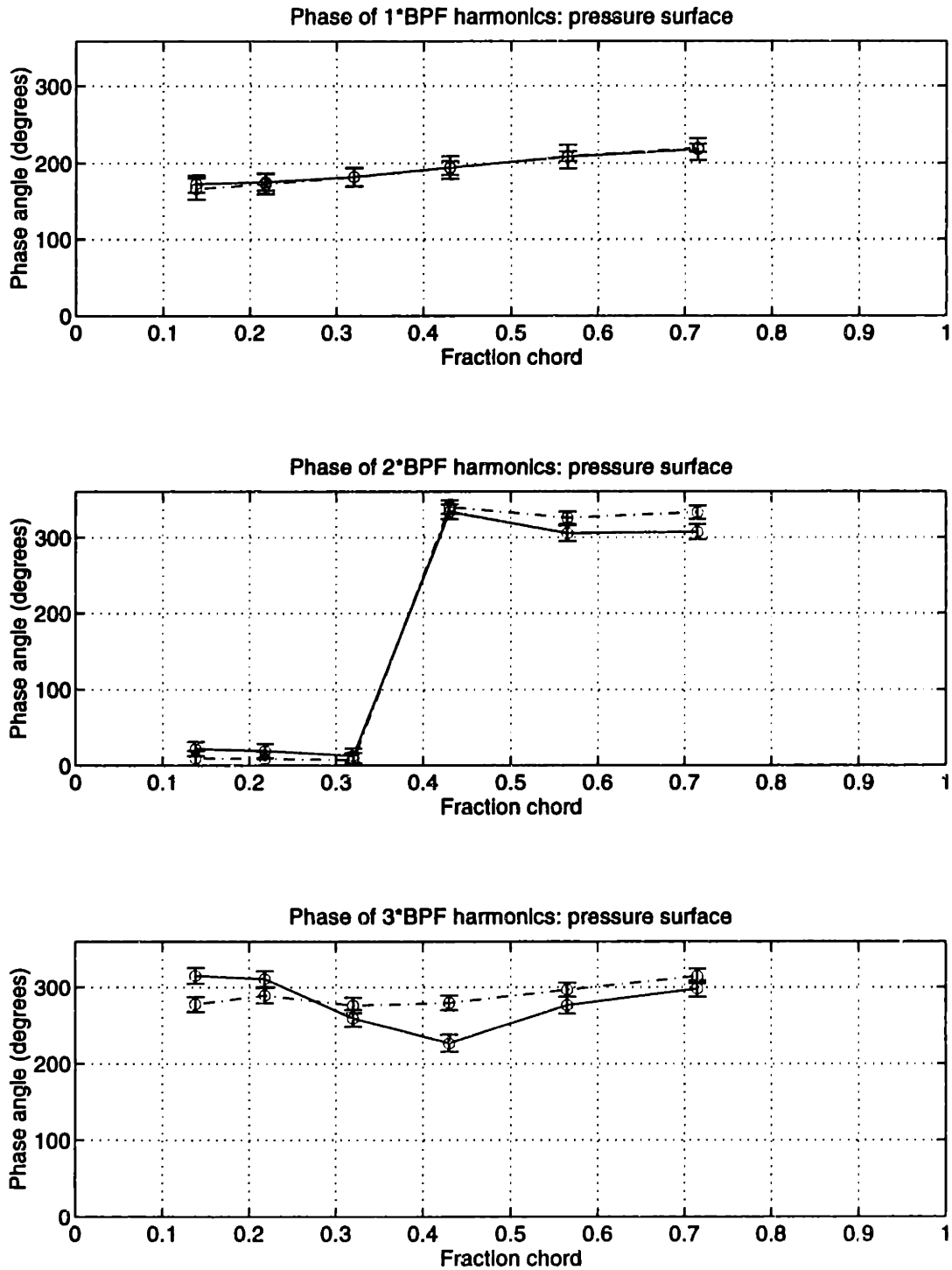

Figure 8-15: Stator pressure surface harmonic phases at 87.5% span for the baseline solid-bladed rotor (—) and the trailing edge blowing rotor with no injection (– .)

blade passing frequency amplitudes and phases at 1.5 chord remain fairly consistent between the baseline rotor and trailing edge blowing rotor (no injection). The stator data presented in Sections 8.1.1 through 8.1.3 appears to correlate well with changes in the wake BPF harmonics observed in Section 7.2.

To gain a better understanding of the change in stator unsteady loading, the pressure fluctuations on the suction surface were linearly interpolated to the chordwise position of the measurements on the pressure surface. The difference in the BPF harmonic on the two surfaces was then taken, and the amplitudes of the pressure differential across the stator blade at 50, 75, and 87.5% span are plotted in Figure 8-16. Again, the wake BPF harmonic amplitudes at 50, 75, and 87.5% span were higher for the trailing edge blowing rotor (no injection) by 25% (1.9 dB), 18% (1.5 dB), and 16% (1.3 dB), respectively.

The differential pressure amplitude of BPF at 87.5% span appears to match that of the upstream wake quite nicely, but the measurements at 50% and 75% span do not match as well. However, since the estimated 95% confidence intervals are generally 1 to 2 dB for these calculated pressure differentials, the changes in the wake harmonics measured at 1.5 chord are within the confidence intervals in the stator data.

The stator pressure differential BPF harmonic phases are shown in Figure 8-17. The 50% span measurements show a 25 degree phase offset compared to a 16 degree phase offset in the wake data, and the measurements at 75% and 87.5% span show similar agreement. Therefore, the stator measurements at BPF were found to be consistent with the changes in the wake structure between the baseline solid-bladed rotor and the trailing edge blowing rotor (no injection). Note, the measurements for these two configurations were taken almost one year apart.

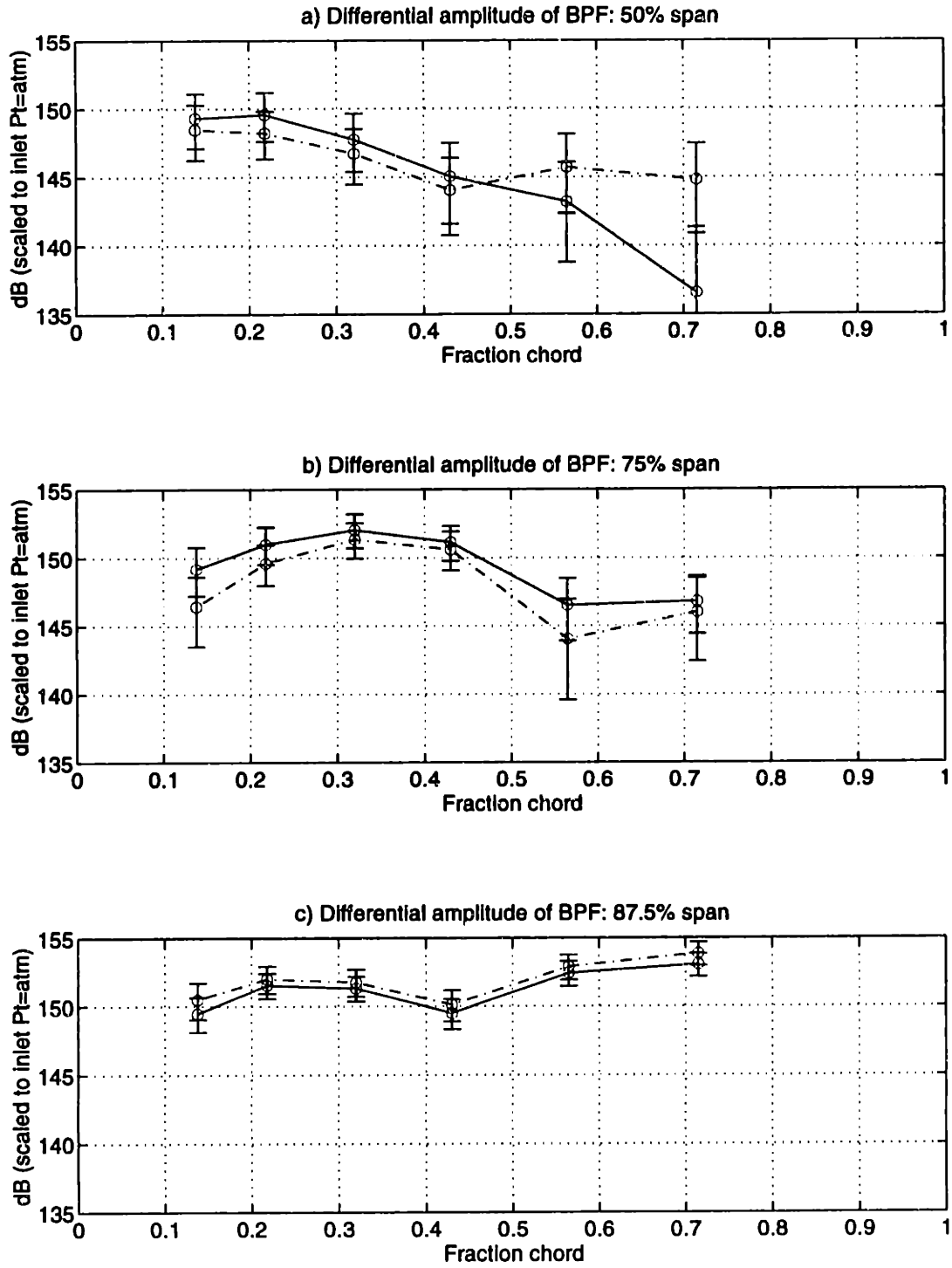

Figure 8-16: Amplitudes of stator surface pressure differential BPF harmonic for the baseline solid-bladed rotor (—) and the trailing edge blowing rotor with no injection (- .)

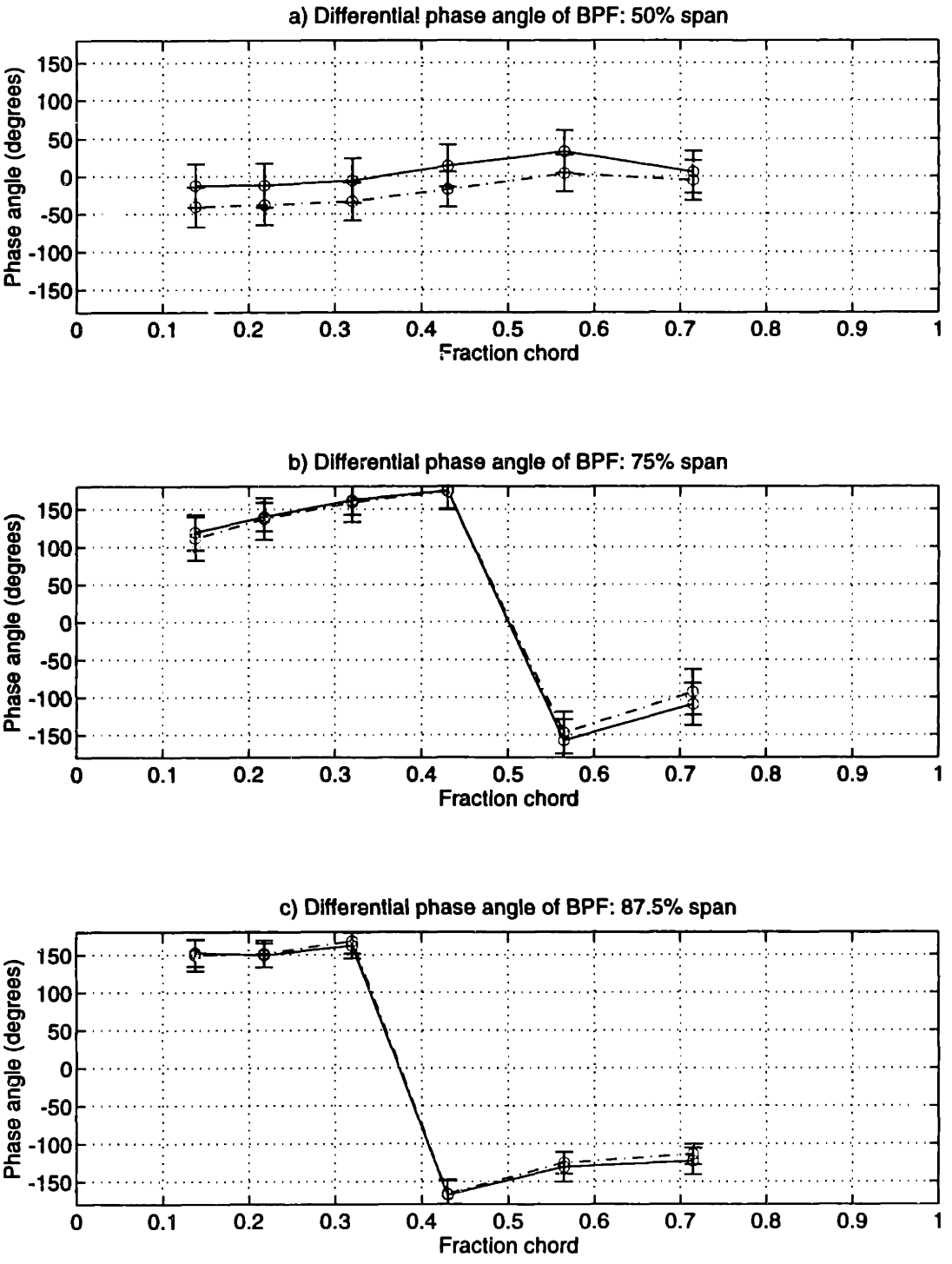

Figure 8-17: Phases of stator surface pressure differential BPF harmonic for the baseline solid-bladed rotor (—) and the trailing edge blowing rotor with no injection (– .)

8.2 Stator Unsteady Pressure Measurements: Trailing edge blowing rotor with and without tip-weighted injection (1.9%)

Unsteady pressure measurements were taken on the stator blade using the instrumented blade with 13 flush-mounted, Kulite pressure transducers. Tests were completed at 50, 75, and 87.5% span, both with and without tip-weighted injection. Again, the amount of injection was approximately 1.9% of the fan throughflow. Two runs at each condition were averaged to obtain the presented plots. The data for the rotor with no injection is shown with solid lines, and the data with tip-weighted injection is shown with dashed lines.

The repeatability of the data presented in Section 8.1, particularly at BPF, gave confidence in the ability of the stator to provide reasonable results. It was hoped that the changes in unsteady loading on the stator blade due to trailing edge blowing could be correlated to changes in the wake upstream of the stator row.

8.2.1 50% span

The stator measurements at 50% span are presented in Figures 8-18 through 8-23. The time-mean pressure envelopes with and without injection are plotted in Figure 8-18. The pressure level with blowing is seen to be higher due to the lower inlet axial Mach number, but the overall loading is approximately the same. In addition to the mean pressure values, the range of periodic pressure fluctuation is also plotted (dash-dot lines). These curves show the ensemble-averaged range of pressure seen at the transducers over the blade passing period.

The amplitudes of the first three BPF harmonics of the stator surface pressure perturbations are shown in Figures 8-19 and 8-20 for the suction and pressure surfaces, respectively. The BPF harmonic amplitudes are seen to be generally higher on the pressure surface with injection and higher over about 50% of the chord on the suction surface with injection. Similarly, the 2*BPF amplitudes are generally higher on the suction surface with injection and show little change on the pressure surface with injection. 3*BPF has similar behavior.

With the wake harmonic amplitudes at 50% span, 1.5 chord reduced by approximately

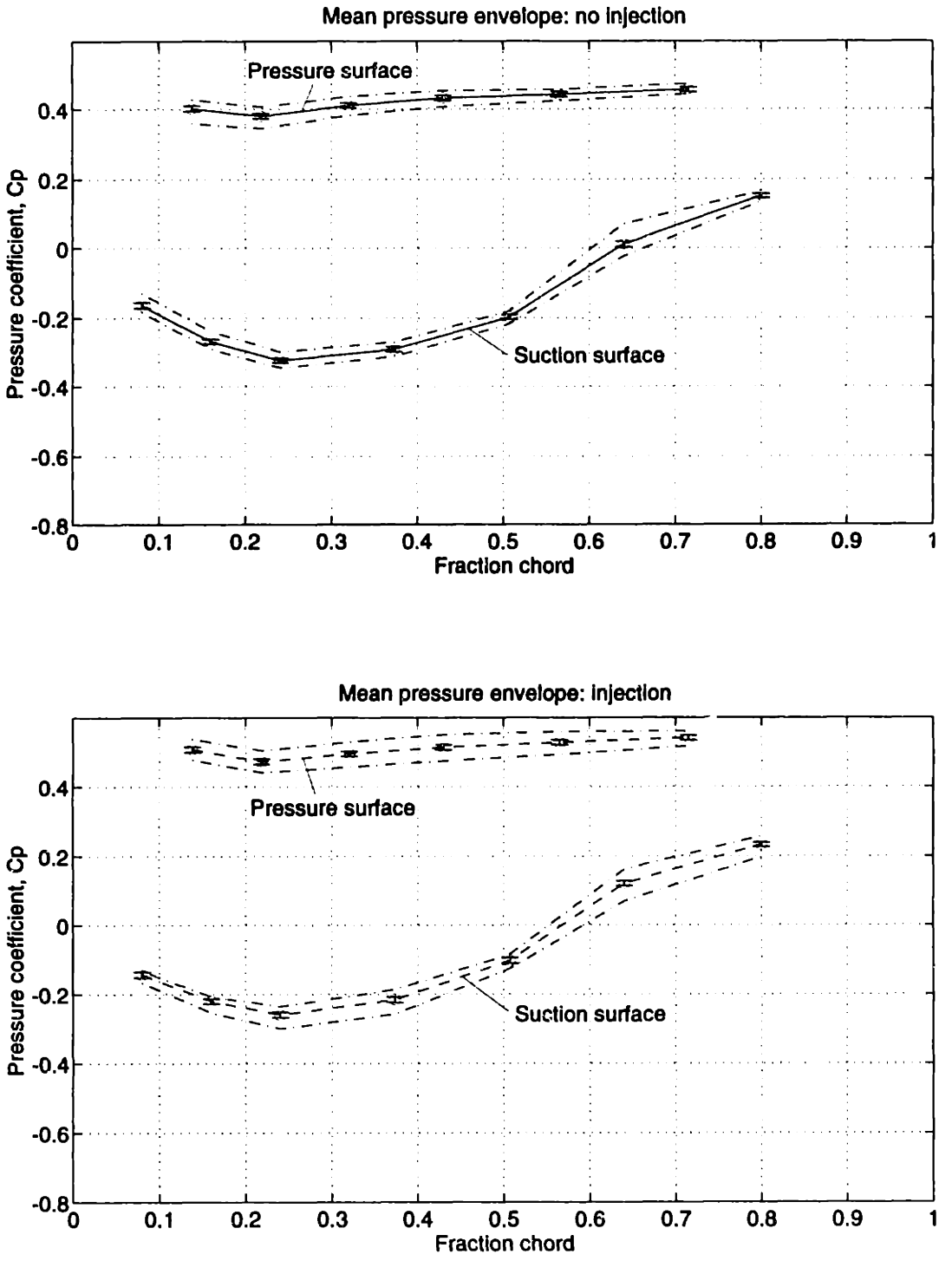

Figure 8-18: Stator time-mean pressure envelope at 50% span for the trailing edge blowing rotor with (- -) and without (—) tip-weighted injection [with periodic unsteady pressure envelope (– .)]

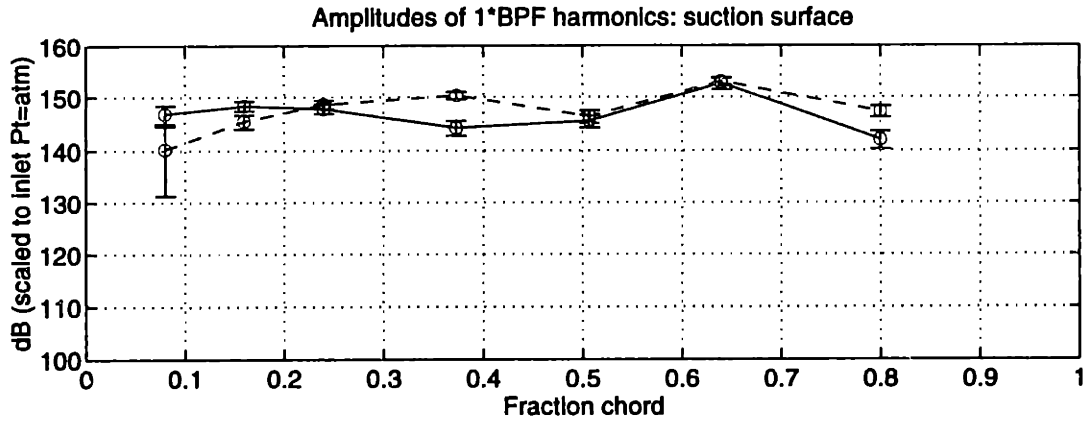

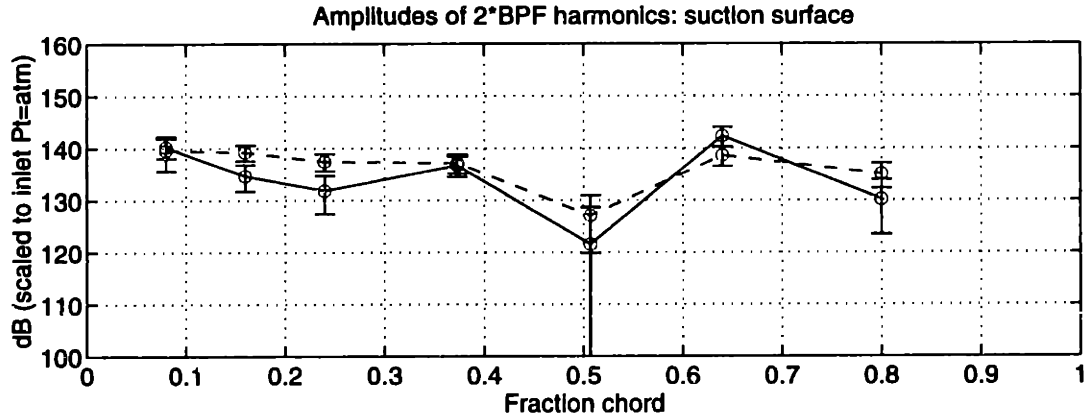

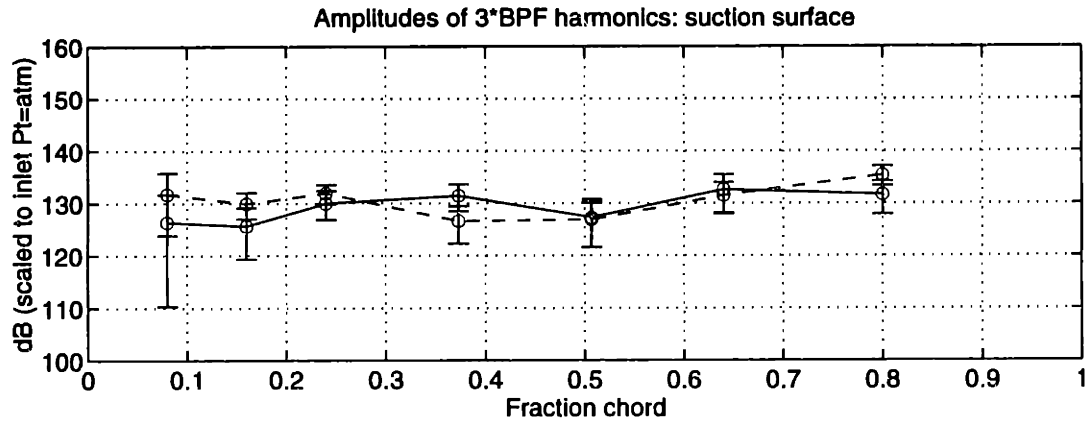

Figure 8-19: Stator suction surface harmonic amplitudes at 50% span for the trailing edge blowing rotor with (- -) and without (—) tip-weighted injection

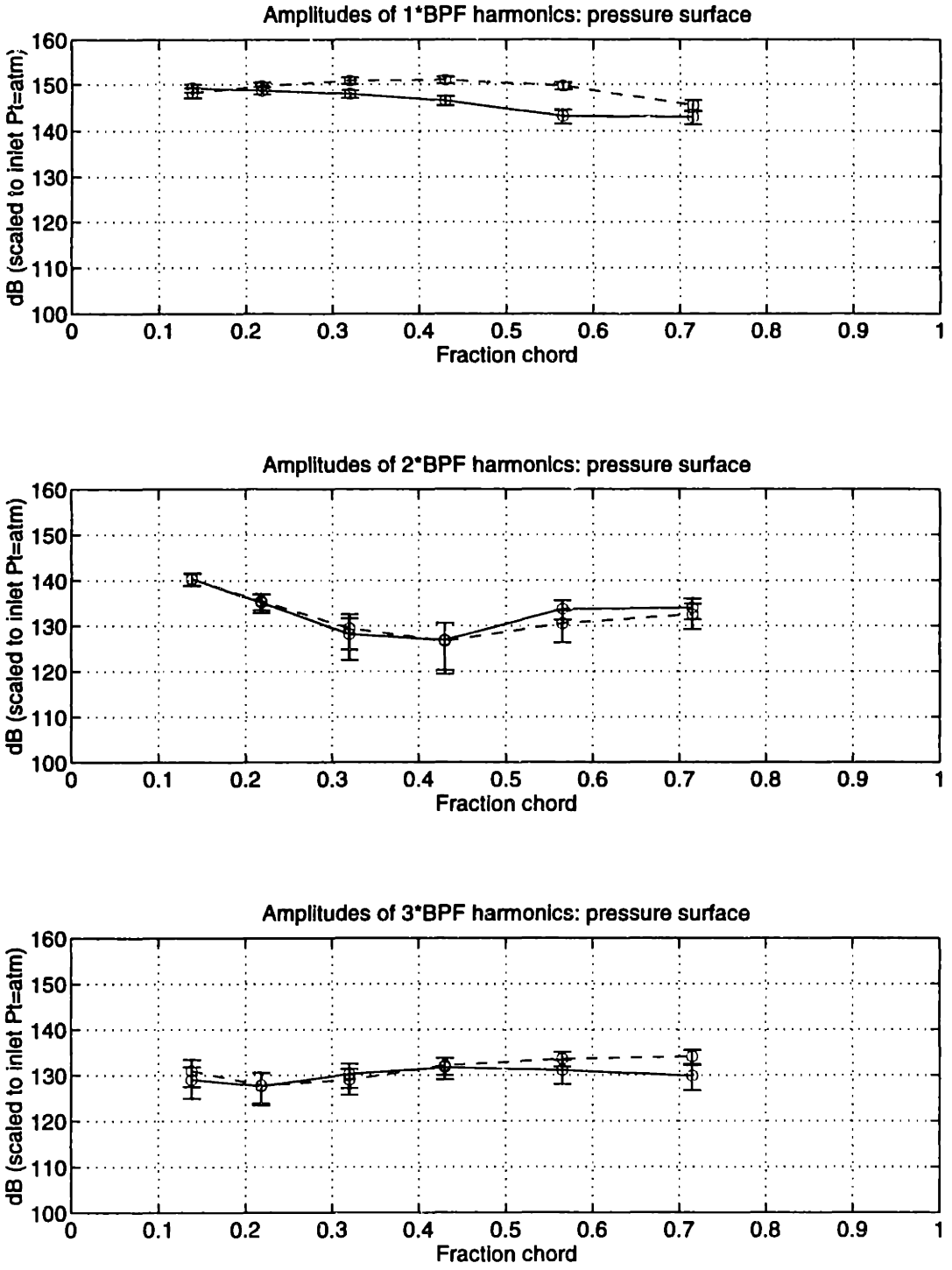

Figure 8-20: Stator pressure surface harmonic amplitudes at 50% span for the trailing edge blowing rotor with (- -) and without (—) tip-weighted injection

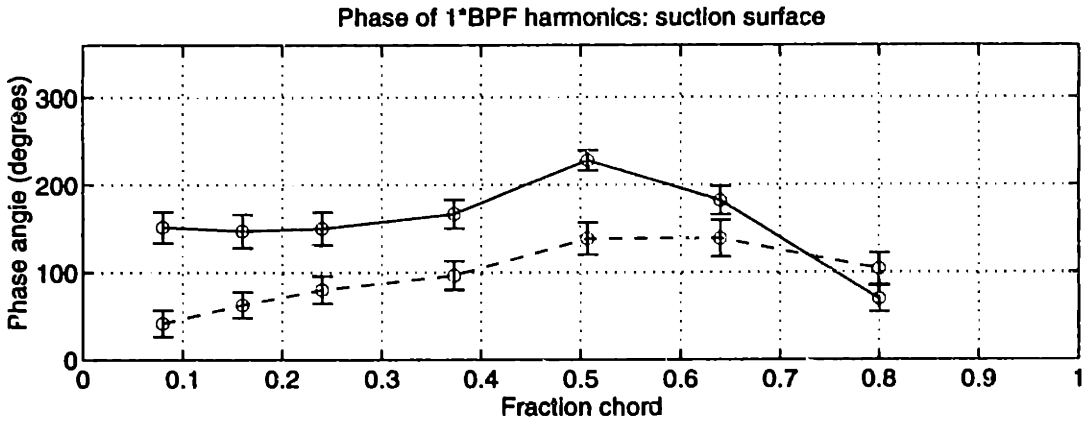

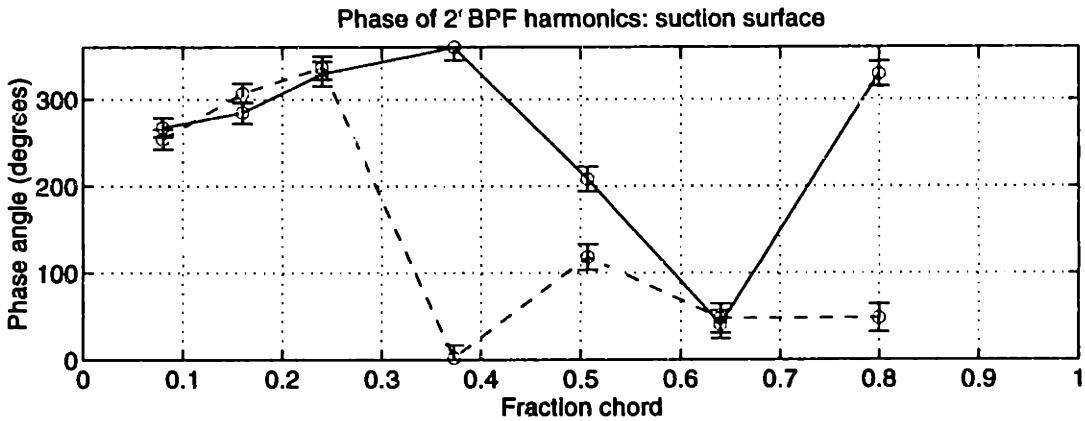

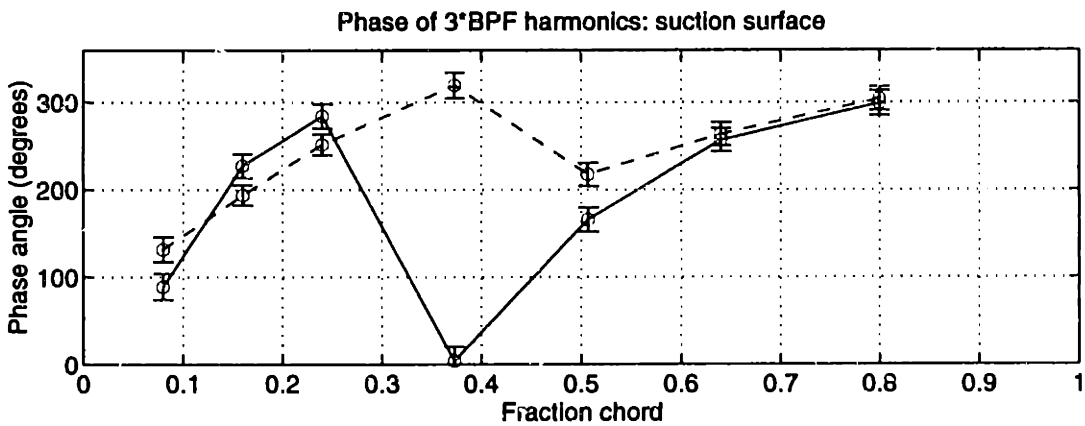

Figure 8-21: Stator suction surface harmonic phases at 50% span for the trailing edge blowing rotor with (- -) and without (—) tip-weighted injection

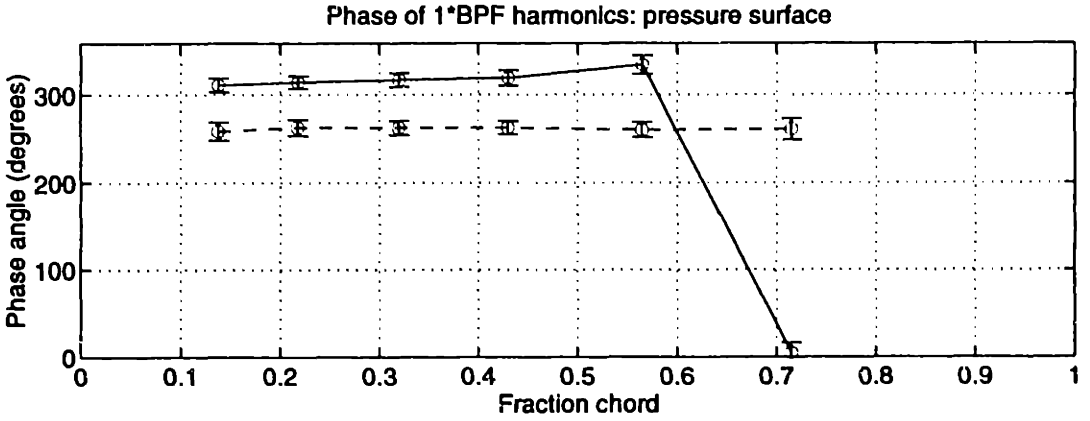

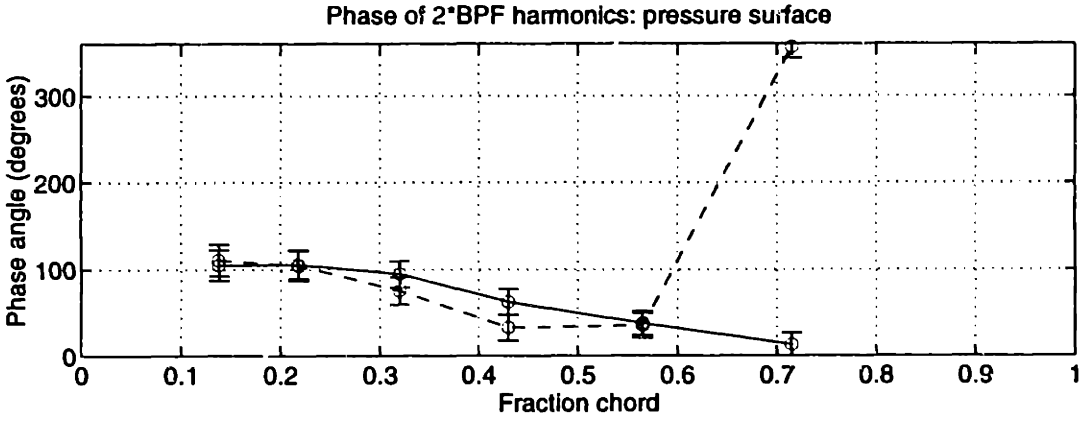

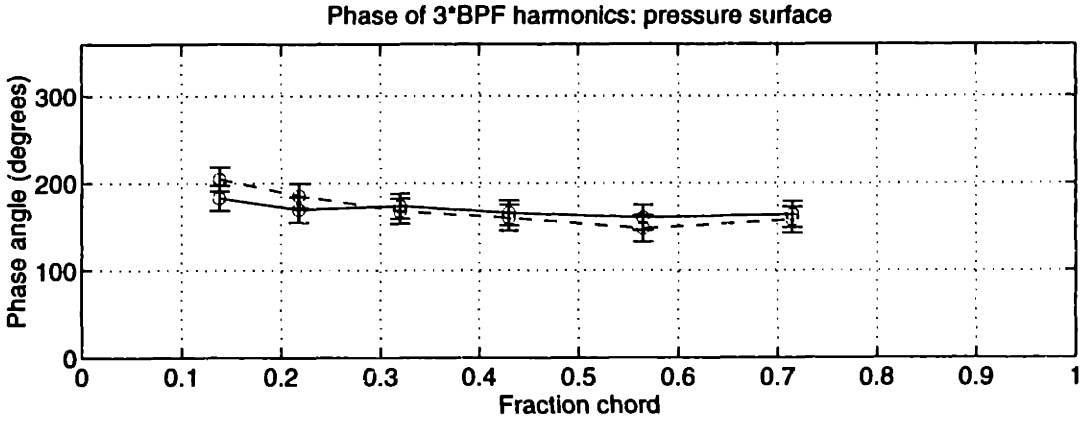

Figure 8-22: Stator pressure surface harmonic phases at 50% span for the trailing edge blowing rotor with (- -) and without (—) tip-weighted injection

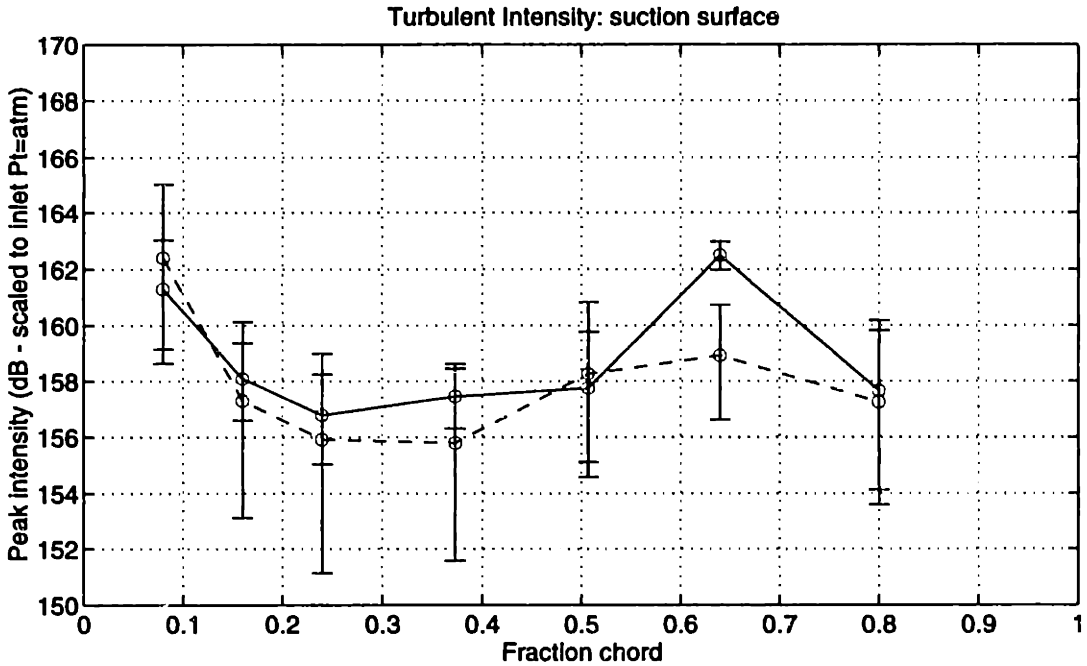

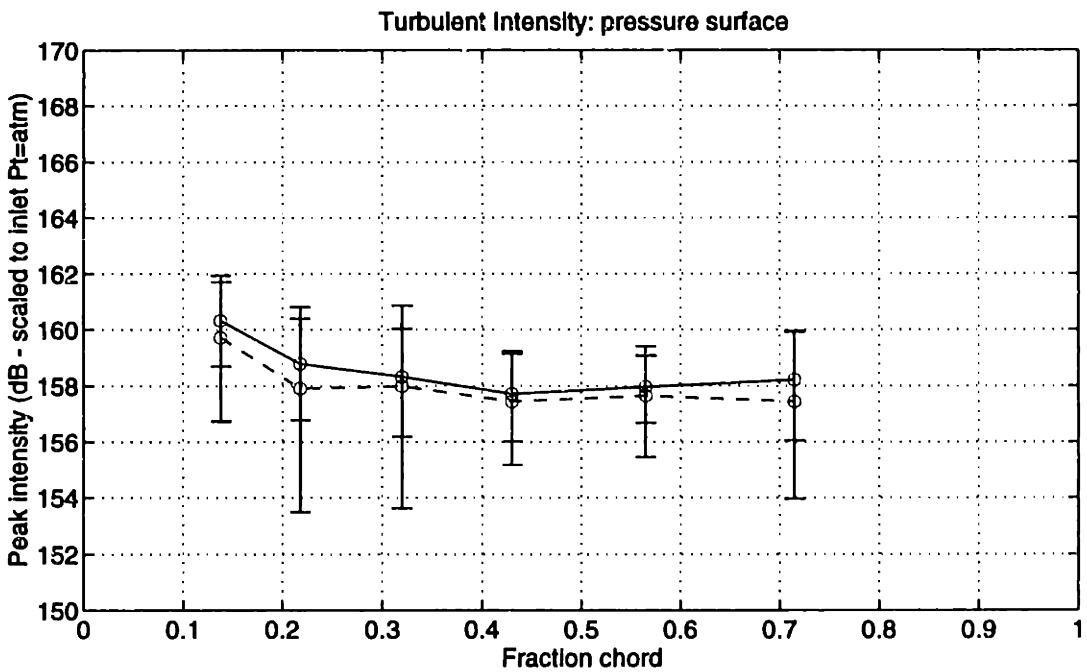

Figure 8-23: Stator pressure turbulence intensity at 50% span for the trailing edge blowing rotor with (- -) and without (—) tip-weighted injection

30% for BPF, 50% for 2*BPF, and 40% for 3*BPF with injection, the stator unsteady harmonic amplitudes are expected to be reduced approximately 3 dB for BPF, 6 dB for 2*BPF, and 4.4 dB for 3*BPF. While the 95% confidence intervals are typically about 2-4 dB for the stator pressure harmonic amplitudes, many of the transducers show clear increases in harmonic amplitude with injection. Much of the reduction in stator surface harmonic amplitudes expected from the decrease in wake harmonic amplitudes are not observed.

In addition to the harmonic amplitudes, the phase of the stator surface pressure perturbations are important to the unsteady loading. The phases of the first three harmonics of blade passing frequency are shown in Figures 8-21 and 8-22 for the suction and pressure surfaces, respectively. The phases of BPF are seen to be approximately 80 degrees lower with injection on the suction surface and about 60 degree lower on the pressure surface. Thus, the phase difference across the stator surface does not change significantly, but the phase shift between the injection and no injection configurations does roughly correspond to the change in wake BPF harmonic observed in Figure 7-55. The phases of the 2*BPF and 3*BPF harmonics do not change significantly over much of the chord, but differences do roughly agree with the wake phase differences.

The level of turbulence intensity at the transducers is shown in Figure 8-23. The random perturbation amplitudes appear to be slightly lower with injection, but changes are well within the 95% confidence intervals except at 64% chord on the suction surface.

8.2.2 75% span

The stator pressure data at 75% span is presented in Figures 8-24 through 8-29. The time-mean pressure envelopes, shown in Figure 8-24, are seen to be very similar with and without injection. The range of periodic pressure is slightly smaller with injection, but the mean pressure coefficients are roughly identical.

Similar to 50% span, the unsteady pressure harmonic amplitudes at 75% span are reduced along some sections of the chord and increased on others. The BPF harmonic amplitude is generally lower on the suction surface and uniformly lower on the pressure surface by approximately 3 dB with injection. The wake BPF harmonic at 75% span, 1.5 chord was reduced by approximately 65% (9 dB).

The 2*BPF stator pressure harmonics are reduced at several locations along the suction surface and increased by approximately 4 dB on most of the pressure surface. The 2*BPF wake harmonic amplitude upstream at 75% span, 1.5 chord was reduced by approximately 80% or 14 dB. The 3*BPF stator pressure harmonic amplitudes show more uniform reduction of a few dB with only about 40% reduction in the wake harmonic amplitude seen at 1.5 chord.

The stator pressure harmonic phase angles are shown in Figures 8-27 and 8-28, and the turbulence intensity at the transducers is shown in Figure 8-29. Changes of approximately 50 degrees are seen in the phase angles. Despite a reduction in the wake turbulence intensity at 75% span, the turbulence intensity on the stator surface is increased by about 1 dB. However, these changes are within the confidence intervals and are thus not conclusive.

8.2.3 87.5% span

The stator pressure measurements at 87.5% span for the tip-weighted injection are shown in Figures 8-30 through 8-35. The time-mean pressure envelopes along with the range of periodic pressure perturbations are shown in Figure 8-30, both with and without injection. The mean profiles are again very similar with injection, but there is a small offset. The range of periodic fluctuations is seen to be smaller with injection.

The stator surface harmonic amplitudes are shown in Figures 8-31 and 8-32 and generally show reductions with injection. The BPF harmonics, show the same behavior on the suction side as at 50 and 75% span, with some positions along the chord showing an increase in harmonic amplitude and some locations showing a decrease in amplitude. The pressure surface, however, has about a 10 dB reduction in the BPF harmonic amplitude along the entire chord. This 10 dB decrease approximately correlates with the decrease in the wake BPF harmonic amplitude observed in the flow field measurements at 87.5% span, 1.5 chord (about 13.5 dB).

The 2*BPF and 3*BPF harmonics again show some increases and some decreases along the chord. The 2*BPF has nearly opposite behavior on the suction and pressure surfaces, i.e. where the harmonic amplitude is decreased on the suction surface, it is increased on the pressure surface by roughly the same amount. The result is nearly the same differential

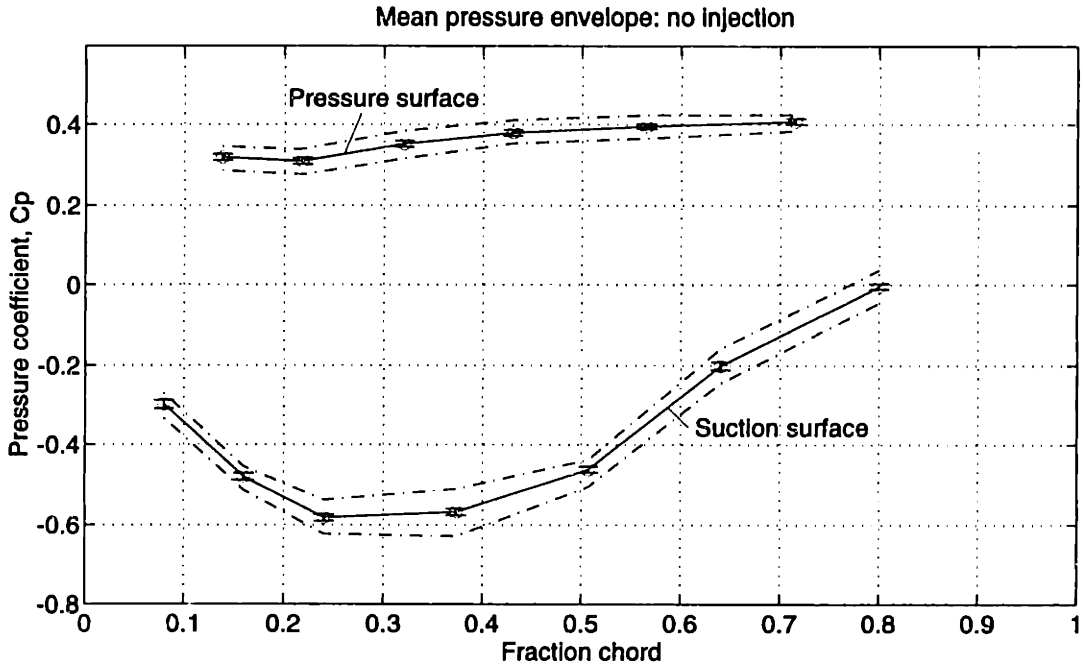

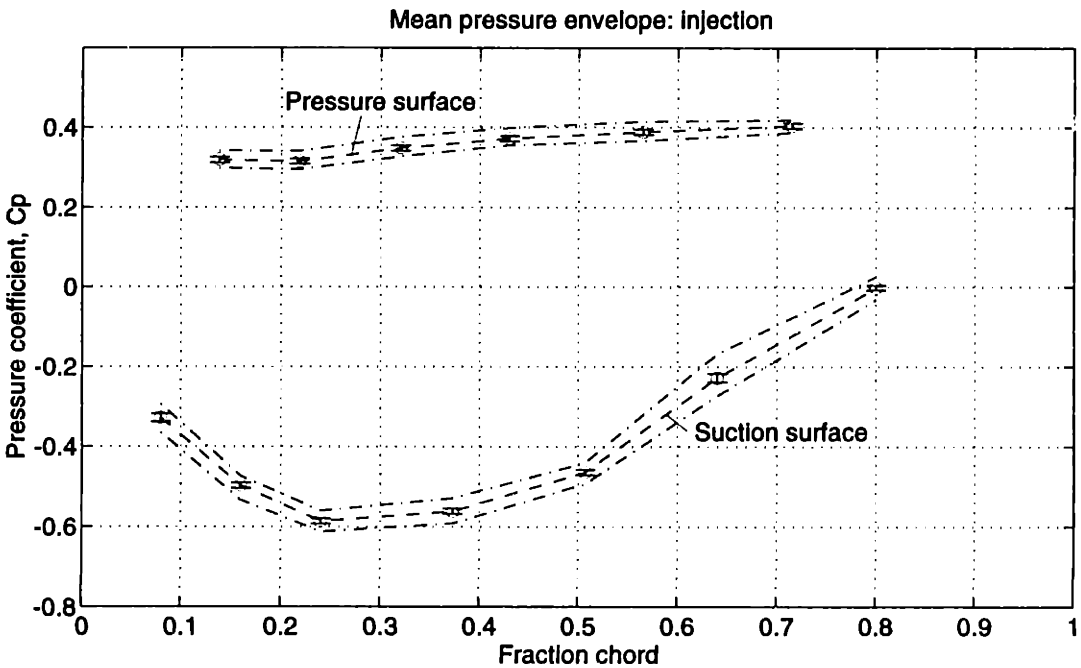

Figure 8-24: Stator time-mean pressure envelope at 75% span for the trailing edge blo\ ıg rotor with (- -) and without (—) tip-weighted injection [with periodic unsteady :essure envelope (-· .)]

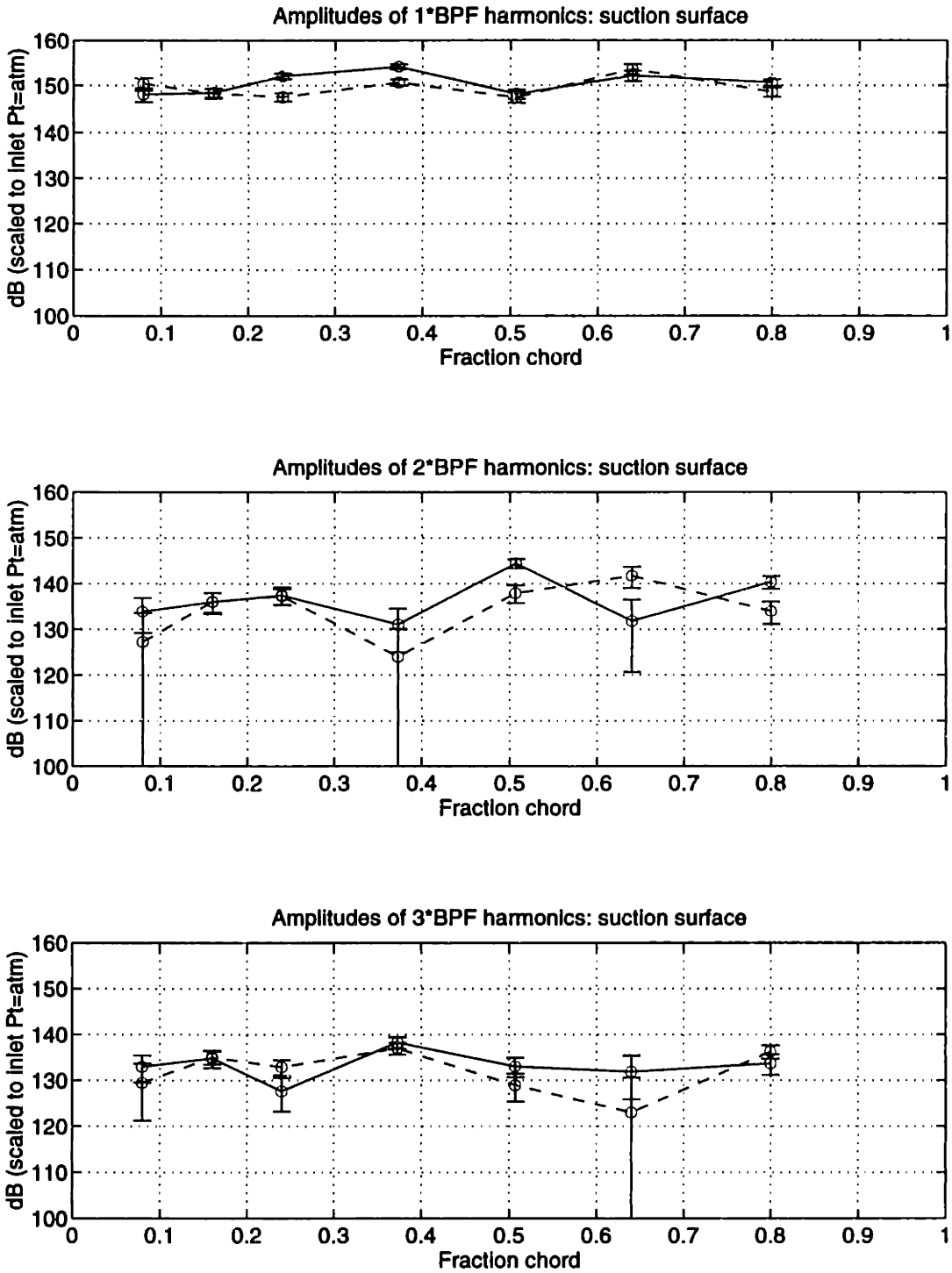

Figure 8-25: Stator suction surface harmonic amplitudes at 75% span for the trailing edge blowing rotor with (- -) and without (—) tip-weighted injection

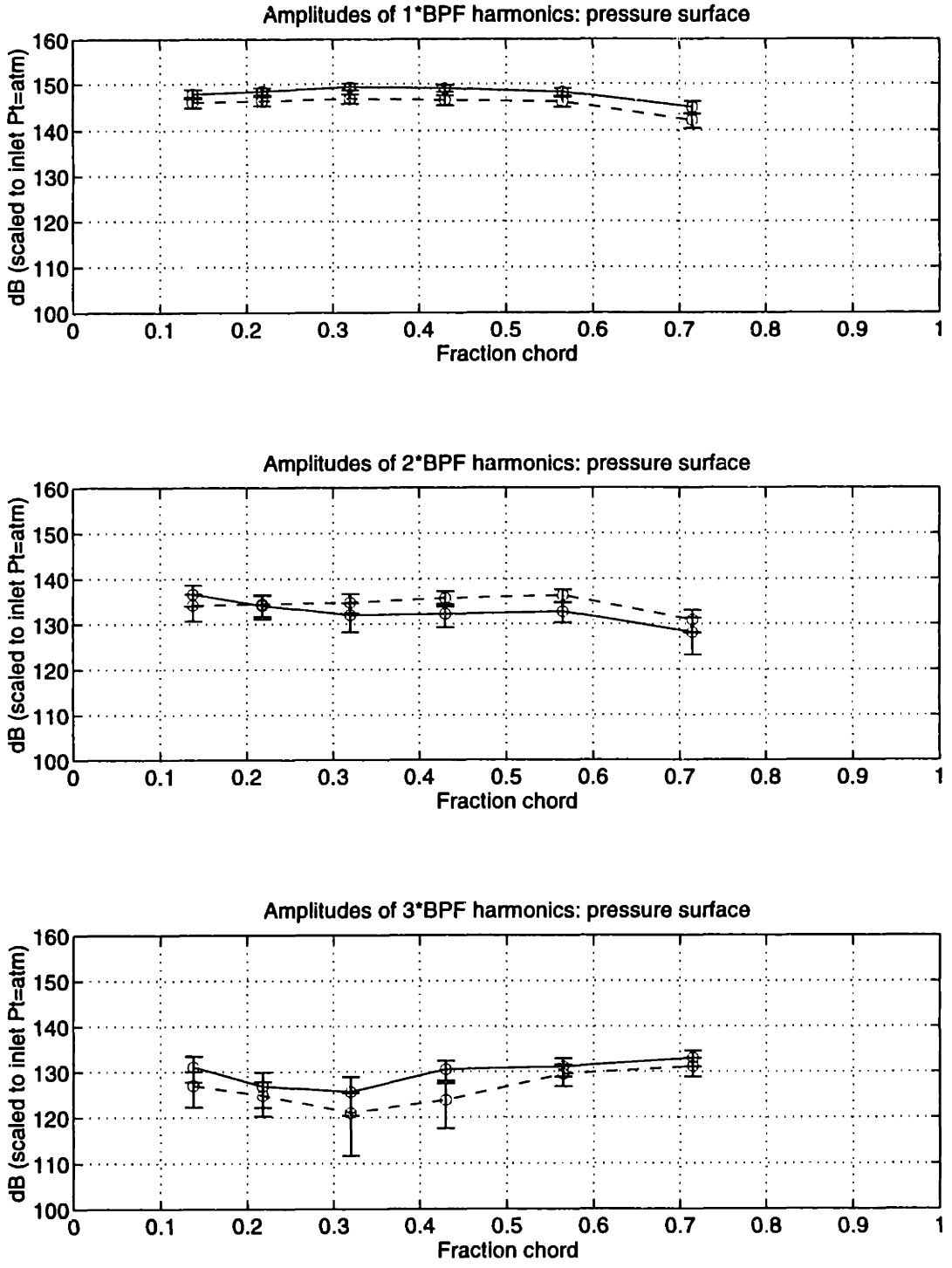

Figure 8-26: Stator pressure surface harmonic amplitudes at 75% span for the trailing edge blowing rotor with (- -) and without (—) tip-weighted injection

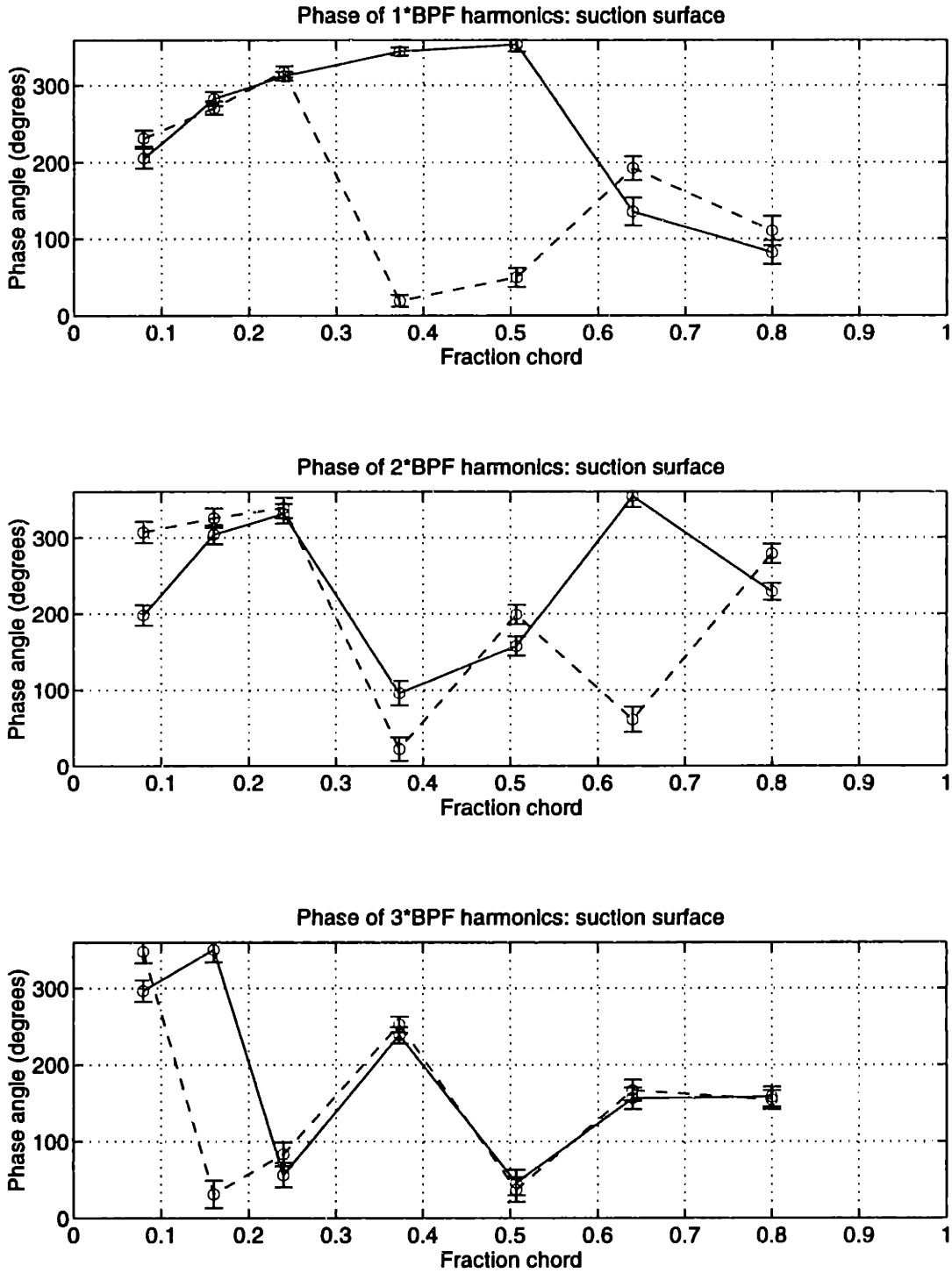

Figure 8-27: Stator suction surface harmonic phases at 75% span for the trailing edge blowing rotor with (- -) and without (—) tip-weighted injection

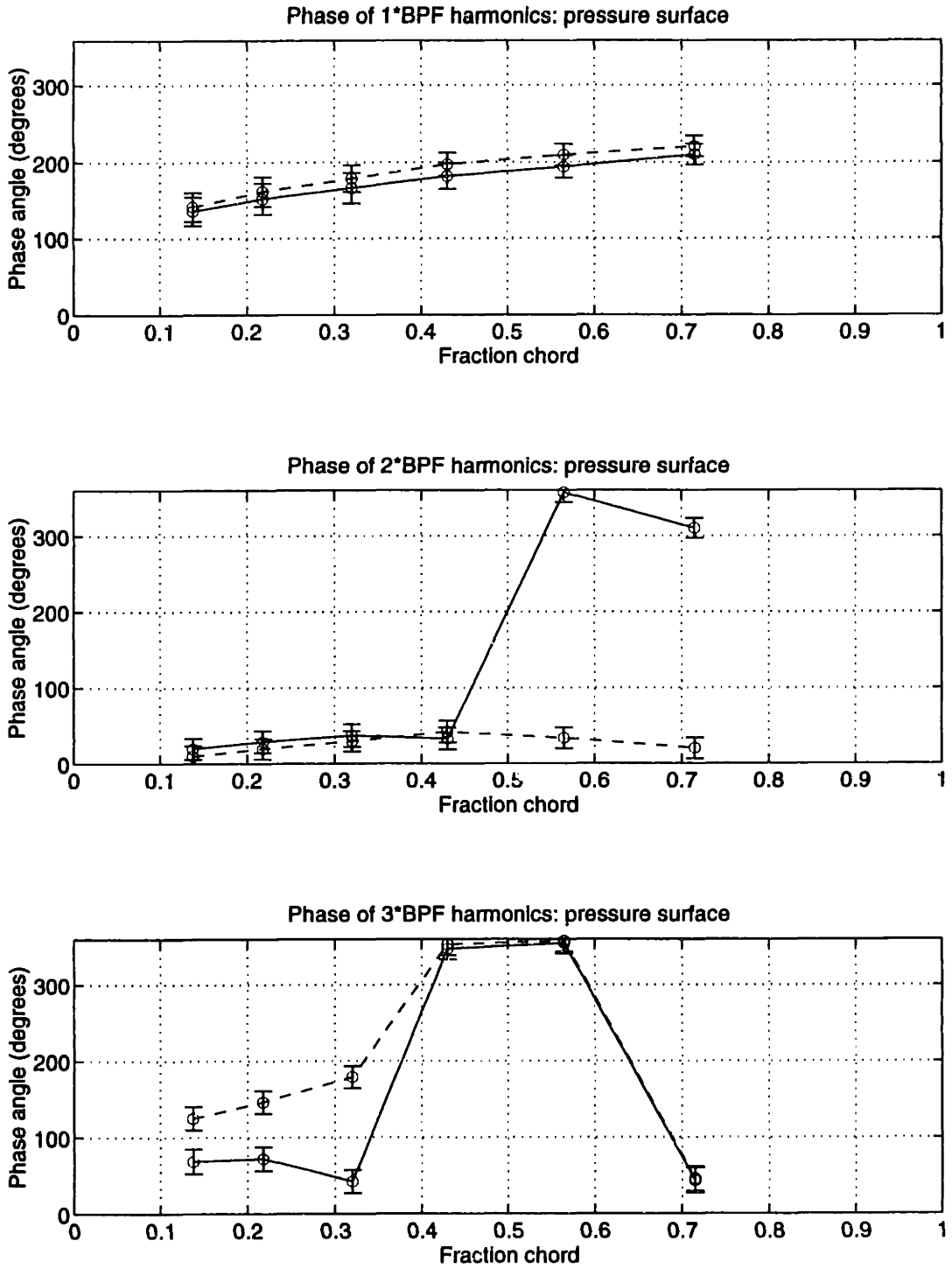

Figure 8-28: Stator pressure surface harmonic phases at 75% span for the trailing edge blowing rotor with (- -) and without (—) tip-weighted injection

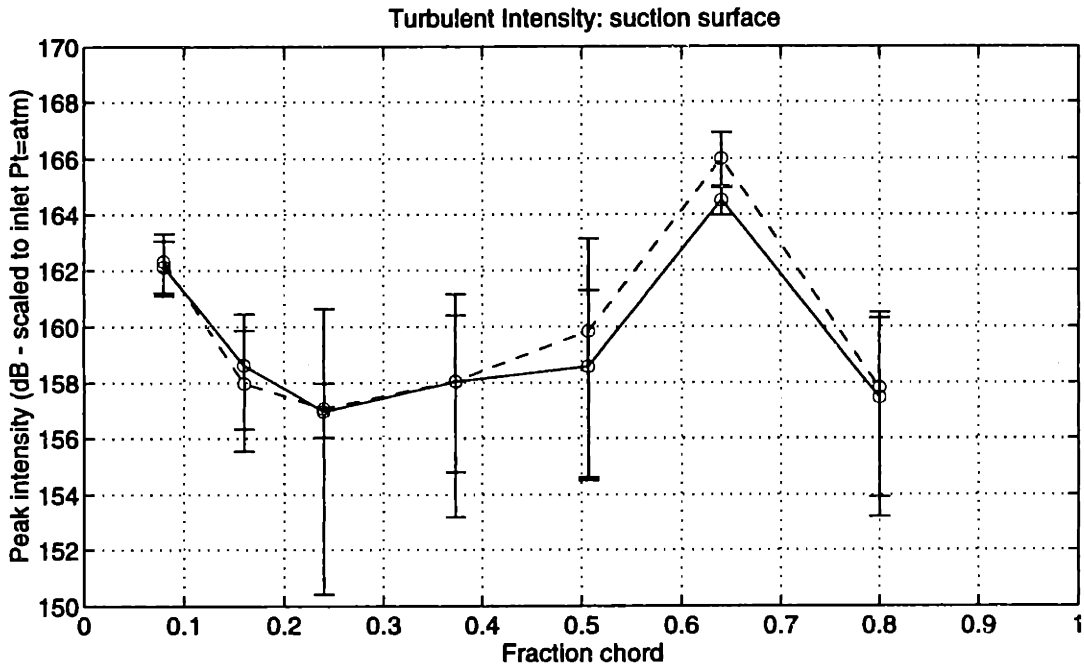

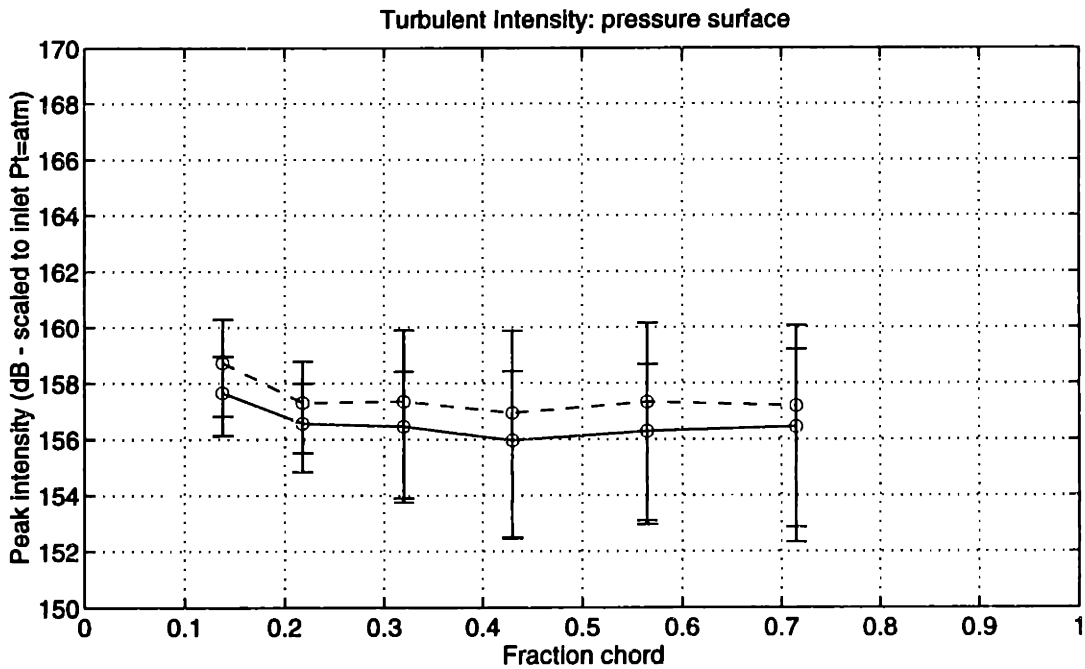

Figure 8-29: Stator pressure turbulence intensity at 75% span for the trailing edge blowing rotor with (- -) and without (—) tip-weighted injection

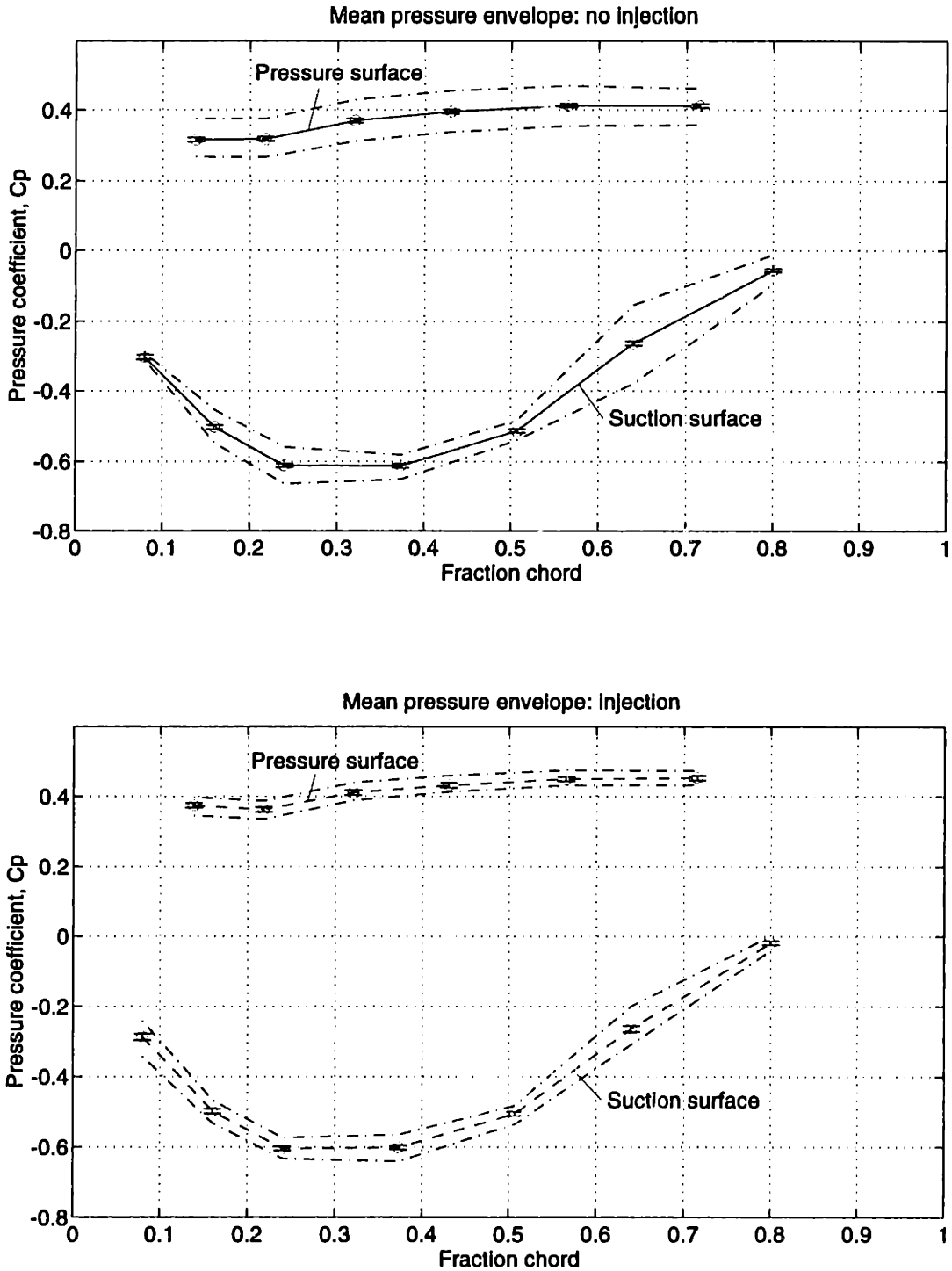

Figure 8-30: Stator time-mean pressure envelope at 87.5% span for the trailing edge blowing rotor with (- -) and without (—) tip-weighted injection [with periodic unsteady pressure envelope (– .)]

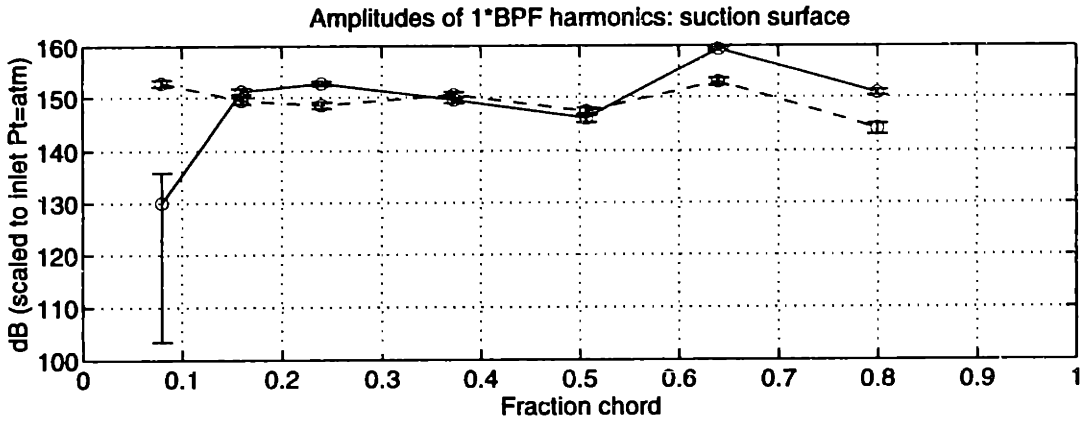

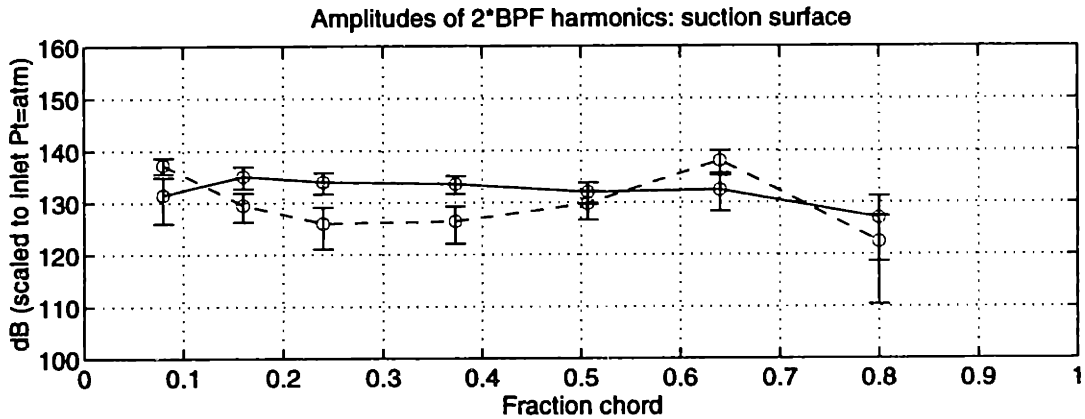

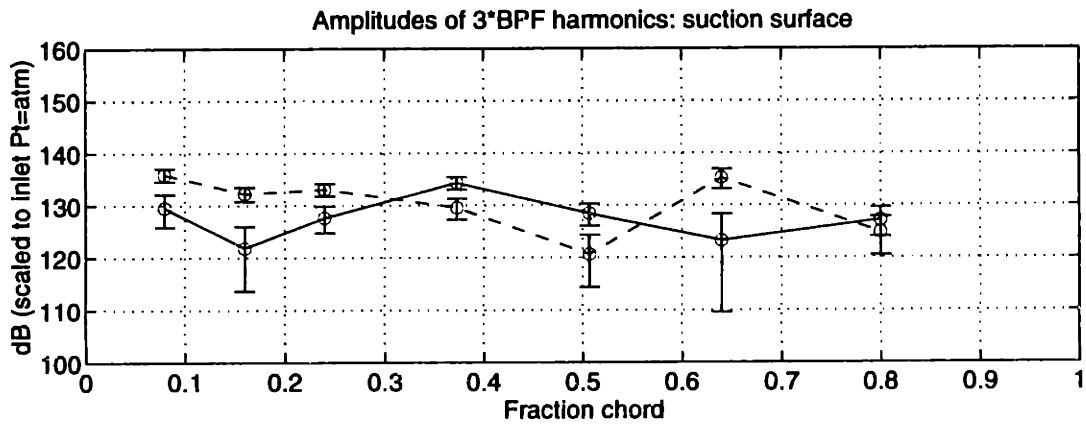

Figure 8-31: Stator suction surface harmonic amplitudes at 87.5% span for the trailing edge blowing rotor with (- -) and without (—) tip-weighted injection

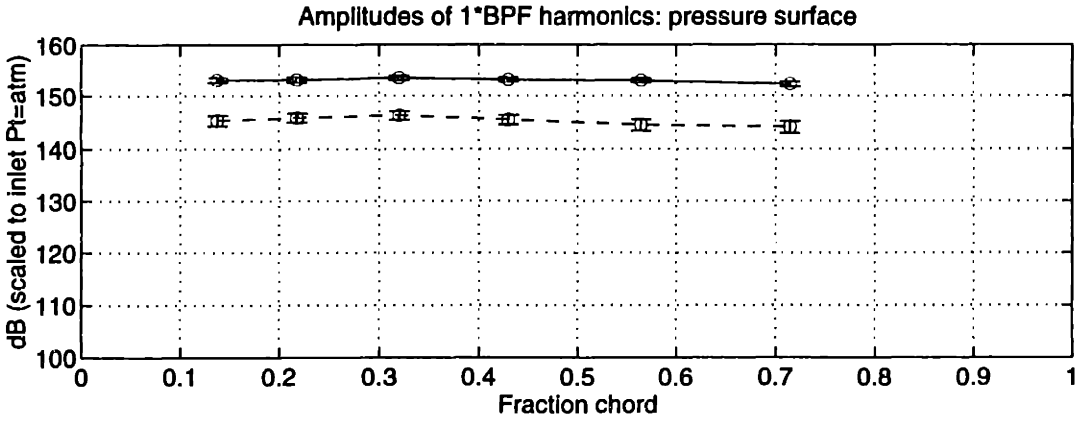

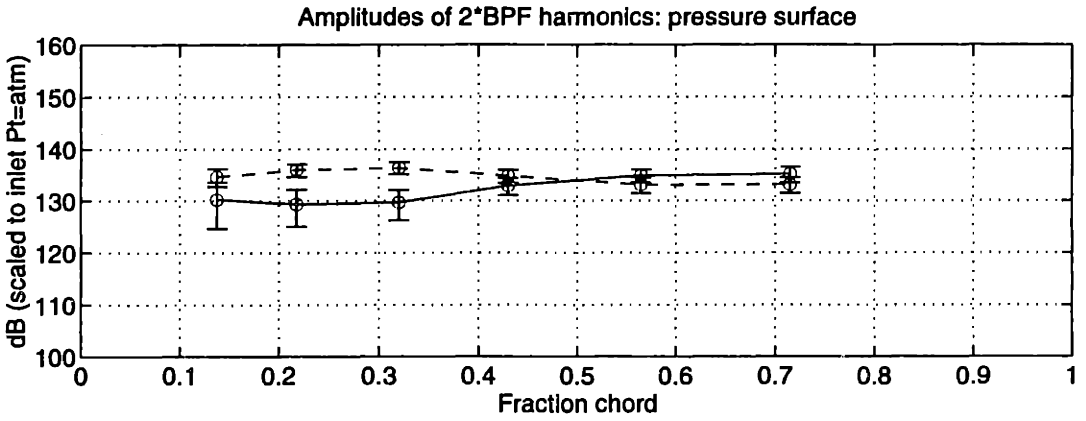

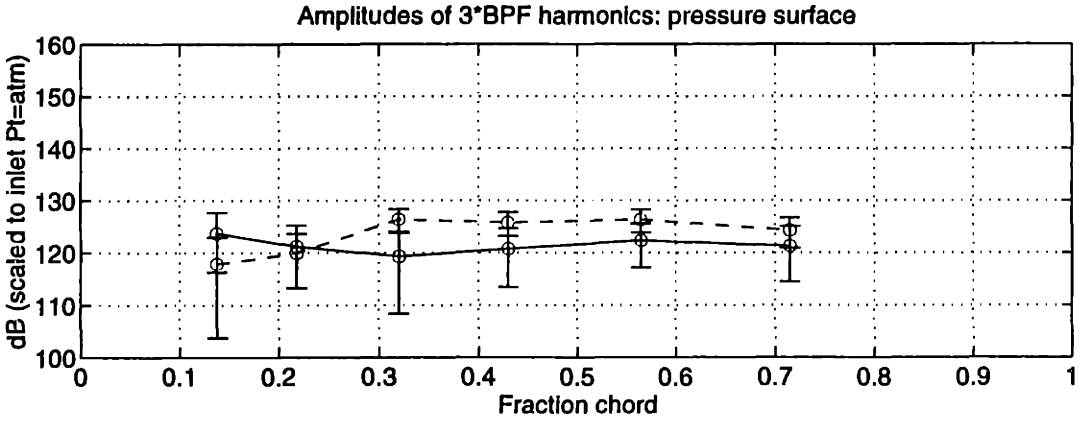

Figure 8-32: Stator pressure surface harmonic amplitudes at 87.5% span for the trailing edge blowing rotor with (- -) and without (—) tip-weighted injection

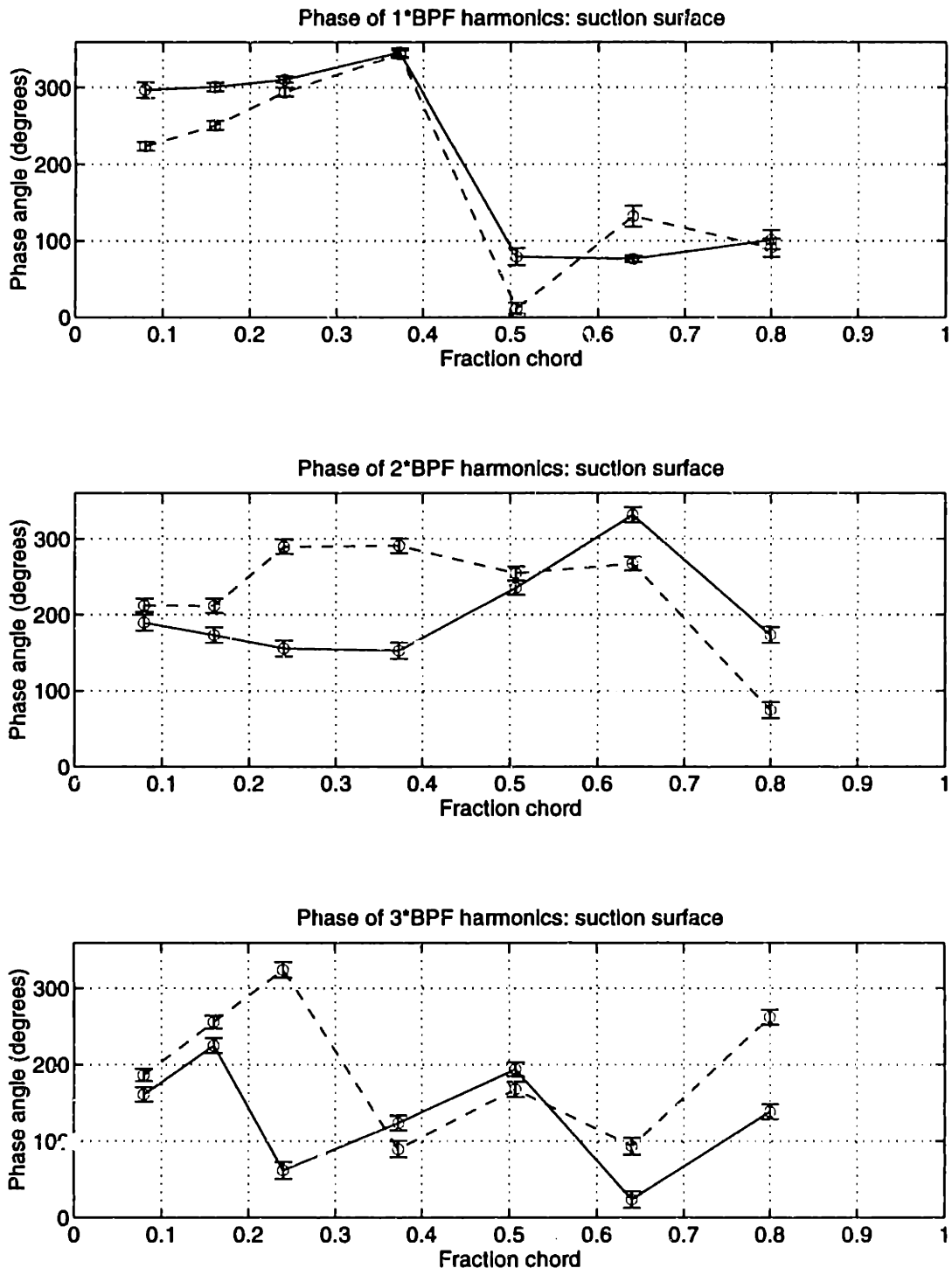

Figure 8-33: Stator suction surface harmonic phases at 87.5% span for the trailing edge blowing rotor with (- -) and without (—) tip-weighted injection

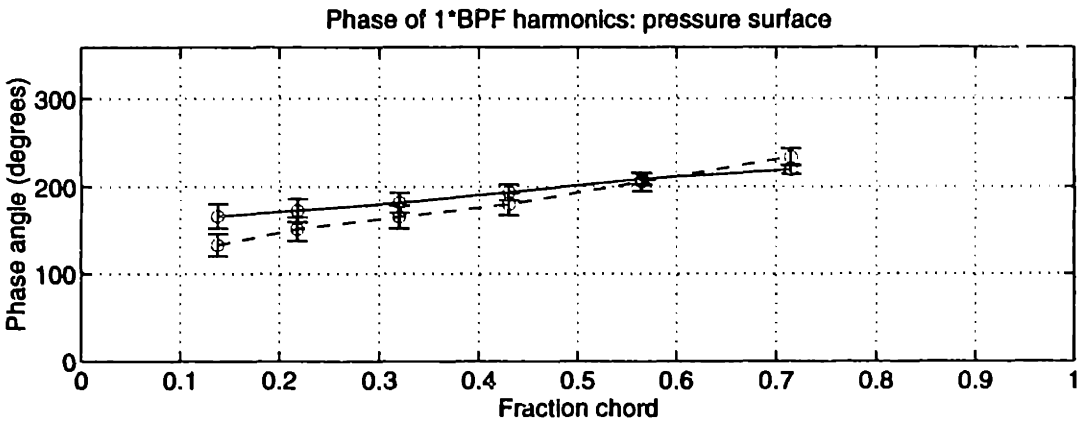

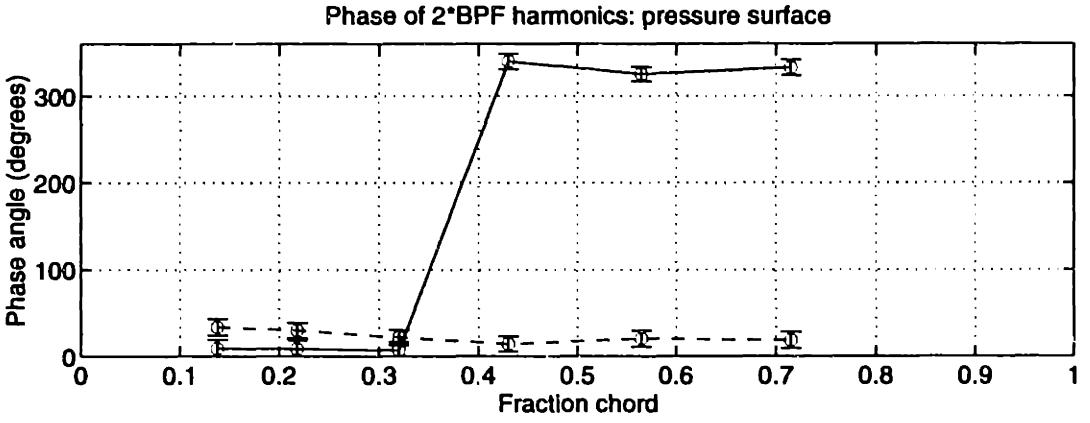

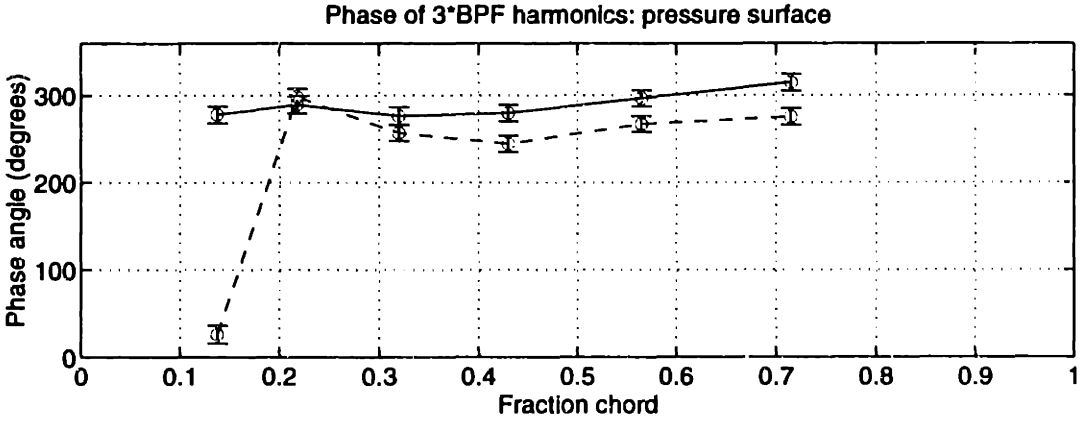

Figure 8-34: Stator pressure surface harmonic phases at 87.5% span for the trailing edge blowing rotor with (- -) and without (—) tip-weighted injection

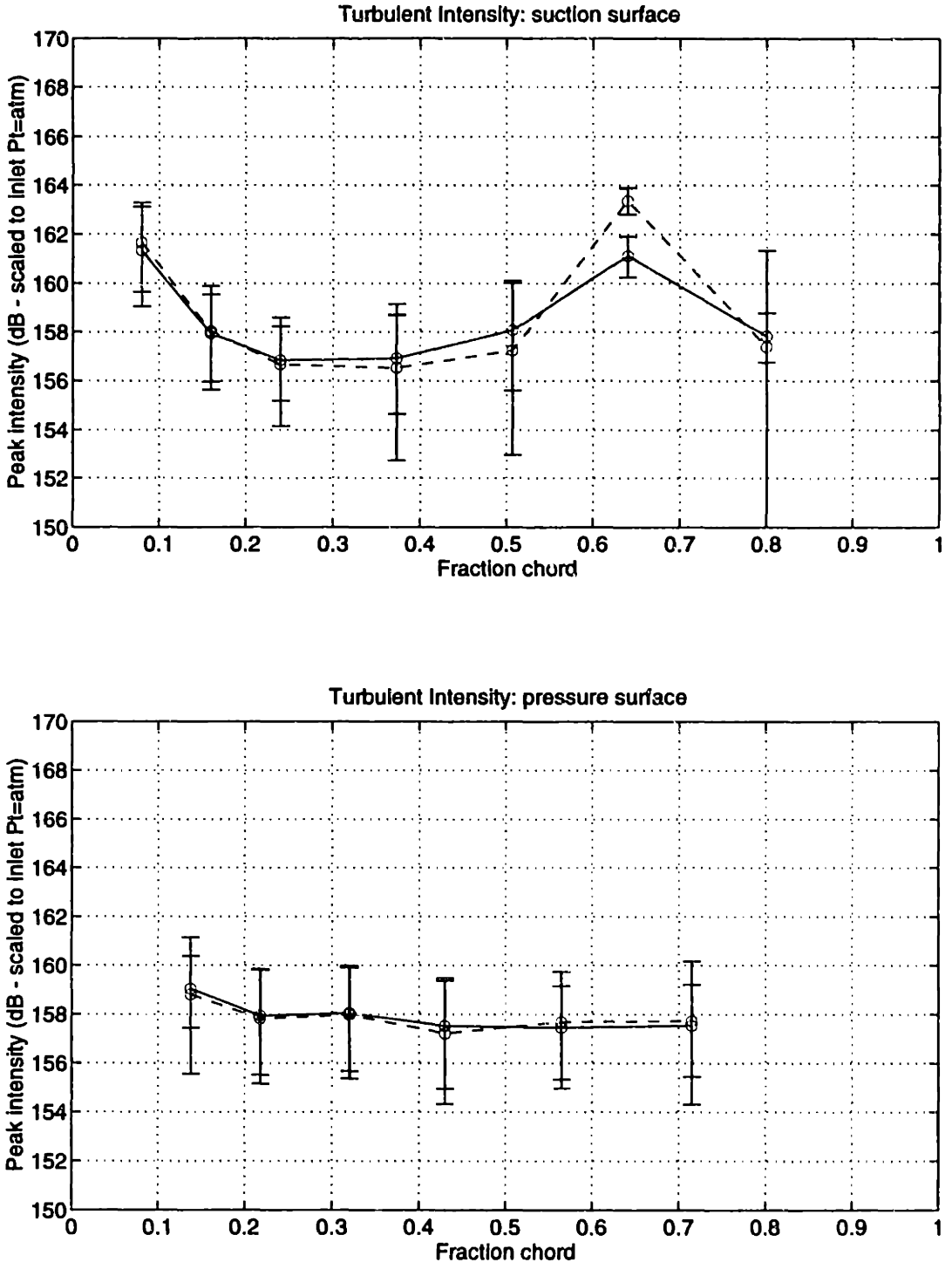

Figure 8-35: Stator pressure turbulence intensity at 87.5% span for the trailing edge blowing rotor with (- -) and without (—) tip-weighted injection

pressure across the blade and thus little change in the distributed dipole strength.

The harmonic phase angles for the suction and pressure surfaces are shown in Figures 8-33 and 8-34, respectively. As at 50 and 75% span, changes in the phase angles of about 50 to 100 degrees are seen. The wake 2*BPF phase angle was measured to have shifted approximately -240 degrees (or +120 degrees), and the stator 2*BPF harmonics are similarly shifted on the suction side about 100 degrees, but only about 50 degrees on the pressure side. The BPF harmonics on the stator appear to only have phase shifts of approximately 50 degrees, while the wake BPF harmonic was shifted about 160 degrees with injection. At this spanwise location, the BPF harmonic amplitudes correlate fairly well with the wake BPF harmonic upstream, but the phases do not.

The turbulence intensity at 87.5% span is plotted in Figure 8-35, but there is no discernible change in the turbulence levels with injection (except at 64% chord on the suction surface where the turbulence intensity is increased by approximately 2.5 dB with injection).

8.2.4 Amplitude and phase of pressure difference

The pressure differential harmonics across the stator blade were calculated from the data in Sections 8.2.1 through 8.2.3, as described in Section 8.1.4. The amplitudes of the BPF harmonics at 50, 75, and 87.5% span are plotted in Figure 8-36. The amplitudes at 50% span are seen to generally increase by about 3 dB with injection, even though the wake BPF harmonic is decreased by about 30% (3 dB). Most of the confidence intervals overlap, but a clear increase in the BPF pressure difference harmonic is observed at mid-chord.

At 75% span, the pressure difference BPF harmonic amplitude is seen to be reduced about 4 dB. The wake BPF harmonic amplitude at 1.5 chord was reduced about 65% (9.5 dB) with injection. Similarly, the differential amplitude at 87.5% span was reduced 3 to 10 dB along the chord, while the wake harmonic amplitude was reduced about 80% (13.7 dB).

The phases of the pressure difference are shown in Figure 8-37. The phase at 50% span shows a consistent offset of approximately 60 degrees, roughly corresponding to the shift in wake phase of about 39 degrees. At 75% span, there is similar correspondence between

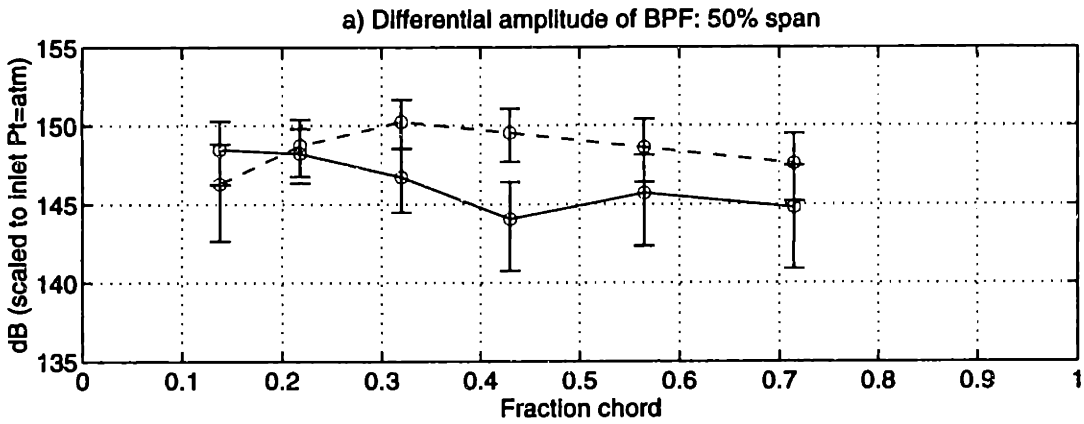

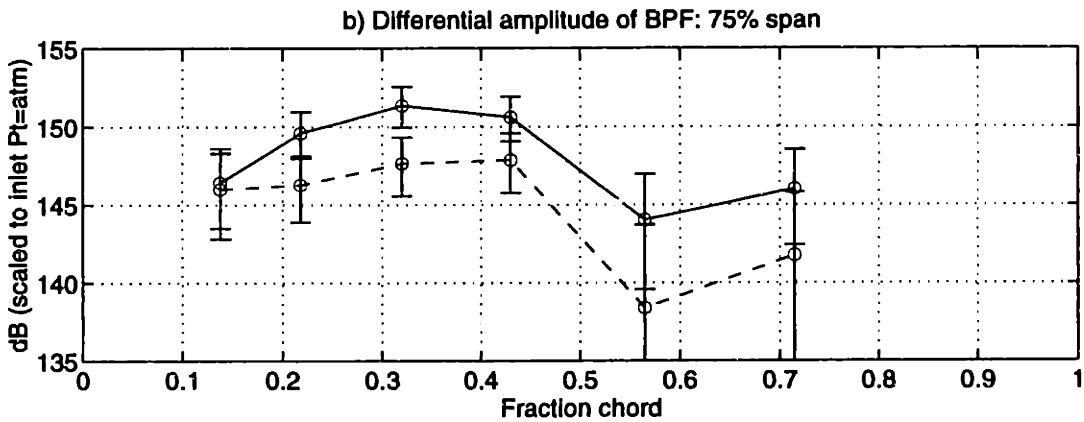

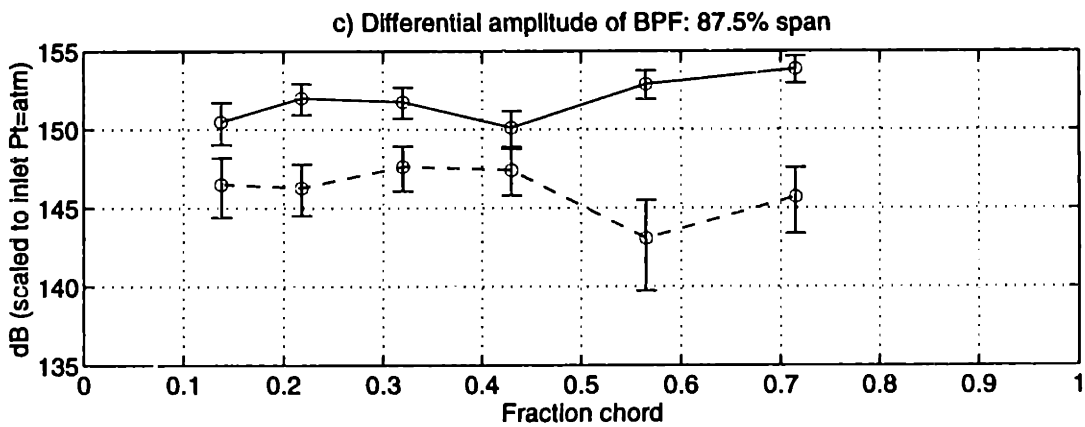

Figure 8-36: Amplitudes of stator surface pressure differential BPF harmonic for the trailing edge blowing rotor with (- -) and without (—) tip-weighted injection

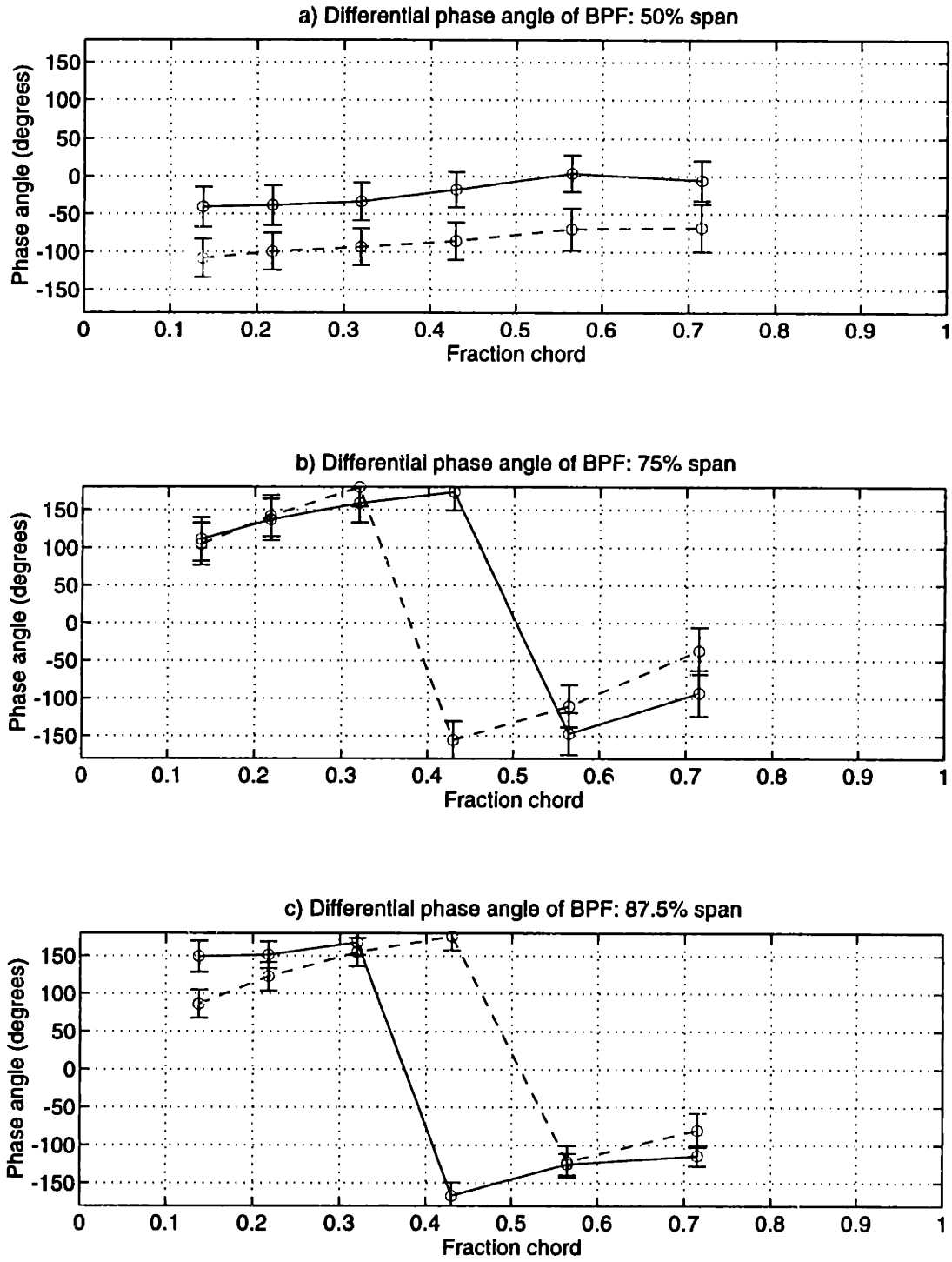

Figure 8-37: Phases of stator surface pressure differential BPF harmonic for the trailing edge blowing rotor with (- -) and without (—) tip-weighted injection

the wake phase angle shift of 68 degrees and the phase shift seen in the stator pressure differential of -10 to +65 degrees. However, at 87.5% span, where the wake BPF harmonic was shifted by approximately 156 degrees due to overblowing (as seen in Figure 7-55), there are only 5 to 70 degree phase angle shifts observed in the stator data from the no injection to tip-weighted injection configurations.

8.3 Summary of Stator Surface Pressure Measurements

Stator unsteady pressure measurements were taken downstream of the trailing edge blowing rotor with and without tip-weighted injection. The data with no injection was compared to measurements taken with the baseline solid-bladed rotor, and changes in the stator measurements were seen to correlate reasonably well (within 2 dB) with changes in the wake measurements at 1.5 chord. However, when examining the stator measurements for the rotor with tip-weighted injection, changes in the harmonic amplitudes and phases on the stator had only partial correlation to changes in the wake harmonics at 1.5 chord.

In particular, the pressure differences across the stator blade were calculated, and while some phase shifts observed in the stator data corresponded fairly well to those observed in the wake measurements, others did not. Changes in the BPF harmonic amplitudes on the stator did not correlate well with the wake measurements either. Reductions on the stator were only 50 to 70% of the reductions observed in the wake. These results imply that the use of strip theory for calculation of the stator unsteady pressures with trailing edge blowing may lead to erroneous results. Additional data and numerical simulation will be required to accurately determine the cause of these unexpected results on the stator due to trailing edge blowing.

The cause for the lack of correlation between the wake harmonic changes and the changes on the stator blade is currently believed to be the significant alteration in radial wake harmonic phase variation due to injection. It was shown in Chapter 5.4 that the coupling of neighboring stator blades during wake/stator interaction causes the pressure fluctuations on the stator blade surfaces to move upstream over the rotor blade passing period for rotor-stator blade count ratios similar to that for the fan stage used in this research. In addition, the shape of the harmonic amplitudes and phases along the chord

are complicated.

If neighboring blades that are spaced circumferentially 0.5 to 1.0 stator chords (hub to tip) cause significant interaction between them, then wake harmonics that have phase variations on the order of 360 degrees over about 1.7 stator chords (one-half the stator span) can certainly be expected to cause significant coupling of the stator unsteady pressure fields at different spanwise locations. Thus, if trailing edge blowing creates large changes to the spanwise wake harmonic phase and amplitude variation, the stator unsteady pressure fields can not be expected to behave in the traditional strip-theory sense. That is to say, the unsteady pressure harmonics at each spanwise position on the stator will most likely not have the same amplitude and phase changes as the wake harmonics upstream of the stator at the same spanwise position.

It should be noted, however, that the BPF, m=-24 mode was estimated to be just on the verge of cut-on in the swirling, midstage region (i.e. changes of about 1 percent in Mach number will create cut-on conditions). Therefore, even if the mode is evanescent, the decay rate is less than about 20 dB per rotor/stator spacing and some 'mode trapping' will occur (see Section 1.3.3). Some of the differences observed between changes in the wake harmonics and changes in the stator pressure harmonics may be due to changes in the trapping of the BPF mode.

8.4 Microphone Duct Acoustic Measurements

Flow field measurements presented in Chapter 7 show that significant reduction of the periodic unsteadiness entering the stator row can be achieved. Stator unsteady pressure measurements discussed in Section 8.2, however, show that changes in the radial variation in wake harmonic amplitude and phase cause alterations in the stator unsteady response that do not follow traditional linear strip theory approximations. Because of these changes in the spanwise distribution of stator unsteady loading, the acoustic coupling will be altered. In particular, the radial mode content for each circumferential mode at multiples of rotor blade passing frequency, BPF, is expected to change.

Pairs of microphones were placed in the outer shroud upstream and downstream of

both the rotor and stator. One pair was placed approximately one rotor chord upstream of the rotor; one pair was placed one stator chord downstream of the stator; and, the third pair was placed between the blade rows approximately one rotor chord downstream of the rotor and one stator chord upstream of the stator. Each pair was placed 22.5 degrees apart circumferentially (1/16th of the circumference). This spacing was used since, ideally, all of the propagating acoustic modes for the 16/40, rotor/stator blade count are multiples of 8. By adding and subtracting the signals at each pair of microphones, the different circumferential modes at each multiple of blade passing frequency could be distinguished.

For example, the dominant propagating acoustic mode for this fan stage, as determined from LINSUB [34], is the 2*BPF, m=-8 mode downstream of the stator. This mode has eight wavelengths around the circumference and thus is out-of-phase at the microphone pair. Downstream of the stator, the out-of-phase acoustic spectra should produce this 2*BPF out-of-phase tone, and the in-phase spectra should have no 2*BPF content.

Because the acoustic measurements were taken at the shroud wall, however, they measure the sum of the radial modes present for each circumferential mode. If all the radial modes are uniformly reduced, then the wall measurements will accurately capture the change in the overall acoustics. Any change in the radial variation of the stator unsteady pressure field (amplitude and/or phase) will change the radial coupling and the radial acoustic mode content. Therefore, the wall microphones will measure a sum of radial modes that have different amplitudes and different tangential phases than for the baseline condition. Even though the total acoustic power in the modes may be reduced (for a given circumferential mode and frequency) the measurements at the wall may indicate an increase in amplitude. In addition, if the wake harmonic phases change such that they are approximately constant along the span, the low order radial modes (which generally do not couple well due to large wake skew) may couple strongly and increase the radiated noise even for significant reduction in the wake harmonic amplitudes.

In the next several sections, acoustic spectra will be shown for all the rotor configurations discussed in the thesis. First, measurements from the baseline rotor with solid blades are shown. Next, measurements from the trailing edge blowing rotor with no injection are presented, followed by the high loading condition of the solid-bladed rotor. Finally, acoustic spectra for trailing edge blowing is shown for 1.9% tip-weighted injection, and for 2.0%

and 1.8% midspan-weighted injection. Tables of the tonal levels (from the full data trace spectra) from all the rotor configurations are provided in Section 8.4.7.

The acoustic spectra are plotted with 95% confidence intervals calculated by using the harmonic content of each blade passing period sum or difference. These harmonics from each rotor period are averaged over several runs and the standard deviation taken. The 95% confidence interval is then calculated assuming a χ^2 distribution. The mean harmonic tone levels calculated in this manner are shown as round symbols and match the tones calculated using the full data trace within about 1.5 dB for tones that stand clearly above the broadband noise. For tonal levels in the broadband noise floor, the blade period averaging gives inconsistent results.

8.4.1 Baseline solid-bladed rotor acoustic spectra

The in and out-of-phase acoustic spectra at the microphones upstream of the rotor are shown in Figure 8-38 for the solid-bladed rotor at the baseline takeoff condition. There are in-phase BPF and 2*BPF tones present, which are most likely due to the rotor potential field. The out-of-phase BPF tone is due to the evanescent m=-24, BPF acoustic mode upstream of the rotor and/or inlet distortion.

The spectra in the midstage region are plotted in Figure 8-39. Several tones stand out in the midstage region, both in and out-of-phase. In the swirling flow between the rotor and stator, a m=-24 BPF mode is close to cut-on, but is evanescent upstream of the rotor and downstream of the stator. Circumferential mode pairs propagate for 3,4, and 5*BPF that are in and out-of-phase. The propagating acoustic modes for this fan stage are shown in Table 3.2.

Downstream of the stator row, the out-of-phase BPF does not propagate and the acoustic field is dominated by the m=-8, 2*BPF mode. The spectra downstream of the stator are shown in Figure 8-40. There is a 'tone' at BPF that is in-phase. It is assumed that this peak is due to the wake and tip clearances flows near the endwall. In the out-of-phase spectra, the 2*BPF tone is about 10 dB above the broadband noise floor, and smaller tones are seen at 4 and 5*BPF. The spectra for the baseline rotor are the average of two runs.

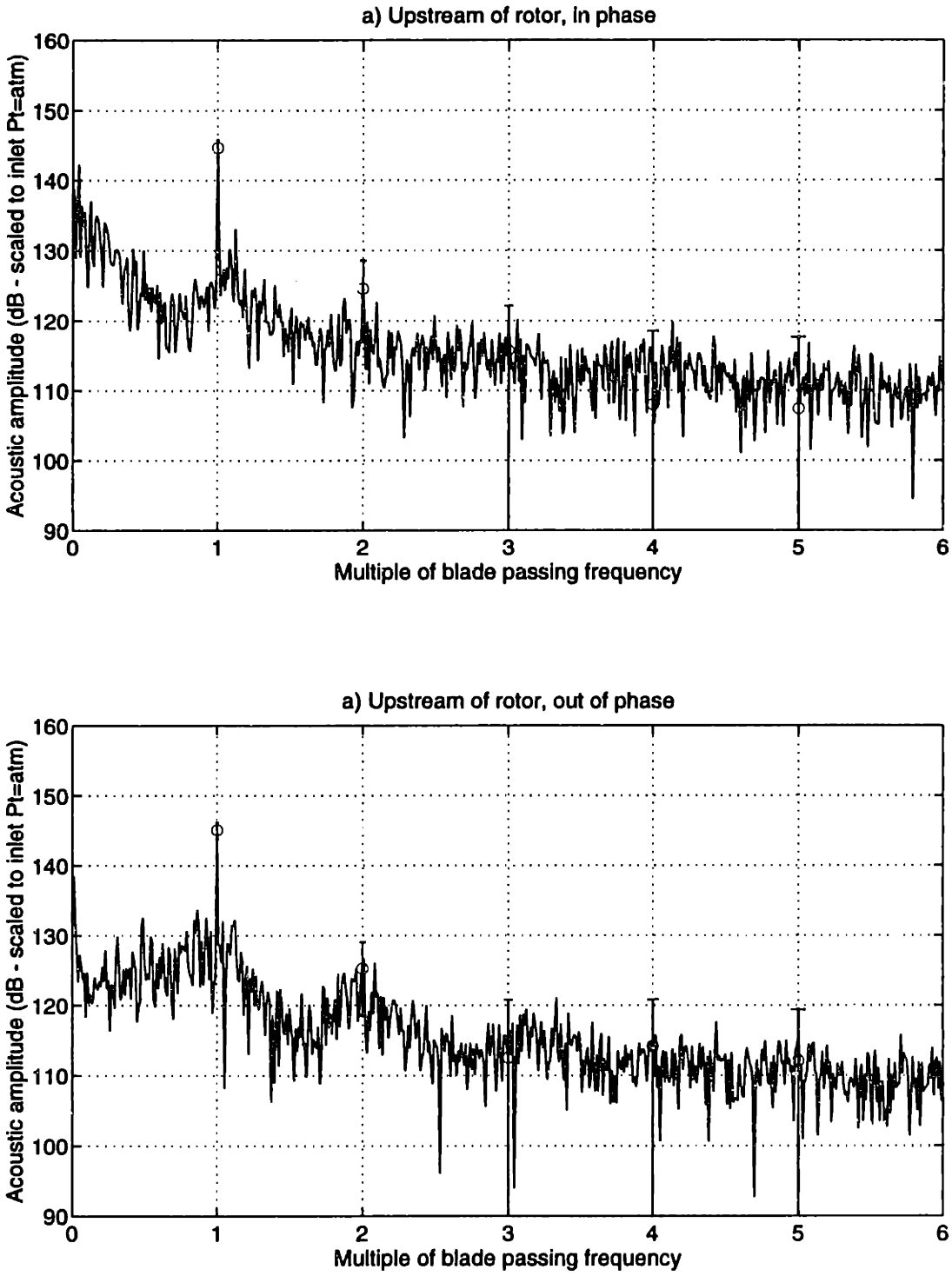

Figure 8-38: Acoustic spectra upstream of the rotor: baseline rotor

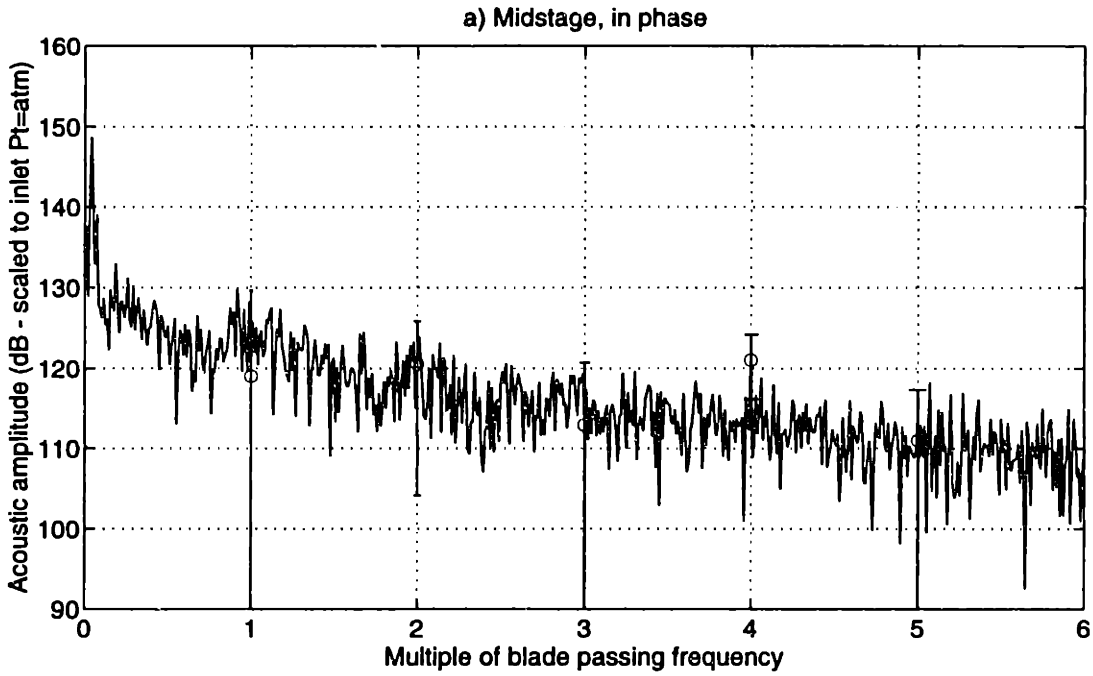

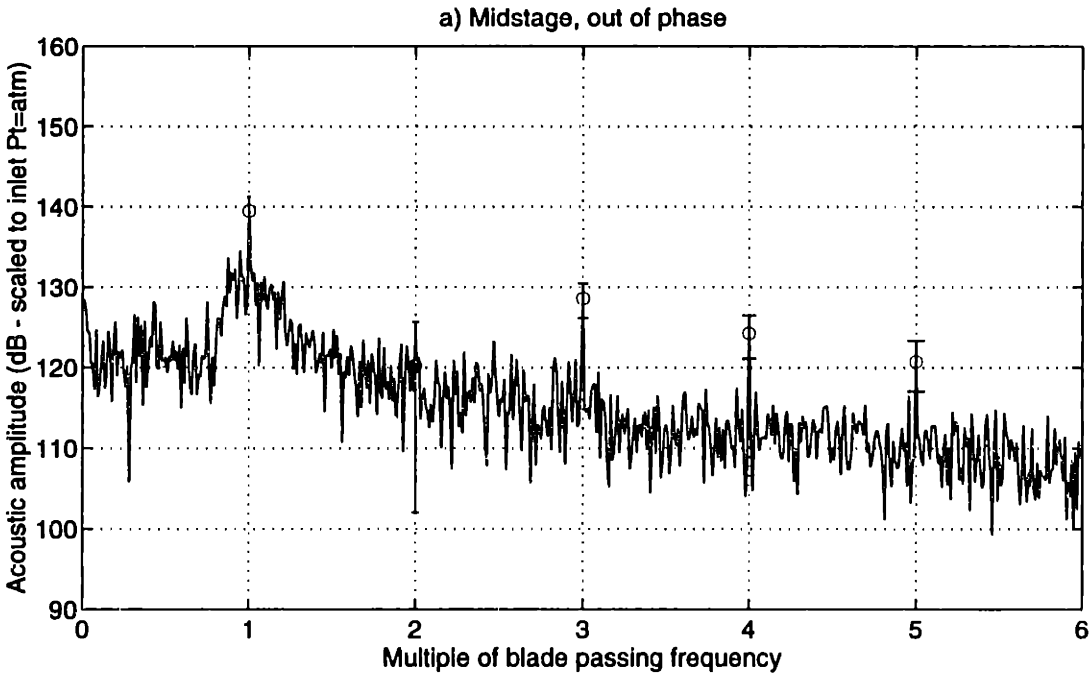

Figure 8-39: Acoustic spectra upstream in the midstage region: baseline rotor

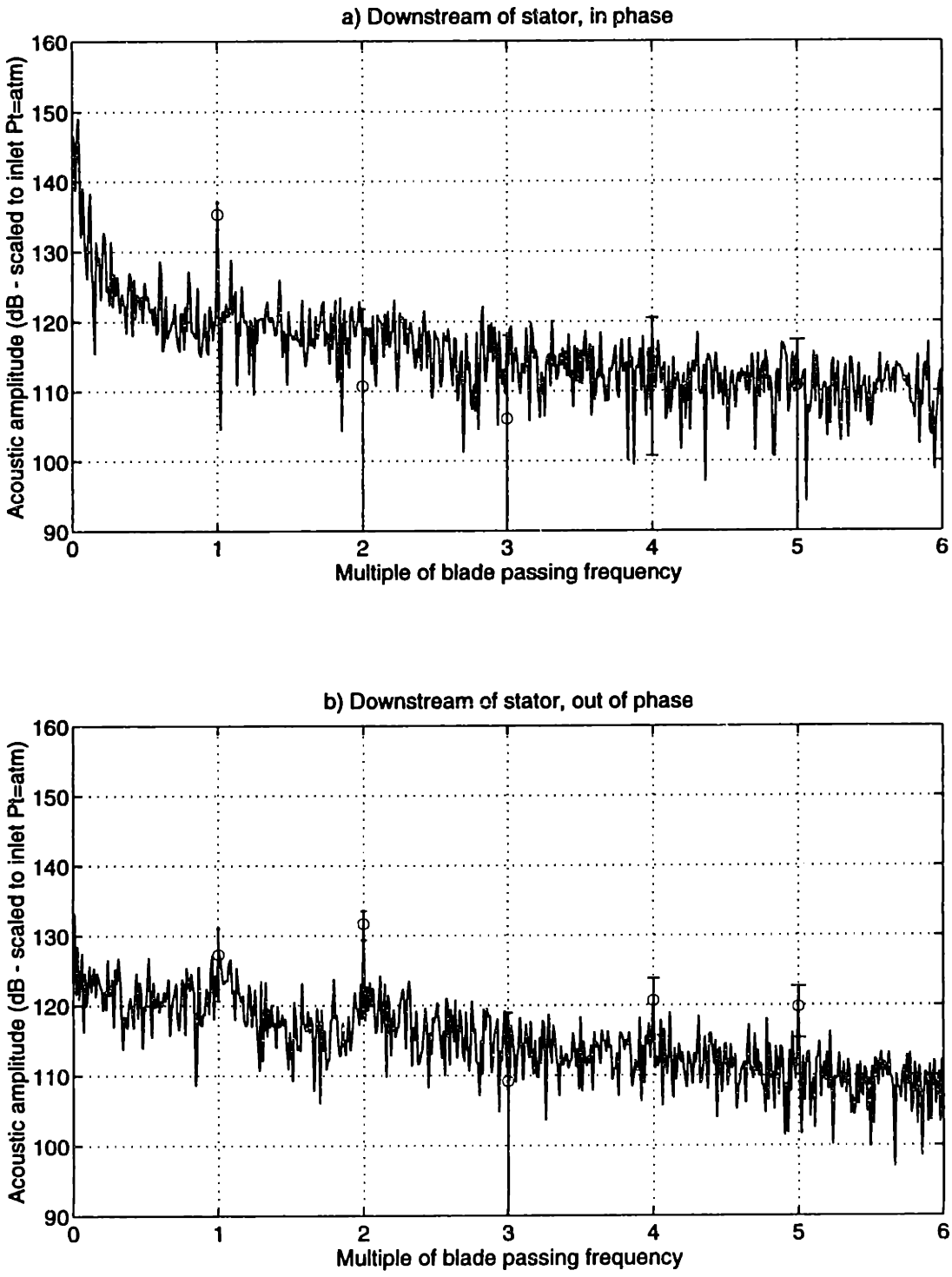

Figure 8-40: Acoustic spectra downstream of the stator: baseline rotor

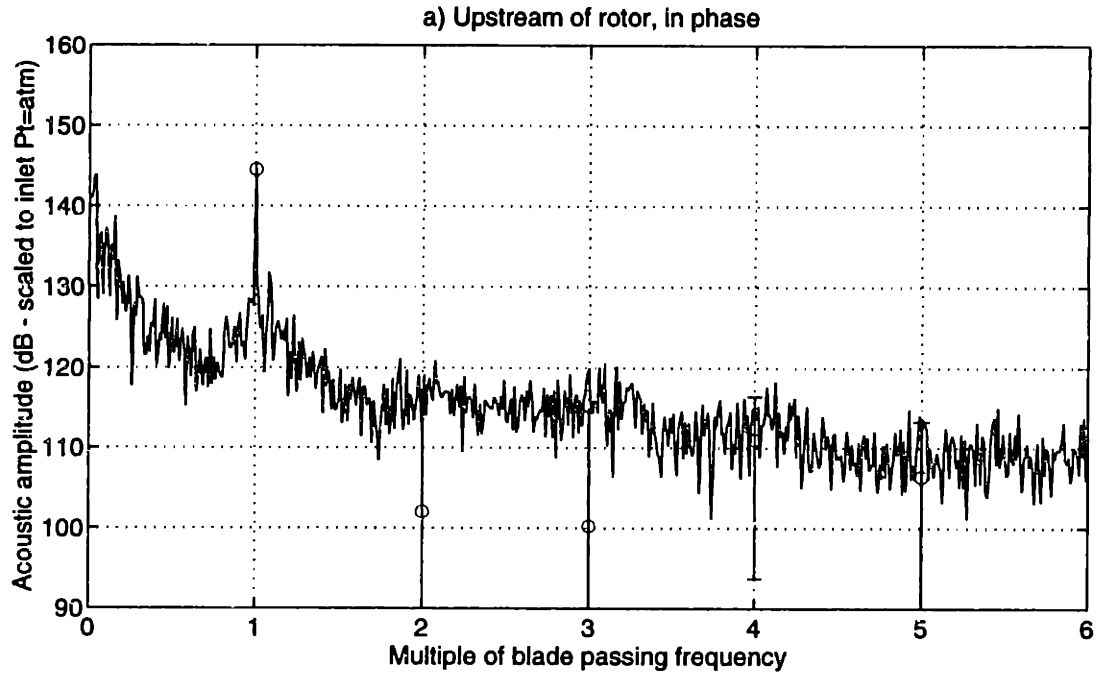

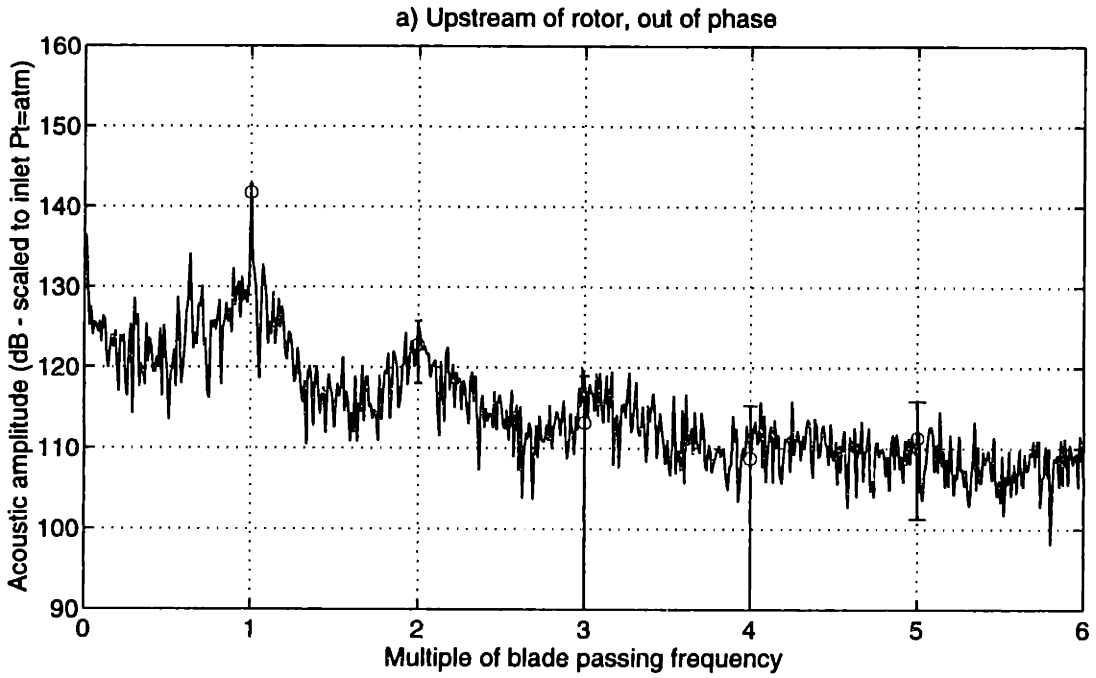

Figure 8-41: Acoustic spectra upstream of the rotor: trailing edge blowing rotor (no injection)

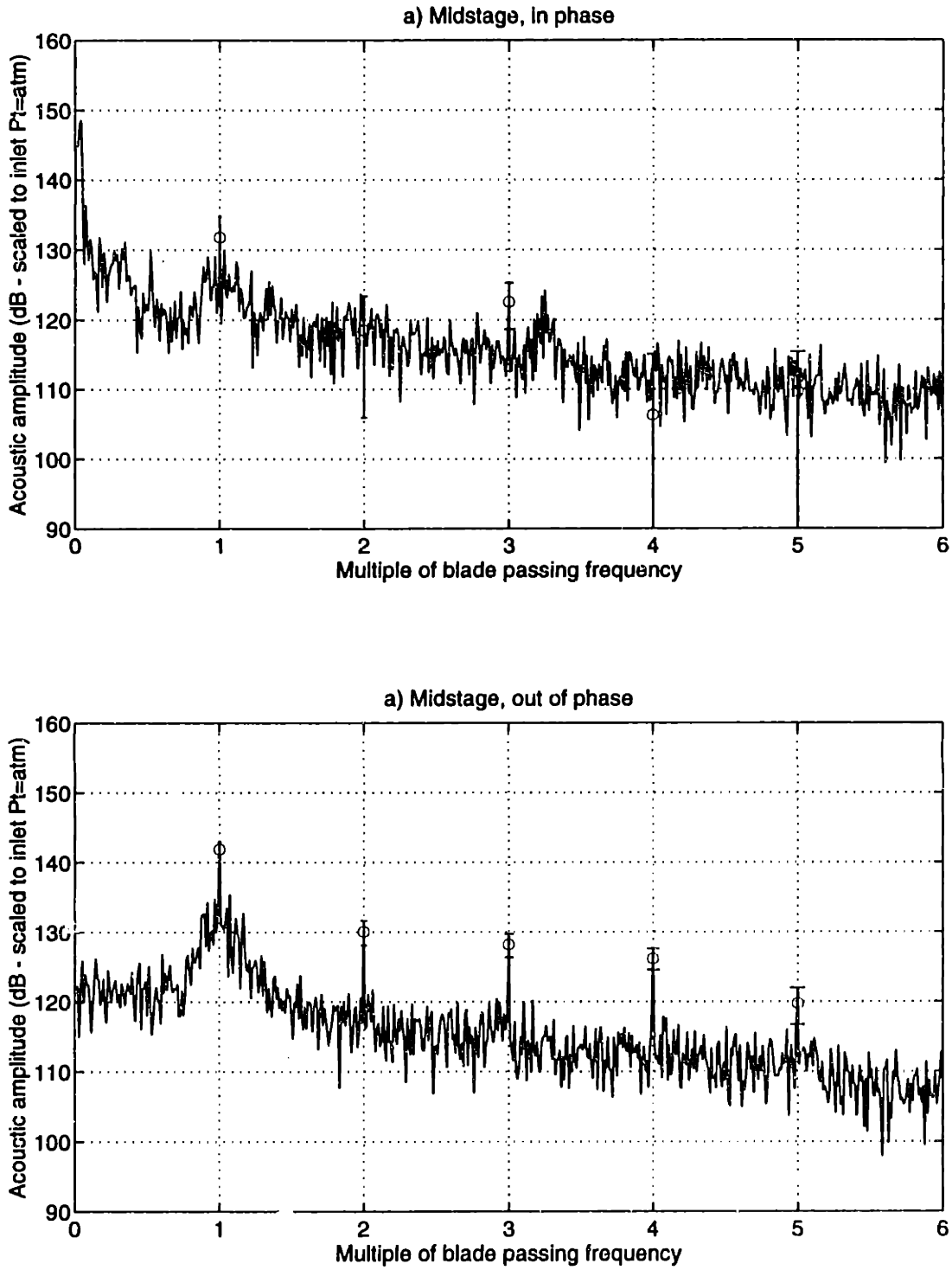

Figure 8-42: Acoustic spectra upstream in the midstage region: trailing edge blowing rotor (no injection)

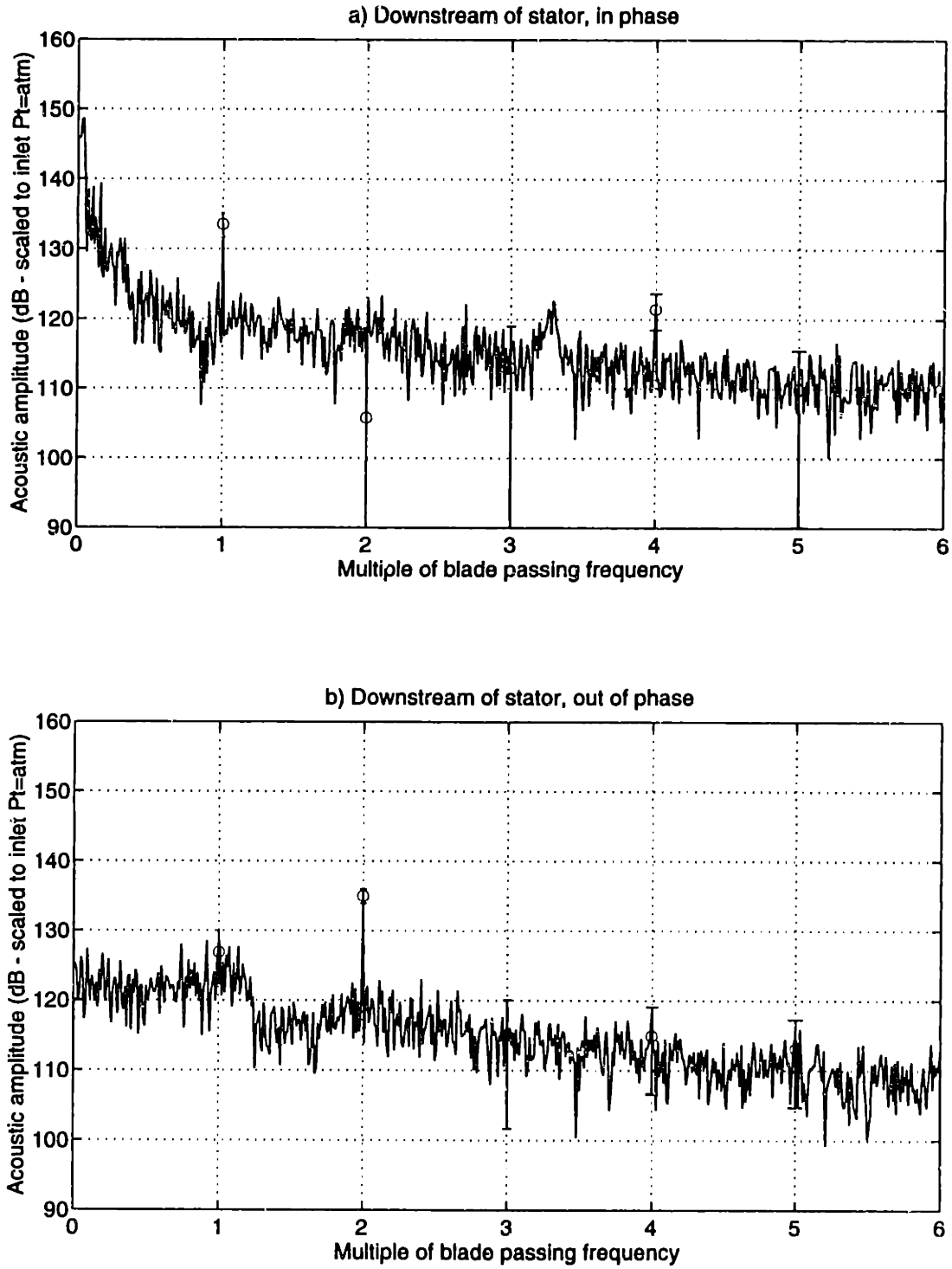

Figure 8-43: Acoustic spectra downstream of the stator: trailing edge blowing rotor (no injection)

8.4.2 Trailing edge blowing rotor (no injection) acoustic spectra

The acoustic spectra upstream of the trailing edge blowing rotor with no injection are plotted in Figure 8-41. The spectra are seen to be very similar to the upstream spectra for the baseline rotor in Figure 8-38, except for a slight decrease in the out-of-phase BPF tone and a smoother broadband noise floor due to the averaging of four runs.

The spectra in the midstage region are plotted in Figure 8-42 and show similar behavior to the baseline rotor spectra with some changes in the various tonal levels. The spectra downstream of the stator (shown in Figure 8-43) are also similar for the two rotors with a slight increase in the out-of-phase 2*BPF tone for the trailing edge blowing rotor. Since the wake harmonic amplitudes and phases at 1.5 chord were approximately the same for the baseline solid-bladed rotor and the trailing edge blowing rotor without injection, the acoustics should be very similar. Again, all the tonal levels are shown in Table 8.1.

8.4.3 High loading solid-bladed rotor acoustic spectra

The first case examined with markedly different flow conditions than the baseline configuration is the high loading condition of the solid-bladed rotor. The flow field for this case is discussed in Appendix C and has a mass flow rate approximately 15% lower than the baseline loading and a 1.5% increase in total pressure ratio. The wake harmonic amplitudes at 1.5 chord are generally larger than the baseline loading condition by 20 to 40%, with the largest increase occurring at 75% span. The primary importance of this configuration is that the wake harmonics are increased, but the wake harmonic phase variation remains approximately the same as for the baseline loading condition (see Figure C-25).

The upstream spectra are plotted in Figure 8-44. The in and out-of-phase BPF 'tones' both increase by a few dB and the broadband noise is seen to increase as well by a few dB relative to the baseline loading condition. This is particularly seen in the in-phase spectra around multiples of BPF, where the noise levels are increased approximately 5 dB.

The midstage microphone spectra are shown in Figure 8-45. Like the results from the trailing edge blowing rotor (no injection) there are differences in the tonal levels at high loading compared to the baseline loading of about 10 dB. Downstream of the stator

row, the tonal levels remain approximately the same except for the 2*BPF tone, which is increased by about 7 dB. This increase can be seen in Figure 8-46. As with the upstream measurements, the in-phase broadband noise floor is increased approximately 5 dB.

8.4.4 Tip-weighted injection (1.9%) acoustic spectra

The acoustic spectra presented thus far have been from flow fields with largely equivalent wake harmonic radial phase variation. With the introduction of trailing edge blowing that results in portions of the wake being overblown, the radial phasing is changed significantly. The wake harmonic phases for tip-weighted injection (1.9% of the throughflow) are shown in Figure 7-55. Because of the large change in spanwise distribution of both wake harmonic amplitude and phase, the radial acoustic field is expected to change significantly. However, while the acoustic amplitudes at the outer wall may not correctly indicate the overall change in the radiated acoustic power, they may be useful for validation of acoustic prediction tools.

The upstream acoustic spectra are shown in Figure 8-47 for tip-weighted injection. The results appear very similar to the baseline rotor, except for the appearance of an out-of-phase 2*BPF tone. This tone is about 5 dB above the broadband noise floor. These measurements were taken back-to-back with the no injection configuration, and thus this 2*BPF appearance can not be caused by an inlet distortion. The acoustic radial mode content of this m=-8, 2*BPF mode is certainly changed from the no injection configuration, so the appearance of the 2*BPF tone upstream indicates a different radial mode content that may have overall reduction or increase in radiated power.

The midstage acoustic spectra are plotted in Figure 8-48 and show similar behavior to the previous midstage spectra. Some tones are increased and some are decreased. This midstage region appears to be the most inconsistent of the three microphone measurement positions.

The acoustic spectra from downstream of the stator are presented in Figure 8-49. Except for the appearance of a 4*BPF in-phase tone, the biggest change in the spectra is the near removal of the 2*BPF tone. The 2*BPF out-of-phase amplitude is reduced about 11 dB from the no injection configuration. Of course, like the upstream 2*BPF tone that appeared with tip-weighted injection, this 11 dB decrease may be caused solely by a shift in

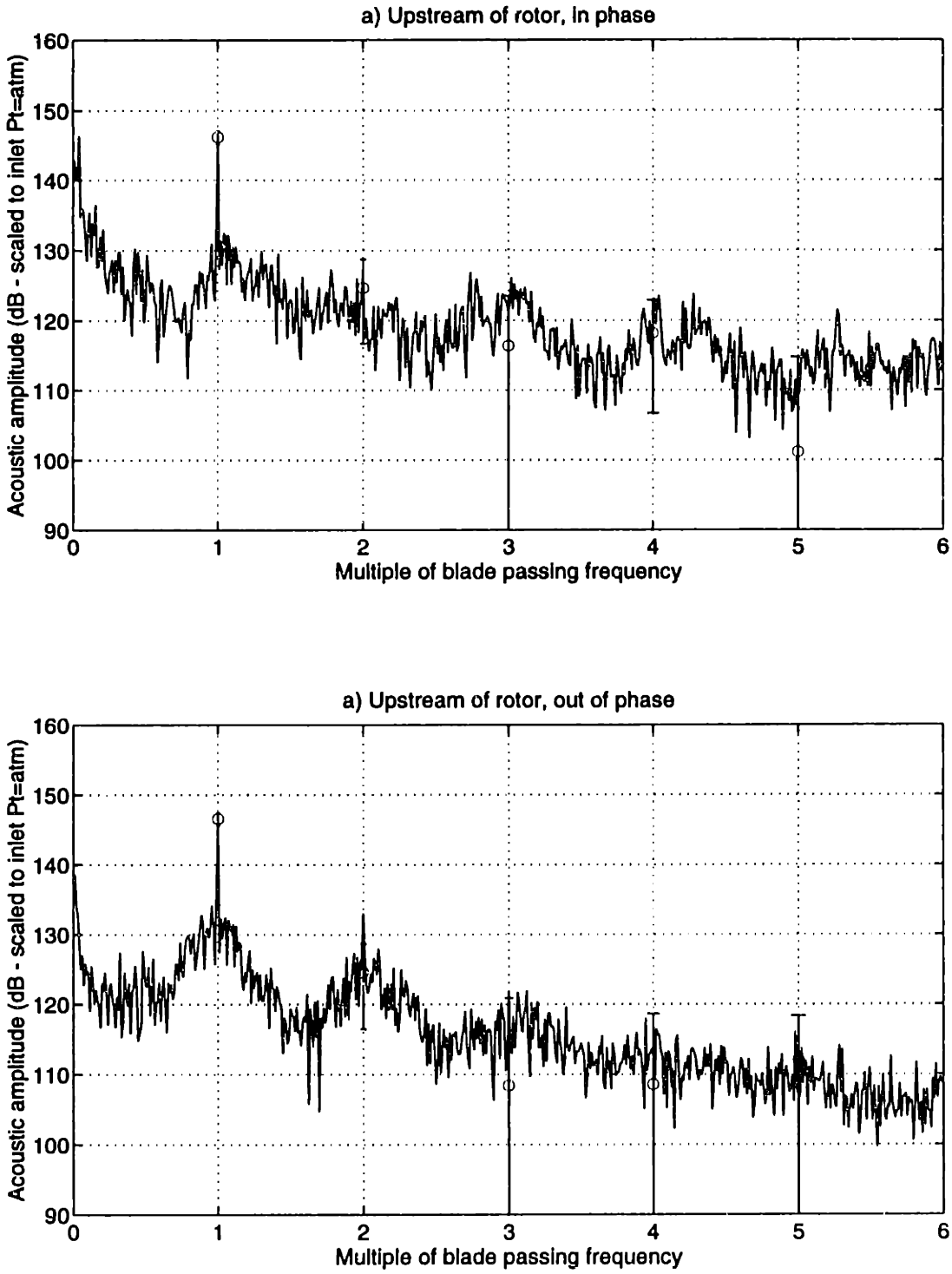

Figure 8-44: Acoustic spectra upstream of the rotor: high loading of solid-bladed rotor

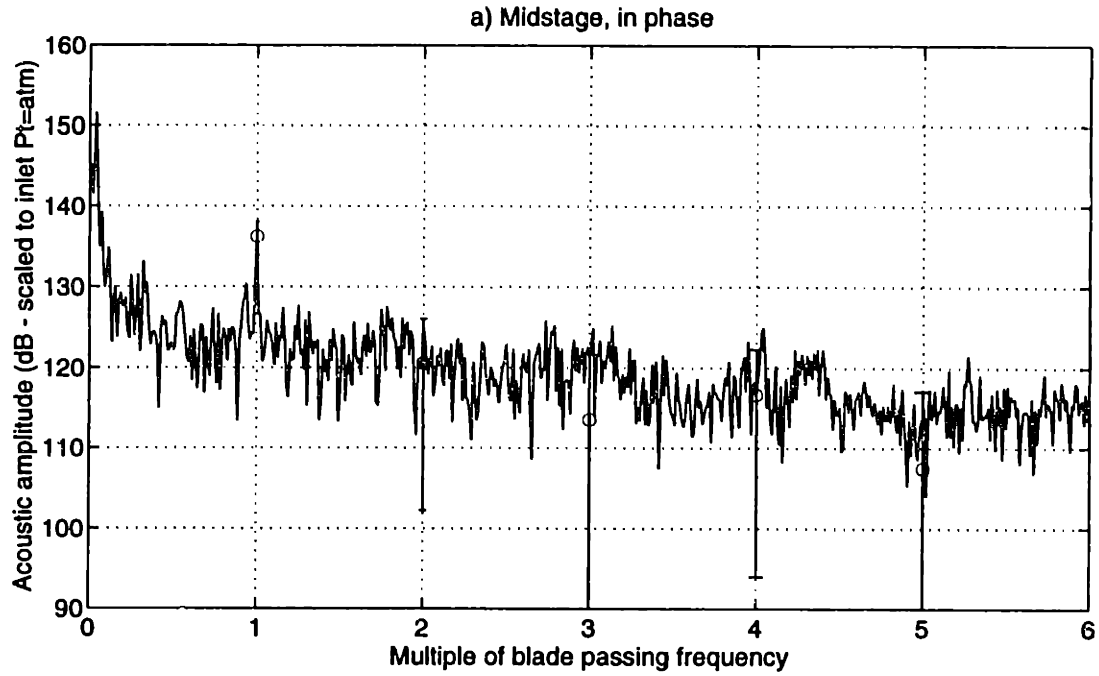

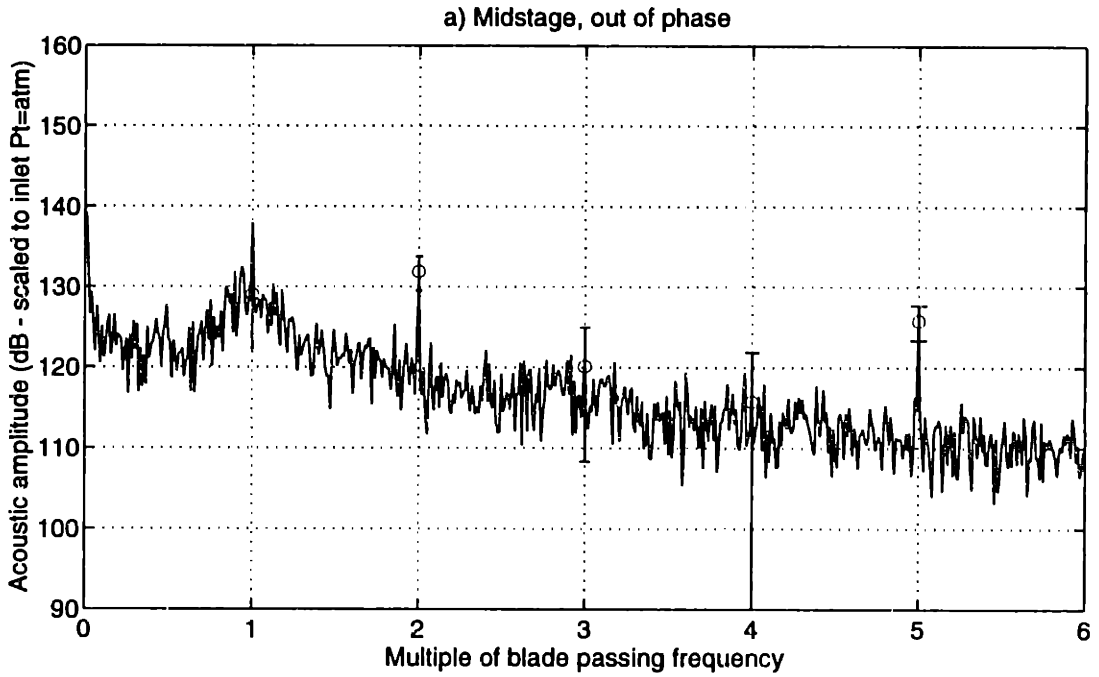

Figure 8-45: Acoustic spectra upstream in the midstage region: high loading of solid-bladed rotor

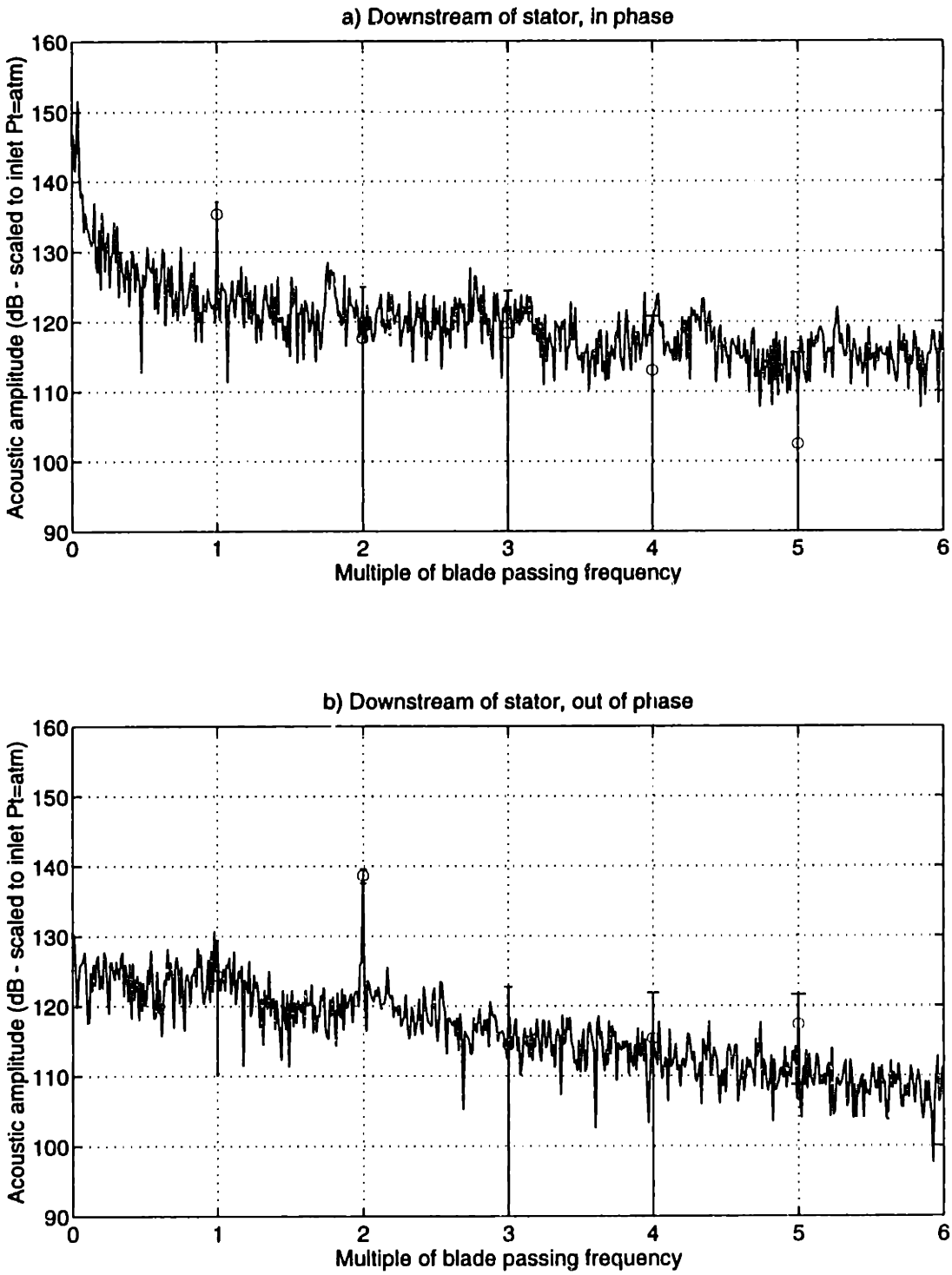

Figure 8-46: Acoustic spectra downstream of the stator: high loading of solid-bladed rotor

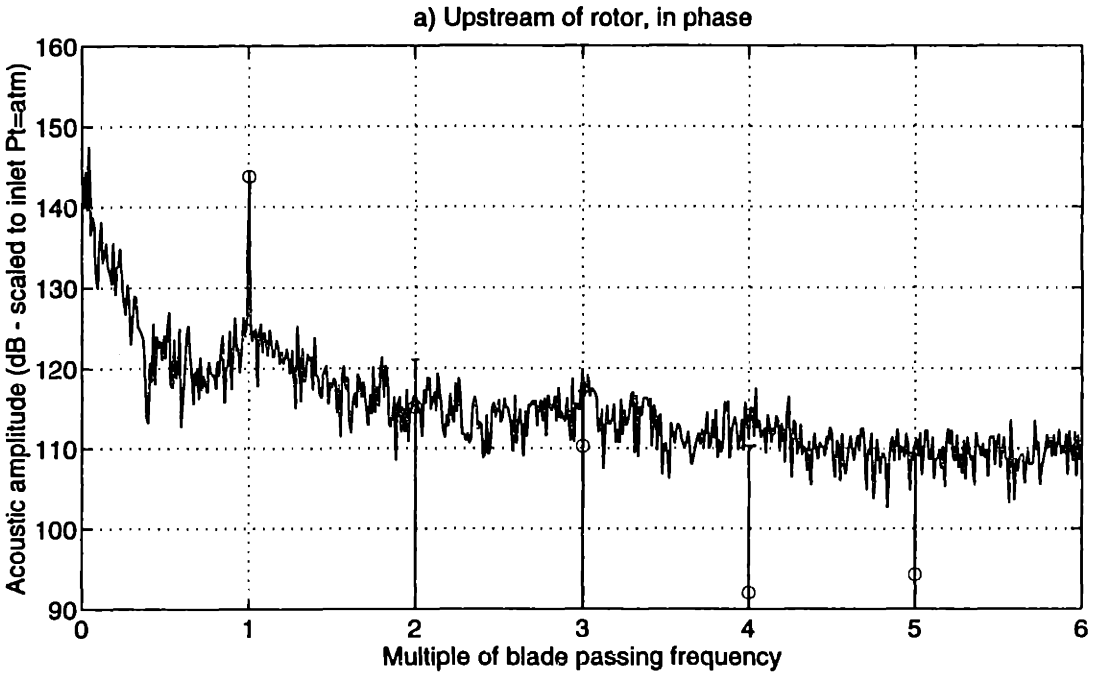

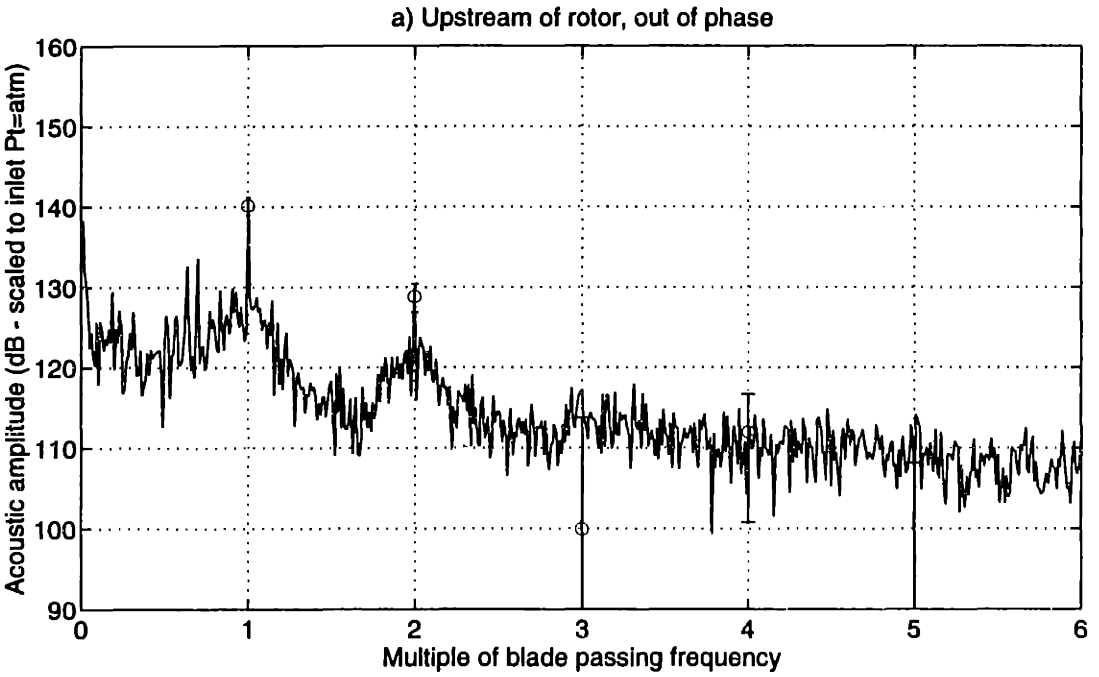

Figure 8-47: Acoustic spectra upstream of the rotor: tip-weighted injection

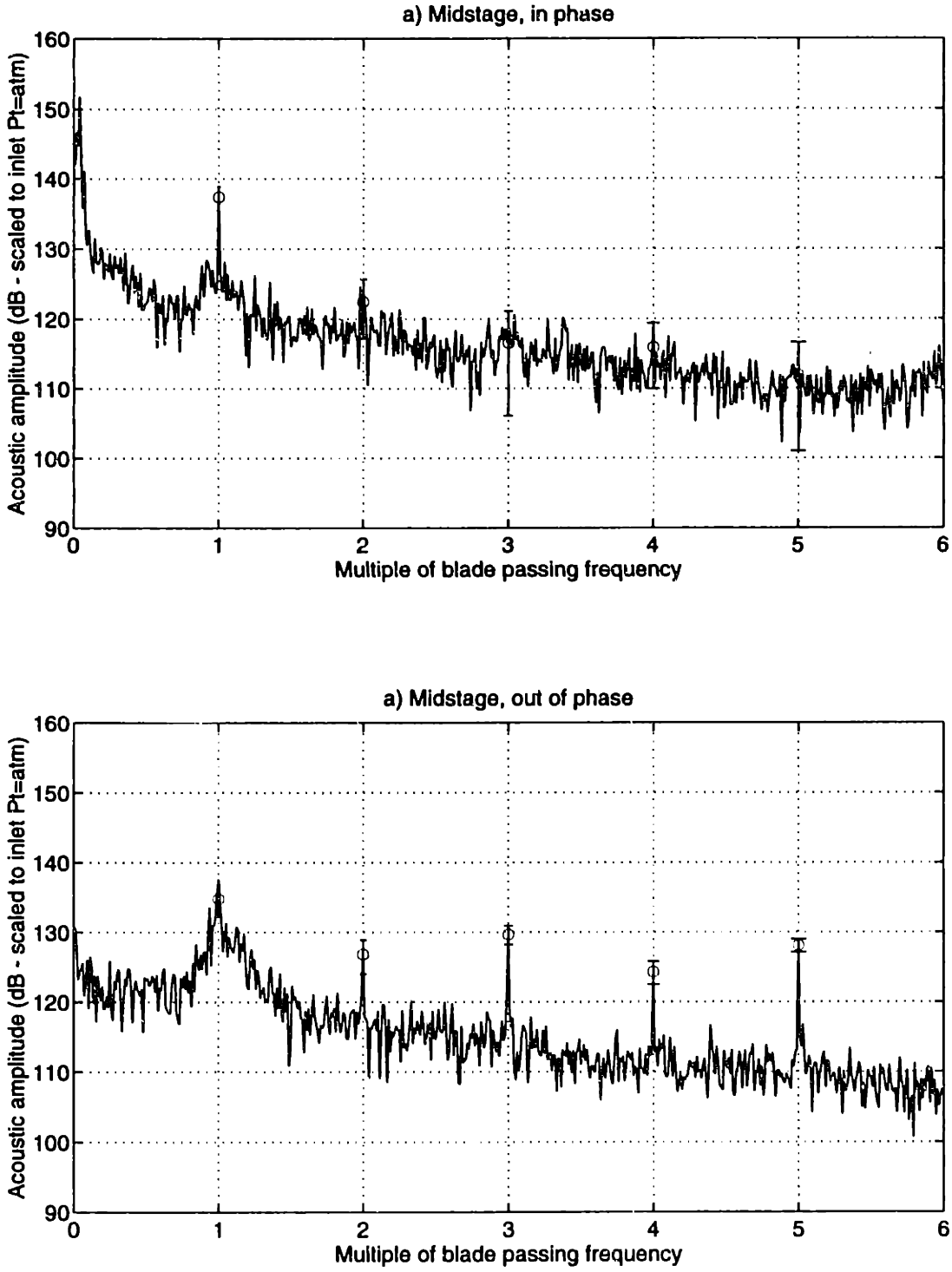

Figure 8-48: Acoustic spectra upstream in the midstage region: tip-weighted injection

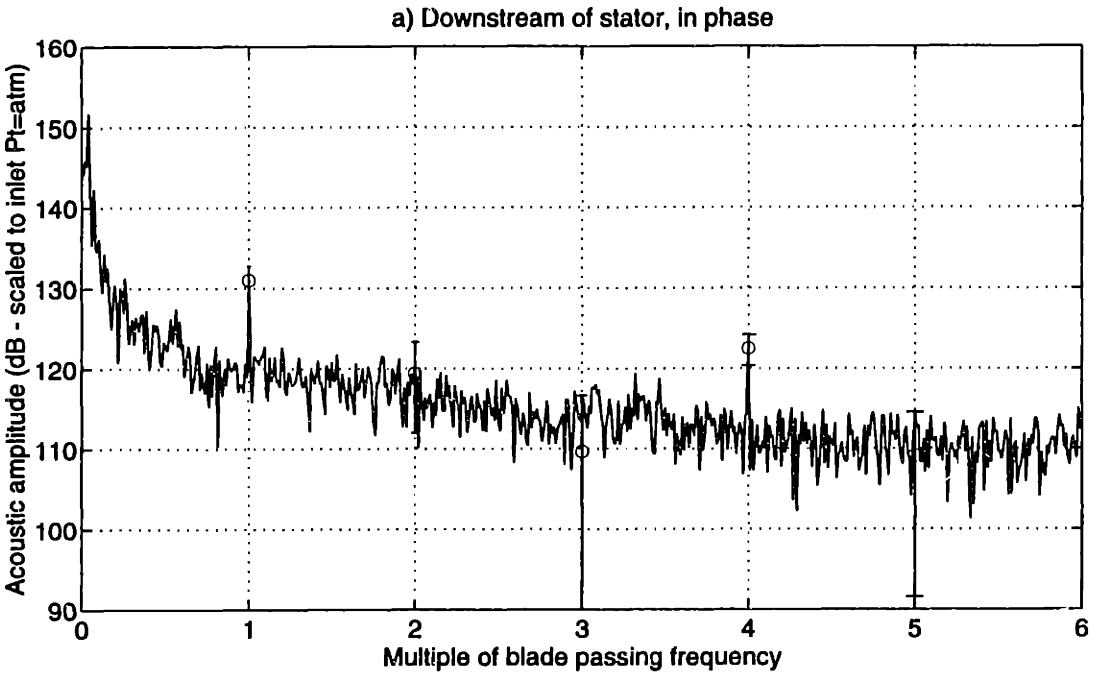

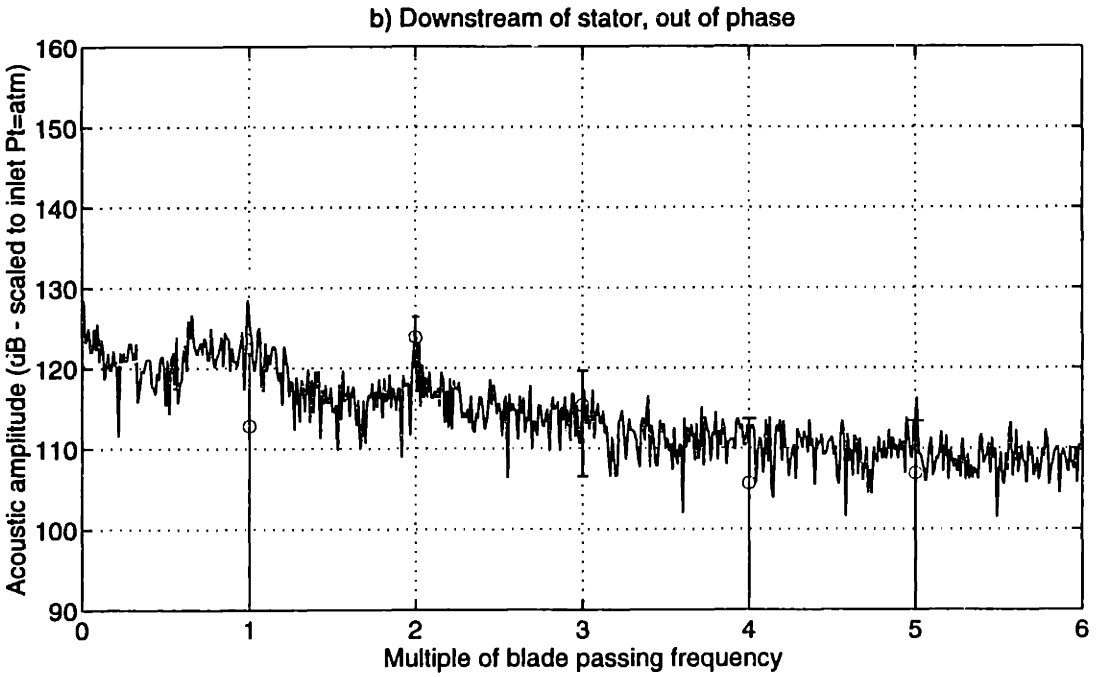

Figure 8-49: Acoustic spectra downstream of the stator: tip-weighted injection

the radial mode content and not necessarily a reduction in the total 2*BPF radiated power.

8.4.5 Midspan-weighted injection (2.0%) acoustic spectra

Similar to the tip-weighted injection, the blowing weighted in the midspan region with 2.0% mass addition had significant wake harmonic phase shifts as seen in Figure 7-72. The radial variation in the wake harmonic amplitudes, of course, also changed. The radial acoustic mode content is thus expected to change significantly.

The upstream acoustic spectra are shown in Figure 8-50. The spectra looks very similar to the tip-weighted injection spectra, including the out-of-phase 2*BPF tone. The rougher nature of the broadband noise is due to the averaging of only two runs. The midstage spectra are plotted in Figure 8-51. Except for the persistence of the BPF and 2*BPF tones, all higher harmonic tones disappear into the broadband noise.

However, at the downstream position, shown in Figure 8-52, the 2*BPF tone is virtually unchanged compared to the baseline rotor configuration (11 dB higher than the tip-weighted injection), while both BPF 'tones' are reduced more than 10 dB. The acoustic results of the tip (1.9%) and midspan (2.0%) weighted injection are quite interesting. Due to changes in the wake harmonic radial variations, one case has significantly reduced the downstream 2*BPF tone (at the shroud wall) and the other has significantly reduced the midstage tones. Both, however, increase the 2*BPF tone upstream of the rotor. The acoustic measurements alone demonstrate the complicated nature of rotor wake/stator interaction and the coupling to the acoustic field.

8.4.6 Midspan-weighted injection (1.8%) acoustic spectra

The tip (1.9%) and midspan (2.0%) weighted injection showed significant changes in the wake harmonic radial structure, and thus generated different radial acoustic mode content. The changes in the shroud acoustic amplitudes upstream, downstream, and in the midstage region demonstrate that the acoustic modes up and downstream of a given blade row do not even behave similarly for changes to the wake. In an attempt to keep the wake harmonic phase angles as similar as possible to the no injection configuration, the midspan-weighted

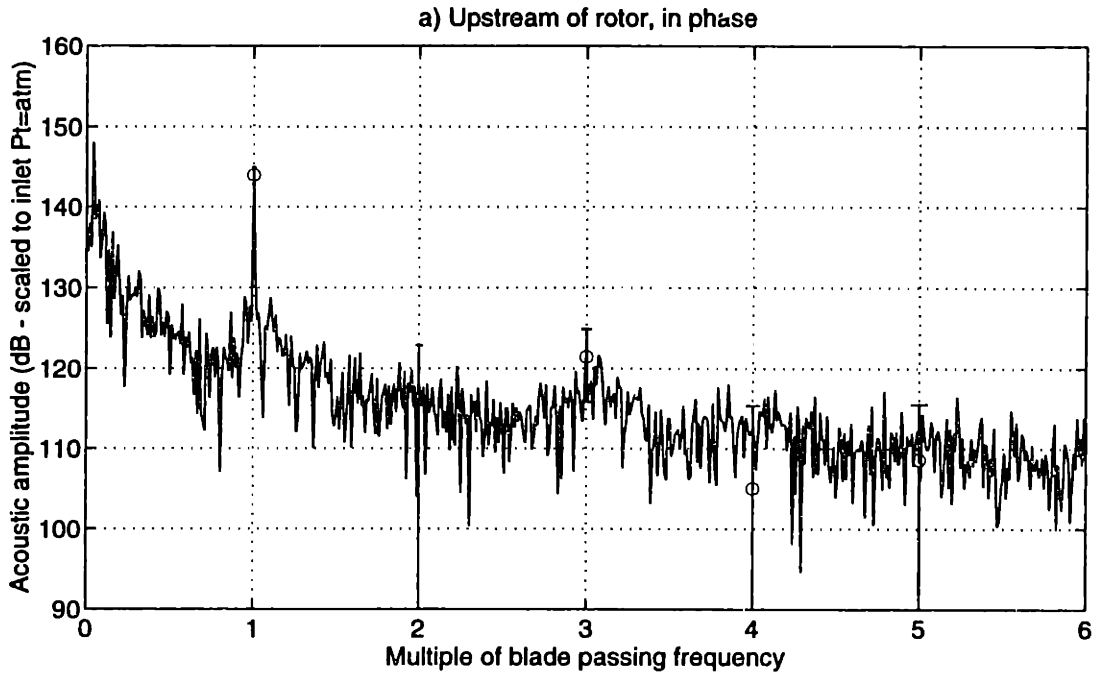

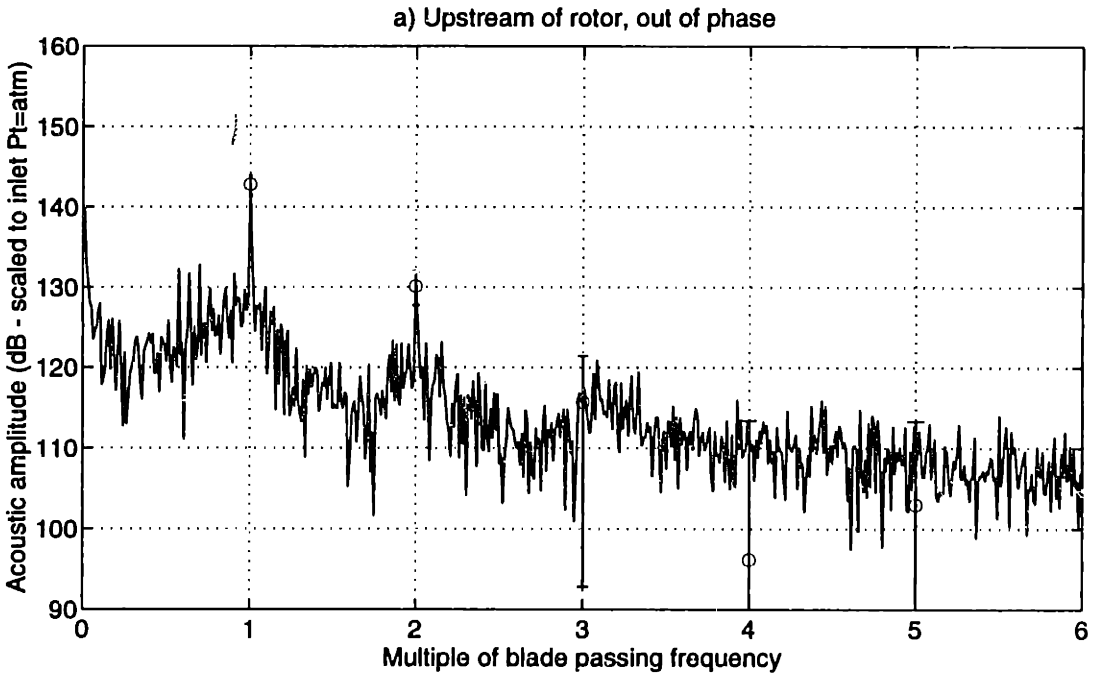

Figure 8-50: Acoustic spectra upstream of the rotor: 2.0% midspan-weighted injection

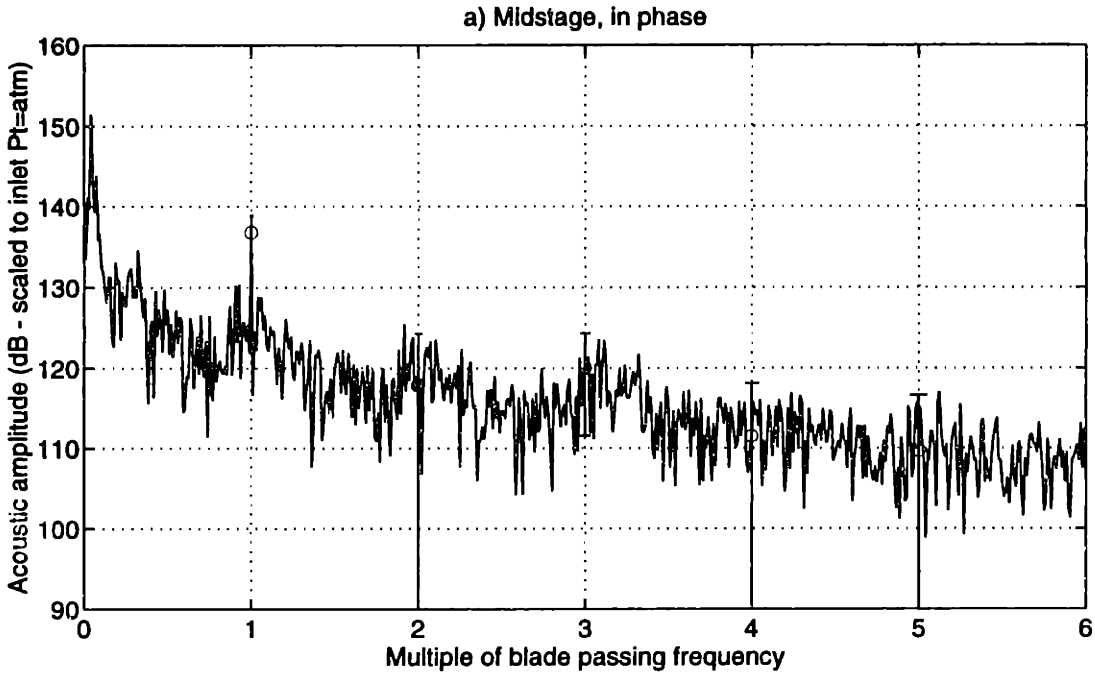

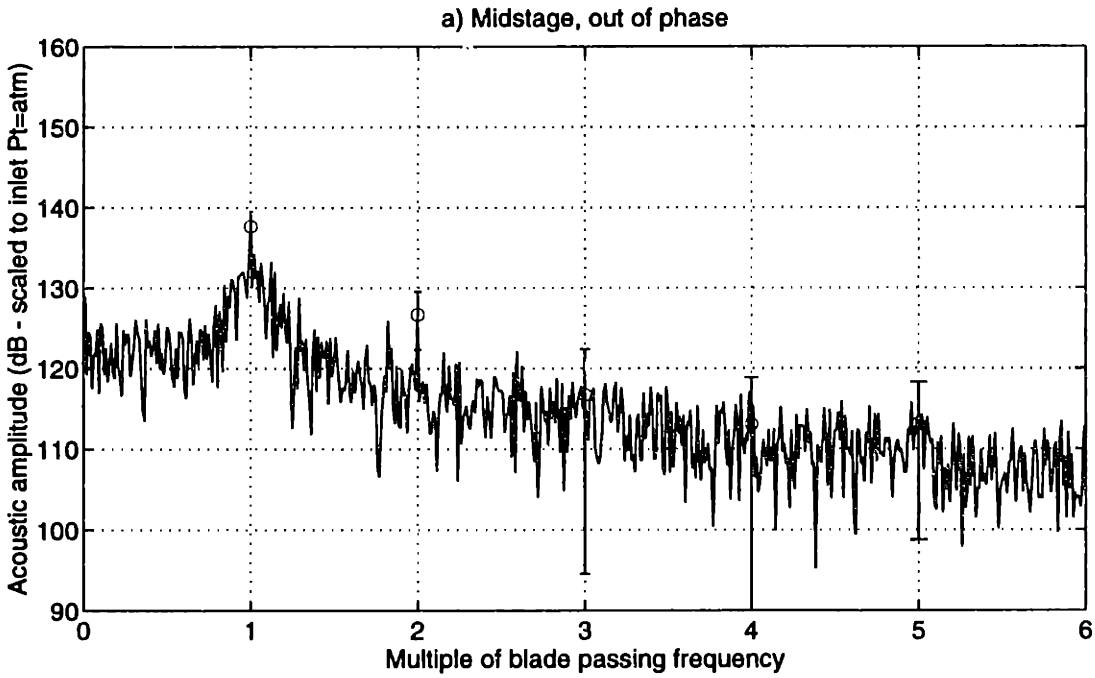

Figure 8-51: Acoustic spectra upstream in the midstage region: 2.0% midspan-weighted injection

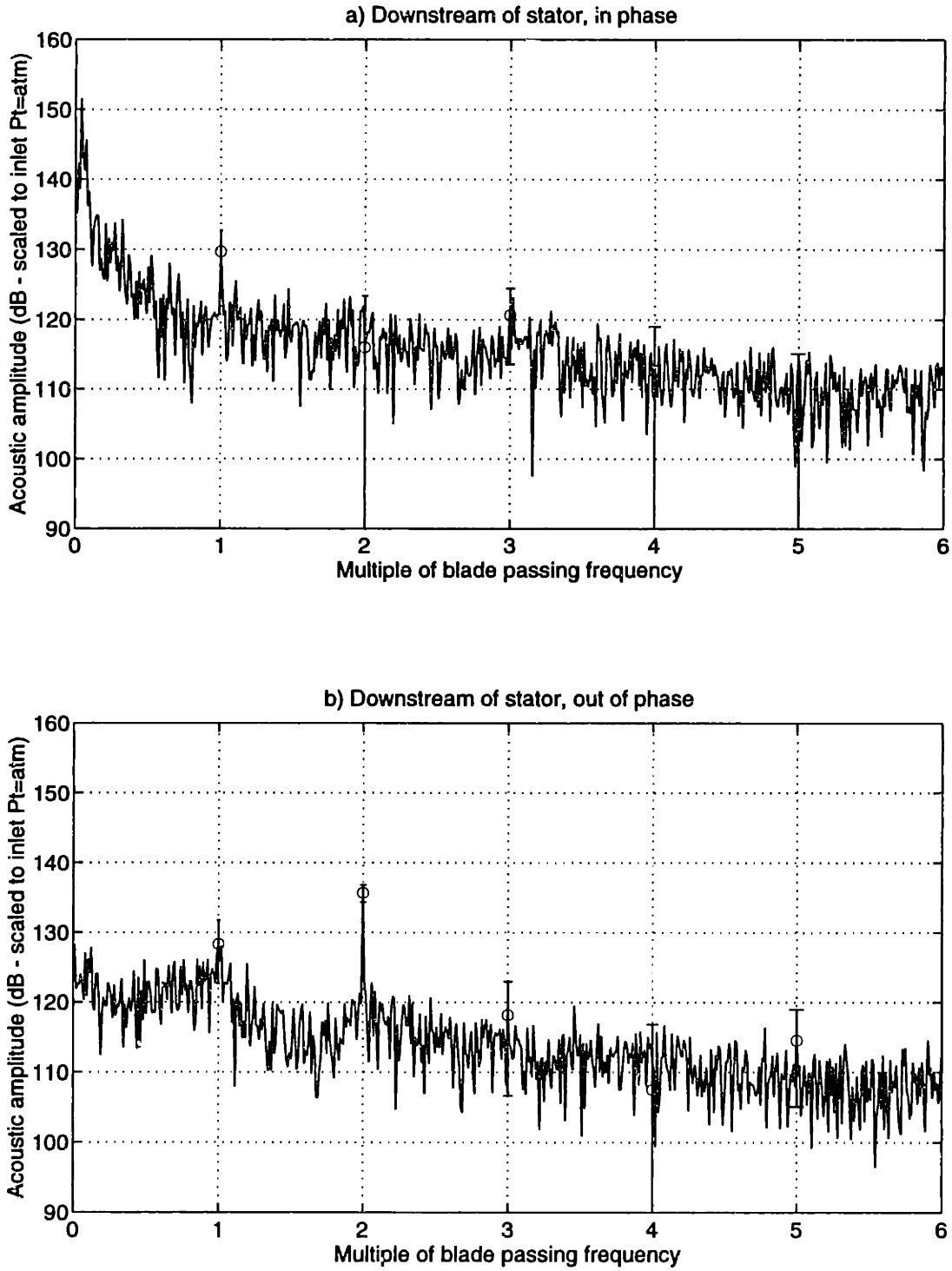

Figure 8-52: Acoustic spectra downstream of the stator: 2.0% midspan-weighted injection

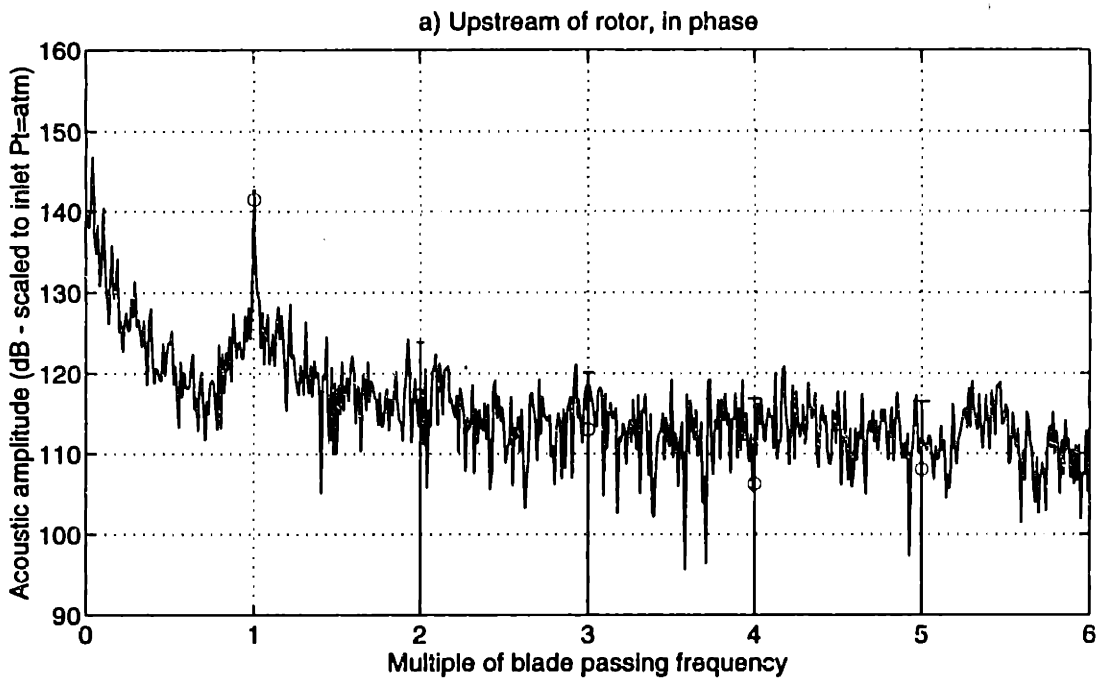

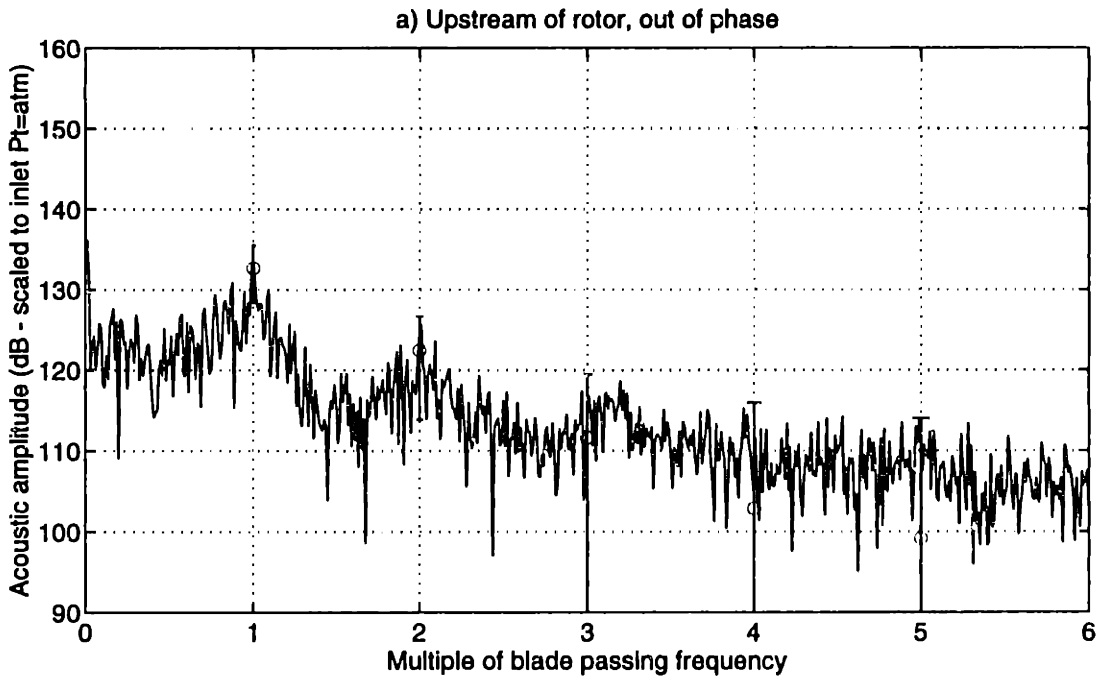

Figure 8-53: Acoustic spectra upstream of the rotor: 1.8% midspan-weighted injection

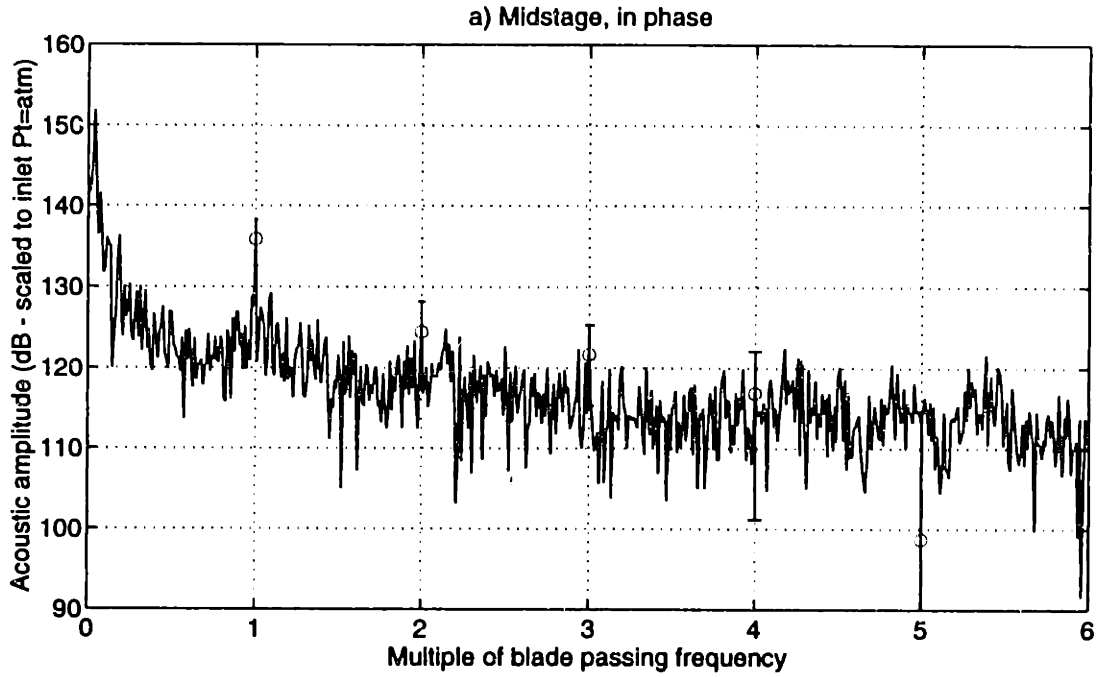

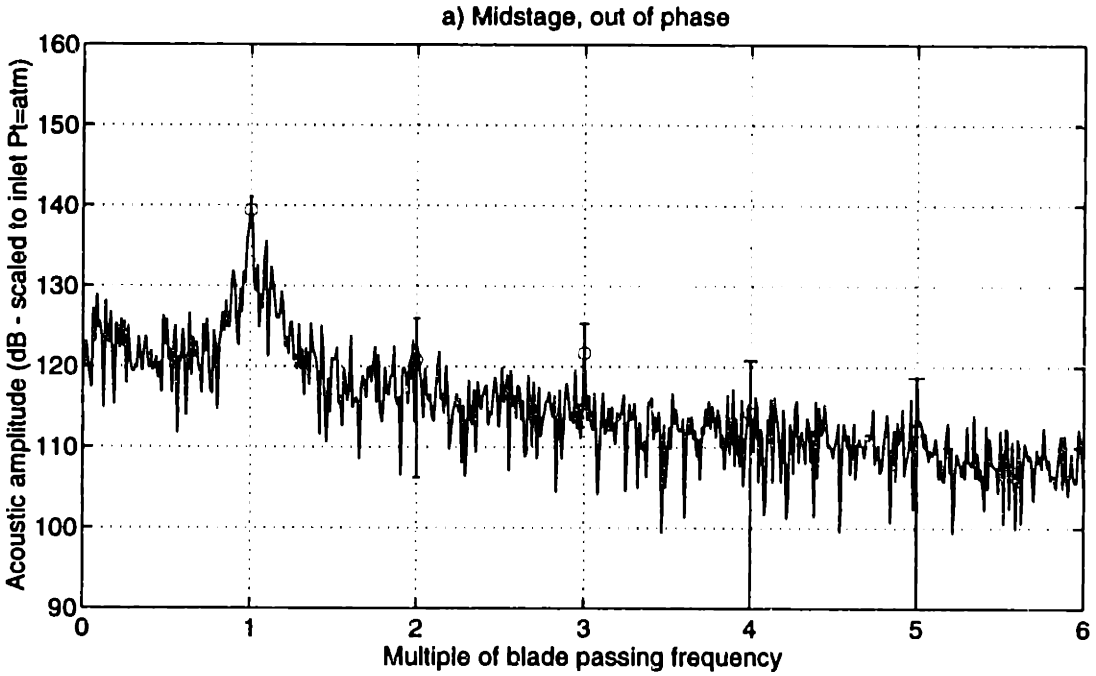

Figure 8-54: Acoustic spectra upstream in the midstage region: 1.8% midspan-weighted injection

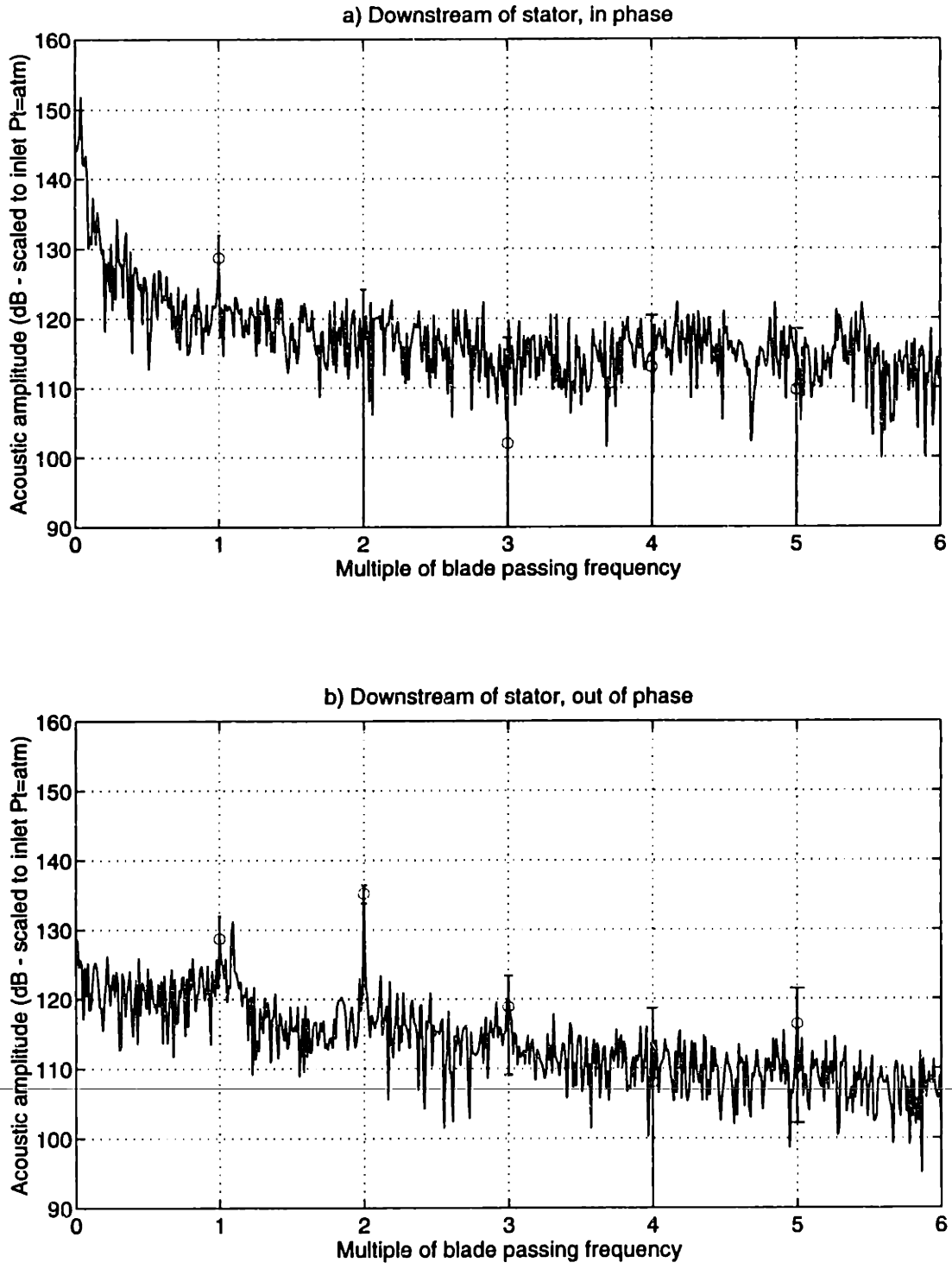

Figure 8-55: Acoustic spectra downstream of the stator: 1.8% midspan-weighted injection

injection was throttled back to 1.8% of the fan throughflow. The resulting phase angles are plotted in Figure 7-78, and the wake harmonic amplitudes are tabulated in Table 7.6.

The upstream acoustic spectra at the shroud wall are plotted in Figure 8-53. The spectra look very similar to the results for the baseline rotor and the trailing edge blowing rotor without injection. The BPF 'tones' are a little smaller and there is no distinguishing 2*BPF tone.

In the midstage region, plotted in Figure 8-54, the spectra show similar reductions to the 2.0% midspan-weighted injection. Nearly all higher harmonics of BPF are in or near the broadband noise floor. Downstream of the stator, shown in Figure 8-55, the spectra is again very similar to the 2.0% midspan-weighted injection. There is no conclusive change to the 2*BPF tone relative to the no injection configuration.

8.4.7 Conclusions regarding microphone acoustic measurements

Due to changes in the radial variation of the wake harmonic amplitudes and phases with trailing edge blowing, reductions in the duct acoustic modes can not be conclusively quantified. The radial mode content of the acoustic field will be altered due to nonuniform changes in the wake harmonics along the span. The acoustic pressures measured at the wall will thus produce a different combination of radial modes, depending on the trailing edge blowing performed. Changes in the wall amplitude, therefore, may have little or no correspondence to the overall radiated power. The wall measurements, however, can be used to validate acoustic prediction tools.

In addition, changes in the wake harmonics due to injection do not appear to have the same effects on the acoustics upstream and downstream of the stator row. This effect was seen in the data when modes in the midstage region were significantly reduced with little change to the tones downstream (midspan-weighted injection), as well as the opposite result (tip-weighted injection). Tables showing the acoustic harmonic amplitudes for the different rotor configurations are shown in Tables 8.1 and 8.2.

Baseline rotor	BPF	2*BPF	(dB) 3*BPF	4*BPF	5*BPF
Upstream (in)	145	126	119	111	111
Upstream (out)	145	126	113	114	116
Midstage (in)	122	121	113	121	114
Midstage (out)	140	124	129	125	121
Downstream (in)	136	119	117	118	116
Downstream (out)	128	132	114	121	120
T.e. blowing rotor (no injection)	BPF	2*BPF	(dB) 3*BPF	4*BPF	5*BPF
Upstream (in)	145 (0)	112 (-14)	120 (+1)	114 (+3)	111 (0)
Upstream (out)	142 (-3)	125 (-1)	118 (+5)	109 (-5)	112 (-4)
Midstage (in)	132 (+10)	119 (-2)	124 (-11)	113 (-8)	110 (-4)
Midstage (out)	142 (+2)	130 (+6)	128 (-1)	127 (+2)	120 (-1)
Downstream (in)	134 (-2)	112 (-7)	117 (0)	122 (+4)	112 (-4)
Downstream (out)	129 (+1)	135 (+3)	116 (+2)	1.? (-3)	115 (-5)
Solid rotor (high loading)	BPF	2*BPF	(dB) 3*BPF	4*BPF	5*BPF
Upstream (in)	148 (+3)	128 (+2)	122 (+3)	120 (+9)	115 (+4)
Upstream (out)	146 (+1)	129 (+3)	122 (+9)	114 (0)	114 (-2)
Midstage (in)	135 (+13)	122 (+1)	121 (+8)	119 (-2)	114 (0)
Midstage (out)	136 (-4)	131 (+7)	121 (-8)	120 (-5)	126 (+5)
Downstream (in)	135 (-1)	123 (+4)	117 (0)	116 (-2)	113 (-3)
Downstream (out)	127 (-1)	139 (+7)	117 (+3)	115 (-6)	115 (-5)

Table 8.1: Acoustic harmonic amplitudes (dB scaled to atmospheric conditions): upstream and downstream of both blade rows (no injection trailing edge blowing rotor data and high loading solid-bladed rotor data also shown as dB change from baseline rotor data)

T.e. blowing rotor (1.9% tip-weighted inj.)	BPF	2*BPF	(dB) 3*BPF	4*BPF	5*BPF
Upstream (in)	145 (0)	114 (+2)	121 (+1)	113 (-1)	112 (+1)
Upstream (out)	140 (-2)	131 (+6)	119 (+1)	112 (+3)	104 (-8)
Midstage (in)	138 (+6)	125 (+6)	115 (-9)	120 (+7)	118 (+8)
Midstage (out)	134 (-8)	127 (-3)	131 (+3)	124 (-3)	128 (+8)
Downstream (in)	133 (-1)	119 (+7)	118 (+1)	122 (0)	114 (+2)
Downstream (out)	126 (-3)	124 (-11)	112 (+4)	114 (-4)	109 (-6)
T.e. blowing rotor (2.0% mid-weighted inj.)	BPF	2*BPF	3*BPF	4*BPF	5*BPF
Upstream (in)	144 (-1)	118 (+6)	122 (+2)	113 (-1)	110 (-1)
Upstream (out)	143 (+1)	131 (+6)	116 (-2)	112 (+3)	109 (-3)
Midstage (in)	137 (+5)	119 (0)	120 (-4)	112 (-1)	111 (+1)
Midstage (out)	138 (-4)	127 (+3)	118 (-10)	114 (-13)	114 (-6)
Downstream (in)	130 (-4)	116 (+4)	123 (+6)	114 (-8)	114 (+2)
Downstream (out)	128 (-1)	136 (+1)	119 (+3)	111 (-7)	115 (0)
T.e. blowing rotor (1.8% mid-weighted inj.)	BPF	2*BPF	3*BPF	4*BPF	5*BPF
Upstream (in)	142 (-3)	117 (+5)	114 (-6)	111 (-3)	112 (+1)
Upstream (out)	133 (-9)	125 (0)	117 (-1)	105 (-4)	111 (-1)
Midstage (in)	136 (+4)	125 (+6)	123 (-1)	117 (+4)	113 (+3)
Midstage (out)	140 (-2)	123 (-7)	122 (-6)	114 (-13)	119 (-1)
Downstream (in)	129 (-5)	118 (+6)	111 (-6)	114 (-8)	114 (+2)
Downstream (out)	129 (0)	136 (+1)	120 (+4)	113 (-5)	118 (+3)

Table 8.2: Acoustic harmonic amplitudes (dB scaled to atmospheric conditions): upstream and downstream of both blade rows (injection results are also shown as dB change from trailing edge blowing rotor with no injection)

CHAPTER 9

SUMMARY AND CONCLUSIONS

Trailing edge blowing wake management was completed on a high bypass ratio next-generation fan stage. Mitigation of the wake was performed by incorporating internal passages in the fan blade and injecting gas into the rotor wake through orifices in the blade suction surface near the trailing edge. Flow field, stator unsteady surface pressure, and acoustic measurements were taken for a baseline rotor with solid blades and for three different trailing edge blowing configurations. The range of trailing edge blowing mass addition was 1.8 to 2.0% of the fan throughflow. Both tip-weighted and midspan- weighted injection distributions were tested. Below, the results of each set of measurements are discussed, followed by a summary of the contributions and recommendations for future work.

9.1 Flow Field Measurements

Flow field measurements downstream of the rotor showed significant reduction of the wake harmonic amplitudes. For spanwise positions with momentumless wake injection, the reductions in the first two rotor blade passing frequency, BPF, harmonic amplitudes were 68 to 85% at 1.5 chord downstream of the rotor.

In addition to the reductions at 1.5 chord, significant reductions in at least the first five wake BPF harmonic amplitudes were achieved at 0.1 chord, just downstream of the rotor. For momentumless wake mass injection, the wake harmonic amplitudes at 0.1 chord

were reduced approximately 70% relative to the no injection configuration. Perhaps more importantly, the BPF and 2*BPF wake harmonic amplitudes at 0.1 chord with momentumless wake injection were more than 40% smaller than the wake harmonic amplitudes at 1.5 chord without injection. This result implies that the rotor/stator axial spacing could be significantly reduced without increasing the radiated acoustic power. However, effects due to wake skew must be taken into account when considering any design changes.

While significant reductions in the wake harmonic amplitudes were achieved, there were also large changes in the wake harmonic phase angles. The wake harmonic phase angles do not change significantly for mass injection that results in less than complete filling of the wake momentum deficit. Higher injection rates, however, result in a 'jet' and a shift in the BPF harmonic of approximately 180 degrees, with similar changes in the higher harmonics. These wake harmonic phase shifts change the radial variation in phase along the span and can significantly alter the radial coupling of the stator unsteady pressure and acoustic modes. While the radial coupling can be maintained approximately the same by performing slightly less than momentumless wake injection along the entire span, overblowing offers the potential for tailoring the wake harmonic amplitude and phase distribution to achieve maximum noise reduction.

9.2 Stator Unsteady Pressure Measurements

Stator unsteady pressure measurements were taken downstream of the baseline solid-bladed rotor and the trailing edge blowing rotor with and without tip-weighted injection. The results from the trailing edge blowing rotor without injection matched reasonably well with the baseline rotor in both amplitude and phase of the stator surface unsteady pressure harmonics. Measurements downstream of the rotor with tip-weighted injection, however, demonstrated some interesting characteristics.

The tip-weighted injection configuration resulted in a wake that was momentumless at approximately 80% span. The wake outboard of 80% span was overblown, resulting in a 'jet' and large shifts in the wake harmonic phases. At 87.5% span, the wake BPF harmonic amplitude (at 1.5 chord) was reduced about 80% (14 dB) and the phase angle shifted about 160 degrees with injection, compared to the no injection measurements. The amplitudes

and phases of the pressure differences across the stator blade were calculated from the stator surface measurements and showed decreases in stator BPF unsteady loading along the chord of 3 to 10 dB. Phase changes in the differential pressure BPF harmonics were less than 60 degrees. The phase shift of the differential pressure BPF harmonic at 50% span did roughly correlate with the phase shift in the wake at 50% span (1.5 chord), but the wake harmonic phase variation was not greatly altered in this region.

These stator unsteady pressure results show only partial correlation with changes in the wake harmonics at 1.5 chord, and indicate that strip theory approximations may not accurately capture changes in the stator unsteady loading when the radial variations in wake harmonic amplitude and phase are significantly altered. However, changes in mode trapping (see Section 1.3.3) of the BPF, m=-24 mode (which is very close to being cut-on in the midstage region) may also influence the stator unsteady surface pressures. Additional experimental data and numerical simulation will be required to enhance understanding of the complicated three-dimensional interaction of the wake unsteady flow field and the stator blades. Not only do the neighboring blades alter the interaction process (causing the pressure minimum to travel upstream on the chord), but the large radial phase variations (on the order of 360 degrees over one-half the span) and mode trapping can significantly alter the stator pressure fields as well. Regardless, both sets of measurements could be used in acoustic radiation prediction tools to examine the possible far-field noise reduction due to trailing edge blowing.

9.3 Acoustic Measurements

Duct acoustic measurements were taken upstream and downstream of both the rotor and stator rows at the outer shroud wall. Since the wake harmonic amplitudes were not uniformly reduced along the span and the harmonic phases were shifted, the radial mode content of the acoustic field changed. Because the data collected at the wall is a sum of all radial modes present, quantitative assessment of overall radiated noise was not possible. The wall amplitudes can, however, be used for validation of acoustic prediction tools.

One interesting result of the microphone measurements was the relative changes upstream and downstream of the blade rows. For the tip-weighted injection (1.9% of the

throughflow), the 2*BPF amplitude measured downstream of the stator was reduced 11 dB compared to the no injection configuration. In the midstage region, the 2*BPF amplitude was reduced only about 3 dB. Upstream of the rotor where there was no apparent tone without injection, a 2*BPF tone approximately 5 dB above the broadband resulted from the injection. These results show the complexity of the rotor/stator interaction noise generation mechanism.

9.4 Wake Decay

The evolution of rotor wakes was shown to depend on the freestream swirl. The swirl (imparted to the flow by the rotating blade row) skews the wakes as they are convected downstream. This skewing stretches the wake elements (wake vorticity), increasing the mixing within the wakes. The wake centerline velocity deficit can be reduced by 50% due to stretching in typical fan stages, compared to the velocity deficit that would result with no wake skewing/stretching (two-dimensional approximation). The effects of skewing are observed predominantly in rotor/stator geometries with large axial spacings and low hub-to-tip ratios.

9.5 Contributions

1) First-of-their-kind trailing edge blowing experiments were completed on a high-bypass ratio next-generation fan stage. Results demonstrated the ability to adjust the injection distribution and that sufficient mass flow could be attained to perform any reasonable distribution of injection required.

2) The methodology and a simplified model for designing trailing edge blowing blades were developed. The model calculates the flow in the blade internal passages, incorporating empirical estimates for the flow losses around corners and through large area changes. The methodology for designing trailing edge blowing blades, as well as boundary layer suction, was filed with the United States Patent and Trademark Office.

3) Significant reduction of the wake harmonic amplitudes at 1.5 chord with trailing edge injection were shown. Reductions in the BPF and 2*BPF harmonic amplitudes of approximately 80% were obtained, with smaller reductions in the higher harmonics.

4) Large reductions in the wake harmonic amplitudes at 0.1 chord were also observed with injection. Momentumless wake injection resulted in BPF and 2*BPF harmonic amplitudes at 0.1 chord that were 40% smaller than the harmonic amplitudes at 1.5 chord without injection. These results suggest that significant reduction of the rotor/stator spacing may be possible without increasing the radiated noise.

5) Injection that overfills the wake momentum deficit results in a 'jet' and shifts in the wake harmonic phases of approximately 180 degrees. These results demonstrate the ability to use trailing edge blowing to leverage not only the wake harmonic amplitude, but also the phase variation along the span. Significant changes in the radial coupling on the stator can be created, and increases in the radiated acoustic power could result for inappropriate injection distributions.

6) Stator unsteady pressure data did not fully correlate with changes in the wake harmonics at 1.5 chord. These measurements suggest that traditional linear strip theory may not accurately capture changes in stator unsteady loading due to trailing edge blowing.

7) The effects of swirl on the decay of rotor wakes was shown to be significant for geometries with large rotor/stator axial spacings and low hub-to-tip ratios. Much of the difference between two-dimensional wake decay and the evolution of wakes in turbomachinery can be attributed to the effects of wake skewing/stretching. These results suggest that small noise reductions may be possible by tailoring the rotor loading distribution to create large wake skewing in spanwise regions where the wake/stator interaction is critical for noise production.

9.6 Recommendations for Future Work

Trailing edge blowing was shown to significantly reduce the wake harmonic amplitudes, particularly for momentumless wake injection. However, the coupling of the wake unsteady flow field to the stator, and eventually the acoustic modes, is not fully understood. Linear strip theory approximations did not apply for the measurements presented in this thesis. While these traditional tools may achieve roughly consistent results for wakes that look very similar (high skew angle, roughly constant wake profiles along the span, etc.) large changes in the wake harmonic amplitudes and phases along the span cause significant changes in the radial coupling on the stator that strip theory will not capture. Thus, additional experimental data and numerical simulation is required to better understand the complicated interaction of the rotor wakes and stator blades. Once the interaction is understood, then the ideal injection distribution for a given geometry can be determined and applied to the rotor. It is certainly possible, that injection at only a few portions of the span is needed to reduce the critical radiated acoustic modes.

Time did not allow for optimizing the injection distribution in the current research, but tuning the injection to obtain a momentumless wake along the entire span is achievable. With a fully momentumless wake, the harmonic amplitudes would be dramatically reduced in the entire flow field, and the radial variation in the harmonics should not significantly change. A detailed mapping of the flow field and stator unsteady loading could be completed to enhance understanding of the wake/stator interaction process, and the wall microphone measurements would provide reductions in the overall radiated noise level (no change in radial mode content relative to no injection). Individual passages could then be throttled to determine spanwise sensitivities. However, to truly test the ability of rotor trailing edge blowing to reduce engine fan noise, the technique must be completed in an anechoic wind tunnel to accurately capture changes in the far-field noise.

Finally, a full system analysis needs to be done to determine the impact of trailing edge blowing on an engine's overall performance. While it is clear that significant noise reduction is possible, the performance, weight, and cost penalties of incorporating these techniques into a production engine must be evaluated.

BIBLIOGRAPHY

[1] BROOKFIELD, J., WAITZ, I., AND SELL, J. "Wake Decay: Effect of Freestream Swirl". *Journal of Propulsion and Power, Vol. 14*, No. 2 (March-April 1998), pp. 215–224.

[2] CORCORAN, T. "Control of the Wake from a Simulated Blade by Trailing Edge Blowing". Master's thesis, Lehigh University, Bethelem, PA, 1992.

[3] CUMPSTY, N. personnel communication, 1997.

[4] CUMPSTY, N. *Compressor Aerodynamics.* Wiley, New York, 1989.

[5] DAWES, W. "The Practical Application of Solution-Adaption to the Numerical Simulation of Complex Turbomachinery Problems". *Prog. Aerospace Sci., Vol. 29* (1992), pp. 221–269.

[6] DRELA, M. "Two-Dimensional Transonic Aerodynamic Design and Analysis Using the Euler Equations". Gas Turbine Lab 187, Massachusetts Institute of Technology, Cambridge, MA, 1986.

[7] EPSTEIN, A., GERTZ, J., OWEN, P., AND GILES, M. "Vortex Shedding in High-Speed Compressor Blade Wakes". *AIAA Journal of Propulsion and Power, Vol. 4*, No. 3 (May-June 1988), pp. 236–244.

[8] FLEETER, S., JAY, R., AND BENNETT, W. "Rotor Wake Generated Unsteady Aerodynamic Response of a Compressor Stator". *Transactions of the ASME, Vol. 100* (Oct. 1978), pp. 664–675.

[9] GILES, M. "UNSFLO: A Numerical Method for the Calculation of Unsteady Flow in Turbomachinery". Gas Turbine Lab 205, Massachusetts Institute of Technology, Cambridge, MA, 1991.

[10] HANSON, D. "Coupled 2-Dimensional Cascade Theory for Noise and Unsteady Aerodynamics of Blade Row Interaction in Turbofans, Volume 1- Theory Development and Parametric Studies". NASA CR 4506 (Jan. 1994).

[11] HANSON, D., AND WAGNER, B. personal communication, United Technologies Pratt & Whitney, 1995.

[12] HAYDEN, B. "Two-Dimensional Analysis of Rotor Suction and the Impact on Rotor-Stator Interaction Noise". Master's thesis, Massachusetts Institute of Technology, Cambridge, MA, 1994.

[13] HILL, P., SCHAUB, U., AND SENOO, Y. "Turbulent Wakes in Pressure Gradients". *Transactions of the ASME* (Dec. 1993), pp. 518–524.

[14] HOUDEVILLE, R., AND FOURNIER, G. "Manipulation of the Wake of a 2D Wing in Order to Reduce Propeller Noise". 13th Colloquium on Aero- and Hydro-acoustics.

[15] IDELCHIK, I. *Handbook of Hydraulic Resistance, 3rd Edition.* Begell House, Inc, 1996.

[16] INCORPORATED, D. E. "Analysis of MIT Fan Blades", unpublished report to MIT, 1994.

[17] INGARD, K. MIT-AERL internal document, 1995.

[18] KERREBROCK, J. *Aircraft Engines and Gas Turbines*, 2nd ed. The MIT Press, Cambridge, MA, 1972.

[19] KERREBROCK, J. "The MIT Blowdown Compressor Facility". Gas Turbine Lab 108, Massachusetts Institute of Technology, Cambridge, MA, 1972.

[20] LAKSHMINARAYANA, B., GOVINDAN, T., AND REYNOLDS, B. "Effects of Rotation and Blade Incidence on the Properties of the Turbomachinery Rotor Wake". AIAA-81-0054 (1981).

[21] LEU, T.-S., AND HO, C.-M. "Free Shear Layer Control and Its Application to Fan Noise". AIAA Paper 93-3242 (July 1993).

[22] MANWARING, S., AND WISLER, D. "Unsteady Aerodynamics and Gust Response in Compressors and Turbines". American Society of Mechanical Engineers 37th International Gas Turbine and Aeroengine Congress and Exposition (1992).

[23] MILLER, D. *Internal Flow Systems*, 2nd ed. Unwin Brothers Limited, The Gersham Press, Martins Printing Group, Surrey, 1990.

[24] MIRANDA, J., AND DEVENPORT, W. "Two-Point Measurements in Trailing Vortices". AIAA-96-0804 (1996).

[25] NASA. *Aeroacoustics of Flight Vehicles: Theory Practice, Volumes 1&2, NASA RP-1258* (1991).

[26] NAUMANN, R. "Control of the Wake from a Simulated Blade by Trailing Edge Blowing". Master's thesis, Lehigh University, Bethlehem, PA, 1992.

[27] NG, W., AND EPSTEIN, A. "Unsteady Losses in Transonic Compressors". *Journal of Engineering for Power, Vol. 107* (April 1985), pp. 345–353.

[28] PARK, W., AND CIMBALA, J. "The Effect of Jet Injection Geometry on Two-Dimensional Momentumless Wakes". *Journal of Fluid Mechanics, Vol. 224* (March 1991), pp. 29–47.

[29] PHILBRICK, D., AND TOPOL, D. "Development of a Fan Noise Design System Part I: System Design and Source Modeling". AIAA-93-4415 (1993).

[30] PRATO, J., AND LAKSHMINARAYANA, B. "Investigation of Compressor Rotor Wake Structure at Peak Pressure Rise Coefficient and Effects of Loading". *Journal of Turbomachinery, Vol. 115* (July 1993), pp. 487–500.

[31] REIJNEN, D. *An Experimental Study of Boundary Layer Suction in a Transonic Compressor.* PhD thesis, Massachusetts Institute of Technology, Cambridge, MA, Feb. 1997.

[32] SCHLICHTING, H. *Boundary Layer Theory.* McGraw-Hill Book Company, New York, NY, 1979.

[33] SELL, J. "Cascade Testing to Assess the Effectiveness of Mass Addition/Removal Wake Management Strategies for Reduction of Rotor-Stator Interaction Noise". Master's thesis, Massachusetts Institute of Technology, Cambridge, MA, Feb. 1997.

[34] SMITH, S. "Discrete Frequency Sound Generation in Axial Flow Turbomachines". Aeronautical Research Council R&M 3709 (March 1972).

[35] SUCCI, G. "System and Method for Suppressing Noise Produced by Rotors". US Patent 5217349 (1993).

[36] SURYAVAMSHI, N., AND LAKSHMINARAYANA, B. "Numerical Prediction of Wakes in Cascades and Compressor Rotors Including the Effects of Mixing Part II - Rotor Passage Flow and Wakes Including the Effects of Spanwise Mixing". ASME 91-GT-222 (1991).

[37] TYLER, J., AND SOFRIN, T. "Axial Flow Compressor Noise Studies". *SAE Trans., Vol. 70* (1962), pp. 309–332.

[38] WAITZ, I., BROOKFIELD, J., SELL, J., AND HAYDEN, B. "Preliminary Assessment of Wake Management Strategies for Reduction of Turbomachinery Fan Noise". *AIAA Journal of Propulsion and Power, Vol. 12*, No. 5 (Sept.-Oct. 1996), pp. 958–966.

[39] WAITZ, I., BROOKFIELD, J., SELL, J., HAYDEN, B., AND INGARD, K. "Reduction of Turbomachinery Fan Noise". patent pending.

[40] WAITZ, I., ELLIOT, J., FUNG, A., KERWIN, J., KRASNODEBSKI, J., O'SULLIVAN, M., QUI, Y., TEW, D., GREITZER, E., MARBLE, F., TAN, C., AND TILLMAN, T. "Streamwise-Vorticity-Enhanced Mixing". *Progress in Aerospace Sciences, Vol. 33*, No. 5-6, pp. 323–351.

[41] WHITE, F. *Viscous Fluid Flow.* McGraw-Hill, New York, 1989.

[42] ZIMINSKY, W. "Design of a high pressure ratio transonic compressor stage with active boundary layer control". Master's thesis, Massachusetts Institute of Technology, 1996.

APPENDIX A

DATA REDUCTION METHODOLOGY

Analog signals from the pressure transducer amplifiers were converted to digital form by ADTEK A/D boards and stored on the computer hard drive as board data counts. With 12-bit boards, the counts range from 0 to 4095 (-10 to +10 volts). Using MATLAB files, all the data was converted to voltages and then the transducer data was converted to pressures using the measured calibration slopes. For linear position instrumentation (4-way probe, stator, and valve), the voltages were converted to position (inches or percent span) using appropriate calibration measurements. The data reduction for the flow field, stator, and microphone measurements are described in more detail in the following sections. Tables of the data files are provided in Section A.0.5.

As discussed in Chapter 1, the wakes downstream of high speed rotors are complex and unsteady. Therefore, to obtain the mean component of the wake, measurements from each rotor blade passage were averaged to remove the random components. This mean wake profile is related to the tonal noise generated from the fan stage, and thus the spatial harmonic content of the wake profile is presented. In addition, the stator unsteady loading (caused by the wake) was averaged over rotor blade passing time and decomposed to obtain the loading at multiples of rotor blade passing frequency. These two quantities are related to the levels of tonal noise generated by the fan stage. Microphone measurements were also used to estimate the duct acoustic amplitudes.

To obtain estimates of the broadband noise generated by the stage, the turbulence intensity over the blade passing period and the temporal decomposition of the signals were

calculated. The decomposition produced noise spectra typical of gas turbine engines with a broadband noise floor and sharp tones (perhaps 15 dB above the broadband) at multiples of the blade passing frequency. For Mach number traces, the broadband noise floor is representative of the turbulence in the flow, and the tones are the amplitudes of the wake harmonics. The amplitudes of the tones from this spectrum are identical to those calculated by performing the blade passing average and then decomposing the mean profiles into harmonics. The turbulence intensity profile produces the amplitude of the flow unsteadiness, but does not provide any spectral information. Discussion of the data reduction and averaging will be presented in the following sections.

A.0.1 Shaft Encoder

Unlike experiments performed in continuous flow facilities, the rotor in the Blowdown Compressor decelerates during the test time, such that the blade passing period increases during the run (the change from the beginning to the end of the test window is approximately 6 percent). To apply the averaging techniques, the data was scaled by the instantaneous blade passing period.

The shaft encoder used in the Blowdown Compressor is an optical encoder with 400 lines per revolution, as well as a once-per-revolution index. The index was used for all data reduction to start the averaging process. This was done so that all data was synchronized to the same rotor position. The 400 count signal was used to calculate the rotor speed throughout the test and scale the data for averaging. The speed was calculated using a sliding window around the data point of interest, measuring the time to observe a given number of pulses from the encoder. Using the instantaneous rotor speed, time during the test was nondimensionalized marching from t=0 to the final time using the formula $t^*(n) = t^*(n-1) + dt[fr(n)/fr(1)]$, n = 2 $\rightarrow$ number of data points, where dt is the time step between computer data points, and fr is the wheel speed, rev/sec (fr is fitted with a polynomial to remove noise). Data was typically averaged over several runs, each comprised of four to six rotor revolutions (64 to 96 blade passing periods). Over this time period, the time nondimensionalization described above has an error of approximately 4 computer data counts, or about 2 percent of a rotor blade passing period.

The time nondimensionalization resulted in later blade passing periods having a larger number of data points than earlier blade passing periods for a given run. The number of data points (sampling at 333 kHz) per period was roughly 200. To average all the blade periods, the data was loaded into a new data vector having 100 equally spaced bins per period. The time vector over which the averaging was to be done was examined for which bin a data point lied within and the value stored in that bin. The samples (usually 2) in a given bin were then averaged to obtain the new data trace. The data could then be averaged since each blade passing period had an equal number of points.

A.0.2 Flow Field Data Reduction

Flow field measurements downstream of the rotor were taken with the 4-way probe described in Section 2.6.3. The probe consists of four flush-mounted pressure transducers and through data reduction procedures described in Reijnen [31], four quantities are output: total pressure, static pressure, tangential flow angle, and radial flow angle. With these values the absolute Mach number and its components (axial, tangential, and radial) can also be directly determined. In addition, by knowing the wheel speed and radial position of the measurements, relative Mach number and total pressure can be calculated. For all the data presented in this thesis, the relative Mach number will be that in a surface of constant radius, *i.e.* it will not include the radial Mach number component. This is done to exhibit the harmonics of most interest, which are the harmonics that cause unsteady loading on the stator blade (axial and tangential), not harmonics of velocity along the blade span (radial). However, since typical radial Mach numbers are approximately 10% of the freestream, the difference between the relative Mach number used here and that including radial Mach number is small ($< 1\%$), particularly more than 1.0 chords downstream of the rotor.

Having obtained data vectors for all required quantities of the flow field over the time window desired, the blade passing periods can be averaged together to obtain the ensemble-averaged signal over one blade period. To do this, the individual bins from each passage period (from several runs) are averaged together. This results in a 100 element vector for the mean signal. To obtain the harmonic content of the mean flow field, these averaged signals

are decomposed[1] with a Fast Fourier Transform (FFT) function built in to MATLAB. The amplitude of each harmonic of the wake and its phase can then be determined.

To determine a confidence interval in the mean value, the standard deviation of each data point (100 per period) was calculated. This value is a combination of all random errors in the system and the turbulence in the flow. In general, the system errors were much smaller than the turbulence (particularly in the wake) and thus the flow unsteadiness dominates. Measurements were taken with no flow in the facility to verify the level of measurement unsteadiness due to sources other than flow turbulence (*e.g.* electrical noise). These tests found the level of induced unsteadiness (both in the calculated turbulence intensity and in the spectrum up to 10 BPF) were less than 30% of the level of unsteadiness measured in any flow field or stator pressure measurement test. The standard deviation can be plotted across the blade pitch to visualize the variation in turbulence level, and 95% confidence intervals were placed on the mean data assuming a χ squared distribution and using the formula $\sigma_{mean} = (1.96/\sqrt{n})\sigma_{samples}$, where n is the number of samples (number of runs times number of blade passing periods per run). In addition, the full data signal can be run through the FFT to obtain the full turbulent noise floor spectrum, if desired.

The confidence intervals for the harmonic amplitudes are obtained by calculating the harmonics for each blade passing period used for the ensemble-average. The standard deviation of these harmonics is then calculated and the mean confidence interval determined using the expression above. To obtain confidence intervals for the ensemble-averaged turbulence intensity, the intensity for each rotor revolution used in the ensemble-averaging process is calculated. The standard deviation of these profiles is then obtained and used in the expression above (with appropriate constant) like that for the harmonics and the mean profiles. Similar results can be obtained by calculating the standard deviation of the turbulence intensity from each run, instead of each rotor revolution.

In general, the plots of most interest for noise estimation purposes are the ensemble-averaged relative Mach number profile harmonics and the turbulence level. The harmonic content of the wake in the relative and absolute frames is identical. However, since the wake velocity perturbation in the absolute frame is not in the freestream direction, it is easier to

[1]The identicle answer would result if each separate blade passing period was decomposed spatially and the complex Fourier coefficients averaged together.

calculate the harmonics in the relative frame. At 1.5 chords downstream of the rotor, all the flow variables output from the 4-way probe are presented.

Data reduction for a typical 4-way probe run is as follows. The base program **w4red.m** is first run which converts all quantites to voltages and then to pressure if appropriate. The wheel speed is calculated and the 4-way probe data is run through the calibration routine to calculate pressures, flow angles, and Mach numbers. The window of data is then chosen (steady state and probe position) and **w4pass.m** is run. This program nondimensionalizes the data (time) and produces data vectors 100 points/blade passing period, **a4w**. These vectors can then be put in to **w4avep.m** alone or with other runs to create the ensemble-averaged plots.

A.0.3 Stator Data Reduction

Like the flow field measurements obtained with the 4-way probe, the unsteady pressure measurements from the instrumented stator blade were ensemble-averaged to obtain the average pressure signal over one blade passing period. This signal was then decomposed to obtain the mean pressure and the harmonics for each transducer on the stator blade surface. The standard deviation was also determined and the confidence intervals calculated. The steady pressure envelope over the blade surface could then be presented by plotting values from all the transducers on the blade surface at their respective chordwise position. The unsteady amplitudes and phase can be shown similarly. The confidence intervals for the harmonic amplitudes and phase were obtained by calculating the standard deviation of all the blade passing period harmonics (amplitude and phase, respectively). The primary data plots from the stator will be the amplitudes and phase of the unsteady component of the pressure signals on the blade, particularly at 2*BPF, since 2*BPF is the dominant radiated acoustic mode from rotor wake-stator interaction.

The data reduction for a stator run is completed very similarly as for a 4-way probe run. The base file **stred.m** is first run to convert the signals to pressure and to calculate the wheel speed. **stpass.m** is then run to perform the time nondimensionalization and finally **stavep.m** is run to ensemble-average the data from one or more runs.

A.0.4 Acoustic Mode Data Reduction

Data reduction of the microphone measurements for estimating the acoustic duct modes in the Blowdown Compressor test section was completed in a similar manner to the 4-way probe and stator data. The data vectors from several runs were averaged together to obtain an ensemble-averaged blade passage period signal. These signals from the six microphones were decomposed spatially, and the harmonics used to calculate the in- and out-of-phase components. To obtain the in-phase mode amplitude, the microphone harmonics for the pair at a given axial station were averaged together, and the out-of-phase amplitude obtained by taking the difference, divided by 2. Identical results would be obtained by adding and subtracting the full data signals and then decomposing.

To obtain the full noise spectrum, the data vector from a given microphone was put through an FFT. This produced a plot of the broadband noise floor, as well as the tones. Using data vectors having 100 data points per blade period, frequencies up to 50*BPF can be calculated and the resolution of the plots are 1/50th BPF, or about 40Hz.

The microphone data is reduced similar to the 4-way probe data. **w4red.m** is first run to convert the signals to pressure and calculate the wheel speed. **micpass.m** is then run to nondimensionalize the data to even blade passing periods, and then **w4mics.m** is run to generate the spectral content.

A.0.5 Summary of Data Files

The data files used for all the fan stage results presented in this thesis are summarized in the following tables. Flow field, stator unsteady pressure, and microphone runs were completed and the files averaged together to obtain the presented plots. The number of runs averaged for any given measurement type and location ranges from one to four. The data files are listed by date of measurement and the number of run on the given day, i.e. the third run on February 13, 1998 would be given as fb13983. The first run of the day has no additional number beyond the date.

Baseline Rotor Takeoff condition	25% span	50% span	75% span	87.5% span
0.1 chord		my0197 my01972	my0297 my02972	
0.5 chord		ap3097 ap30972	ap30973 ap30974	
1.0 chord		ap1697 ap2397 ap2897	ap2997 ap29972 ap29973	
1.5 chord	ap10973 ap1197 ap11972 ap11973	ap0597 ap05972 ap05973 ap0797	ap0897 ap08973 ap08974 ap0997	ap09972 ap09973 ap1097 ap10972
High loading				
0.1 chord		ag2597 ag25972	ag2297 ag22972	
1.5 chord	ag1297 ag12972	jl2397 jl2497	jl24972 jl24973	jl3097 jl30972

Table A.1: Flow field (4-way probe) data files: Baseline solid-bladed rotor

Trailing Edge Blowing Rotor No injection	25% span	50% span	75% span	87.5% span
0.1 chord	mr0698	mr0598	mr06983	mr0798
1.5 chord	fb2198 fb21982	fb2098 fb20982	fb1898 fb18982	fb1998 fb19982
1.9% tip weighted injection				
0.1 chord	mr06982	mr05982	mr06984	mr07982
1.5 chord	fb21983 fb21984	fb20983 fb20984	fb18983 fb18984	fb19983 fb19984
2.0% mid weighted injection				
0.1 chord	mr1898	mr1698	mr16982	mr18982
1.5 chord	mr2598	mr2398	mr2498	mr24982
1.8% mid weighted injection				
1.5 chord	mr2898	mr2698	mr26982	mr26983

Table A.2: Flow field (4-way probe) data files: Trailing edge blowing rotor

Baseline Rotor	25% span	50% span	75% span	87.5% span
Takeoff condition	mr2197*	mr0697*	mr27972	mr28973
	mr24972*	mr06972*	mr27973	mr28974
	mr2597	mr0797*	mr2897	mr3197
	mr2697	mr07972*	mr28972	mr31972
Trailing Edge Blowing Rotor				
No injection		fb23983	fb2298	fb22985
		fb23984	fb22982	fb22986
				fb2498
				fb24982
1.9% tip weighted injection		fb23985	fb22983	fb2398
		fb23986	fb22984	fb23982
				fb24983
				fb24984

Table A.3: Stator pressure data files (* indicates channels 8-13 are switched: prior to mr2597)

Baseline Rotor				
Takeoff loading	ap22972	ap22973		
High Loading	ag2897	ag2997	ag29972	
Trailing Edge Blowing Rotor				
No injection	fb2698	fb26982	fb2798	fb27982
1.9% tip weighted injection	fb26983	fb26984	fb27983	fb27984
2.0% mid weighted injection	mr1398	mr13982		
1.8% mid weighted injection	mr3098	mr30982		

Table A.4: Microphone data files

APPENDIX B

INLET DISTORTION

To examine the effects of inlet distortion on the radiated noise, a 0.5 inch aluminum rod was inserted into the baseline (solid- bladed) fan stage flow path through the total pressure probe port, approximately 1.50 inches upstream of the rotor, to a depth of 3.0 inches. (This type of distortion is typical of that present in production turbofan engines generated by inlet total temperature probes.) The rod thus generated an inlet distortion on the outer one-half span of the rotor blades having approximately 50% wake centerline axial velocity deficit and a wake width of about 1% of the circumference at the face of the rotor. The axial velocity harmonic content of this distortion is shown in Figure B-1. The rod inlet distortion causes perturbation harmonic amplitudes of about 0.5 percent of the freestream velocity for harmonics up to about 3*BPF. Since the relative tangential velocity is high in the outer portion of the flow field, the blades see the inlet distortion primarily as an angle of attack variation. Calculations with MISES showed the variation in steady lift force on the blades was roughly the same as the variation in axial Mach number, i.e. 0.5% variation in axial Mach number resulted in roughly 0.5% variation in lift force.

Effects of inlet distortion on duct acoustic modes

The result of the inlet distortion is shown in Figures B-2 through B-7, where noise spectra are plotted upstream of the rotor, in the midstage region, and downstream of the stator (two run average). Figure B-2 shows the in-phase component of the acoustic signature measured one chord upstream of the rotor for both clean inlet flow (a) and for the 0.5 inch

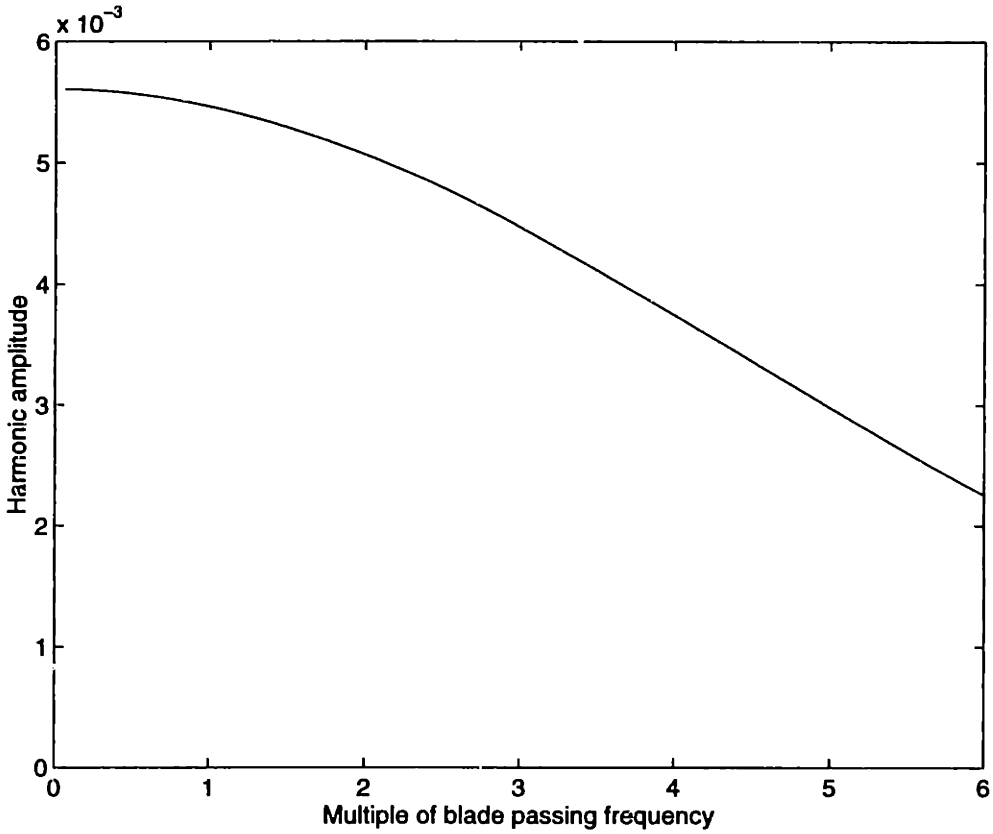

Figure B-1: Harmonic content of 1/2" rod inlet distortion: 4-5 diameters downstream

rod inlet distortion (b). Unlike the clean flow which has a BPF component but little else, the flow with the rod has virtually no in phase BPF, but does have a 2*BPF component. The out-of-phase component of the acoustic signal in Figure B-3, however, shows a strong effect of the inlet distortion with a very strong BPF amplitude, as well as 2*BPF.

For this fan stage geometry, BPF should be cut-off upstream of the rotor with clean inflow. However, even the 'clean' inlet flow experimental data shows some BPF, both in and out-of-phase. These acoustics are expected to be caused by 1) the steady (rotating) pressure field of the rotor, 2) the evanescent rotor wake-stator interaction BPF mode upstream of the rotor, and 3) inlet distortion. The main purpose of this study was to examine what level of inlet distortion is required to produce the acoustic amplitudes seen upstream of the rotor at BPF. With the 0.5% inlet distortion generated amplitude of BPF upstream of the rotor being about 152 dB, the BPF seen with 'clean' flow (about 145 dB) would only need about 0.22% distortion in the axial velocity field to generate acoustics of the amplitudes measured. Clearly, the size of the distortion and thus its harmonic content, is important to

the resulting acoustics that are generated, but a distortion of this magnitude could easily be generated due to nonuniform boundary layer loading, casing or spinner geometry, etc.

Even more than upstream of the rotor, the 0.5 inch rod dramatically changes the acoustics in the midstage region. The in-phase acoustics are shown in Figure B-4 for clean flow and with the inlet distortion. With clean flow the acoustic modes are all nearly in the broadband noise floor. Inlet distortion, however, generates modes at 1-4*BPF which are about 15 dB above the noise floor. The out-of-phase acoustics in the midstage region are plotted in Figure B-5 where both the BPF and 2*BPF modes are increased by about 10 dB.

The changes in acoustics are similar downstream of the fan stage in Figures B-6 and B-7. As before, acoustics at multiples of BPF are generated that were not present with 'clean' inlet flow, but the increases are not nearly as large as upstream of the rotor or in the midstage region.

It should be noted, however, that it is very difficult to make comments that are more specific than whether the acoustics are in or out-of-phase, since the signals are the sum of many different modes. With clean inlet flow and perfect blades (no geometrical differences) there are only certain modes generated from rotor wake-stator interaction at each multiple of BPF. Therefore, each mode can be easily identified, even with only two microphones at each axial station. However, with inlet distortion (especially with broad harmonic content) every mode order (number of wavelengths around the circumference) is generated so the acoustic field is very complicated. One would expect to see a strong in-phase amplitude upstream of the rotor from the plane wave mode. For this case at least, the other modes appear to sum in such a way as to obscure this mode. It is clear from the data, however, that inlet distortion must be minimized to gain maximum benefit from wake management strategies.

Broadband noise floor

Two important aspects of the noise signature can be seen in the plots presented here. The first is that the broadband noise floor does not seem to be increased by the inlet distortion. Perhaps this is because the unsteadiness in the wake of the rod at the rotor face

(only 3 diameters downstream) is still mostly at the unsteady vortex shedding frequency of approximately 0.9 BPF (1.8 kHz).

In addition, the high amplitude noise below about 0.1 BPF (or 200 Hz) is seen quite clearly in the in-phase plots, but nearly disappears in the out-of-phase plots. In fact, the noise level up to about 0.5 BPF (1 kHz) is lower in the out-of-phase plots. This indicates that most of this noise is electrical noise in the transducer signals (the same on each channel) and thus is not a flow field phenomena.

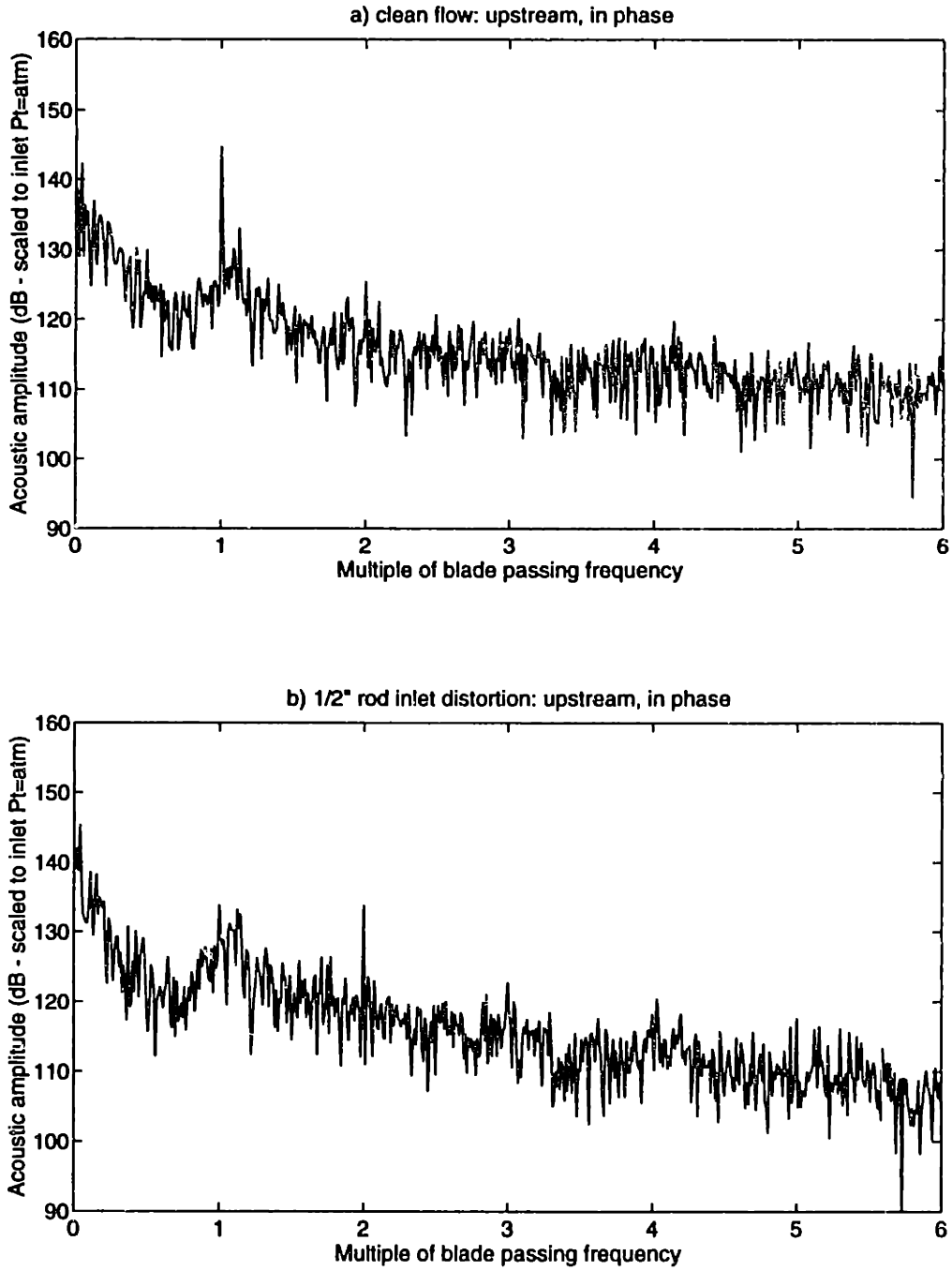

Figure B-2: Upstream, in-phase acoustic spectra for clean and inlet distortion

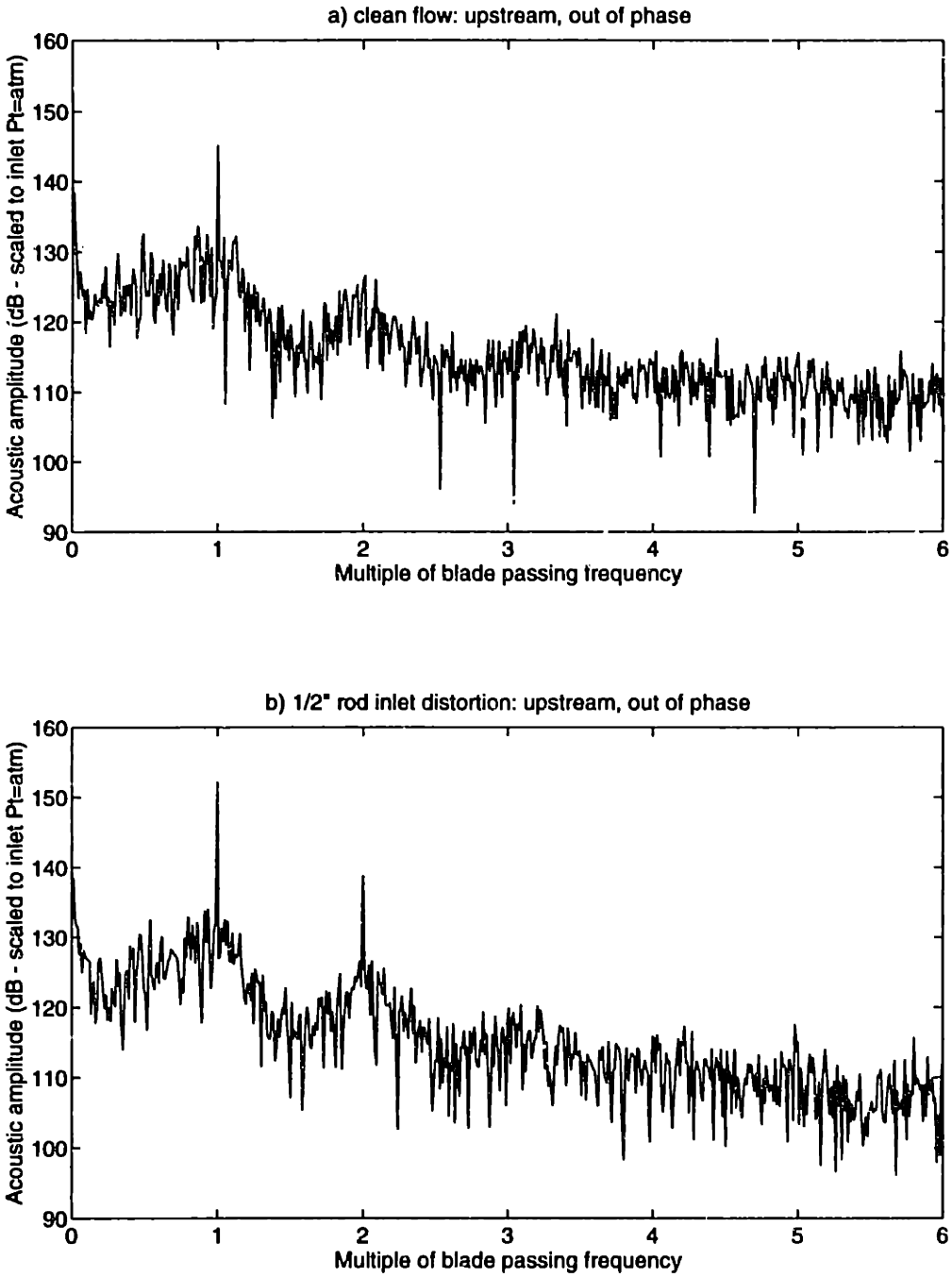

Figure B-3: Upstream, out-of-phase acoustic spectra for clean and inlet distortion

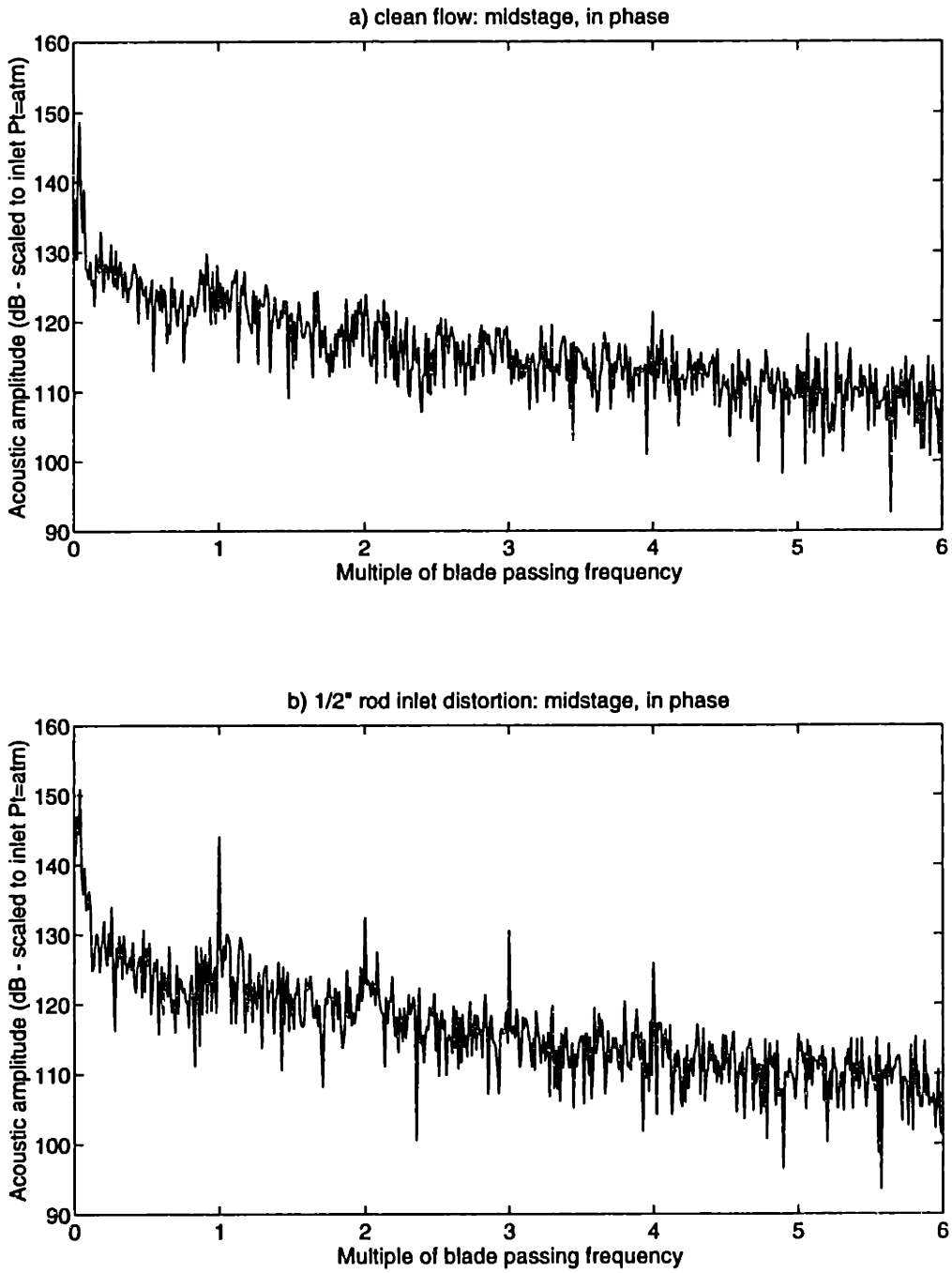

Figure B-4: Midstage, in-phase acoustic spectra for clean and inlet distortion

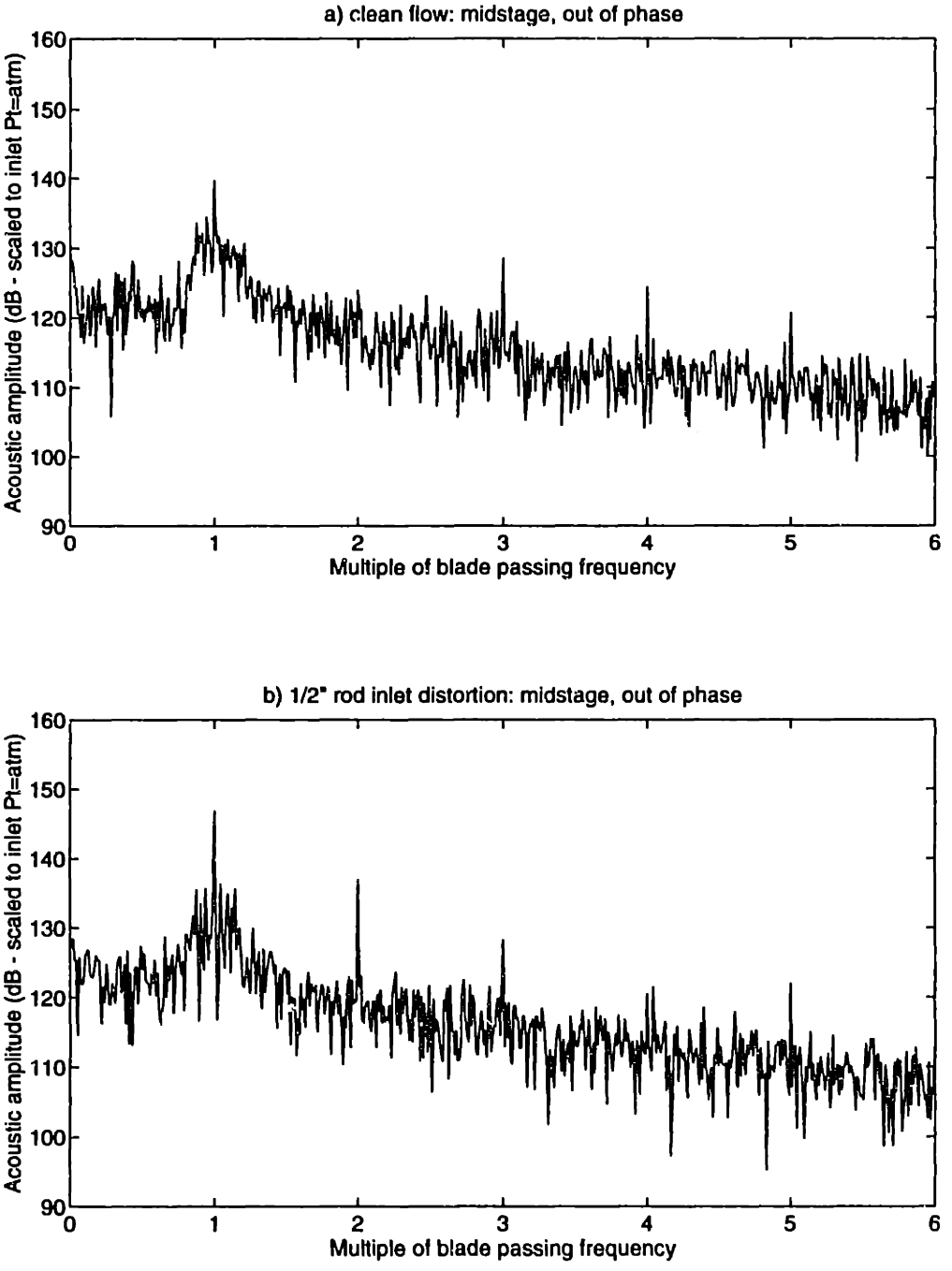

Figure B-5: Midstage, out-of-phase acoustic spectra for clean and inlet distortion

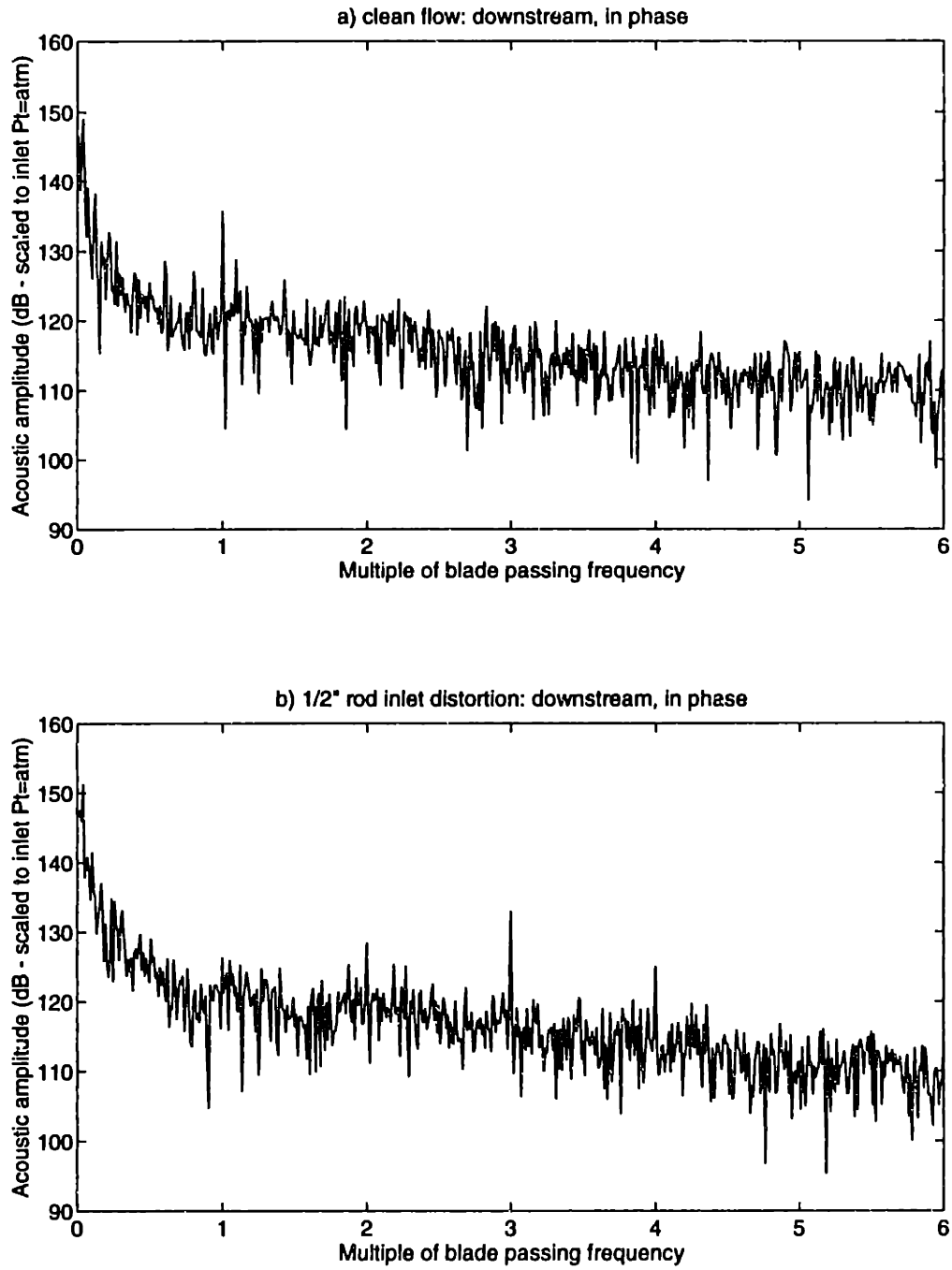

Figure B-6: Downstream, in-phase acoustic spectra for clean and inlet distortion

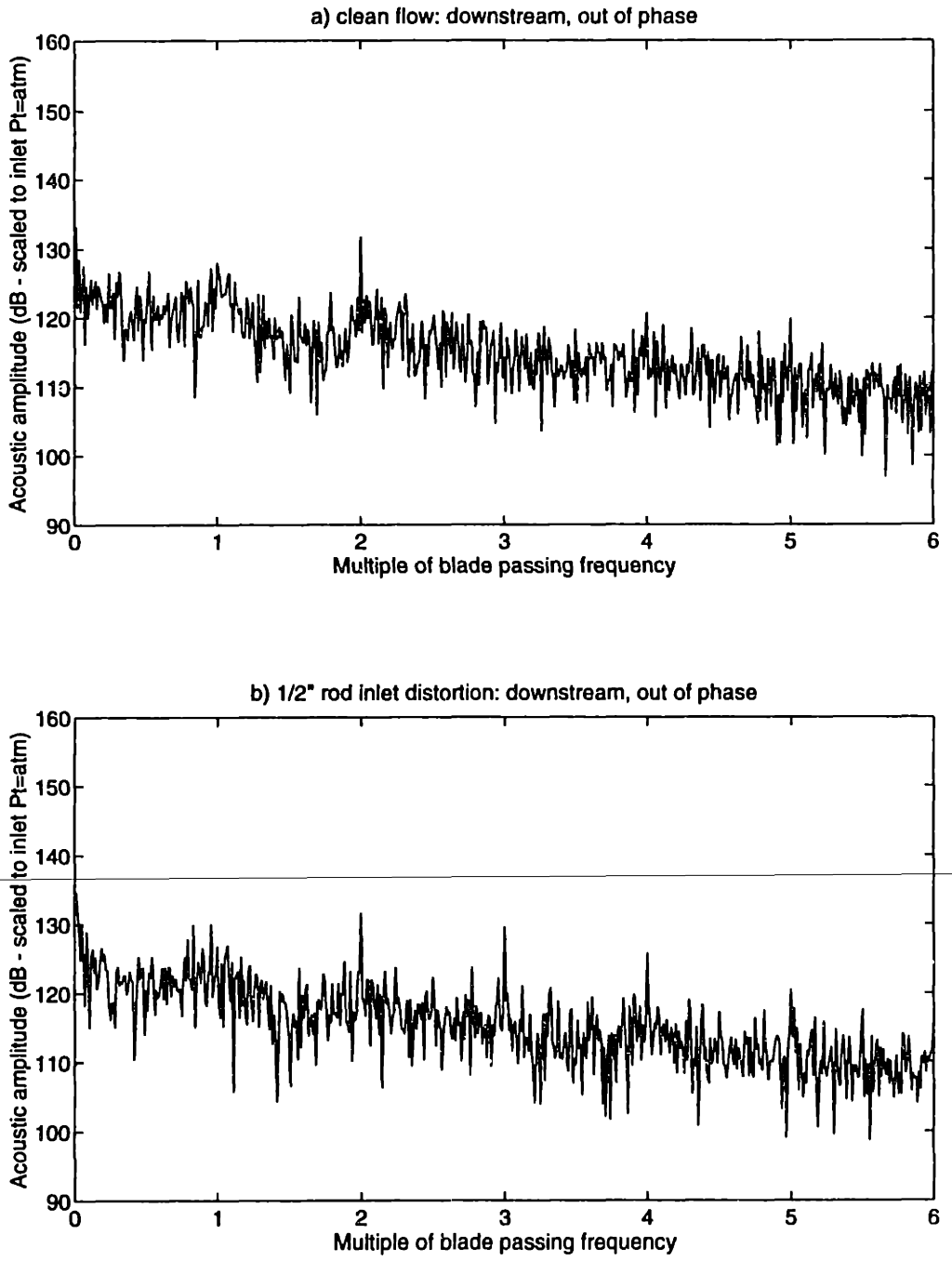

Figure B-7: Downstream, out-of-phase acoustic spectra for clean and inlet distortion

APPENDIX C

HIGH LOADING CONDITION: BASELINE FAN STAGE

To examine the effects of loading on the flow field downstream of the baseline solid-bladed fan, tests were completed at a condition near the stall point. This high loading operating condition corresponded to approximately a 15% drop in axial Mach number, or mass flow, and a 1.5% increase in total-to-total pressure ratio. In addition to providing flow field and acoustic data near stall, the data at high loading provides an opportunity to assess the trailing edge blowing wake management blade performance relative to the baseline solid-bladed rotor. Since the hollow blades have different structural characteristics, the blades will untwist and bend differently and thus may have a different overall loading and spanwise loading distribution as the baseline fan. Having data at both nominal take-off and high loading will provide some basis for evaluating the wake management rotor blade characteristics.

C.1 Flow Field Measurements

Data was taken at 0.1c (just behind the trailing edge of the rotor) at 50% and 75% span and at 1.5c (just in front of the stator row) at 25%, 50%, 75%, and 87.5% span. Plots of relative Mach number (mean profile, harmonic content, and turbulence intensity), flow angles, Mach number components, and components of pressure will be presented in Figures C-1 through C-24. The data is shown compared to the baseline takeoff loading condition.

The baseline loading flow measurements are shown as solid lines and the high loading measurements are shown as dashed lines. As expected, the high loading mean wake profiles are generally wider and deeper than the baseline take-off condition profiles. At 0.1 chords, the suction side of the wake (right side of the wake in the plots) is much wider than the baseline take-off condition wake. This is due to the substantially thickened (or separated) suction surface boundary layer at high loading, with little change to the pressure side of the wake (left side in the plots). This result is seen most clearly at 75% span, 0.1c is Figure C-5. The harmonic content changes accordling with more low harmonic content due to the increase in wake width. The increase in wake width is also evident at 1.5 chords, with a corresponding increase in the 1*BPF harmonic at 50%, 75% and 87.5% span. At 87.5% span, the combination of tip clearance flow and wake in the outboard region have resulted in a near complete 1*BPF flow field perturbation at the high loading condition. In addition, the peak turbulence intensity levels at 75 and 87.5% span increase with loading, as well as the pitch average level. Therefore, the broadband noise would be expected to increase.

C.1.1 Wake phase angles

The relative Mach number wake harmonic phase angles were calculated and are shown for the first four multiples of blade passing frequency, BPF in Figure C-25. The wake skew is seen to have approximately the same shape and variation as the baseline loading condition but the wake is offset by approximately 40 degrees due to the increase in tangential flow angle. Because the phase variation is about the same as the baseline condition, changes in the acoustics can be more accurately determined than in the trailing edge blowing configurations if the wake harmonic amplitudes change uniformly along the span. Microphone measurements will be shown in the next section.

In general, the changes in flow field characteristics from the nominal take-off design operating conditions are:

1) The first four harmonics of BPF increase by approximately 20% at 0.1c.

2) The turbulence intensity is slightly increased at 0.1c.

3) The 1*BPF harmonic at 1.5c is approximately 34% lower at 25% span, and approx-

imately 18% higher at 50% span, 42% higher at 75% span, and approximately 33% higher at 87.5% span.

4) The 2*BPF harmonic at 1.5c follows the same trends as 1*BPF, except at 87.5% where it is decreased by approximately 75%.

5) The turbulence intensity at 1.5c is slightly lower at 25% and 50% span, and about 24% and 11% higher at 75% and 87.5% span, respectively.

6) The tangential flow angle is approximately 5 degrees higher at 1.5c.

7) The axial Mach number is approximately 15% lower at 1.5c.

8) The tangential Mach number is approximately 3% higher at 1.5c.

9) The absolute total pressure divided by the inlet total pressure is approximately 1.5% higher at 1.5c.

10) The static pressure divided by the inlet total pressure is approximately 4% higher at 1.5c.

In addition to the mean profiles, the relative Mach number spectra at 1.5 chords are shown in Figures C-26 through C-29. The tones at multipes of blade passing frequency (BPF) match the harmonic content plots, and the spectral distribution of turbulence can also be seen. Comparing these plots to the spectra content at the baseline take-off condition (Figures 5-5 through 5-8), the level of turbulence intensity is not higher to any significant degree at 25%, 50% and 75% span, but is increased at 87.5% span.

C.2 Microphone measurements

Microphone measurements were taken with the 4-way probe removed from the test section. The test section was clean with only flush mounted duct microphone probes upstream and downstream of both blade rows. The acoustic spectra at the shroud (in-phase and out-of-phase) are shown in Figures 8-44 through 8-46. The increase in the 2*BPF out-of-phase amplitude downstream of the stator row (which corresponds to the strongest propogating acoustic mode) is approximately 7 dB. This increase is substantially larger than the increase

in the 2*BPF wake harmonic amplitudes (largest increase was 26%), especially since the wake harmonic decreases in the outboard region. This may indicate the the outboard region is not critical to the 2*BPF acoustic mode, since the 2*BPF wake harmonic is small in this region and the phase variation is large. However, changes in the wake harmonic amplitudes and phase along the entire span must be considered when trying to estimate noise reductions.

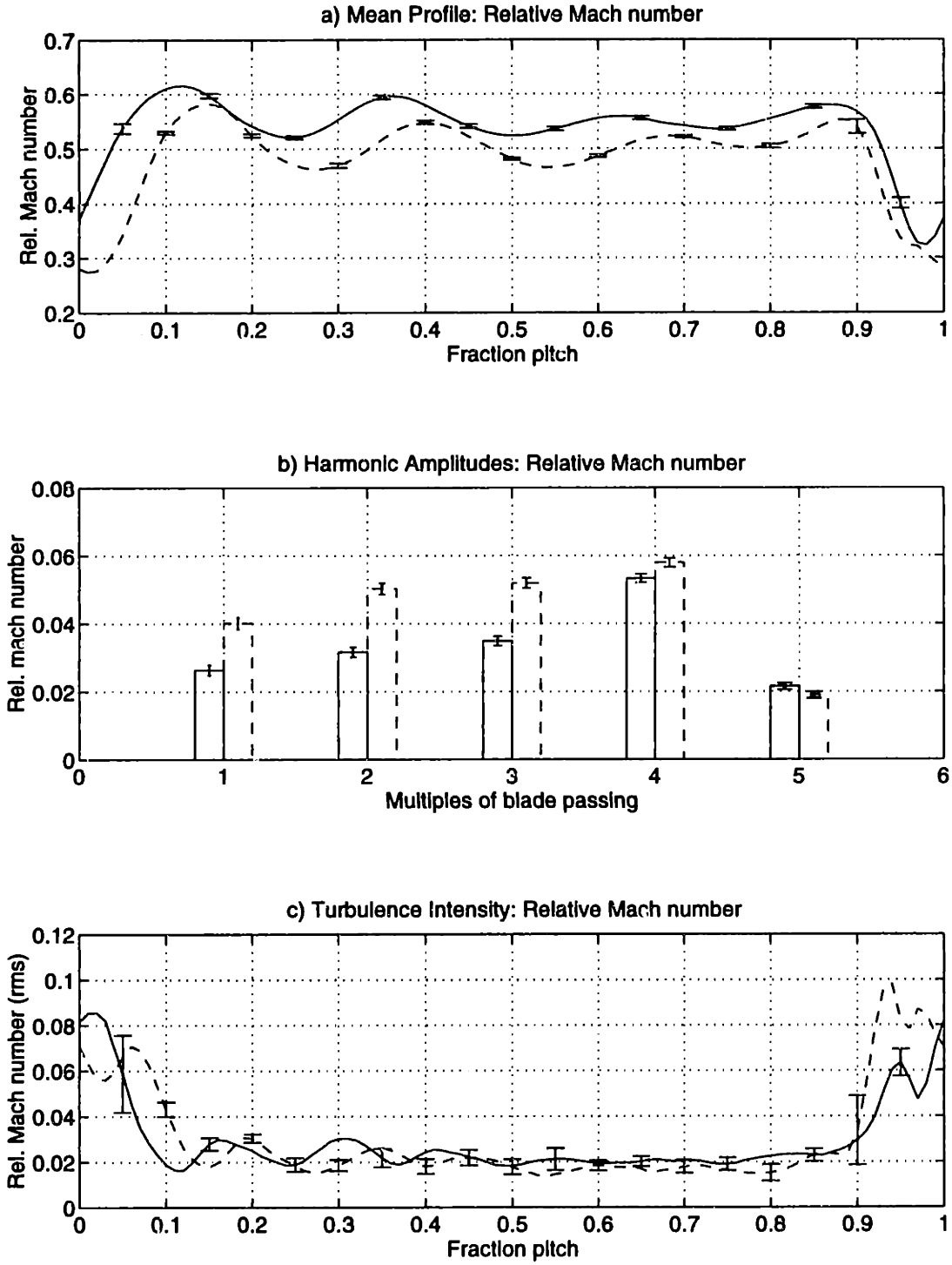

Figure C-1: Relative Mach number flow measurements at 50% span, 0.1c: baseline loading (—) and high loading (- -)

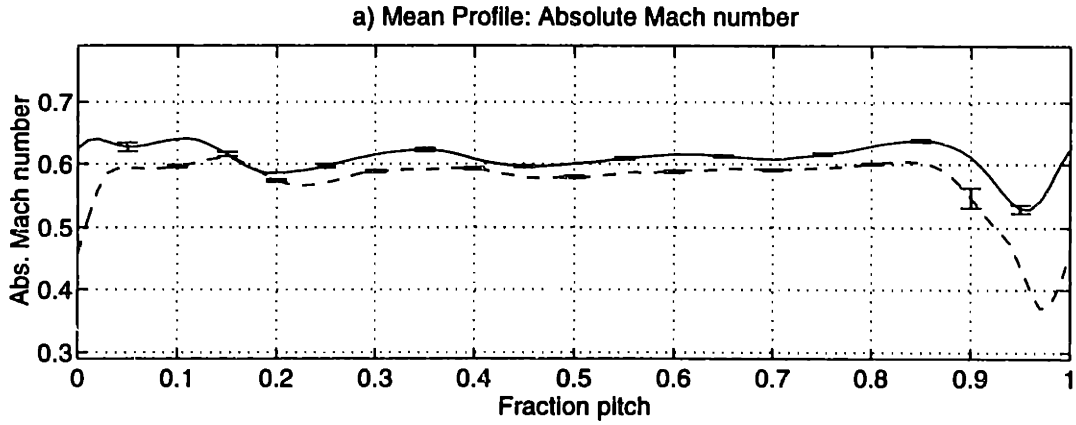

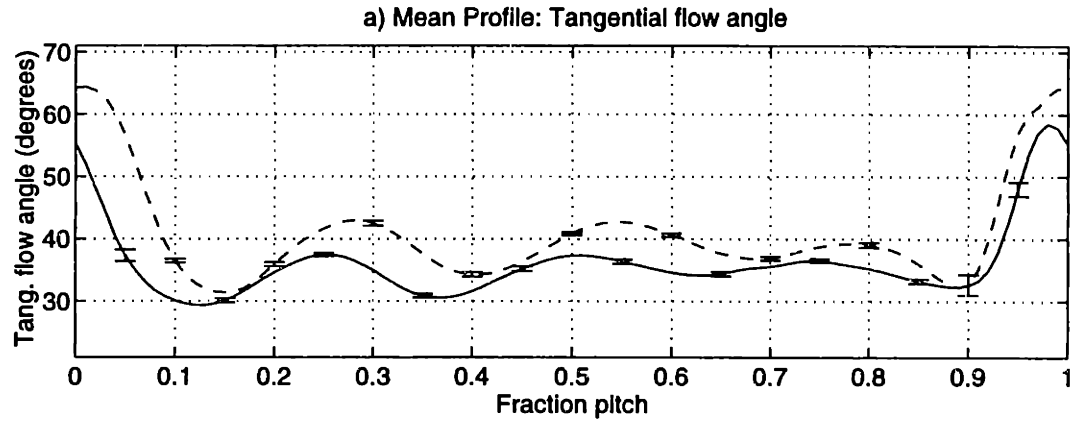

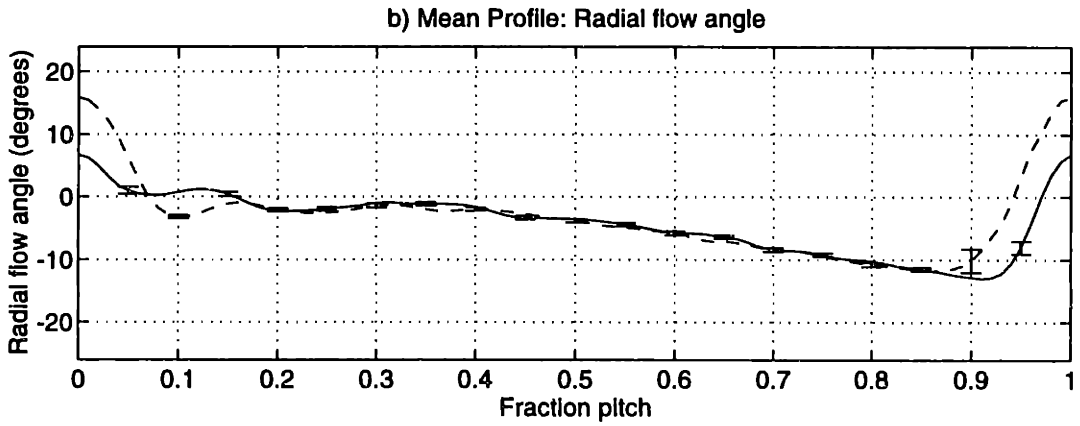

Figure C-2: Flow angle measurements at 50% span, 0.1c: baseline loading (—) and high loading (- -)

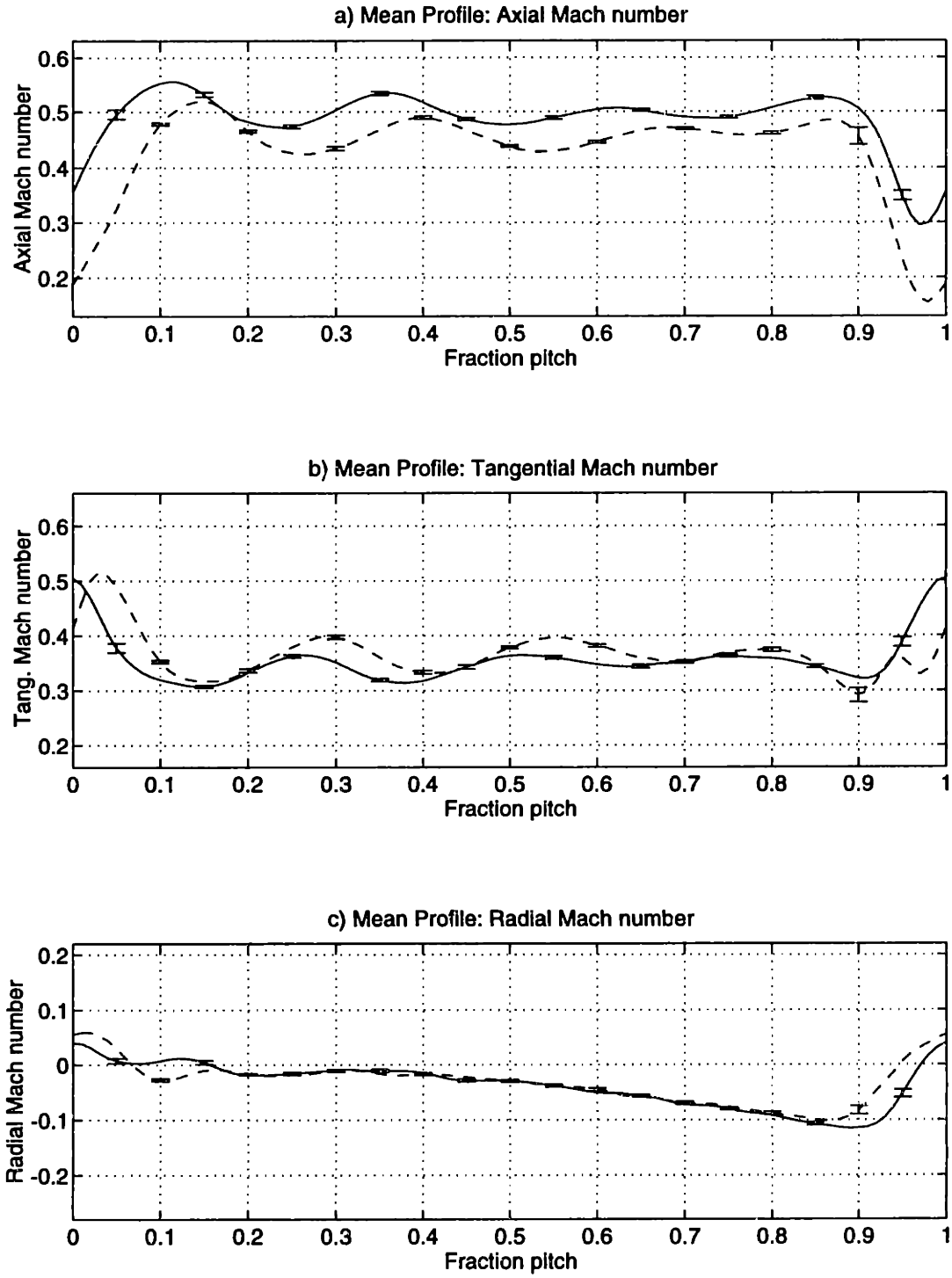

Figure C-3: Mach number component flow measurements at 50% span, 0.1c: baseline loading (—) and high loading (- -)

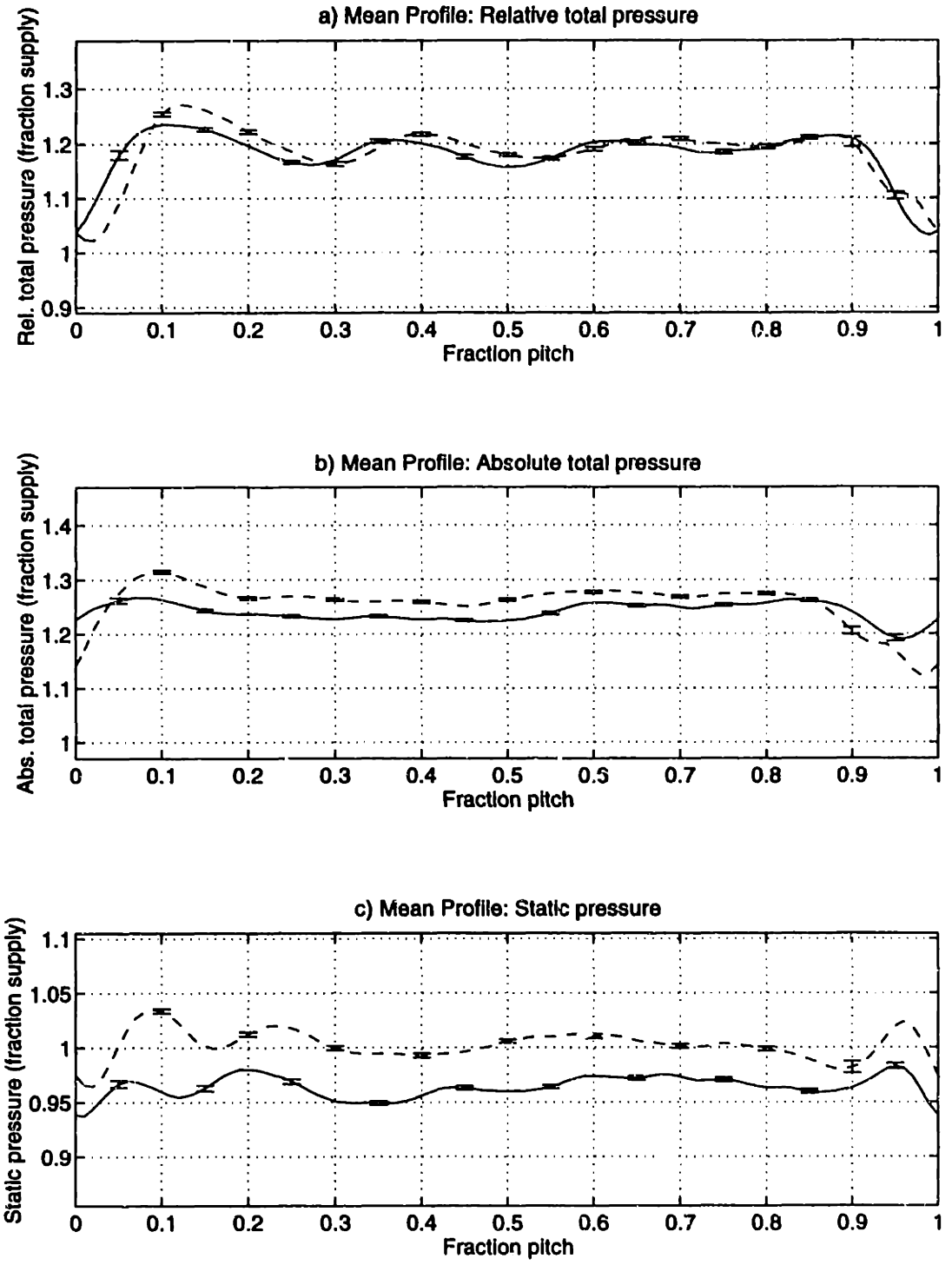

Figure C-4: Pressure component measurements at 50% span, 0.1c: baseline loading (—) and high loading (- -)

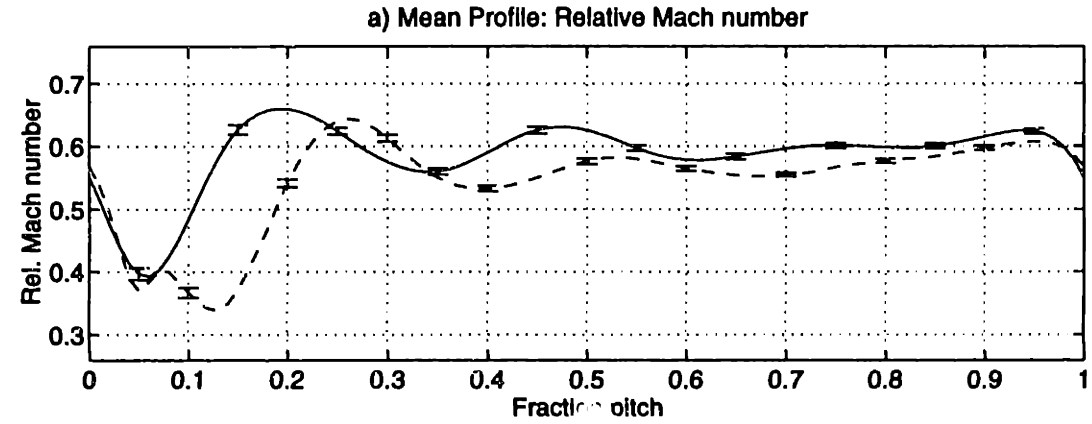

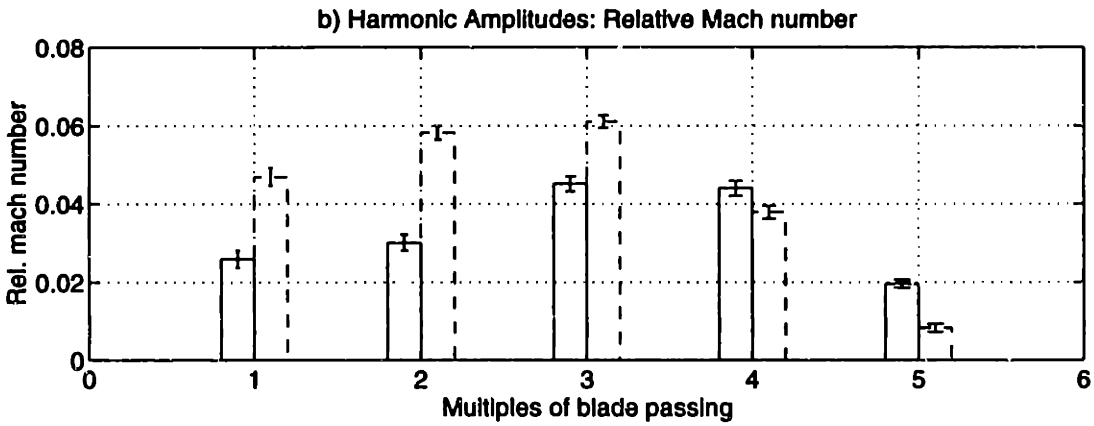

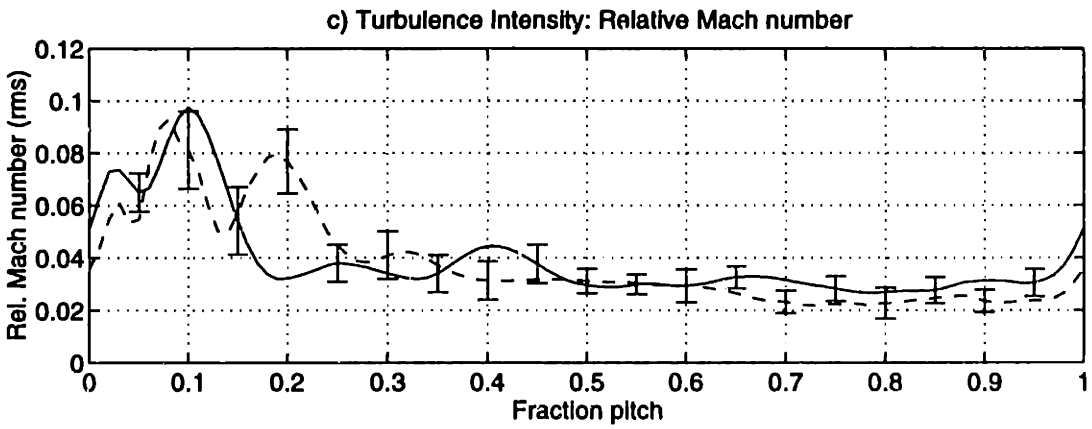

Figure C-5: Relative Mach number flow measurements at 75% span, 0.1c: baseline loading (—) and high loading (- -)

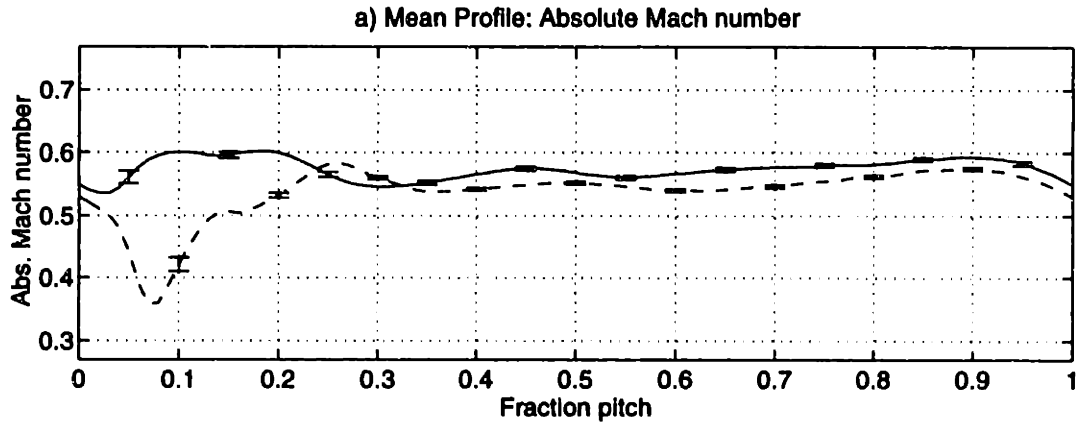

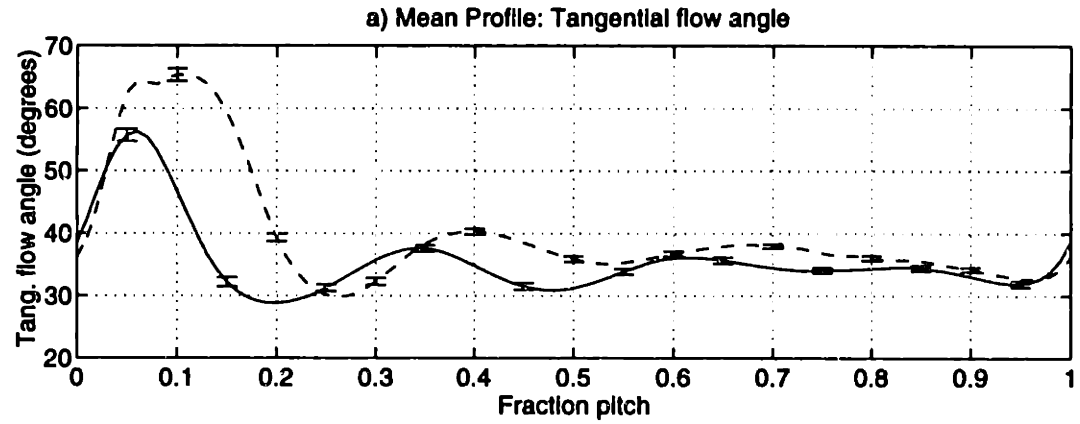

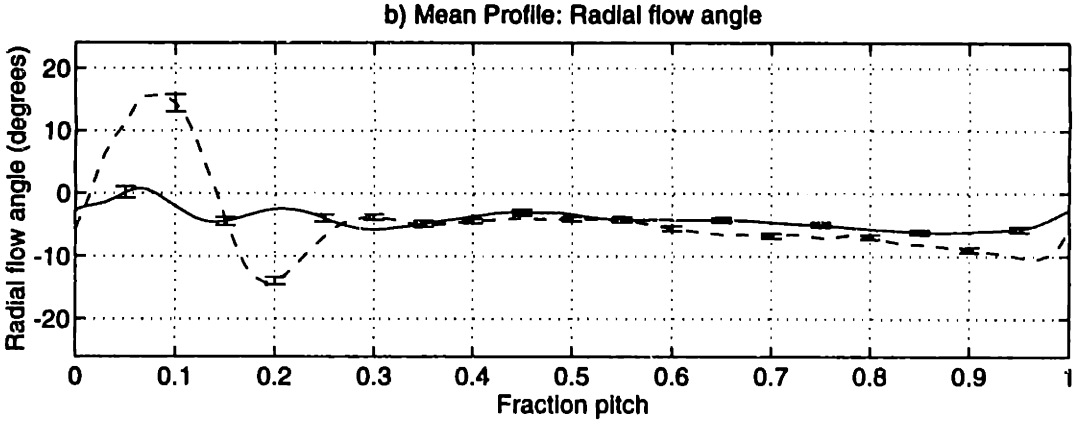

Figure C-6: Flow angle measurements at 75% span, 0.1c: baseline loading (—) and high loading (- -)

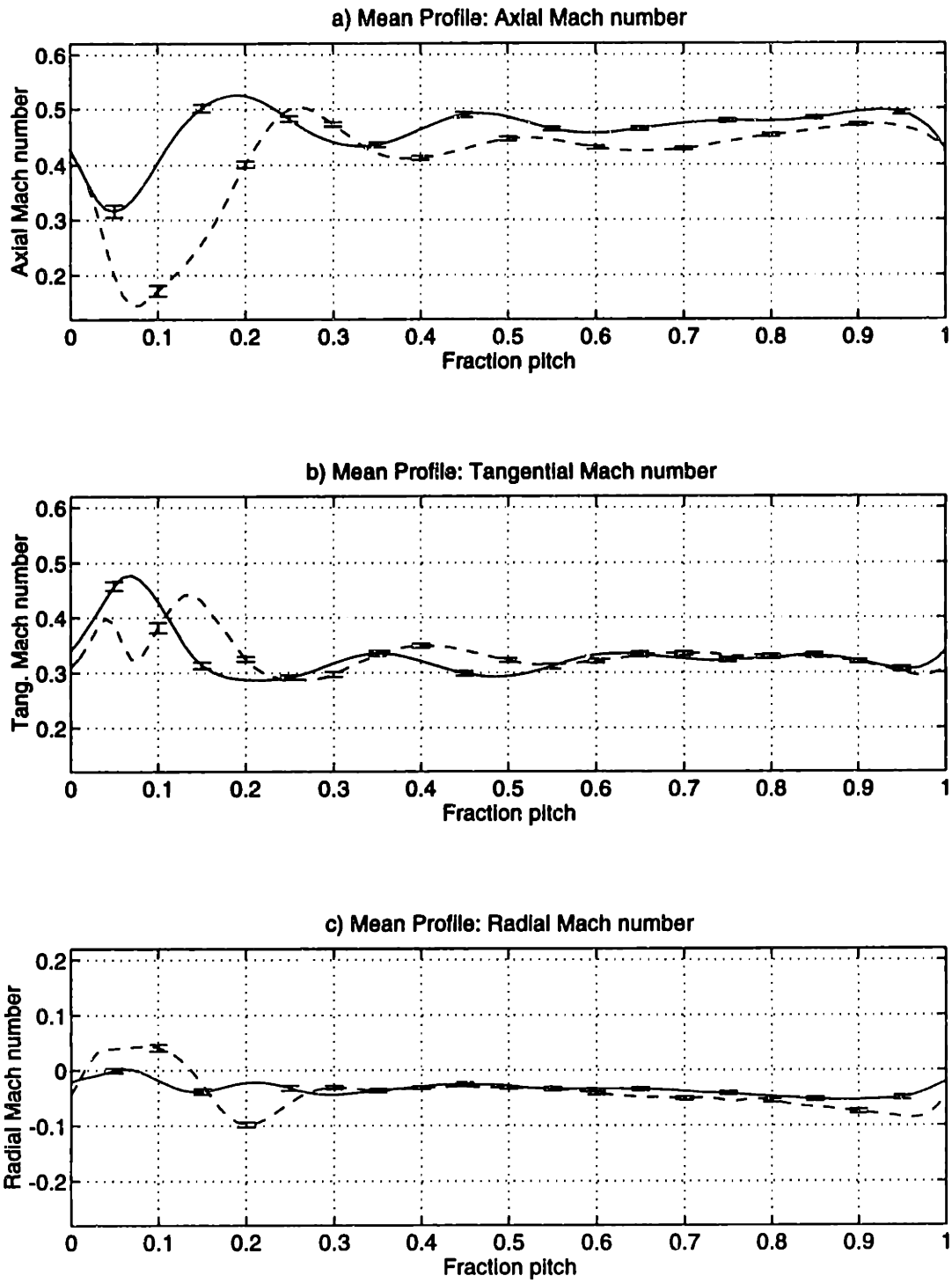

Figure C-7: Mach number conponent measurements at 75% span, 0.1c: baseline loading (—) and high loading (- -)

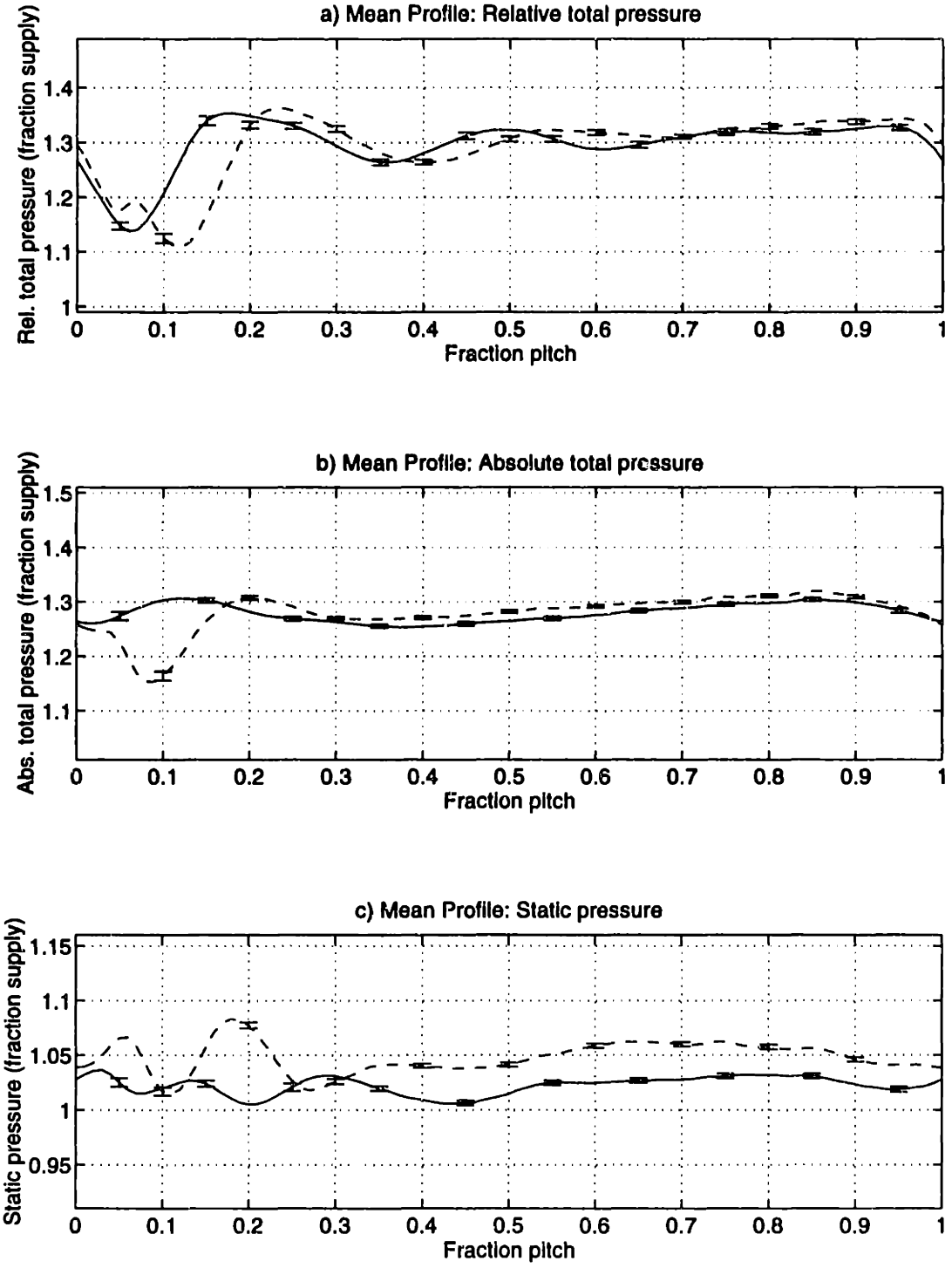

Figure C-8: Pressure component measurements at 75% span, 0.1c: baseline loading (—) and high loading (- -)

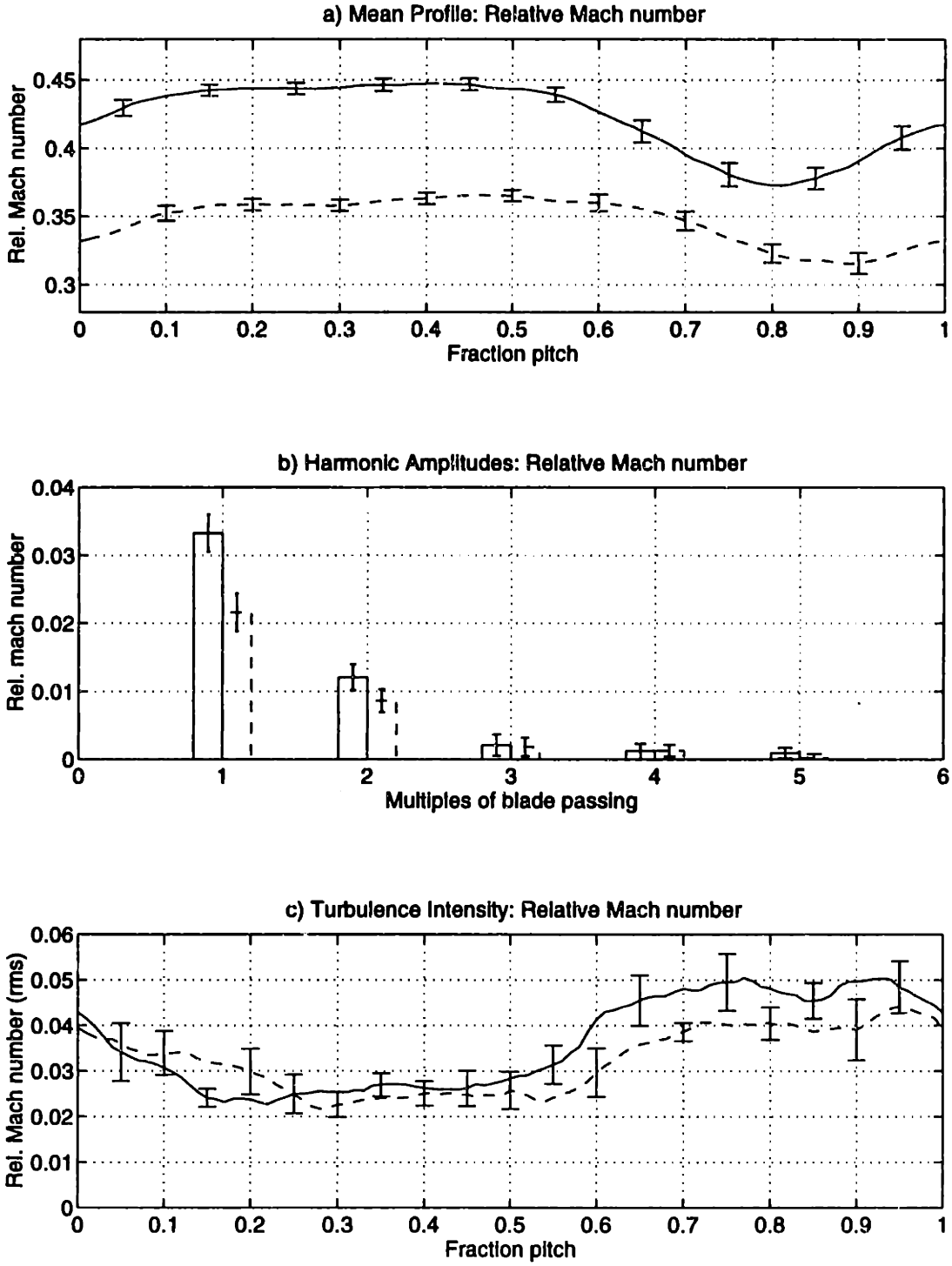

Figure C-9: Relative Mach number measurements at 25% span, 1.5c: baseline loading (—) and high loading (- -)

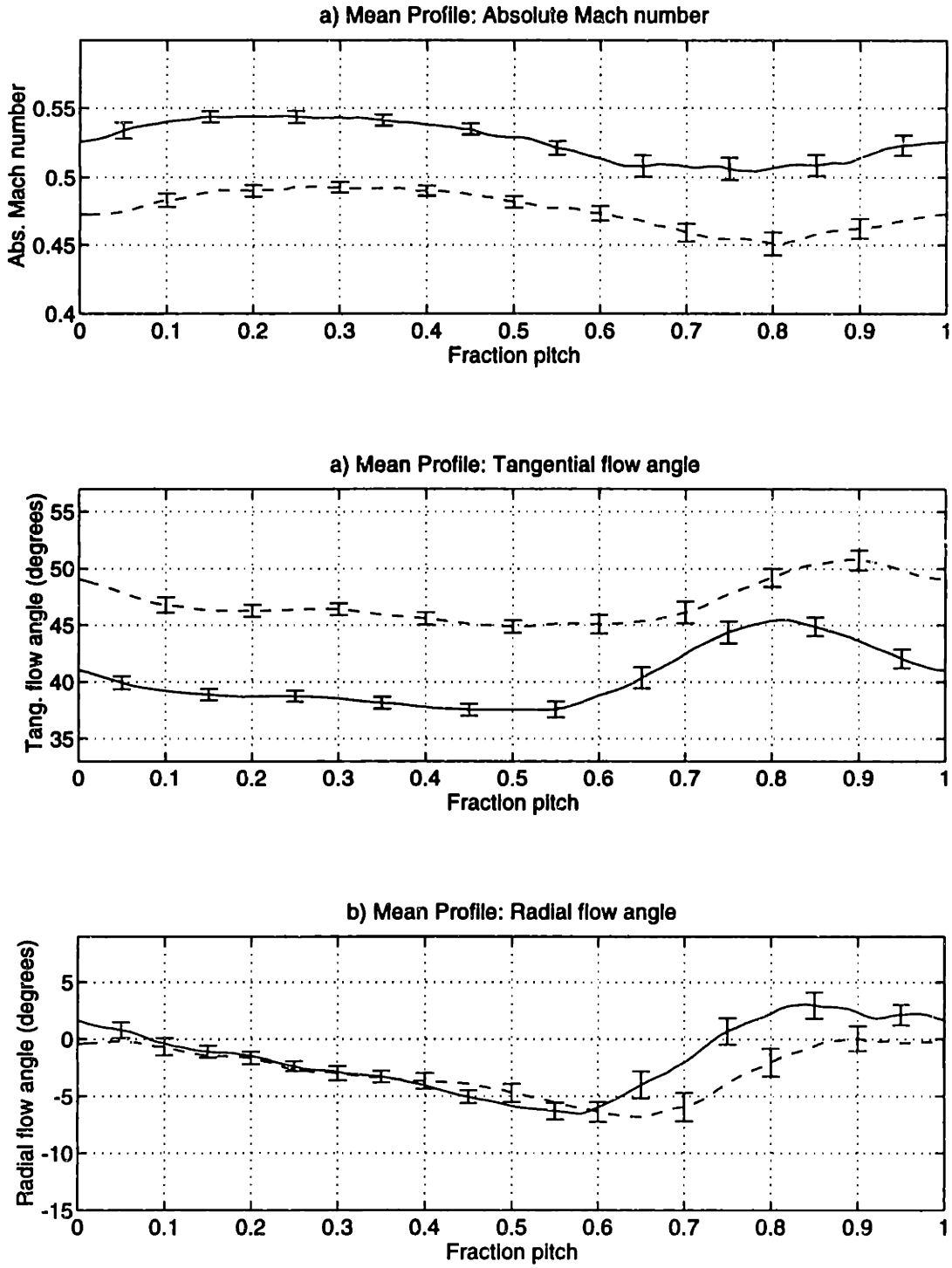

Figure C-10: Flow angle measurements at 25% span, 1.5c: baseline loading (—) and high loading (- -)

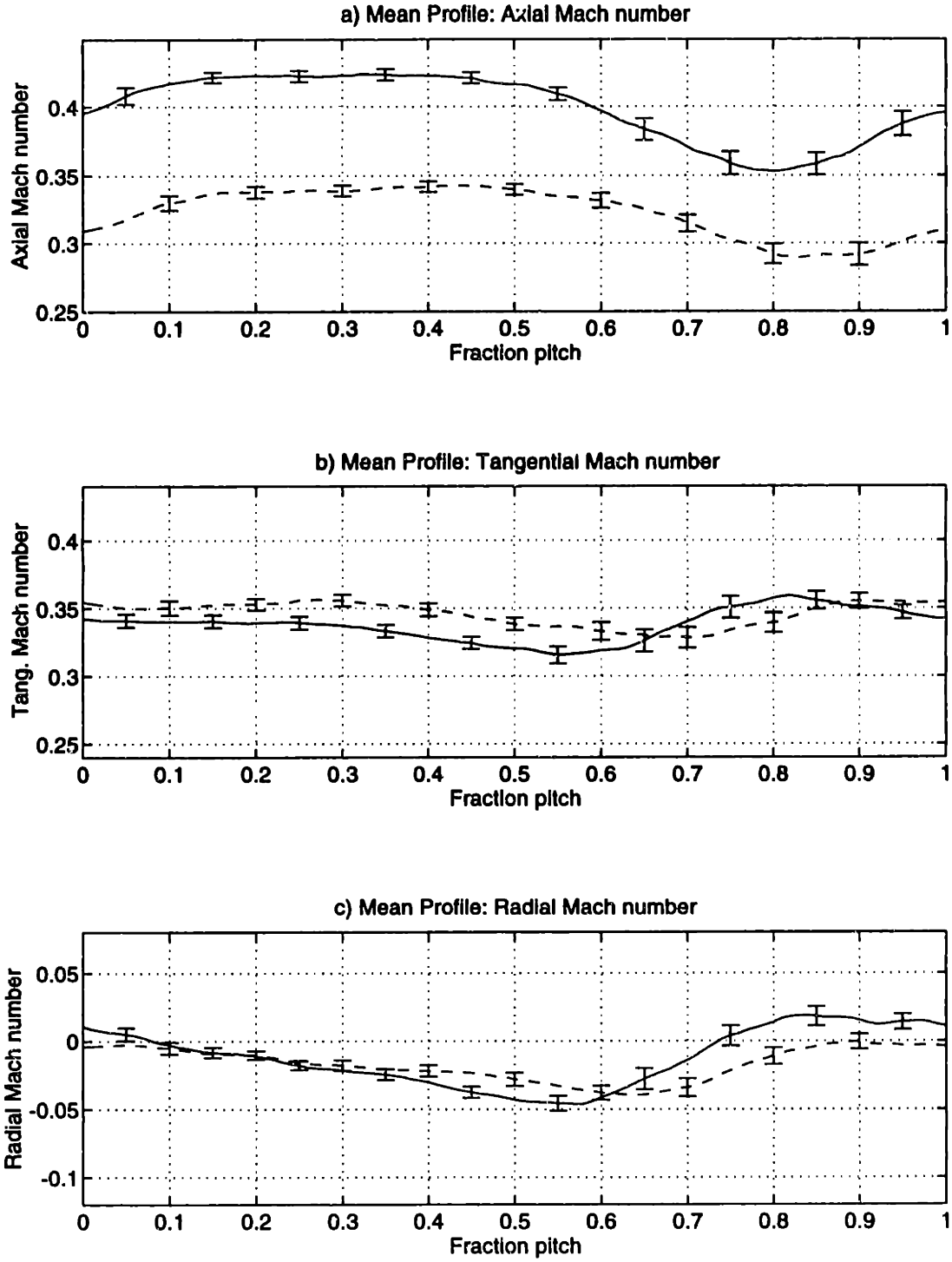

Figure C-11: Mach number component measurements at 25% span, 1.5c: baseline loading (—) and high loading (- -)

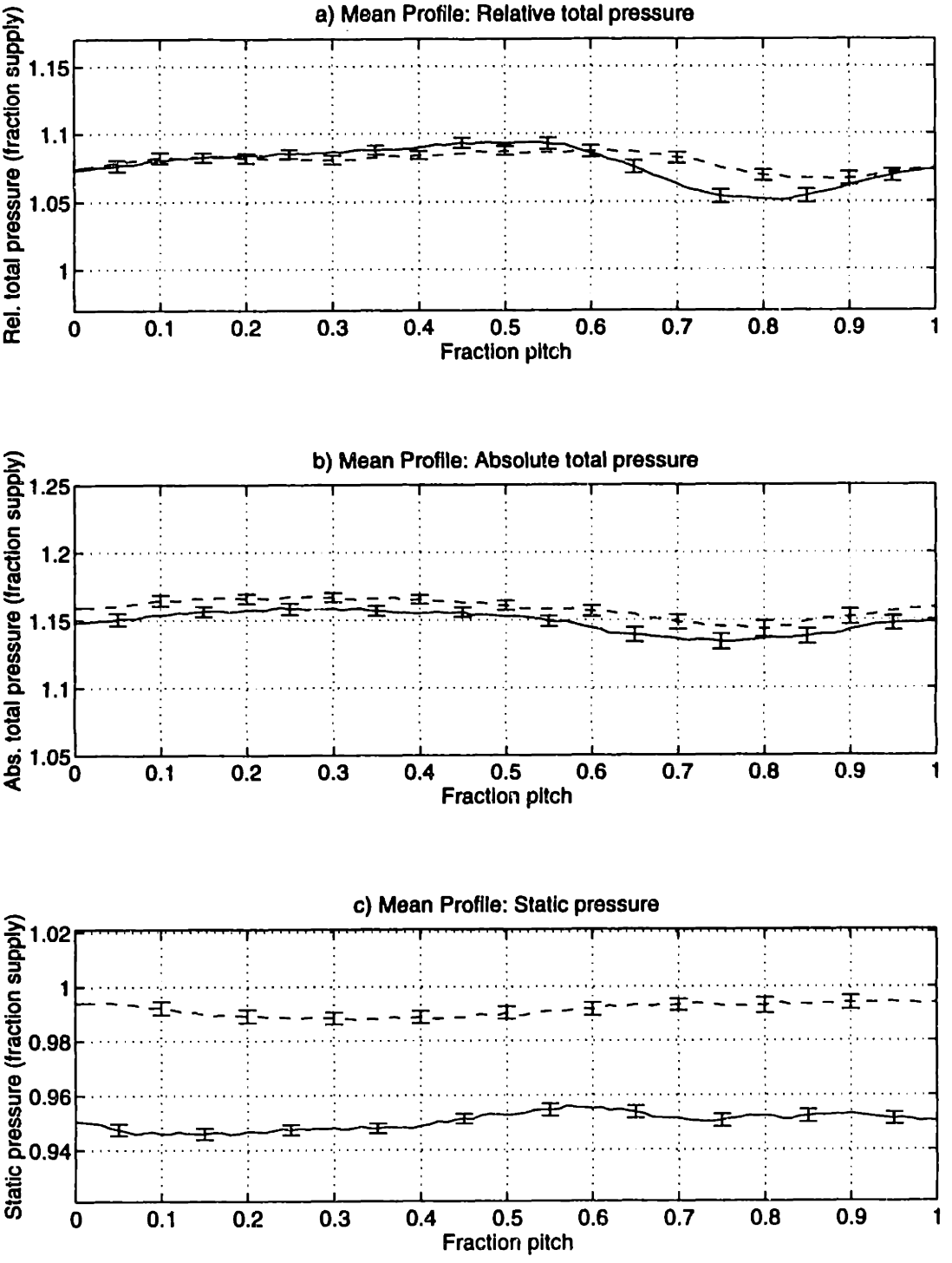

Figure C-12: Pressure component measurements at 25% span, 1.5c: baseline loading (—) and high loading (- -)

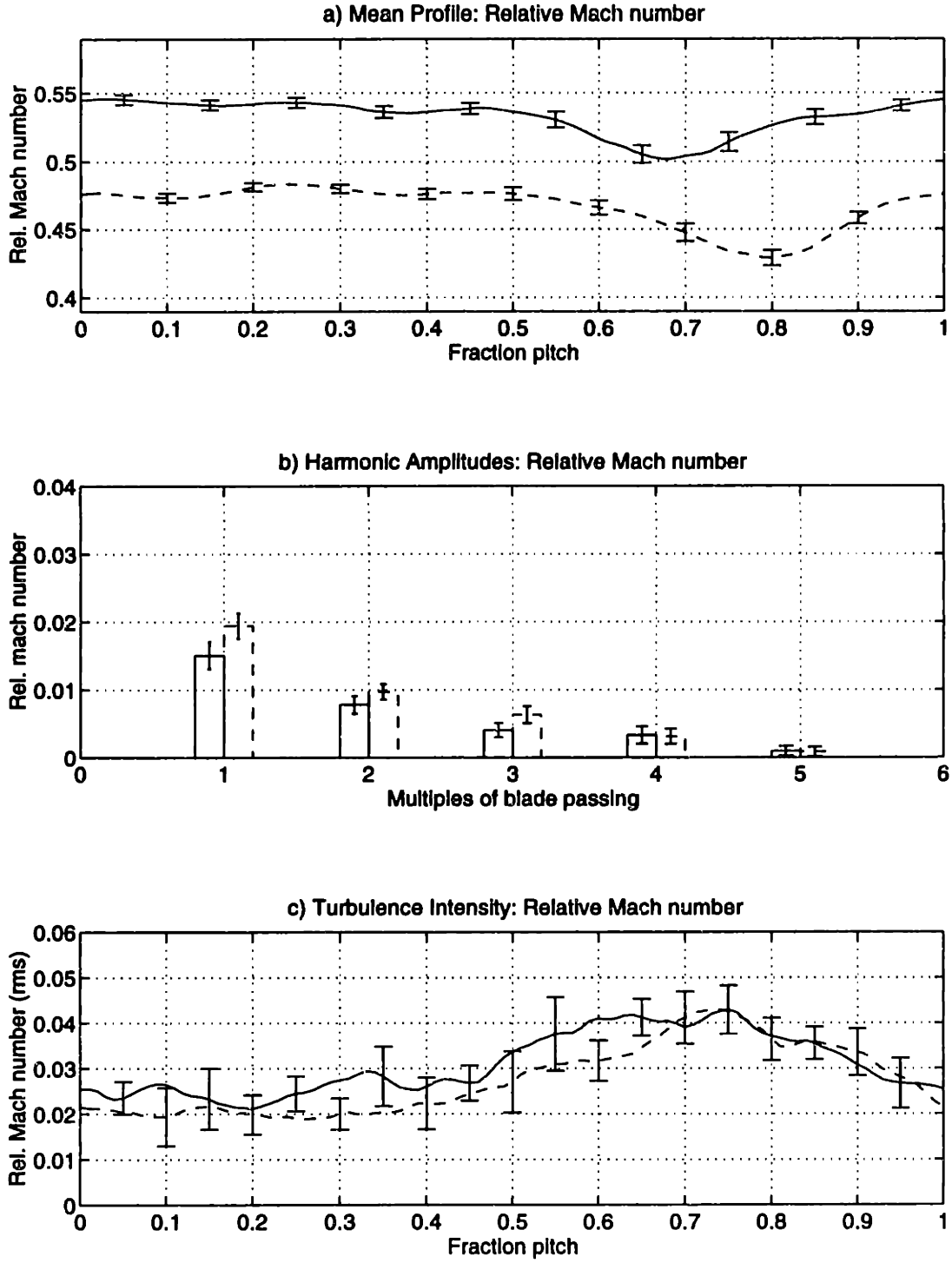

Figure C-13: Relative Mach number measurements at 50% span, 1.5c: baseline loading (—) and high loading (- -)

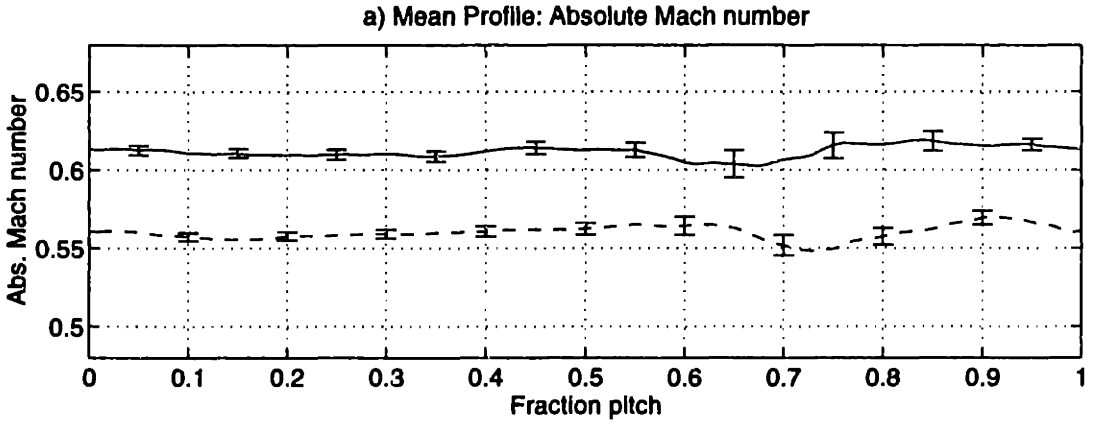

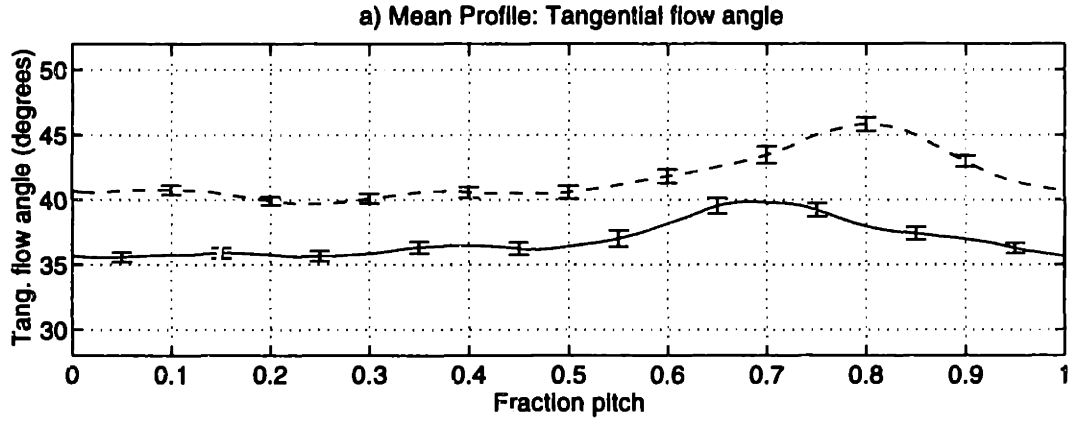

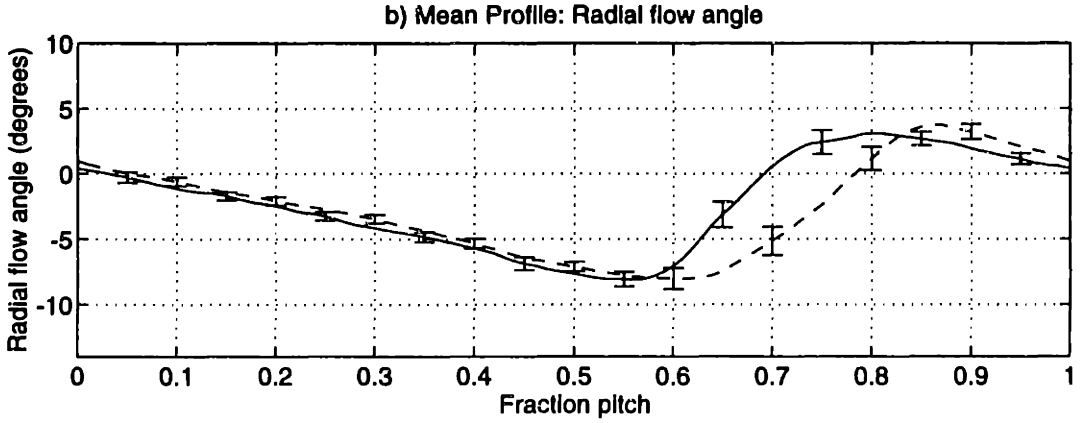

Figure C-14: Flow angle measurements at 50% span, 1.5c: baseline loading (—) and high loading (- -)

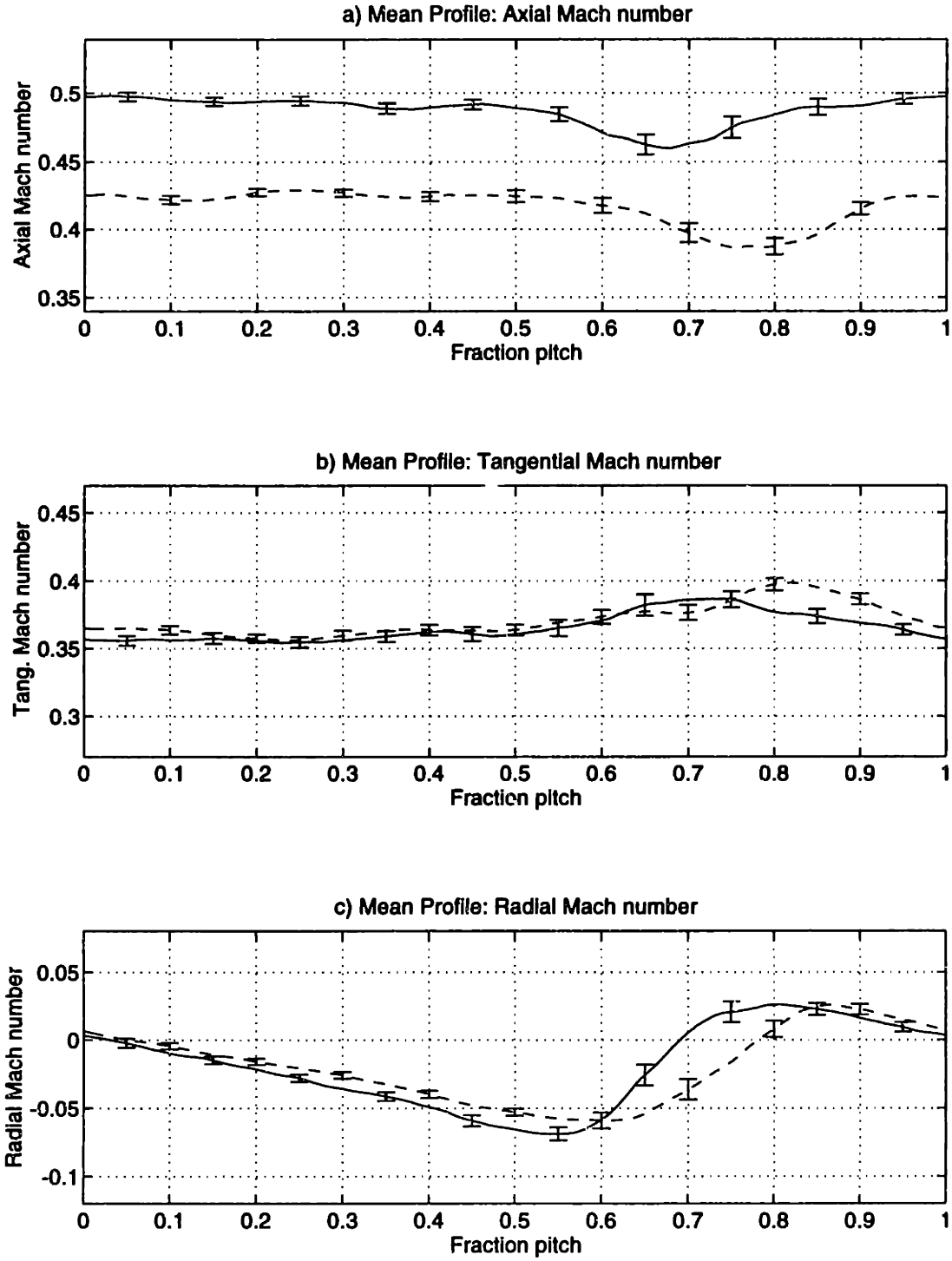

Figure C-15: Mach number component measurements at 50% span, 1.5c: baseline loading (—) and high loading (- -)

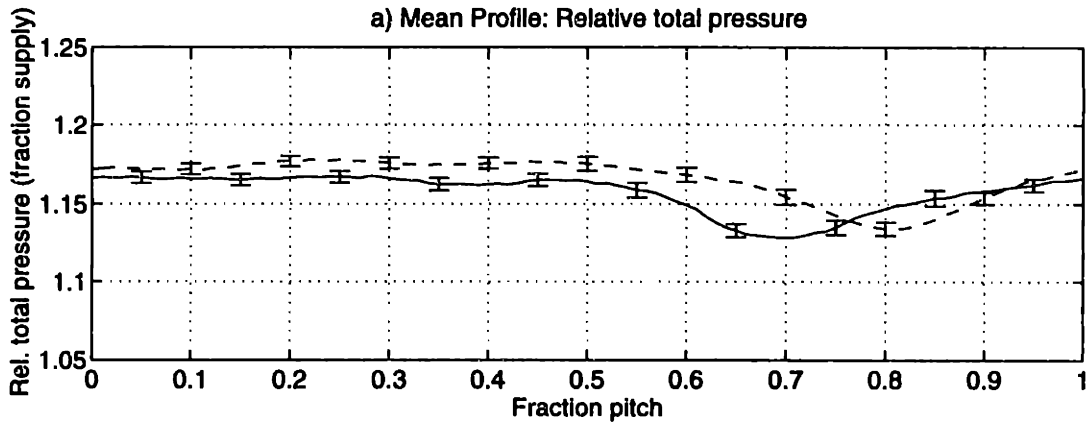

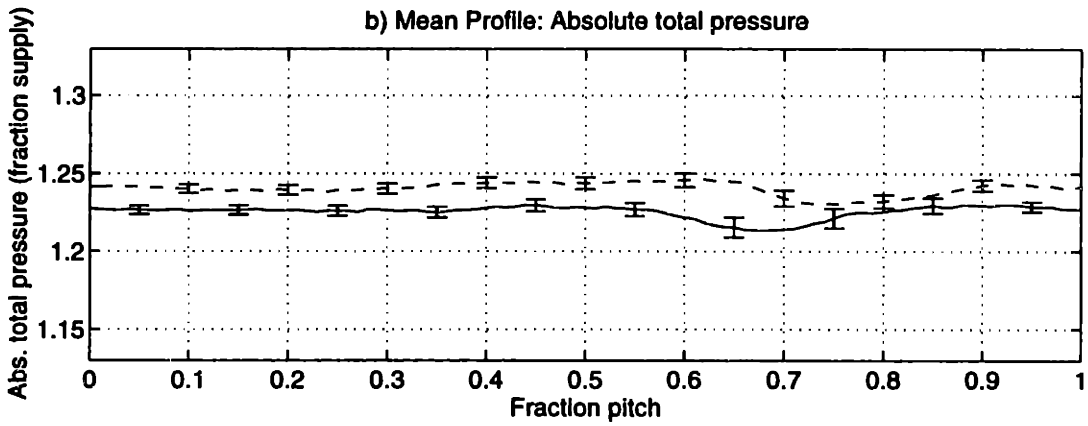

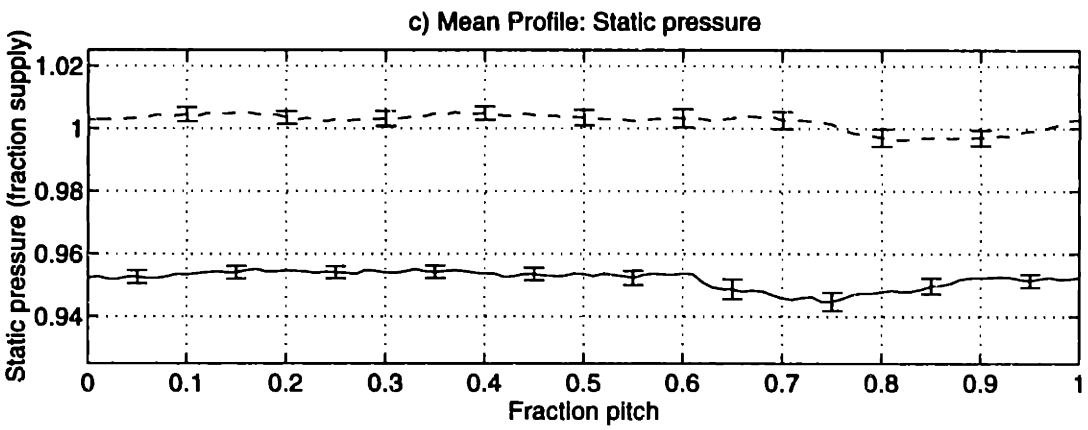

Figure C-16: Pressure component measurements at 50% span, 1.5c: baseline loading (—) and high loading (- -)

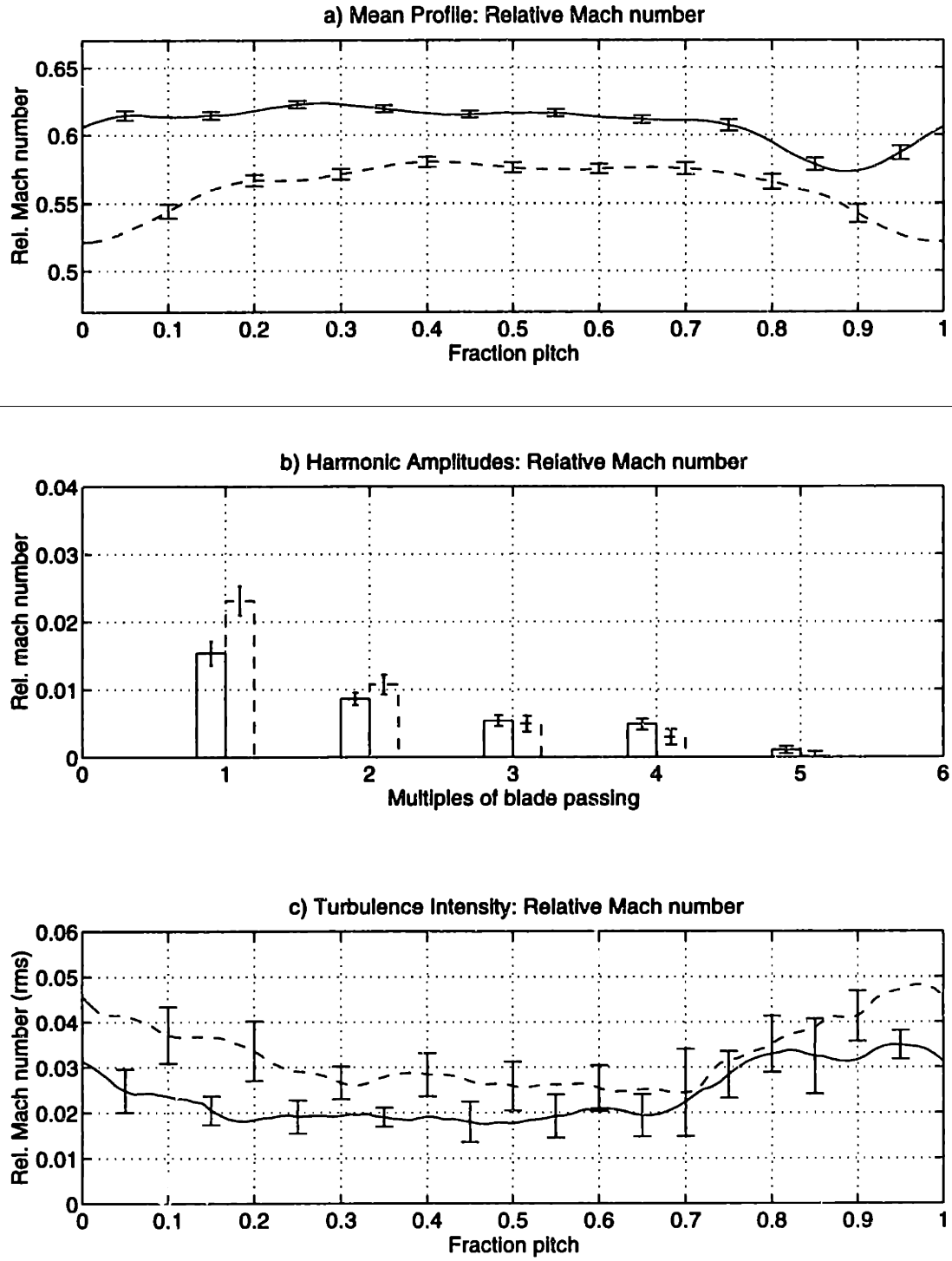

Figure C-17: Relative Mach number measurements at 75% span, 1.5c: baseline loading (—) and high loading (- -)

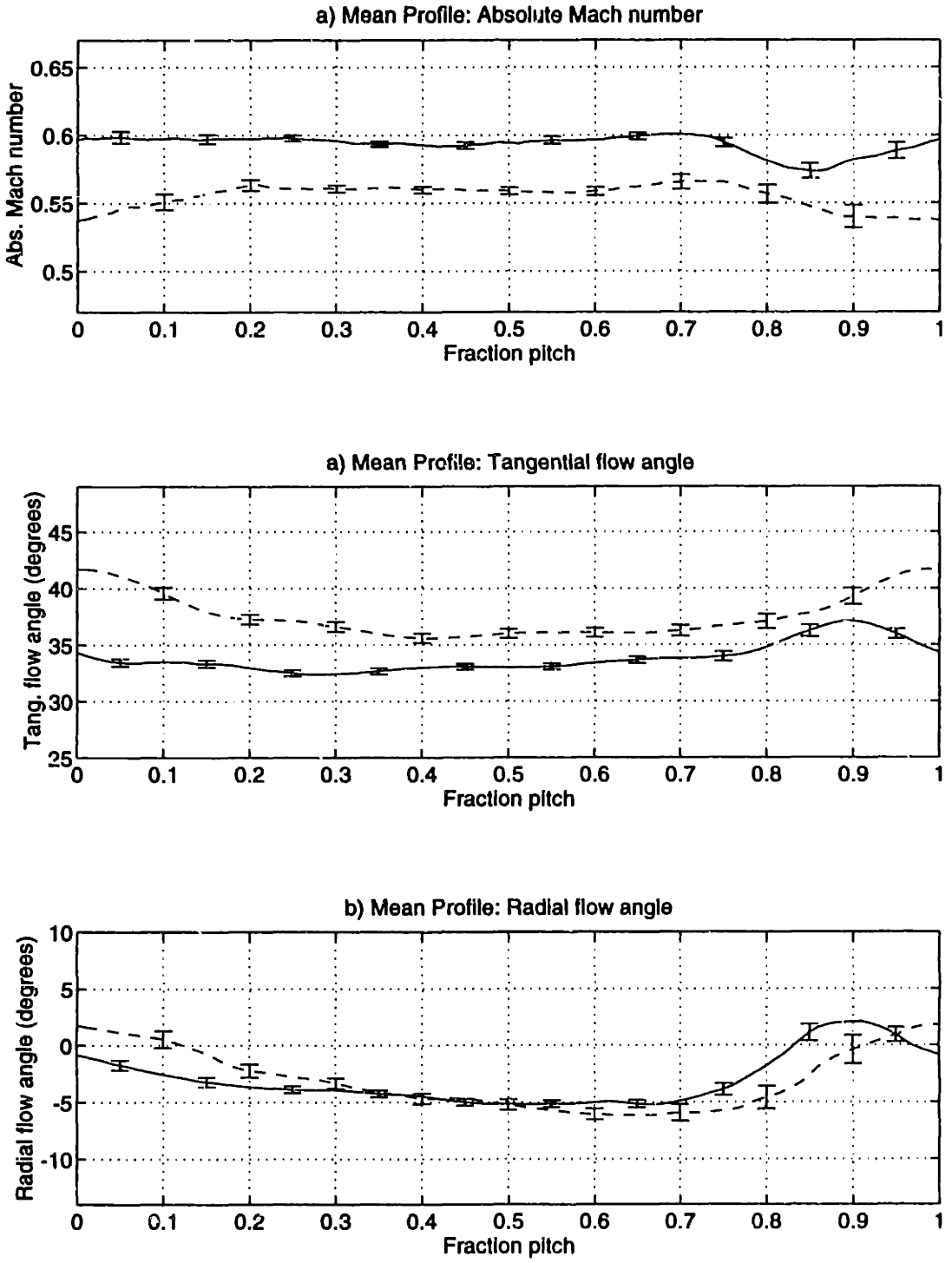

Figure C-18: Flow angle measurements at 75% span, 1.5c: baseline loading (—) and high loading (- -)

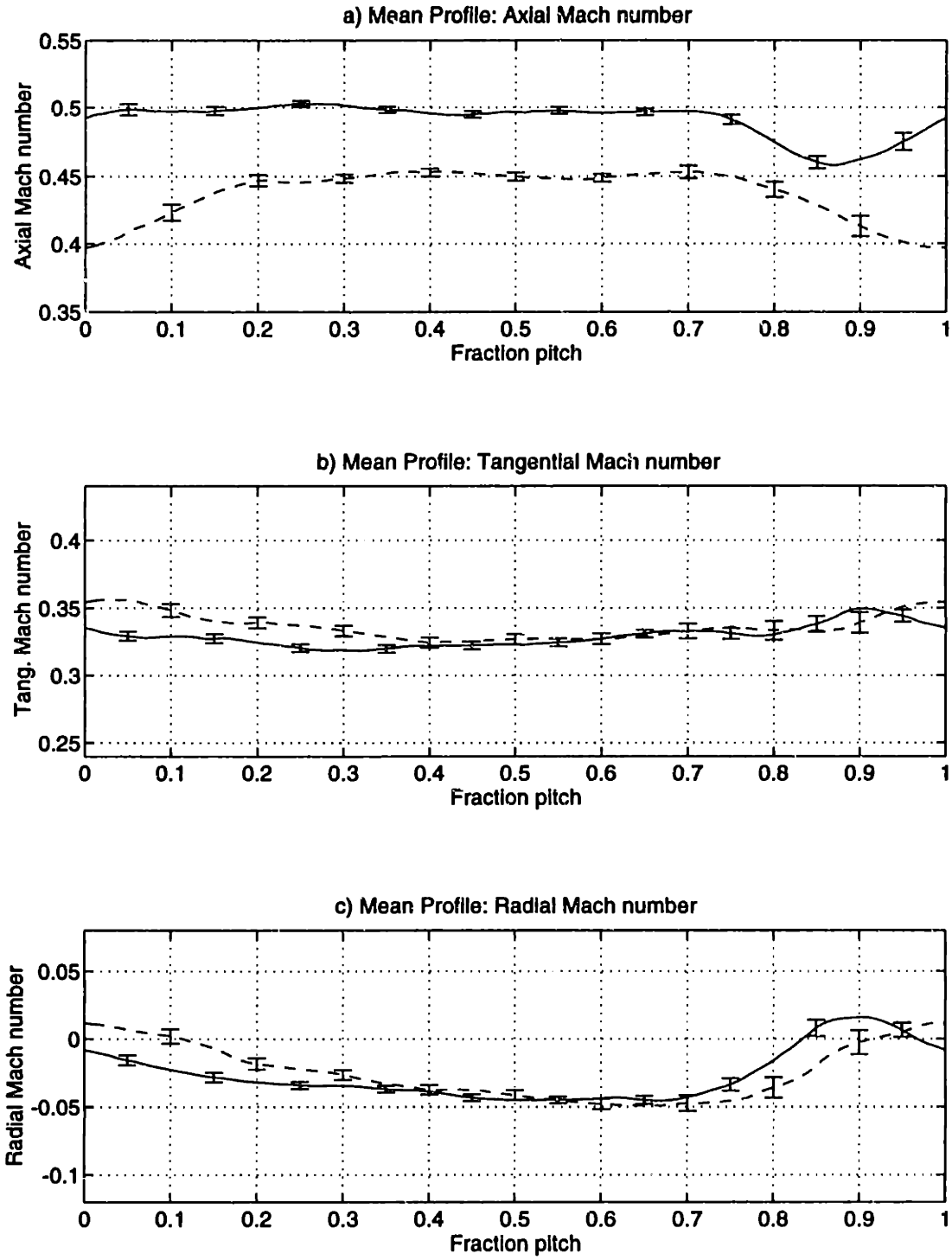

Figure C-19: Mach number compnoent measurements at 75% span, 1.5c: baseline loading (—) and high loading (- -)

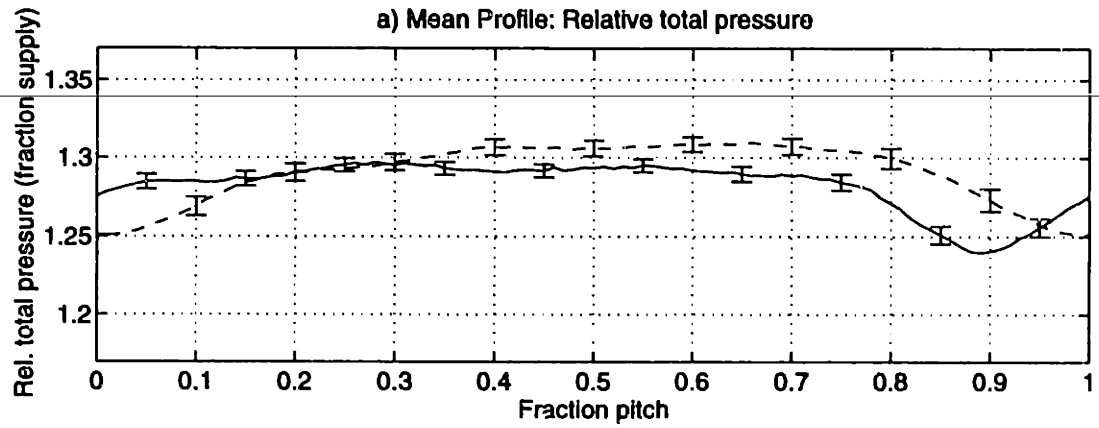

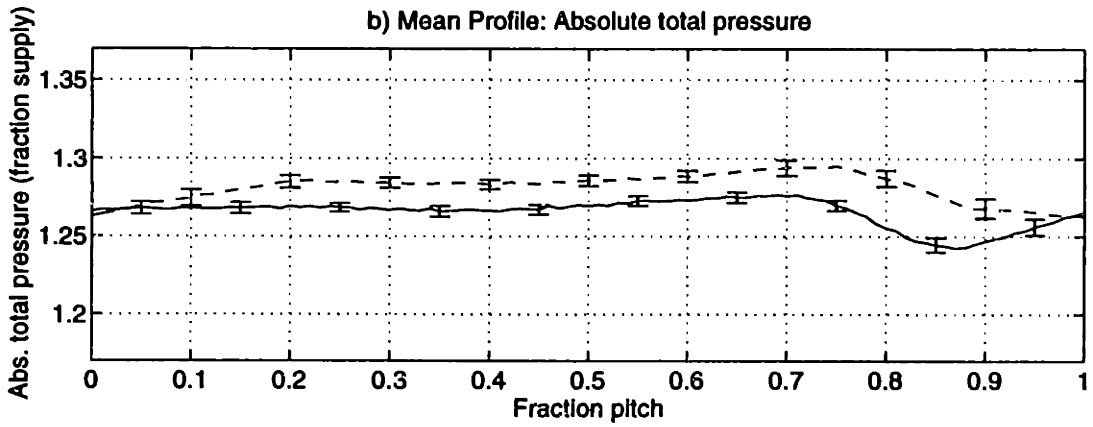

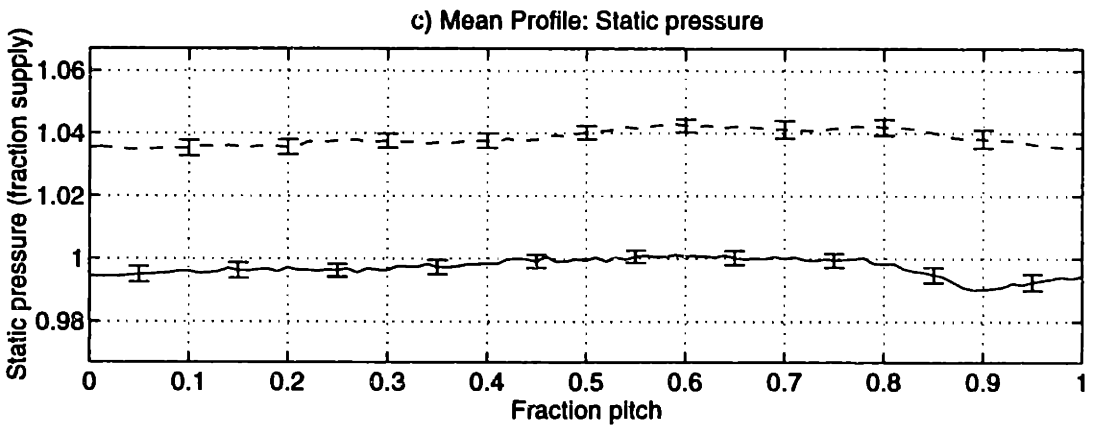

Figure C-20: Pressure component measurements at 75% span, 1.5c: baseline loading (—) and high loading (- -)

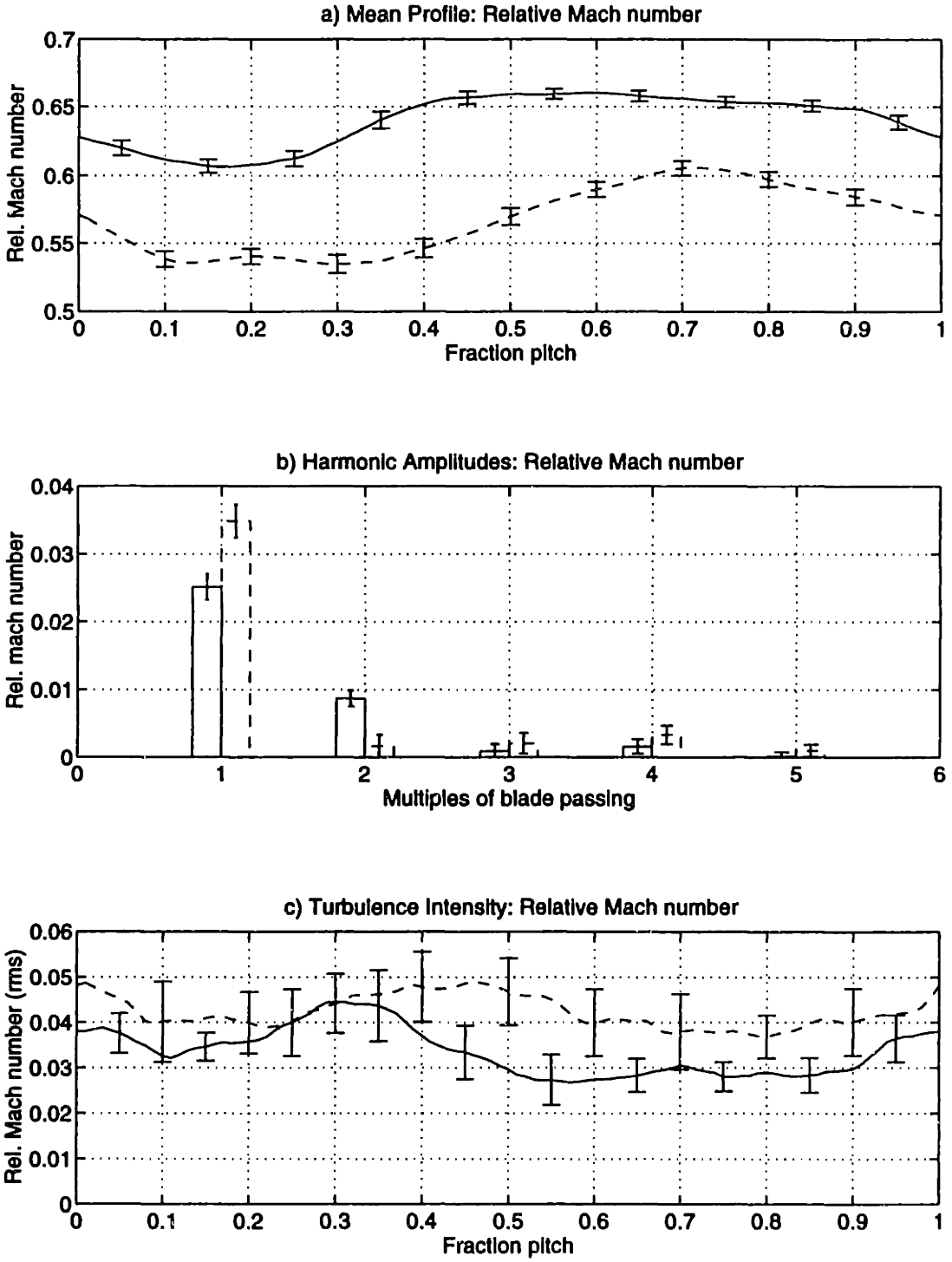

Figure C-21: Relative Mach number measurements at 87.5% span, 1.5c: baseline loading (—) and high loading (- -)

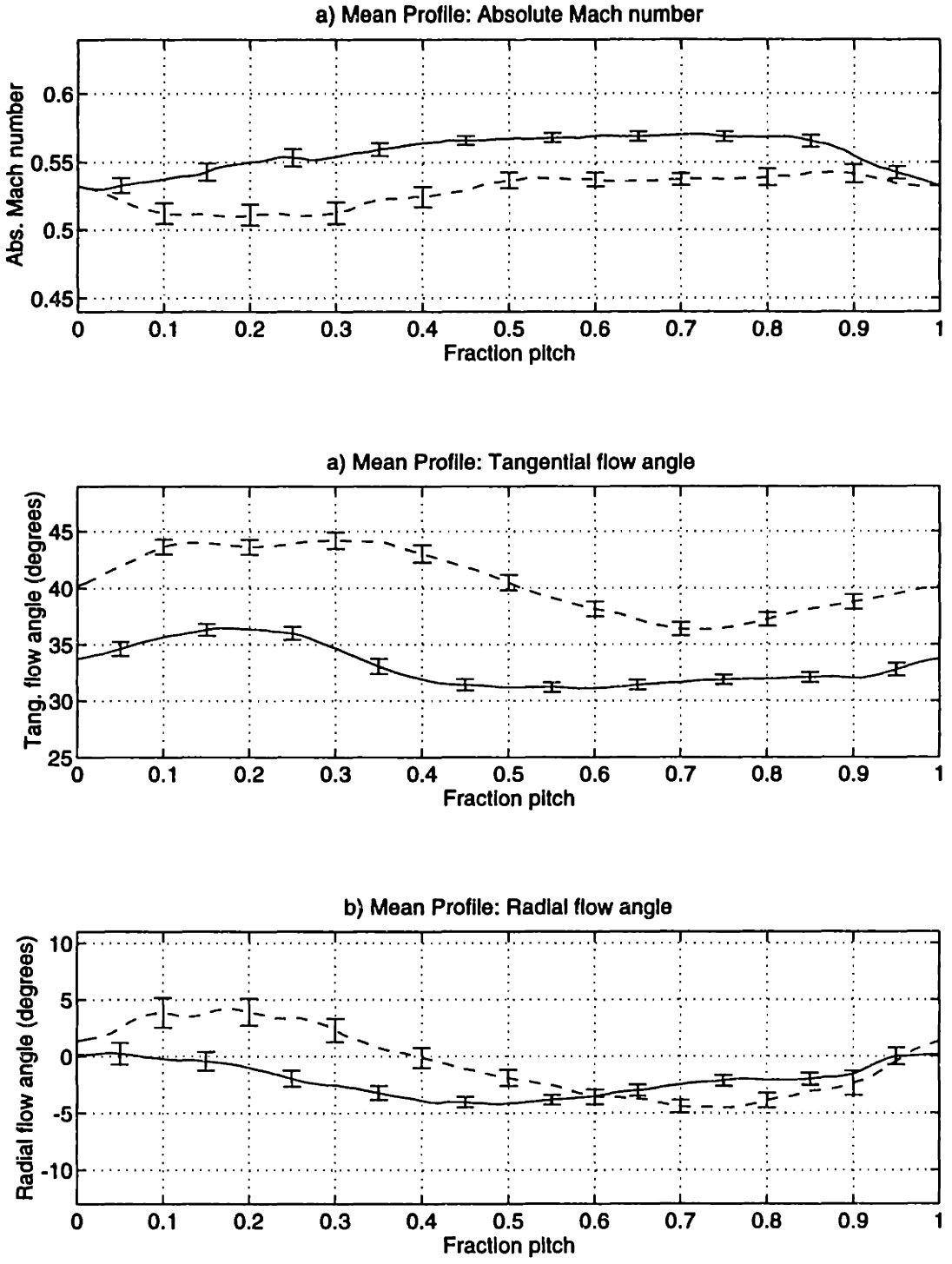

Figure C-22: Flow angle measurements at 87.5% span, 1.5c: baseline loading (—) and high loading (- -)

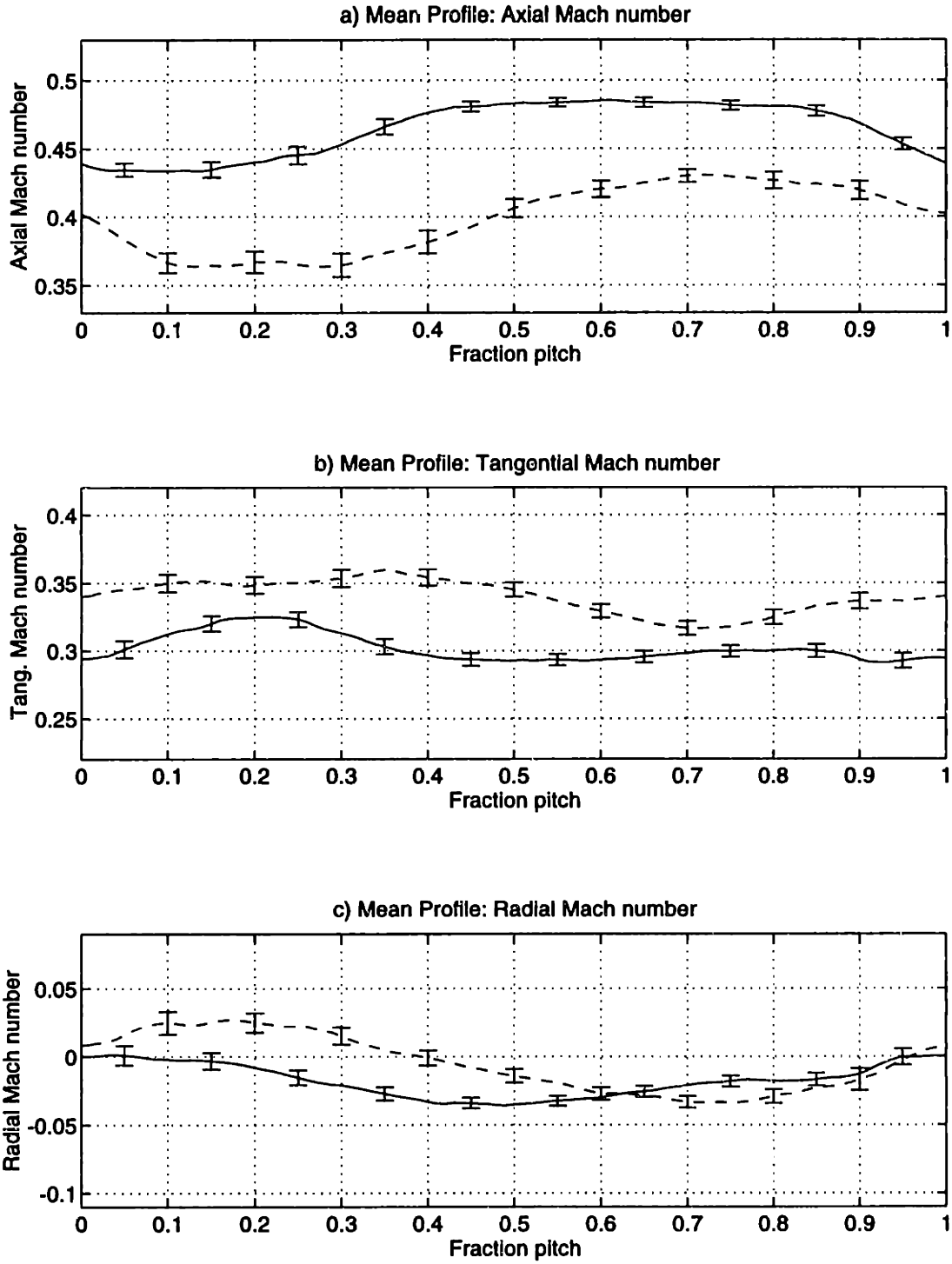

Figure C-23: Mach number component measurements at 87.5% span, 1.5c: baseline loading (—) and high loading (- -)

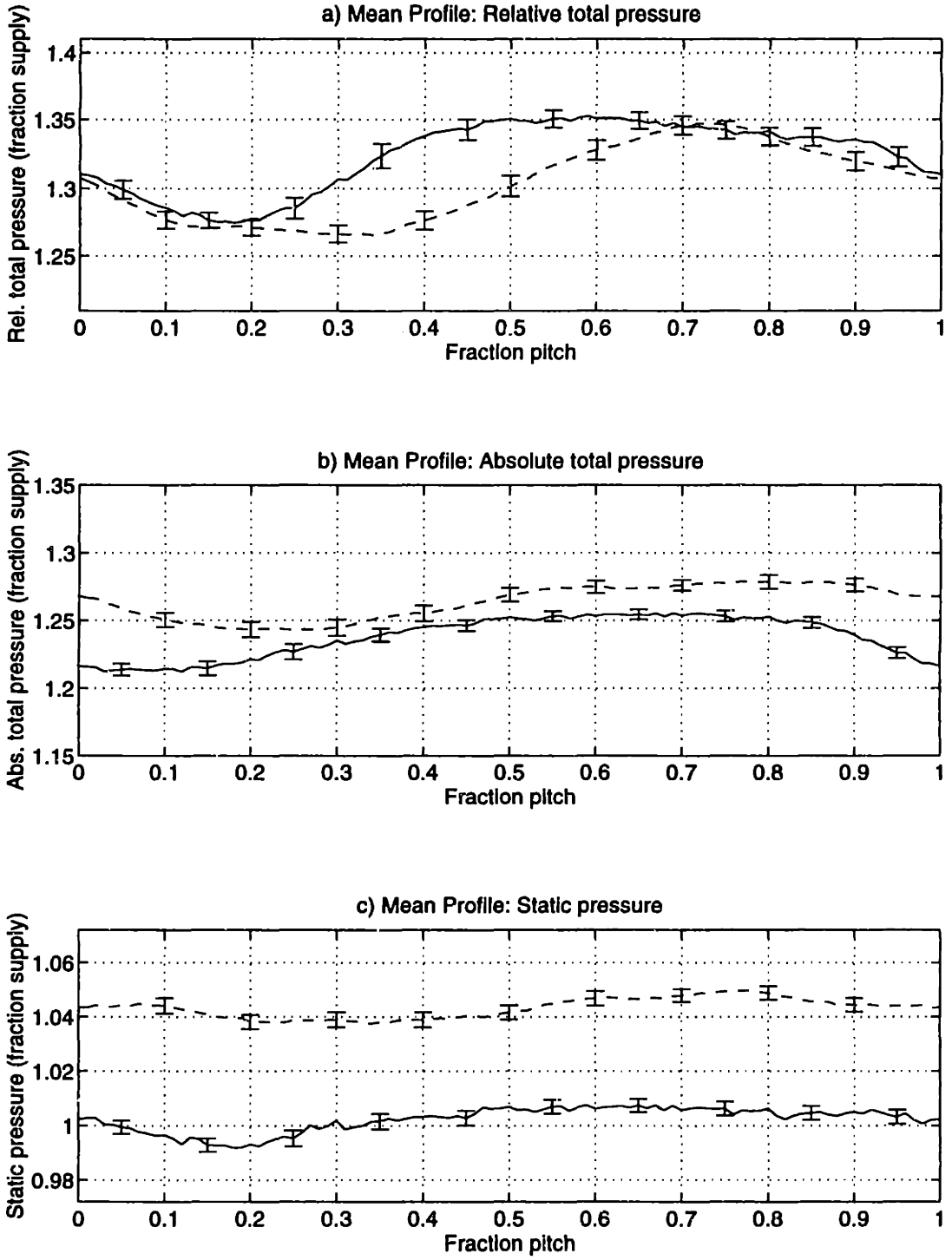

Figure C-24: Pressure component measurements at 87.5% span, 1.5c: baseline loading (—) and high loading (- -)

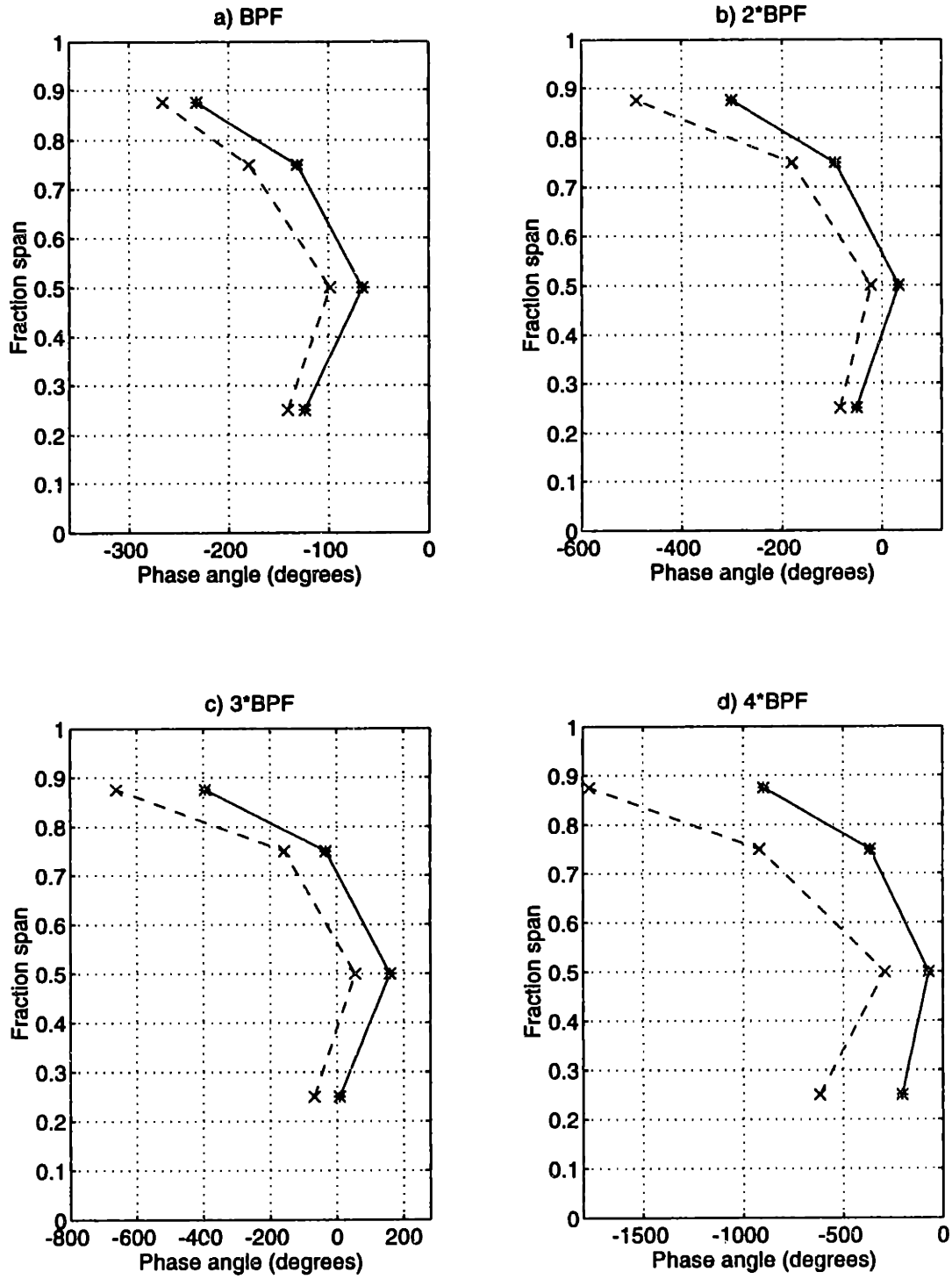

Figure C-25: Relative Mach number wake harmonic phase angles at 1.5 chord: baseline loading (—) and high loading (- -)

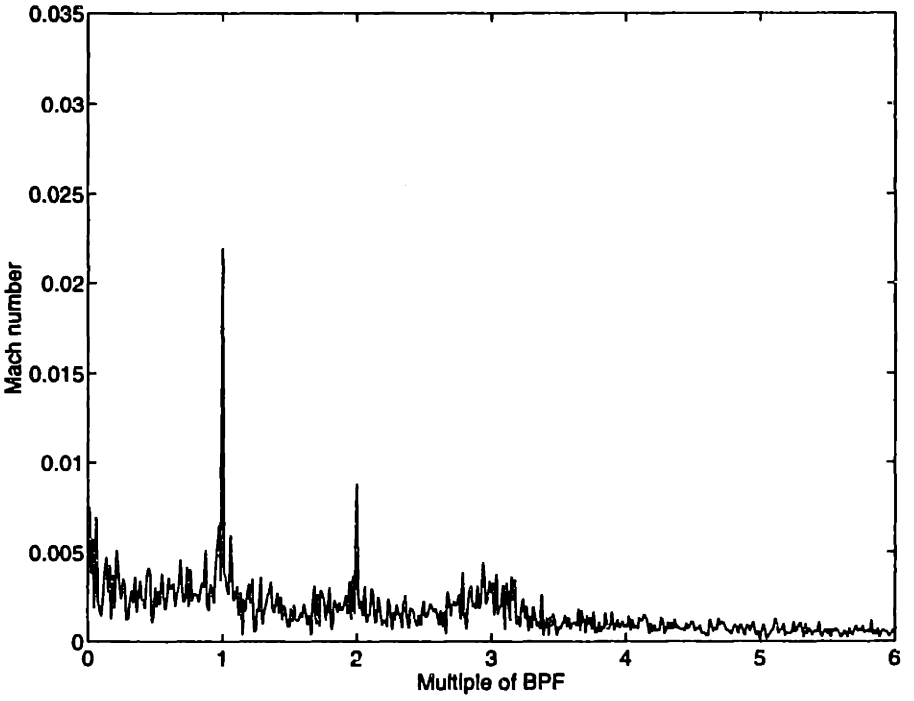

Figure C-26: Relative Mach number spectra at 25% span, 1.5c: high loading (baseline)

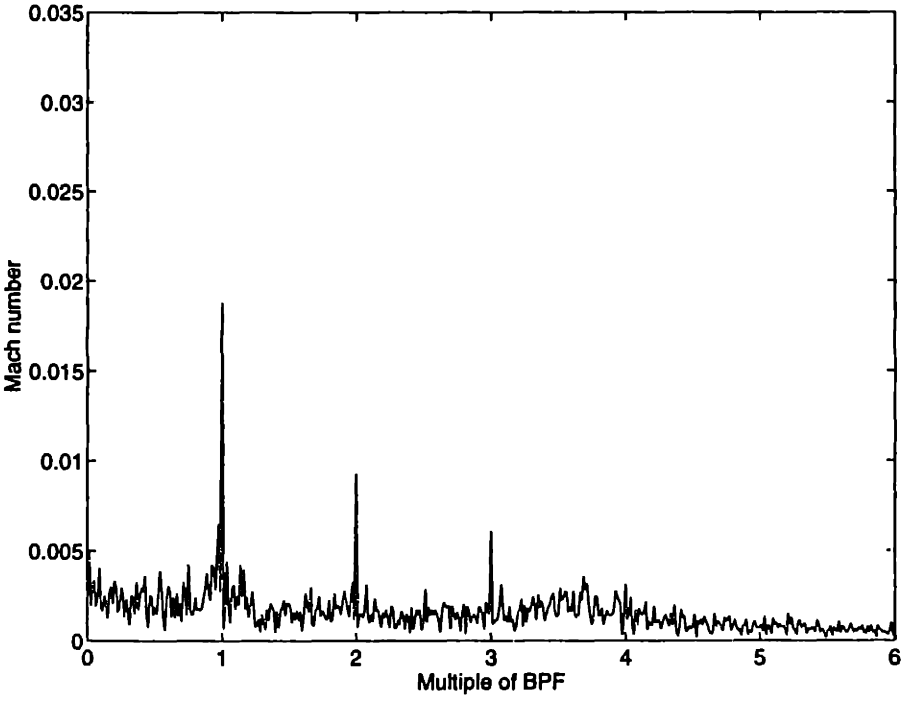

Figure C-27: Relative Mach number spectra at 50% span, 1.5c: high loading (baseline)

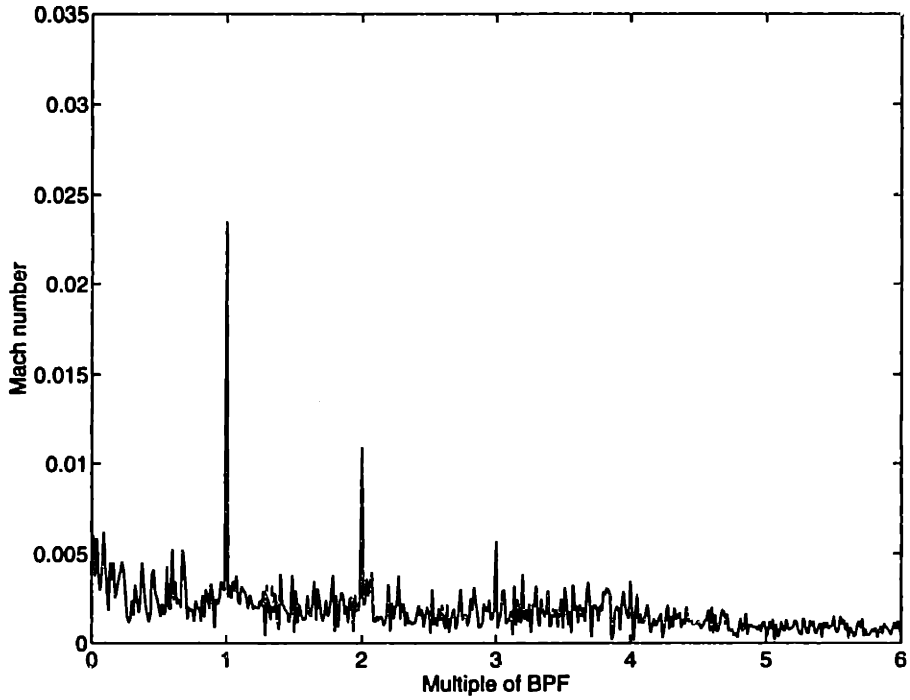

Figure C-28: Relative Mach number spectra at 75% span, 1.5c: high loading (baseline)

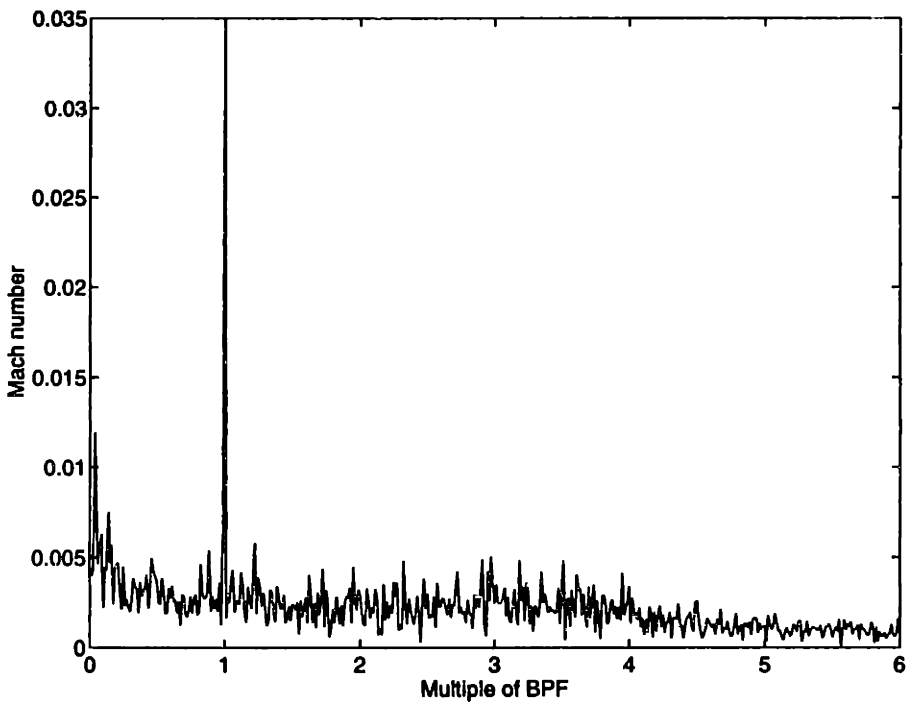

Figure C-29: Relative Mach number spectra at 87.5% span, 1.5c: high loading (baseline)

Appendix D

Wake Management Fan Stage: Drawings

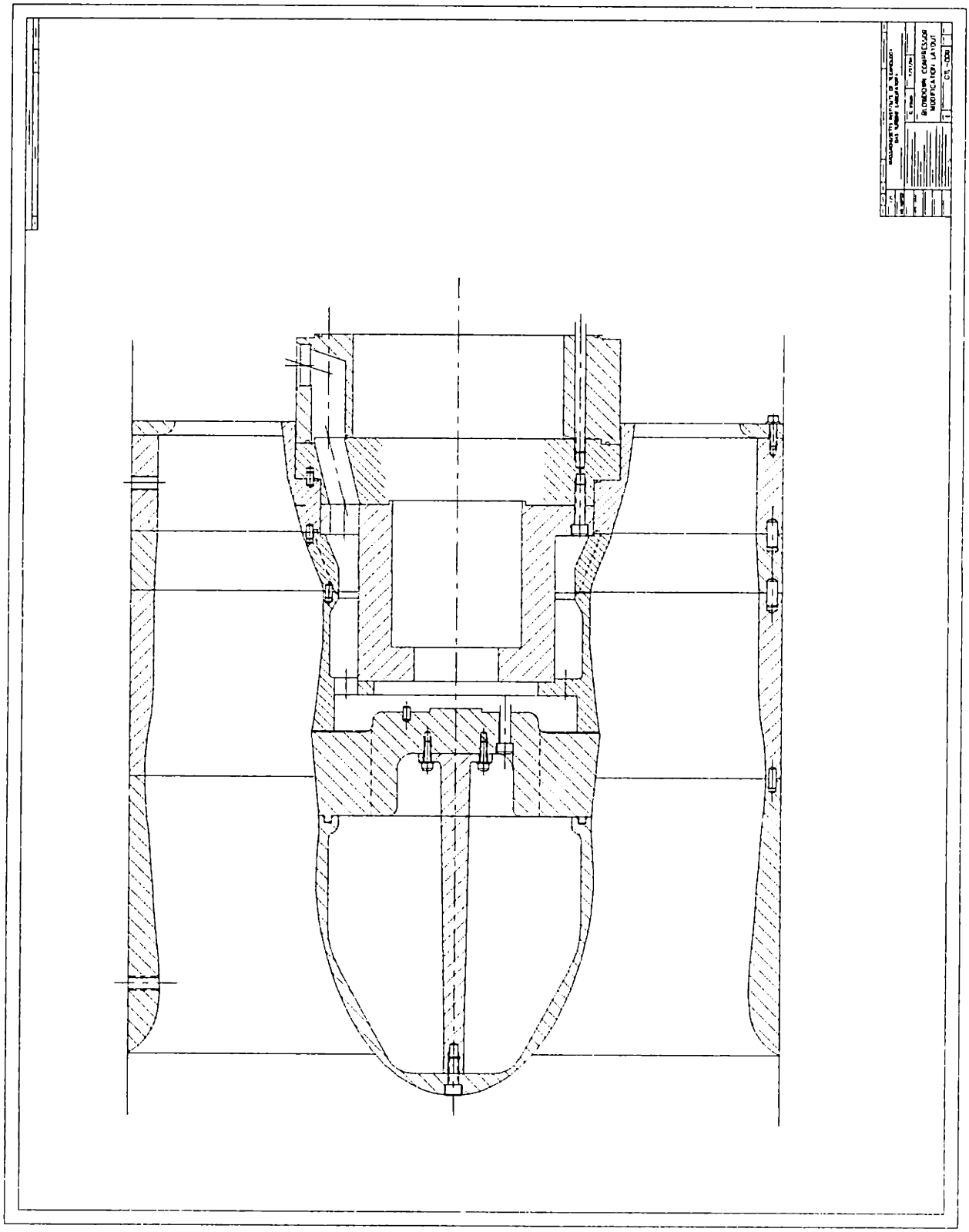

Figure D-1: Fan stage drawing (GTL-000): layout drawing

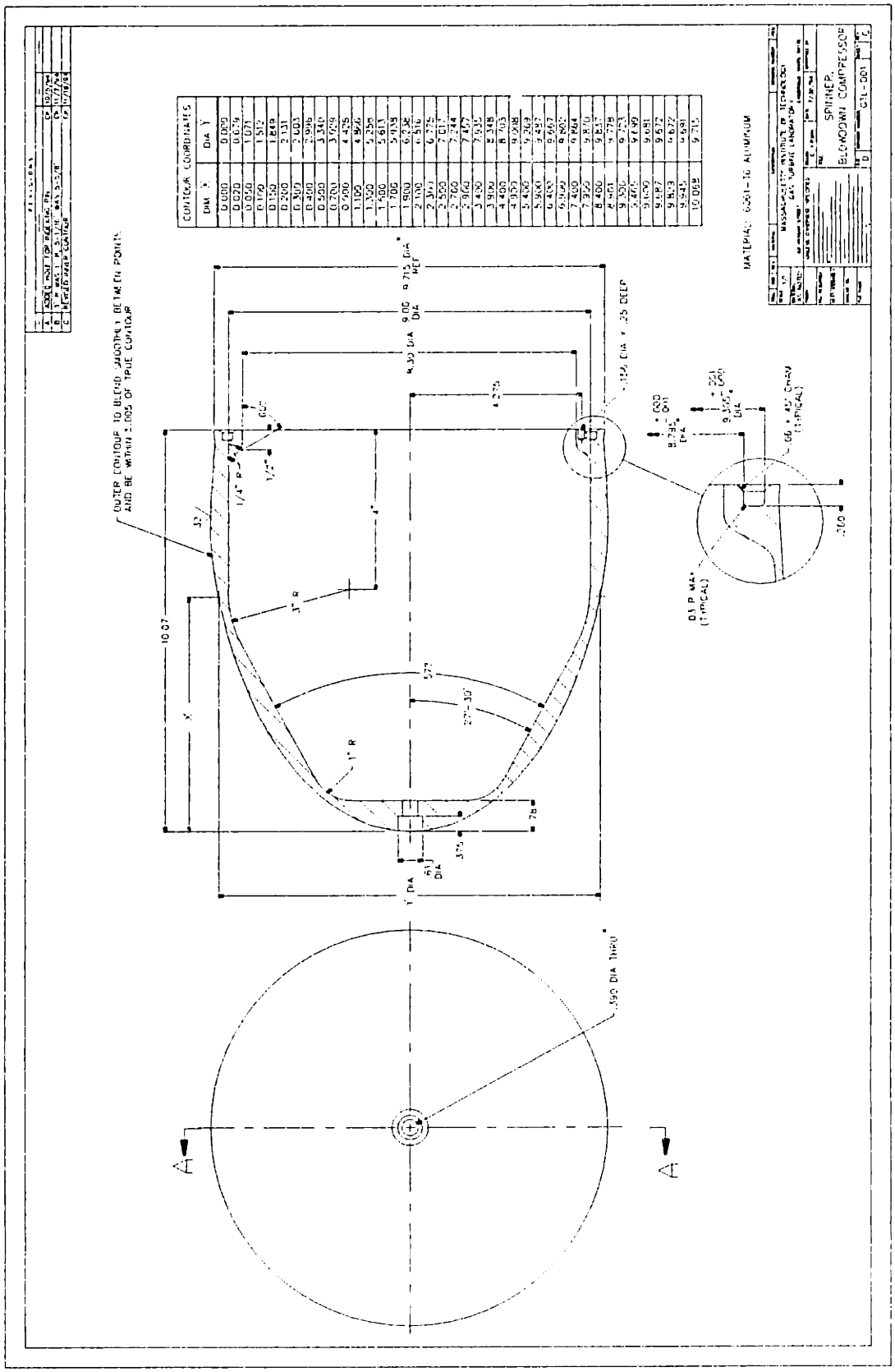

Figure D-2: Fan stage drawing (GTL-001): spinner

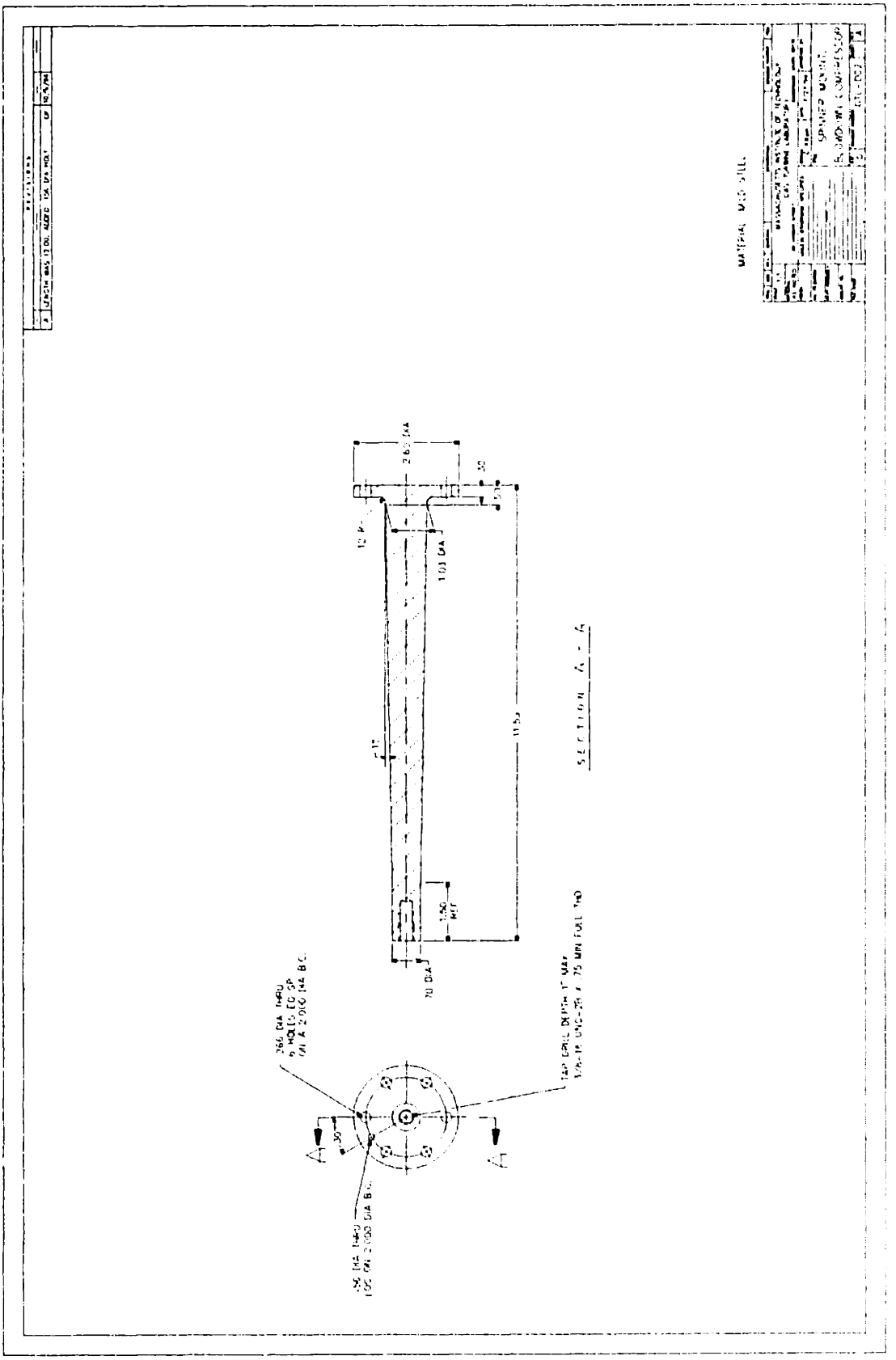

Figure D-3: Fan stage drawing (GTL-002): spinner mount

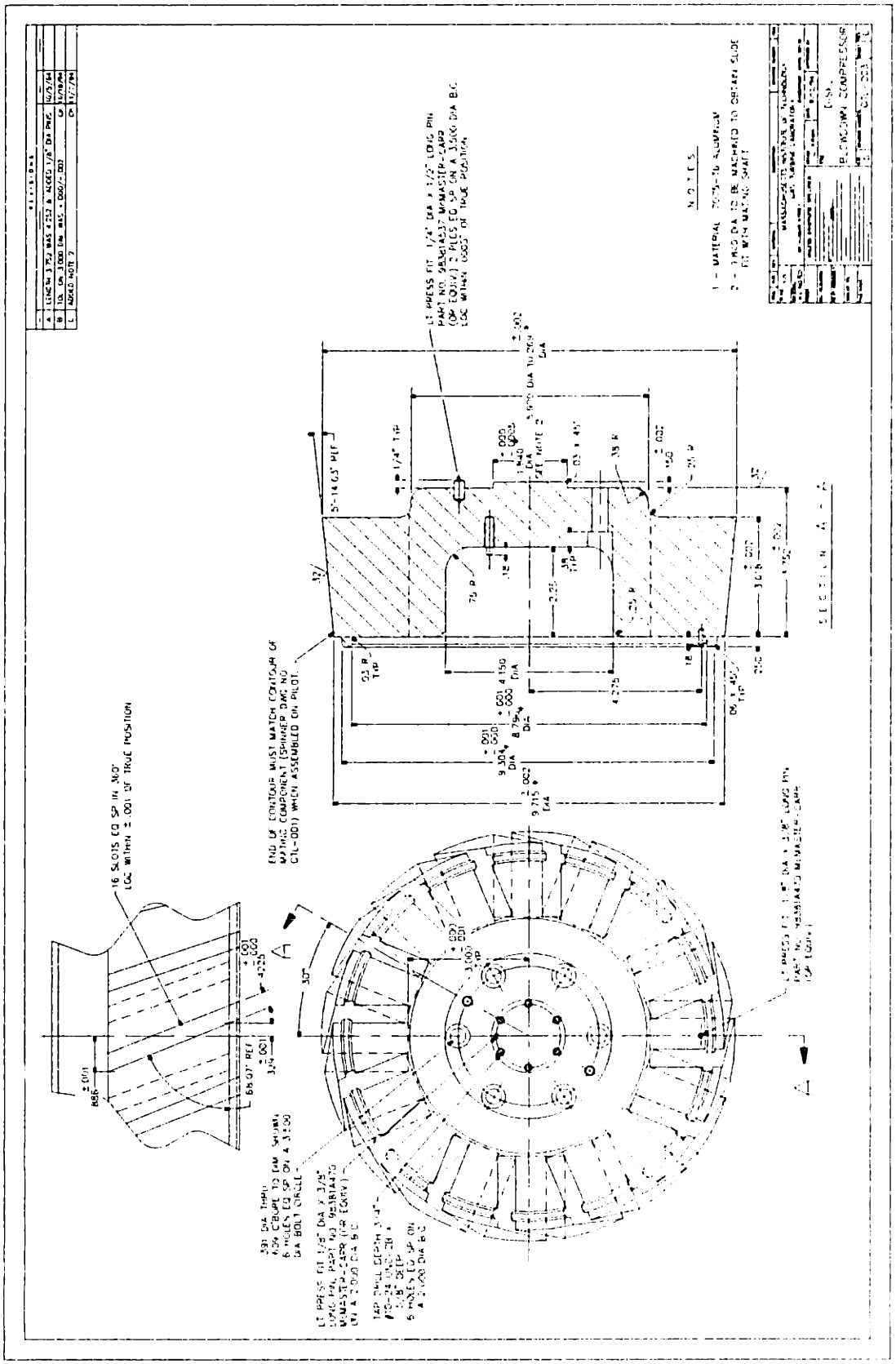

Figure D-4: Fan stage drawing (GTL-003): rotor disk (baseline)

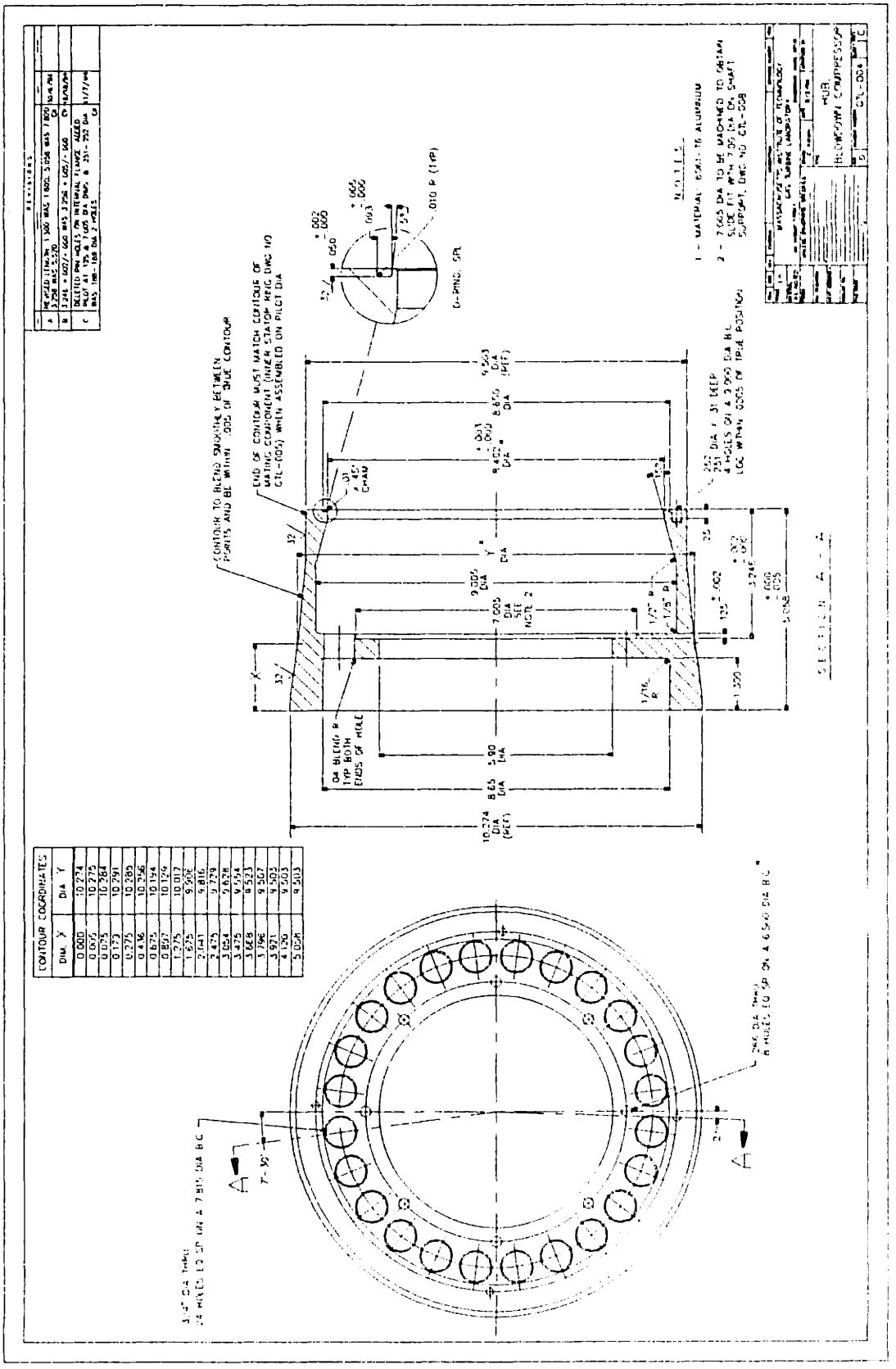

Figure D-5: Fan stage drawing (GTL-004): midstage hub section

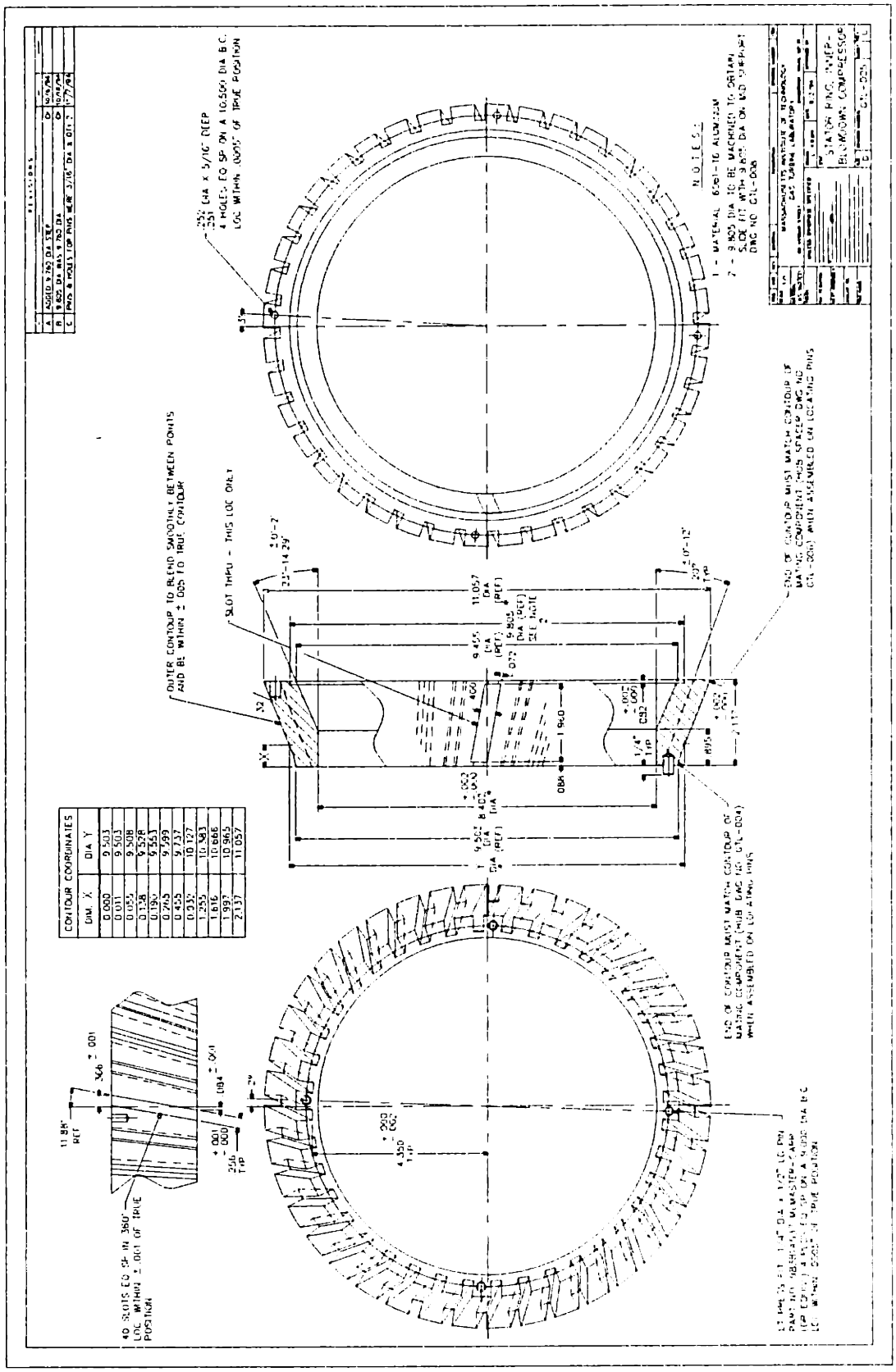

Figure D-6: Fan stage drawing (GTL-005): stator hub ring

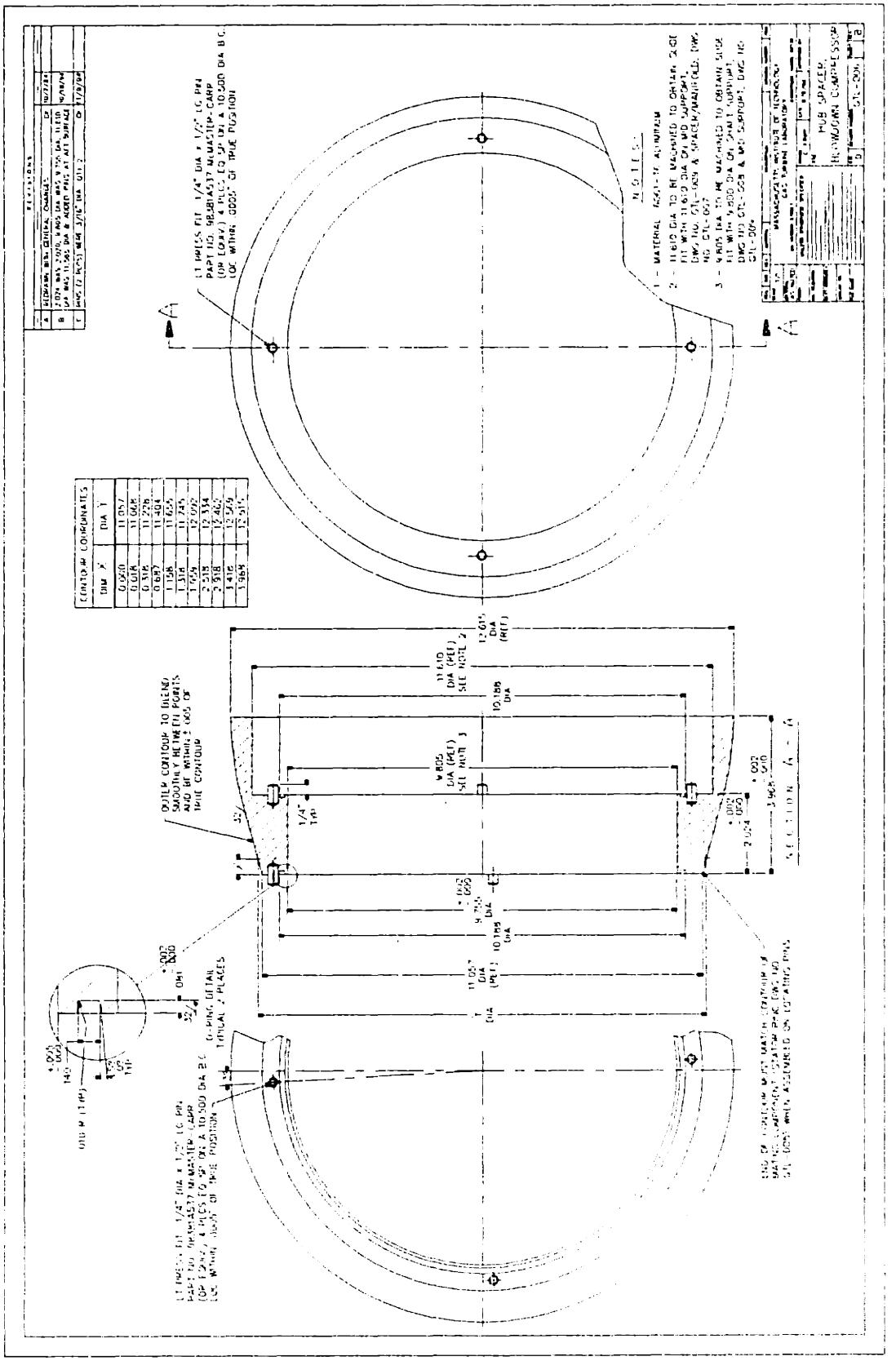

Figure D-7: Fan stage drawing (GTL-006): downstream hub section

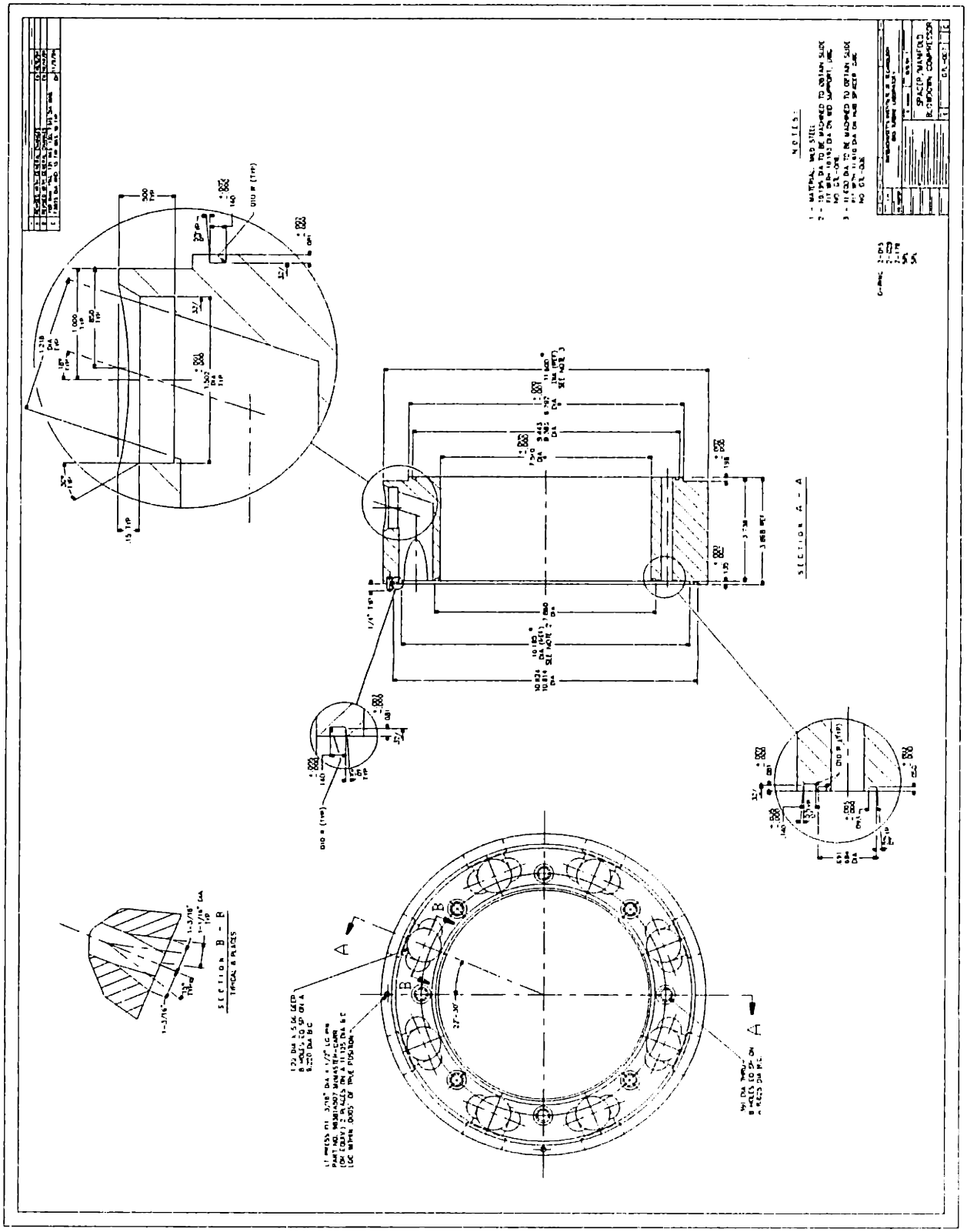

Figure D-8: Fan stage drawing (GTL-007): wake management manifold

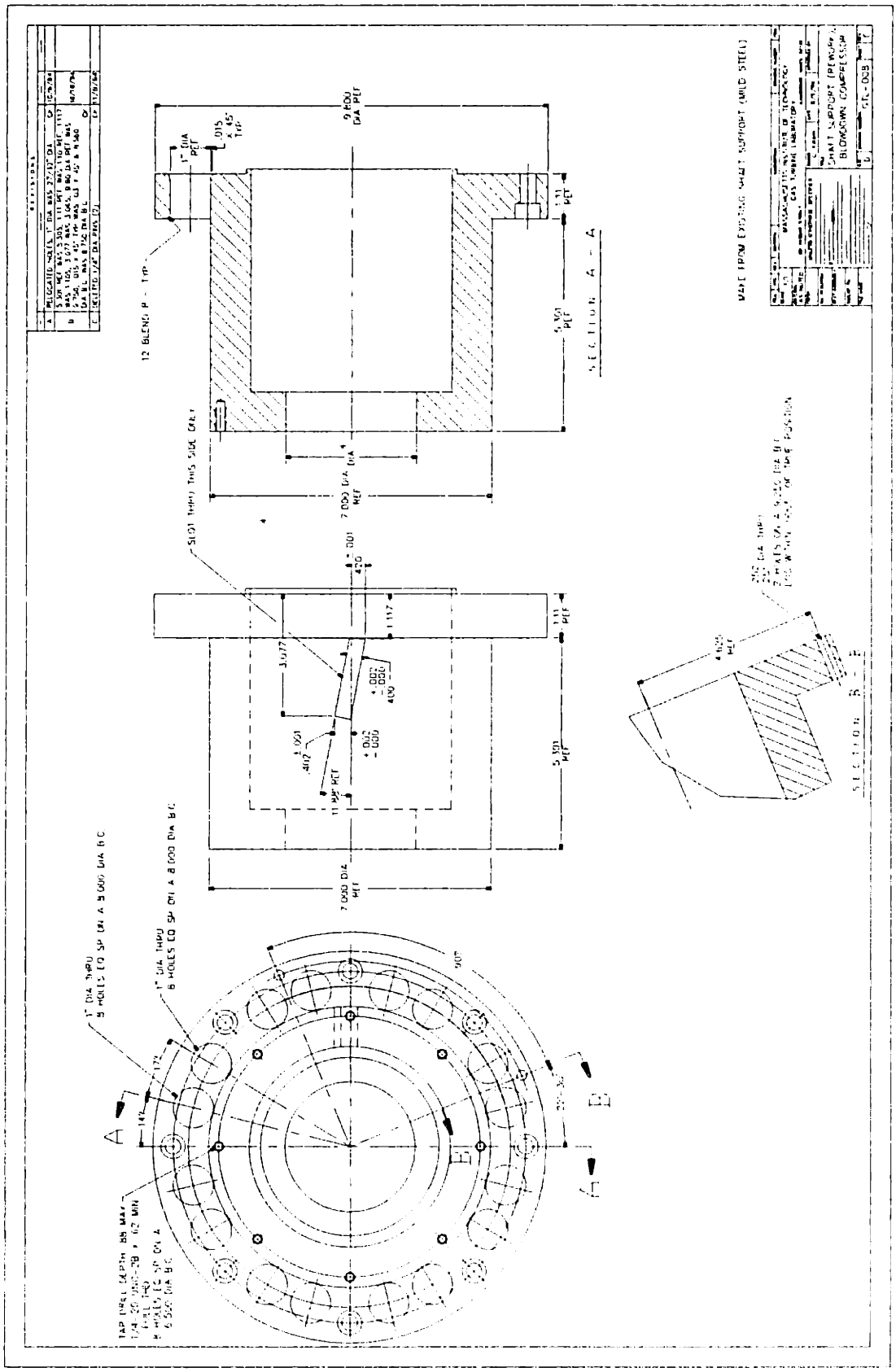

Figure D-9: Fan stage drawing (GTL-008): modification to front bearing housing

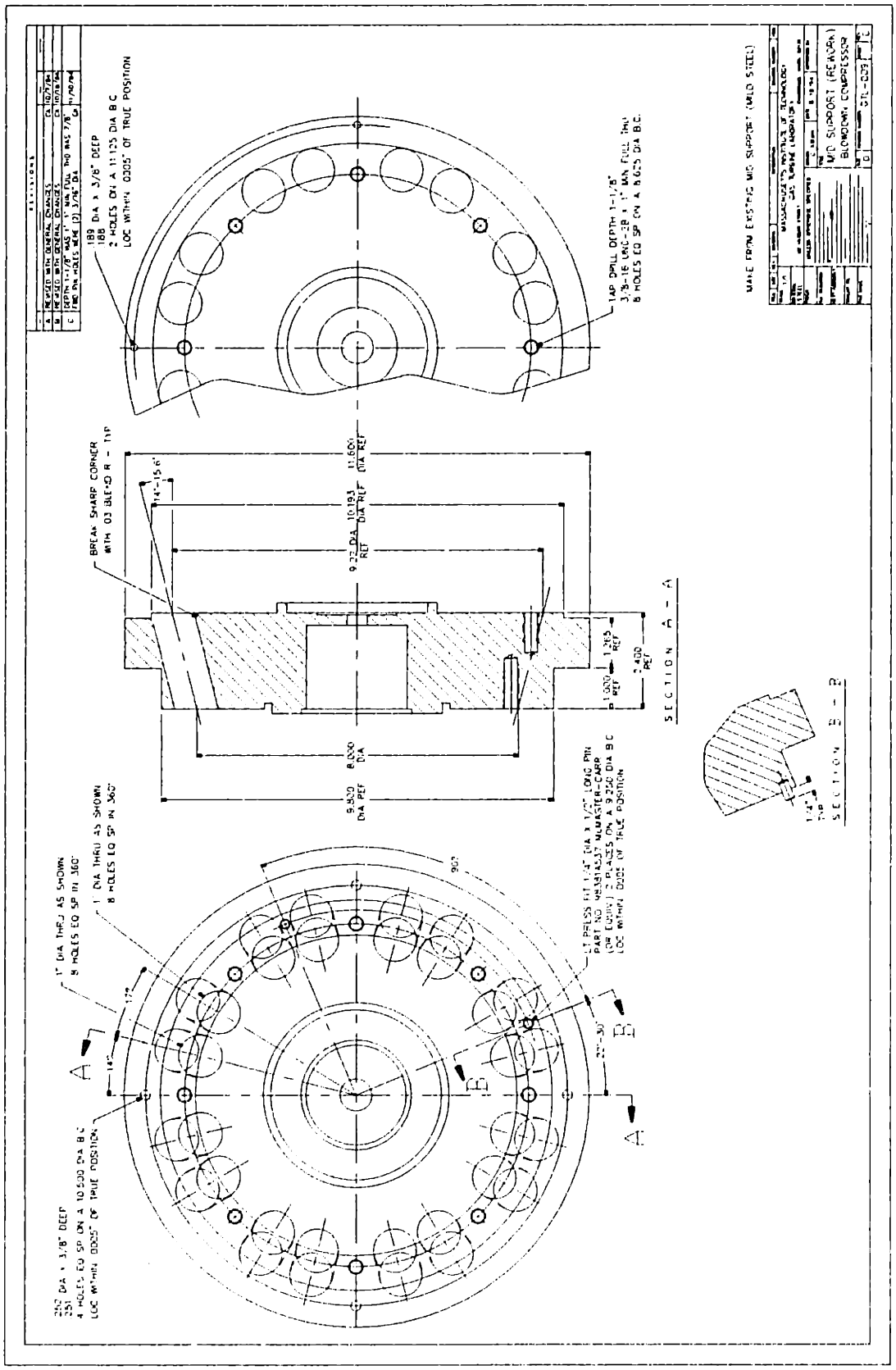

Figure D-10: Fan stage drawing (GTL-009): modification to rear bearing housing

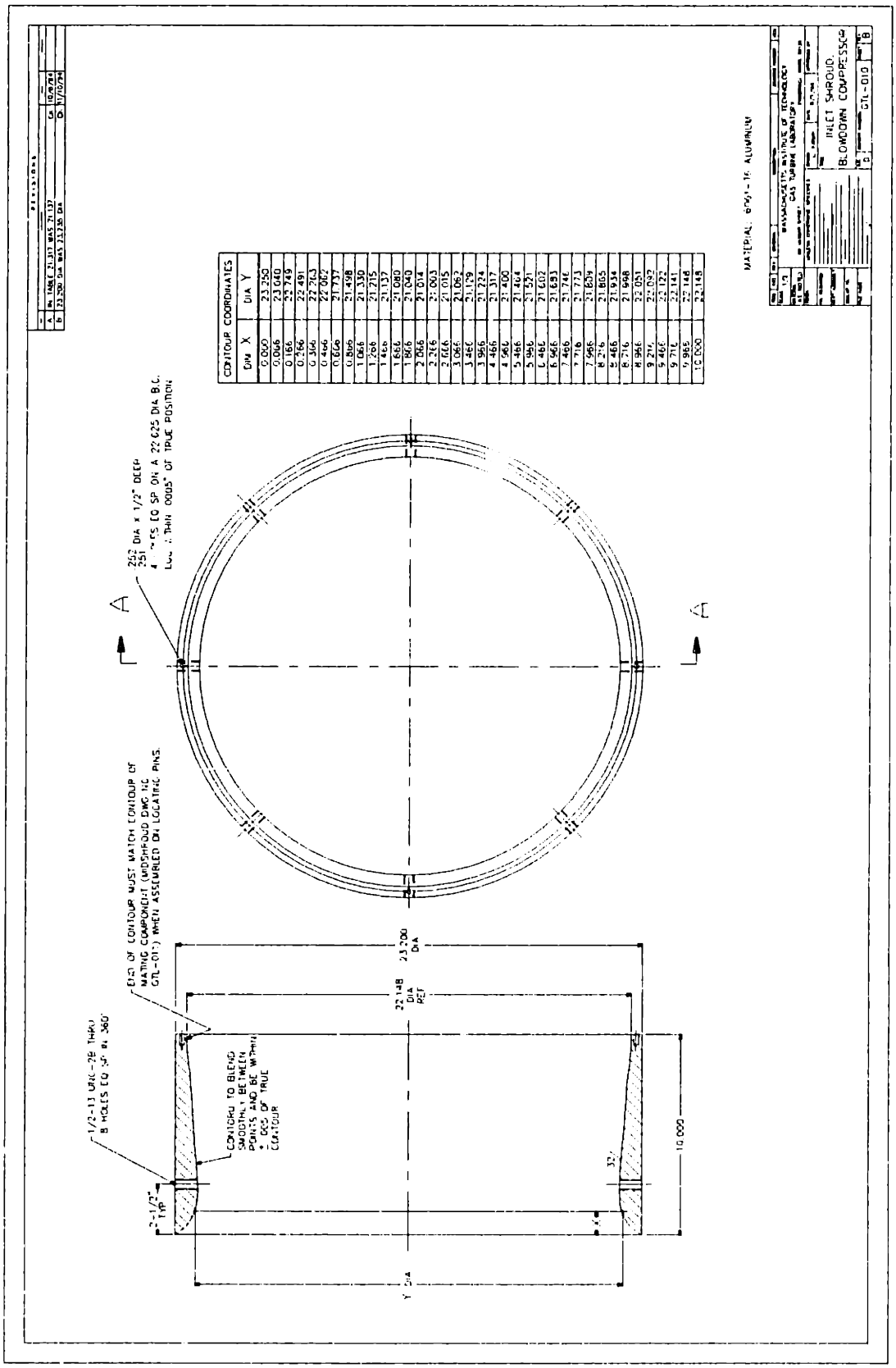

Figure D-11: Fan stage drawing (GTL-010): inlet shroud section

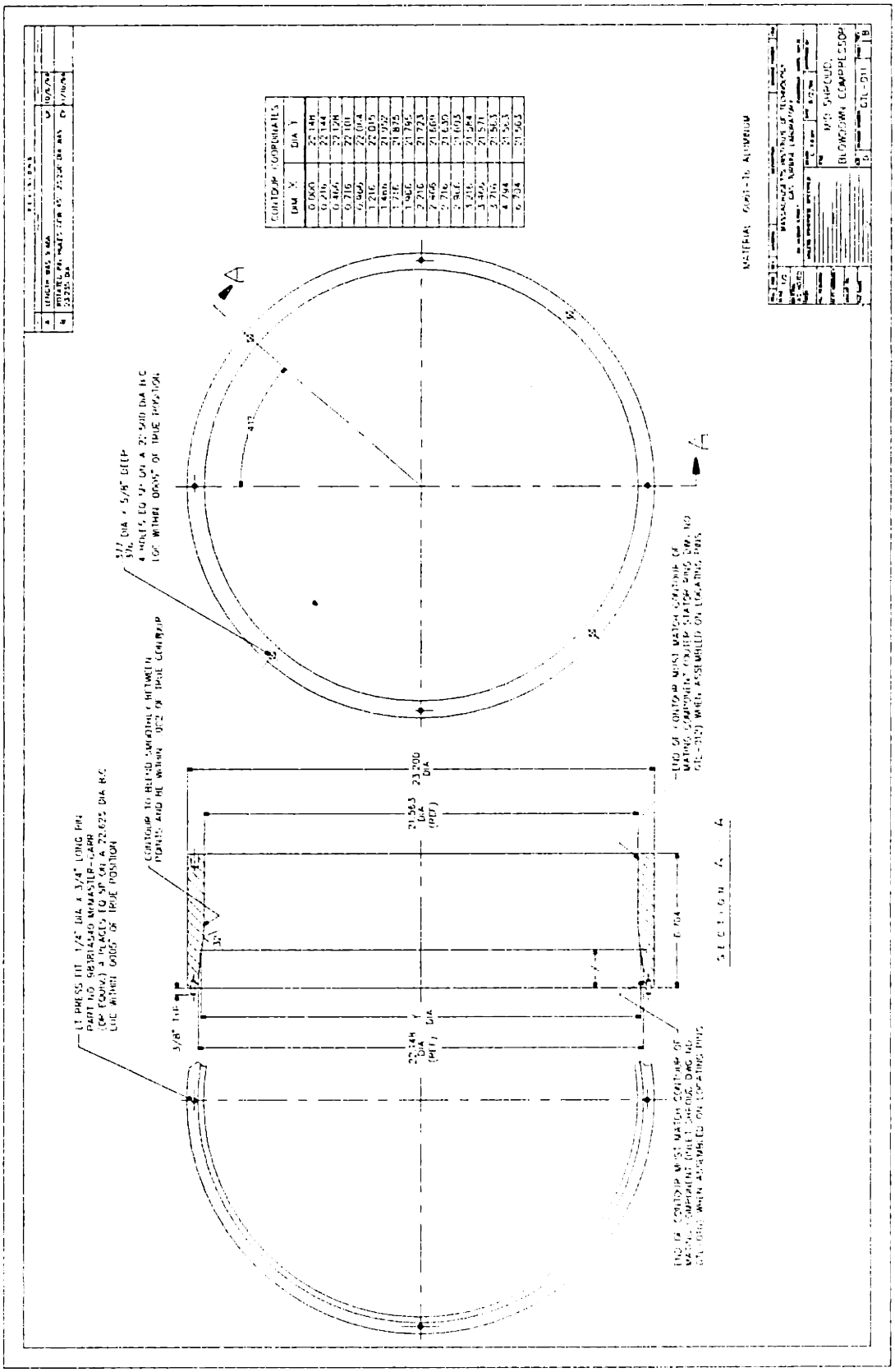

Figure D-12: Fan stage drawing (GTL-911): midstage shroud section

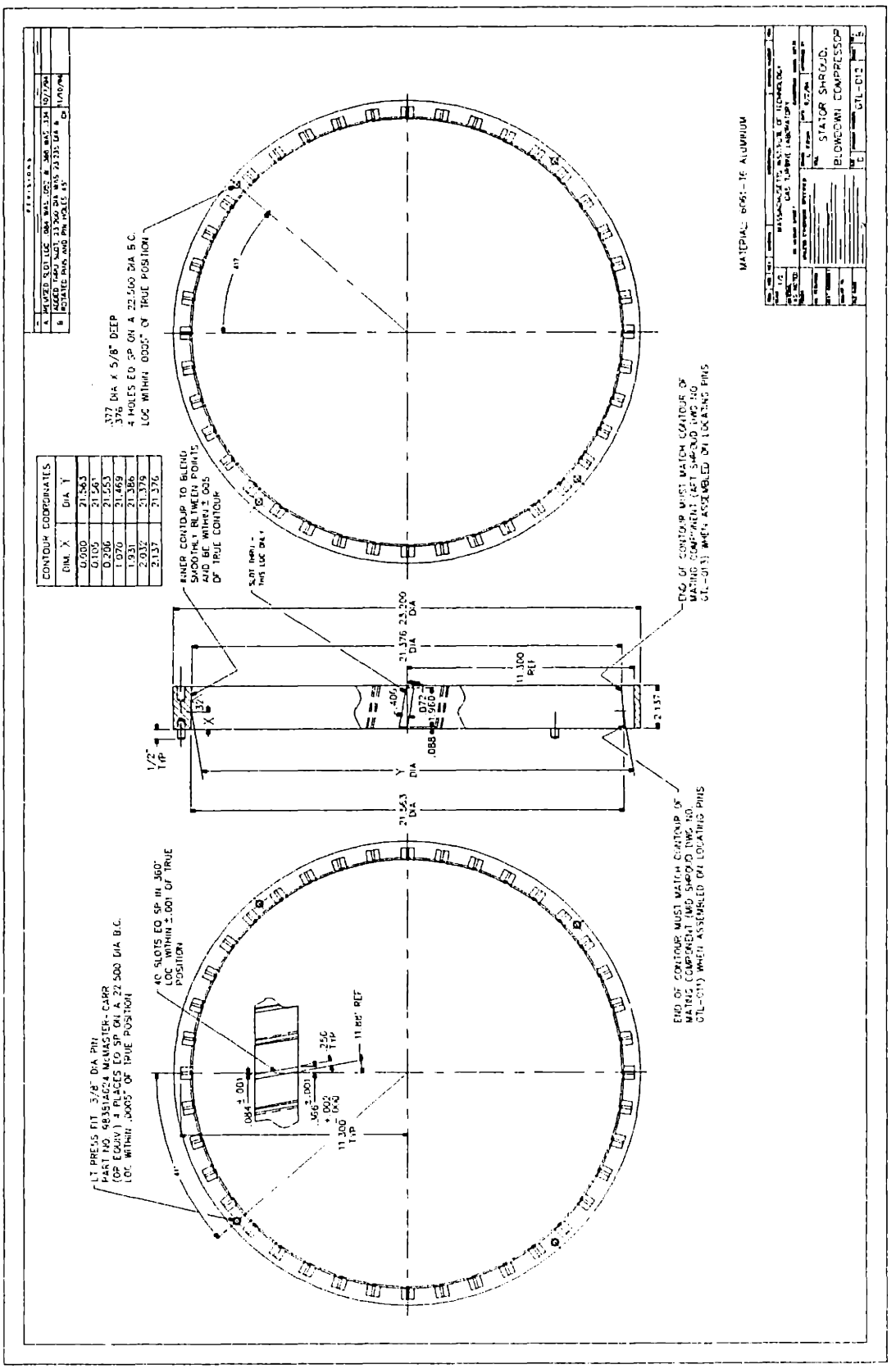

Figure D-13: Fan stage drawing (GTL-012): stator shroud ring

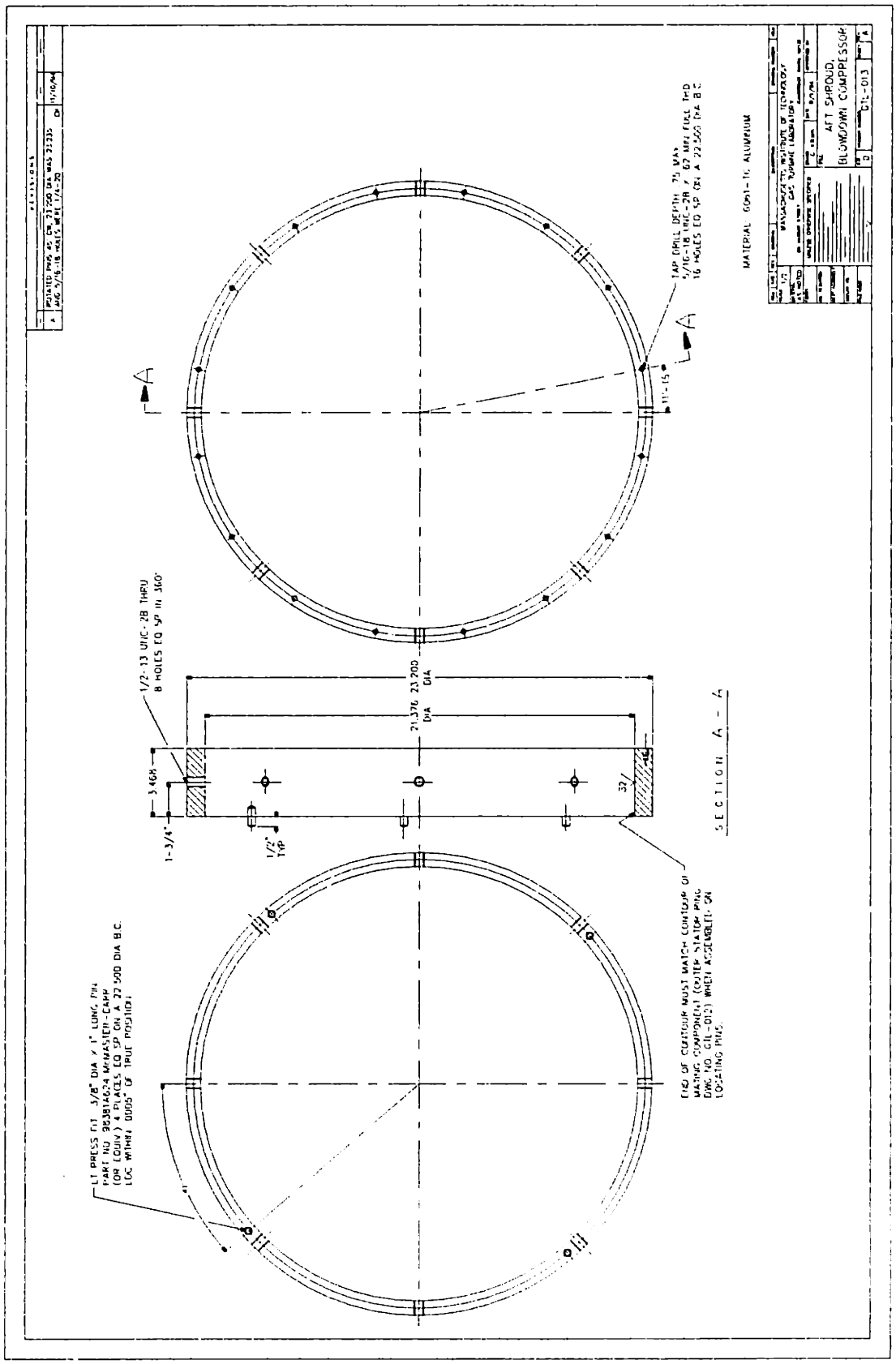

Figure D-14: Fan stage drawing (GTL-013): downstream shroud section

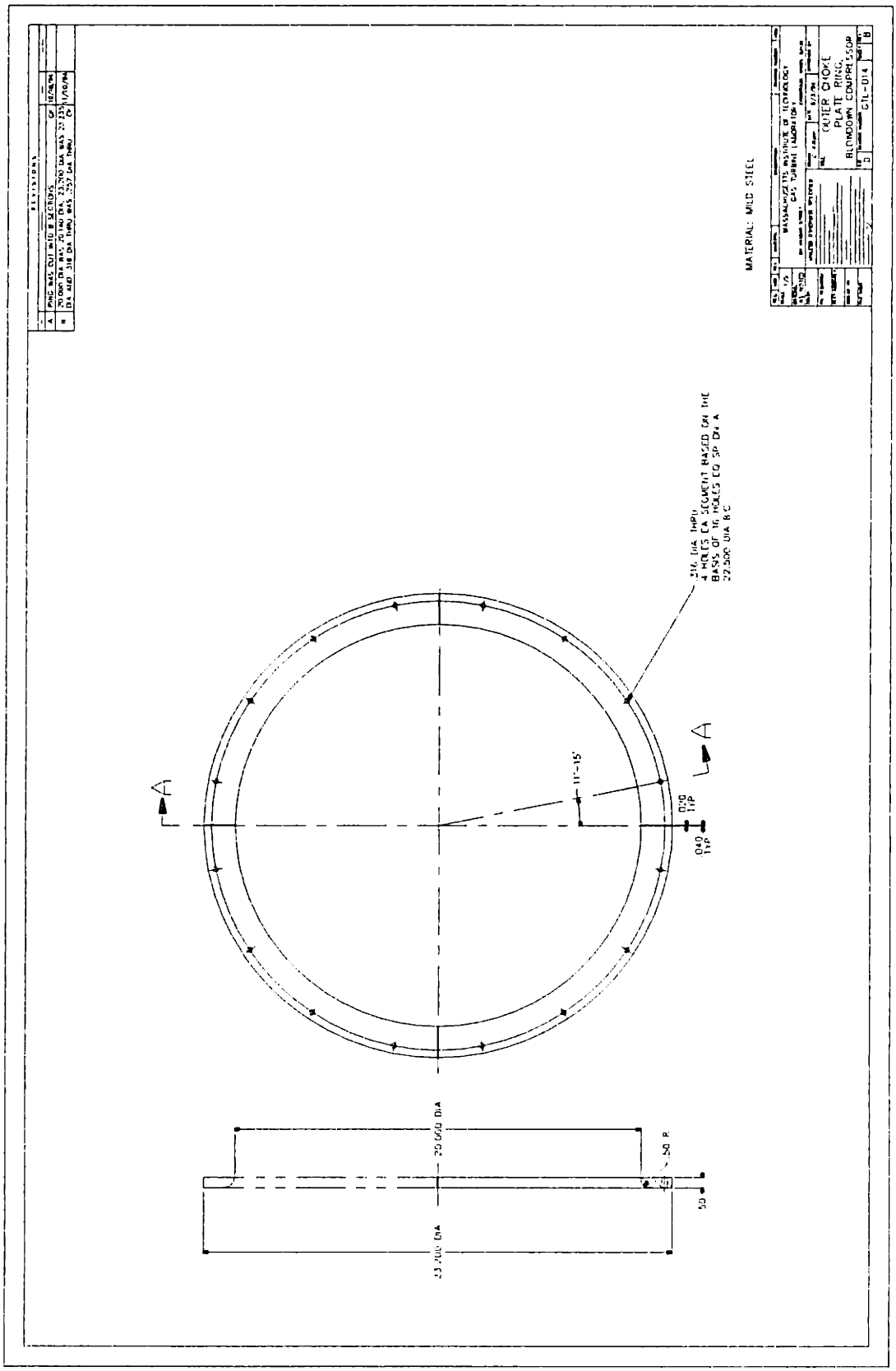

Figure D-15: Fan stage drawing (GTL-014): choke plate (baseline)

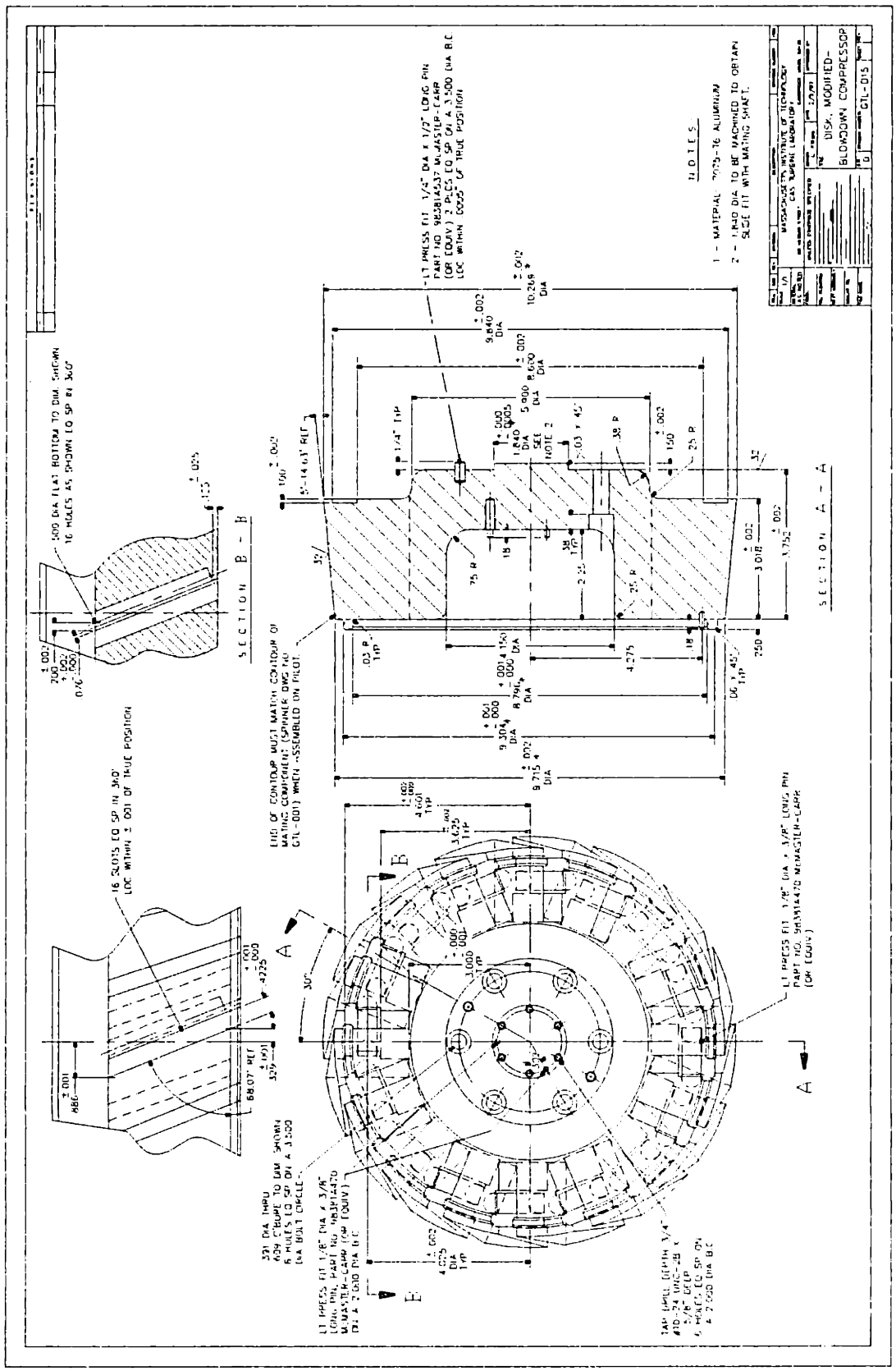

Figure D-16: Fan stage drawing (GTL-015): rotor disk (trailing edge blowing)

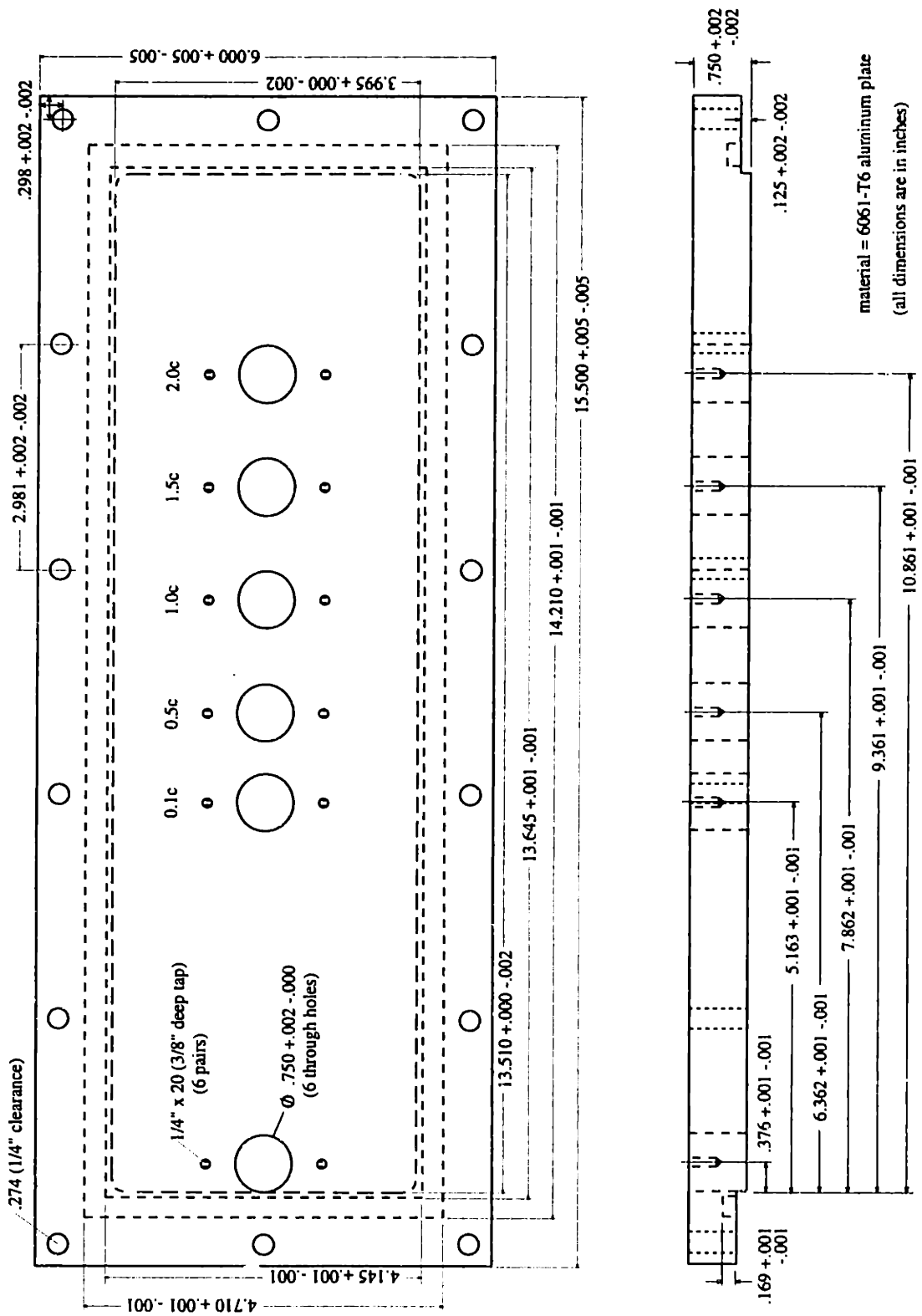

Figure D-17: Instrumentation window for flow field measurements with total pressure and 4 way probe ports

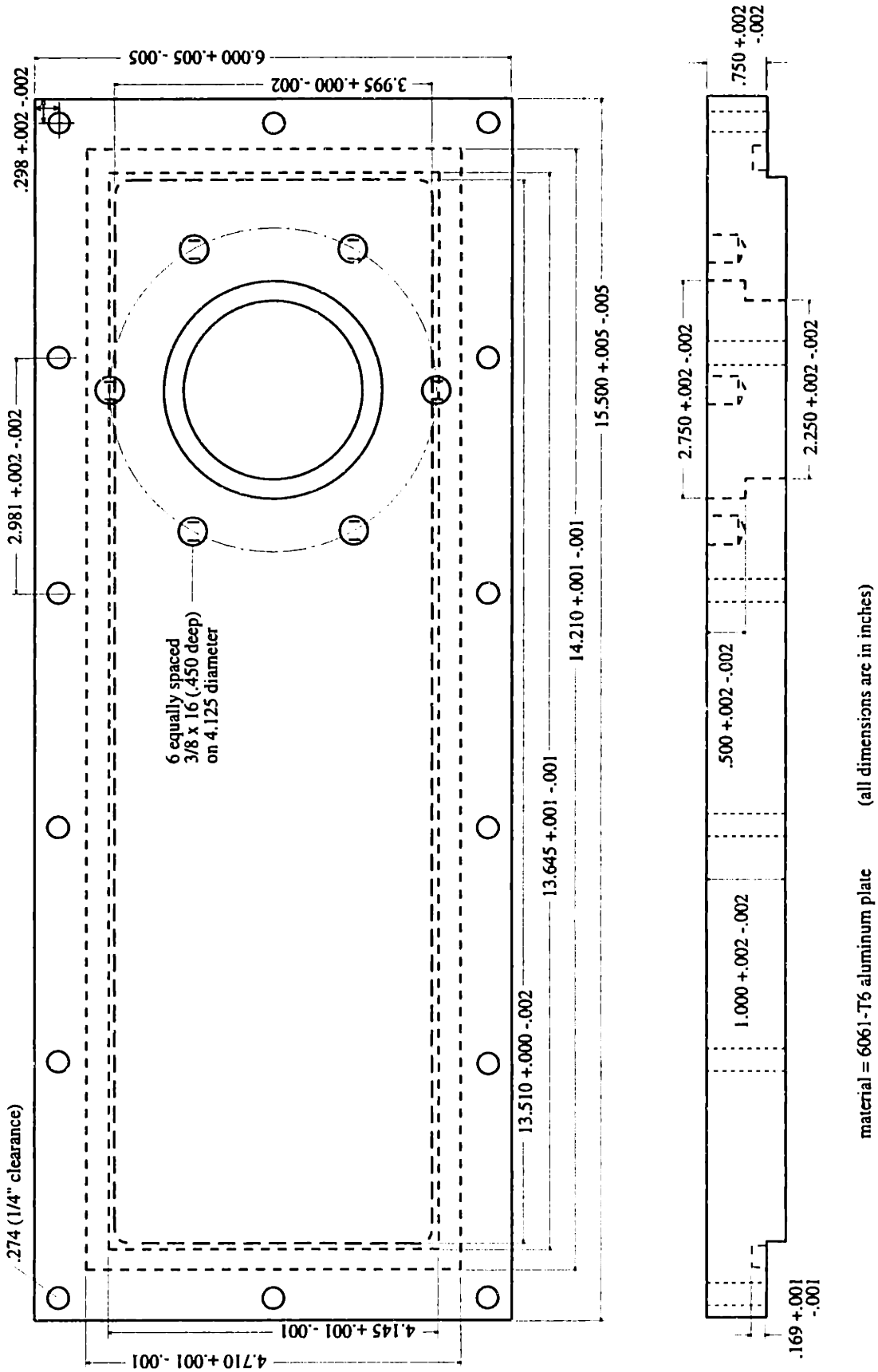

Figure D-18: Instrumentation window for unsteady stator pressure measurements

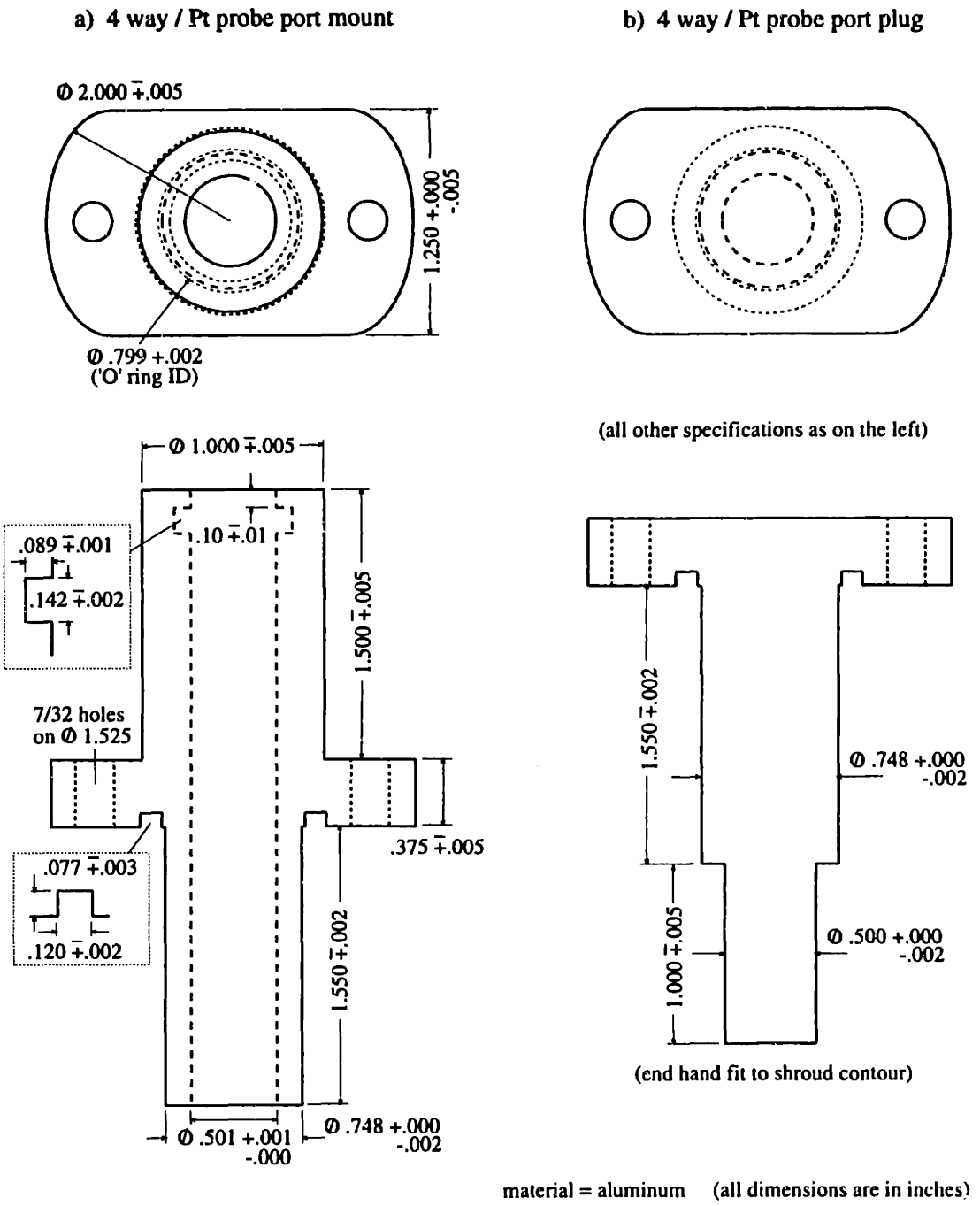

Figure D-19: 4-way and total pressure probe mounts and plugs for use on instrumentation window

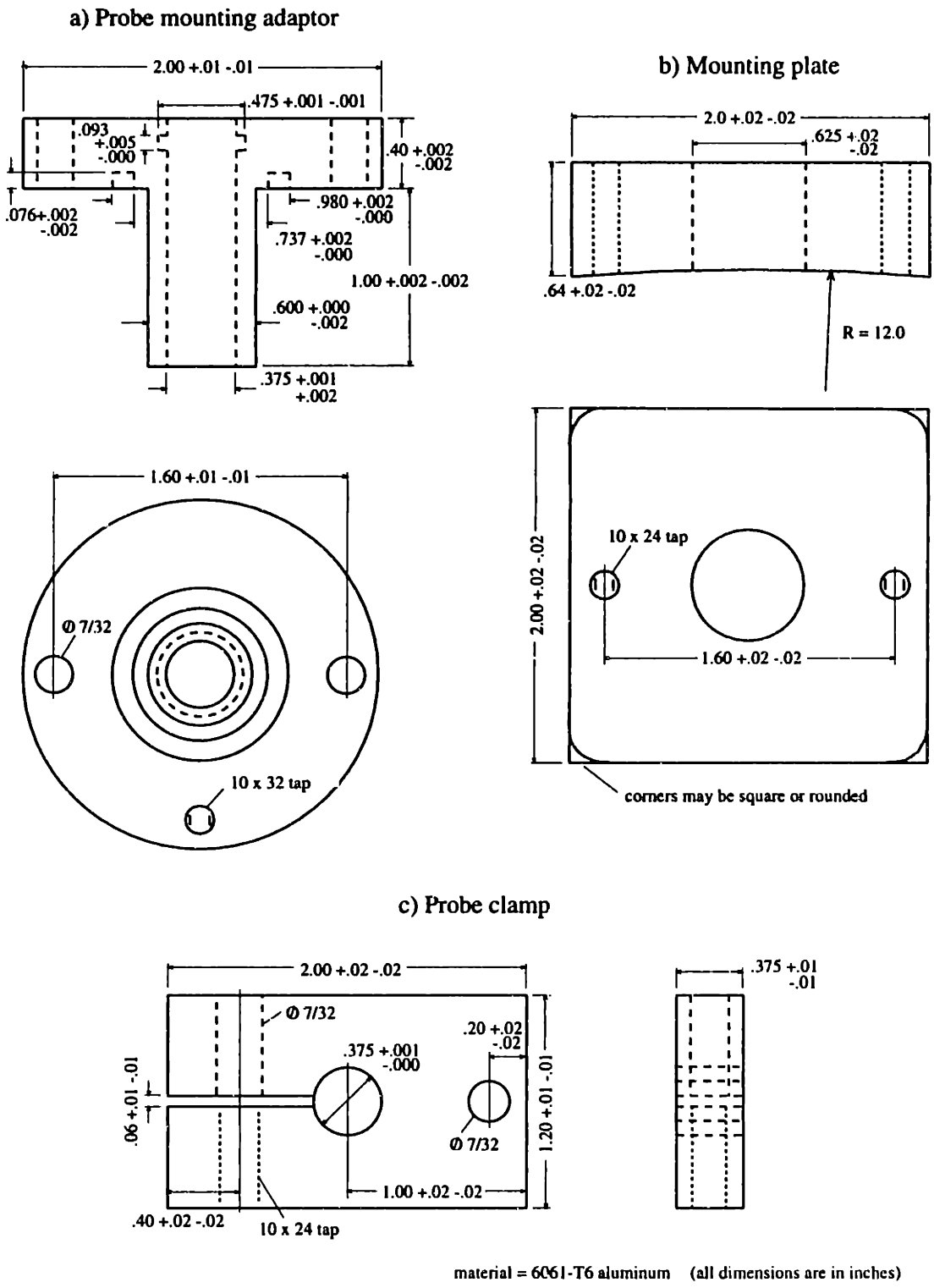

Figure D-20: Mounting hardware for microphones and wall static pressure probes

a) Graphite seal support ring

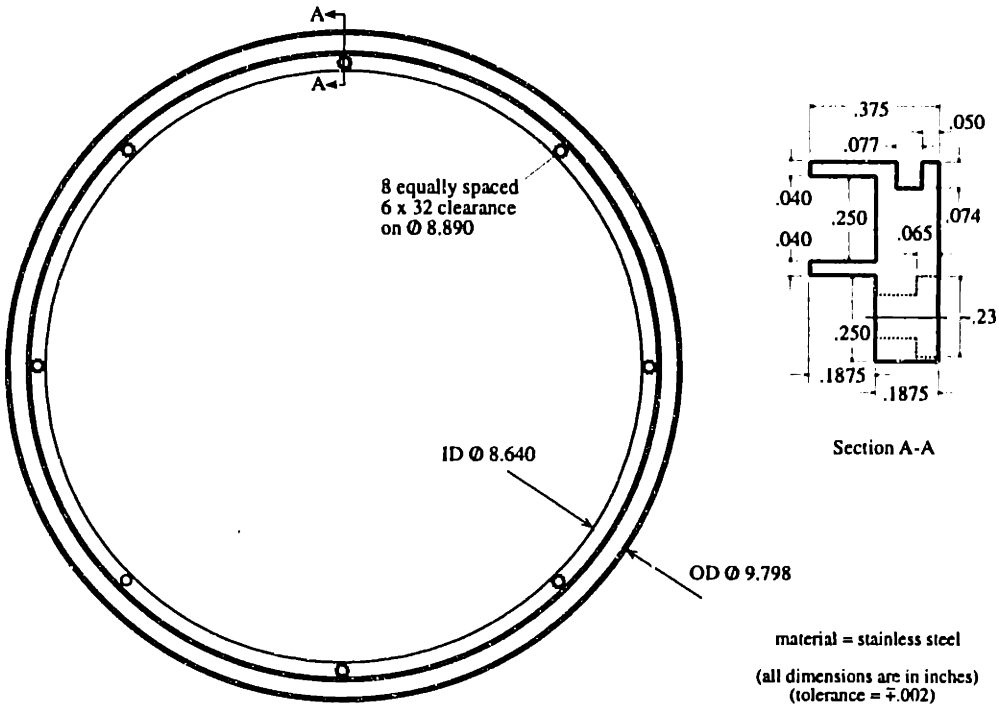

b) Graphite seal ring

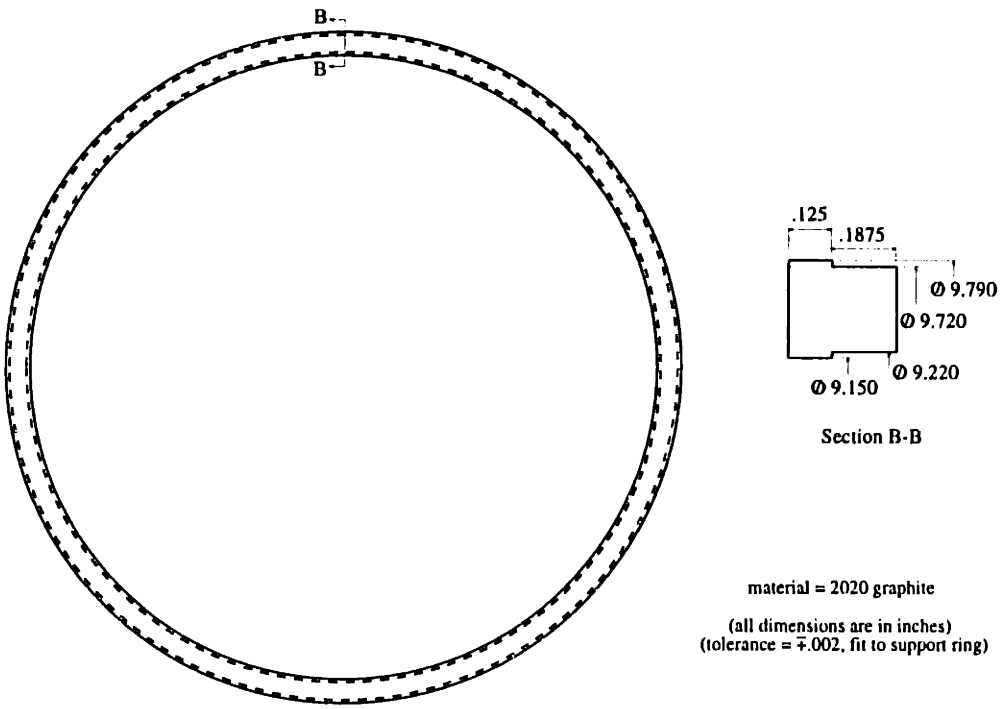

Figure D-21: Hub graphite face seal: stainless steel support and graphite rings

a) Graphite seal actuators

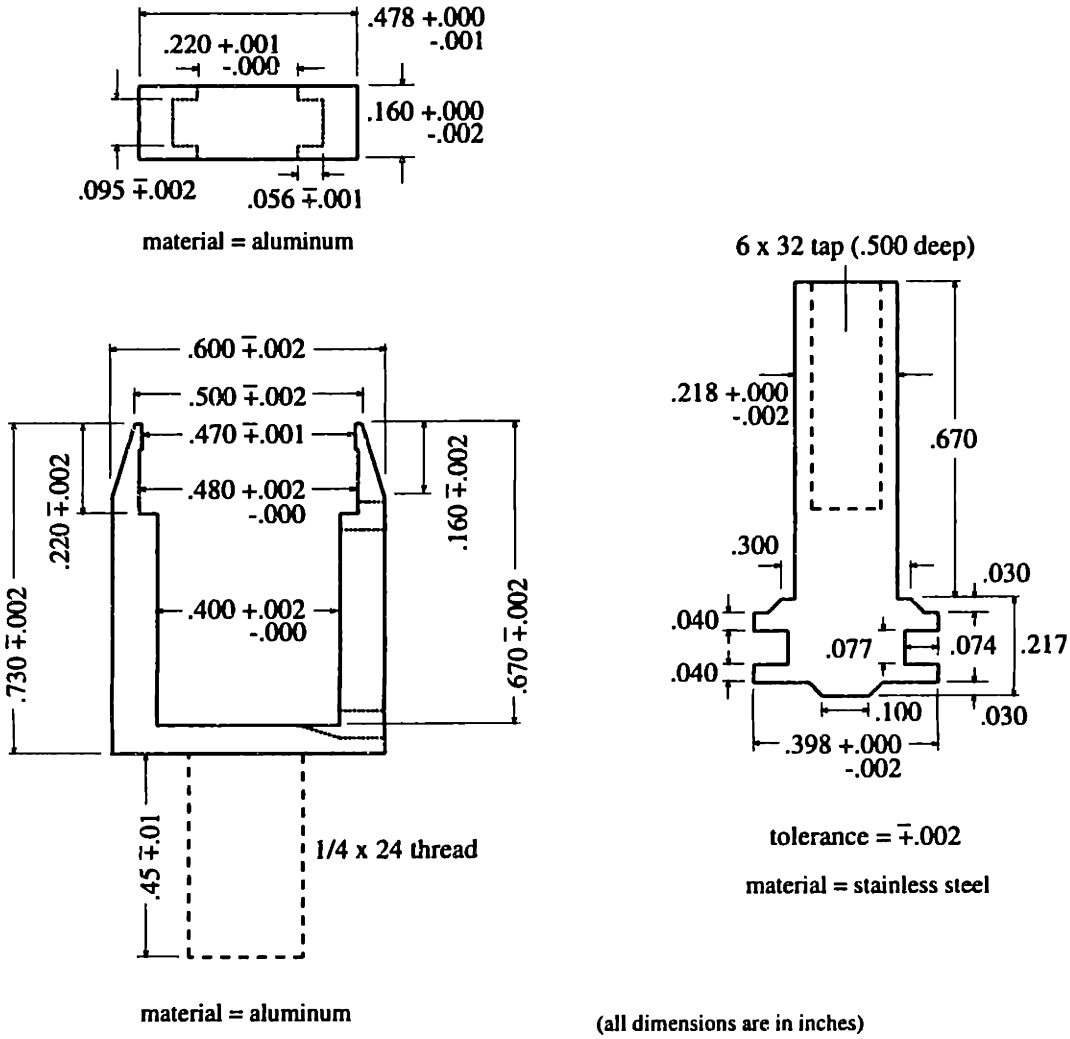

(all dimensions are in inches)

b) Hub modification (GTL-004)

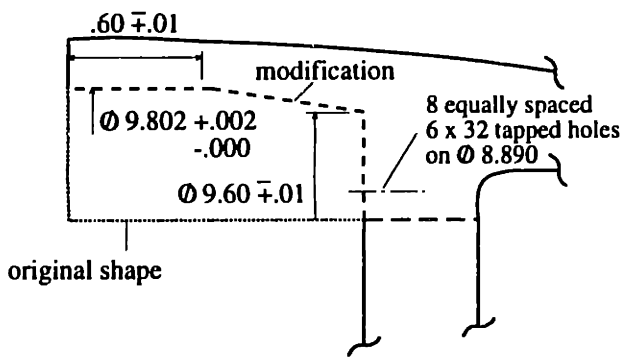

Figure D-22: Hub graphite face seal: actuators (8)

a) Ring for graphite face seal

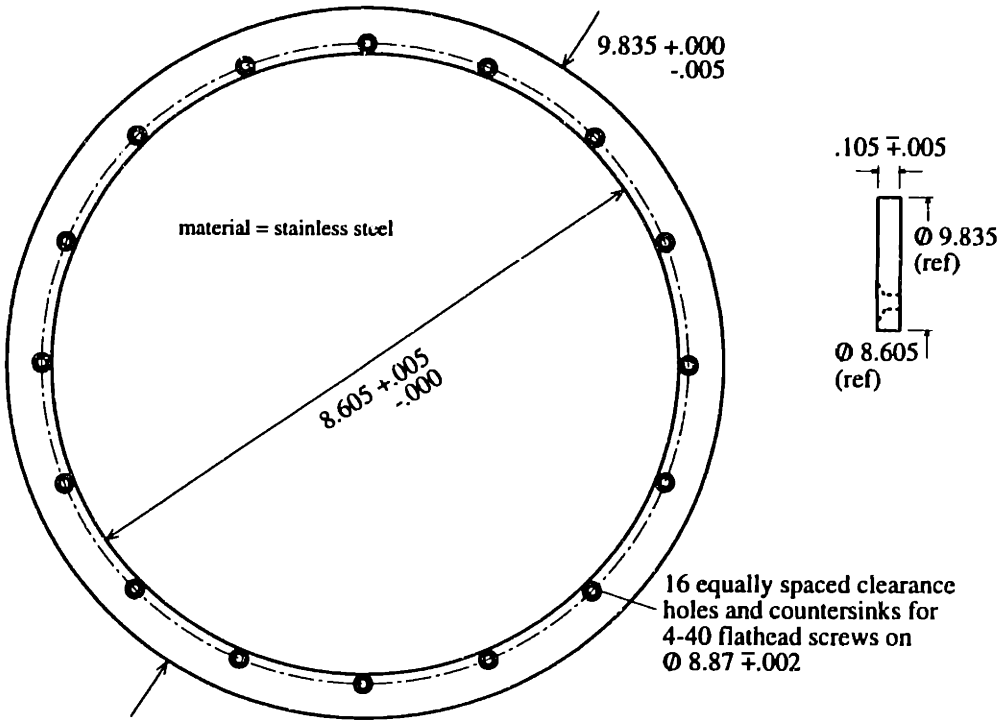

(all dimensions are in inches)

b) Balancing rings

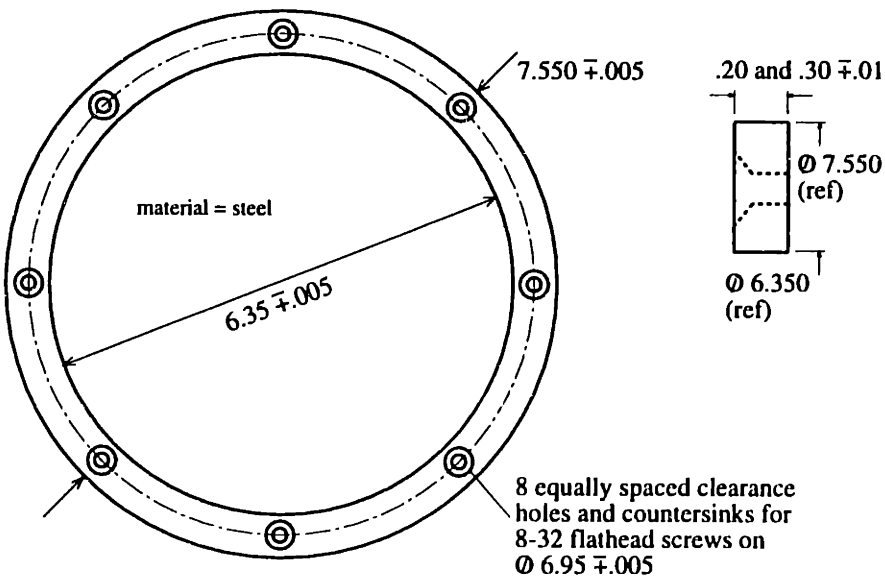

Figure D-23: Steel rings for wake management rotor: 1) stainless steel ring for graphite seal seat, 2) blade containment and balancing rings (for and aft)

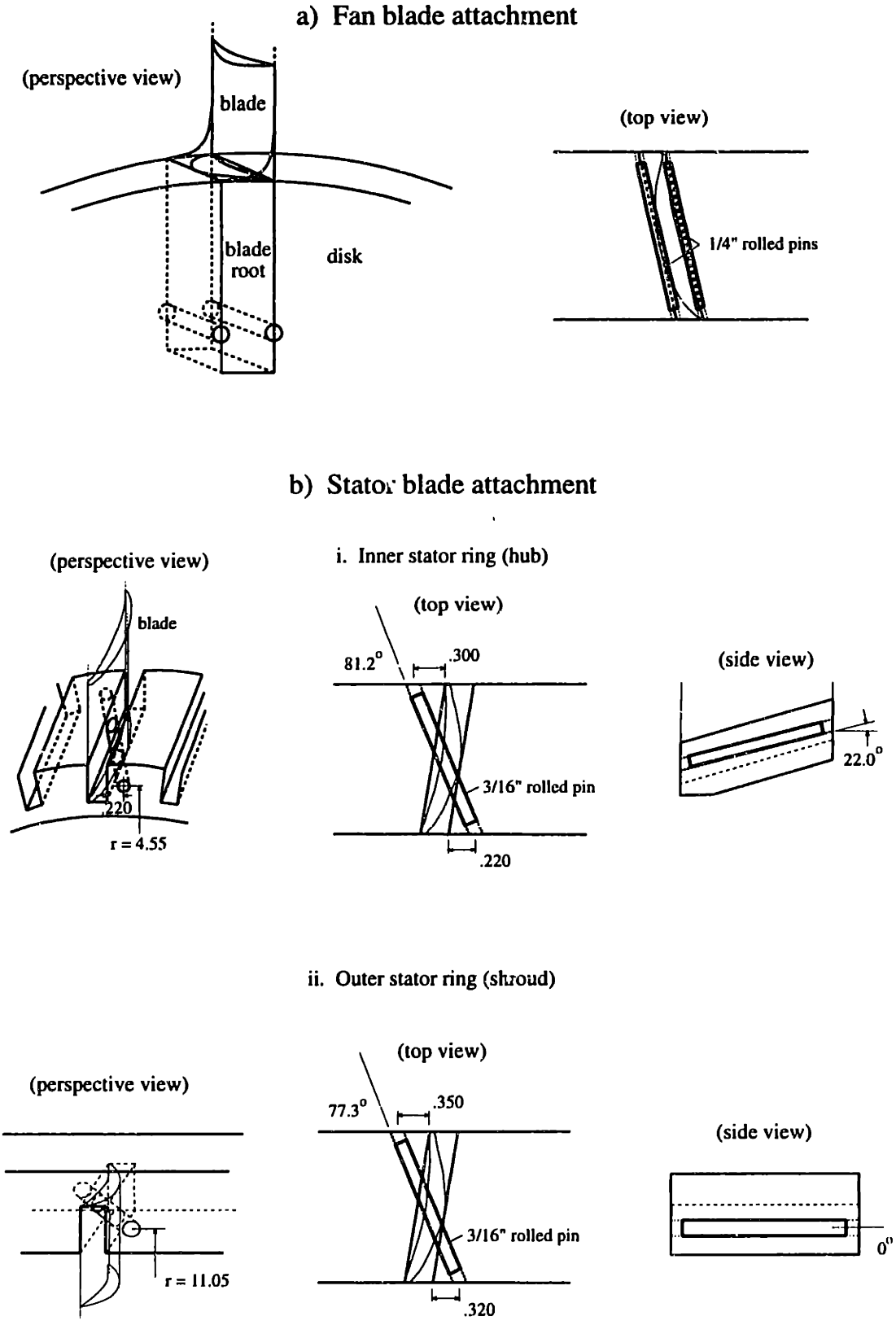

Figure D-24: Rotor and stator blade attachment pinning

APPENDIX E

EXPERIMENTAL DATA

In addition to the experimental data presented in Chapters 5 and 7, flow field variables (other than relative Mach number) measured with the 4-way probe are presented here. Although the mean relative Mach number profile harmonics, as well as the turbulence level in the flow field, are the most relevant for the noise generation process and were presented in the above mentioned chapters, the profiles of axial, tangential, and radial Mach number, flow angles, and pressure (static and total) are useful for examining the overall performance of the fan stage. First the data from the baseline solid-bladed rotor will be shown (0.1, 0.5, and 1.0 chord), and then the data from the trailing edge blowing rotor with midspan weighted injection at 0.1 and 1.5 chord will be shown.

E.1 Baseline Fan Stage Data

The following plots at 0.1c, 0.5c, and 1.0c all use the same plot scales for similar flow variables. Thus, the profiles at the different downstream positions can be directly compared to examine the decay of the wake.

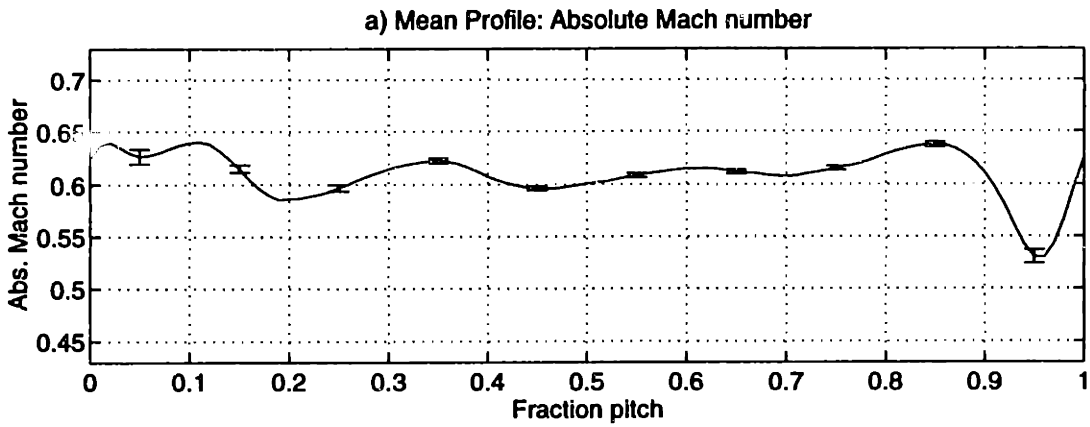

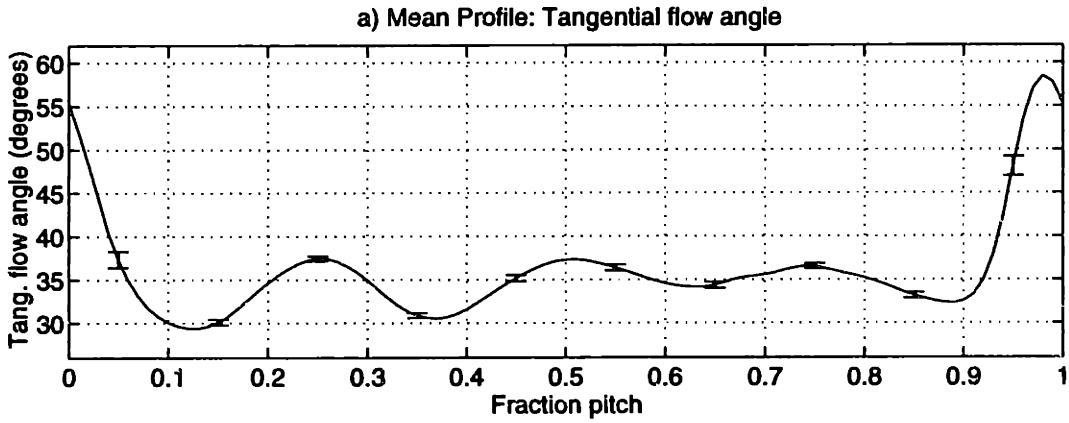

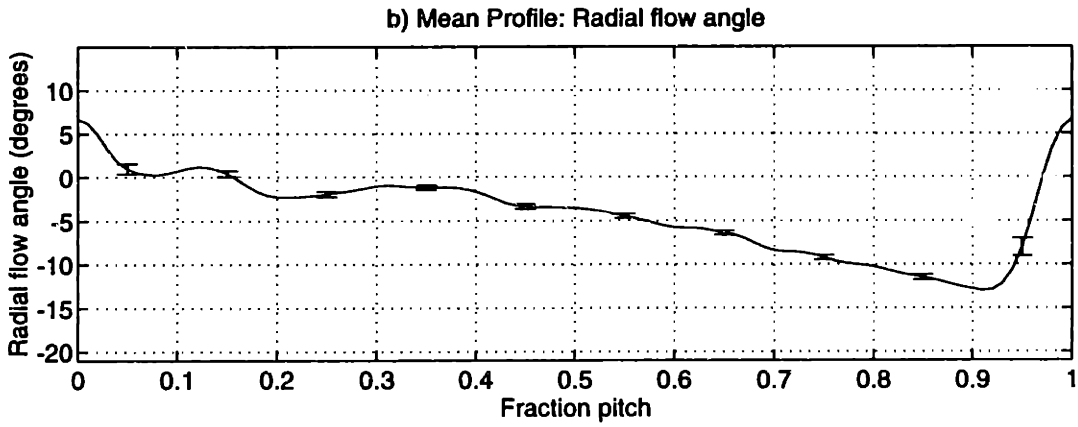

Figure E-1: Measured baseline flow field data at 50% span, 0.1c

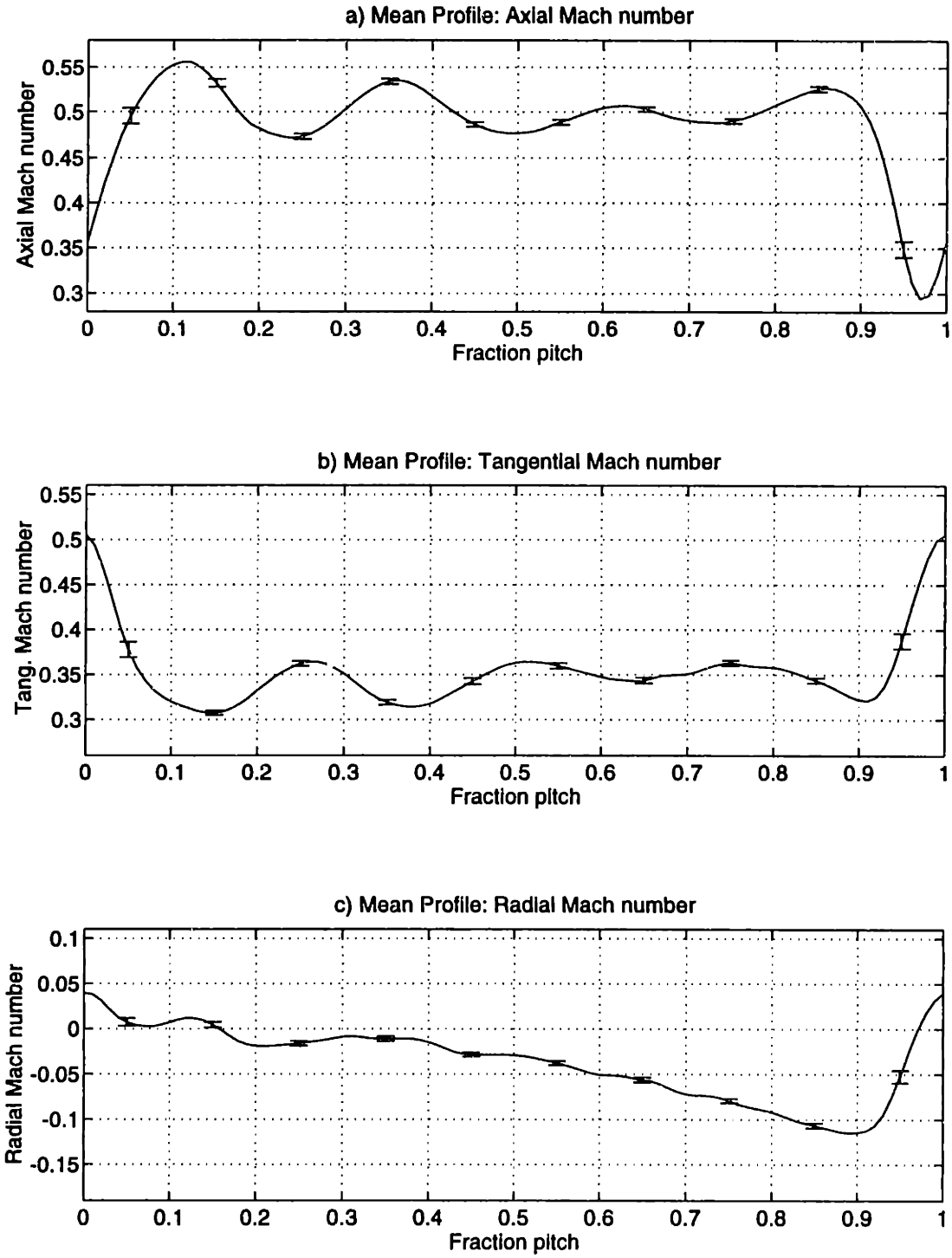

Figure E-2: Measured baseline flow field data at 50% span, 0.1c

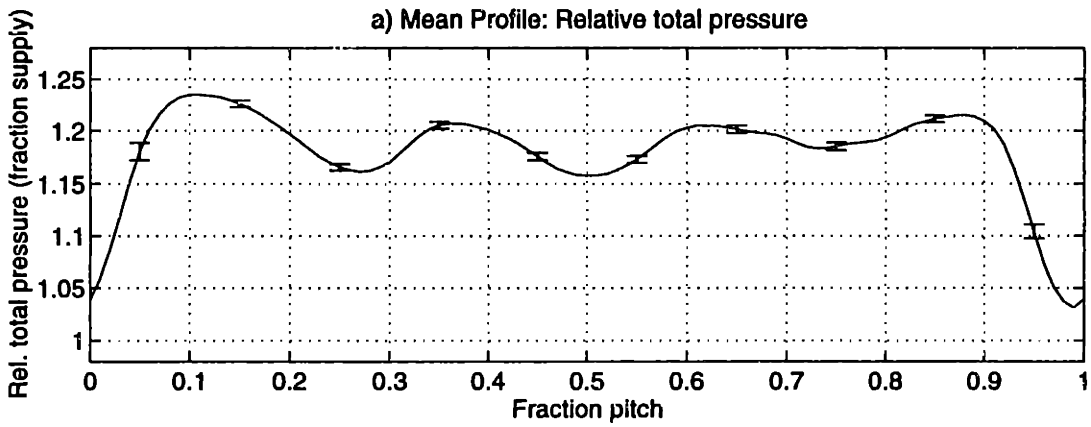

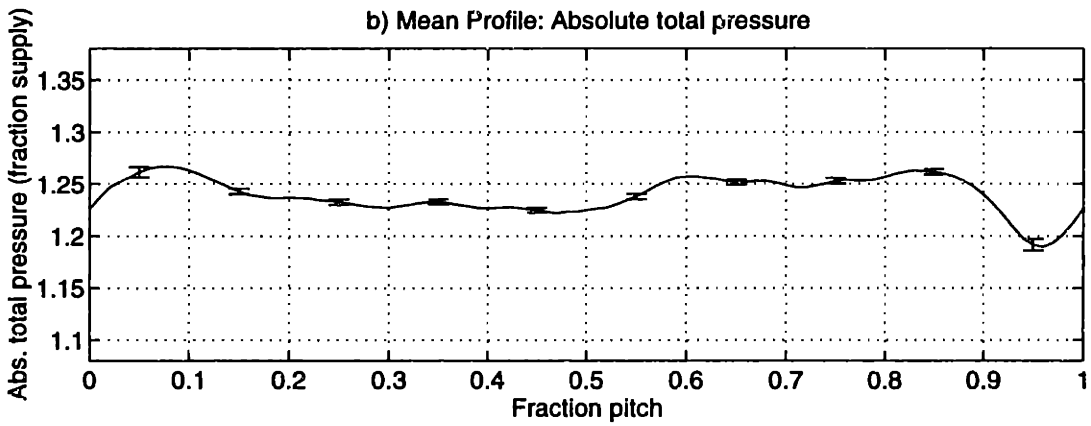

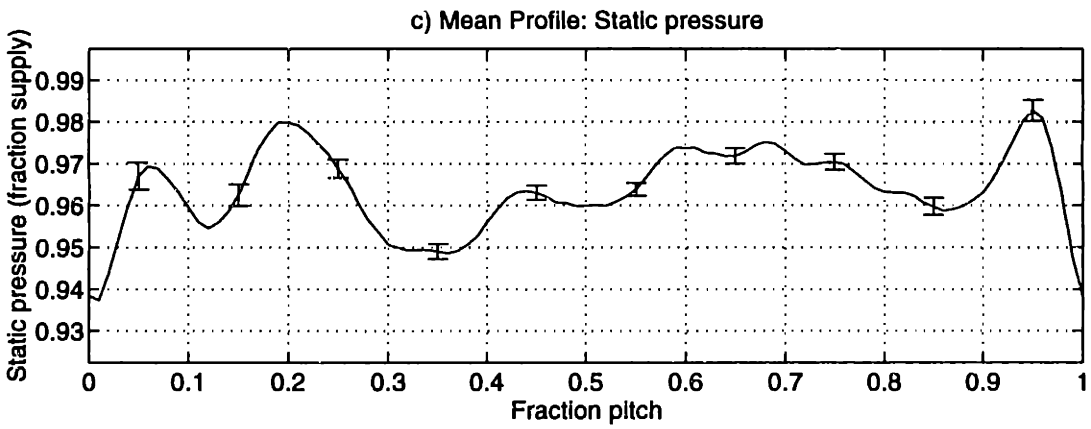

Figure E-3: Measured baseline flow field data at 50% span, 0.1c

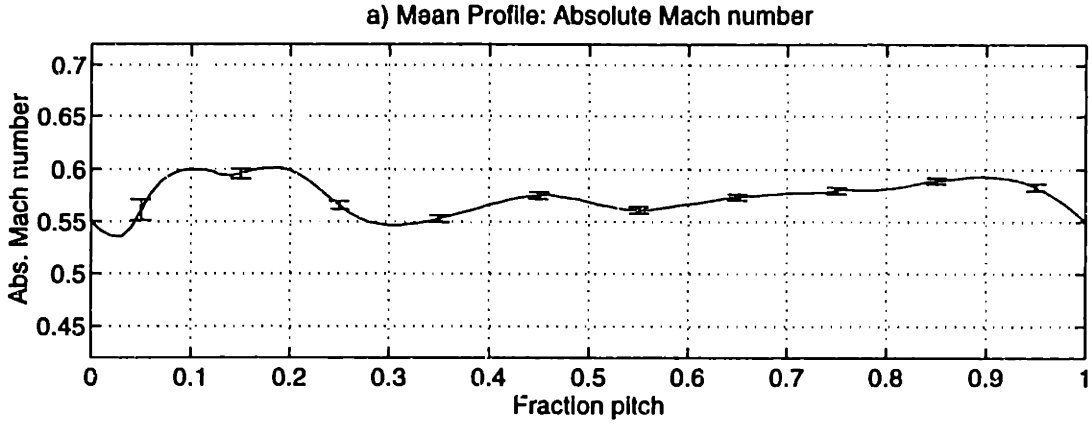

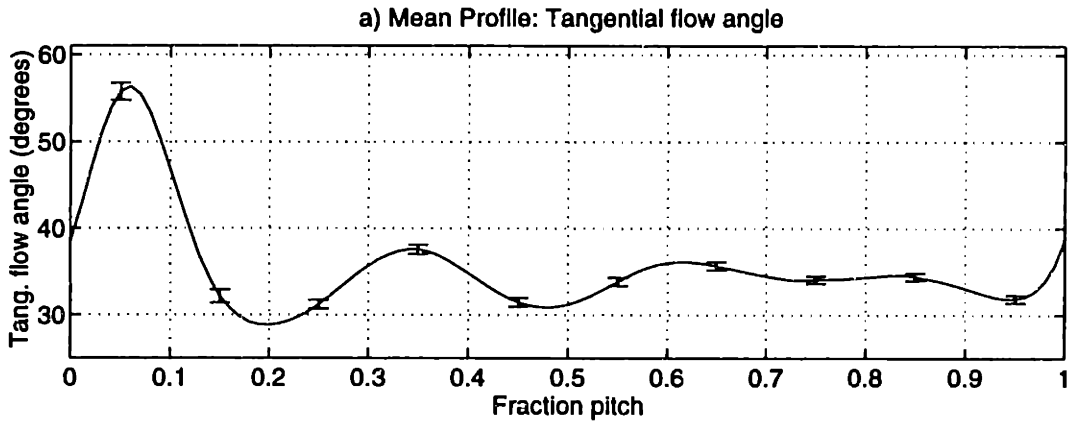

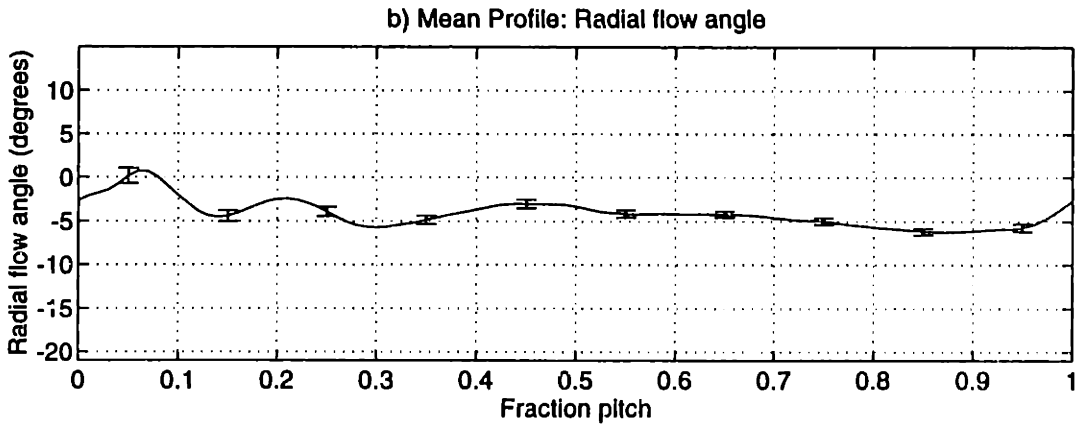

Figure E-4: Measured baseline flow field data at 75% span, 0.1c

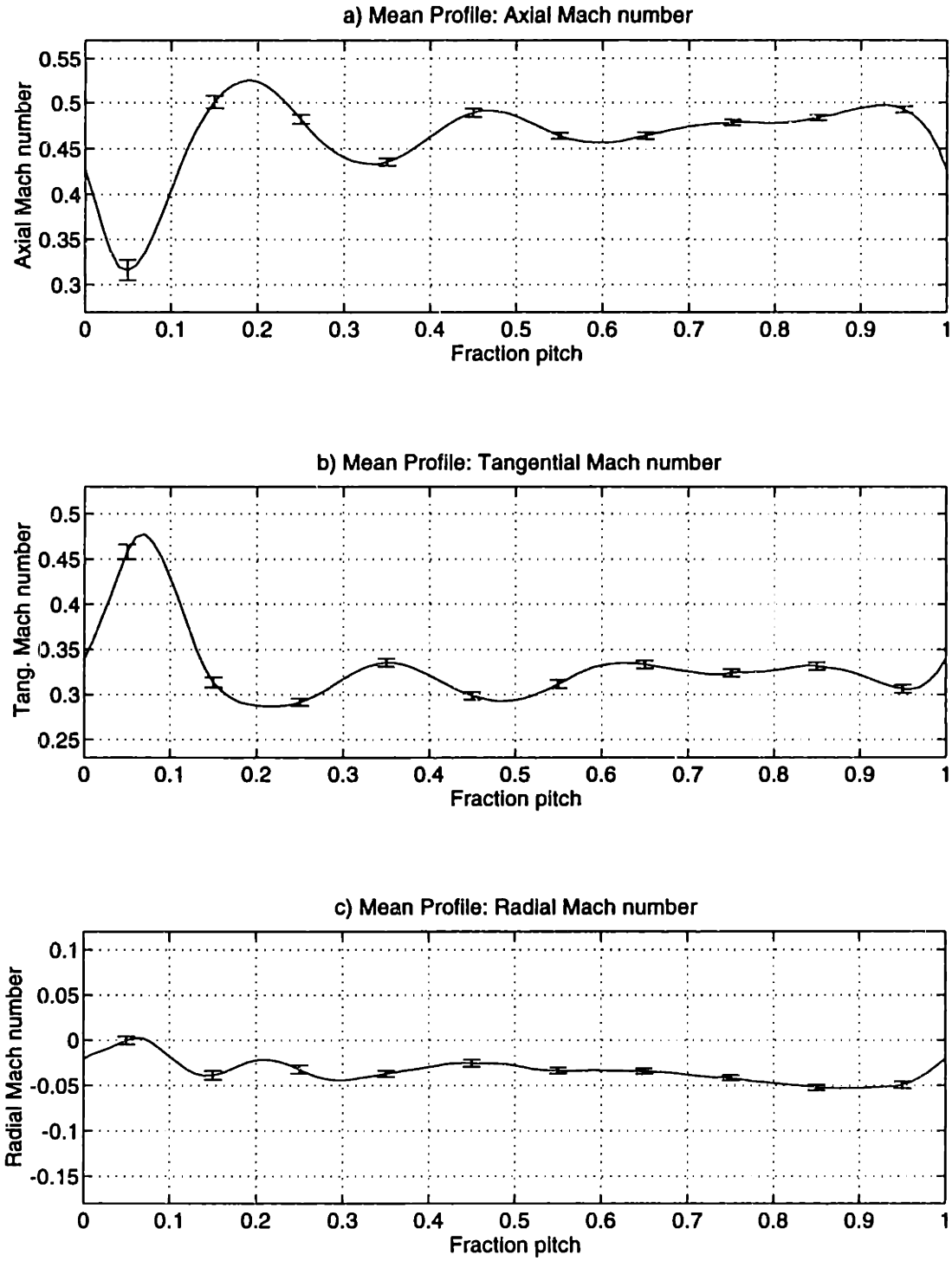

Figure E-5: Measured baseline flow field data at 75% span, 0.1c

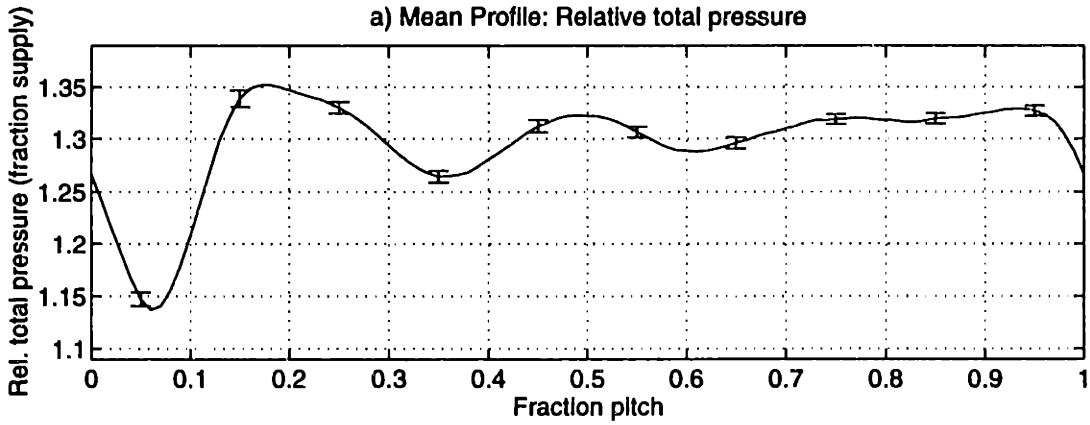

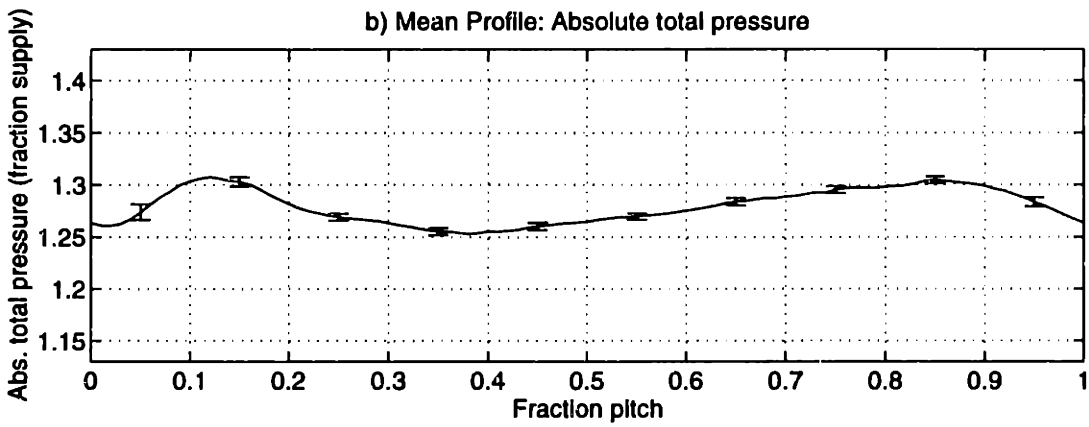

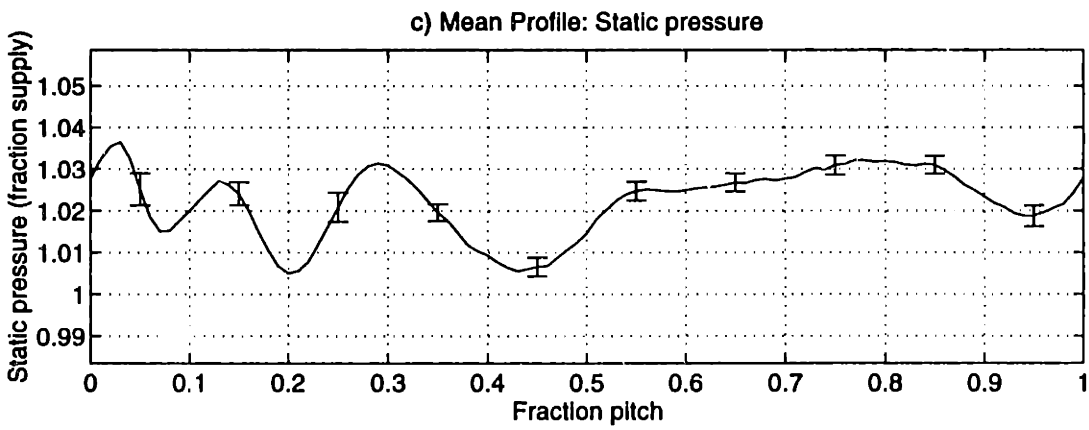

Figure E-6: Measured baseline flow field data at 75% span, 0.1c

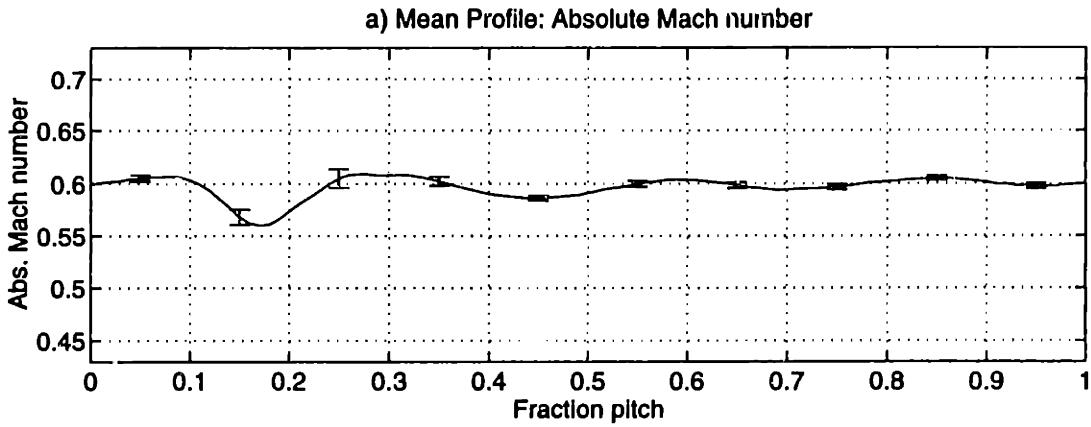

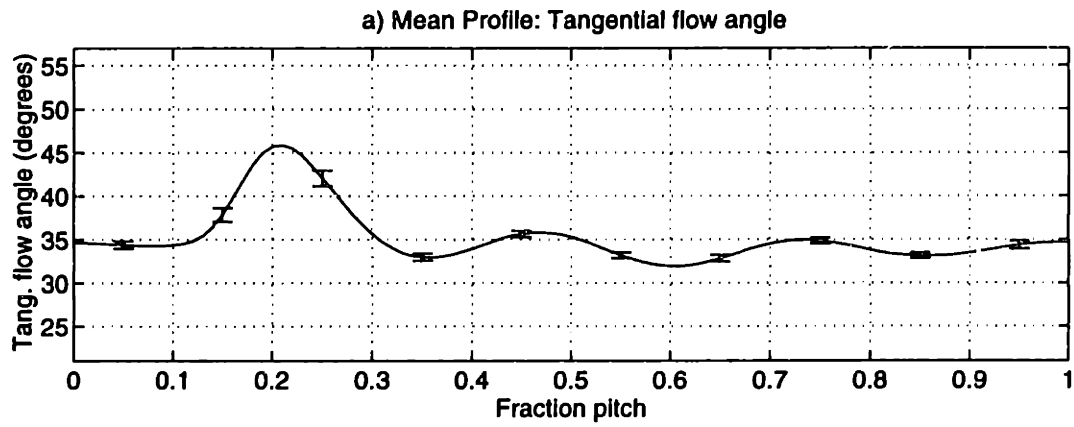

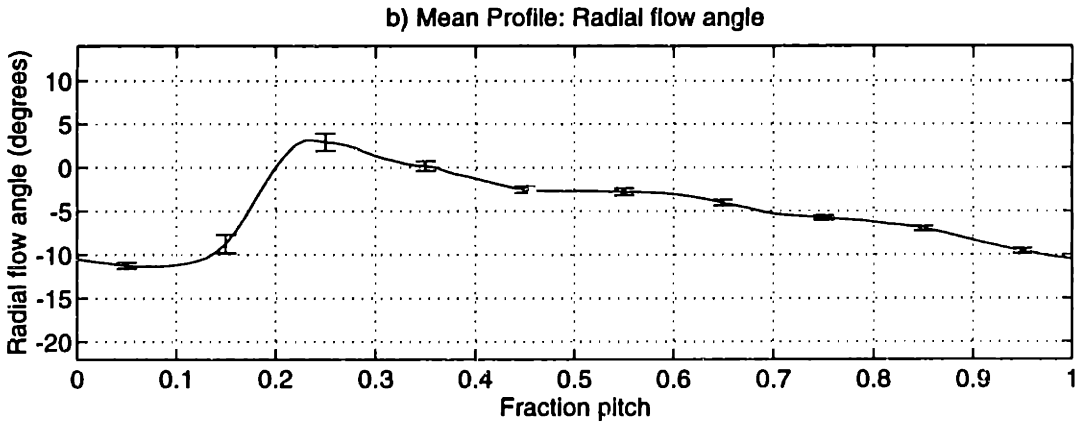

Figure E-7: Measured baseline flow field data at 50% span, 0.5c

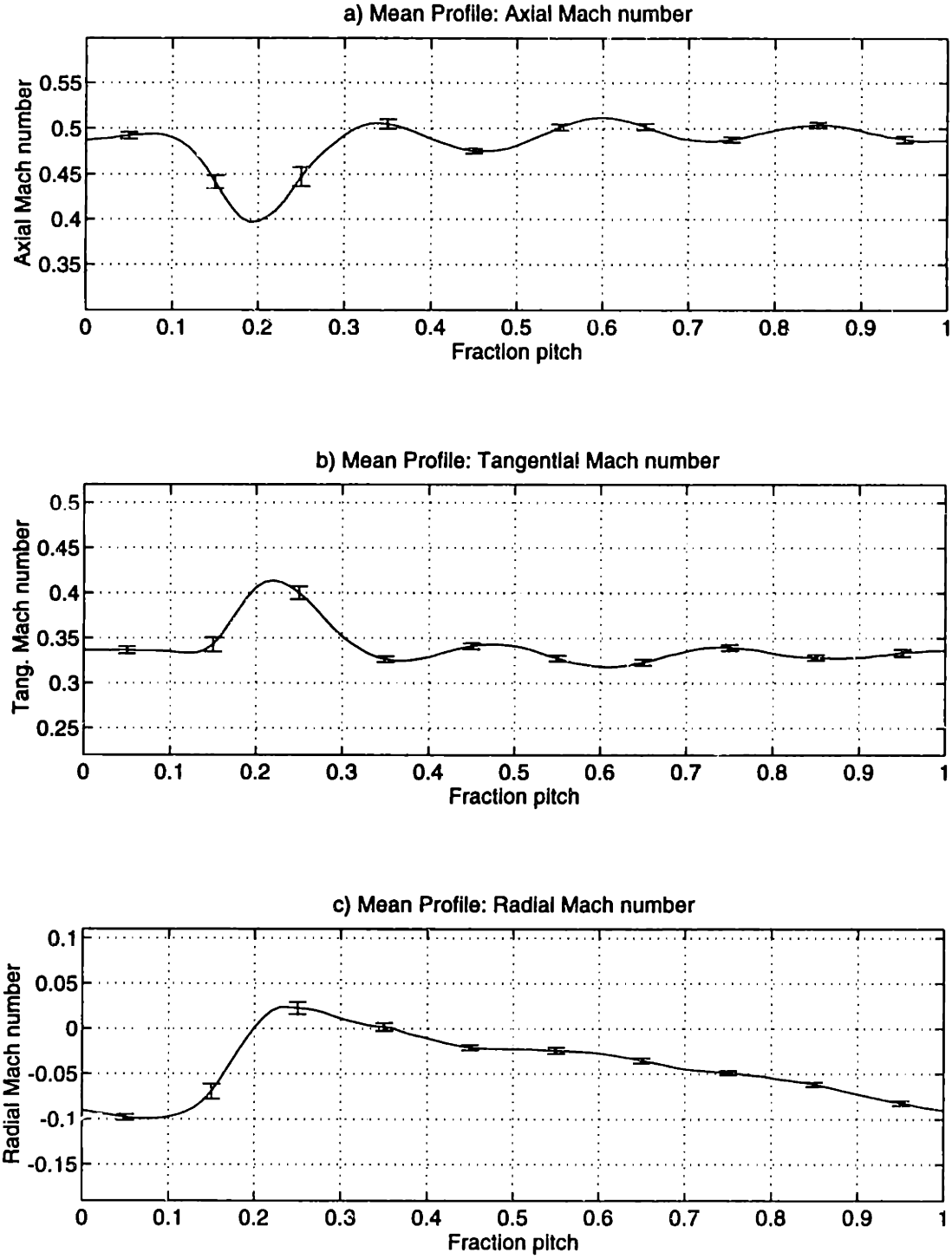

Figure E-8: Measured baseline flow field data at 50% span, 0.5c

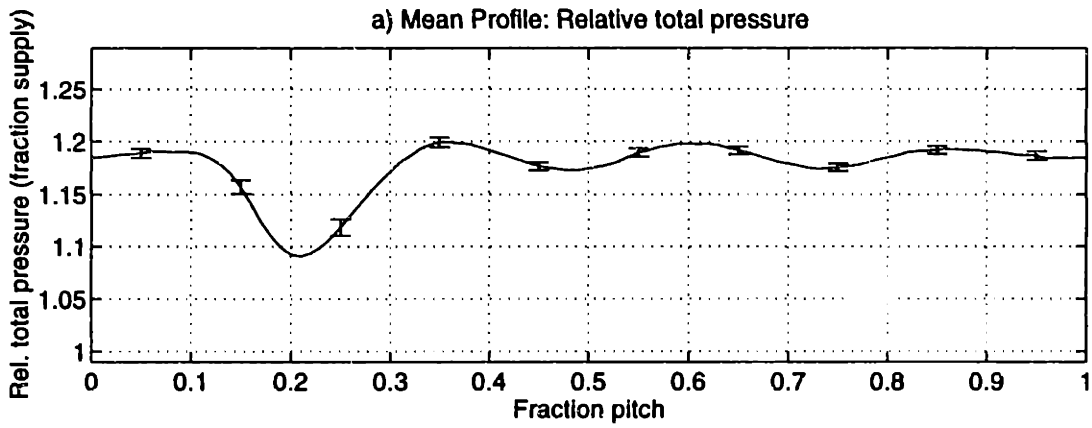

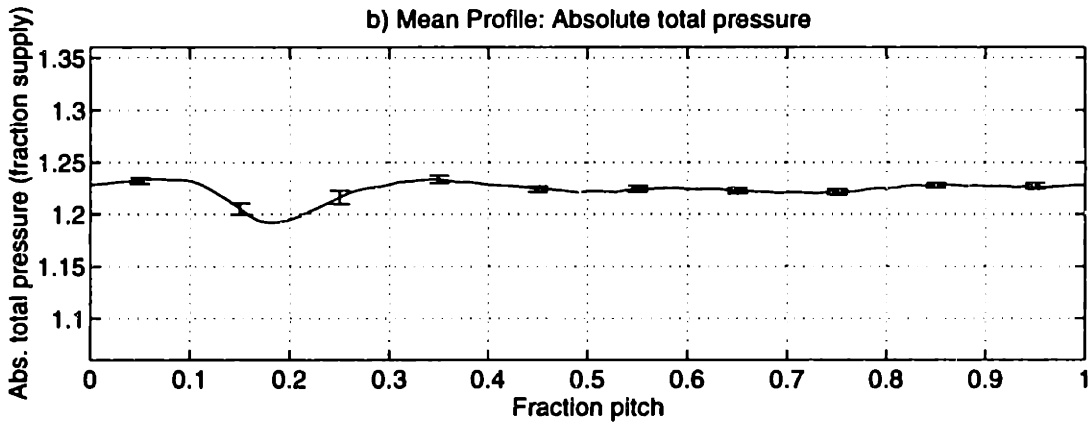

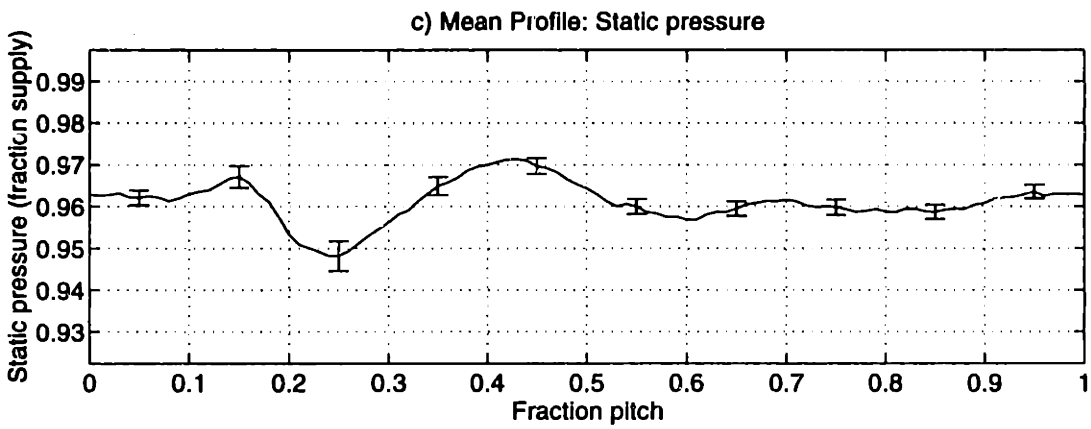

Figure E-9: Measured baseline flow field data at 50% span, 0.5c

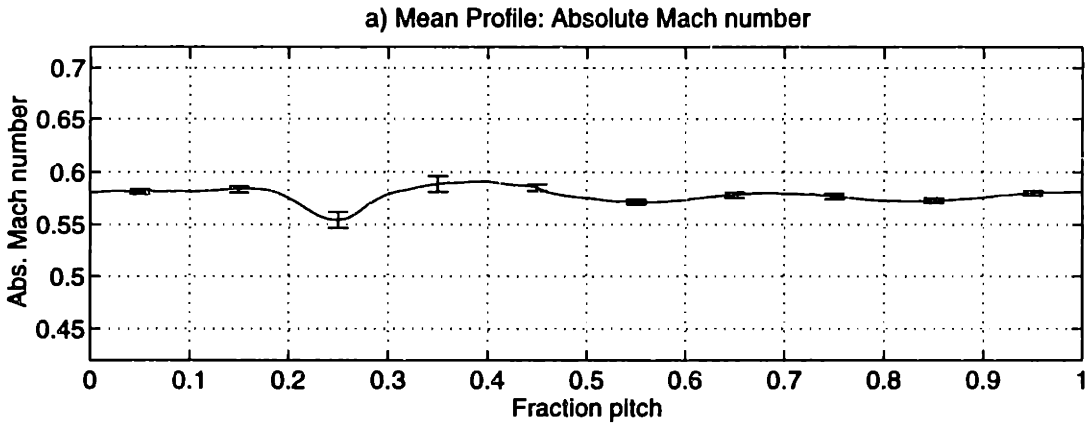

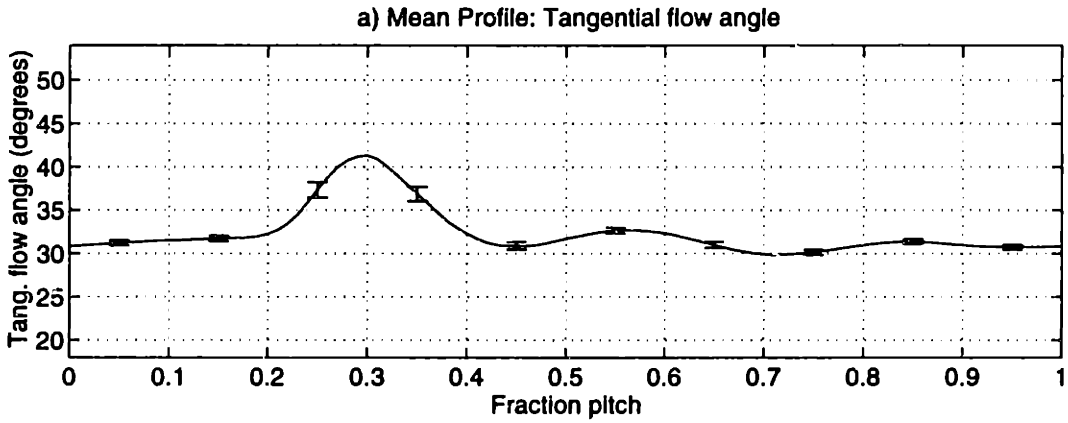

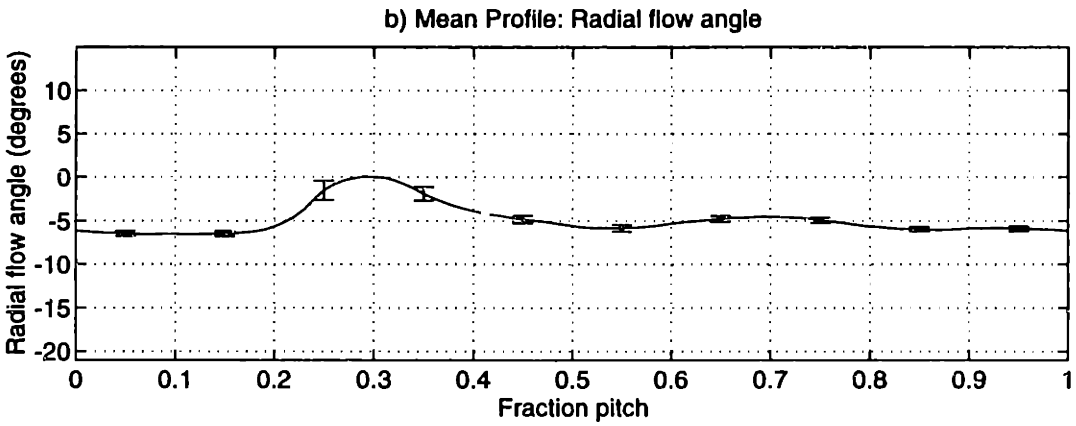

Figure E-10: Measured baseline flow field data at 75% span, 0.5c

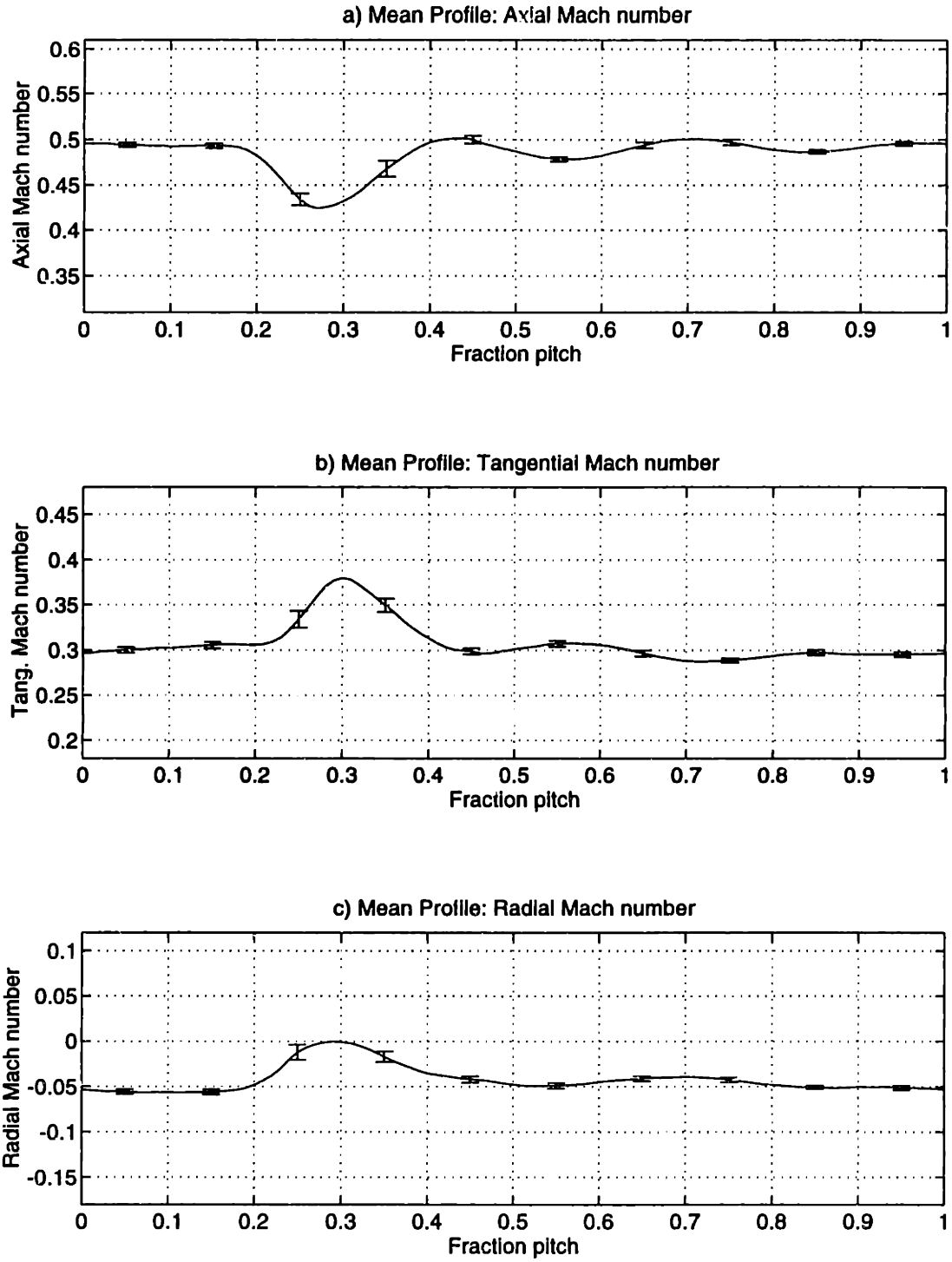

Figure E-11: Measured baseline flow field data at 75% span, 0.5c

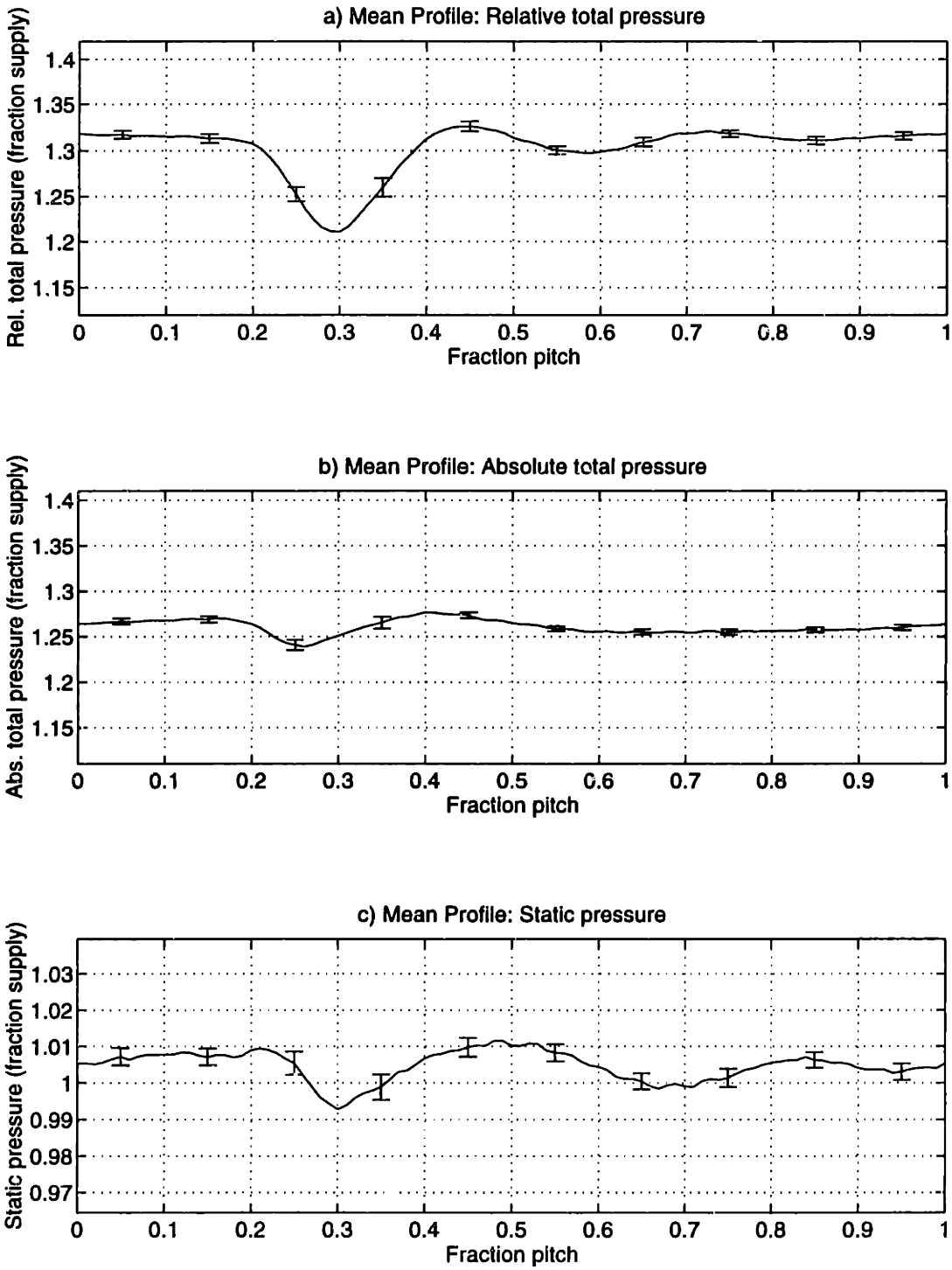

Figure E-12: Measured baseline flow field data at 75% span, 0.5c

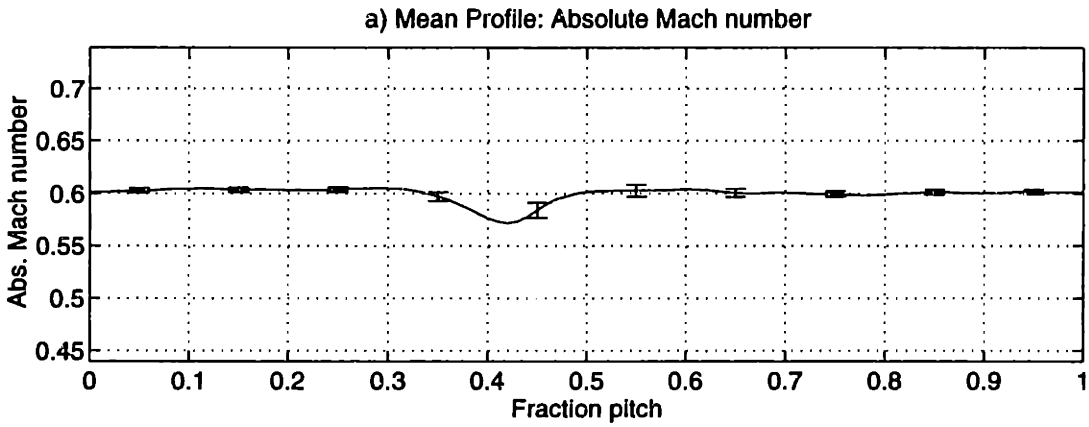

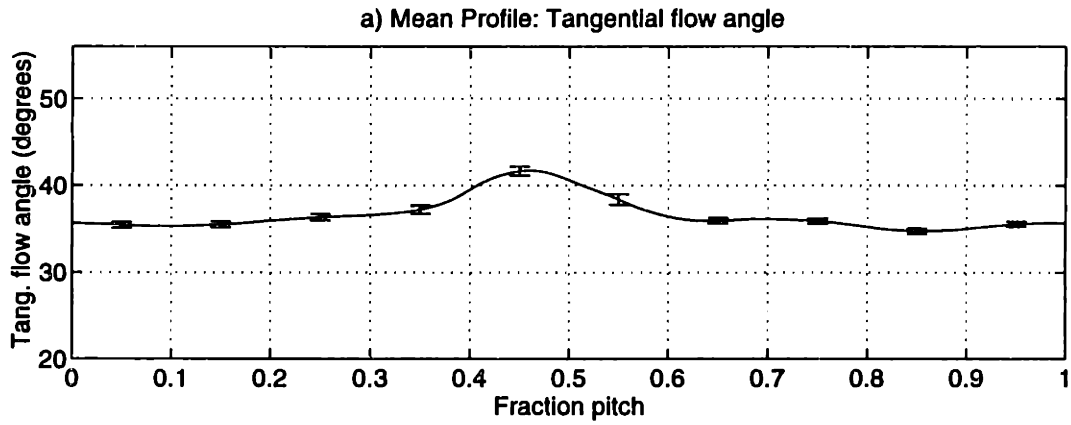

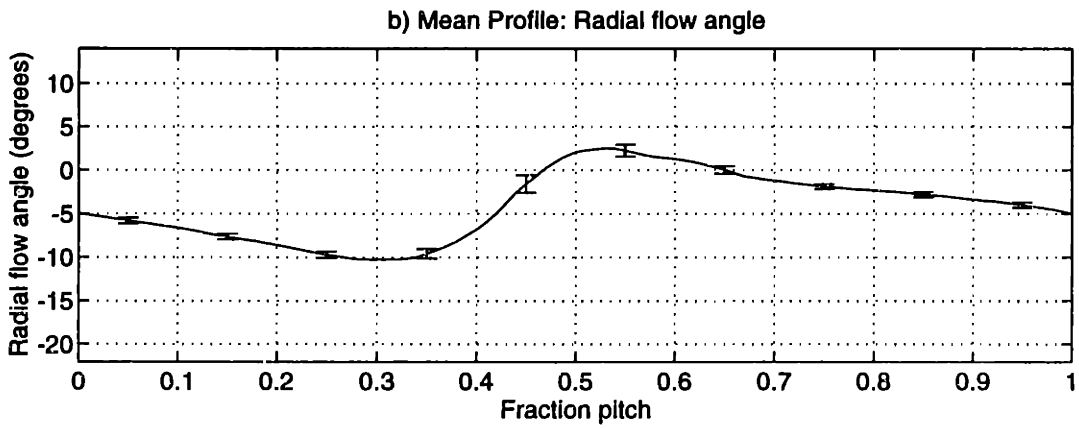

Figure E-13: Measured baseline flow field data at 50% span, 1.0c

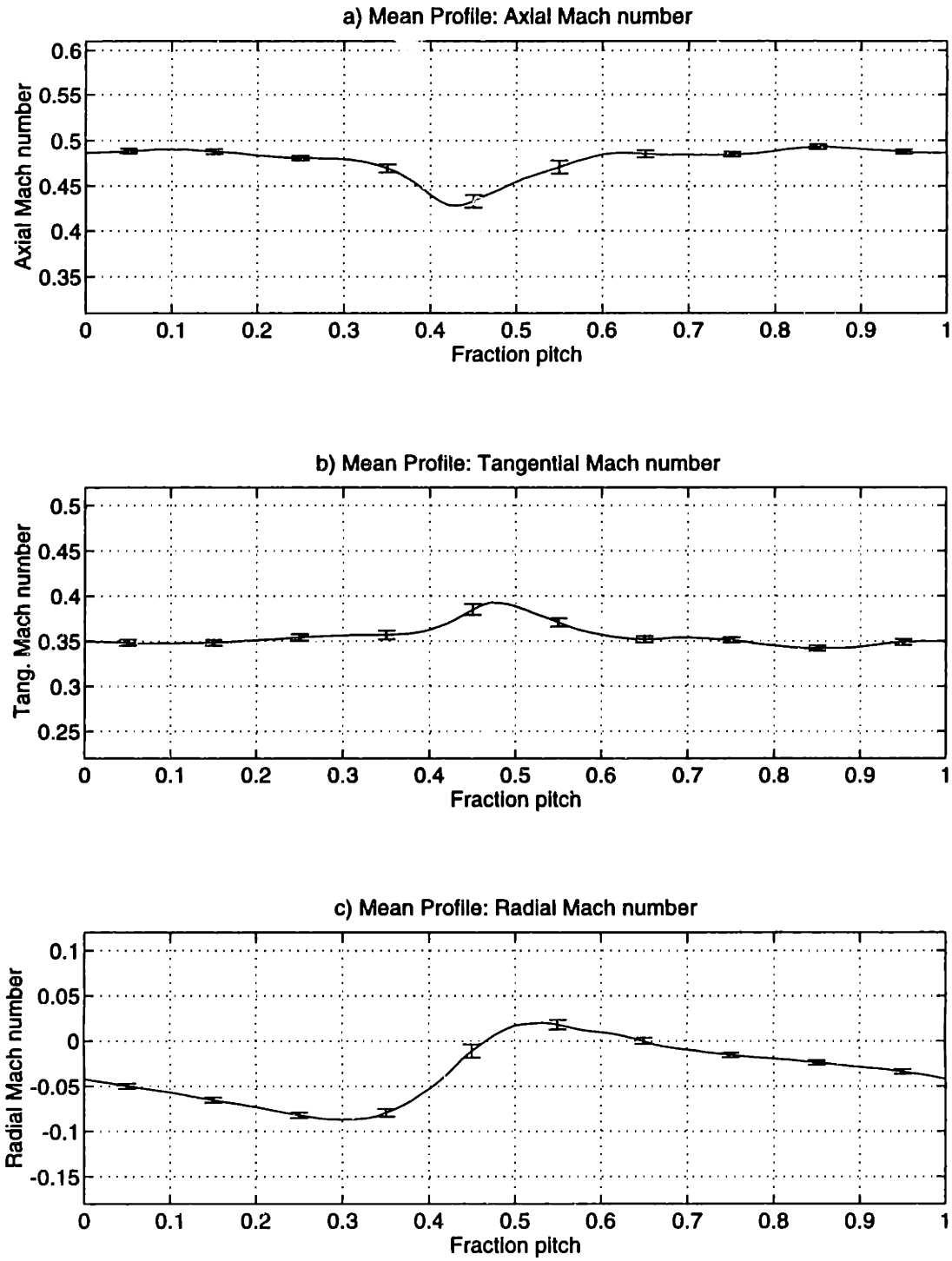

Figure E-14: Measured baseline flow field data at 50% span, 1.0c

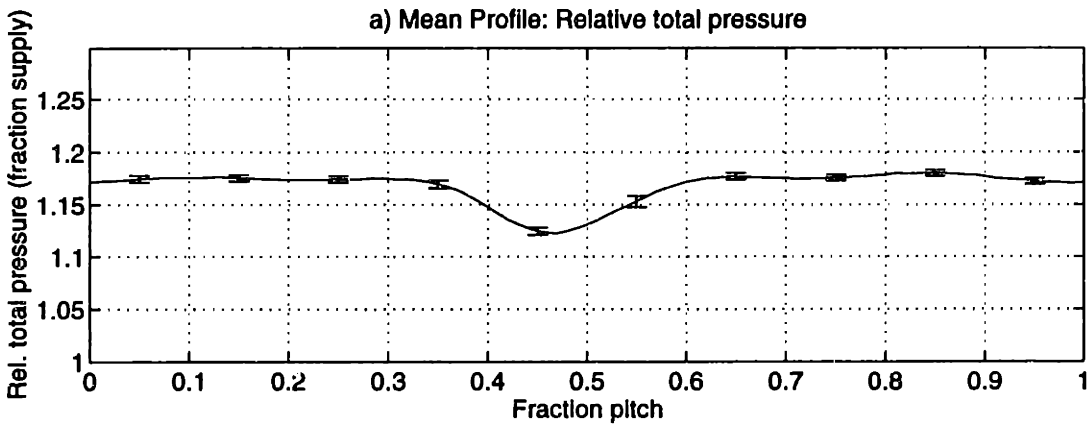

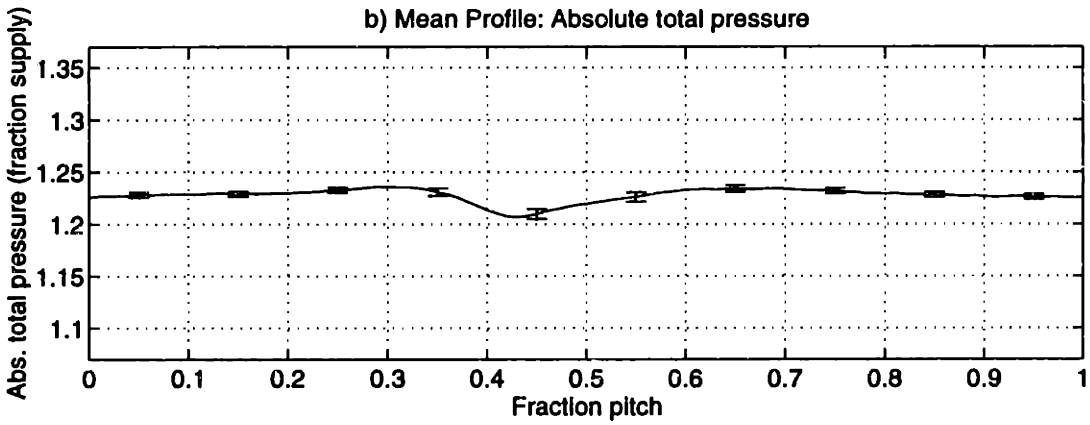

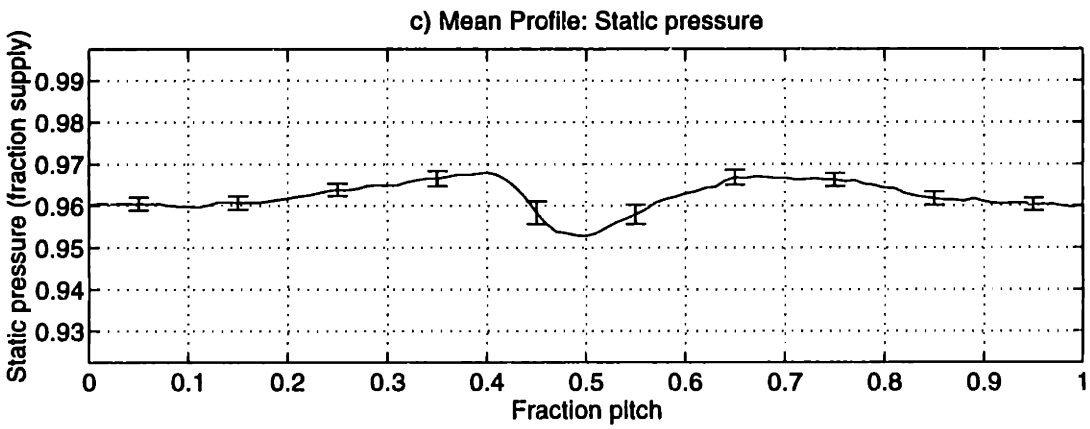

Figure E-15: Measured baseline flow field data at 50% span, 1.0c

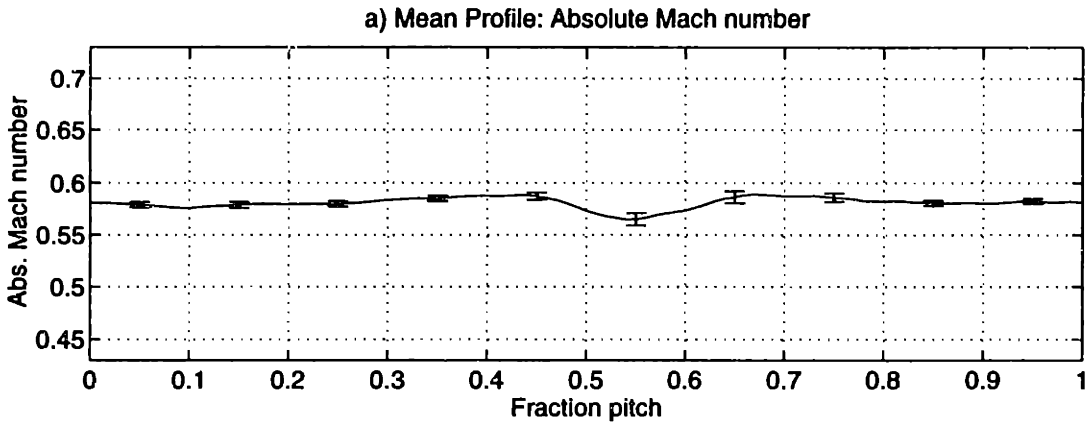

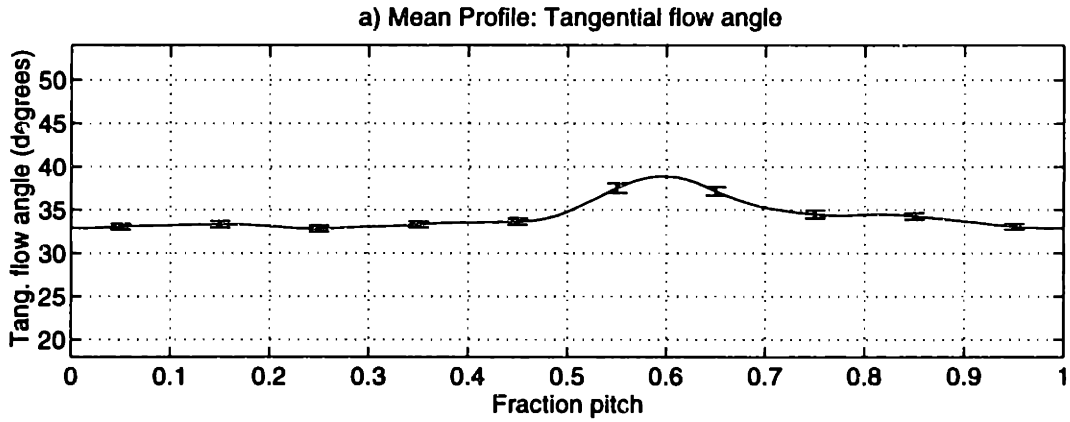

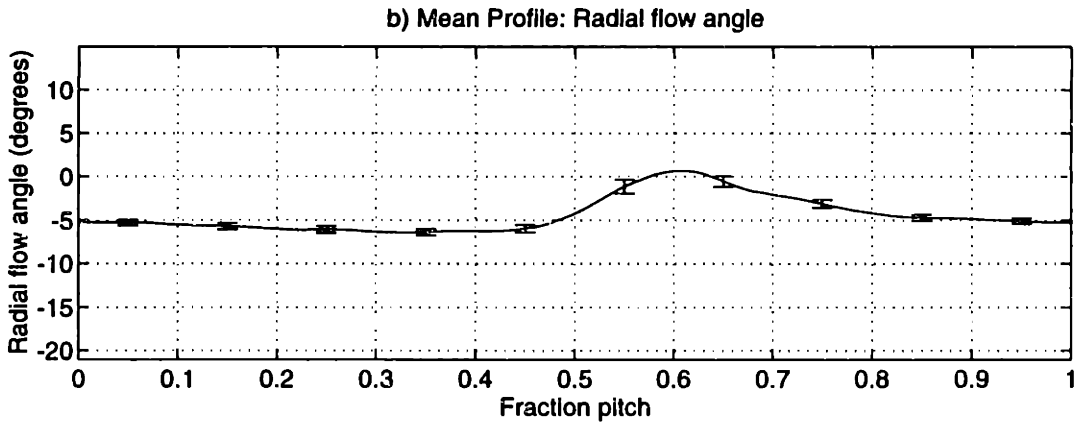

Figure E-16: Measured baseline flow field data at 75% span, 1.0c

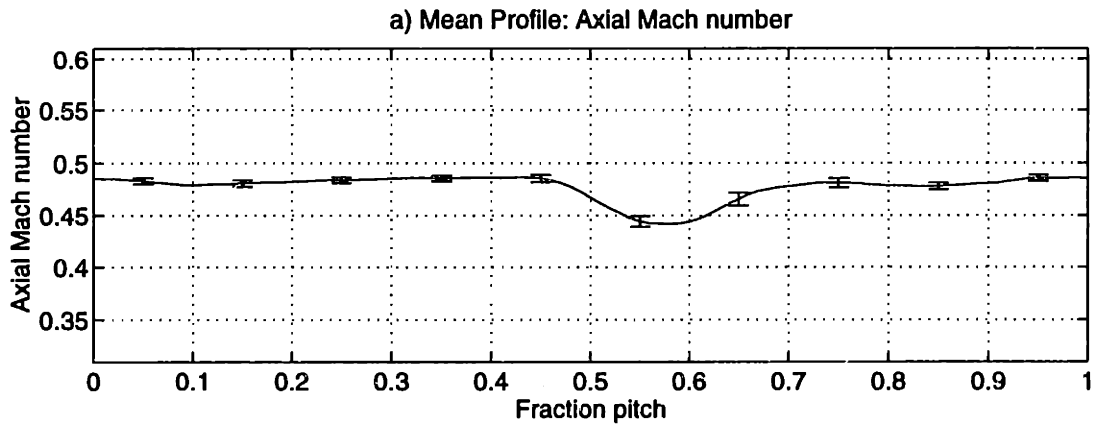

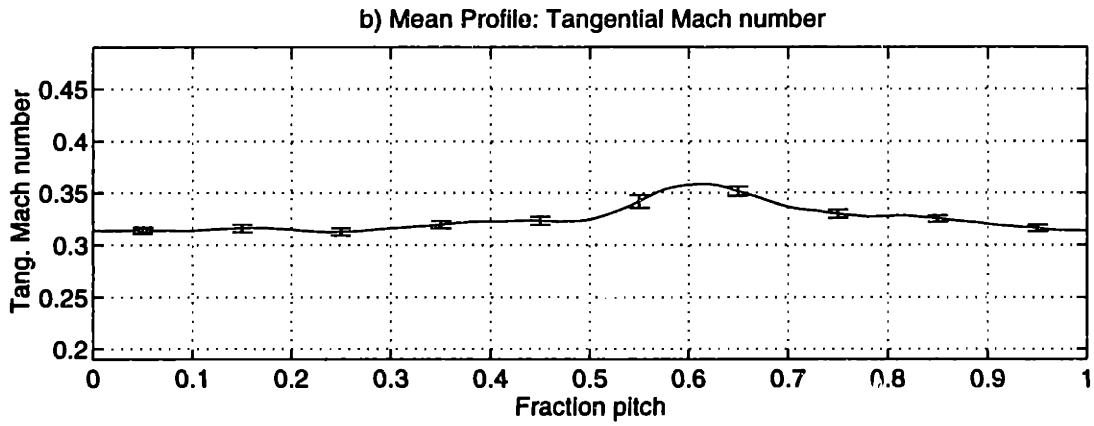

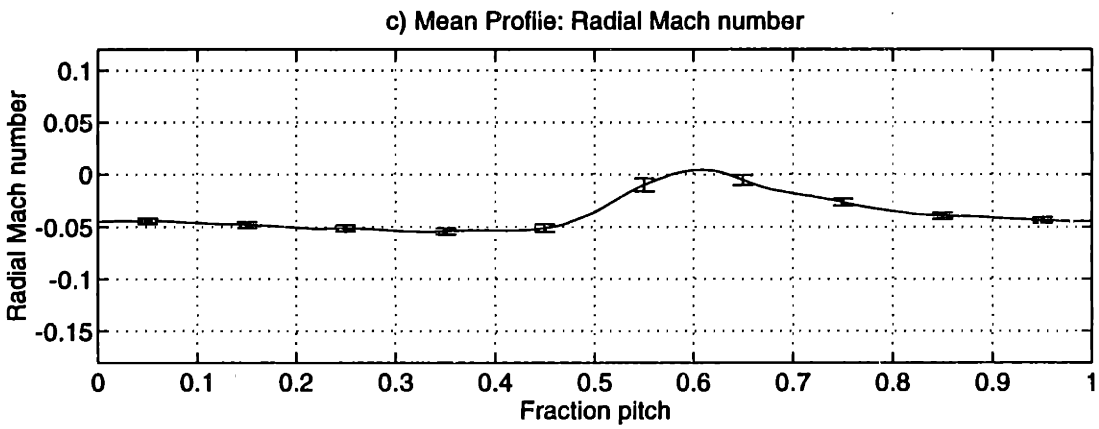

Figure E-17: Measured baseline flow field data at 75% span, 1.0c

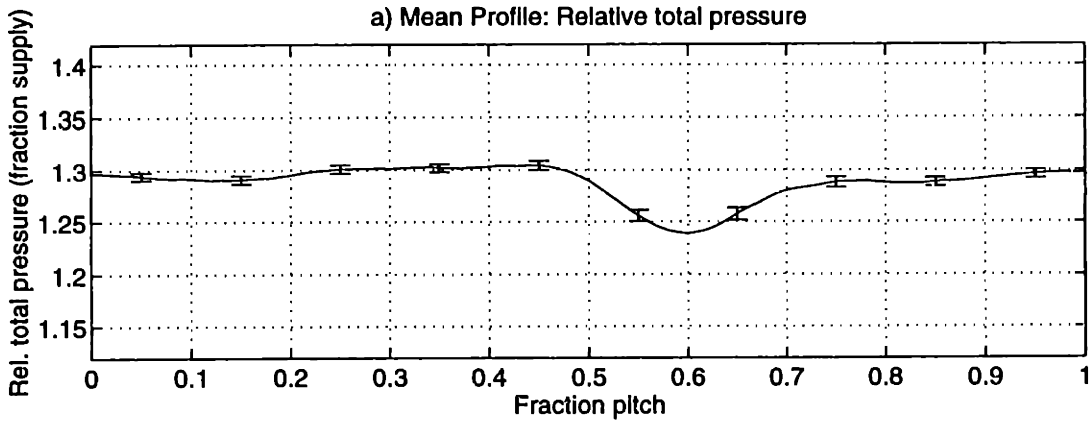

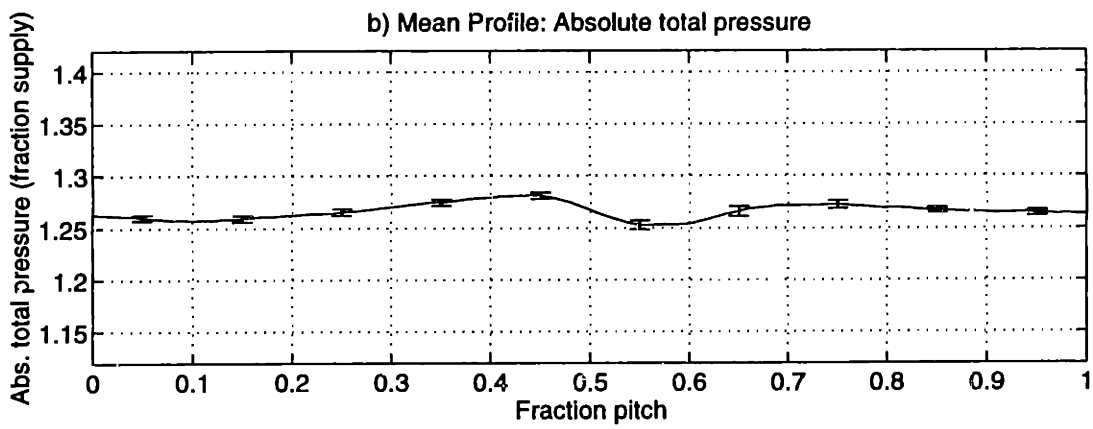

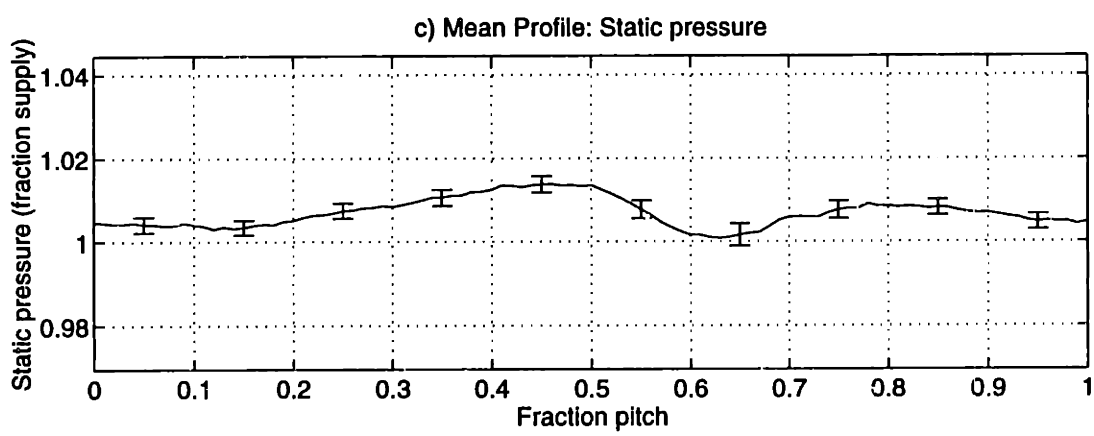

Figure E-18: Measured baseline flow field data at 75% span, 1.0c

E.2 Wake Management Fan Data

Flow variables other than relative Mach number for the midspan weighted injection trailing edge blowing rotor are shown at 0.1 and 1.5 chord for 2.0% injection and at 1.5 chord for 1.8% injection.

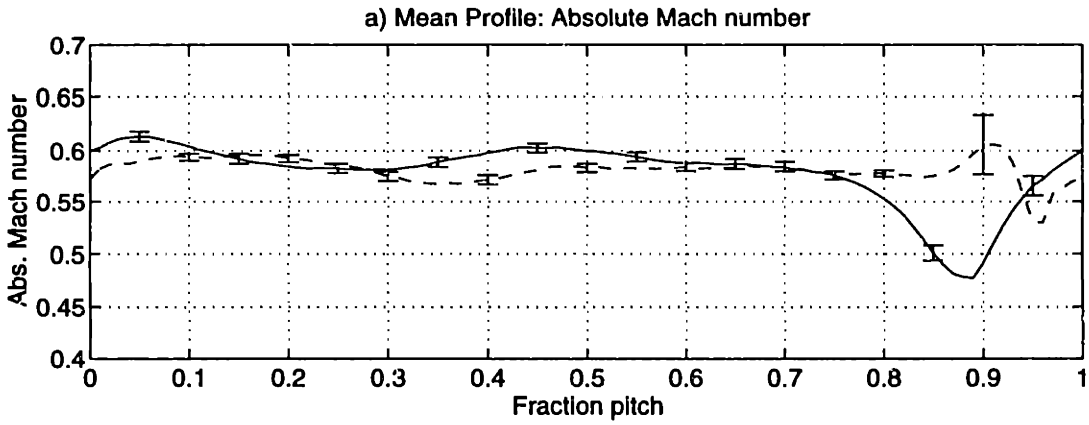

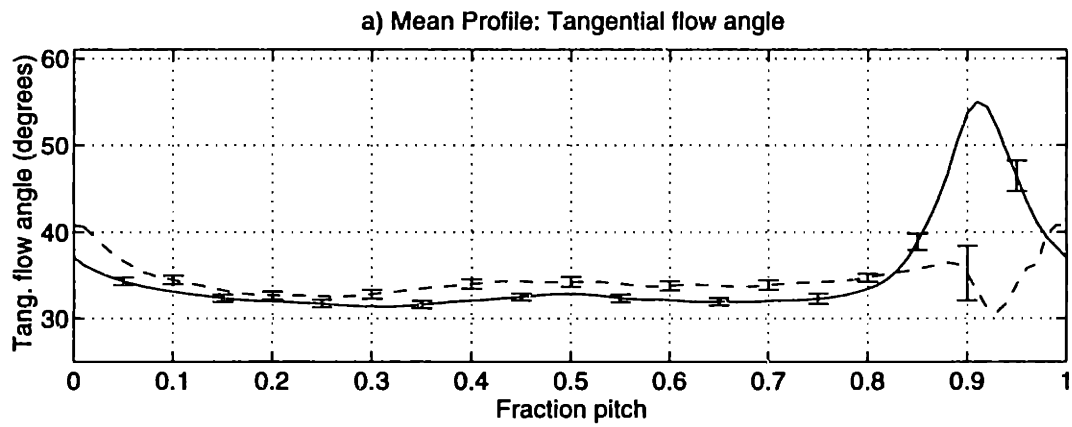

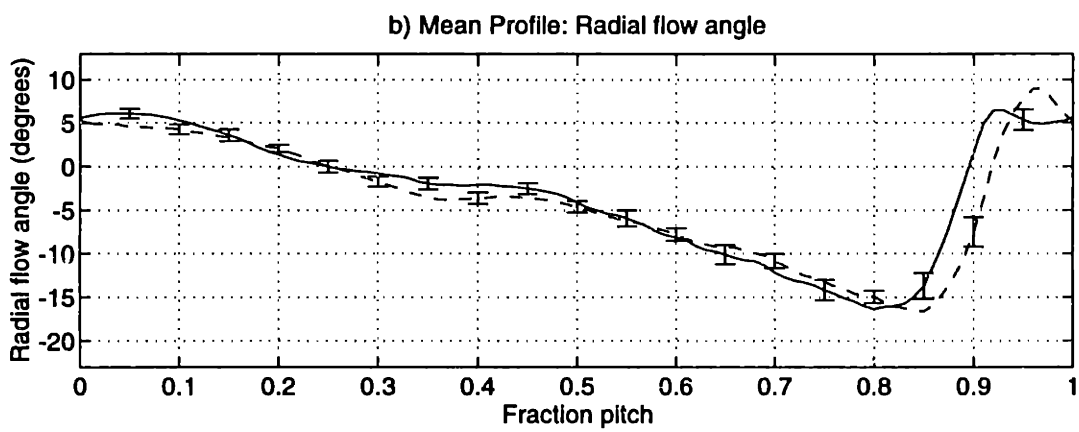

Figure E-19: 2.0% midspan weighted injection flow field data at 25% span, 0.1c: flow angles

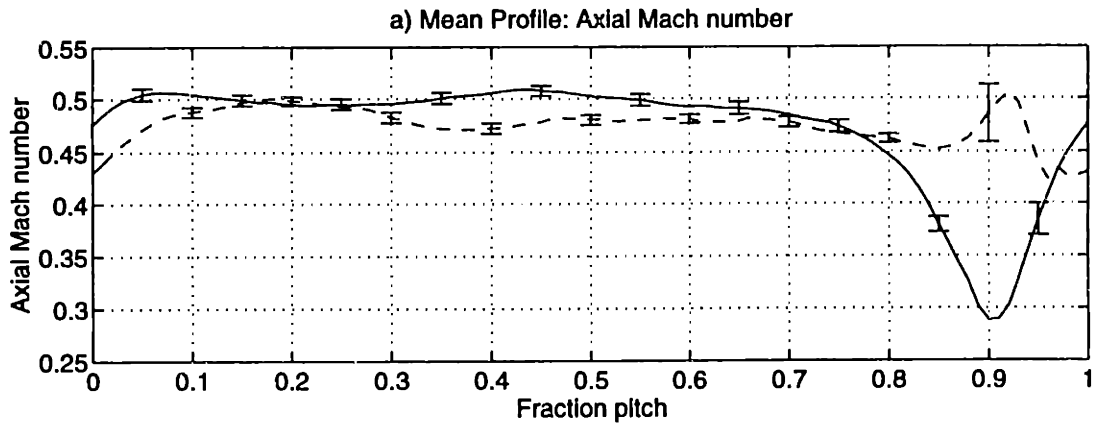

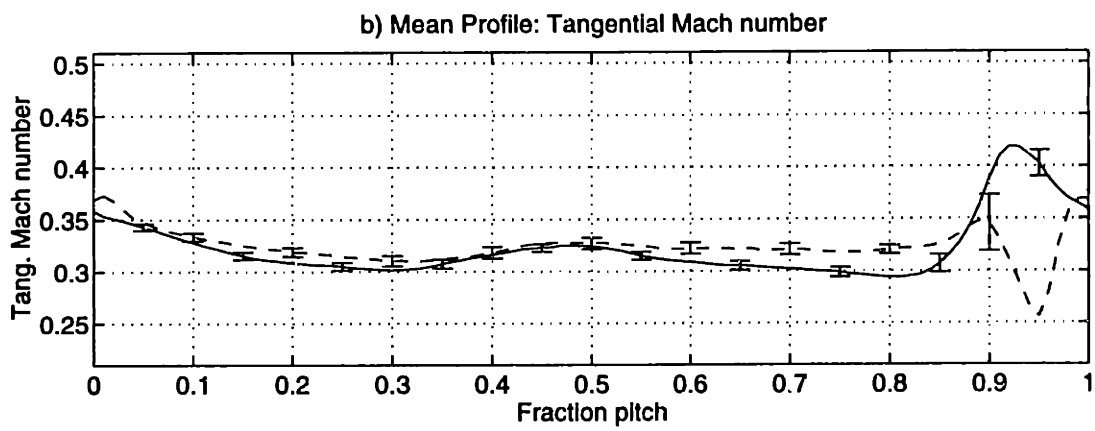

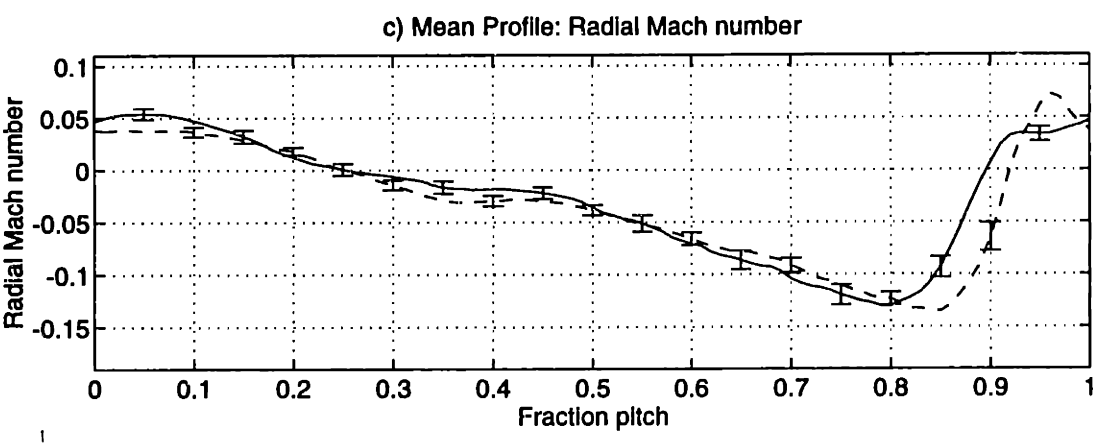

Figure E-20: 2.0% midspan weighted injection flow field data at 25% span, 0.1c: Mach number components

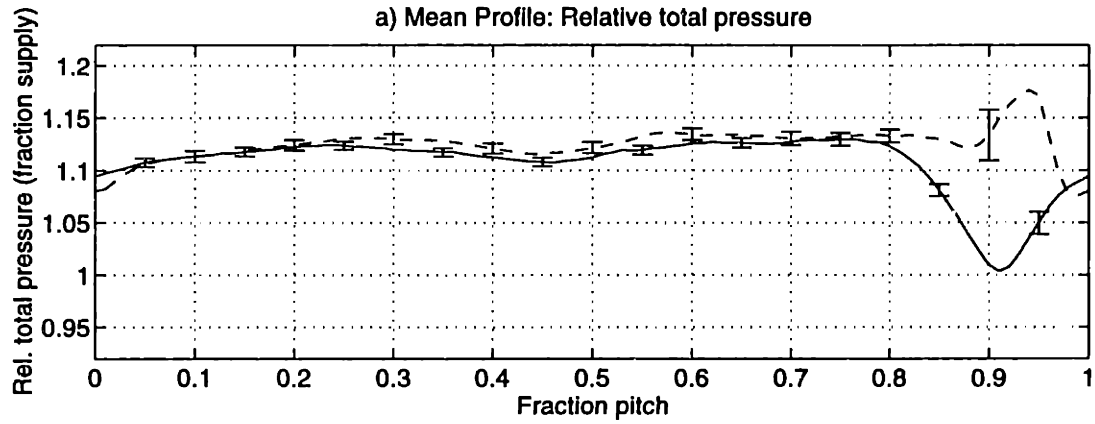

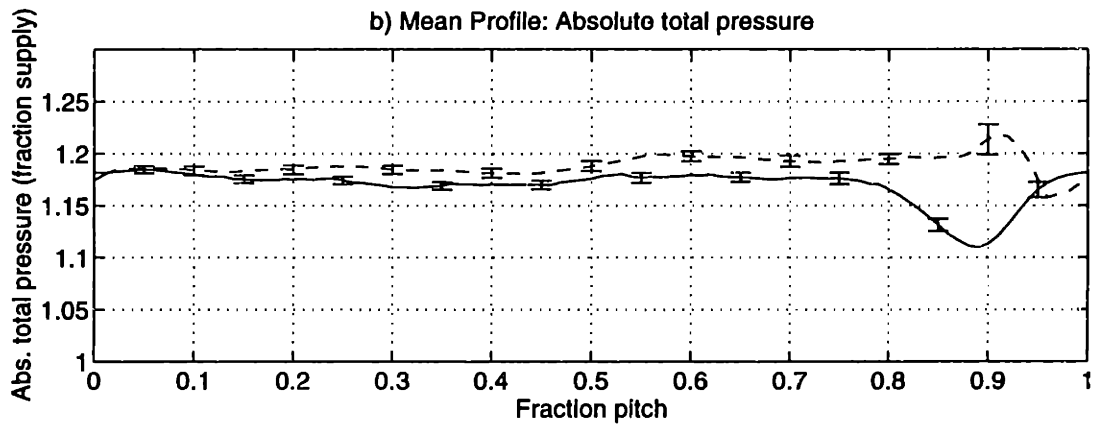

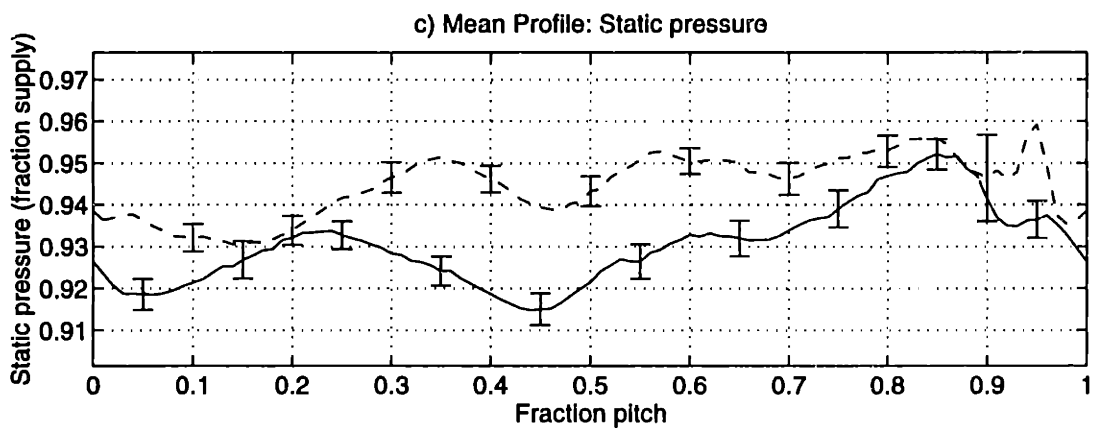

Figure E-21: 2.0% midspan weighted injection flow field data at 25% span, 0.1c: pressures

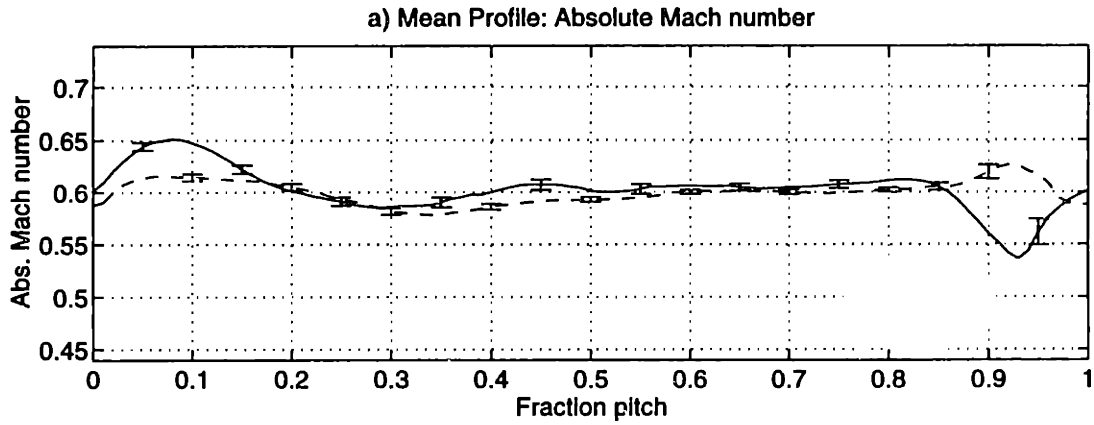

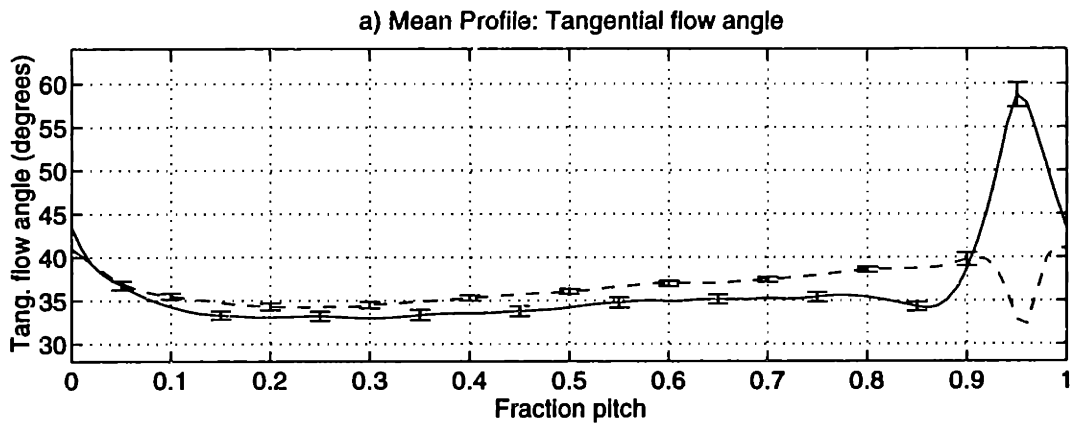

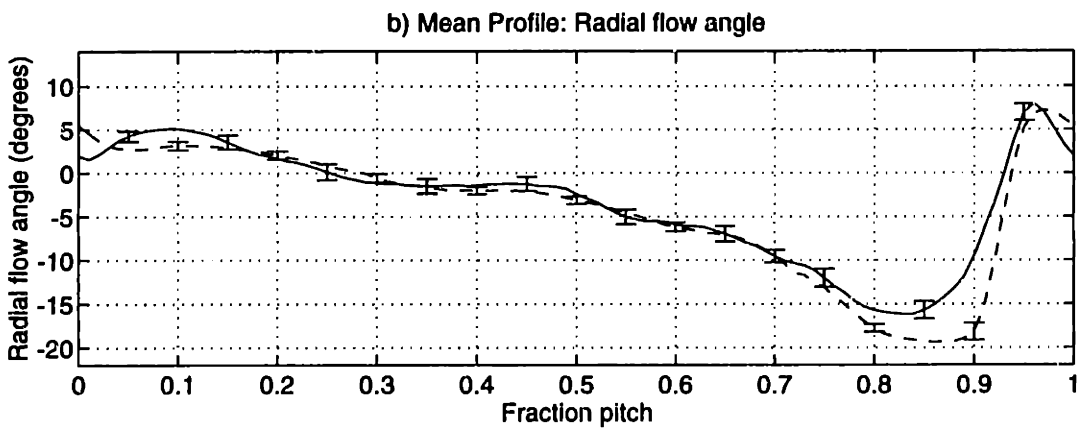

Figure E-22: 2.0% midspan weighted injection flow field data at 50% span, 0.1c: flow angles

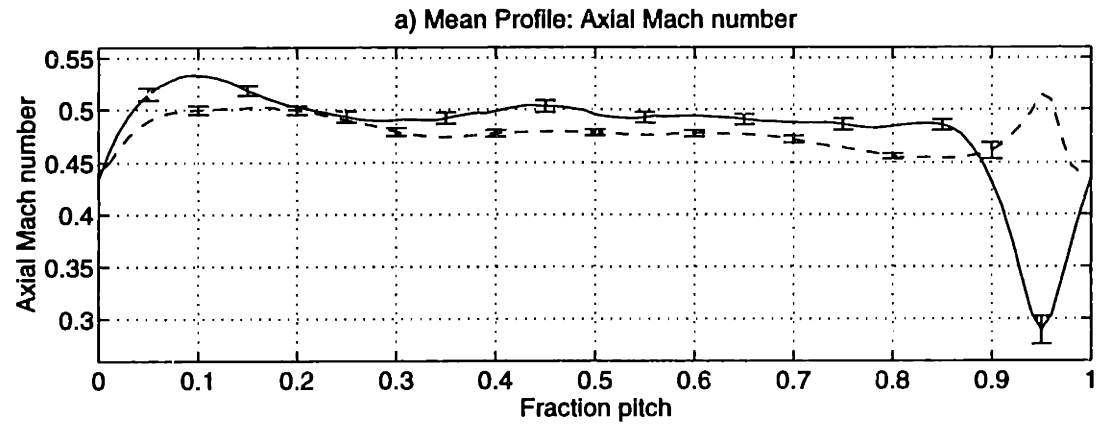

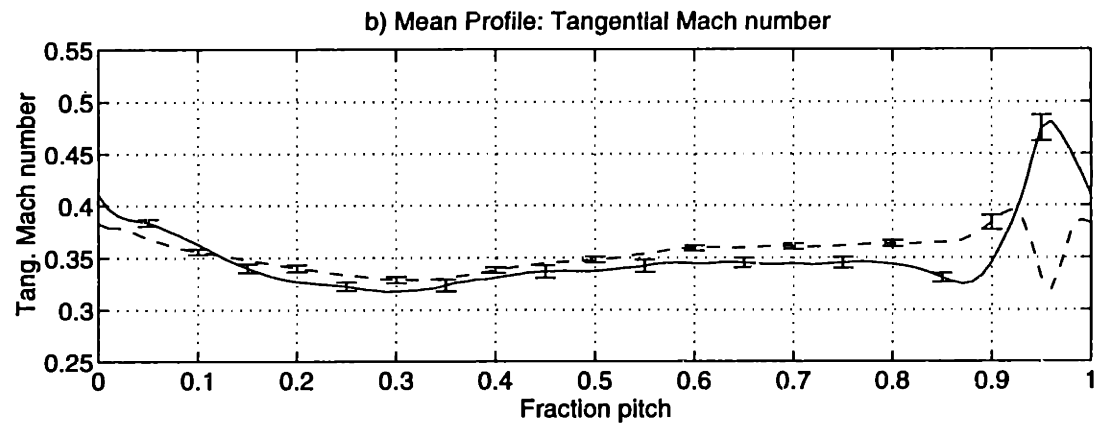

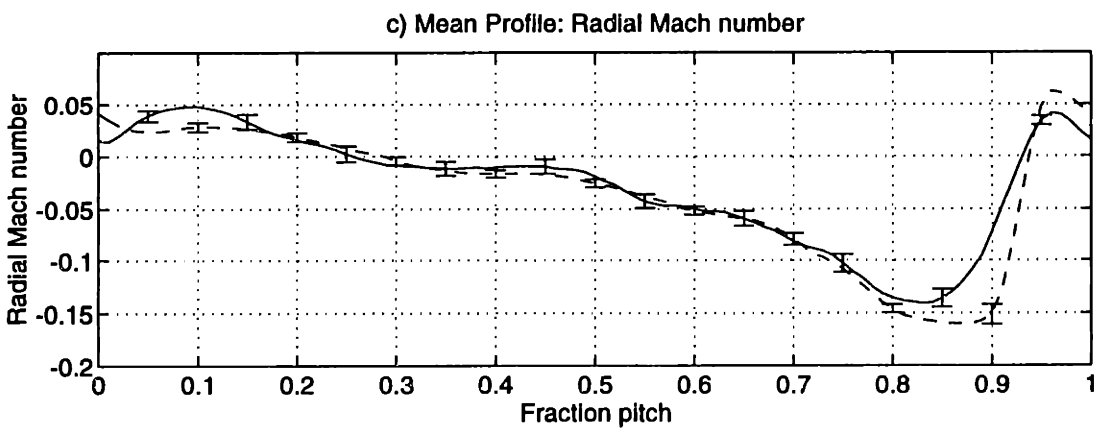

Figure E-23: 2.0% midspan weighted injection flow field data at 50% span, 0.1c: Mach number components

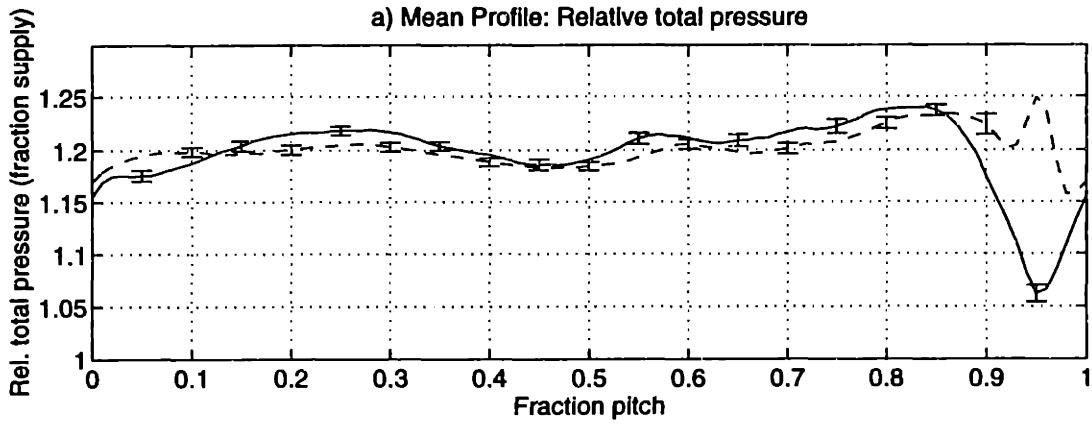

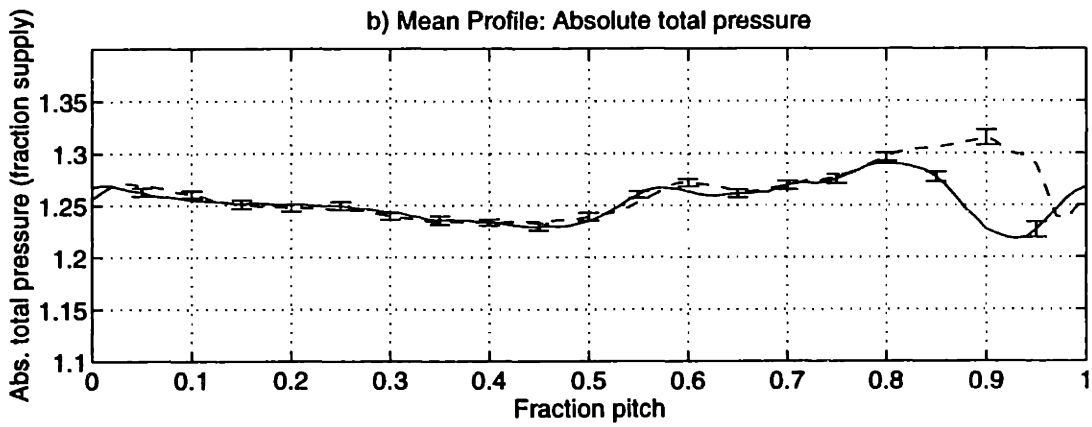

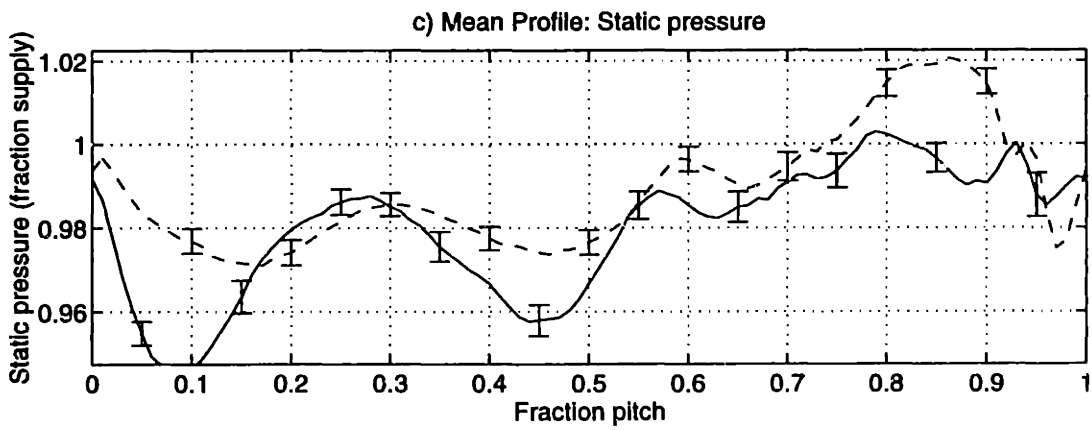

Figure E-24: 2.0% midspan weighted injection flow field data at 50% span, 0.1c: pressures

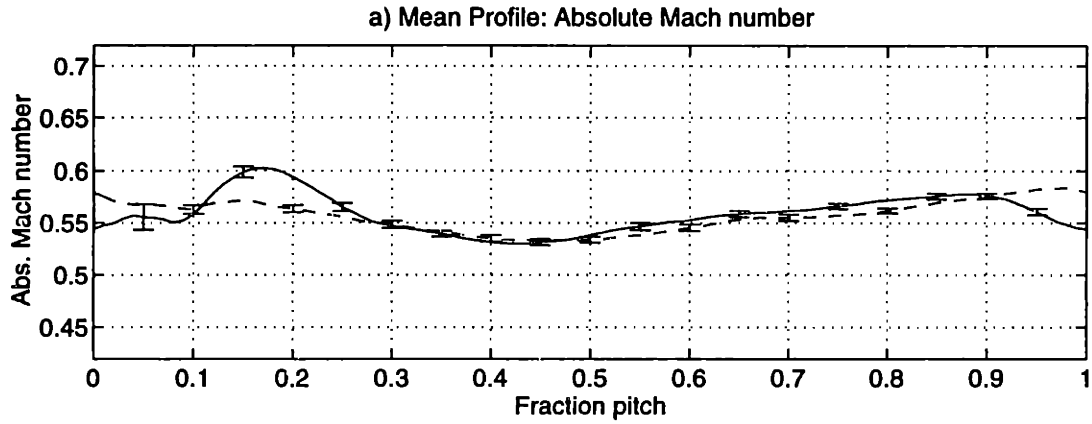

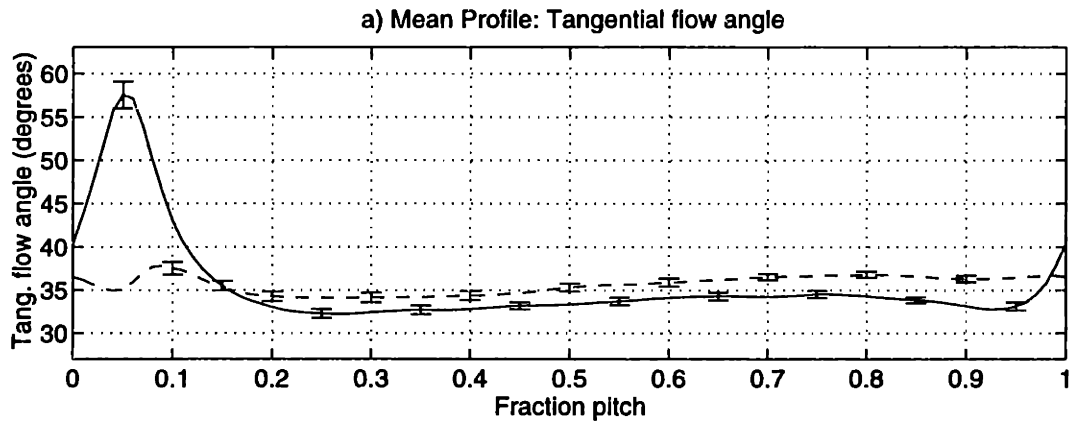

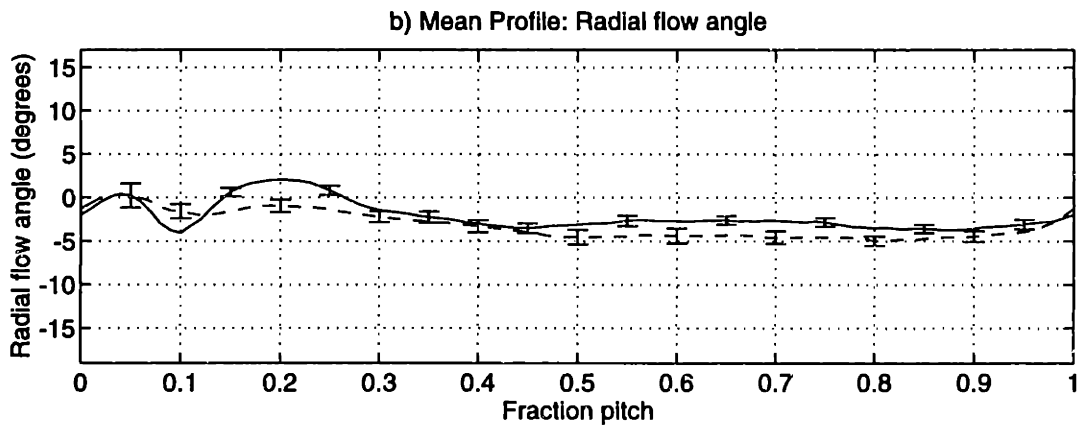

Figure E-25: 2.0% midspan weighted injection flow field data at 75% span, 0.1c: flow angles

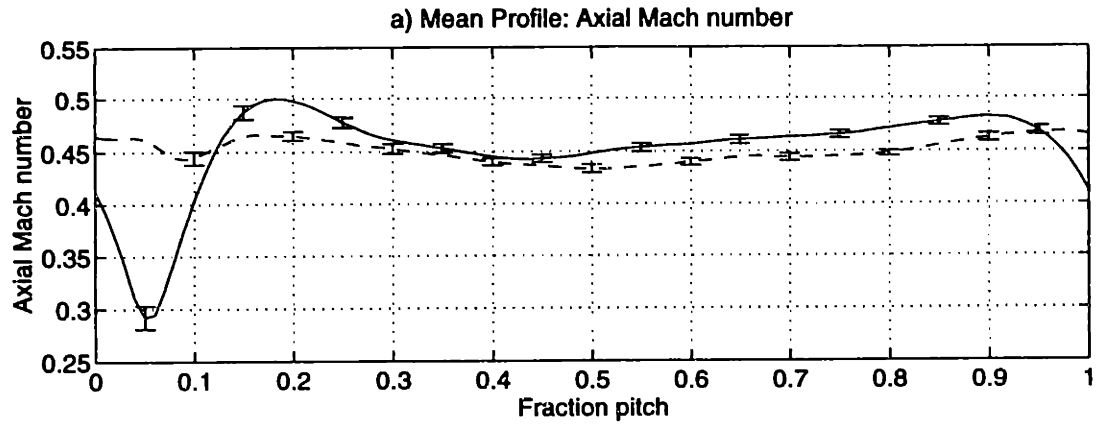

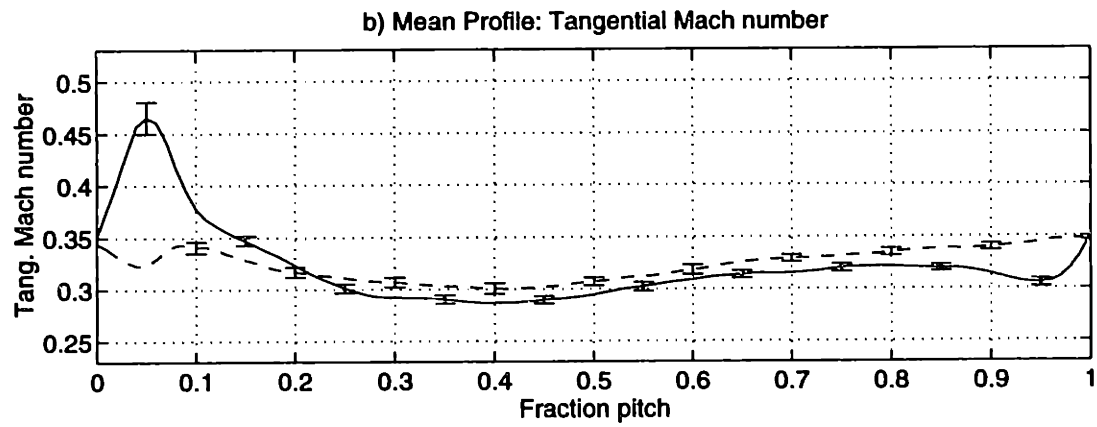

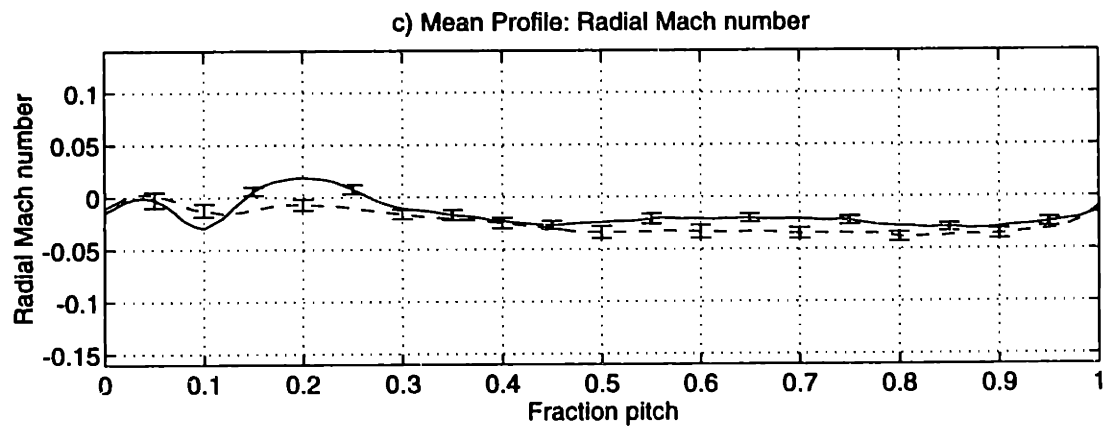

Figure E-26: 2.0% midspan weighted injection flow field data at 75% span, 0.1c: Mach number components

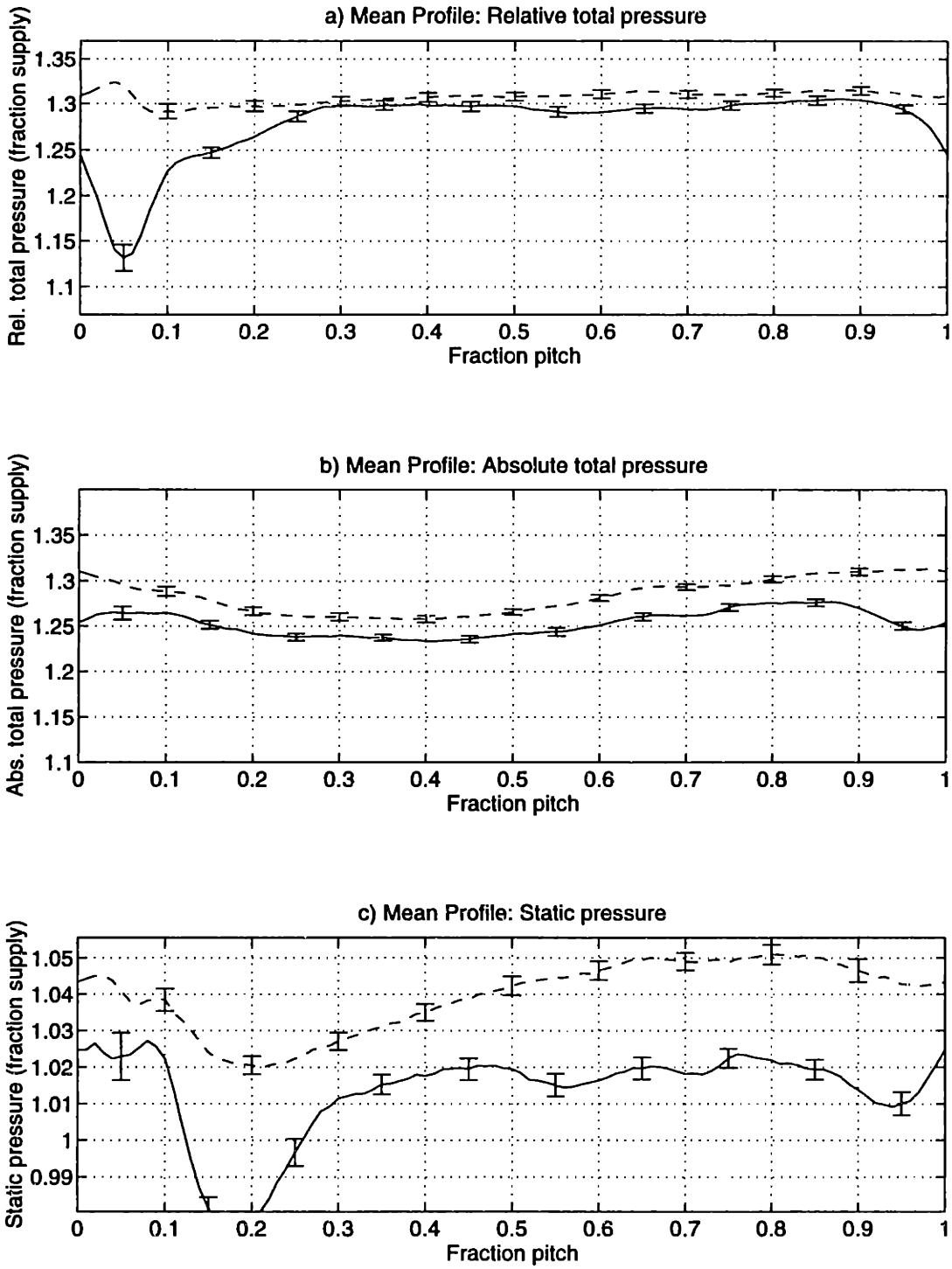

Figure E-27: 2.0% midspan weighted injection flow field data at 75% span, 0.1c: pressures

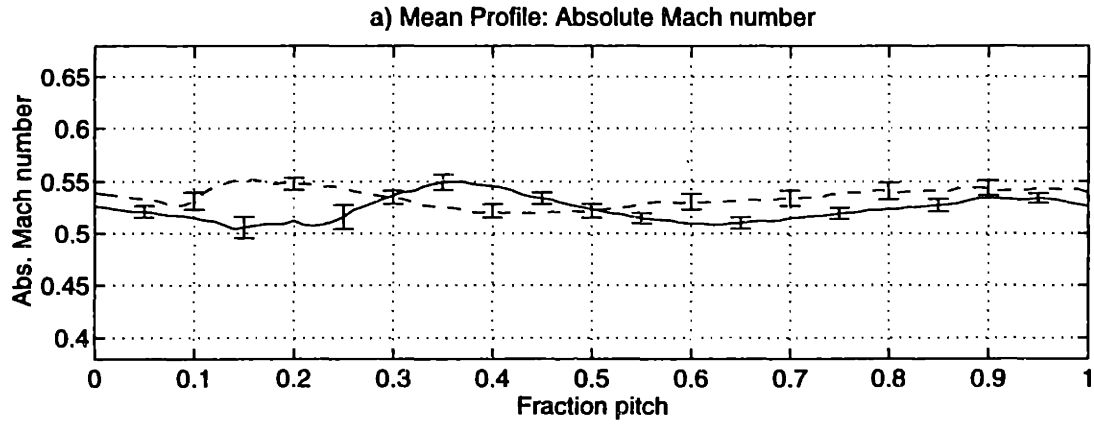

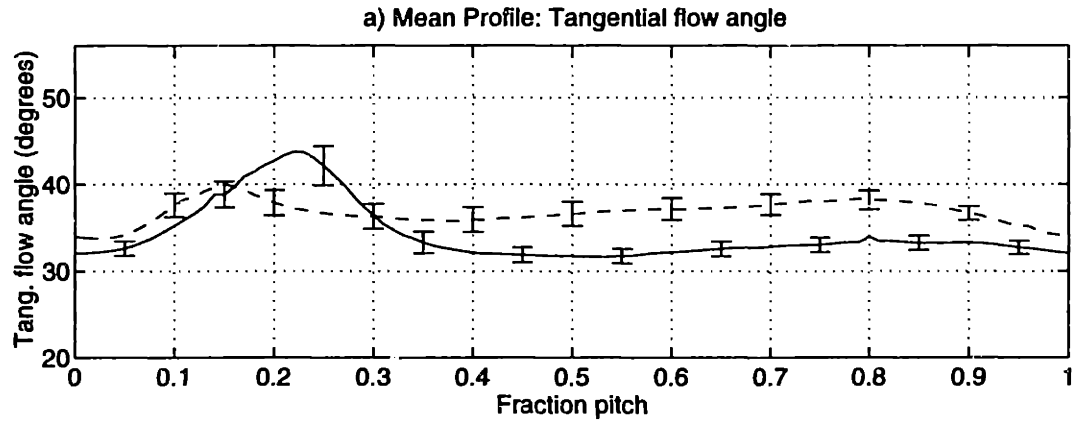

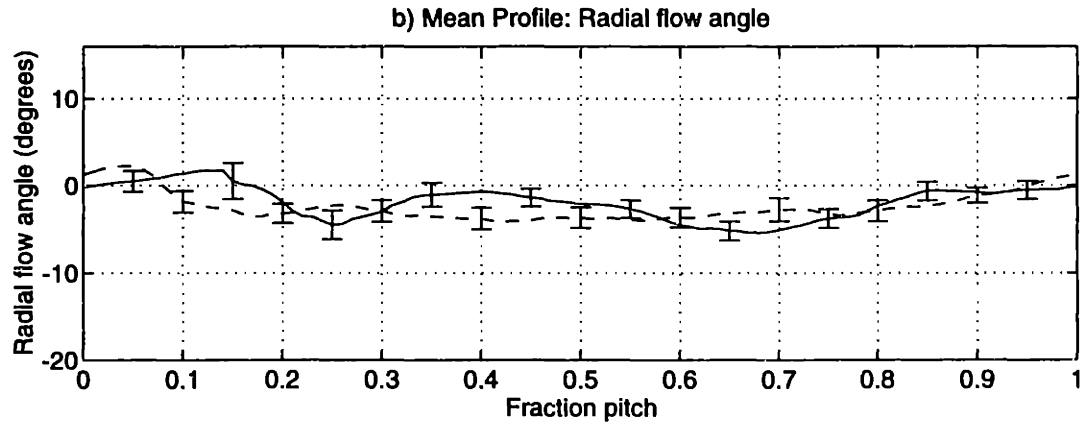

Figure E-28: 2.0% midspan weighted injection flow field data at 87.5% span, 0.1c: flow angles

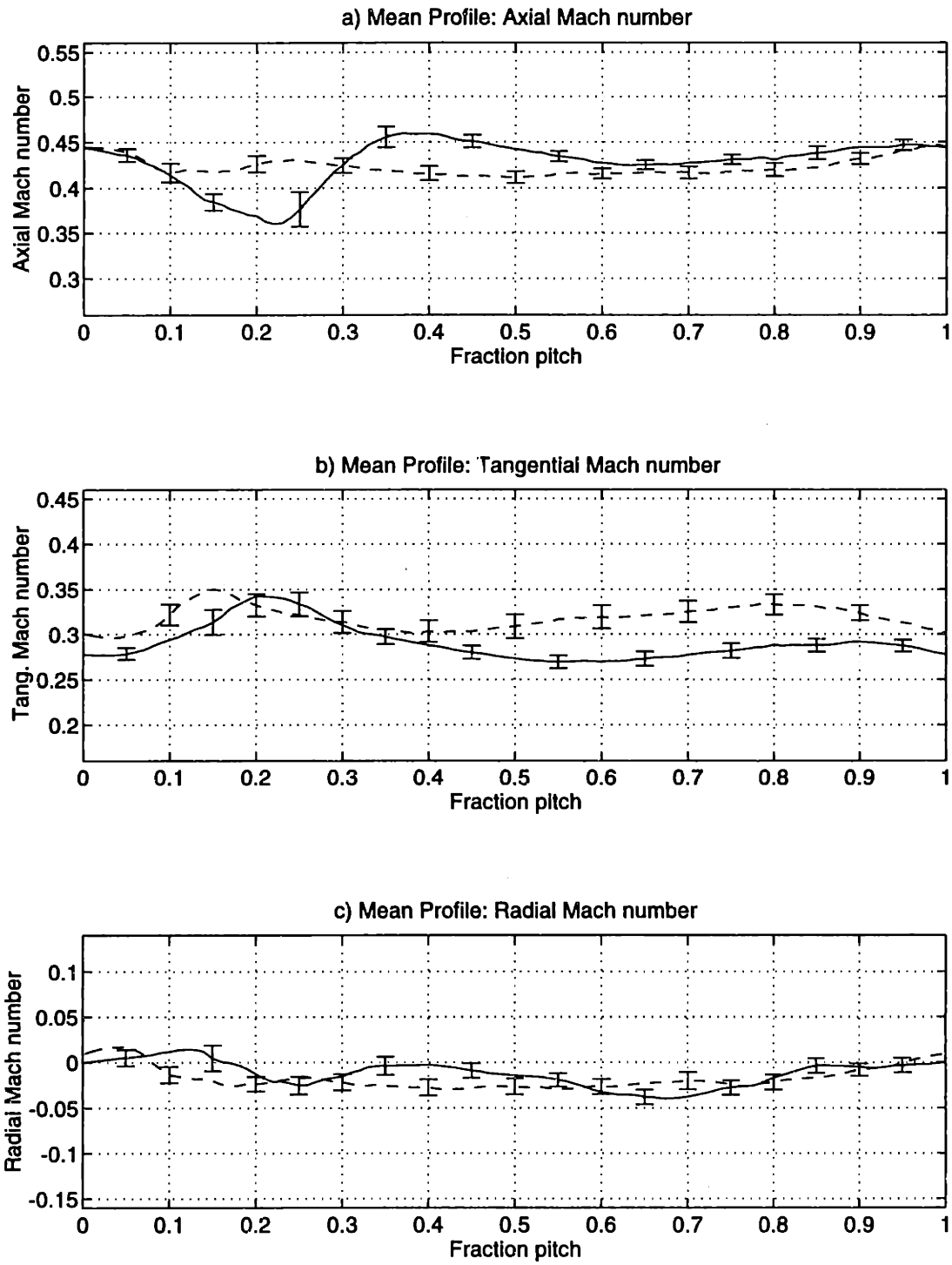

Figure E-29: 2.0% midspan weighted injection flow field data at 87.5% span, 0.1c: Mach number components

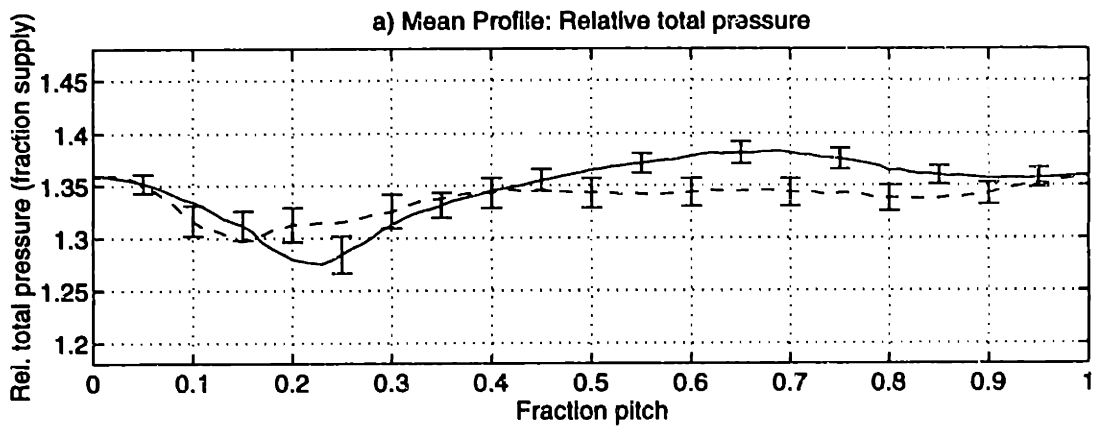

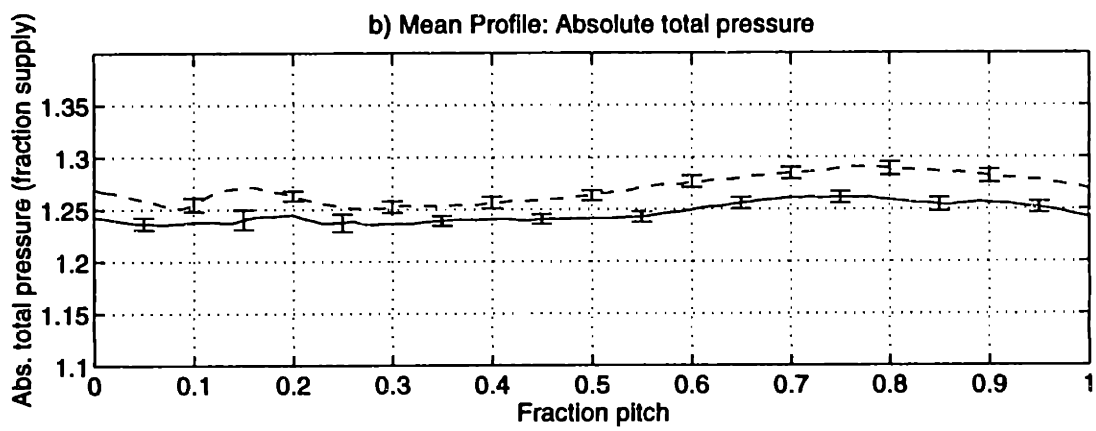

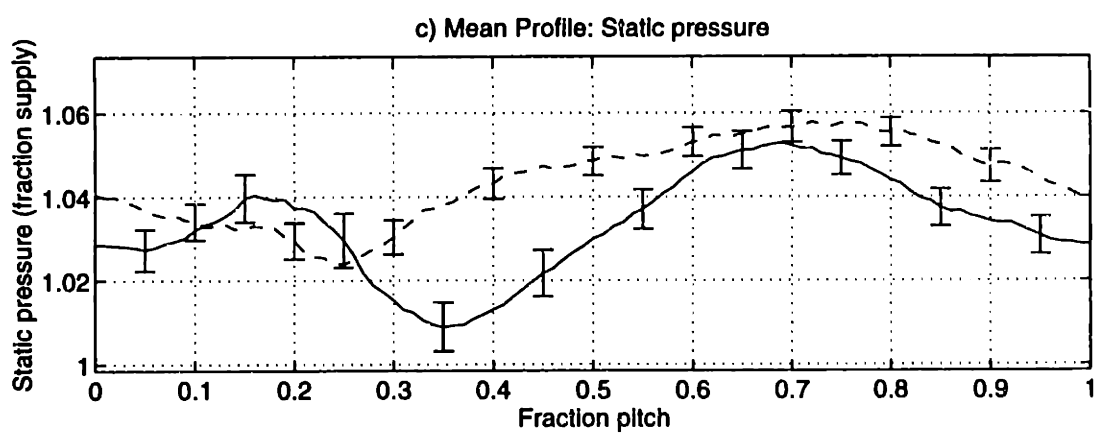

Figure E-30: 2.0% midspan weighted injection flow field data at 87.5% span, 0.1c: pressures

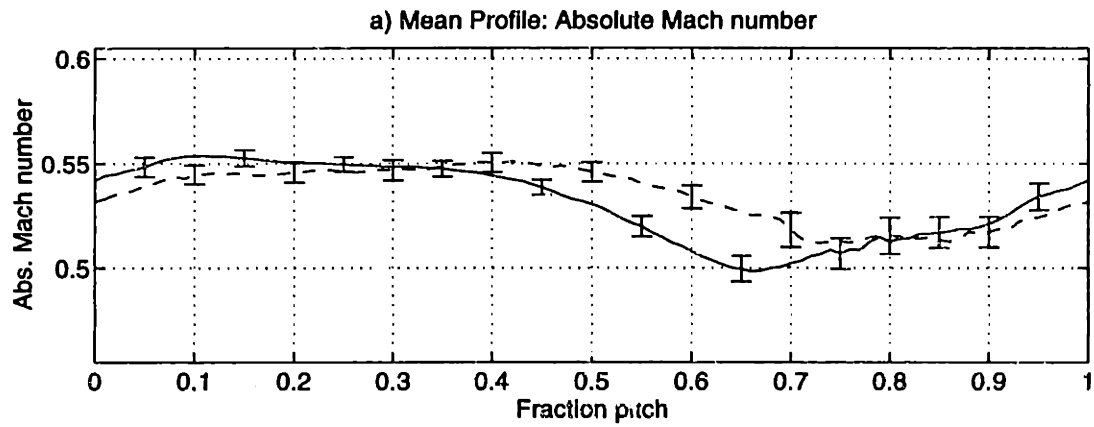

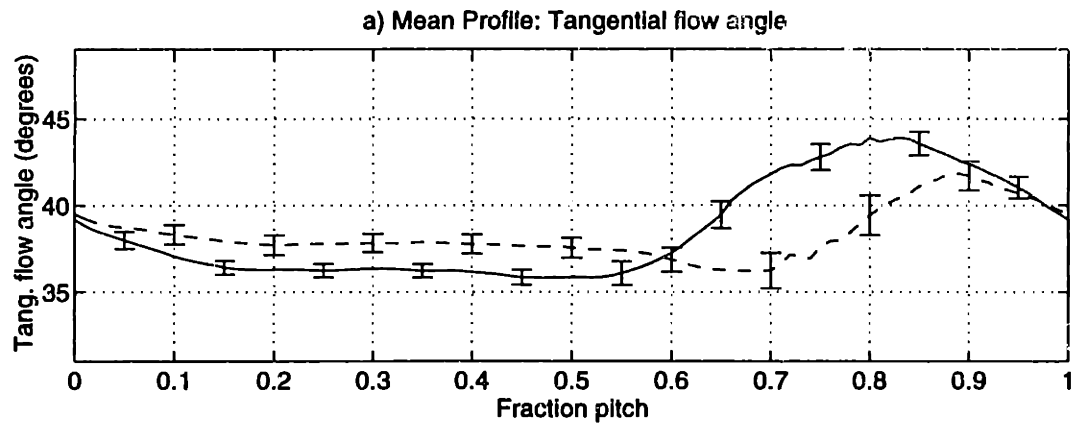

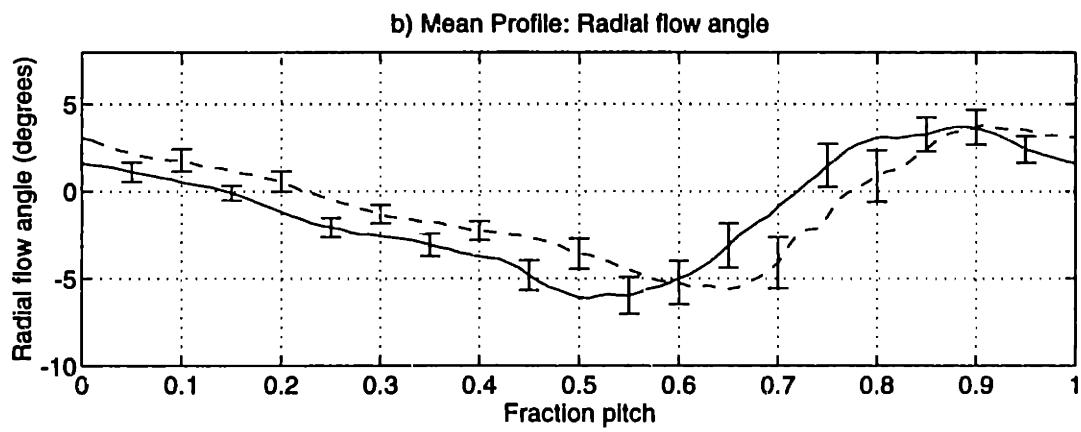

Figure E-31: 2.0% midspan weighted injection flow field data at 25% span, 1.5c: flow angles

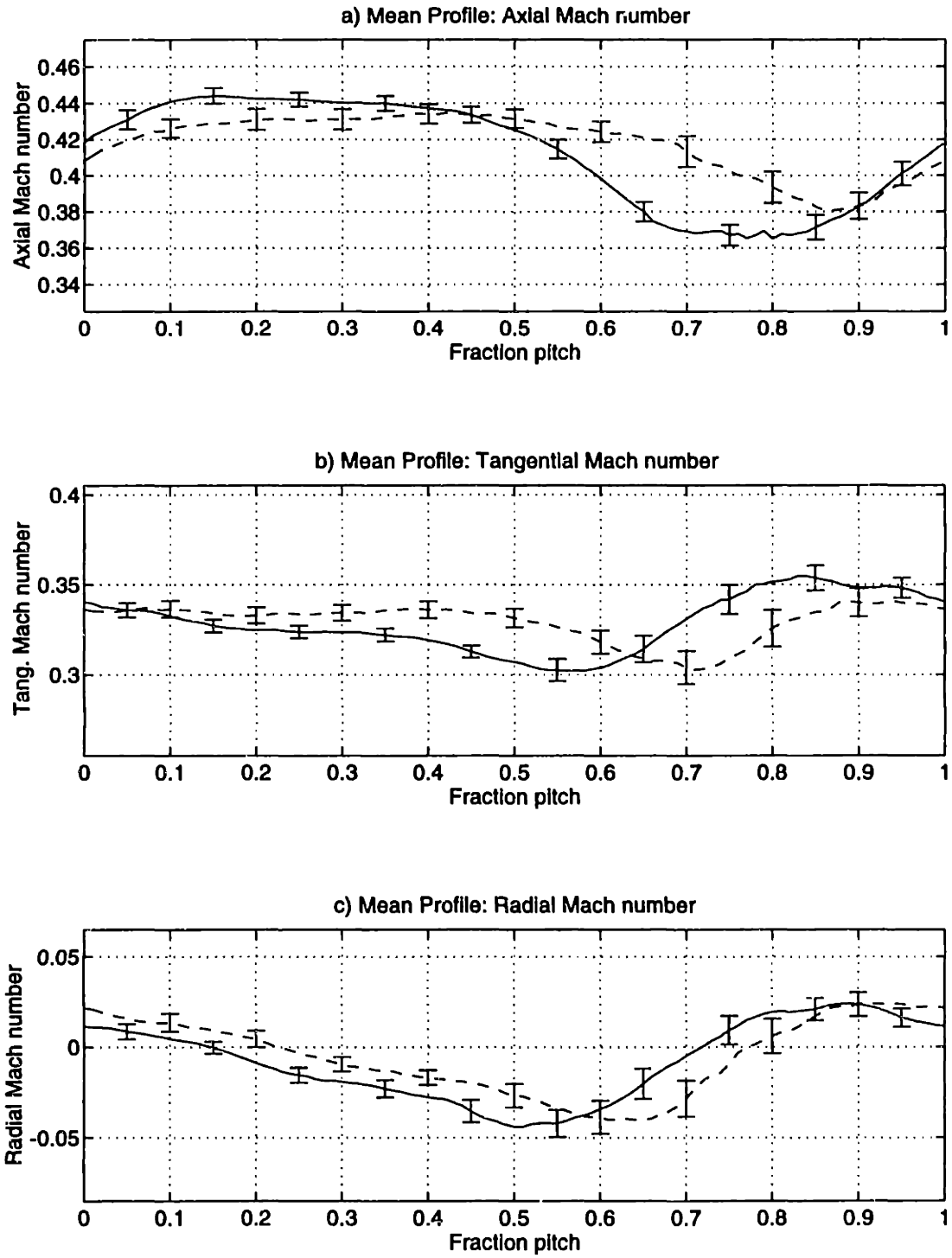

Figure E-32: 2.0% midspan weighted injection flow field data at 25% span, 1.5c: Mach number components

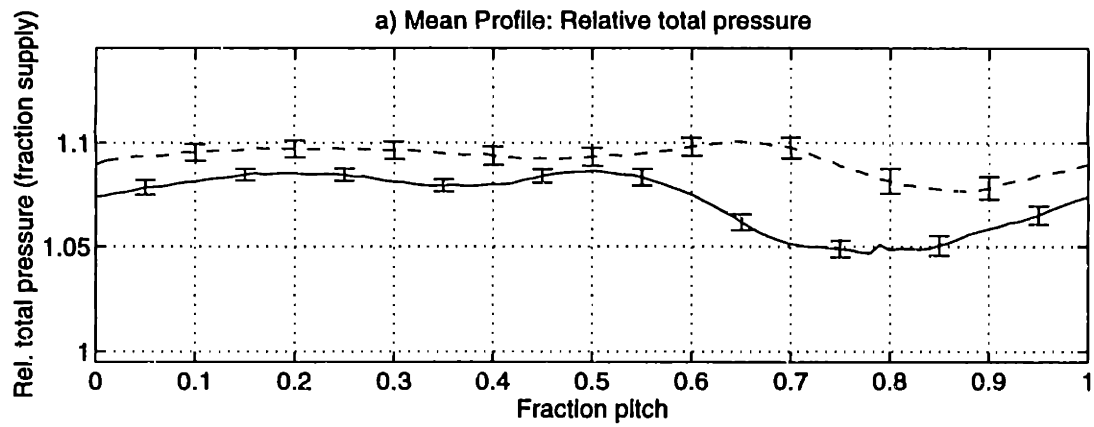

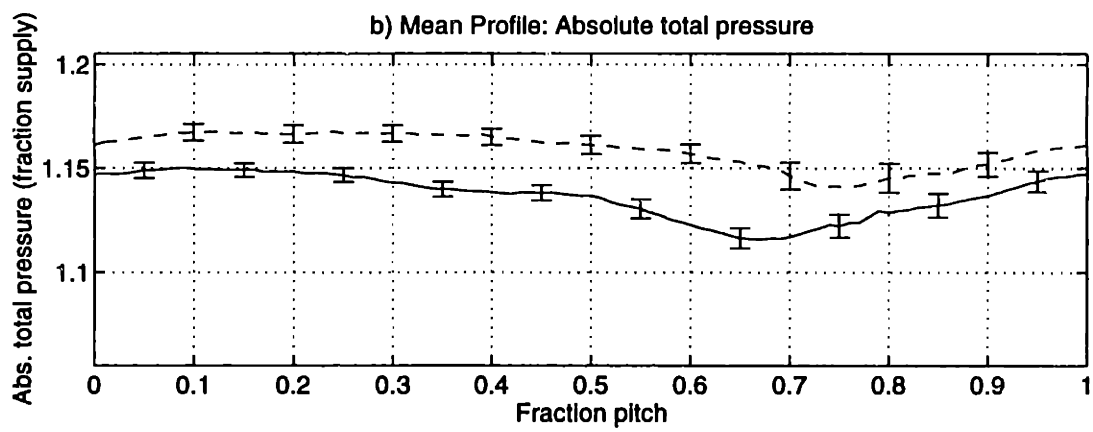

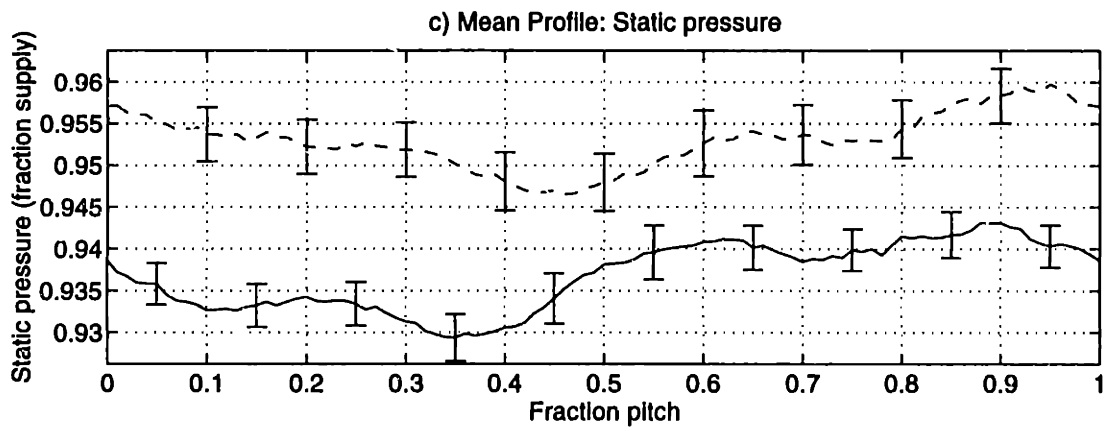

Figure E-33: 2.0% midspan weighted injection flow field data at 25% span, 1.5c: pressures

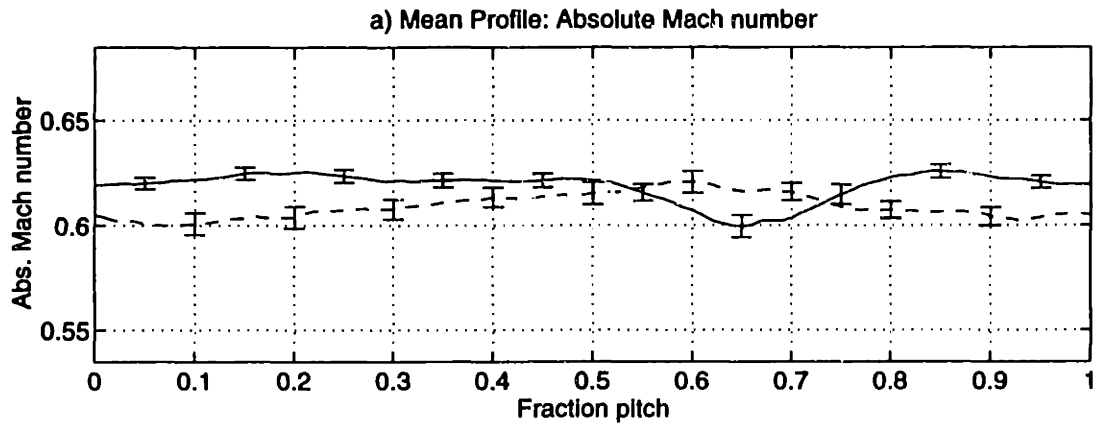

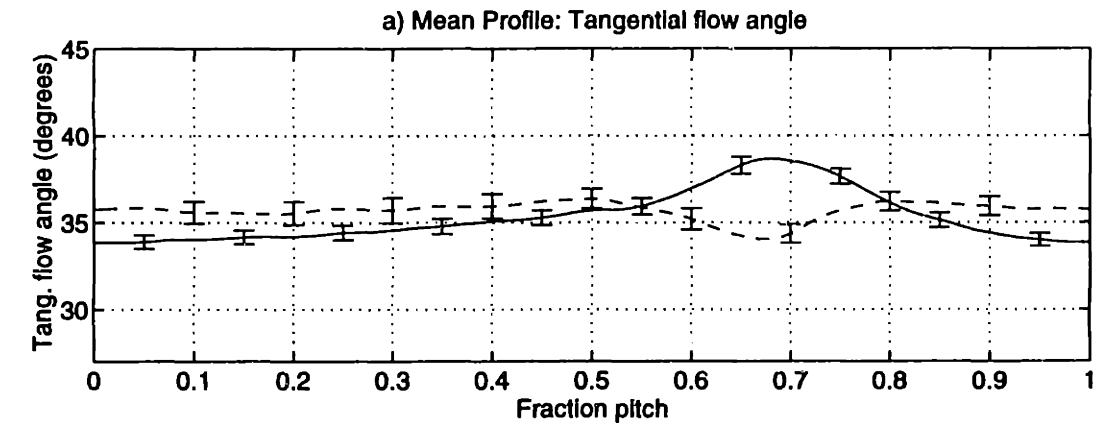

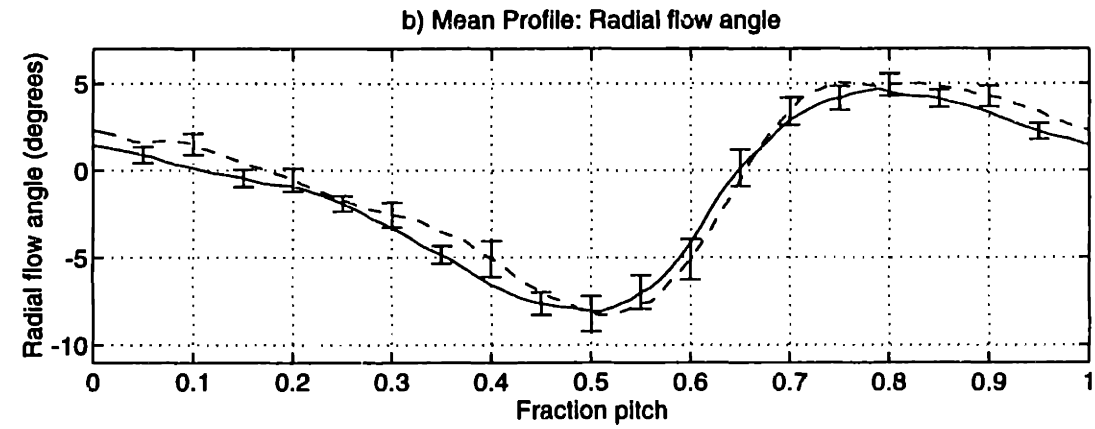

Figure E-34: 2.0% midspan weighted injection flow field data at 50% span, 1.5c: flow angles

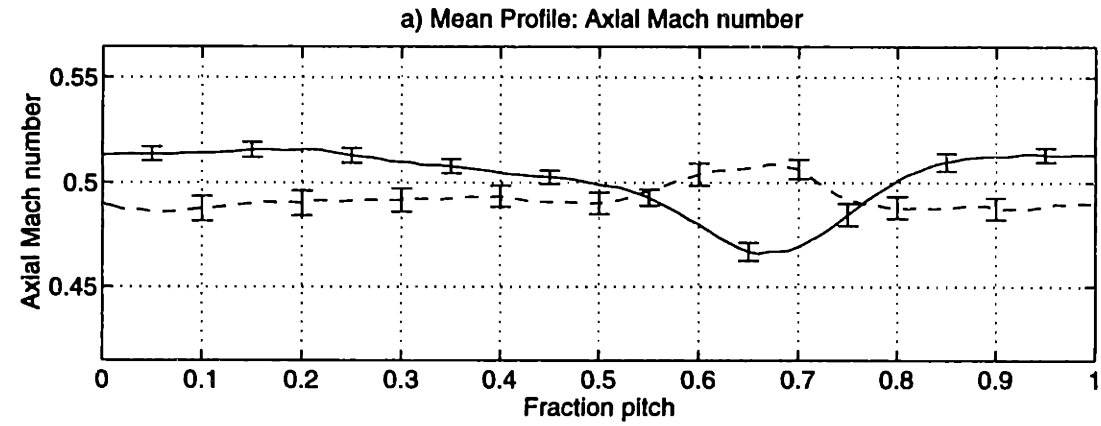

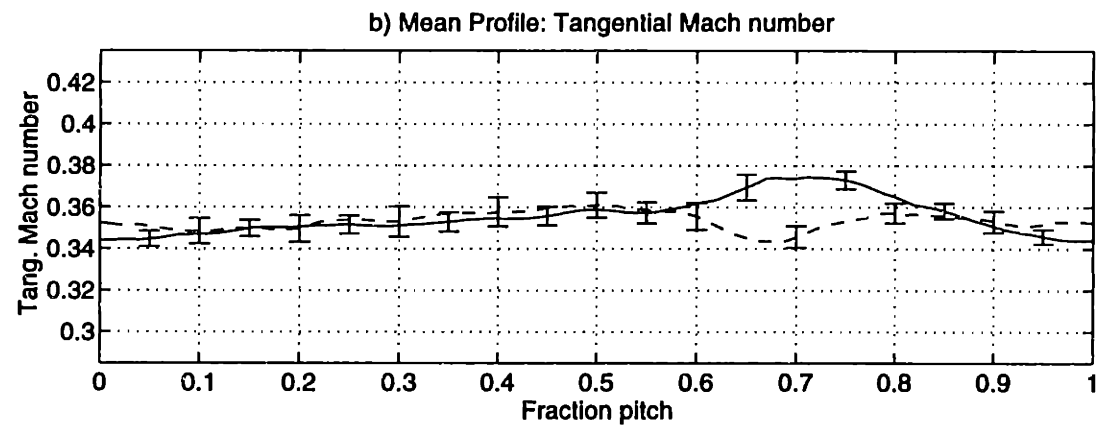

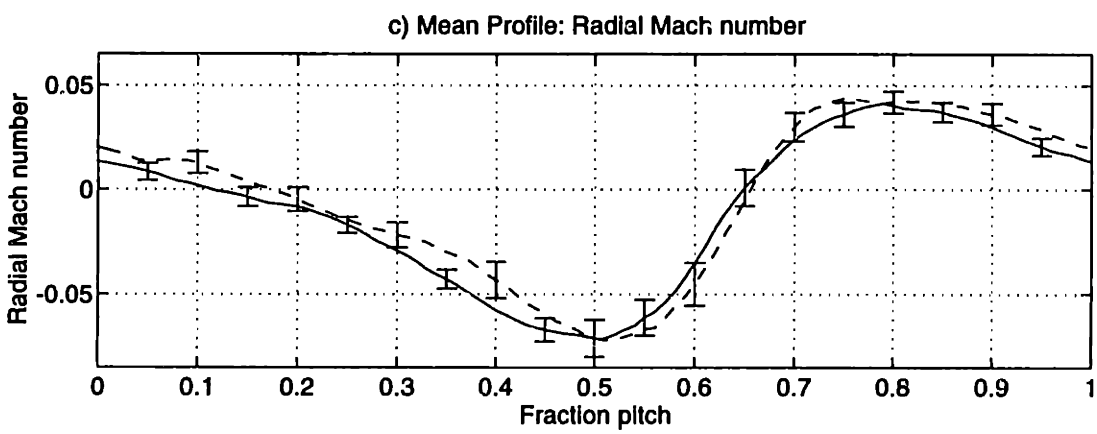

Figure E-35: 2.0% midspan weighted injection flow field data at 50% span, 1.5c: Mach number components

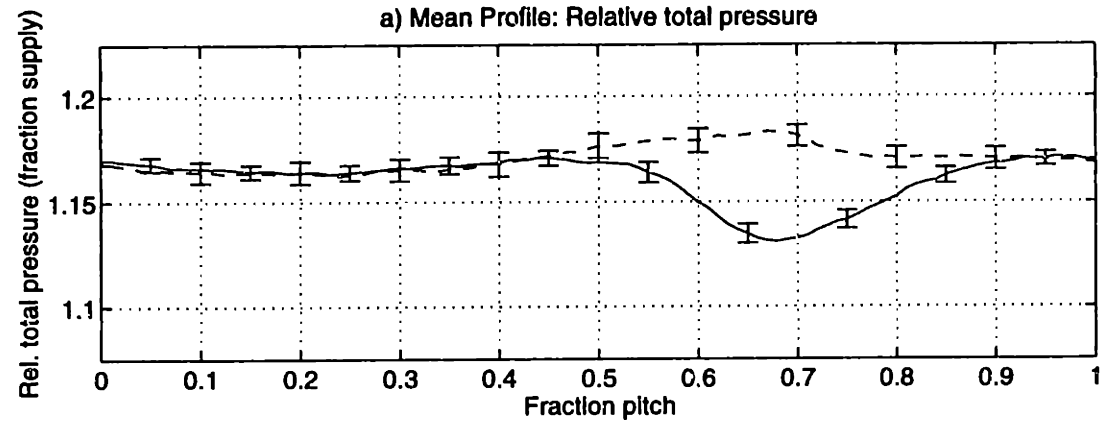

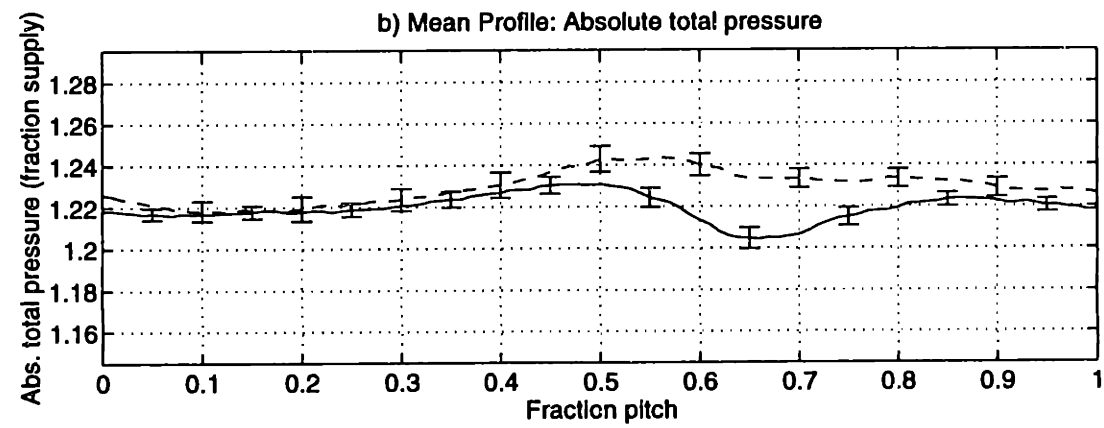

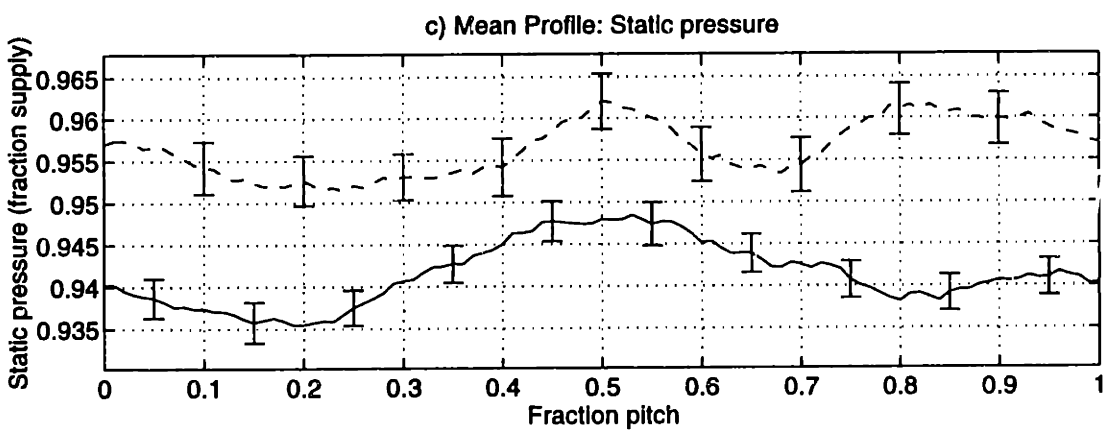

Figure E-36: 2.0% midspan weighted injection flow field data at 50% span, 1.5c: pressures

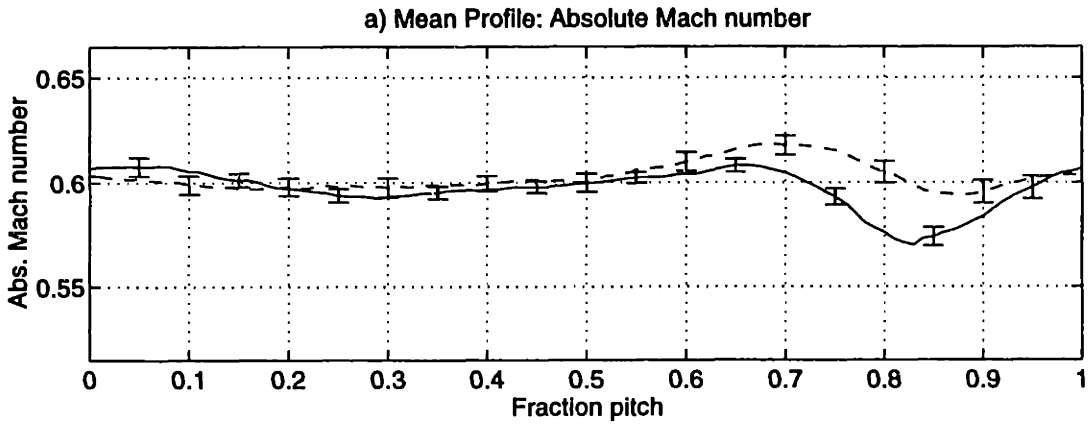

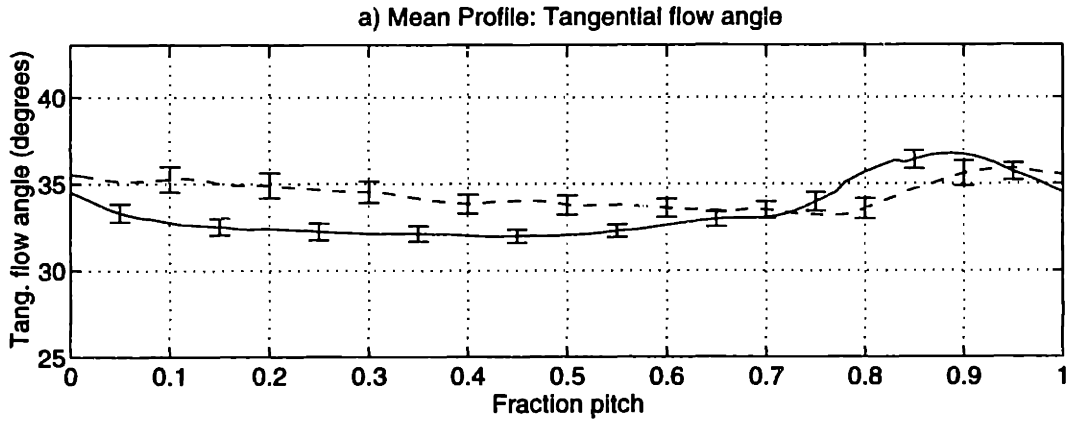

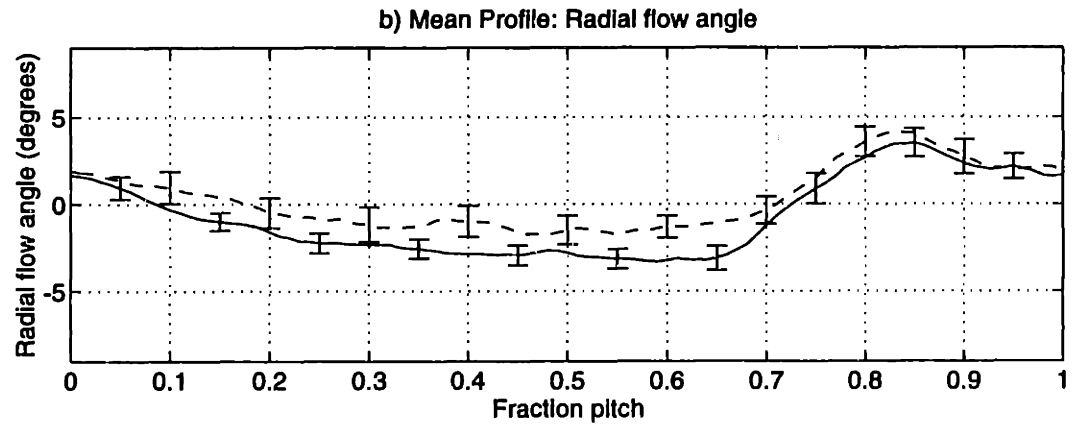

Figure E-37: 2.0% midspan weighted injection flow field data at 75% span, 1.5c: flow angles

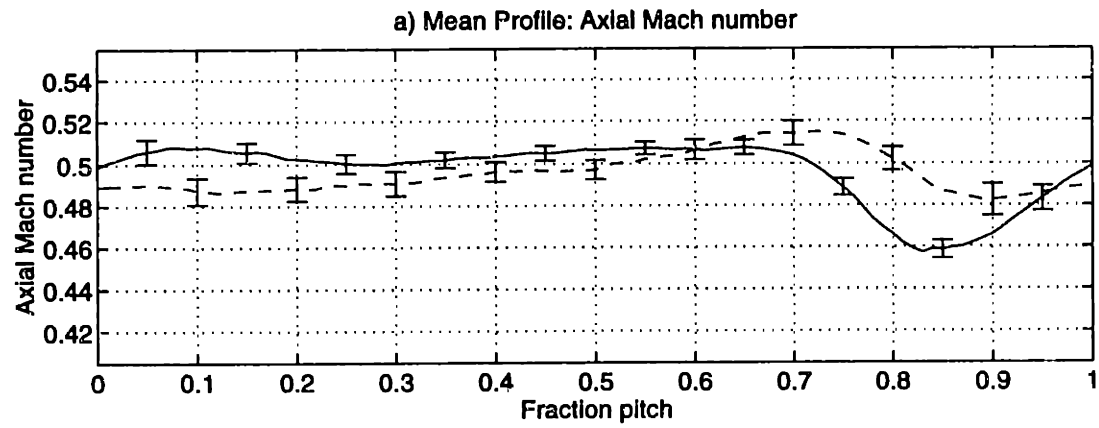

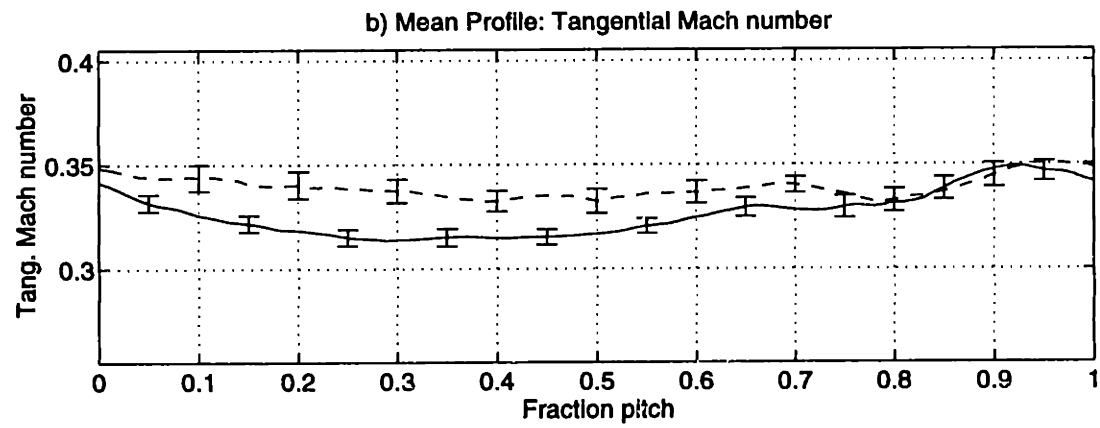

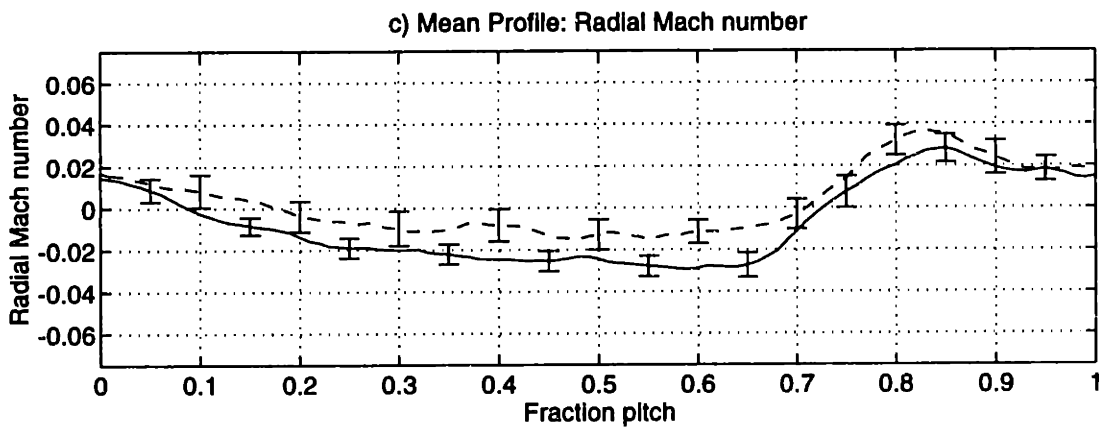

Figure E-38: 2.0% midspan weighted injection flow field data at 75% span, 1.5c: Mach number components

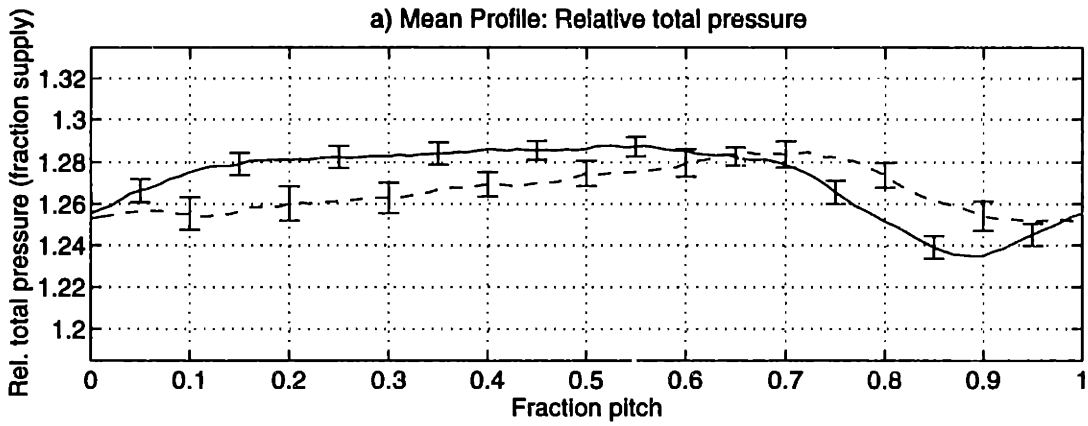

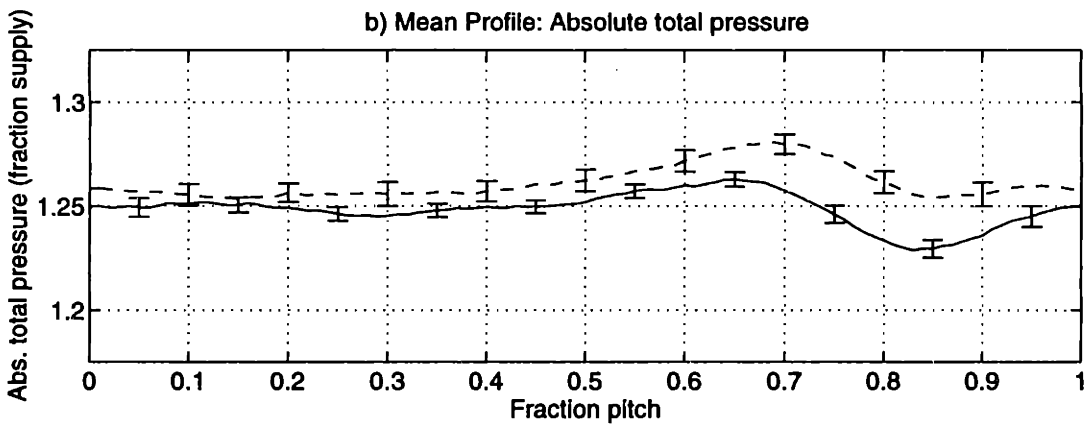

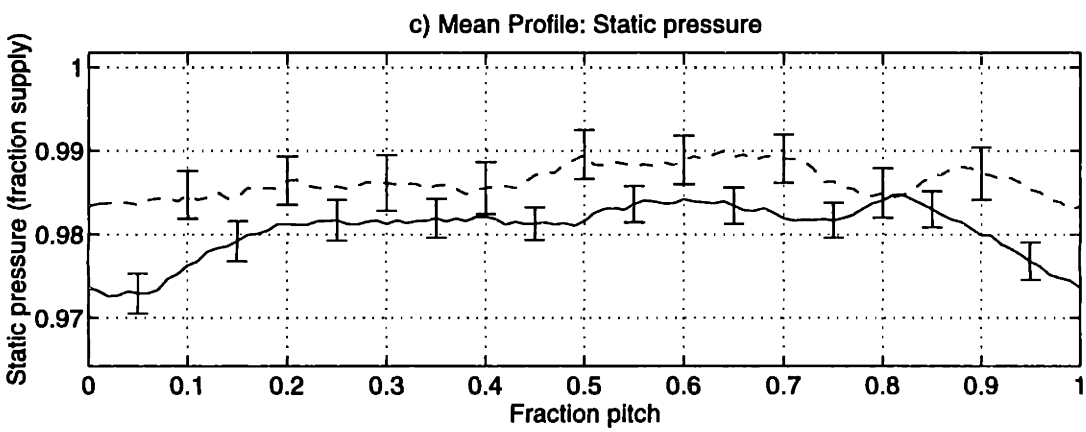

Figure E-39: 2.0% midspan weighted injection flow field data at 75% span, 1.5c: pressures

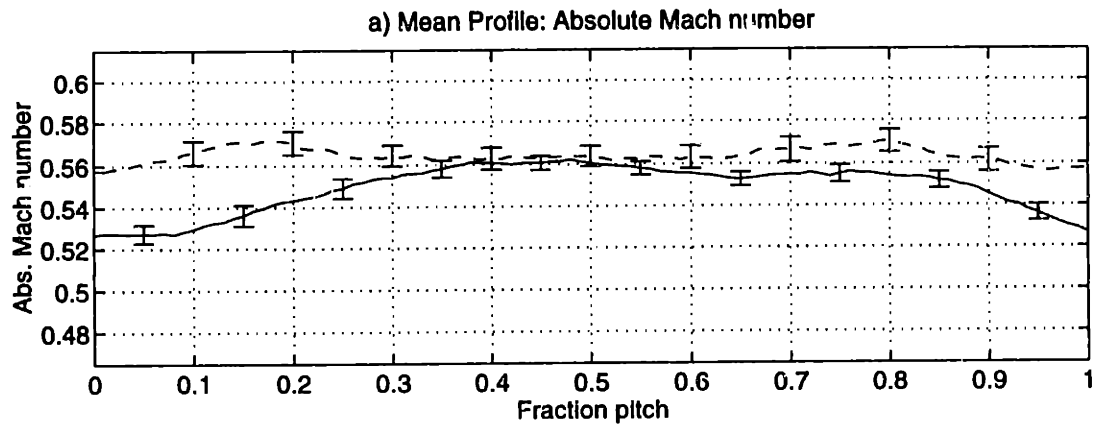

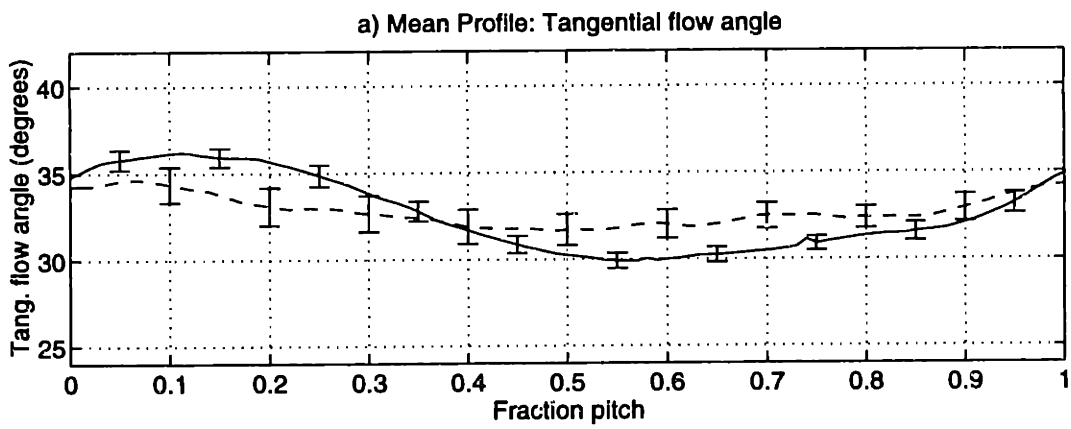

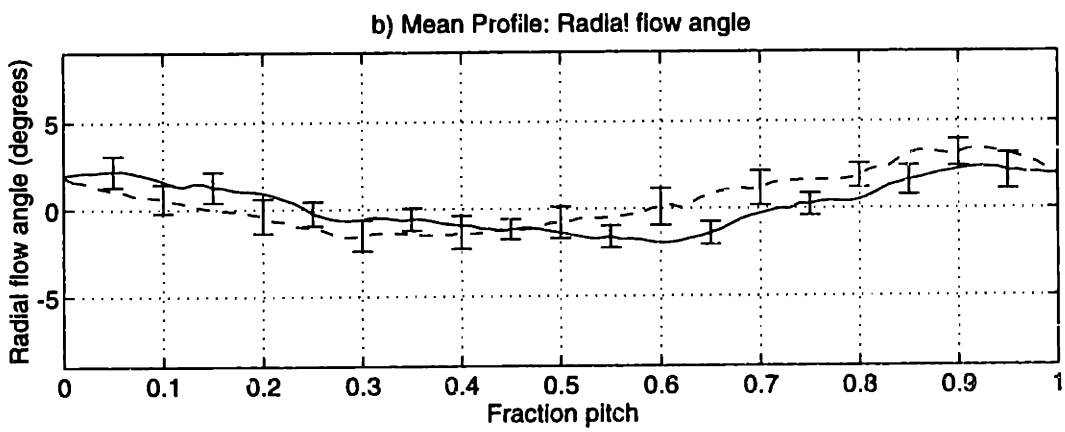

Figure E-40: 2.0% midspan weighted injection flow field data at 87.5% span, 1.5c: flow angles

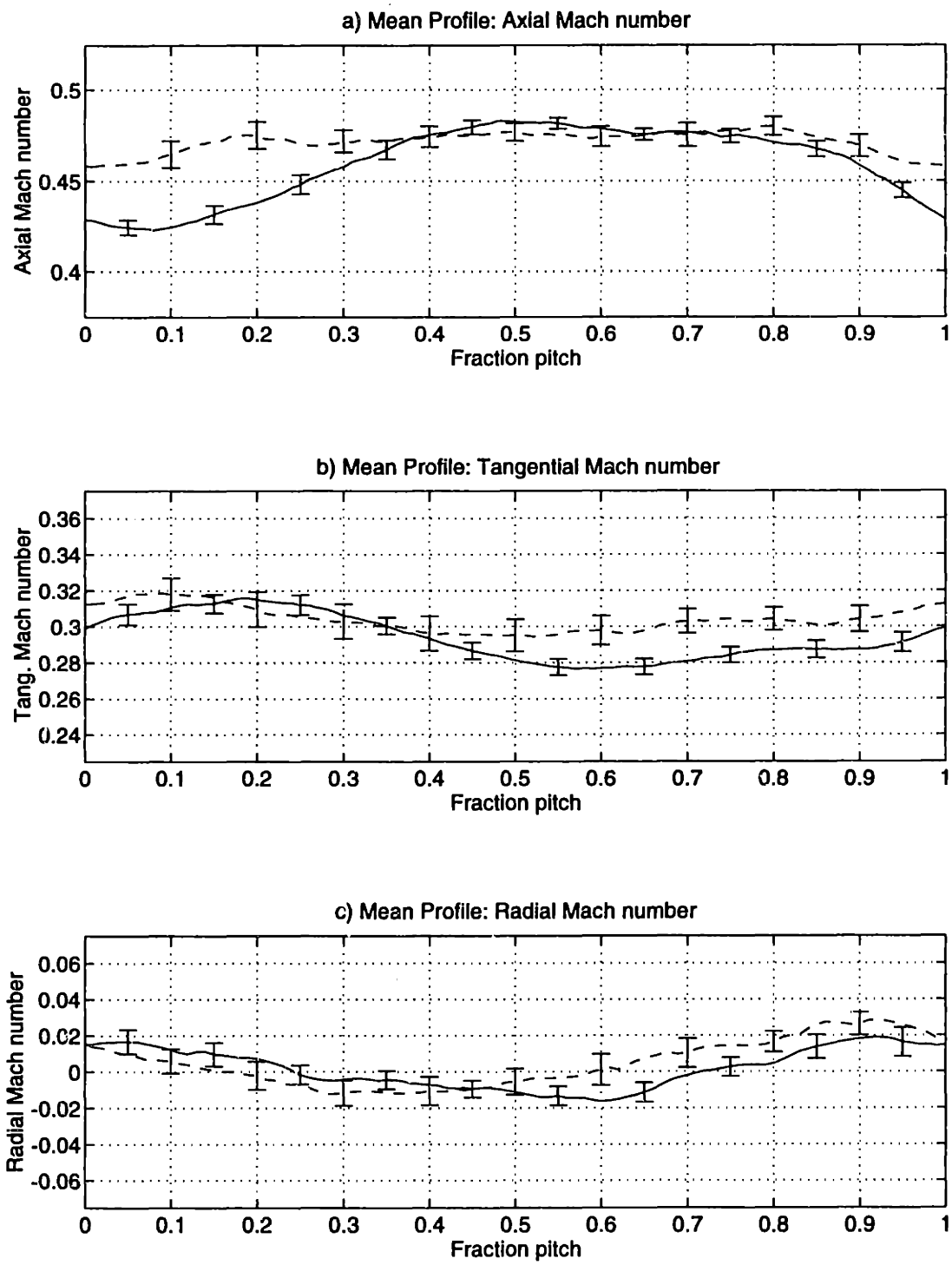

Figure E-41: 2.0% midspan weighted injection flow field data at 87.5% span, 1.5c: Mach number components

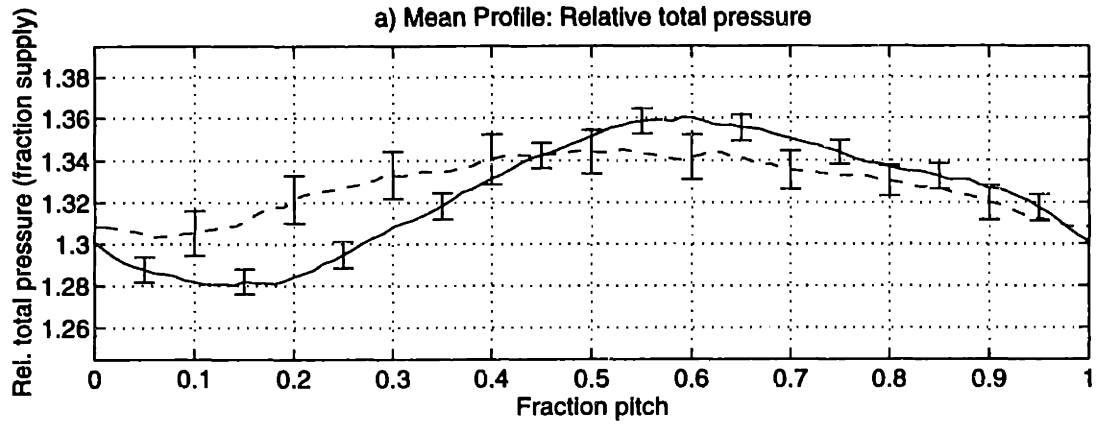

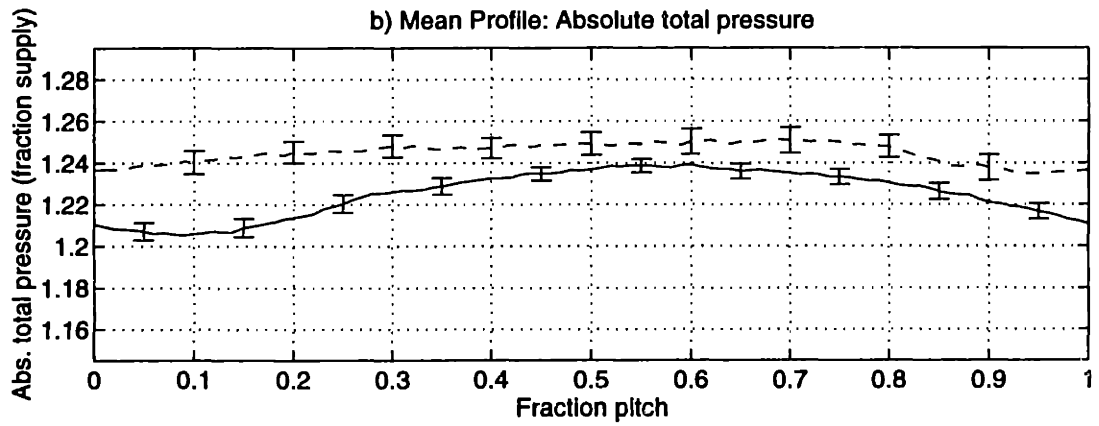

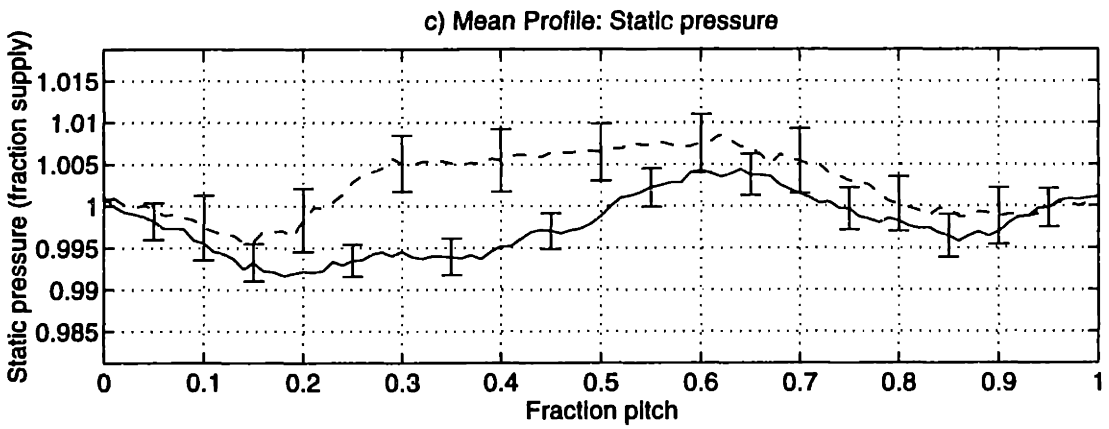

Figure E-42: 2.0% midspan weighted injection flow field data at 87.5% span, 1.5c: pressures

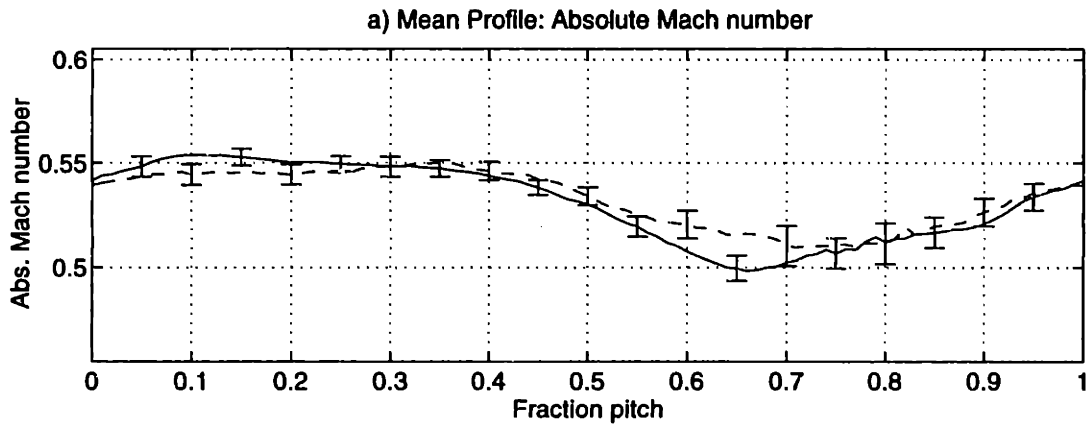

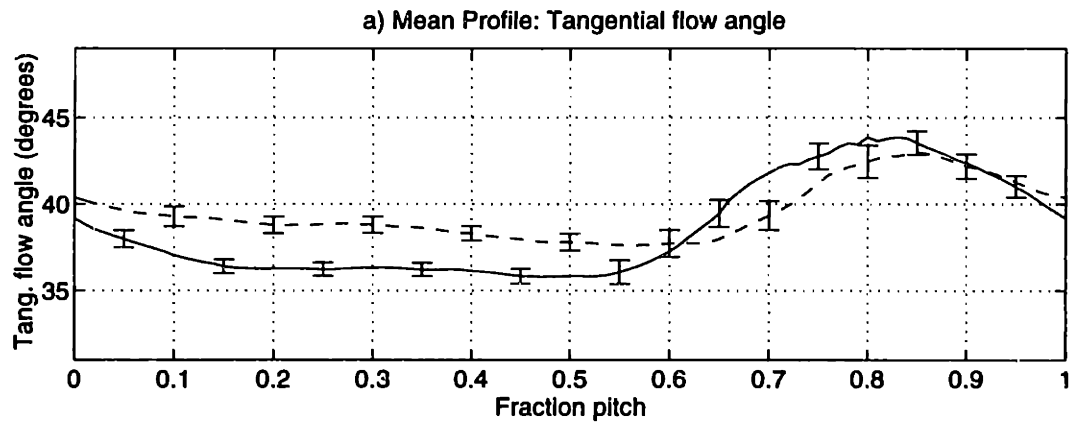

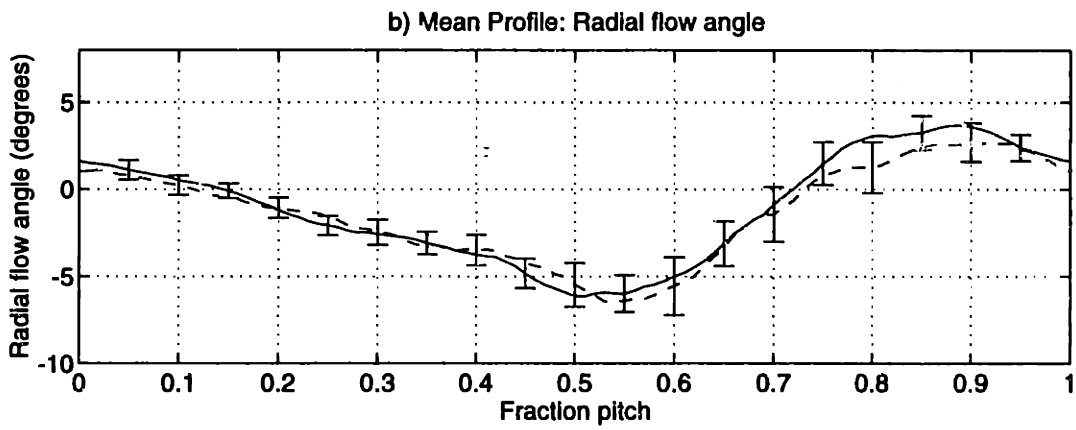

Figure E-43: 1.8% midspan weighted injection flow field data at 25% span, 1.5c: flow angles

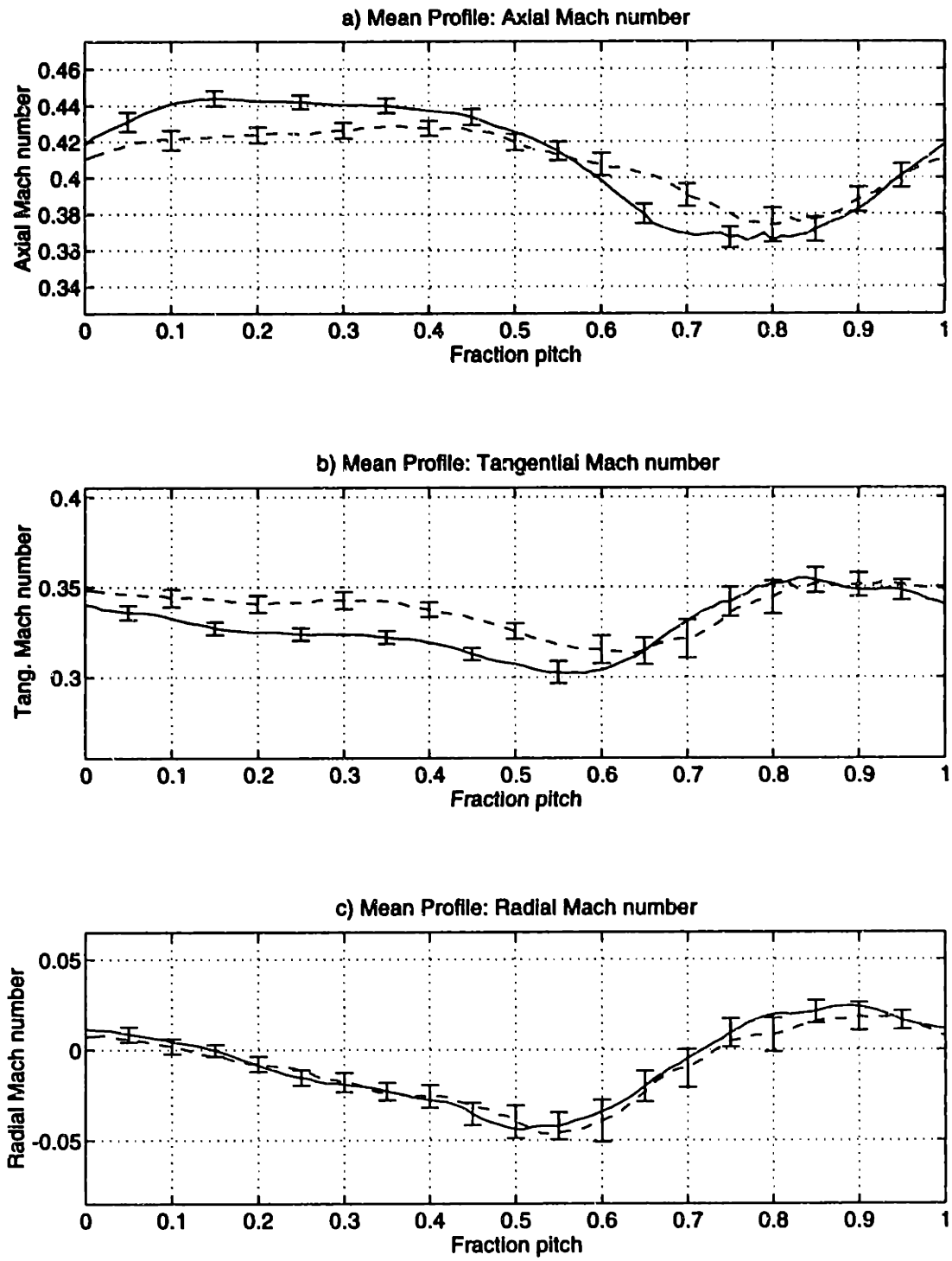

Figure E-44: 1.8% midspan weighted injection flow field data at 25% span, 1.5c: Mach number components

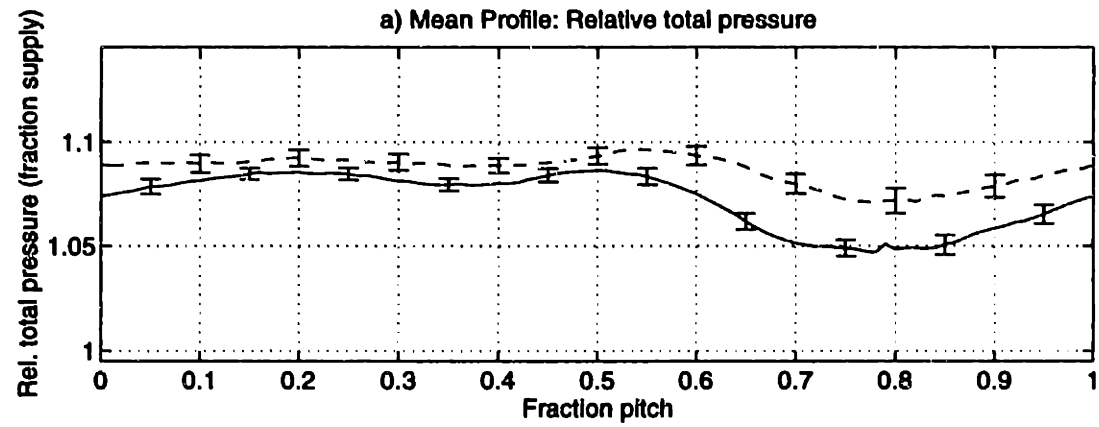

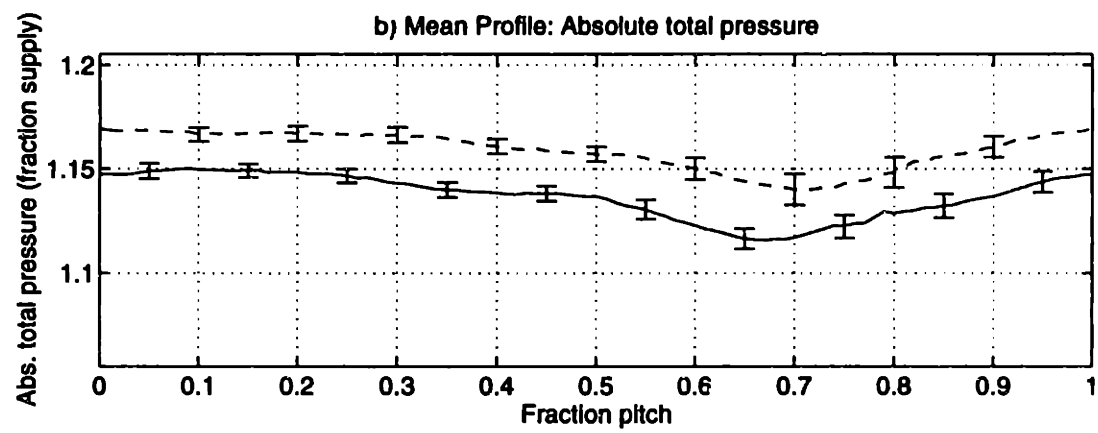

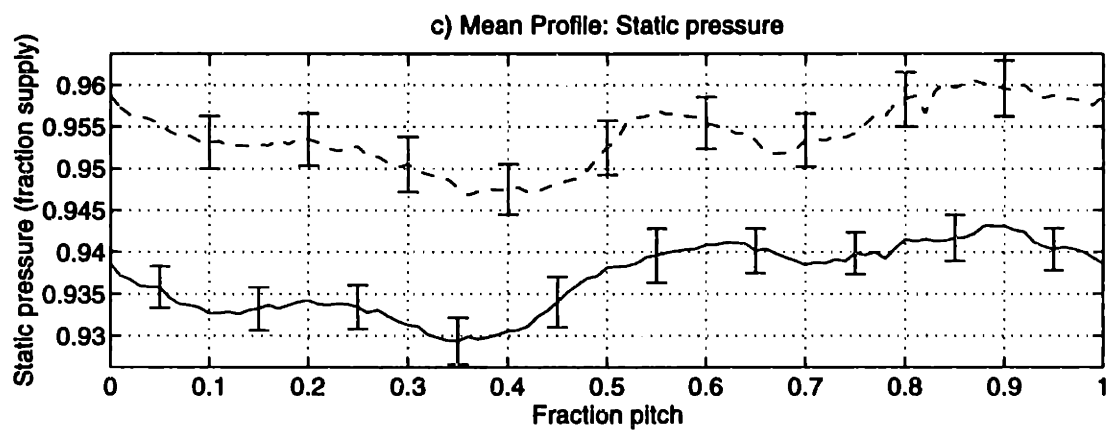

Figure E-45: 1.8% midspan weighted injection flow field data at 25% span, 1.5c: pressures

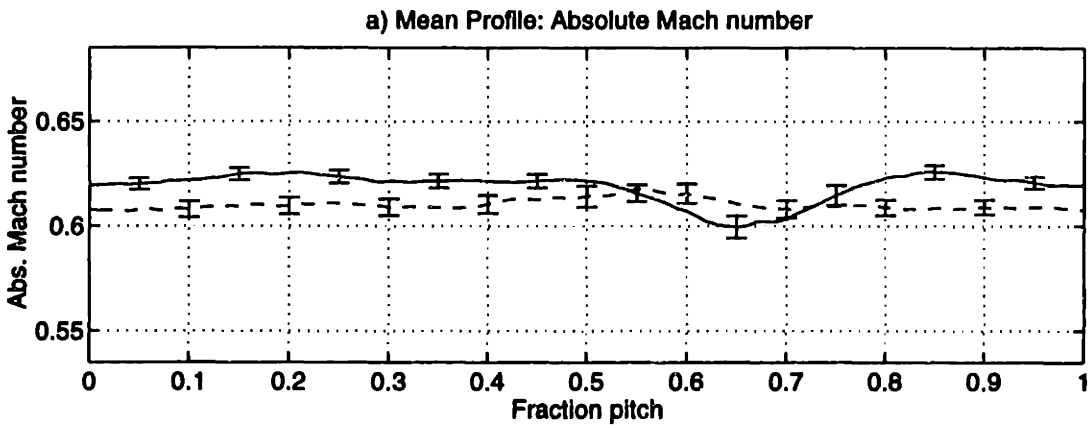

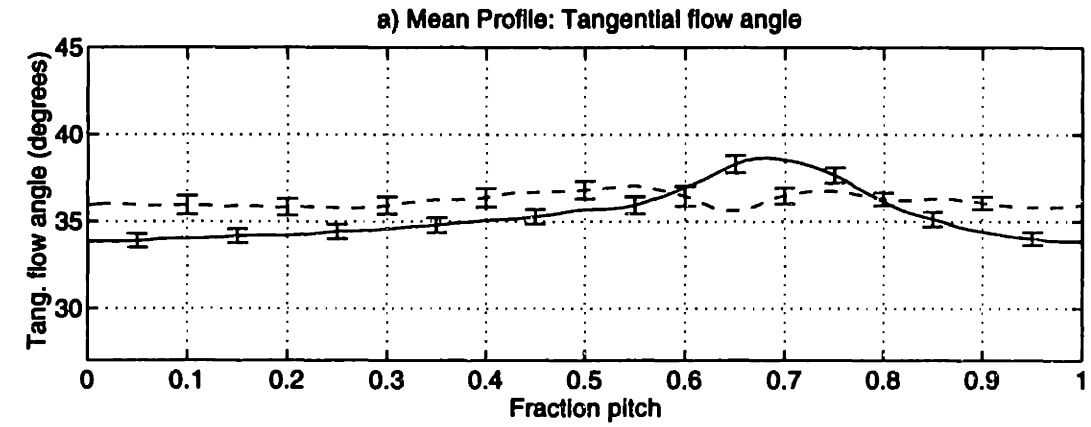

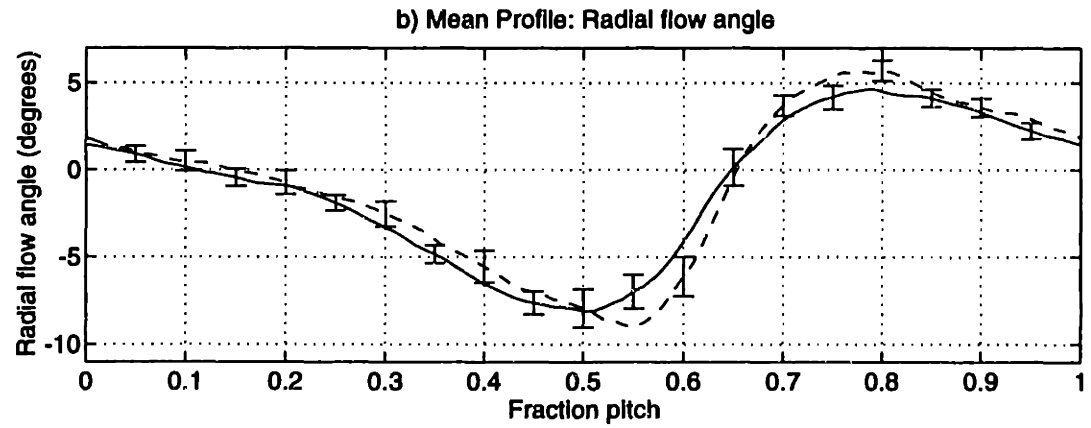

Figure E-46: 1.8% midspan weighted injection flow field data at 50% span, 1.5c: flow angles

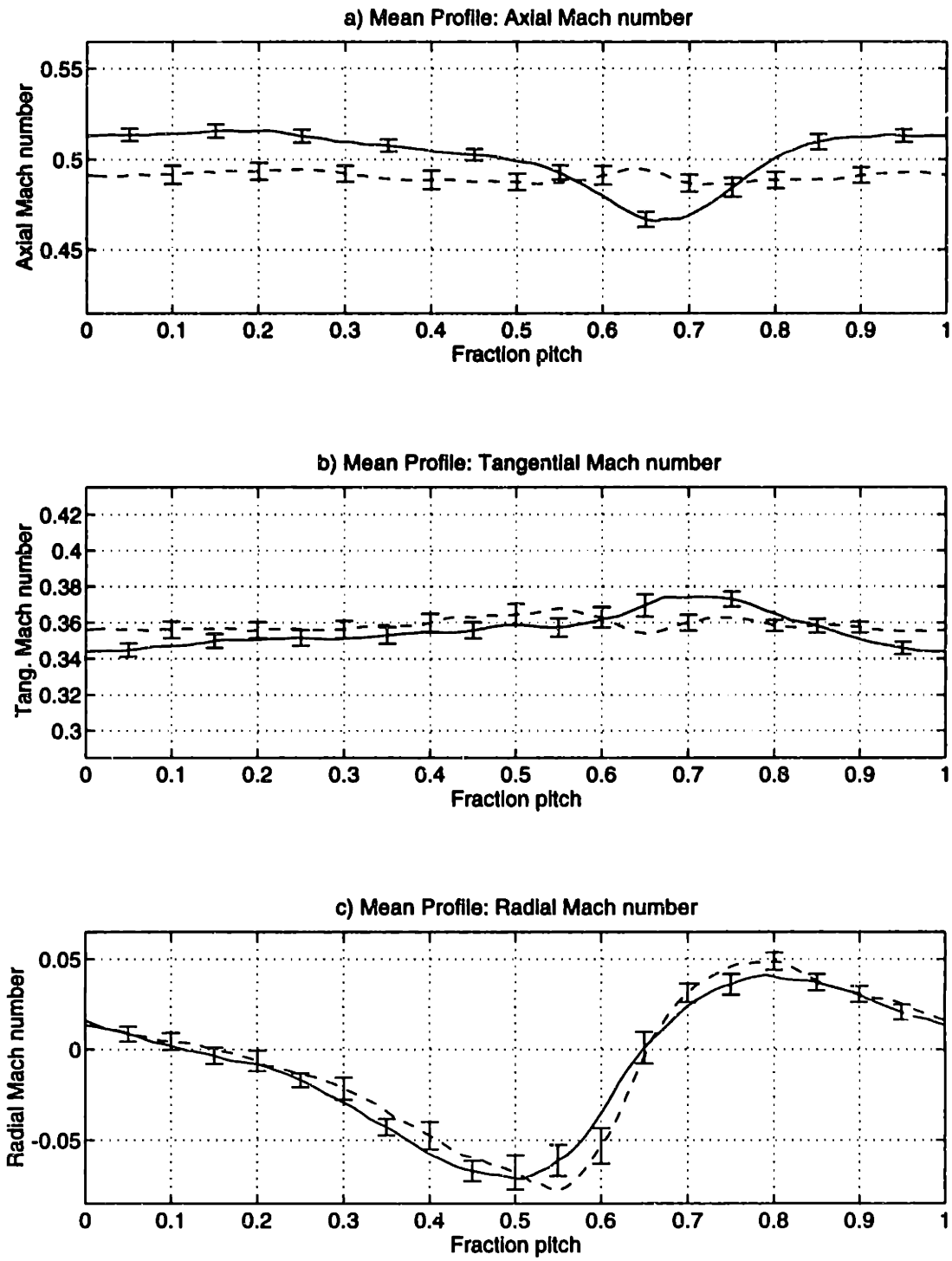

Figure E-47: 1.8% midspan weighted injection flow field data at 50% span, 1.5c: Mach number components

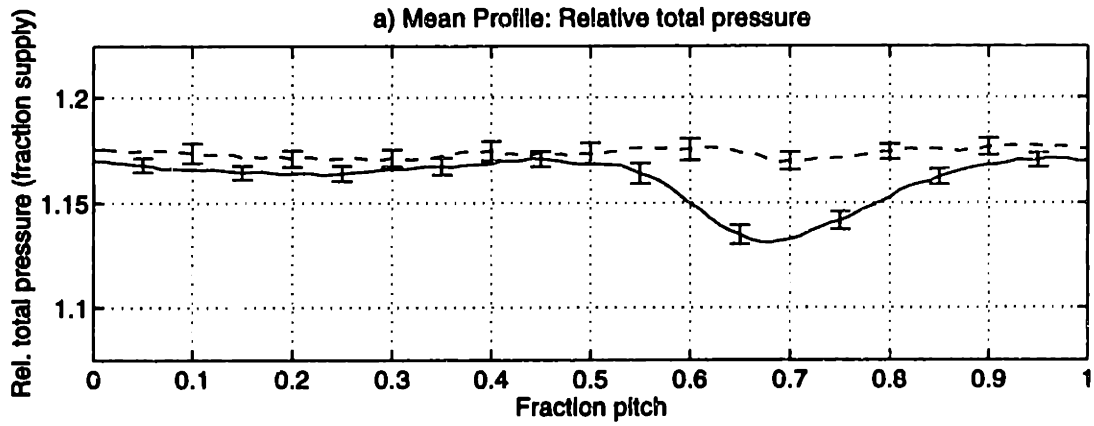

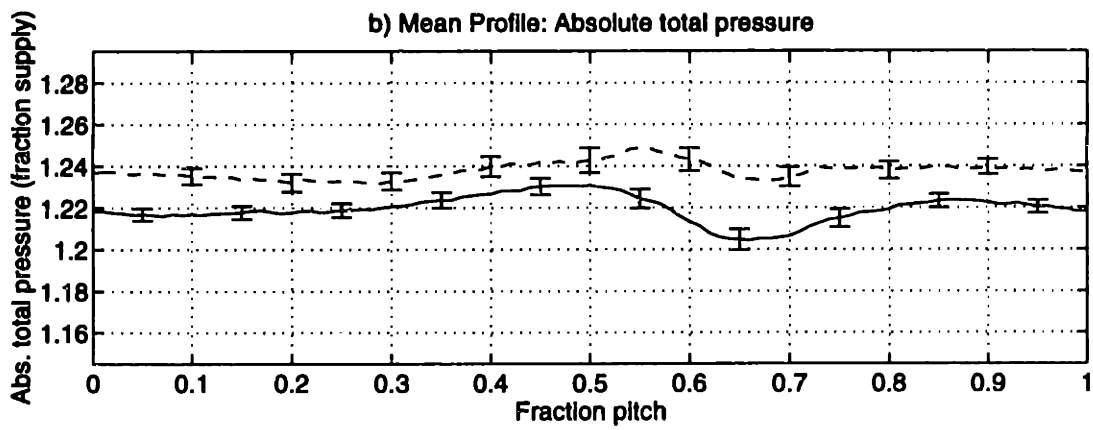

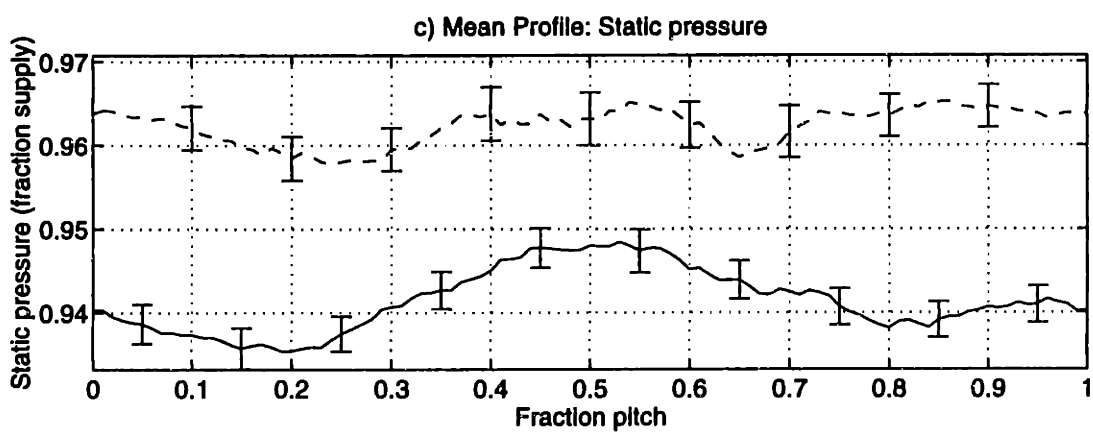

Figure E-48: 1.8% midspan weighted injection flow field data at 50% span, 1.5c: pressures

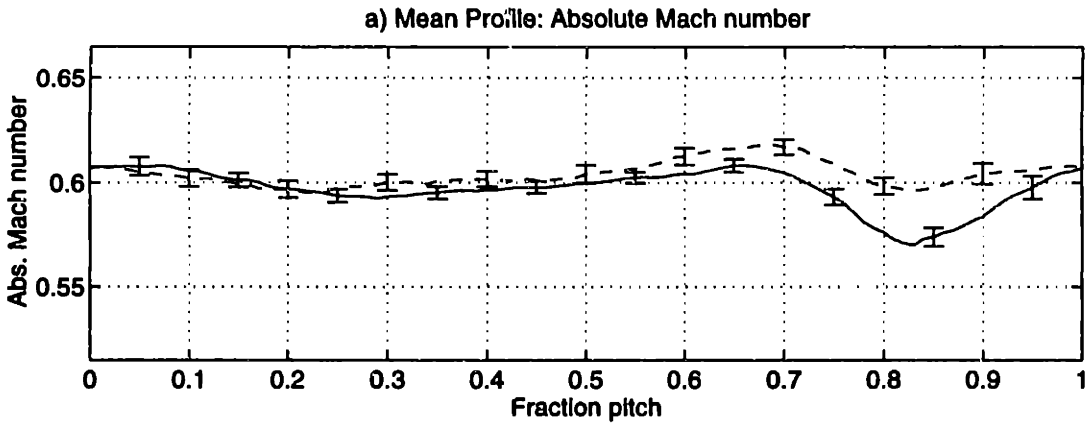

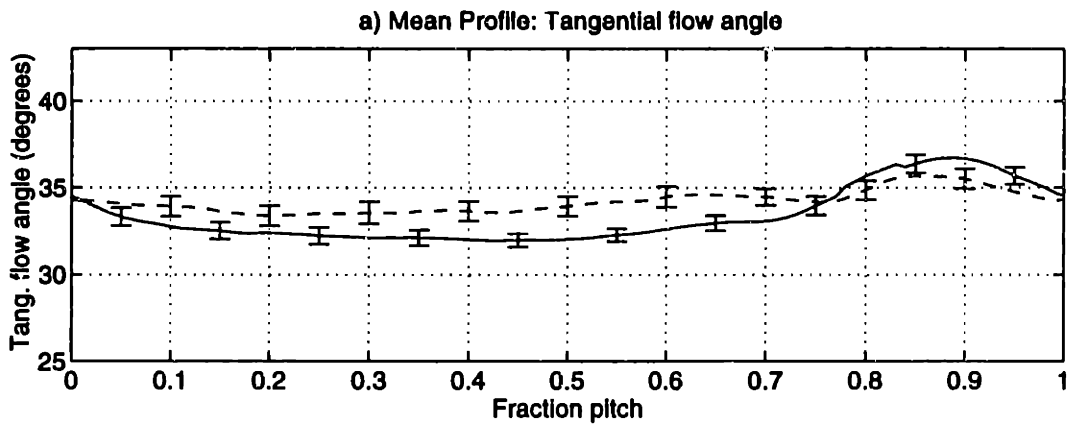

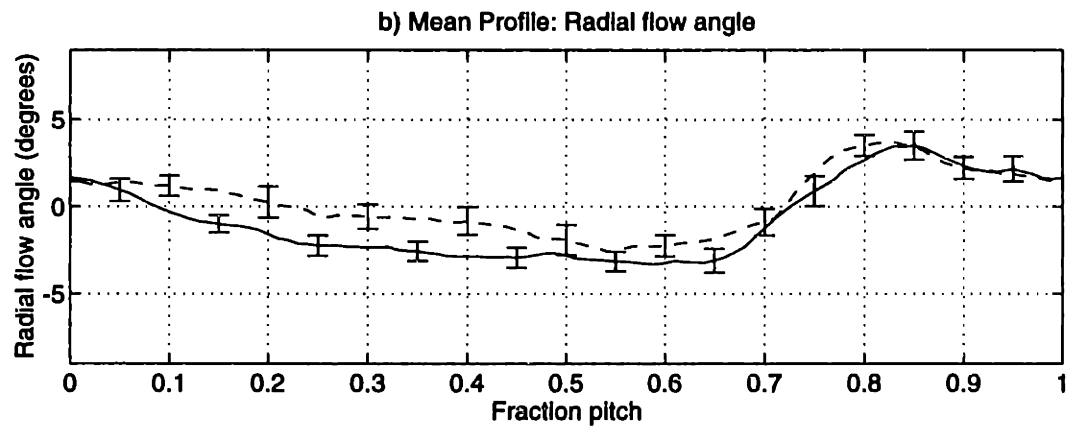

Figure E-49: 1.8% midspan weighted injection flow field data at 75% span, 1.5c: flow angles

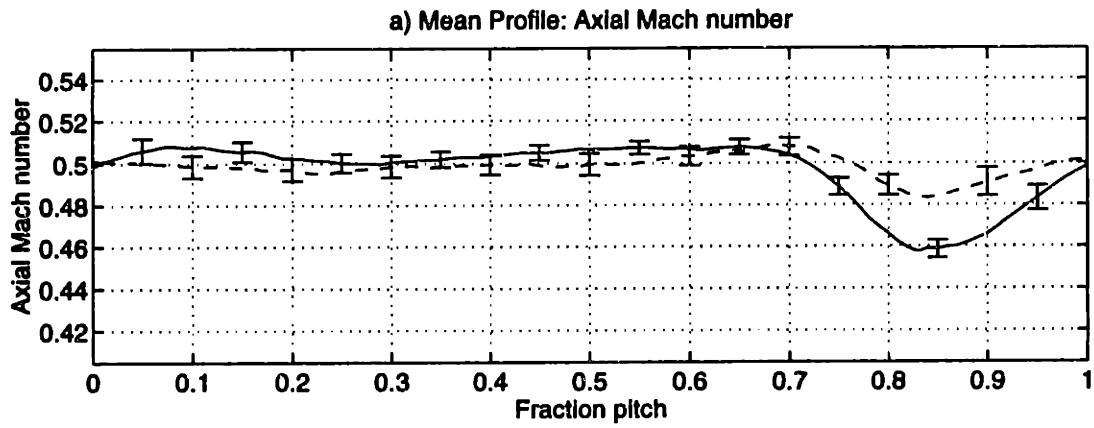

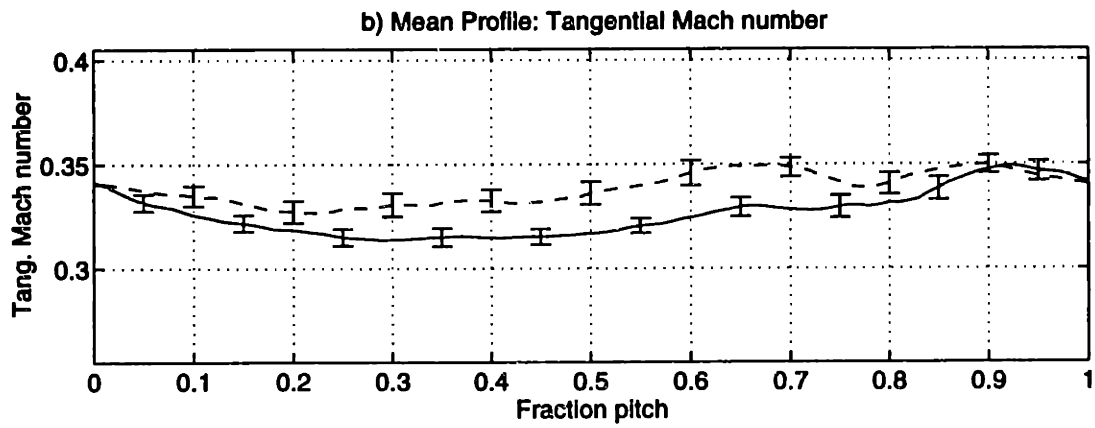

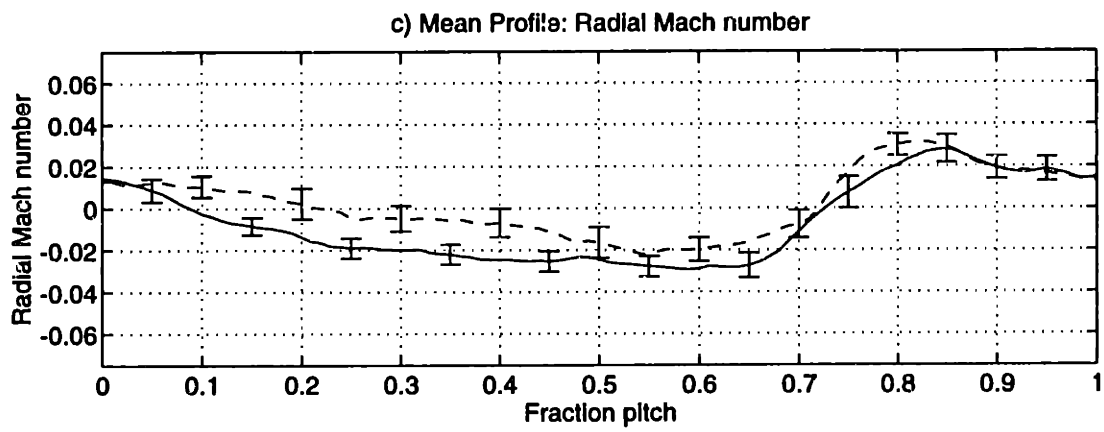

Figure E-50: 1.8% midspan weighted injection flow field data at 75% span, 1.5c: Mach number components

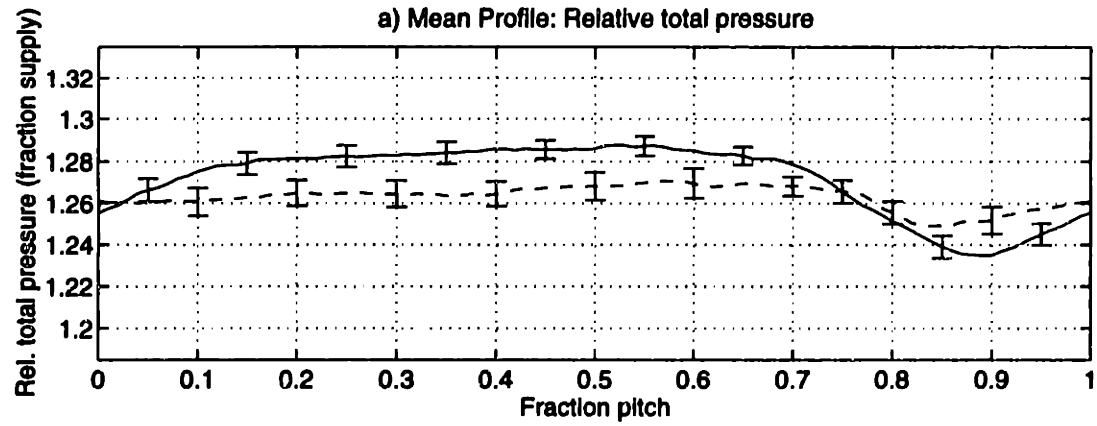

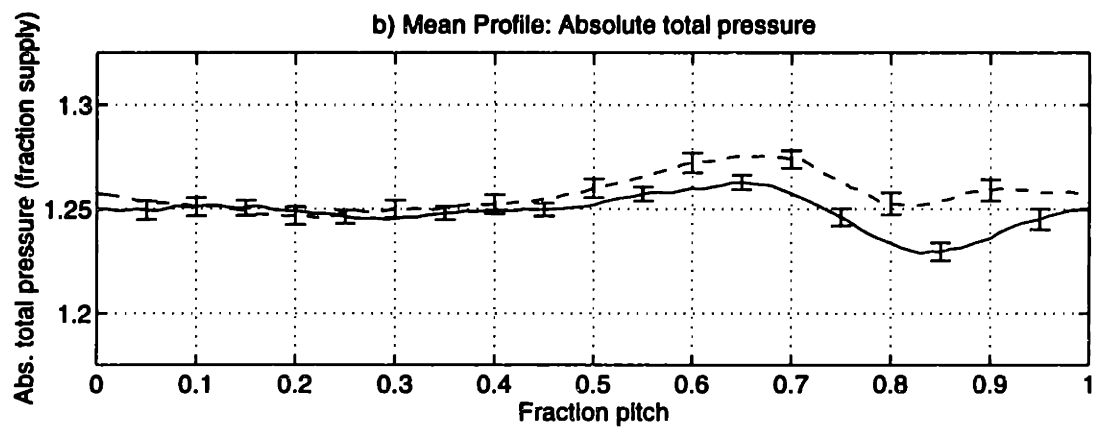

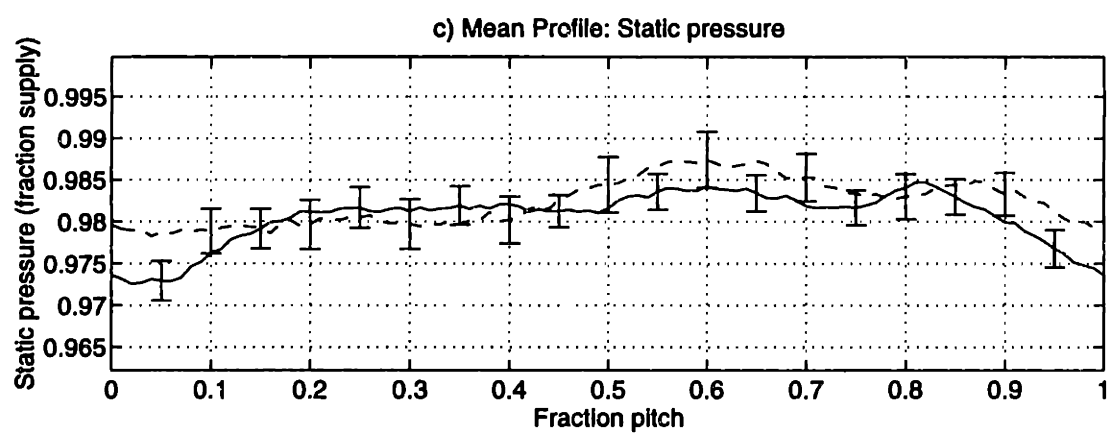

Figure E-51: 1.8% midspan weighted injection flow field data at 75% span, 1.5c: pressures

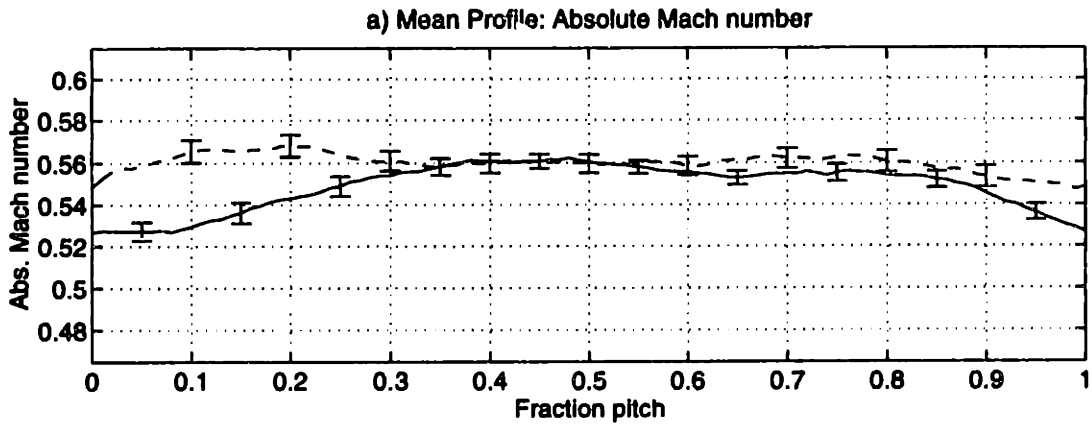

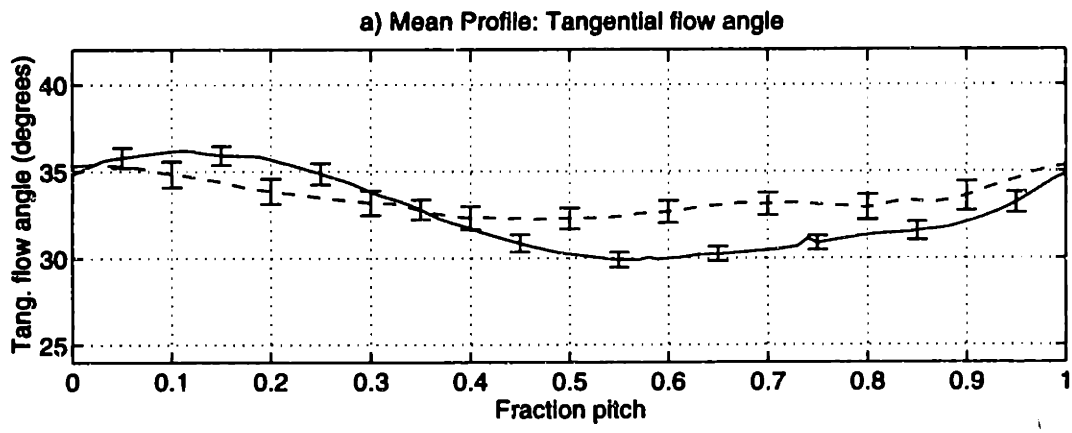

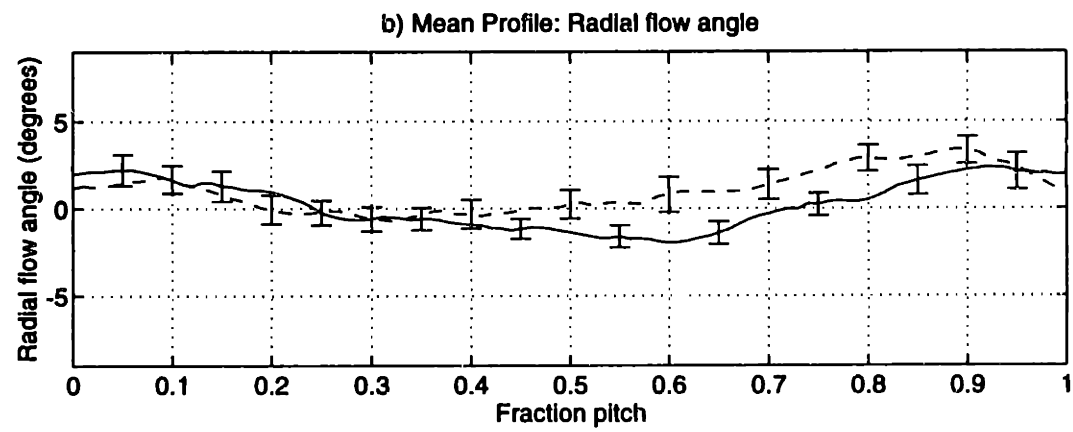

Figure E-52: 1.8% midspan weighted injection flow field data at 87.5% span, 1.5c: flow angles

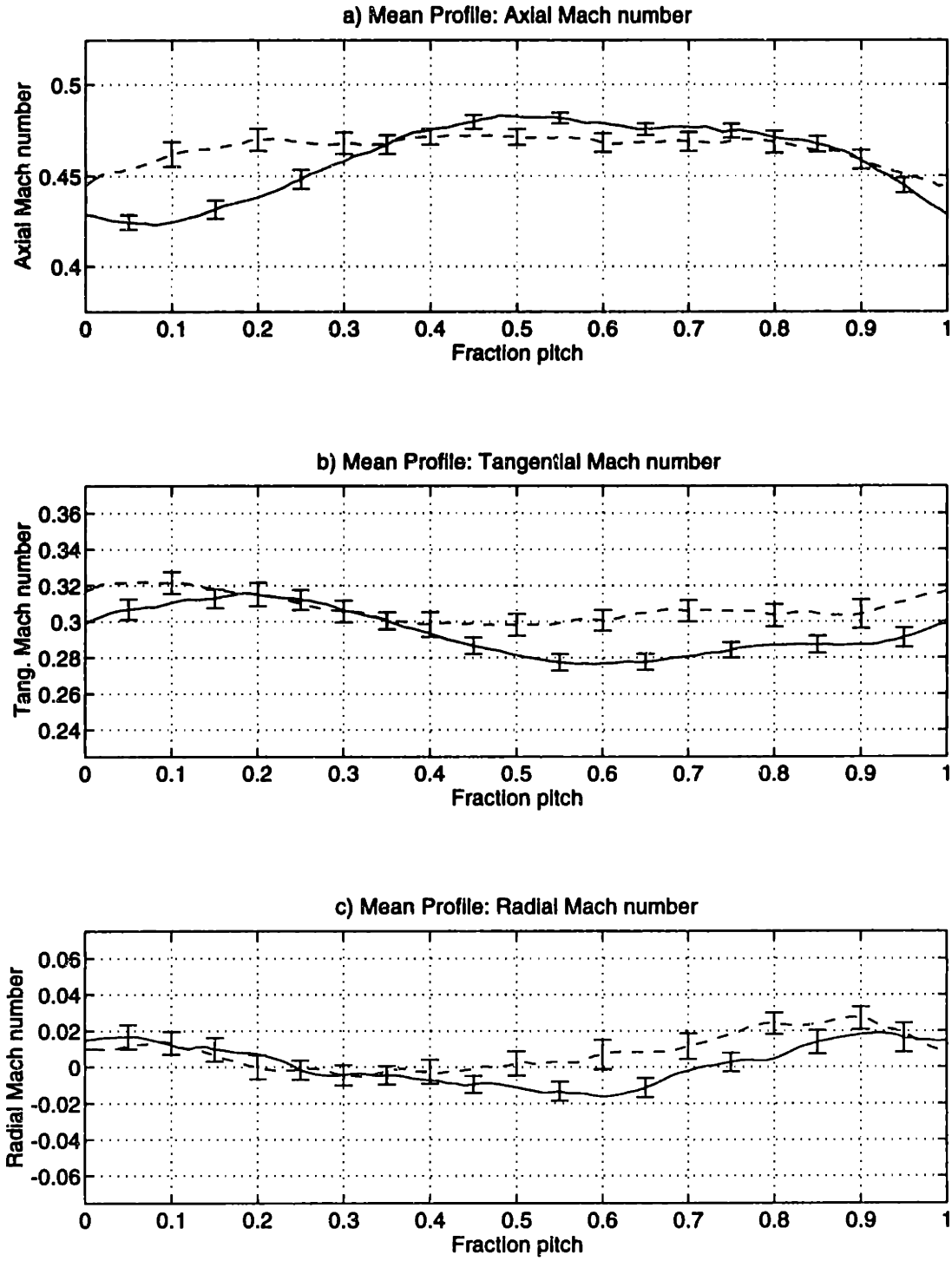

Figure E-53: 1.8% midspan weighted injection flow field data at 87.5% span, 1.5c: Mach number components

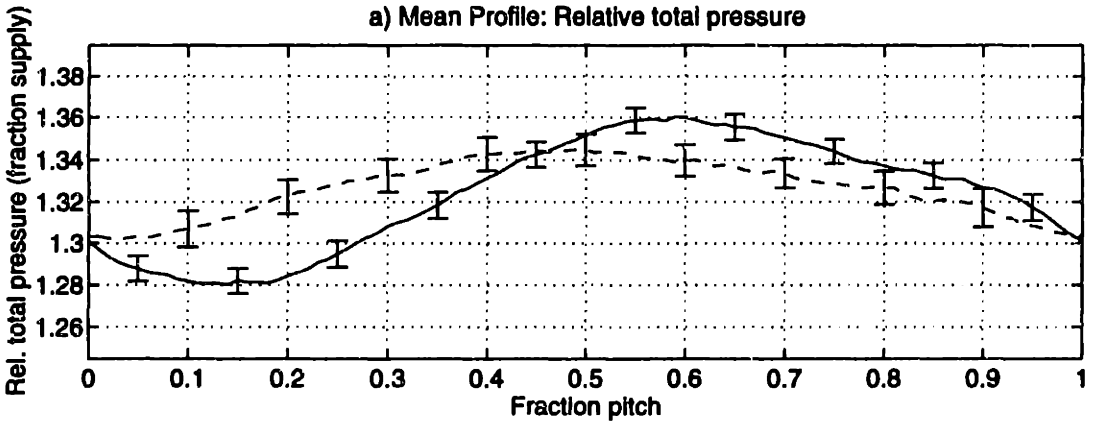

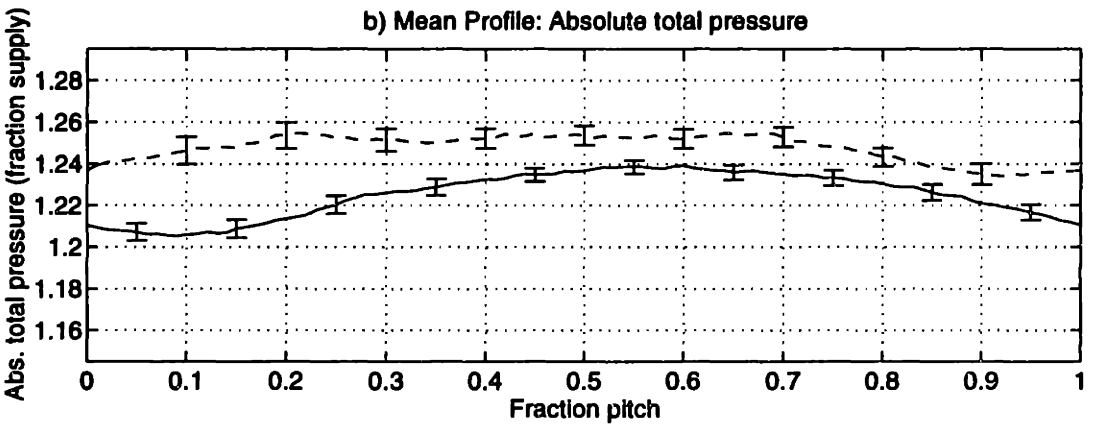

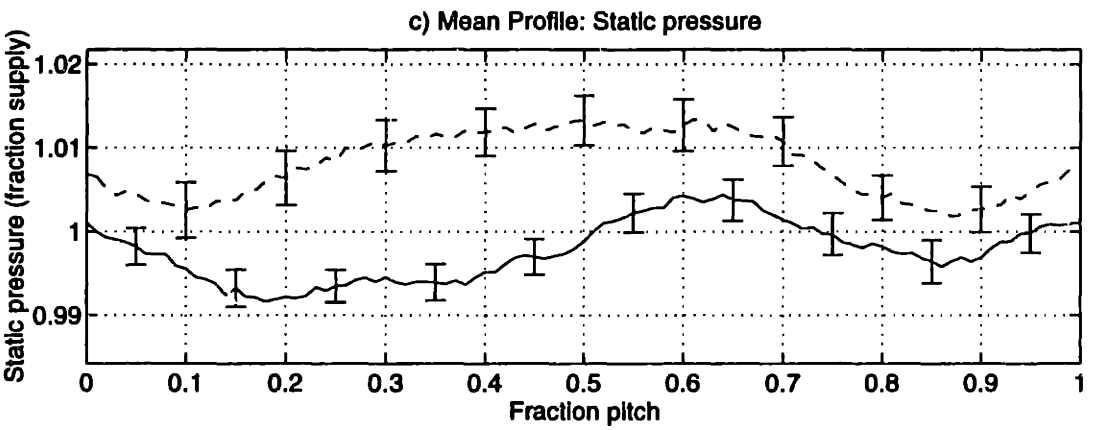

Figure E-54: 1.8% midspan weighted injection flow field data at 87.5% span, 1.5c: pressures